Coastal enhanced olivine weathering for climate change mitigation: investigating the CO$_2$ sequestration potential and ecotoxicological risks

Versnelde olivijnverwering in kustzones voor klimaatmitigatie: onderzoek naar het CO$_2$-vastleggingspotentieel en ecotoxicologische risico's

Proefschrift voorgelegd tot het behalen van de graad van Doctor in de Wetenschappen: Biologie aan de Universiteit Antwerpen

Te verdedigen door **Gunter Flipkens**

Promotoren:

Prof. Dr. Ronny Blust

Prof. Dr. Raewyn M. Town

Antwerpen, 2024

Members of the jury

Chairwoman:

Prof. Dr. Gudrun De Boeck, University of Antwerp, Belgium

Promotors

Prof. Dr. Ronny Blust, University of Antwerp, Belgium

Prof. Dr. Raewyn M. Town, University of Antwerp, Belgium

Members

Prof. Dr. Ir. Filip J.R. Meysman, University of Antwerp, Belgium

Prof. Dr. Stijn Temmerman, University of Antwerp, Belgium

Prof. Dr. Tamzin A. Blewett, University of Alberta, Canada

Prof. Dr. Willie J.G.M. Peijnenburg, Leiden University, the Netherlands

Contact information

Gunter Flipkens

University of Antwerp – Department of Biology

Groenenborgerlaan 171, 2020 Antwerpen, Belgium

Gunter.flipkens@uantwerpen.be

2

Acknowledgements

It all started just over four years ago when I successfully defended my master thesis on metal toxicity in common carp. At that time, Gudrun De Boeck, my former thesis supervisor, told me about an upcoming PhD position under the supervision of Ronny Blust and Raewyn M. Town. Looking back, I still vividly remember the interview and the moment Ronny informed me that I could start my PhD journey revolving around coastal enhanced olivine weathering. Now, after a period of four years with ups and downs (including a global pandemic) I can happily say that I am approaching the finish line! It is a cliché, but time has really flown by. This journey would not have been possible alone, and therefore I would like to express my sincere gratitude to the people that supported and guided me along the way.

First and foremost, I would like to express my deepest gratitude to my supervisors, Ronny Blust and Raewyn M. Town. They entrusted me with the opportunity to conduct research and their unwavering support, guidance, and invaluable scientific insights shaped me into the researcher I am today. I must offer a special acknowledgement to Raewyn for always providing prompt feedback on my work and taking the time to discuss new experimental ideas, results, and inevitable challenges I encountered along the way.

Besides my supervisors, I would also like to thank my other jury members: Gudrun De Boeck, Filip J.R. Meysman, Stijn Temmerman, Tamzin A. Blewett, and Willie J.G.M. Peijnenburg for their valuable time, interest, constructive comments and useful questions that helped me improve the quality of my thesis.

Throughout my PhD, Filip J.R. Meysman provided meticulous and constructive criticism which elevated the quality of my work to new heights and taught me to scrutinize my research with a critical eye. I cherish the small scientific discussions we had when I was conducting scanning electron microscopy or total alkalinity titrations in his lab. I also

appreciate the opportunity he gave me to join the bi-weekly olivine group meetings during the last year of my PhD. I will definitely miss the cookies and outstanding team members talking about olivine, worms, water changes, pore water sampling, and our favourite topic: trace metals.

Speaking of trace metals, I of course need to acknowledge the pivotal role of Steven Joosen and Valentine M. Kayawe. I am profoundly thankful for their analysis of numerous samples and for generously taking time to discuss digestion protocols, data abnormalities, and data analysis. The rest of the technical staff: Karin Van den Berg, Nemo Maes, Femke De Croock, Jetta Vlaming, Dimitri Van Pelt, Anne Cools, and Anke De Boeck of course also deserves a big thank you! Special thanks to Karin for all the DIC and DOC analyses she conducted for me. My appreciation also extends to Thanos Gritzalis from VLIZ for his support in obtaining natural seawater for my olivine weathering experiments. Lastly, a warm thank you also goes to Bieke Rutten for her friendly assistance with all administrative tasks.

To my amazing colleagues from ECOSPHERE and Geobiology at UAntwerp and PProGRess at UGent: thank you for creating a nice working environment both in the lab and abroad at conferences. All your support, thoughtful discussions, and encouragement helped me immensely in navigating this challenging journey.

I would also want to extend my gratitude to my friends, with special thanks to Michiel Lathouwers and Käthe Robert. Their unwavering support, which often included lending a sympathetic ear and arranging much-needed relaxation through board games and memorable trips, has been invaluable to me. Thanks Michiel for taking me outside of the lab to catch nightjars on warm summer evenings or do bird watching in the weekends. The endless talks about our PhD struggles were very therapeutic, but will now come to an end. I look forward to attending your PhD defence soon and our birding trips in the future!

To a very special person in my life: Laura, I want to convey my deepest gratitude. You have been a very loving and caring girlfriend who has also continuously supported me with my work. From proofreading my manuscripts to catching amphipods on a mudflat in the middle of winter (sorry again for the freezing hands). As a physiotherapist, your dedication to my scientific endeavours is truly remarkable, and I look forward to our future together!

Last but certainly not least, my parents also deserve an immense thank you for their continuous support throughout the years. Special thanks to my dad who always helped me by reading my manuscripts, and thinking along when I was brainstorming about future experiments or possible explanations for my experimental results. Big credits to you for finding the rock tumblers on Alibaba.com. Although they were very noisy (what can you expect for 40 euro…), they did what they were supposed to do and provided me with results that are now published in a highly prestigious geochemical journal. Who would have thought… Your infectious interest in nature was undeniably a driving force behind my decision to study biology after completing high school. Therefore, I can with certainty say that without you I would not be where I am today. So thank you for everything!

List of abbreviations

Abbreviation	Meaning	Abbreviation	Meaning
CDR	Carbon dioxide removal	DIC	Dissolved inorganic carbon
CESW	Coastal enhanced silicate weathering	US	United States
ESW	Enhanced silicate weathering	XRD	X-ray diffraction
OAE	Ocean alkalinity enhancement	IAP	Ion activity product
GrIS	Greenland Ice Sheet	BSi	Biogenic silicon
IPCC	Intergovernmental Panel on Climate Change	DOC	Dissolved organic carbon
COP	Conference of the Parties	PNEC	Predicted no-effect concentration
NETs	Negative emission technologies	PEC	Predicted effect concentration
BECCS	bioenergy with carbon capture and storage	AF	Assessment factor
DACCS	direct air capture and storage	SSD	Species sensitivity distribution
GHG	Greenhouse gases	NOEC	No observed effect concentration
OA	Ocean acidification	SI	Saturation index
TA	Total alkalinity	TRIS	2-amino-2-hydroxy-1,3-propanediol
EC10	10% effect concentration	AMP	2-aminopyridine
HC5	hazardous concentration for 5% of species	FTU	Formazine turbidity unit
EQS	Environmental quality standard	NTU	Nephelometric turbidity unit
ROS	Reactive oxygen species	SOM	Sediment organic matter

List of abbreviations

Abbreviation	Meaning	Abbreviation	Meaning
TBARS	Thiobarbituric acid reactive substances	SOPs	Standard operating procedures
HDPE	High density polyethylene	ICP-OES	Inductively coupled plasma optical emission spectroscopy
MQ	Milli-Q	d.w.	Dry weight
B.E.T.	Brunauer-Emmett-Teller	w.w.	Wet weight
RPM	Rotations per minute	CT	Computed tomography
RSD	Residual standard deviation	ol	Olivine
HR-ICP-MS	High Resolution Inductively Coupled Plasma Mass Spectrometry	sed	Sediment
TIC	Total inorganic carbon	GEO	Geometric
Mg/Si	Magnesium to silicon	TEL	Threshold effect level
SEM	Scanning electron microscopy	PEL	Probable effect level
EDS or EDX	Energy dispersive X-ray spectroscopy	FDEP	Florida Department of Environmental Protection
FEG	Field emission gun	BLMs	Biotic ligand models
PE	Polyethylene	ANOVA	Analysis of variance
DO	Dissolved oxygen	GLMM	Generalized linear mixed model
ASW	Artificial seawater	FWO	Fonds voor Wetenschappelijk Onderzoek
MDA	Malondialdehyde	ML	Metasomatic length
HABs	Harmful algal blooms		

Table of contents

Thesis abstract

Human-induced climate change is currently considered as the biggest global threat to natural ecosystems and human societies. To mitigate its adverse impacts, it is essential to limit global warming to well below 2 °C, ideally 1.5 °C. Achieving this climate goal requires drastic reductions in anthropogenic greenhouse gas emissions and gigaton-scale atmospheric carbon dioxide removal (CDR). One proposed CDR method is ocean alkalinity enhancement (OAE) via coastal enhanced silicate weathering (CESW), which aims to accelerate the natural CO_2-consuming weathering of silicate minerals by distributing finely ground olivine ($Mg_xFe_{(2-x)}SiO_4$) rich rock in dynamic coastal environments. Olivine has received most attention for CESW application due to its global abundance, relatively fast dissolution rate, and theoretically high CO_2 sequestration potential. However, the *in situ* CO_2 sequestration potential remains uncertain due to limited experimental data under environmentally relevant conditions. Additionally, olivine contains high levels of nickel (Ni) and chromium (Cr), which could be toxic to marine biota during large-scale coastal applications. Yet, the effects of olivine exposure on marine biota are poorly understood, preventing accurate ecological risk assessment. This thesis aimed to advance our understanding of olivine dissolution and CO_2 sequestration kinetics under the influence of hydrodynamics and assess potential ecotoxicological effects of CESW.

The impact of grain collisions on olivine reactivity in natural seawater was investigated during a 70-day experiment using benchtop rock tumblers (**Chapter 2**). Continuous physical agitation resulted in olivine dissolution rates which were 8 to 19 times higher than those observed under stagnant conditions, most likely attributed to advective pore water flushing. Consequently, coastal areas with high bed shear stress and pore water exchange rates (e.g. nearshore zones) can be considered as suitable olivine deployment sites. To subsequently bridge the gap between laboratory experiments and complex field studies, a 175-day flume experiment was conducted in which the effect of current on olivine dissolution in permeable sediment was investigated (**Chapter 3**). Although the

current stimulated alkalinity release from natural sediment, olivine dissolution was more than one order of magnitude lower than expected. Air-seawater CO_2 equilibration did not limit mineral dissolution and passivating layers were absent. Pore water saturation and secondary calcium carbonate ($CaCO_3$) precipitation could not be confirmed due the lack of pore water chemistry data and abundance of $CaCO_3$ originally present in the natural sediment. Hence, the reason for the low olivine reactivity remains unknown and requires further research.

In **Chapter 4**, an initial assessment of the environmentally safe olivine deployment scale was conducted based on existing environmental quality standards for Ni and Cr in seawater and marine sediment. Calculations made under the assumption that all trace metals released during olivine weathering would either remain in the sediment, or get flushed into the overlying water, showed that benthic biota would be at highest risk for trace metal toxicity. Depending on the background sedimentary Ni concentration, only 0.059 to 1.4 kg of olivine m^{-2} of seabed could be supplied without future exceedance of existing sediment Ni quality guidelines. These results indicate that trace metal toxicity effects could possibly limit the sustainable CDR potential of CESW, signifying the need for more in-depth studies on olivine exposure effects on marine biota. Coastal olivine deployments would change local sediment physicochemical properties, which could alter habitat suitability and possibly result in community composition changes. The degree of olivine avoidance in the marine gastropod *Littorina littorea* and amphipod *Gammarus locusta* was investigated during several short term choice experiments (**Chapter 5**). Pure olivine was avoided by both species, while natural sediment with 3 or 30% w/w olivine added was not. *Littorina littorea* avoided pure olivine due to its pale green colour (i.e. positive scototaxis), while *G. locusta* possibly tried to minimize trace metal exposure. Furthermore, the distance to a food source was found to be an important factor controlling the degree of olivine avoidance in *L. littorea*. Overall, the results indicate that relatively coarse olivine will not be significantly avoided by *L. littorea* and *G. locusta* at environmentally relevant concentrations and that environmental factors such as food or shelter availability could affect the avoidance response. Finally, short term (24 to 72 h)

bioaccumulation and chronic (35 d) olivine toxicity were investigated in *G. locusta* (**Chapter 6**). The accumulation of Ni was found to be significantly higher compared to Cr in both seawater and olivine-exposed amphipods, indicating that most Cr remained in particulate form of low bioavailability. Metal bioaccumulation was inversely related to olivine grain size, and thousands of olivine grains (mainly ≤ 10 µm) were ingested upon exposure. Chronic fine-grained olivine (3 – 99 µm) exposure reduced amphipod survival, reproduction, and growth, likely as a result of metal-induced ionoregulatory disruption and oxidative stress. Amphipod reproduction was adversely affected at olivine concentrations of 10% w/w and higher. Following the arbitrary assessment factor method, a very low predicted no-effect concentration of 0.01% w/w olivine was derived. These findings highlight the need for additional olivine toxicity data (especially for Ni-sensitive species) to accurately derive the environmentally safe coastal olivine deployment scale.

Overall, our work provides valuable novel insights into the stimulating effect of hydrodynamics on olivine reactivity in marine environments and shows possible trace metal related adverse ecological impacts of CESW (**Chapter 7**). The observed low olivine dissolution rate in natural permeable sediment and ecotoxicological effects at relatively low olivine concentrations highlight the need for additional research on the environmental safety and *in situ* CO_2 sequestration potential of CESW. Specifically, additional large-scale mesocosm and flume experiments in combination with small field trials are needed to assess olivine reactivity and CO_2 sequestration efficiency under environmentally relevant conditions. Further research on *in situ* olivine Ni and Cr release rates, environmental fate, bioavailability, and potential mixture toxicity are also warranted to ultimately derive robust, bioavailability-based, site specific coastal olivine application guidelines for climate change mitigation.

Nederlandstalige samenvatting

Door de mens veroorzaakte klimaatverandering wordt momenteel beschouwd als de grootste wereldwijde bedreiging voor natuurlijke ecosystemen en menselijke samenlevingen. Om de nadelige gevolgen ervan te beperken, is het essentieel om de opwarming van de aarde te beperken tot ruim onder de 2 °C, idealiter 1,5 °C. Het bereiken van dit klimaatdoel vereist ingrijpende verminderingen van antropogene broeikasgasemissies en grootschalige verwijdering van koolstofdioxide uit de atmosfeer (CDR). Een voorgestelde methode voor CDR is alkaliniteitsverhoging van de oceanen (OAE) via versnelde silicaatverwering in kustzones (CESW), die tot doel heeft de natuurlijke CO_2-verbruikende verwering van silicaatmineralen te versnellen door fijngemalen olivijn ($Mg_xFe_{(2-x)}SiO_4$) rijk gesteente te verspreiden in dynamische kustomgevingen. Olivijn heeft de meeste aandacht gekregen voor toepassing in CESW vanwege zijn wereldwijde abundantie, relatief snelle oplossingssnelheid en theoretisch hoog CO_2-vastleggingspotentieel. Toch blijft het *in-situ* CO_2-vastleggingspotentieel van olivijn onzeker vanwege beperkte experimentele data onder milieurelevante omstandigheden. Daarnaast bevat olivijn grote hoeveelheden nikkel (Ni) en chroom (Cr), die toxisch kunnen zijn voor mariene biota tijdens grootschalige toepassing aan de kust. De effecten van olivijnblootstelling op mariene biota zijn echter grotendeels ongekend, waardoor een nauwkeurige ecologische risicobeoordeling onmogelijk is. Dit proefschrift had tot doel onze kennis van olivijnoplossing en CO_2-vastleggingskinetiek onder invloed van hydrodynamica te verbeteren en potentiële ecotoxicologische effecten van CESW te onderzoeken.

De impact van korrelbotsingen op de reactiviteit van olivijn in natuurlijk zeewater werd onderzocht tijdens een experiment van 70 dagen met behulp van steenpolijsttrommels (**Hoofdstuk 2**). Continue fysieke beweging resulteerde in olivijnoplossingssnelheden die 8 tot 19 keer hoger waren dan die waargenomen onder stilstaande omstandigheden, hoogstwaarschijnlijk toe te schrijven aan advectieve poriewaterverversing. Daarom

kunnen kustgebieden met hoge bodemspanningen en verversingssnelheden van poriewater (bv. nearshore zones) beschouwd worden als geschikte locaties voor olivijndistributie. Om de kloof tussen laboratoriumexperimenten en complexe veldstudies te overbruggen, werd een flume experiment uitgevoerd van 175 dagen waarbij het effect van stroming op olivijnoplossing in permeabel sediment werd onderzocht (**Hoofdstuk 3**). Hoewel de stroming de afgifte van alkaliniteit uit natuurlijk sediment stimuleerde, was de oplossing van olivijn meer dan één grootteorde lager dan verwacht. De lucht-zeewater-CO_2-equilibratie beperkte de mineraaloplossing niet en passiverende oppervlaktelagen waren afwezig. Poriewater verzadiging en secundaire calciumcarbonaat ($CaCO_3$) precipitatie kon niet worden bevestigd vanwege het gebrek aan chemische poriewater data en de overvloed aan $CaCO_3$ dat oorspronkelijk aanwezig was in het natuurlijke sediment. De reden voor de lage olivijnreactiviteit kon daarom niet worden bevestigd en vereist verder onderzoek.

In **Hoofdstuk 4** werd een initiële beoordeling uitgevoerd van de ecologisch veilige schaal voor olivijndistributie, gebaseerd op bestaande milieunormen voor Ni en Cr in zeewater en marien sediment. Berekeningen onder de aanname dat alle sporenmetalen die tijdens de olivijnoplossing worden vrijgegeven in het sediment blijven, of naar het bovenliggende water worden gespoeld, toonden aan dat benthische biota het grootste risico lopen op metaaltoxiciteit. Afhankelijk van de achtergrondconcentratie van Ni in het sediment kon slechts 0,059 tot 1,4 kg olivijn per vierkante meter zeebodem worden uitgespreid zonder toekomstige overschrijding van de bestaande normen voor Ni in sediment. Deze resultaten geven aan dat toxische effecten van metalen mogelijk het duurzame CDR-potentieel van CESW kunnen beperken, wat indiceert dat verder onderzoek naar de effecten van olivijnblootstelling op mariene biota noodzakelijk is. Olivijndistributie in kustzones zou lokale fysicochemische eigenschappen van het sediment wijzigen, wat habitatgeschiktheid zou kunnen veranderen en mogelijk tot wijzigingen in de samenstelling van de levensgemeenschap zou kunnen leiden. De mate van olivijnvermijding door de mariene gastropode *Littorina littorea* en de amfipode *Gammarus locusta* werd onderzocht tijdens verschillende korte keuze-experimenten

(**Hoofdstuk 5**). Beide soorten vermeden puur olivijn, terwijl natuurlijk sediment waar 3 of 30 massapercentage olivijn was aan toegevoegd niet werd vermeden. *Littorina littorea* vermeed puur olivijn vanwege zijn lichtgroene kleur (i.e. positieve scototaxis), terwijl *G. locusta* mogelijk metaalblootstelling probeerde te beperken. Bovendien bleek de afstand tot een voedselbron een belangrijke factor te zijn die de mate van olivijnvermijding bij *L. littorea* beïnvloedde. Globaal gezien geven de resultaten aan dat relatief grofkorrelig olivijn niet significant wordt vermeden door *L. littorea* en *G. locusta* bij milieurelevante concentraties, en dat omgevingsfactoren zoals voedsel- of schuilplaatsbeschikbaarheid de mate van vermijdingsreactie kunnen beïnvloeden. Tenslotte werd de korte termijn (24 tot 72 uur) bioaccumulatie en chronische (35 dagen) olivijntoxiciteit onderzocht bij *G. locusta* (**Hoofdstuk 6**). De accumulatie van Ni bleek significant hoger te zijn dan die van Cr in zowel zeewater als in amfipoden, wat aangeeft dat het meeste Cr in een partikelvorm met lage bio-beschikbaarheid bleef. De metaalbio-accumulatie was omgekeerd evenredig met de korrelgrootte van olivijn, en duizenden olivijnkorrels (voornamelijk ≤ 10 µm) werden ingenomen bij blootstelling. Chronische blootstelling aan fijnkorrelig olivijn (3 - 99 µm) leidde tot verminderde overleving, voortplanting en groei van de amfipoden, waarschijnlijk als gevolg van door metaal geïnduceerde ionoregulatorische verstoring en oxidatieve stress. De voortplanting van de amfipoden werd negatief beïnvloed bij olivijnconcentraties van 10% w/w en hoger. Volgens de arbitraire beoordelingsfactor methode werd een zeer lage voorspelde concentratie zonder effect van 0,01% w/w olivijn afgeleid. Deze resultaten benadrukken de noodzaak van aanvullende data over olivijntoxiciteit (vooral voor Ni gevoelige soorten) om nauwkeurig de ecologisch veilige schaal voor olivijndistributie in kustzones te bepalen.

Over het geheel genomen biedt ons werk waardevolle nieuwe inzichten in het stimulerende effect van hydrodynamica op de reactiviteit van olivijn in mariene omgevingen en toont nadelige ecologische effecten van CESW die mogelijk verband houden met metalen (**Hoofdstuk 7**). De waargenomen lage oplossingssnelheid van olivijn in natuurlijk permeabel sediment en ecotoxicologische effecten bij relatief lage olivijnconcentraties benadrukken de nood aan verder onderzoek rond de ecologische

veiligheid en het *in-situ* CO_2-vastleggingspotentieel van CESW. Specifiek zijn aanvullende grootschalige mesocosm- en flume-experimenten in combinatie met kleine veldproeven nodig om de reactiviteit van olivijn en de efficiëntie van CO_2-vastlegging onder milieurelevante omstandigheden te beoordelen. Verder onderzoek naar *in-situ* afgiftesnelheden van Ni en Cr, verspreiding in het milieu, bio-beschikbaarheid en potentiële mengseltoxiciteit is ook noodzakelijk om uiteindelijk robuuste, bio-beschikbaarheid-gebaseerde, locatiespecifieke richtlijnen voor olivijndistributie in kustzones te ontwikkelen in het kader van klimaatmitigatie.

Chapter 1   General Introduction

1.1 **The Earth's climate**

The stable and mild climate conditions on Earth have ensured the availability of liquid water, making the development and sustenance of life possible (Henderson-Sellers and Meadows, 1977; Clarke et al., 2013). The climate in a given region is defined by the average atmospheric conditions (e.g. temperature, humidity, wind) over a period typically longer than 30 years and is controlled by the radiation balance (Hartmann et al., 1986; Serreze, 2010). This balance between the incoming radiation from the sun and outgoing radiation to space depends on various factors such as the solar irradiance, the Earth's orbit, and degree of radiation reflection and absorbance. The latter is affected by cloud coverage, surface albedo, and atmospheric aerosol and greenhouse gas (GHG) concentrations (Serreze, 2010).

Greenhouse gases absorb infrared radiation from the sun and re-emit a fraction to the Earth's surface causing an increase in temperature. This phenomenon is known as the greenhouse effect and is responsible for the hospitable average temperature of 14 °C on the Earth's surface compared to -19 °C in case greenhouse gases would be absent. The main gases in the atmosphere responsible for this greenhouse effect are water vapour (H_2O), carbon dioxide (CO_2), methane (CH_4), nitrous oxide (N_2O), and ozone (O_3) (Kweku et al., 2018; Tuckett, 2019).

Throughout Earth's climate history, colder periods with significant ice coverage across the globe known as icehouse states were alternated by warmer periods known as greenhouse states as a result of changes in the radiation balance (Serreze, 2010). For example, the widespread glaciation during the Makganyene "snowball Earth" period (~2.3 – 2.2 billion years ago) could have been caused by the oxidation-induced drop in atmospheric CH_4 concentrations after the evolution of oxygenic photosynthesis (Kopp et al., 2005). Furthermore, several sudden short (0.1 – 0.2 million years) temperature rises occurred since the Mesozoic era. For instance, during the Paleocene-Eocene Thermal Maximum around 55.8 million years ago more than 10,000 gigatons of carbon were released to the

atmosphere resulting in an estimated 4 to 5 °C average global warming over a period of around 200,000 years (Cui et al., 2011; Jones et al., 2013; Gutjahr et al., 2017). This event was possibly caused by volcanism during the formation of the North Atlantic Ocean (Gutjahr et al., 2017) and led to mass extinction of marine foraminifera and drastic shifts in marine and terrestrial ecosystems (McInerney and Wing, 2011).

The global average temperature has risen by an estimated 1.1 °C since 1850 according to the Intergovernmental Panel on Climate Change (IPCC). This rate of climate change is unprecedented and can be entirely ascribed by greenhouse gas emissions from human activities such as agriculture, deforestation, and burning of fossil fuels (Figure 1.1A) (IPCC, 2021). Industrialization has benefitted human societies by increasing living standards, economic growth, technological developments, and facilitating transportation (Das, 2014). Nevertheless, the large scale combustion of coal, oil and natural gas for energy production has already led to a rise of atmospheric CO_2 concentrations from 286 ppm in 1850 to around 420 ppm in 2023 (Figure 1.1B) and a resulting 1.1 °C global warming. Depending on future anthropogenic greenhouse gas emissions, average global temperatures could rise by up to 4.4 °C by 2100 if humankind remains heavily reliant on fossil fuels during the 21st century (IPCC, 2021).
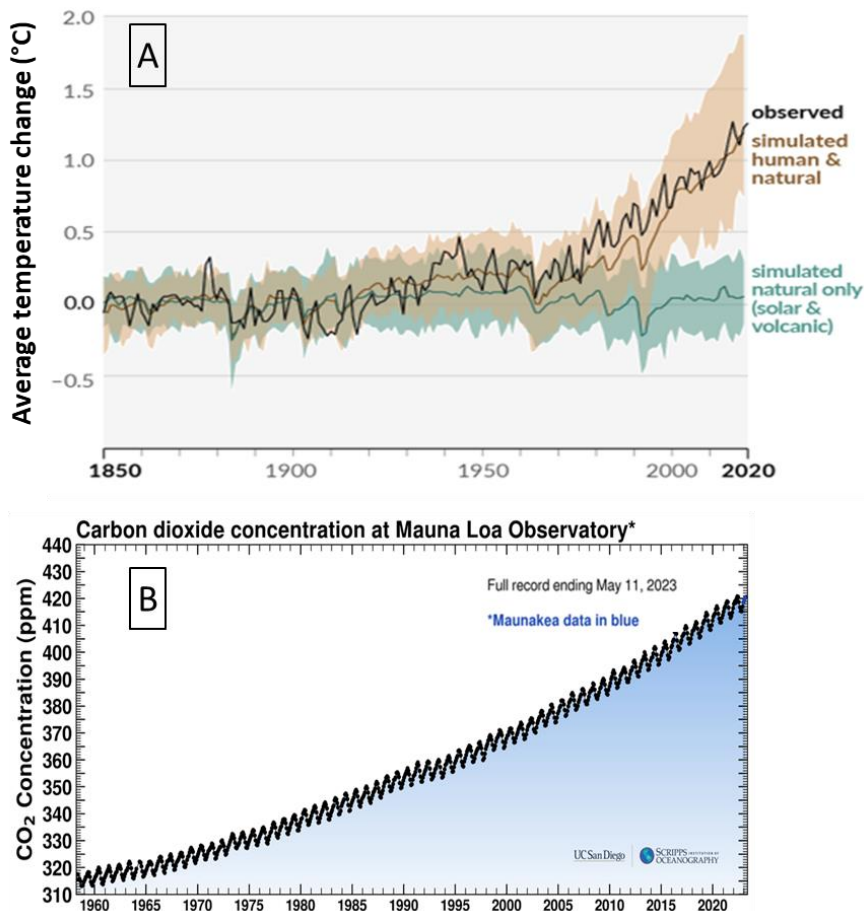
Figure 1.1: (A) Observed and simulated annual average change in global surface temperature in the presence of human and natural (orange) or only natural (green) factors since 1850. (B) Keeling curve showing the daily atmospheric CO_2 concentration (ppm) measured since 1956 at the Mauna Loa Observatory (Hawaii, USA). Figures were adapted from the Sixth Assessment report by the IPCC (IPCC, 2021) and the keeling curve website (https://keelingcurve.ucsd.edu/) maintained by Scripps Institution of Oceanography at UC San Diego.

1.2 Global warming risks and policy

Global warming can pose a range of risks to human societies and the environment. These risks include increased frequency and intensity of extreme weather events (e.g. heat waves, droughts, storms), sea level rise, ecosystem function and structure disruption, and loss of biodiversity. Furthermore, global warming would increase water scarcity, affect agricultural productivity, reduce societal and economic stability, and directly or indirectly

endanger human health (Kim et al., 2014; IPCC, 2022a). These impacts of climate change are already apparent across the globe today and will increase in intensity with every 0.1 °C of additional global warming (Hashim and Hashim, 2016; IPCC, 2022a). Moreover, it is important to mention that temperature thresholds, known as climate tipping points, exist above which adverse consequences are irreversible (Lenton et al., 2019). For example, the western Greenland Ice Sheet (GrIS) has melted to a point where recovery might not be possible (Boers and Rypdal, 2021). Complete melting of the GrIS would lead to a rise in global sea level up to 7 m and disruption of the Atlantic Meridional Overturning Circulation via the large freshwater influx in the North Atlantic which could trigger a cascade of other climate tipping points (Aschwanden et al., 2019; Orihuela-Pinto et al., 2022).

The problem of climate change was already discovered in the 19th century, but it was only first discussed globally in 1979 at the World Climate Conference in Geneva (Switzerland) (WMO, 1979; Gupta, 2010). Afterwards, several other international conferences were organized and the IPCC was formed in 1988 by the United Nations Environment Programme and the World Meteorological Organization to provide policymakers scientific assessments of the knowledge and state of global warming on a regular basis. The first IPCC report about the state of global warming, future risks, and need for mitigation measures was released in 1990 (IPCC, 1990; Gupta, 2010). In 1992, the United Nations Framework Convention on Climate Change (UNFCC) was signed by 154 countries with the main aim to keep atmospheric GHG concentrations below a level that would lead to dangerous anthropogenic interference with the climate system. In 1995, the Conference of the Parties (COP) was established to monitor and review the implementation of the UNFCC on a yearly basis. During the third COP in 1997, the international Kyoto protocol was adopted with individual targets to reduce GHG emission in developed countries by 4% compared to 1990 emissions in the period from 2008 to 2012 (Nations, 1998; Gupta, 2010; Mor et al., 2023). This protocol was implemented in 2005 and the progress was discussed at the 21st COP in Paris where the Paris Agreement was adopted by 196 countries (UNFCC, 2015; Mor et al., 2023).

The Paris Agreement is a milestone in global climate efforts since it was the first universal legally binding agreement with the ambitious goal to keep average global temperature rise well below 2 °C, ideally 1.5 °C compared to pre-industrial levels. In contrast to the Kyoto protocol, countries are free to set their own climate change mitigation targets under the Paris Agreement. Nevertheless, these targets are revised every five years to pressure for more ambitious climate change mitigation and adaptation measures worldwide (UNFCC, 2015; Falkner, 2016).

1.3 Climate change mitigation

Keeping global warming below the 2 °C will require drastic reductions in anthropogenic GHG emissions in the coming decades. The European Union pledged to reduce GHG emissions by at least 55% (compared to 1990 levels) by 2030 and achieve net zero emissions by 2050 (Skjærseth, 2021). This necessitates a decarbonization of the energy sector by transitioning from fossil fuels to renewables such as solar, wind and hydroelectric energy. Furthermore, energy efficiencies should be improved by for example developing energy efficient technologies and improving insulation of buildings (Noailly, 2012; Al-Ghussain, 2019; IPCC, 2022b). Additionally, sustainable land use should be practiced and a circular economy should be promoted (IPCC, 2022b). Moreover, both financial and policy support are needed to facilitate the transition to a net zero emissions economy and people should try to reduce their carbon footprint by for example eating less meat and reducing flying for business trips or holidays abroad (Whitmarsh et al., 2021; IPCC, 2022b).

In addition to drastic GHG emission cuts, active removal of atmospheric CO_2 and storage in geological, terrestrial or ocean reservoirs is needed on a gigaton scale to meet the climate goals (Minx et al., 2018; IPCC, 2022b). Specifically, carbon dioxide removal (CDR), also known as negative emission technologies (NETs), are required to offset residual GHG emissions from hard-to-abate sectors such as aviation, agriculture, and steel industry and to compensate for carbon budget overshoot. An estimated cumulative 25 to 800 Gt or

115 to 1180 Gt of CDR is needed to keep global warming below 2 °C, or 1.5 °C, respectively depending on the rate of conventional mitigation (Gasser et al., 2015; Minx et al., 2018). Achieving this scale requires urgent implementation of CDR methods and yearly gigaton scale atmospheric carbon removal between 2030 and 2050 (Minx et al., 2018). Various CDR methods have been put forward (Figure 1.2) and will be briefly introduced in the next paragraphs. Importantly, the dependence on these CDR techniques to achieve the climate goals should be kept to a minimum given their relatively high cost (ranging from ≤ $20 to $1000 t^{-1} CO_2), and currently uncertain CO_2 sequestration potential, and environmental safety. Furthermore, a portfolio of CDR techniques should be implemented to achieve the required CDR targets in order to minimize the scale of each individual technology (Minx et al., 2018).
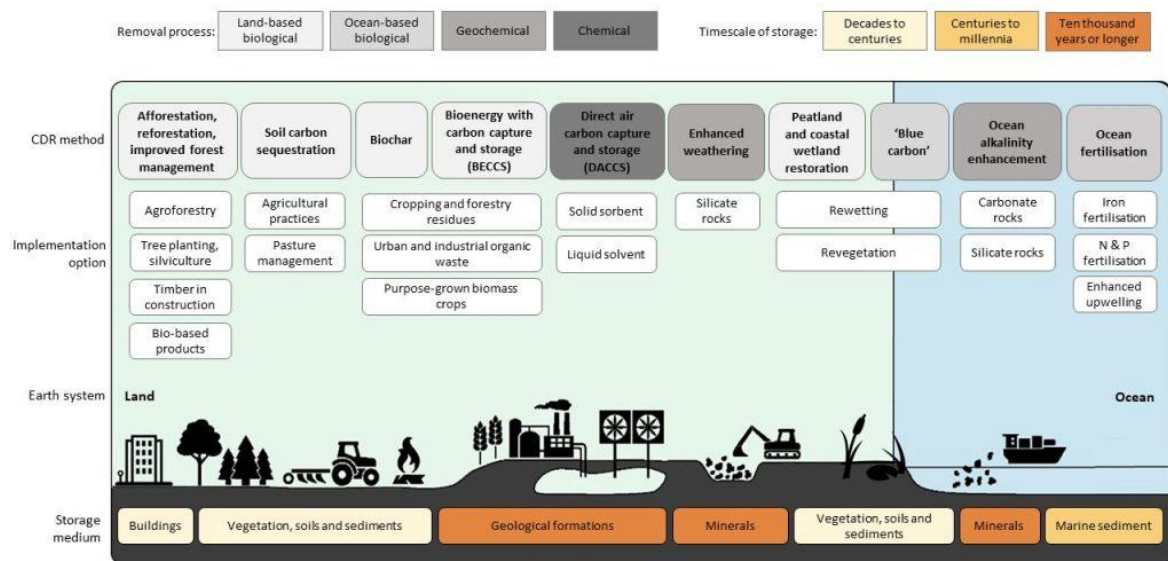
Figure 1.2: Proposed carbon dioxide removal (CDR) technologies in the 6th assessment report of the IPCC (Cross-Chapter box 8, Figure 1) adapted from Minx et al. (2018). The CO_2 removal process (grey shaded boxes), storage time and medium (yellow/brown shaded boxes) and implementation option(s) (white boxes) are given for each CDR technology.

A range of terrestrial and marine CDR techniques with a megaton to gigaton scale mitigation potential have been proposed (Figure 1.2). Terrestrial options include planting trees, soil carbon sequestration, biochar, bioenergy with carbon capture and storage (BECCS), direct air capture and storage (DACCS), enhanced weathering, and restoration of wetlands and "blue carbon" ecosystems (i.e. mangroves, tidal marshes, seagrasses) (IPCC, 2022b). Most terrestrial CDR methods have the possible co-benefits that they could enhance biodiversity and improve soil quality (e.g. increase soil pH and nutrient content and retention) and associated crop productivity when implemented correctly. However, competition for land with agriculture and biodiversity conservation could prevent large scale implementation. Furthermore, terrestrial carbon storage is generally more prone to disturbance (e.g. forest fires, drought, diseases) compared to marine or geological storage and hence potentially less reliable for long term carbon storage (Fuss et al., 2018; IPCC, 2022b).

Marine CDR methods comprise of "blue carbon" ecosystem restoration and conservation, ocean fertilization, and ocean alkalinity enhancement. These methods have the benefit that they do not compete for land and aid in counteracting ocean acidification (OA). Furthermore, blue carbon ecosystems could improve coastal protection and biodiversity and ocean fertilization could potentially enhance fisheries by providing additional biomass for consumption at the base of the marine food web. Nevertheless, seawater chemistry changes (e.g. pH, mineral saturation states, trace metal concentrations) could also be potentially harmful for marine biota above certain thresholds (IPCC, 2022b). Furthermore, marine CDR methods do not directly remove CO_2 from the atmosphere in contrast to most terrestrial CDR methods, but rely on creating a seawater CO_2 deficit (via photosynthetic CO_2 fixation or CO_2 conversion to HCO_3^-) to achieve atmospheric CO_2 drawdown (Bach et al., 2023).

1.4 Ocean alkalinity enhancement via enhanced weathering

The ocean serves as the Earth's largest carbon sink (~93% of total C storage) and currently takes up approximately 25% of the yearly anthropogenic CO_2 emissions (Holmén, 1992; Heinze et al., 2015). This ocean carbon cycling is governed by three pumps, namely the (I) the biological pump, (II) the carbonate pump, and (III) the solubility pump. The biological and carbonate pump are driven by photosynthesis of phytoplankton and $CaCO_3$ formation by calcifying organisms (e.g. molluscs, corals, coccolithophores), respectively (Heinze et al., 2015; Duan et al., 2022). The solubility pump is the result of CO_2 dissolution in seawater (Eq. 1.1 and 1.2) which is affected by seawater temperature, salinity, partial pressure of CO_2 (pCO$_2$), pH, total alkalinity (TA), and ocean circulation (Zeebe and Wolf-Gladrow, 2001).

$$CO_2(atm) \rightleftharpoons CO_2(aq) \qquad [1.1]$$

$$CO_2(aq) + H_2O \rightleftharpoons HCO_3^- + H^+ \rightleftharpoons CO_3^{2-} + 2H^+ \qquad [1.2]$$

Ocean alkalinity enhancement (OAE) aims to enhance the solubility pump by increasing seawater TA. The TA (Eq. 1.4) can be interpreted as the acid buffering capacity of seawater and is formally described as "the number of moles of hydrogen ion equivalent to the excess of proton acceptors (bases formed from weak acids with a dissociation constant $K \leq 10^{-4.5}$ at 25 °C and zero ionic strength) over proton donors (acid with $K > 10^{-4.5}$) in 1 kilogram of sample" by Dickson (1981). TA addition to seawater would shift the partitioning of inorganic carbon species by proton consumption, which would lower dissolved CO_2 concentration (CO_2(aq)) (Eq. 1.2) driving atmospheric CO_2 drawdown (Eq. 1.1) (Meysman and Montserrat, 2017). The sequestered CO_2 would remain in seawater as dissolved inorganic carbon (DIC) (Eq. 1.3) over time scales associated with alkalinity cycling in the ocean, on the order of up to 100,000 years (Middelburg et al., 2020).

$$DIC = \Sigma CO_2 = [CO_2] + [HCO_3^-] + [CO_3^{2-}] \qquad [1.3]$$

$$TA = [HCO_3^-] + 2[CO_3^{2-}] + [B(OH)_4^-] + [OH^-] + [HPO_4^{2-}] + 2[PO_4^{3-}] + [SiO(OH)_3^-] +$$
$$[NH_3] + [HS^-] + \cdots - [H^+]_F - [HSO_4^-] - [HF] - [H_3PO_4] - \cdots \qquad [1.4]$$

Seawater TA can be increased electrochemically by various methods which rely on the splitting of water molecules with renewable electricity in H⁺ and OH⁻ ions at the cathode and anode, respectively. The OH⁻ rich water can be discharged in the ocean to increase seawater TA, while the acid stream can be neutralized with for example alkaline silicate minerals (Rau et al., 2018). Additionally, alkaline materials such as hydrated lime (Ca(OH)$_2$) or olivine (Mg$_{2x}$Fe$_{2(1-x)}$SiO$_4$) release alkalinity upon dissolution (Eq. 1.5 and 1.6) and could therefore potentially be used for OAE (Renforth and Henderson, 2017).

$$Ca(OH)_2 + 2CO_2 \rightarrow Ca^{2+} + 2HCO_3^- \qquad [1.5]$$

$$Mg_xFe_{2-x}SiO_4 + 4H_2O + 4CO_2 \rightarrow xMg^{2+} + (2-x)Fe^{2+} + H_4SiO_4 + 4HCO_3^- \qquad [1.6]$$
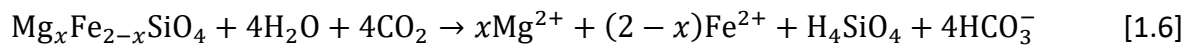
The chemical weathering of silicate rocks is an important carbon sink over geological time scales (thousands to millions of years) and is responsible for the relatively constant climate on earth during the past 4 billion years despite a steady (~30%) increase in the sun's luminosity (Penman et al., 2020). Currently, chemical weathering of silicates consumes an estimated 0.26 Gt of carbon per year (Hartmann et al., 2010). Coastal enhanced silicate weathering (CESW) aims to accelerate this climate regulating process to human time scales by distributing finely ground (ultra)mafic silicate rocks rich in fast weathering minerals (e.g. olivine) in the dynamic coastal environment (Figure 1.3) (Meysman and Montserrat, 2017). Dunite rock has received most attention for this technique due its global abundance and fast weathering kinetics of the most abundant (≥ 90%) mineral olivine (Mg$_x$Fe$_{(2-x)}$SiO$_4$) present in this rock type (Köhler et al., 2010; Schuiling and De Boer, 2011; Rimstidt et al., 2012; Hartmann et al., 2013; Taylor et al., 2016; Meysman and Montserrat, 2017; Caserini et al., 2022; Fuhr et al., 2022). During olivine dissolution in seawater (Eq. 1.6), protons are consumed which increases seawater

alkalinity and subsequent seawater CO_2 uptake (Figure 1.3). The geochemical properties of olivine are discussed in more detail in section 1.5.
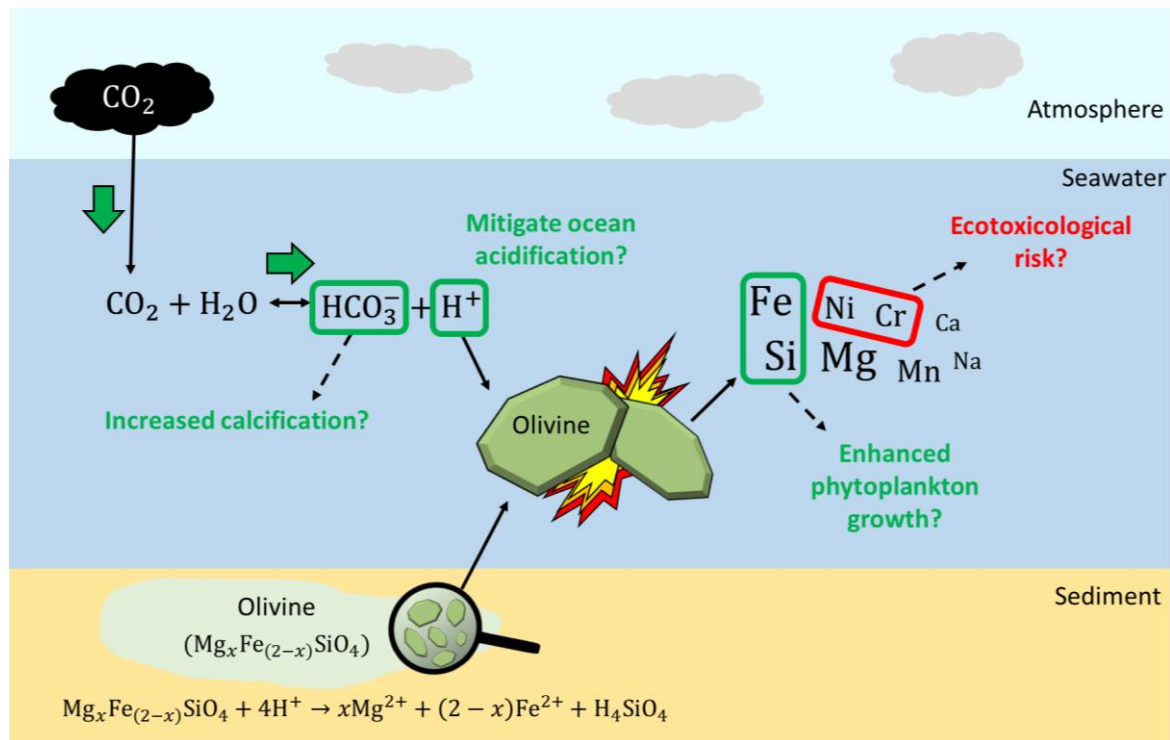
Figure 1.3: Schematic representation of the CO_2 sequestration mechanism (section 1.4) and possible beneficial (green text) and adverse (red text) ecosystem impacts from changes in seawater chemistry (section 1.7) during coastal enhanced olivine weathering.

Continental shelf seas could be suitable for enhanced silicate weathering (ESW) because of the large surface area (24-29 x 10^6 km²) and relatively easy implementation of olivine spreading in existing coastal zone management practices (e.g. beach nourishment, land reclamation) (Mackenzie and Lerman, 2006; Meysman and Montserrat, 2017; Montserrat et al., 2017). Furthermore, the natural grinding of rocks by waves and currents and proportionally large mixing layer where CO_2 exchange between the atmosphere and TA-enriched seawater is possible, favour the distribution of olivine in coastal areas compared to the open ocean (Schuiling and De Boer, 2011; Köhler et al., 2013; Meysman and Montserrat, 2017). Moreover, porewater flushing by coastal hydrodynamics and benthic macrofauna (i.e. bio-irrigation) could prevent porewater saturation effects that would

hamper olivine dissolution (Meysman and Montserrat, 2017; Montserrat et al., 2017). Finally, microbial porewater acidification and passage of olivine through the acidic, bacteria rich guts of deposit feeders could potentially enhance mineral reactivity since acidic conditions are known to accelerate olivine dissolution (Needham et al., 2004; Rao et al., 2012; Meysman and Montserrat, 2017; Oelkers et al., 2018).

1.5 Olivine

Olivine represents a group of magnesium-iron silicate minerals ($Mg_xFe_{(2-x)}SiO_4$) which are formed deep in the Earth's upper mantle (Harben and Smith jr., 2006; Kremer et al., 2019). Forsterite (Mg_2SiO_4) is the magnesium rich end-member, while fayalite is the iron rich end-member (Fe_2SiO_4). On the earth's surface olivine with a Mg-to-Fe ratio of 1.6:0.4 ($Mg_{1.6}Fe_{0.4}SiO_4$) is most common, which has an olive green colour from which the mineral's name is derived. Olivine naturally occurs in (ultra)mafic ($\leq 55\%$ SiO_2 content) magmatic rocks and certain metamorphic rocks and is most commonly present in peridotite rocks such as dunite and serpentinite (Kremer et al., 2019; Caserini et al., 2022). Currently, approximately 8 Mt of olivine is mined each year mainly for metallurgical use as a slag conditioner in iron and steel industries, refractory, foundry sand, and as a fertilizer. Additionally, the low free silica content (<1%), Mohns hardness of 6.5 to 7.0, specific gravity of 3.3 g cm^{-3}, conchoidal (i.e. curved, shell-like) fracture, and light coloured dust make it attractive for use as an airblast abrasive, filtration medium, and weighting agent in concrete oil-production platforms (Olerud, 1993; Harben and Smith jr., 2006).

From the yearly olivine production, roughly 3.5 Mt originates from the 2000 Mt high quality dunite bodies of the Fjordane Complex in Norway. Japan is the second largest olivine producer with 2 Mt per year from serpentine reserves (~100 Mt) in the Horoman Hill region. Other countries such as Austria, Argentina, Brazil, Italy, Korea, Mexico, Spain, Taiwan, and the United States (US) also mainly rely on serpentine reserves for olivine production. In Italy, olivine reserves are estimated at 650 Mt and located in the Piedmont

region. For the US, olivine is only produced in relatively small amounts (0.1 Mt per year) in the Cascade Mountains of Washington State and Smoky Mountains of North Carolina. The latter location contains several bodies of dunite and serpentine, with the largest one estimated at 300 Mt. Furthermore, a huge body of 200 Gt unaltered dunite is believed to be present in the Twin Sisters Mountains (Harben and Smith jr., 2006; Kremer et al., 2019; Caserini et al., 2022). Overall, the estimated gigaton scale CDR potential of coastal enhanced olivine weathering should not be limited by suitable rock availability if the estimated reserves are correct (Köhler et al., 2010; Renforth, 2012). However, significant upscaling of the mining operations and world fleet size for olivine distribution would be required (Hangx and Spiers, 2009).

The experimental work of this thesis was conducted with various grain sizes of VANGUARD® refractory grade dunite sand from Sibelco's Åheim mining site in Norway (Figure 1.4). The mineral and elemental composition of this dunite sand as given by the manufacturer, reported by previous studies and measured in the current study are shown in Table 1.1 Norwegian dunite contains on average 92% olivine, of which 94% is forsterite and 6% is fayalite according to Olerud (1993). Kremer et al. (2019) and Santos et al. (2015) reported a ferroan-forsterite (i.e. forsterite with iron substitution) content of 75 to 80% and 84.5%, respectively in Norwegian dunite based on X-ray diffraction (XRD) analysis. Here, we measured a similar ferroan-forsterite content via XRD analysis ranging between 69 and 86% (Table 1.1). Dunite is primarily composed of Mg, O, Si, and Fe as can be seen from the chemical formula of olivine (Eq. 1.5) (Table 1.1). Additionally, several trace elements are present of which Ni and Cr are of potential ecotoxicological concern (see section 1.7.4). Throughout this thesis, "olivine" will refer forsterite rich dunite unless specified otherwise.

Table 1.1: Mineral and elemental composition of Norwegian dunite analysed via X-ray diffraction (XRD) and ICP-MS or ICP-OES, respectively. All concentrations are given in wt%. Values for the current study are averages for the different grain sizes. Note that oxygen makes up the remaining ~40 wt% of the dunite elemental composition. N.A. = not available, N.D. = not detected.

Mineral composition	Unit	Manufacturer	Santos et al. (2015)	Kremer et al. (2019)	Current study
Ferroan-forsterite	wt%	N.A.	84.5	75 - 80	69 – 86
Enstatite	"	N.A.	N.D.	10 – 15	5 – 8
Antigorite	"	N.A.	N.D.	N.D.	1 – 6
Chlorite	"	N.A.	N.D.	N.D.	2 – 9
Hornblende	"	N.A.	N.D.	N.D.	1 – 2
Talc	"	N.A.	0.5	N.D.	1 – 7
Quartz	"	N.A.	0.2	N.D.	≤1
Lizardite	"	N.A.	2.7	≤5	N.D.
Fayalite	"	N.A.	2.5	N.D.	N.D.
Clinochlore	"	N.A.	2.1	N.D.	N.D.
Tirodite	"	N.A.	3.1	N.D.	N.D.
Magnesian calcite	"	N.A.	1.0	N.D.	N.D.
Magnesite	"	N.A.	0.2	N.D.	N.D.
Periclase	"	N.A.	0.1	N.D.	N.D.
Brucite	"	N.A.	0.7	N.D.	N.D.
Chromite	"	N.A.	1.1	N.D.	N.D.
Elemental composition					
Mg	wt%	30.4	27.2	24.8	22.0 – 30.4
Si	"	26.6	20.7	22.7	N.A.
Fe	"	5.0	3.7	5.5	3.6 – 5.0
Cr	"	0.30	0.24	N.A.	0.11 – 0.30
Ni	"	0.25	0.27	0.94	0.21 – 0.25
Al	"	0.081	0.17	0.26	0.00081 – 0.0032

| Mn | " | 0.068 | 0.09 | N.A. | 0.062 – 0.068 |
| Co | " | 0.011 | 0.02 | N.A. | 0.0093 – 0.011 |

Figure 1.4: Picture of the experimental Norwegian dunite sand (93 – 332 µm) and a detailed scanning electron microscope image of a singular olivine grain that is covered with fine (<10 µm) olivine particles originating from the industrial grinding process.

In addition to the global abundance, olivine is one of the fastest weathering silicate minerals (Hartmann et al., 2013; Oelkers et al., 2018). This fast dissolution rate is the result of olivine's relatively simple structure comprised of silicate (SiO_4^-) tetrahedra connected by divalent cations Me^{2+} (e.g. Mg^{2+}, Fe^{2+}, Ni^{2+}) via ionic bonds. These ionic Me^{2+}-O bonds are easier to break compared to the covalent Si-O-Si bonds typically found in other silicate minerals, resulting in a relatively fast dissolution rate (Oelkers et al., 2018). Laboratory olivine weathering experiments have shown that the olivine dissolution rate is mainly influenced by mineral reactive surface area and solution pH and

temperature (Rimstidt et al., 2012; Oelkers et al., 2018). Olivine grains dissolves faster when they are ground to a small size (large surface area) and exposed to acidic, high temperature conditions (Oelkers et al., 2018). These conclusions were drawn from experiments conducted in simple salt (e.g. NaCl) or acid (H_2SO_4) solutions rather than actual seawater (Golubev et al., 2005; Kleiv and Thornhill, 2008; Rimstidt et al., 2012). Currently, only four studies have investigated olivine dissolution in artificial or natural seawater (Montserrat et al., 2017; Rigopoulos et al., 2018; Fuhr et al., 2022; Fuhr et al., 2023). Furthermore, the possibly stimulating effect of bioturbation and coastal hydrodynamics (i.e. waves and currents) on olivine reactivity (see section 1.4) has not been investigated. Therefore, *in situ* olivine dissolution rates remain uncertain, which prevents accurate assessment of the CO_2 sequestration potential of coastal enhanced olivine weathering in the 21st century (Meysman and Montserrat, 2017).

1.6 Marine CO_2 sequestration potential with olivine

The potential contribution of coastal enhanced olivine weathering to climate change mitigation depends on the rate of atmospheric CO_2 removal R_{CO_2} (µmol CO_2 m^{-2} seafloor s^{-1}) which can be calculated from the net CO_2 sequestration efficiency $\gamma_{CO_2}^{net}$ (µmol CO_2 µmol^{-1} olivine) and olivine (ol) dissolution rate R_{ol} (µmol olivine m^{-2} seafloor s^{-1}) (Meysman and Montserrat, 2017) according to:

$$R_{CO_2} = \gamma_{CO_2}^{net} R_{ol} = [(\delta DIC/\delta TA)_{pCO_2} \alpha_{TA} 4(1-\varepsilon)] [k_{ol} A(1-\Omega)C] \qquad [1.7]$$

Where $\gamma_{CO_2}^{net}$ represents the net amount of CO_2 that is sequestered upon dissolution of a given amount of olivine, and is dependent on the seawater CO_2 sensitivity $(\delta DIC/ \delta TA)_{pCO_2}$, the alkalinity release during olivine dissolution, and the CO_2 emissions during mining, grinding and transport of the olivine, which are accounted for by the dimensionless factors α_{TA} and ε, respectively. The olivine dissolution rate R_{ol} is depended on the olivine dissolution rate constant k_{ol} (µmol olivine m^{-2} s^{-1}), mineral reactive surface area A (m² g^{-1}), mass of supplied olivine C (g m^{-2} of seafloor), and the pore water

saturation state with respect to olivine Ω (dimensionless). The CO_2 sensitivity can be accurately quantified when local seawater conditions (e.g. pH, salinity, temperature) at the olivine deployment site are known (Hofmann et al., 2009). Similarly, CO_2 emissions associated with mining, grinding, and transport of the olivine can be assessed with relatively low uncertainty (Moosdorf et al., 2014; Meysman and Montserrat, 2017). However, the alkalinity release during olivine dissolution α_{TA} remains uncertain due to possible serpentinization of olivine and formation of secondary minerals that scavenge alkalinity (Table 1.2) (Griffioen, 2017; Fuhr et al., 2022).

Various secondary mineral have been hypothesized and observed to form during olivine dissolution in seawater including calcium carbonates (mainly aragonite), iron (hydr)oxides, and phyllosilicates (e.g. sepiolite and talc) (Table 1.2) (Griffioen, 2017; Rigopoulos et al., 2018; Fuhr et al., 2022). The rate of secondary mineral precipitation is dependent on the mineral saturation state Ω, and the quality and quantity of nucleation sites where mineral formation is initiated (Moras et al., 2022; Hartmann et al., 2023). The dimensionless mineral saturation state Ω is defined as the quotient of the ion activity product (IAP) and the solubility product K_{sp}. The IAP is equal to the product of the activities of the dissolved ions involved in the mineral precipitation reaction, while K_{sp} is a thermodynamic constant that indicates the equilibrium solubility of a specific mineral in a solution with a given temperature, salinity, and pressure (Doney et al., 2009; Griffioen, 2017). Significant secondary mineral formation is expected in solutions with high levels of supersaturation (i.e. high Ω) and an abundance of high-quality nucleation sites (Hartmann et al., 2023). However, knowledge about the kinetics and critical saturation state thresholds for secondary mineral precipitation is largely lacking (Moras et al., 2022). Consequently, the $\gamma_{CO_2}^{net}$ for coastal enhanced olivine weathering can currently not be accurately estimated.

Table 1.2: Possible secondary mineral formation reactions during olivine dissolution in seawater reported by previous studies (Griffioen, 2017; Rigopoulos et al., 2018; Fuhr et al., 2022). The formation of these minerals

is undesirable since it would reduce the net CO₂ sequestration efficiency of coastal enhanced olivine weathering.

Aragonite/ calcite	$Ca^{2+} + 2HCO_3^- \rightarrow CaCO_3 + CO_2 + H_2O$	[1.8]
Amorphous ferrihydrite	$Fe^{2+} + \frac{1}{4}O_2 + H^+ + 3H_2O \rightarrow Fe(OH)_3 + 3H^+ + 0.5H_2O$	[1.8]
Sepiolite	$2Mg^{2+} + 3H_4SiO_4 \rightarrow Mg_2Si_3O_{7.5}(OH)(H_2O)_3 + 4H^+ + 0.5H_2O$	[1.9]
Talc	$3Mg^{2+} + 4H_4SiO_4 + 4H_2O \rightarrow Mg_3Si_4O_{10}(OH)_2 + 6H^+$	[1.10]
Chrysotile	$3Mg^{2+} + 2H_4SiO_4 + H_2O \rightarrow Mg_3Si_2O_5(OH)_4 + 6H^+$	[1.11]
Serpentinization	$3Mg_2SiO_4 + 4H_2O + SiO_2 \rightarrow 2Mg_3Si_2O_5(OH)_4$	[1.12]
	$2Mg_2SiO_4 + 3H_2O \rightarrow Mg_3Si_2O_5(OH)_4 + Mg(OH)_2$	[1.13]

To date, olivine dissolution rate constants have mainly been derived from laboratory experiments where olivine is weathered in idealized solutions, rather than in actual seawater as mentioned in section 1.5. Furthermore, the impact of biota and coastal hydrodynamics on olivine dissolution could potentially be significant, but has not been experimentally studied (Meysman and Montserrat, 2017). Finally, limited knowledge on changes in reactive mineral surface area during olivine dissolution prevent accurate predictions of temporal changes in olivine dissolution rates (Oelkers et al., 2018; Strefler et al., 2018). Overall, various crucial parameters needed to accurately assess the atmospheric CO₂ removal rate of coastal enhanced olivine weathering are currently poorly constrained, signifying the urgent need for additional experimental work on this topic.

1.7 Ecological impacts of coastal olivine spreading

Environmental changes induced by coastal enhanced olivine weathering need to be carefully assessed to ensure that the technique will be deployed at a scale where benefits significantly outweigh any potential adverse ecosystem effects. Coastal olivine spreading will result in both physical and chemical environmental changes that could affect marine

biota either positively or negatively (Hartmann et al., 2013; Köhler et al., 2013; Bach et al., 2019). An overview of the possible co-benefits and ecological risks of coastal enhanced olivine weathering that have currently been recognized will be provided in the following sections.

1.7.1 Physical perturbations

Dedicated studies about the physical impacts of coastal enhanced olivine weathering are currently lacking. However, it is reasonable to anticipate that these impacts would be comparable to those of beach nourishment and be dependent on the olivine supply rate and grain size. Mortality through burial is an immediate threat to benthic fauna during beach nourishment that is dependent on the thickness of the deposited sediment layer (Speybroeck et al., 2006; Schlacher et al., 2012). Typically, during beach nourishments, sediment layers ranging from 1 to 2.5 m in thickness are supplied, resulting in mortality of all resident benthic biota (Speybroeck et al., 2006). For CESW, the olivine supply rate should ideally be chosen based on the local environmental conditions to minimize the risk of secondary mineral precipitation and adverse ecosystem impacts (Riebesell et al., 2023). The supplied olivine layer needed to achieve gigaton-scale atmospheric CO_2 removal would likely only be a couple cm thick at most, depending on how homogenously it would be spread along coastal zones (Köhler et al., 2013). Mobile benthic organisms such as polychaetes would therefore be at minor risk of burial-induced mortality, although the survival of less mobile taxa such a microphytobenthos might be compromised (Speybroeck et al., 2006).

Olivine particles larger than 10 μm would likely quickly sink to the seafloor (within days), while very fine particles (≤ 1 μm diameter) could theoretically remain in suspension for several years (Köhler et al., 2013). Suspended olivine particles would increase seawater turbidity and potentially reduce light transparency in low-productive ocean waters (Köhler et al., 2013). However, due to the low photosynthetic activity in these areas, the impact on the biological carbon pump would likely be limited (Köhler et al., 2013).

Furthermore, limited shading would be expected for coastal zones in Europe, since suspended particulate matter concentrations (~0.02 – 50 g m^{-3}) would typically be higher than olivine input rates (Köhler et al., 2013).

Additionally, suspended olivine particles could potentially physically damage marine biota through grain abrasion and adversely affect the feeding efficiency of marine suspension feeders (e.g. bivalves, sponges, and tunicates). For examples, Cheung and Shin (2005) observed a significant depletion in cilia on the gill lamellae of the green-lipped mussel (*Perna viridis*) during a 14-day exposure to suspended marine sediment at concentrations 500 mg L^{-1} and higher. Notably, adverse effects were found to be dependent on the grain size, with increased damage during exposure to larger grain sizes (Cheung and Shin, 2005). A strong correlation between suspended sediment concentrations and structural gill damage (including epithelium lifting and reduction of epithelial volume) was also observed for the green grouper *Epinephelus coioides* after a six-week exposure (Au et al., 2004). Sponges exhibit little particle selectivity during filter feeding and are therefore prone to ingest olivine particles that could damage and clog their feeding structures (Bell et al., 2015; Godefroy et al., 2019). Additionally, suspension feeding bivalves are known to be vulnerable to elevated concentrations of suspended solids, which can adversely affect various physiological processes including clearance rate, oxygen consumption and growth (Bricelj et al., 1984; Grant and Thorpe, 1991; Ward and MacDonald, 1996; Cheung and Shin, 2005). Moreover, suspended sediments can also adversely affect adult corals by reducing solute exchange (smothering), decreasing feeding activity, and increasing energy expenditure for self-cleaning (Jones et al., 2016). These adverse effects on lower trophic levels could potentially also reduce prey availability for marine mammals and fish (Kjelland et al., 2015; Todd et al., 2015). Hence, dedicated experiments on the effects of suspended olivine particles on marine biota may be warranted if large amounts of olivine would be deployed.

Once olivine gets mixed in the seafloor through biological and hydrodynamic processes, it would alter the physical and chemical characteristics of the surficial sediment. Olivine

grains would possibly be smaller and less rounded compared to local sediment grains. Additionally, the density of olivine grains (3.3 g cm^{-3}) could be higher than most minerals that naturally occur in the sediment at the deployment site (e.g. quartz, 2.65 g cm^{-3}) (Veerasingam et al., 2014; Kermani et al., 2016; Montserrat et al., 2017). These changes in the physical sediment properties could lead to increased compaction of the sediment, which would alter sediment porosity, permeability, capillarity, and exchange of gases and nutrients (Speybroeck et al., 2006). Furthermore, sediment compaction could adversely affect the feeding of wading bird and movement of infauna (Speybroeck et al., 2006). Moreover, changes in sediment grain size distribution would change the habitat suitability for marine biota and thus possibly result in changes of the benthic community species composition (Speybroeck et al., 2006; de Schipper et al., 2021). Changes in sediment colour resulting from the addition of light green coloured forsterite sand could also possibly have ecological consequences (Speybroeck et al., 2006). Organisms that are unable to change their colour to match the environment could for example be at a higher risk of predation by visual predators (Johannesson and Ekendahl, 2002). In addition to these physical changes, olivine addition could reduce the organic matter concentration in the surface sediment and increase the concentration of trace metals, notably nickel (Ni) and chromium (Cr) (Speybroeck et al., 2006; Hartmann et al., 2013). Dilution of the sediment organic matter content through olivine addition could temporarily reduce the food availability for benthic deposit feeders (Lopez and Levinton, 1987). The ecological risks of trace metal release during olivine dissolution are discussed in detail in section 1.7.3.

1.7.2 Ocean alkalinization and fertilization

Coastal enhanced olivine weathering changes the seawater carbonate chemistry (i.e. increased pH, TA, and DIC after atmospheric CO_2 equilibration) and results in the release of various elements (mainly Mg, Si, Fe, Ni, and Cr) to the marine environment. These chemical changes could have a range of effects on marine ecosystems and biogeochemical cycling therein (Hauck et al., 2016; Meysman and Montserrat, 2017; Bach

et al., 2019). Findings from both *in silico* and *in vivo* experiments will be described in the following paragraphs.

Rising atmospheric CO_2 concentrations have resulted in increased anthropogenic CO_2 uptake by the oceans which reduces seawater pH and lowers the $CaCO_3$ saturation state (Doney et al., 2009). This process of OA has resulted in a decrease of seawater pH by 0.1 units (from approximately 8.21 to 8.10) since the industrial revolution, which could further decline by 0.3 to 0.4 units in the 21st century if anthropogenic CO_2 emissions continue to rise (business-as-usual scenario) (Orr et al., 2005). Ocean acidification most notably reduces the calcification and growth rate of shell forming organisms including planktonic species (e.g. coccolithophores and foraminifera) and benthic invertebrates (e.g. molluscs, echinoderms, and corals) (Doney et al., 2009; Das and Mangwani, 2015; Meyer and Riebesell, 2015). However, other marine organisms are also affected by OA either directly (e.g. increased N_2 fixation by cyanobacteria, or increased growth of seagrasses) or indirectly (e.g. through habitat loss) (Hutchins et al., 2007; Palacios and Zimmerman, 2007; Nagelkerken and Connell, 2022).

A proposed co-benefit of coastal enhanced silicate weathering is mitigation of OA via proton consumption during olivine dissolution in seawater (Eq. 1.6) (Hartmann et al., 2013; Meysman and Montserrat, 2017). However, biogeochemical modelling by Köhler et al. (2013) showed that seawater pH would only increase by 0.007 units after yearly homogeneous application of 3 Gt olivine over the global ocean. Similarly, Hauck et al. (2016) concluded that the mitigation of OA through olivine dissolution is limited after seawater CO_2 equilibration with the atmosphere. Additionally, OAE from CESW increases seawater CO_3^{2-} concentrations and thus elevates the $CaCO_3$ saturation state. Therefore, coastal enhanced olivine spreading could improve $CaCO_3$ formation in calcifying organisms (Bach et al., 2023). However, at mineral dissolution hotspots phytoplankton growth could potentially decrease if seawater pCO$_2$ falls below approximately 100 µatm due to poor seawater mixing and slow CO_2 in-gassing (Bach et al., 2011; Bach et al., 2019).

The number of experimental studies about the effects of ocean alkalinity enhancement on marine biota has risen significantly during the past years, but remains limited (Cripps et al., 2013; Gore et al., 2019; Ferderer et al., 2022; Subhas et al., 2022; Ferderer et al., 2023; Gately et al., 2023; Guo et al., 2023). Increased seawater TA (by ~1000 µEq L^{-1}) enhanced $CaCO_3$ production by 60% in the red calcifying algae *Corallina* sp. with no significant effects on respiration, primary production, or photophysiology during the 21-day exposure (Gore et al., 2019). Moderate (~700 µmol kg^{-1}) and high (~2700 µmol kg^{-1}) alkalinity additions did not significantly alter the growth rate or elemental ratios of the diatom *Chaetoceros* sp. and coccolithophore *Emiliania huxleyi* during single species laboratory experiments (Gately et al., 2023). Similarly, mostly negligible responses were observed on natural microbial communities of the oligotrophic North Atlantic Subtropical Gyre exposed to various total alkalinity additions (~512 to 2050 µeq kg^{-1}) during a 4-day microcosm experiment at sea (Subhas et al., 2022). In contrast to these positive or neutral effects, Ferderer et al. (2022) observed a reduction in silicic acid drawdown and biogenic Si build-up by diatoms during a 22-day microcosm experiment in which a coastal plankton community was exposed to alkalinity enriched seawater (+500 µmol kg^{-1}). In a follow-up pelagic mesocosm experiment in Norway, silicate- and calcium-based mineral OAE (0 to 600 µmol kg^{-1} TA additions and corresponding Ca or Mg addition) had limited genus-specific impacts on diatoms (Ferderer et al., 2023). Observed effects included increased diatom silicification for the silicate-based OAE treatment and increased silicification of diatoms from the genus *Pseudo-nitzschia* at elevated seawater total alkalinity (Ferderer et al., 2023). Furthermore, enhanced seawater alkalinity through addition of 0.28 or 0.54 mmol L^{-1} Ca(OH)$_2$ resulted in disruption of acid-base regulation in acutely (6 h) exposed green crabs (*Carcinus maenas*) (Cripps et al., 2013).

A range of elements (mainly Mg, Si, Fe, Ni, and Cr) are released during olivine dissolution in seawater (Meysman and Montserrat, 2017). Magnesium is considered of low ecological importance, since the expected release would be relatively low compared to the high background concentration in seawater (~55 mmol L^{-1}) (Meysman and Montserrat, 2017; Bach et al., 2019). Iron is an essential co-factor for many enzymes involved in

photosynthesis, respiration, and nitrogen fixation and considered as a limiting micronutrient for phytoplankton growth in various oceanic regions (Behrenfeld et al., 2009; Smetacek et al., 2012). Iron addition via olivine dissolution could therefore enhance primary production if other essential elements are not limited (Hauck et al., 2016; Bach et al., 2019). Additionally, N_2-fixing cyanobacteria (e.g. *Trichodesmium* spp.) could potentially benefit from the higher Fe and Ni availability, further stimulating CO_2 drawdown via photosynthesis (Bach et al., 2019). Model results from Hauck et al. (2016) indicated that Fe fertilization could account for up to 37% of the global CO_2 uptake by olivine dissolution (5.8 to 7.8 Gt C yr^{-1} for 3 Gt olivine dissolution yr^{-1}). However, at least 40% of the fertilizing effect occurred in the Antarctic Ocean, which is likely not a suitable olivine deployment site due to its poor accessibility and low seawater temperatures that would reduce olivine reactivity (Köhler et al., 2013; Hauck et al., 2016). Additionally, iron concentrations are higher in coastal regions compared to the open ocean due to riverine input and release from sediment resuspension (Boyd and Ellwood, 2010). Hence, the fertilizing effect of Fe addition through coastal olivine spreading could be lower than expected (Bach et al., 2019).

Silicon is an essential element for marine silicifiers, of which diatoms are the most important group. Diatoms sustain the marine food web and significantly contribute to the biological carbon pump (Struyf et al., 2009; Tréguer et al., 2018). However, Si availability limits diatom productivity over large parts of the global ocean (Sarmiento et al., 2004). Olivine weathering would supply Si to coastal environment in amounts that could potentially exceed natural aeolian and riverine inputs (Struyf et al., 2009; Bach et al., 2019). Hence, coastal enhanced olivine weathering may feasibly enhance growth of marine silicifiers (Hartmann et al., 2013; Köhler et al., 2013; Bach et al., 2019). Bach et al. (2019) hypothesized that silicifiers would benefit more from CESW than calcifiers, resulting in the transition to a more productive "green(er) ocean" where diatoms would be more dominant than they already are today (Bach et al., 2019). The impact of coastal olivine spreading on the frequency of harmful algal blooms (HABs) is currently unknown, but possibly limited. This is because dinoflagellates, the primary phytoplankton species of

concern in HABs (Hallegraeff, 2003), are not anticipated to benefit significantly from changes in seawater chemistry induced by olivine weathering. However, certain diatom species from the genus *Pseudo-nitzschia* and the cyanobacterium *Nodularia spumigena* are also associated with HABs (Hallegraeff, 2003) and may potentially benefit from coastal enhanced olivine weathering (Bach et al., 2019). Therefore, research on the olivine exposure effects in these HAB-associated species is recommended to gain a more comprehensive understanding of potential environmental risks of coastal enhanced olivine weathering.

The shift in phytoplankton community composition could also have important implications for the CO_2 sequestration potential of coastal enhanced olivine weathering. If production and burial of $CaCO_3$ would be reduced by for example 10%, then the seawater total alkalinity and olivine CO_2 sequestration efficiency would remain 20% higher (Bach et al., 2019). Additionally, increases in diatom biomass could possibly enhance the ballast potential of biogenic Si (BSi) for export of organic carbon from the surface ocean to the deep ocean for long term storage (Bach et al., 2019). If true, these benefits for oceanic CO_2 sequestration would favour the use of silicates rather than carbonates for OAE. However, modelling of marine particle cycling by Fakhraee et al. (2023) indicated that a low applications (100 g m^{-2} yr^{-1} or 6.2 Gt yr^{-1}) of fine grained olivine (D80 = 10 μm) along coastlines within the 60°N/S could reduce the organic matter content of marine particles by over an order of magnitude, which would significantly reduce zooplankton feeding and fecal pellet production. These changes could have significant implications for the biological carbon pump and ocean trophic structure (Fakhraee et al., 2023).

Currently, only four studies have experimentally investigated the effects of olivine exposure on aquatic biota (Ren et al., 2021; Guo et al., 2023; Hutchins et al., 2023; Xie et al., 2023). Ren et al. (2021) observed an increase in the abundance of marine biofilm-forming particle attached microbes during a 10-day laboratory exposure to 1% w/w fine grained olivine (D50 = 30 μm) in natural seawater. Furthermore, the growth of the freshwater green microalgae *Chlamydomonas reinhardtii* and *Chlorella pyrenoedosa* was

increased during a 9-day exposure to 8 g olivine L^{-1} as a result of the increased Mg availability (Xie et al., 2023). Neutral to positive physiological responses were observed for two silicifying diatoms, a calcifying coccolithophore, and three cyanobacteria species exposed to a range of olivine dissolution product concentrations (Hutchins et al., 2023). Silicifiers and calcifiers benefitted from additional Fe and Si availability or enhanced alkalinity, respectively, while metals such as Ni and Co promoted cyanobacterial growth (Hutchins et al., 2023). The diatom *Ditylum* sp. did not outcompete the coccolithophore *Emiliana huxleyi* during co-culturing in contrast to the "green ocean" hypothesis by Bach et al. (2019), but both species benefitted from the available olivine dissolution products (Hutchins et al., 2023). Finally, after a 21-day exposure to olivine particles (D10 – D90 = 22 – 228 μm) at a concentration of 1.9 gram per liter in natural seawater, Guo et al. (2023) observed significant changes in the abundance of several phyto- and zooplankton taxa. Particularly, small (<20 μm) phytoplankton taxa and the dinoflagellate *Noctiluca scintillans* increased in abundance, while ctenopods (*Penilia sp.*) and tunicates (*Oikopleura sp.*) reduced in number. The authors hypothesize that the observed effects may be attributed to the adverse impact of suspended olivine particles on the grazing efficiency of the different zooplankton taxa (Guo et al., 2023).

1.7.3 Trace metal toxicity risk

Enhanced silicate weathering would release various trace metals to the environment, with the specific metals dependent on the composition of the source rock (Hartmann et al., 2013; Dupla et al., 2023). Notably, dunite rock contains relatively high amounts of Ni (0.17 to 0.94 wt%) and Cr (0.0001 to 0.30 wt%) (De Hoog et al., 2010; Keefner et al., 2011; Kleiv and Thornhill, 2011; Santos et al., 2015; Shur and Perchuk, 2015; Lynn et al., 2017; Montserrat et al., 2017; Kremer et al., 2019). During dissolution in a marine setting, these trace metals could accumulate in seawater and sediment to levels that significantly exceed natural background concentrations (Meysman and Montserrat, 2017).

Nickel is classified as a transition metal and is essential as a cofactor in urease and hydrogenase enzymes for both terrestrial and aquatic plants (Yusuf et al., 2011). Additionally, microorganisms also employ nine Ni-containing enzymes involved in carbon, oxygen, and nitrogen cycling (Mulrooney and Hausinger, 2003). However, the essentiality of Ni for aquatic animals is debated, since no studies have shown Ni deficiency or Ni-depended biochemistry in aquatic organisms, although Ni is actively regulated in aquatic invertebrates and fish (Muyssen et al., 2004; Blewett and Leonard, 2017; Nielsen, 2021). Nickel is naturally present in the Earth's crust, often in oxide and sulphide forms. Its release to the environment occurs via processes such as weathering of Ni-bearing rocks, forest fires, and volcanic eruptions (Genchi et al., 2020). Nickel concentrations are generally between 1.7 and 8.5 nmol L^{-1} in seawater and 0.20 to 1.3 mmol kg^{-1} in pristine marine sediment (Cempel and Nikel, 2006; Birch, 2017).

Nickel serves diverse functions in both commercial and industrial sectors, notably in stainless steel and nickel alloy production (Cempel and Nikel, 2006). As a result of diverse usage, Ni release to the environment is enhanced via multiple anthropogenic sources, including burning of fossil fuels, mining, smelting, municipal and industrial waste, steel manufacturing, and cement production (Shahzad et al., 2018). Consequently, High Ni concentrations have been documented in seawater and marine sediment at human-impacted coastal regions. For example, at the Alang-Sosiya ship scrapping yard in the gulf of Cambay (India) Ni concentrations up to 16 µmol L^{-1} and 2.9 mmol kg^{-1} have been reported in coastal seawater and sediment, respectively (Reddy et al., 2004; Reddy et al., 2005).

Upon olivine dissolution in seawater, Ni is liberated as Ni^{2+} ions which can remain as free metal ions or form complexes with organic (e.g. dissolved organic carbon (DOC)) and inorganic (e.g. SO_4^{2-}, Cl^-, and CO_3^{2-}) ligands (Blewett and Leonard, 2017). The free metal ion is generally considered the most bioavailable and thus potentially toxic chemical species (Blewett and Leonard, 2017). Complexation of Ni with DOC has been shown to reduce Ni toxicity in mussels and sea urchin early life stages, with the degree of

protection being inversely related to the DOC concentration and dependent on the DOC quality (Nadella et al., 2009; Blewett et al., 2016; Blewett et al., 2018). Similarly, Ni is expected to be less bioavailable and toxic at higher salinity due to complexation with SO_4^{2-} and Cl^- and competition with Ca and Mg for uptake (Leonard et al., 2011; Blewett and Leonard, 2017). The effect OAE on marine Ni bioavailability and toxicity remains unclear due to a lack of experimental data. A potential reduction in Ni bioavailability at elevated total alkalinity would be expected as a result of Ni^{2+} complexation with HCO_3^- ions (Kozlova et al., 2009). However, freshwater Ni toxicity tests at different alkalinity levels show that the effect of alkalinity on Ni toxicity is more complex than hypothesized and remains poorly understood (Hoang et al., 2004; Deleebeeck et al., 2007; Deleebeeck et al., 2008; Kozlova et al., 2009). Finally, differences in osmoregulation strategies among species and salinity levels can affect Ni uptake rates and potential toxicity (Leonard et al., 2011; Henry et al., 2012; Blewett et al., 2015).

The exact mechanisms for uptake of free Ni^{2+} ions by aquatic biota remain unclear, but likely occurs via the following three routes. Existing transepithelial transporters for the uptake of essential ions such as Ca^{2+} and Mg^{2+} could be exploited by Ni^{2+} via a process referred to as ion mimicry. Furthermore, Ni may be taken up via non-specific metal carriers such as the divalent metal transporter (DMT1). Finally, Ni could potentially enter via the spaces between cells where tight junctions are not completely impermeable (Blewett and Leonard, 2017).

Accumulation of Ni in metabolically active compartments of the body can result in toxic effects (e.g. reduced survival, growth, or reproduction) once metal concentrations exceed species specific thresholds (Adams et al., 2011). Four main mechanisms of Ni toxicity have been put forward for aquatic organisms, including (I) ionoregulatory disruption (mainly Ca^{2+}, Mg^{2+}, and $Fe^{2+/3+}$), (II) respiratory toxicity as a result of allergic reactions at respiratory epithelia, and (III) disruption of energy metabolism, and (IV) oxidative stress (Blewett and Leonard, 2017; Brix et al., 2017). However, the relative importance of the

different mechanisms in explaining toxic effects remains unclear for marine biota (Blewett and Leonard, 2017).

Ecological risk assessment aims to derive threshold contaminant concentrations below which no adverse effects are expected for aquatic organisms (ECHA, 2008; Sorgog and Kamo, 2019). This threshold concentration is referred to as the predicted no-effect concentration (PNEC) and is compared to the predicted environmental concentration (PEC) to determine the risk of toxicological effects. A PEC/PNEC ratio larger than 1 indicates a potential toxicological risk and need for further assessment and potential risk management measures (Sorgog and Kamo, 2019). PNEC values are generally derived from data of laboratory ecotoxicity tests in which individual biological species are exposed to single contaminants under optimal conditions (ECHA, 2008). The assessment factor (AF) method and species sensitivity distribution (SSD) method are the two main approaches used to derive PNEC values (Sorgog and Kamo, 2019). For the AF method, the lowest effect concentration (e.g. highest no observed effect concentration (NOEC), or 10% effect concentration (EC10)) from the available ecologically relevant toxicity data is divided by an arbitrary AF between 10 and 10,000 to obtain the PNEC (Chapman et al., 1998; ECHA, 2008). Mortality, immobilisation, growth, development, population growth, and reproduction or the equivalent are considered ecologically relevant endpoints (Gissi et al., 2016). The AF depends on the number and quality of the available toxicity data and is used to account for the uncertainty when extrapolating findings from laboratory toxicity data for a limited number of species to complex natural ecosystems (ECHA, 2008). When sufficient chronic high-quality ecologically relevant toxicity data are available, an SSD can be constructed to derive the hazardous concentrations for 5% of the species (HC5) (Posthuma et al., 2019). This HC5 value is then divided by an AF between 1 and 5 (justified on a case by case basis) to derive a PNEC value (ECHA, 2008; Sorgog and Kamo, 2019). PNEC values are ultimately used by industries, governments, and environmental agencies to set environmental quality standards (EQS) to protect natural ecosystems (Lepper, 2005).

We constructed species sensitivity distributions for Ni(II) and Cr(VI) with marine ecotoxicity data collected from the ECOTOXicology knowledgebase, risk assessment reports, and relevant research articles on Web of Science and Google Scholar (Figure 1.5 and 1.6). Only chronic no-effect or negligible-effect data (i.e. NOEC and ≤10% effect data) for ecologically relevant endpoints that passed the quality criteria by Gissi et al. (2016) were included for SSD construction. For certain data incorporated in the marine Ni SSDs constructed by DeForest and Schlekat (2013) and Gissi et al. (2020), original research articles were not accessible. Despite the unavailability of the original research articles, these data were included for SSD construction since data quality was already assessed in those studies. Data were considered chronic when the test duration was longer than the times defined in Table 1.3 or when an adverse sublethal effect was investigated on a sensitive early life stage (Gissi et al., 2020). For each species, the geometric mean was calculated if multiple chronic NOEC or EC10 values were available for the same endpoint (e.g. growth or reproduction). When several NOEC or EC10 values were available for different toxicological endpoints or organism life stages, the lowest value was determined based on the geometric mean of the toxicity data for the most sensitive endpoint (Tyle and Scott-Fordsmand, 2008; Gissi et al., 2020). The ssdtools package was used to plot SSDs in R and derive HC5 values. The best fitting distribution for the Ni(II) (log-normal) and Cr(VI) (log-logistic) toxicity data was selected based on the lowest aicc value.

Figure 1.5: Nickel (Ni) species sensitivity distribution for marine species. Shaded band reflects the 95% confidence interval. The dotted line indicates the 5% hazardous concentration (HC5) of 0.16 (0.066 – 0.42) µmol L^{-1}.

Significant research efforts during the past 10 years have resulted in a substantial increase in high-quality chronic marine Ni toxicity data that can be used to conduct rigorous risk assessment (Gissi et al., 2020). From the constructed marine Ni SSD we can see that there are considerable differences in Ni sensitivity among the 45 included species and even within taxa (Figure 1.5). The included species that are most sensitive to Ni exposure are the sea urchin *Diadema antillarum* with a 40-h EC10 value for larval development of 0.049 µmol L^{-1} and the copepod *Acartia sinjensis* with an 80-h EC10 value for larval development of 0.094 µmol L^{-1} (Figure 1.5) (Bielmyer et al., 2005; Gissi et al., 2018). The most tolerant species include the green algae *Dunaliella tertiolecta* with a 72-h

EC10 value for specific growth rate of 306 µmol L^{-1} and the sheepshead minnow (*Cyprinodon variegatus*) with a 28-d EC10 value for larval growth of 354 µmol L^{-1} (Figure 1.5) (DeForest and Schlekat, 2013). An HC5 value of 0.14 (0.058 – 0.38) µmol L^{-1} was derived (Figure 1.5). This HC5 value is similar to the value of 0.099 (0.048 – 0.26) µmol L^{-1} reported by Gissi et al. (2020) but significantly lower than the HC5 value of 0.29 µmol L^{-1} that was used in 2008 to set the current European marine Ni-EQS of 0.15 µmol L^{-1} (AF of 2 applied) (Tyle and Scott-Fordsmand, 2008). Differences in HC5 values among studies can be explained by differences in the included data and model selection to construct the SSD (Wheeler et al., 2002). All data used to construct the marine Ni SSD can be found in Supplementary Table A1.

Table 1.3: Criteria for characterizing data as chronic based on taxa-specific test durations, modified from Posthuma et al. (2019). Shorter tests that investigated adverse sublethal effects on sensitive early life stages were also included for SSD construction (Gissi et al., 2020).

Species group	Chronic test duration
Algae	>12 h
Bacteria	>12 h
Unicellular animals	>24 h
Crustaceans	>48 h
Fish	>7 d
Molluscs, Worms, etc.	>7 d

Chromium is a transition metal that is naturally present as chromite ($FeCr_2O_4$) and other chromium spinels in mafic and ultramafic rocks, including dunite (Saha et al., 2011; Santos et al., 2015). Natural (ultra)mafic rock weathering and volcanic emissions form the main natural sources of Cr to the environment (Saha et al., 2011). Chromite is mined for metallurgical (67%), refractory (18%), and chemical (15%) usage. Anthropogenic activities such as electroplating, tanning, industrial water cooling, paper pulp production, and petroleum refining can lead to elevated Cr emissions to natural environments (Saha et al., 2011). Chromium occurs as Cr(III) and Cr(VI) species in seawater, which differ in their

environmental and biological behaviour. Low solubility of Cr(III) species (mainly present as Cr(OH)$_3$ in seawater) infer low bioavailability and toxicological concern (Pettine, 2000; Aharchaou et al., 2018). Moreover, Cr(III) is considered an essential micronutrient for metabolism of glucose, lipids, and proteins in humans and other animals (Eastmond et al., 2008; Monga et al., 2022). On the contrary, Cr(VI) is primarily present as CrO_4^{2-} and $Cr_2O_7^{2-}$ ions in seawater, which can readily be taken up by aquatic organisms through carboxylate, sulphate, and phosphate transporters and are considered highly toxic (Pettine, 2000; Dayan and Paine, 2001). Once inside a cell, Cr(VI) undergoes rapid reduction to Cr(III) which generates reactive oxygen species (ROS). When antioxidant responses are insufficient, these ROS can damage DNA, RNA, proteins, and mitochondria (Dayan and Paine, 2001; Singh et al., 2022). Dissolved concentrations of Cr in seawater typically range from 0.08 to 2.5 nmol L^{-1} for Cr(III) and 0.23 to 3.8 nmol L^{-1} for Cr (VI) (Cranston and Murray, 1978; Jeandel and Minster, 1984; van den Berg et al., 1994). The background Cr content of marine sediment typically varies between 0.15 and 1.7 mmol kg^{-1} (Birch, 2017). Anthropogenic inputs can however lead to significantly elevated Cr concentrations. For example, total dissolved Cr concentration up to 14.7 µmol L^{-1} and sedimentary Cr concentrations up to 5.6 mmol kg^{-1} have been measured at the highly contaminated Alang–Sosiya ship breaking yard in India (Reddy et al., 2004; Reddy et al., 2005).

The presence of Cr in the form of chromite (Cr(III) oxidation state) in dunite rock implies low bioavailability and toxicological concern for marine biota (Santos et al., 2015). However, potential oxidation of chromite nanoparticles could significantly elevate Cr(VI) exposure concentrations for marine biota (Gunkel-Grillon et al., 2014; Das et al., 2021). Hexavalent chromium is currently not considered as a priority substance globally (e.g. not in Europe), which is reflected in the lower abundance of high quality NOEC/EC10 toxicity data compared to Ni(II) (Figure 1.5 and 1.6). Significant differences in Cr(VI) sensitivity can be observed among species (Figure 1.6 and Supplementary Table A2). The most sensitive marine species to Cr(VI) include the red macroalgae *Champia parvula* with a geometric mean NOEC value for cystocarp production after 48 h of exposure of 0.019 µmol L^{-1} and

the marine diatom *Thalassiosira pseudonana* with a 15-d NOEC value for growth of 0.19 μmol L^{-1} (Figure 1.6) (Frey et al., 1983; Jop, 1989). The most tolerant species to Cr(VI) exposure included the coho salmon (*Oncorhynchus kisutch*) with a 11-d NOEC value for juvenile survival of 342 μmol L^{-1} and the sea urchin *Arbacia punctulata* with a geometric mean NOEC value for fertilization after 1 h of exposure of 2859 μmol L^{-1} (Figure 1.6) (Holland, 1960; Jop, 1989). An HC5 value of 0.12 (0.025 – 0.70) μmol L^{-1} was derived from the SSD (Figure 1.6). This value is significantly lower than the marine Cr(VI) EQS of 0.96 μmol L^{-1} that is currently in place in the USA and higher than the marine Cr(VI) EQS of Canada (0.029 μmol L^{-1}) and Australia (0.085 μmol L^{-1}) (USEPA, 1995; CCME, 1999; ANZECC and ARMCANZ, 2000). Variation in EQS among regions can be explained by differences in the methods and data used for guidelines derivation. Insufficient high quality NOEC/EC10 marine ecotoxicity data were available to construct an SSD for Cr(III).
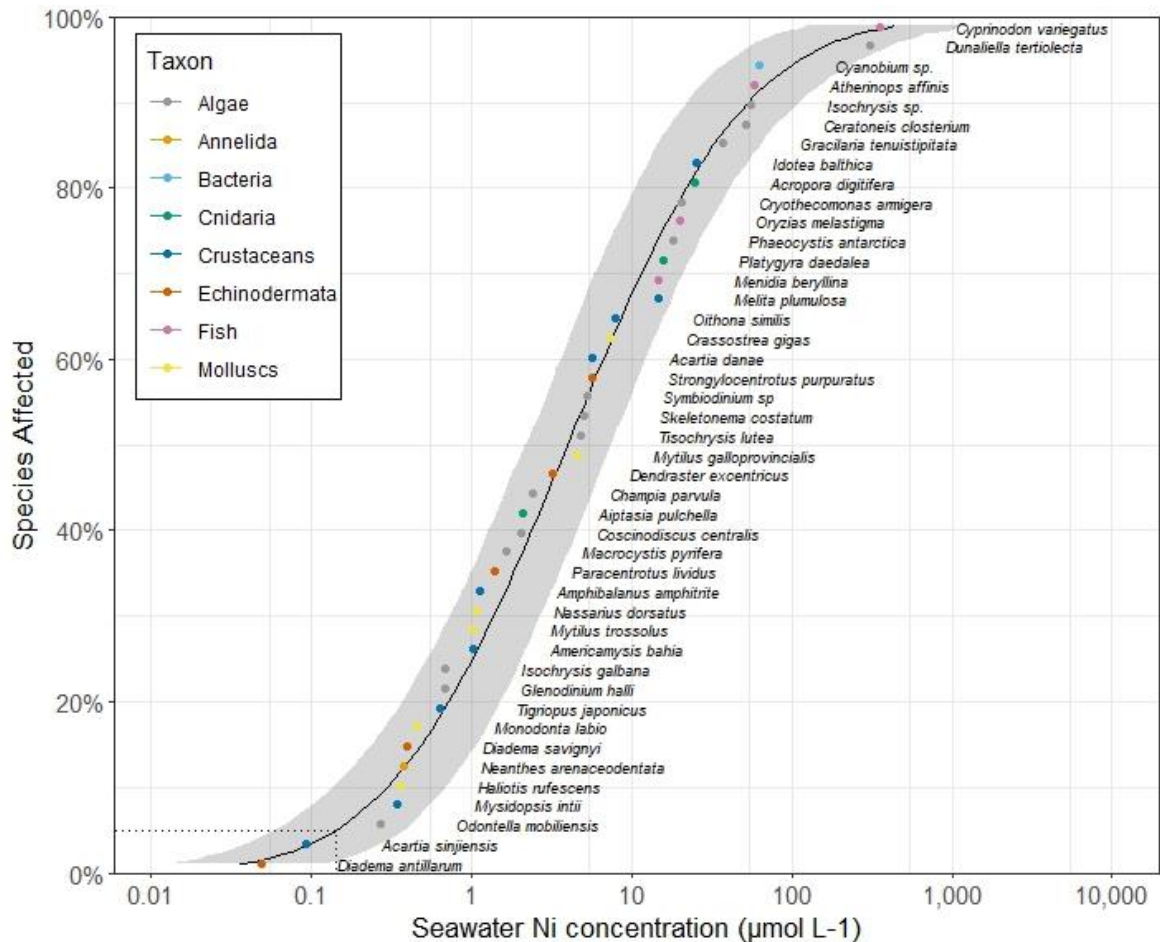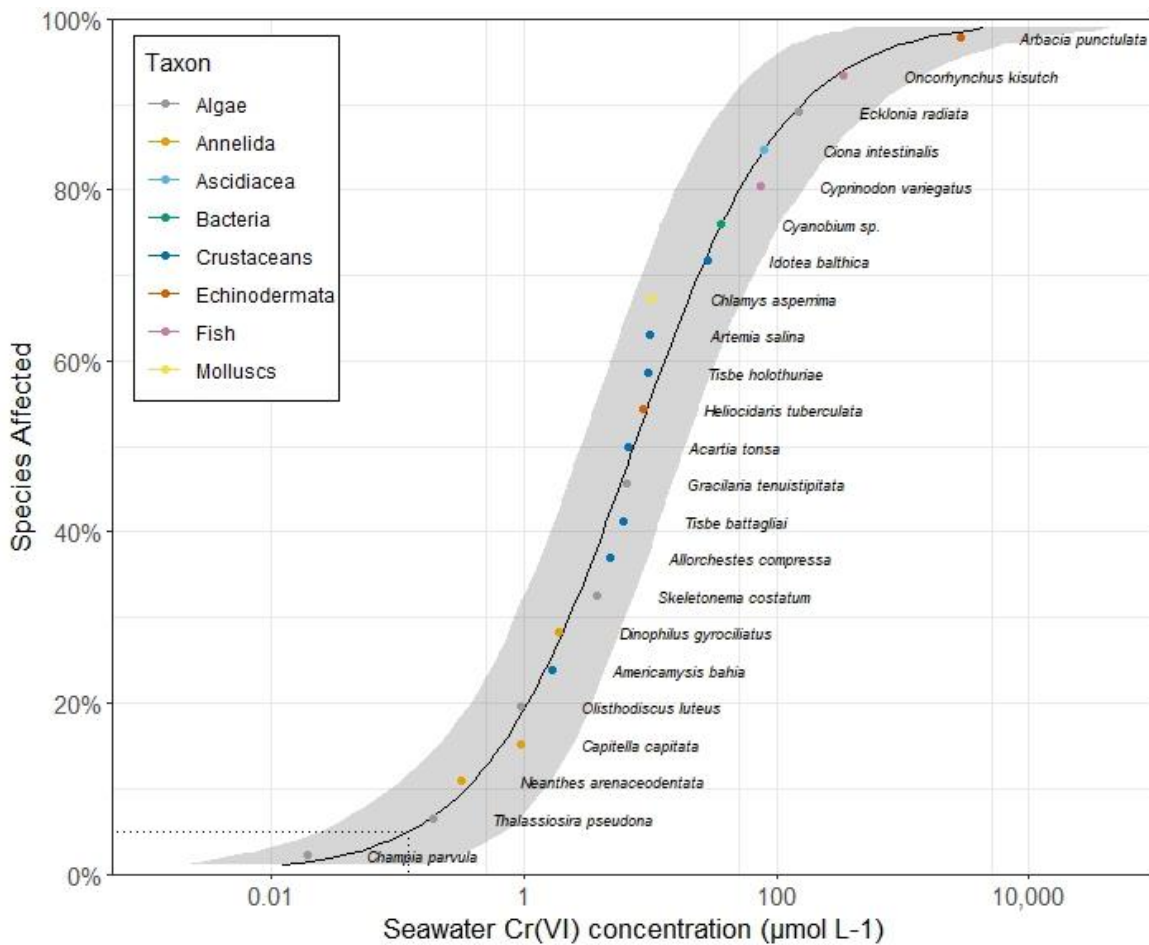
Figure 1.6: Hexavalent chromium (Cr(VI)) species sensitivity distribution for marine species. Shaded band reflects the 95% confidence interval. The dotted line indicates the 5% hazardous concentration (HC5) of 0.13 (0.026 – 0.72) µmol L^{-1}.

Overall, an abundance of marine Ni(II) and Cr(VI) toxicity data are available from single species laboratory toxicity tests conducted under optimal conditions. However, during olivine dissolution in a marine environment, trace metals would be released as a mixture (including Ni, Cr, Fe, Mg, …) accompanied by changes in seawater carbonate chemistry (e.g. pH and TA) (Hartmann et al., 2013; Meysman and Montserrat, 2017). Currently, olivine trace metal release rates and environmental partitioning remain uncertain. additionally, little is known about the bioaccumulation potential and possible toxic effects of olivine and its dissolution products for marine biota (Ren et al., 2021; Hutchins et al., 2023). Robust ecological risks assessment of coastal enhanced olivine weathering is therefore currently not possible. Hence, additional olivine effects data for a range of marine biota are urgently needed to accurately determine the scale at which coastal enhanced olivine weathering could be safely deployed for climate change mitigation (Meysman and Montserrat, 2017).

1.8 Aim and outline of the thesis

Rising atmospheric CO_2 concentrations necessitate the large scale deployment of carbon removal technologies in the coming decades to keep global warming below the Paris Agreement targets of 2 °C, ideally 1.5 °C (UNFCC, 2015; IPCC, 2022b). Ocean alkalinity enhancement via coastal enhanced olivine weathering has been put forward as a promising CDR method (Meysman and Montserrat, 2017). However, the CO_2 sequestration potential and ecosystem impacts of the technique remain uncertain due to the paucity of empirical data. Therefore, the present work aimed to experimentally assess the CO_2 uptake associated with coastal enhanced olivine weathering and quantify possible trace metal related toxicological effects during olivine dissolution. It is important to note that OAE is an emerging field of research, marked by numerous unresolved

questions and uncertainties that could not all be addressed within the scope of this exploratory work. Nevertheless, we remain confident that the results presented herein will play a pivotal role in advancing our understanding of the CDR potential of coastal enhanced olivine weathering.

Chapter 2 and **3** represent two large experiments that were conducted to investigate the potential stimulating effect of coastal hydrodynamics (i.e. waves and currents) on the olivine dissolution and CO_2 sequestration kinetics. **Chapter 2** describes a 70-day laboratory study in which olivine was weathered in natural seawater continuously exposed to various degrees of physical agitation via rotary tumblers. The aim of this study was to assess whether continuous grain-grain collisions would enhanced olivine dissolution. Seawater chemistry changes (i.e. TA, DIC, pH, temperature, salinity, elemental concentrations) were measured weekly, and olivine grain morphology and size distribution were studied to quantify olivine dissolution, CO_2 sequestration, and trace metal release rates.

In **Chapter 3**, we bridged the gap between laboratory experiments and complex field studies by conducting a 175-day flume experiment. The overall goal of this study was to assess the effect of high water current on olivine dissolution kinetics in permeable marine sediment. The experimental set-up consisted of four racetrack flumes which were filled with an approximately 16 cm beach sediment layer and natural seawater. 3.1% w/w olivine was added and a continuous turbulent current was induced in two raceways. Temporal changes in seawater TA, DIC, pH, temperature, salinity, turbidity, and element concentrations were monitored at multiple time points. Furthermore, suspended particulate matter, flume wall precipitates, and sediment grains were examined for the presence of dissolution features and secondary minerals. Mineral saturation indices were calculated for both experiments to assess the possibility of secondary mineral precipitation.

In **Chapter 4**, existing Ni and Cr EQS values were used to derive a first estimate of the maximum amount of olivine that could be supplied to coastal oceans without posing toxicological risks for marine biota. Due to the lack of knowledge on trace metal environmental fate during *in situ* olivine dissolution, calculations were made for the end-member scenarios in which all released trace metal either end up in the water column or the sediment. Subsequently, the CO_2 sequestration potential of coastal enhanced olivine weathering in the 21st century was estimated to assess whether the derived olivine guideline would limit the climate change mitigation potential of this CDR technique.

For **Chapter 5**, we investigated the avoidance response of the marine amphipod *Gammarus locusta* and marine gastropod *Littorina littorea* to sediments containing olivine. Short-term choice experiments were conducted using various mixtures of relatively coarse olivine (83 – 332 µm diameter) and natural marine sediment. We assessed the impact of distance to a food source on sediment avoidance in *L. littorea* and studied the effect of sediment colour on avoidance behaviour for both species. Finally, implications of the observed findings for coastal enhanced olivine weathering were discussed.

Chapter 6 outlines the assessment of acute bioaccumulation, chronic toxicity, and bioaccumulation of olivine in the marine amphipod *G. locusta*. The effect of olivine grain size on trace metal bioaccumulation was studied during a 24-hour exposure followed by a 24-hour depuration period. Additionally, the uptake and depuration kinetics of fine-grained (3 – 99 µm diameter) olivine were investigated during a 7-day experiment. The grain size distribution of ingested olivine grains was quantified and their importance as a trace metal exposure pathway was theoretically explored. Finally, juvenile amphipods were exposed to mixtures of fine-grained (3 – 99 µm diameter) olivine and natural marine sediment for 35-days to assess olivine toxicity. Amphipod survival, growth, reproduction, and whole body element and thiobarbituric acid reactive substances (TBARS) concentrations were measured at the end of the experiment. Olivine NOEC and EC10

values were derived and the assessment factor approach was used to obtain a preliminary olivine PNEC value.

Chapter 7 serves as a comprehensive conclusion where we bring together the key findings from all the previous chapters. Implications of the accumulated data for the CDR potential of coastal enhanced olivine weathering are discussed. Additionally, suggestions and ideas for further research on coastal enhanced silicate weathering are provided.

Chapter 2 Enhanced olivine dissolution in seawater through continuous grain collisions

Flowing seawater — Olivine — Stagnant seawater
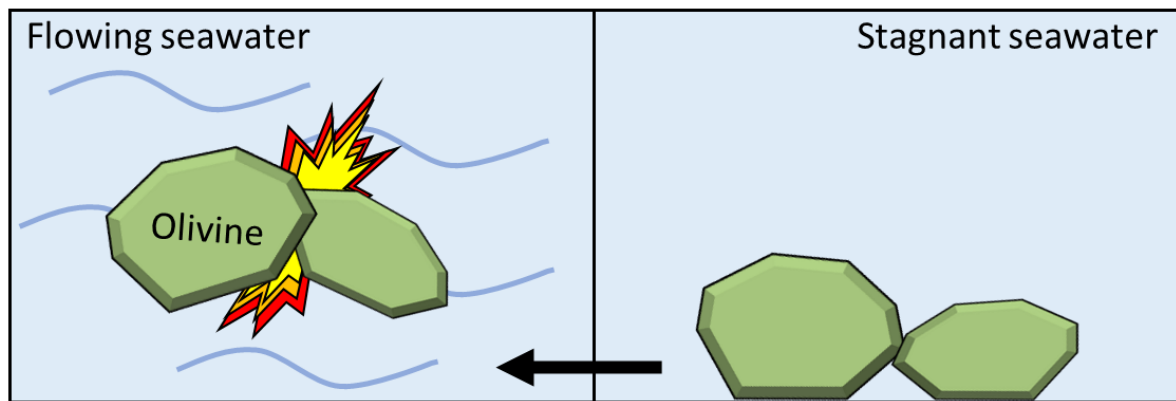
8 – 19 times increase
Olivine dissolution rate

Abstract

Carbon dioxide removal (CDR) technologies at a gigaton scale need to be developed and implemented within the next decades to keep global warming below 1.5 °C. Coastal enhanced silicate weathering is one of the proposed CDR techniques that aims to accelerate the natural process of CO_2-sequestration during marine chemical weathering of silicate minerals. To this end, finely ground rock containing olivine ($Mg_xFe_{2-x}SiO_4$) could be dispersed in dynamic coastal environments, where local biotic and abiotic factors potentially enhance the weathering process. However, accurate predictions of the olivine dissolution rate and the associated CO_2 sequestration under *in situ* conditions are currently lacking and ecosystem impacts remain to be assessed. Previously, it has been hypothesized that *in situ* grain collisions, induced by bed load transport due to currents and waves, could accelerate the *in situ* chemical weathering of olivine particles. To examine this, we investigated the effects of continuous grain tumbling on olivine dissolution in natural seawater. A 70-day experiment was conducted in which forsterite olivine sand was continuously tumbled in filtered seawater at different rotation speeds, and dissolution rates were measured on a weekly basis. Results showed that continuously tumbled olivine dissolved 8 to 19 times faster compared to stagnant (no rotation) conditions. Olivine dissolution was complete and stoichiometric (except for Ni release), air-seawater CO_2 exchange was not significantly rate limiting, and minimal particle fragmentation and secondary mineral formation were observed. Hence, we infer that olivine weathering was mainly enhanced via advective pore water flushing, which limits saturation effects at the grain scale. Overall, this study provides evidence that ambient physical stresses in coastal environments could enhance marine silicate weathering, which has implications for both the natural silicon cycle as well as the use of enhanced coastal weathering of silicates as a CDR technique.

2.1 Introduction

To constrain the adverse effects of climate change, the Paris Agreement foresees strong carbon dioxide (CO_2) emission cuts (UNFCC, 2015). Yet, such traditional mitigation in itself will not be enough, as climate stabilisation by 2100 also requires the implementation of active and large-scale carbon dioxide removal (CDR) from the atmosphere (Minx et al., 2018). A proposed technique for large-scale CDR is ocean alkalinization via coastal enhanced silicate weathering (CESW) (Hangx and Spiers, 2009; Schuiling and De Boer, 2011; Meysman and Montserrat, 2017; Minx et al., 2018). The underlying idea is that relatively coarsely ground particles (< 150 μm grains) of suitable silicate rock are distributed in coastal environments, and that the local dynamics within these systems (including currents, waves, biota) help to speed up the process of natural chemical weathering (Meysman and Montserrat, 2017). During chemical weathering of a silicate mineral, alkalinity is released (i.e. protons are consumed), which drives additional transfer of atmospheric CO_2 to the surface ocean followed by storage as bicarbonate (HCO_3^-) (Eq. 2.1 and 2.2 of Table 2.1) (Schuiling and Krijgsman, 2006; Meysman and Montserrat, 2017). Olivine ($Mg_xFe_{2-x}SiO_4$) has received most attention for CESW application, as it is globally abundant and combines a relatively fast weathering rate with a theoretically high CO_2 sequestration potential (Schuiling and Krijgsman, 2006; Hangx and Spiers, 2009; Köhler et al., 2010; Schuiling and De Boer, 2011; Hartmann et al., 2013; Taylor et al., 2016; Meysman and Montserrat, 2017; Montserrat et al., 2017). However, before CESW can be utilised as a CDR approach, two main uncertainties remain to be addressed, namely environmental impacts and the effectiveness of CO_2 sequestration (Meysman and Montserrat, 2017).

Table 2.1: Chemical reactions relevant for enhanced olivine weathering in seawater. The olivine dissolution, seawater acid-base equilibrium, and possible secondary mineral formation reactions are shown.
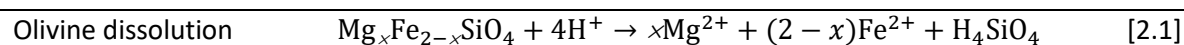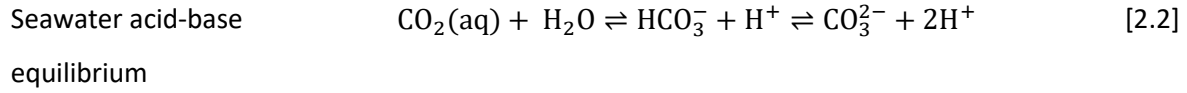
| Olivine dissolution | $Mg_xFe_{2-x}SiO_4 + 4H^+ \rightarrow xMg^{2+} + (2-x)Fe^{2+} + H_4SiO_4$ | [2.1] |

Seawater acid-base equilibrium	$CO_2(aq) + H_2O \rightleftharpoons HCO_3^- + H^+ \rightleftharpoons CO_3^{2-} + 2H^+$	[2.2]

	Potential secondary mineral formation	
Aragonite/calcite	$Ca^{2+} + 2HCO_3^- \rightarrow CaCO_3 + CO_2 + H_2O$	[2.3]
Fe^{2+} oxidation	$Fe^{2+} + 0.25O_2 + H^+ \rightarrow Fe^{3+} + 0.5H_2O$	[2.4]
Iron(III) hydroxide	$Fe^{3+} + 3H_2O \rightarrow Fe(OH)_3 + 3H^+$	[2.5]
Sepiolite	$2Mg^{2+} + 3H_4SiO_4 \rightarrow Mg_2Si_3O_{7.5}(OH)(H_2O)_3 + 4H^+ + 0.5H_2O$	[2.6]
Chrysotile	$3Mg^{2+} + 2H_4SiO_4 + H_2O \rightarrow Mg_3Si_2O_5(OH)_4 + 6H^+$	[2.7]
Talc	$3Mg^{2+} + 4H_4SiO_4 + 4H_2O \rightarrow Mg_3Si_4O_{10}(OH)_2 + 6H^+$	[2.8]
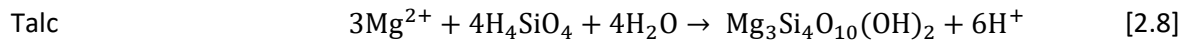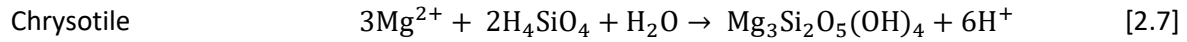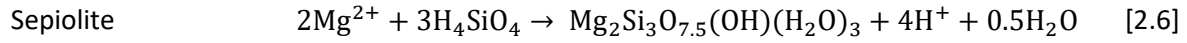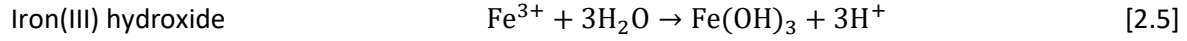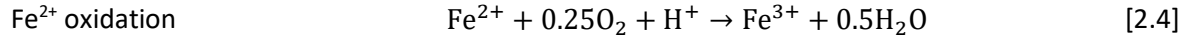
Environmental impacts of coastal enhanced olivine weathering can be geophysical, chemical and biological in nature. From a chemical perspective, the seawater composition can change through addition of dissolved products released during olivine dissolution, including total alkalinity (TA), dissolved inorganic carbon (DIC), Mg, Si, Fe, and potentially toxic Ni and Cr (Montserrat et al., 2017; Flipkens et al., 2021). However, some of these components could be retained within the seafloor, and at present, little experimental data is available on weathering products released under actual *in situ* conditions. Currently, most studies on the environmental impacts of coastal enhanced olivine weathering have been solely computational (Köhler et al., 2013; Hauck et al., 2016; Taylor et al., 2016; Bach et al., 2019; Flipkens et al., 2021), and only a limited number of experimental studies are available, mainly focused on the effects of increased seawater TA and pH (Cripps et al., 2013; Albright et al., 2016; Gim et al., 2018; Gore et al., 2019; Ren et al., 2021; Ferderer et al., 2022; Guo et al., 2022).

The CO_2 sequestration rate of olivine (R_{CO_2}) describes the amount of CO_2 that is removed from the atmosphere during olivine dissolution within a given application area per unit time (e.g. µmol CO_2 per m² of application area per second). It can be written as:

$$R_{CO_2} = \gamma_{CO_2}^{net} R_i = [(\delta DIC/\delta TA)_{pCO_2} \alpha_{TA} 4(1 - \varepsilon)] [k_i A (1 - \Omega)C] \qquad [2.9]$$

This expression features the net CO_2 sequestration efficiency $\gamma_{CO_2}^{net}$ (µmol CO_2 sequestered per µmol of olivine dissolved) and the olivine dissolution rate R_i (Meysman and Montserrat, 2017). The former describes the net amount of CO_2 that is sequestered upon dissolution of a given amount of olivine, and can be written as $\gamma_{CO_2}^{net} = (\delta DIC/\delta TA)_{pCO_2} \alpha_{TA} 4(1 - \varepsilon)$ (Moosdorf et al., 2014; Meysman and Montserrat, 2017; Fuhr et al., 2022). In this $(\delta DIC/\delta TA)_{pCO_2}$ represents the amount of atmospheric CO_2 sequestered upon the addition of 1 µmol of alkalinity to the coastal ocean (µmol DIC µmol^{-1} TA). This thermodynamic quantity is dependent on the partial CO_2 pressure (pCO_2) in the atmosphere, and the salinity, temperature, and chemical composition of the local seawater (Hofmann et al., 2009). Likewise, the dimensionless factor α_{TA} accounts for the alkalinity released during olivine dissolution. In the idealized case, 4 µmol of alkalinity are released per µmol of olivine (Eq. 2.1 and Eq. 2.9), though in practice, dissolution may not be complete (e.g. providing serpentine rather than dissolved silicate) or secondary reactions may scavenge alkalinity (Fuhr et al., 2022). The factor α_{TA} accounts for this and ranges between 0 and 1, where the maximum value 1 is attained at complete olivine dissolution and no secondary reactions removing alkalinity. The factor ε accounts for CO_2 emissions resulting from mining, grinding, and transportation (Moosdorf et al., 2014). The olivine dissolution rate R_i is in itself dependent on the olivine dissolution rate constant k_i (µmol olivine m^{-2} s^{-1}), the reactive surface area A (m^2 g^{-1}), the pore water saturation state Ω with respect to olivine, and the olivine loading C, which represents the amount of olivine per unit of area (g per m² of application area) (Eq. 2.9) (Meysman and Montserrat, 2017). The olivine loading depends on the amount of source rock deployed per unit area and the silicate rock composition (i.e. the olivine content).

To properly assess the feasibility of coastal enhanced silicate weathering, all the factors featured in Eq. 2.9 should be properly constrained under realistic application conditions. Olivine dissolution rate constants have been extensively investigated under idealized laboratory conditions (i.e. $\alpha_{TA} = 1$ and $\Omega = 0$), as reviewed previously (Pokrovsky and Schott, 2000b; Hangx and Spiers, 2009; Rimstidt et al., 2012; Oelkers et al., 2018). The

main factors influencing k_i are solution pH and temperature (Rimstidt et al., 2012; Oelkers et al., 2018). Note however that most data originate from laboratory experiments with idealized electrolyte solutions (e.g. NaCl solutions), rather than actual seawater. Currently, only three studies have investigated olivine dissolution in artificial or natural seawater (Montserrat et al., 2017; Rigopoulos et al., 2018; Fuhr et al., 2022).

Within actual CESW applications, olivine dissolution will occur on or in a coastal seabed, where biological and hydrodynamic processes could significantly affect olivine dissolution and associated CO_2 sequestration (Meysman and Montserrat, 2017). Overall, the effect of these natural biological and hydrodynamic processes on key parameters in Eq. 2.9, related to kinetics (k_i), effective alkalinity release (α_{TA}) and potential saturation effects (Ω), remain largely unexplored. Yet, this information is critically needed for relevant application conditions as to make accurate predictions on the CO_2 sequestration potential and environmental impacts of coastal enhanced olivine weathering (Meysman and Montserrat, 2017).

One important aspect is physical grain abrasion. In shallow marine systems, current and wave induced sediment saltation could potentially lead to significant grain abrasion and development of cracked surfaces (Schuiling and De Boer, 2011; Madhavaraju et al., 2021). This grain abrasion could prevent formation of cation depleted layers, which are known to slow down olivine dissolution (by decreasing k_i), or prevent secondary surface precipitates, which could scavenge alkalinity (by decreasing α_{TA}) (Meysman and Montserrat, 2017; Oelkers et al., 2018). Furthermore, grain fragmentation would increase the olivine surface area exposed to seawater (increasing A), and therefore enhance the olivine dissolution rate (see Eq. 2.9) (Oelkers et al., 2018). Once olivine becomes mixed in the surface sediment, saturation affects which slow down olivine dissolution could be prevented by advective pore water flushing (decreasing Ω) (Schuiling and De Boer, 2011; Meysman and Montserrat, 2017). Finally, waves and currents are essential for ocean mixing (Bates et al., 2001), which is needed to transport CO_2 deficient (i.e. TA rich) bottom water to the ocean surface for atmospheric CO_2 uptake and equilibration (Bach et

al., 2023). This CO_2 uptake constraints the seawater pH increase (and k_i decrease) as seen from Eq. 2.2.

Here, our aim was to investigate the effect of continuous grain collisions on the kinetics of olivine dissolution and metal ion release kinetics in natural seawater by conducting a long-term weathering experiment (70 days) with sequential sampling. We hypothesized that increased grain collisions would result in enhanced olivine dissolution, and so currents and waves could enhance olivine dissolution in CESW via grain abrasion induced during bedload transport.

2.2 Material and Methods

2.2.1 Agitation experiments

A 70-day experiment was conducted, in which a mixture of dunite sand and natural seawater was continuously agitated in commercially available rotary tumblers ("Rock Tumbler", Shandong Qiyang Tools Co.,Ltd) (Figure 2.1). The experiment was conducted in a darkened and temperature-controlled (15 °C) room under ambient pressure (~1 atm) and ambient CO_2 levels (~415 ppm). VANGUARD refractory grade dunite sand was obtained from the Sibelco mine in Åheim (Norway). This dunite sand is composed of 90.54 wt% olivine, of which 93.4% is forsterite (Mg_2SiO_4) and 6.6% is fayalite (Fe_2SiO_4) (Table 2.2; see supplementary section B.1.1 and B.1.2 for characterization procedure), and the experiments using this sand will be further referred to as "olivine treatments". Natural seawater (salinity 33 ± 0.3 ‰) was collected two weeks prior to the start of the experiment from the North Sea coast (Sea Life Centre, Blankenberge, Belgium). Seawater was filtered through 0.2 μm pore-size cellulose acetate filters (OE66, Whatman) and stored in 20 L high density polyethylene (HDPE) containers in the dark at 15 °C until further use. Before experimental use, all equipment was immersed in 2% V/V HCl (VWR International) for at least 24 h and subsequently thoroughly rinsed with ultrapure Milli-Q (MQ) water (Merck).

Table 2.2: Characterization of the forsterite dunite sand used in the experiment. Mineral composition (based on TIMA high-resolution mapping), elemental composition (ICP-OES analysis), and textural composition, including grain size distribution (laser diffraction particle size analysis), specific surface area (geometric and Brunauer-Emmett-Teller (B.E.T.)), and mineral density are given. Details about the geochemical analyses of the olivine are given in supplementary section B.1.1 and B.1.2. Note that oxygen makes up the remaining approximately 44 wt% of the dunite elemental composition.

Mineral composition	Unit	Value
Olivine (Fo$_{93}$)	wt%	90.54
Enstatite	"	6.02
Diopside	"	0.86
Clinochlore	"	0.85
Biotite	"	0.15
Pentlandite	"	0.05
Pyrope	"	0.02
Quartz	"	0.01
Others	"	1.48
Textural composition		
D10	μm	84 ± 1
D20	μm	99 ± 1
D50	μm	136 ± 1
D80	μm	186 ± 2
D90	μm	216 ± 2
Geometric specific surface area	m^2 g^{-1}	0.0161 ± 0.002
B.E.T. specific surface area	m^2 g^{-1}	0.9 ± 0.1
Mineral density	g cm^{-3}	3.3
Elemental composition		
Mg	wt%	30.4
Si	"	20.0
Fe	"	5.0

Cr	"	0.30
Ni	"	0.25
Al	"	0.081
Mn	"	0.068
K	"	0.025
Ca	"	0.018
Co	"	0.011
Ti	"	0.0060
Zn	"	0.0066

At the start of the experiment, HDPE bottles (2 L volume, Lamaplast, VWR International) were filled with a fixed mass of dunite sand (149.53 ± 0.01 g) and fixed amount of filtered natural seawater (718.2 ± 0.1 g or 700.0 ± 0.1 ml). This resulted in a ~1 cm of water-saturated sediment layer (~0.49 porosity) with a ~3.2 cm layer of overlying water on top (Figure 2.1). This ~1 cm layer of mobile sediment mimics a rather intense bedload regime (Pruszak and Zeidler, 1994). Subsequently, bottles were inserted in the rock tumblers and rotated at a constant speed of 18 or 54 rotations per minute (RPM). This rotation speed falls within the range of natural gravity wave frequencies (2 to 60 waves per minute) (Toffoli and Bitner-Gregersen, 2017). These treatments will be respectively referred to as the "low rotation" and "high rotation" treatments. In addition, a "stagnant" treatment with olivine but no agitation (0 RPM) and a rotation treatment with only seawater (54 RPM; referred to as "seawater") were used as controls. Olivine treatments were conducted in triplicate and the seawater control in duplicate. A small hole was made in the bottle cap to allow gas exchange with the atmosphere, so that O_2 and CO_2 concentrations could remain at atmospheric levels.
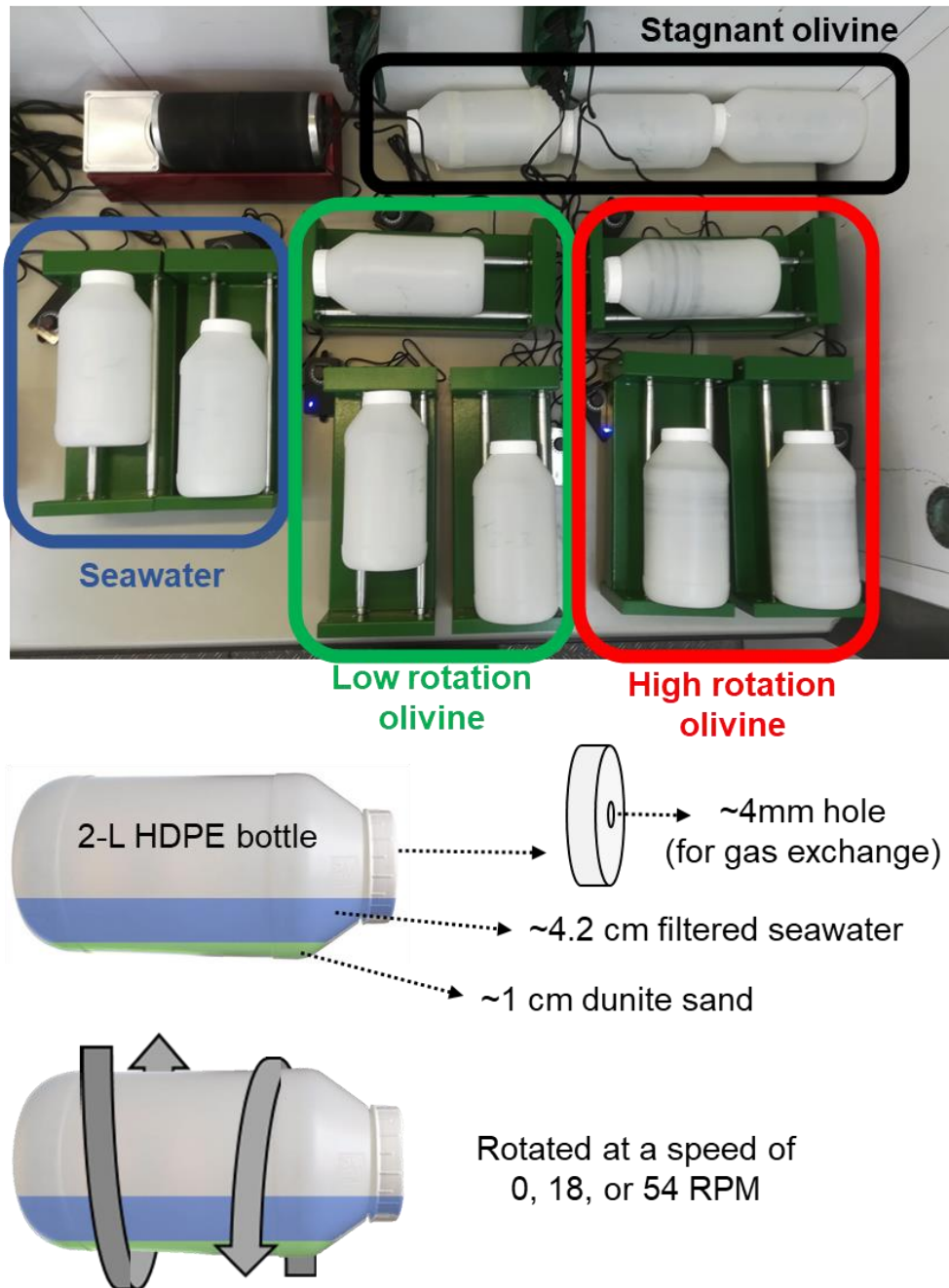
Figure 2.1: Experimental set-up consisting of 11 bottles filled with a fixed amount of dunite sand and a fixed volume of filtered natural seawater. Bottles are rotated in commercial rock tumblers. Olivine treatments were conducted in triplicate and rotated at a rotation speed of 0 (stagnant), 18 (low rotation), or 54 (high rotation) rotations per minute (RPM). A seawater control without olivine was set up in duplicate and rotated at

54 RPM. A hole in the bottle cap allows gas exchange with the atmosphere during incubation.

To determine the olivine dissolution rate as a function of time, consecutive accumulation sessions were performed, which each lasted one week. At the end of each session, water samples were taken from the overlying water of each bottle and the remaining water was replaced (so a new accumulation session could start). Water samples were analysed in duplicate for conductivity, pH, dissolved inorganic carbon (DIC), total alkalinity (TA), grain size distribution of suspended sediment, as well as dissolved metal concentrations. Additionally, sediment was collected at the start and end of the experiment to examine grain size distribution, secondary mineral formation, grain surface dissolution features, and to quantify total extractable metal concentrations.

The weekly water sampling was conducted according to the following procedure. Immediately after removing the bottle from the rock tumblers, 50 mL of seawater was collected with a 20 mL syringe and filtered (0.2 µm pore size, Chromafil XTRA PES-20/25, Macherey-Nagel) for DIC analysis. This filtered seawater was stored in 50 mL Falcon tubes without headspace at 4 °C until further analysis within a week. Subsequently, the HDPE bottle was briefly put on a magnetic stirrer to create a homogeneous suspension. This was done to take standardized samples for the analysis of suspended sediment (and hence to verify whether abrasion led to small particle fragments). After allowing the majority of the sediment to settle for 20 seconds, either 140 or 220 mL (depending on the sample turbidity) of the supernatant was transferred to a 250 mL glass beaker. Water samples were always collected while the HDPE bottle was positioned on a balance (Sartorius CP4202S) to accurately determine the mass of seawater removal.

Subsequently, while stirring the supernatant solution in the glass beaker, a 40 ml sample was passed through a 0.2 µm pore size filter (OE66, Whatman) for dissolved metal analysis. Next, a volume of 20 ml or 100 ml (depending on the sample turbidity) of the unfiltered sample was collected for suspended sediment particle size analysis.

Afterwards, the stirring was halted and the solution in the glass beaker was allowed to settle for 10 minutes before an unfiltered 20 ml seawater sample for pH and conductivity measurements was taken. Finally, the remaining 60 ml of seawater was filtered with 0.2 µm PES membrane filters and stored at 4 °C for TA analysis the subsequent day.

After sampling, the remaining seawater in the HDPE bottle (~400 mL) was gently removed with minimal loss of sediment (as discussed in supplementary section B.2.4). The mass of the HDPE bottle was again determined to assess seawater removal. Subsequently, new filtered seawater was added to a total water volume of 700 ml, and HDPE bottles were put back onto the rock tumblers. This way, a new accumulation session could be started.

2.2.2 Geochemical solute analyses

Seawater salinity was determined using a CDC401 conductivity electrode coupled to a HQ30D portable multimeter (Hach). Calibration of the electrode was performed with a NIST conductivity standard (12880 µS/cm; VWR International) on each sampling day. pH was measured with a FiveEasy pH meter and LE438 pH electrode (Mettler Toledo). The pH electrode was calibrated before each use with three NIST buffers (pH 4.00, 7.00, and 10.01). Furthermore, pH of a TRIS (2-amino-2-hydroxy-1,3-propanediol) and AMP (2-aminopyridine) buffer, prepared according to the procedure by Dickson et al. (2007), were measured to convert pH data to the total hydrogen ion pH scale (Dickson et al., 2007).

The DIC concentration was determined with a Total Organic Carbon Analyzer (Shimadzu TOC-VCPH). For quality control, an ultrapure MQ water sample and 50 mg C L^{-1} TIC standard (Bernd Kraft) were included at the start and end of the analysis. The relative standard deviation (RSD) was better than 7.1% for all samples. Total alkalinity (TA) was analysed via an open cell potentiometric titration with 0.1 M HCl using an automated titrator setup (888 Titrando, Metrohm). The TA was determined from the titrant volume and electromotive force measurement by the pH electrode using a non-linear least-squares method according to Dickson et al. (2007) with RSD values smaller than 1.6%.

Seawater samples for dissolved metal analysis were acidified with TraceMetal™ Grade 67-69% nitric acid (Fisher Scientific) to a final acid concentration of 1.4% V/V and stored at -20 °C to minimize adsorption before further processing. Samples were diluted 20 times or 100 times (only for Na) with 3% V/V HNO_3 to minimize matrix effects during analysis. Element concentrations were analysed by HR-ICP-MS (Element XR, Thermo Scientific). For quality control, NIST SRM 1640a certified reference samples (Merck) and procedural blanks (3% V/V HNO_3) were included in the analysis. A maximum RSD of 5% was allowed for the measurements.

2.2.3 Solid phase analysis

Grain size distribution was determined for the suspended sediment during weekly sampling (see section 2.2.1) as well as for the bulk sediment at the start and end of the experiment. Suspended sediment was not pre-treated before analysis. Recovered bulk olivine sediment was gently rinsed with MQ water and dried at 60 °C for three days. Grain size distribution was determined with a laser diffraction particle size analyzer (Mastersizer 2000, Malvern Panalytical) according to standard operating procedures. Measurement RSD was lower than 16% for all grain size classes.

Total inorganic carbon (TIC) of 66 ± 9 mg fresh and weathered olivine samples was determined in triplicate with an elemental analyzer (Flash 2000 CN Soil Analyser, Interscience). Prior to analysis, samples were dried at 105 °C for 12 h and subsequently combusted in a muffle furnace at 375 °C for 17 h to remove the organic carbon (Wang et al., 2012). Since samples were homogeneous, no sample grinding was required. Results are expressed as a function of the sample dry weight.

2.2.4 Grain surface imaging

Grain morphology, magnesium to silicon (Mg/Si) ratios at the grain surface, and the presence of secondary minerals were investigated with a Phenom ProX scanning electron microscope (SEM) with energy dispersive spectrometer (EDS). To this end, dry olivine grains were fixed on aluminium (Al) pin stubs with double sided carbon tape. The atomic

Mg and Si percentage was determined for 5 spots on the surface of 20 fresh and 10 weathered olivine grains with the accelerating voltage set to 15 kV. Microstructural changes and potential secondary mineral precipitation in the olivine grains were investigated using a Tescan MIRA3 SEM equipped with a Field Emission Gun (FEG) and EDS capability. Samples were fixed on an Al pin stub with double sided carbon tape to study surface features or embedded in an epoxy resin (EpoFix Resin and EpoFix Hardener, Struers), polished and carbon coated to study cross sections. For polishing, sand wetted with deionized water was first ground by hand on silicon carbide grinding paper (grit 500, 1000 and 2400) and subsequently polished on polishing cloths with Tegramin (Struers) using a diamond solution (DiaDuo-2, 6 μm, 3 μm, and 1 μm, Struers). Polished sand was rinsed with deionized water and dried before analysis. The polished cross sections allow for investigating microstructural changes inside an olivine grain.

2.2.5 Olivine dissolution and CO₂ sequestration rate calculations

Olivine dissolution was tracked in weekly accumulation sessions, during which weathering products could accumulate in the overlying seawater. Concentrations of specific compounds C_i^k (μmol L⁻¹, with i = TA, DIC, DSi, DNi) were measured at the end time point t_k of each session k ($C_i^k = C_i(t_k)$). The accumulation ΔN_i^k (expressed in μmol) of a given compound i within a given session k is given by the mass balance expression

$$\Delta N_i^k = V_{\mathrm{OW}}(t_{k-1})\big(C_i(t_k) - C_i^{\mathrm{ASW\ control}}(t_k)\big) + V_{\mathrm{PW}}(t_{k-1})\big(C_i(t_k) - C_i(t_{k-1})\big) \qquad [2.10]$$

Here we assume that during water renewal, the pore water retains the concentration from the previous session $C_i(t_{k-1})$, while the overlying water is replaced with new stock solution. Furthermore, $C_i^{\mathrm{ASW\ control}}(t_k)$ represents the concentration in the seawater control at timepoint t_k. The quantity $V_{\mathrm{OW}}(t_{k-1})$ represents the volume (expressed in L) of stock seawater solution added at the start of a new session and is determined from the added seawater mass m_{OW} and the seawater density ρ_{SW} ($V_{\mathrm{OW}} = m_{\mathrm{OW}}/\rho_{\mathrm{SW}}$). The volume of pore water that remained in the sediment $V_{\mathrm{PW}}(t_{k-1})$ was calculated from the mass of

74

the filled (m_{BF}) and empty (m_{BE}) bottle, the initially added olivine mass ($m_{olivine}$), and the seawater density according to

$$V_{\mathrm{PW}}(t_{k-1}) = \frac{m_{\mathrm{BF}}(t_{k-1}) - m_{\mathrm{BE}} - m_{\mathrm{olivine}}}{\rho_{\mathrm{SW}}}$$

[2.11]

The accumulation ΔN_i^k was subsequently normalized to the molar amount of olivine via

$$\Delta \widehat{N}_i^k = \frac{\Delta N_i^k}{\frac{m_{\mathrm{dunite}} \varphi_{\mathrm{olivine}}}{M_{\mathrm{olivine}}}}$$

[2.12]

Where $\Delta \widehat{N}_i^k$ is the normalized accumulation (µmol mol^{-1} olivine), m_{dunite} the mass of dunite sand (expressed in g), $\varphi_{olivine}$ its olivine fraction (0.9054, Table 2.2), and $M_{olivine}$ the molar mass of the Fo$_{93}$ olivine $M_{olivine}$ (144.88 g mol^{-1}).

The pH excursion $\Delta pH(t_k)$ is defined as the pH difference with reference to the pH of the added seawater pH_{SW}

$$\Delta pH(t_k) = pH(t_k) - pH_{\mathrm{SW}}$$

[2.13]

Using expression [10], we can calculate the compound specific olivine dissolution rate (expressed in µmol of olivine s^{-1}) via

$$R_i(t_k) = \frac{\Delta N_i^k}{v_i(t_k - t_{k-1})}$$

[2.14]

where v_i represents the theoretical stoichiometric coefficient (expressed in µmol µmol^{-1} olivine) for the specific compound in the olivine sand that we used ($v_{TA} = 3.73$, $v_{DIC} = 3.06$, $v_{DSi} = 1$, and $v_{DNi} = 0.0061$; Section B.1.2 provides details on the derivation of these stoichiometric coefficients). The session time ($t_k - t_{k-1}$) was equal to 7 days (604800 s). In general, the olivine dissolution rate can be described by the kinetic rate expression

$$R_i(t_k) = m_{\text{olivine}} k_i(t_k) A(t_k)(1 - \Omega(t_k))$$

[2.15]

In this, m_{olivine} represents the initial mass of olivine derived from the mass of dunite sand and its olivine fraction ($m_{\text{olivine}} = m_{\text{dunite}}\varphi_{\text{olivine}}$), $k_i(t_k)$ is the dissolution rate constant (µmol olivine m^{-2} s^{-1}), A is the specific surface area of the mineral grains (m² g^{-1}) and $\Omega(t_k)$ is the mineral saturation state (dimensionless). Using equation [15], we calculated k_i values from R_i values, assuming that solutions were always far from equilibrium ($\Omega(t_k)$ << 1) and using the geometric surface area A_{GEO} (0.0161 m² g^{-1}) of fresh olivine as calculated from the measured grain size distribution (see Supplementary Section B.1.3). Experimentally determined k_i values were compared to those predicted by the empirical rate expression for the olivine dissolution rate constant (mol m^{-2} s^{-1}) given by Rimstidt et al. (2012)

$$k_{\text{olivine}} = 10^{4.07 - 0.256pH(t) - \frac{3465}{T}}$$

[2.16]

In which *pH(t)* is the pH of the environment at a given time and *T* is the temperature (expressed in K).

The CO_2 sequestration rate (expressed in µmol CO_2 d^{-1}) can be calculated from the alkalinity release rate via

$$R_{CO_2} = \gamma_{CO_2} R_{TA}$$

[2.17]

In this, γ_{CO_2} denotes the CO_2 sequestration efficiency, i.e., the molar amount of CO_2 sequestered (expressed in µmol) per µmol of TA released during olivine dissolution. The CO_2 sequestration efficiency can be directly derived from the accumulation data of DIC and TA as

$$\gamma_{CO_2} = \Delta N_{\text{DIC}}^k / \Delta N_{\text{TA}}^k$$

[2.18]

For comparison, the CO_2 sequestration efficiency was also theoretically calculated from the applicable carbonate system relation in seawater, i.e. as $\gamma_{CO_2} = (\partial DIC/\partial TA)_{pCO_2=420\,ppm}$ at the incubation temperature (15 °C) and salinity (33 ‰) using the R package AquaEnv (Hofmann et al., 2010).

Finally, the seawater pCO_2 values were calculated using the carb function of the seacarb package in R with measured seawater pH and TA as input values. Additionally, seawater salinity, temperature, hydrostatic pressure (0 bar), and dissolved Si concentrations were taken into account and other settings were kept default.

2.2.6 Saturation state calculations

For a given mineral, the saturation state Ω is the ratio of the actual ion activity product and the solubility product. Mineral $\Omega(t_k)$ values were calculated in PHREEQC Interactive (version 3.7.3-15968) using the thermodynamic data from the LLNL database (Parkhurst and Appelo, 2013). The saturation index was subsequently calculated as $SI(t_k)$ = log10($\Omega(t_k)$) (undersaturation occurs at $SI(t_k)$ < 0, supersaturation at $SI(t_k)$ > 0). Weekly measured values of seawater temperature, TA, pH, and concentrations of major (Cl, Na, Mg, SO_4, K, Ca) and minor and trace elements (Ni, Cr, Mn, Fe, Cu, Zn, Pb, Cd, Si) were used as input data for the calculation of $\Omega(t_k)$. Concentrations of Cl and SO_4 were not analytically determined but derived from the chemical composition of natural seawater (fixed ratio with measured Na concentrations) (Hem, 1985).

2.2.7 Modelling olivine dissolution and secondary mineral formation

Rates of olivine dissolution and secondary mineral precipitation were modelled with Wolfram Mathematica using the kinetic box model presented by Fuhr et al. (2022). This model implements olivine dissolution via the rate equation provided by Rimstidt et al. (2012), and accounts for precipitation of the secondary phases aragonite/calcite, sepiolite, chrysotile, talc and $Fe(OH)_3$ through saturation state calculations. The model was adapted to the current conditions accounting for the rock water ratio, flask and sample volumes used in the experimental set-up.

The exchange of the entire water volume after each accumulation session may have led to the removal of small colloids, thus diminishing the available nuclei for formation of secondary mineral phases. For secondary precipitation reactions, the pre-factor $\varepsilon_{\text{pre1}_i}$ that defines when and how fast precipitation of mineral i starts in equation (3) by Fuhr et al. (2022) was changed to:

$$\varepsilon_{\text{pre1}_i} = k_{\text{pre}_i}\left(1 - \frac{1}{1+e^{\frac{t-\alpha_i}{\beta_i}}}\right)\left(2^{-k2_{\text{pre}_i}t}\right) \qquad [2.19]$$

Where k_{pre_i} is a kinetic rate constant, α_i defines the time delay of the precipitation and β_i steers the speed of the precipitation reaction. The tuning variable $k2_{\text{pre}_i}$ was added to the original equation (4) by Fuhr et al. (2022) to simulate a decrease in precipitation rates which can occur after the exchange of the water volume. Thus, with the combination of the two terms the model can simulate secondary mineral precipitation over a certain period of time. The other equations were used as in the original (see Fuhr et al. (2022) and Supplementary Section B.1.5 for details). The constants used for the model calculations are listed in Supplementary Table B.6.

2.2.8 Statistical analyses

All data are reported as mean and range values. Figures were constructed in GraphPad Prism version 9.4.0 for Windows. Statistical analyses were conducted in RStudio (version 1.2.5001) using R version 4.2.1 (R Core Team, 2022). To avoid the assumption of normally distributed data based on few replicate measurements, a non-parametric Kruskal-Wallis ANOVA was used to investigate differences in Mg/Si ratio, A_{GEO}, TIC, and olivine weight loss among treatments. Equal variance of residuals (i.e. homoscedasticity) was assessed visually with residual plots and statistically with Levene's test. Post hoc multiple comparisons were performed with the Dunn's multiple comparisons test. Adjustment of p-values was done using Benjamini-Hochberg's method. Results were considered statistically significant when p-value < 0.05.

2.3 Results

2.3.1 Olivine dissolution in seawater under agitated conditions

Our results show a clear impact of continuous tumbling on the olivine dissolution rate, as shown by the accumulation of the two main weathering products DSi and TA (Figure 2.2). In the stagnant treatment, significant DSi and TA accumulations were only observed during the first week (Figure 2.2A and 2.2C). In contrast, weekly accumulation values $\Delta \widehat{N}_i^k$ for DSi and TA were significantly higher in the rotation treatments compared to the stagnant treatment on most sampling days (Figure 2.2A – 2.2D). At day 70, cumulative TA accumulation was respectively 5.3 and 6.8 times higher in the low and high rotation treatment compared to the stagnant treatment (Figure 2.2B). Similarly, continuous rotation enhanced DSi accumulation by a factor of 4 to 5.6 compared to stagnant conditions (Figure 2.2D).

The olivine dissolution rate showed a marked dependence on time. Immediately after adding seawater to olivine, we already observed a notable increase in DSi and TA (Figure 2.2A and 2.2C). Moreover, at the first consecutive sampling point (day 7), accumulations of TA and DSi were considerably higher compared to most other sampling days (Figure 2.2A and 2.2C). After two weeks, TA and DSi accumulations remained relatively constant in time in the low rotation treatment (Figure 2.2A and 2.2C), thus providing linear cumulative curves (Figure 2.2B and 2.2D). In the high rotation treatment, there was a decreasing trend in TA and DSi accumulations (Figure 2.2A and 2.2C), which resulted in a flattening of the cumulative curve near the end of the experiment (Figure 2.2B, 2.2D). Negative accumulation values are the result of uncertain pore water reaction product concentrations (Eq. 2.10) and possible phyllosilicate formation (Section 2.3.2).

DSi and TA accumulations were strongly correlated, thus suggesting stoichiometric olivine dissolution (Figure 2.2E). Theoretically, 4 moles of TA and 1 mole of DSi should accumulate upon complete dissolution of 1 mole of forsterite olivine in the absence of secondary mineral formation (Table 2.1). However, in addition to Mg-bearing forsterite,

olivine contains a fraction of Fe-bearing fayalite (here 6.6%). Under oxic conditions, the Fe^{2+} released during dissolution of fayalite will be oxidized, which reduces the TA/DSi release ratio to 3.73 for the experimental olivine (dashed line in Figure 2.2E; Supplementary section B.1.2). While there is some variability, this expected relationship compares well with the experimentally observed TA/DSi ratio (slope = 3.43), thus suggesting stoichiometric olivine dissolution for TA and DSi.
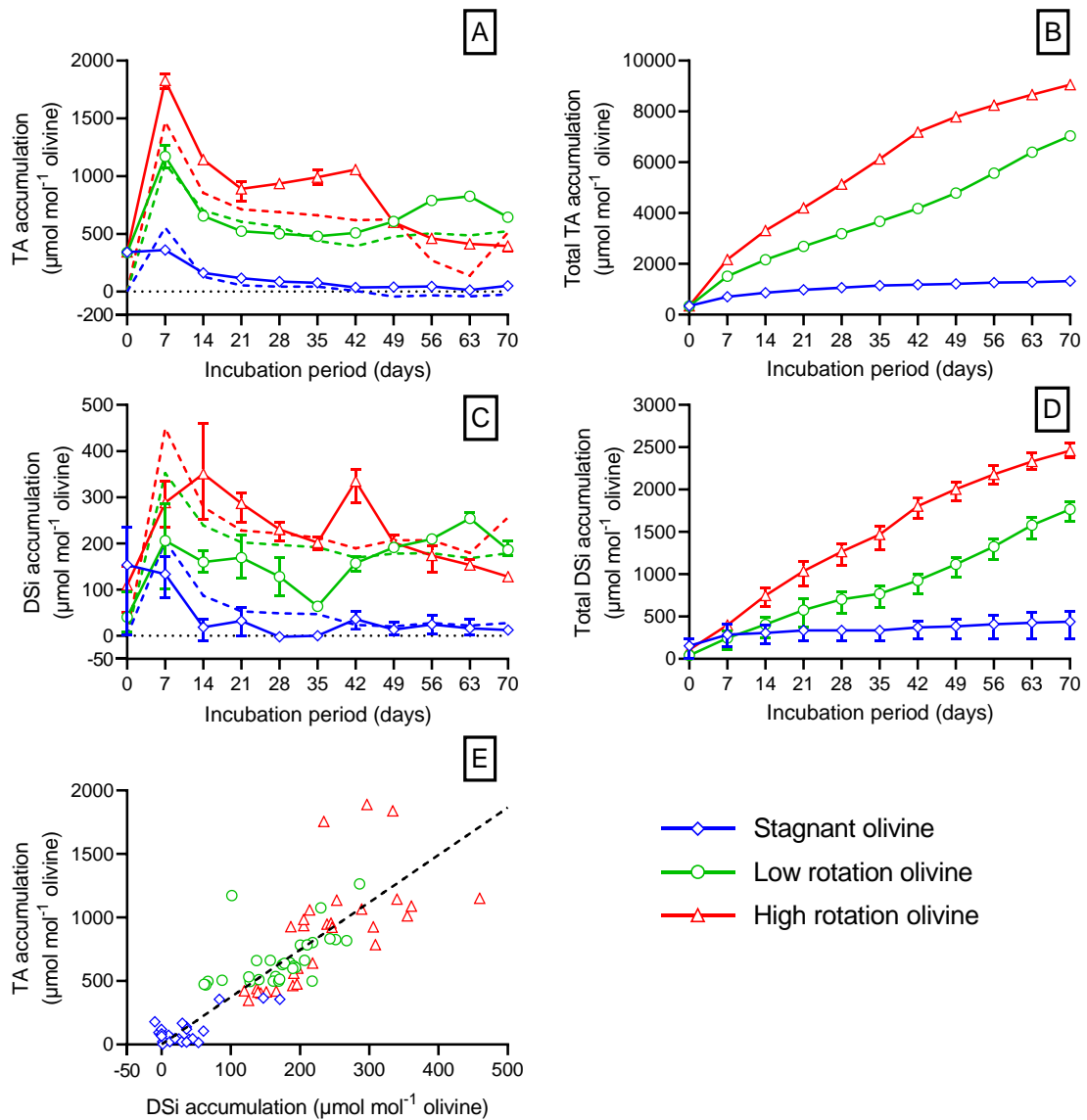
Figure 2.2: Weekly (A, C) and cumulative (B, D) accumulation of (A, B) total alkalinity (TA) and (C, D) dissolved (< 0.2 μm) silicon (DSi) in natural filtered (<0.2 μm) seawater. Mean values with range (N = 3) are shown. (E) The theoretical (black dashed line, TA/DSi ratio = 3.73) and observed relationship between TA accumulation (μmol) and DSi accumulation (μmol) is given. (A, C) Dashed lines for TA and DSi accumulation represent kinetic box model results.

2.3.2 Potential of secondary mineral formation

The pH response is fully in line with the expected response of the seawater carbonate system towards TA changes (i.e. higher TA induces higher pH at constant pCO$_2$). Immediately after olivine addition, the pH of the overlying seawater became significantly elevated ($\Delta pH(t_k = 0)$ = 0.19 – 0.24) in all olivine treatments compared to the seawater control (Figure 2.3A). At subsequent sampling times, the observed pH excursion $\Delta pH(t_k)$ gradually decreased in the stagnant treatment (Figure 2.3A). For the low rotation treatment, $\Delta pH(t_k)$ varied between 0.14 and 0.39 with peak values on day 7 and day 63. For the high rotation treatment, $\Delta pH(t_k)$ varied between 0.09 and 0.35, and showed a peak value on day 7 and a decreasing trend on later sampling days (Figure 2.3A).

Changes in seawater chemistry during olivine dissolution can alter saturation indices of various mineral phases (e.g. aragonite and phyllosilicates) (Griffioen, 2017; Fuhr et al., 2022). The aragonite $SI(t_k)$ was positive for all treatments throughout the experiment (Figure 2.3B). Little variation in aragonite SI was observed in the seawater control ($SI(t_k)$ = 0.29 – 0.42 or $\Omega(t_k)$ = 1.9 – 2.6). Immediately after the start, the stagnant olivine treatment showed a marked increase in aragonite $SI(t_k)$ ($SI(t_k) \approx 0.58$ or $\Omega(t_k) \approx 3.8$) compared to the seawater control (Figure 2.3B), after which it gradually decreased to the seawater control values (Figure 2.3B). In the low rotation and high rotation treatments, the aragonite $SI(t_k)$ also showed a steep initial increase, but remained elevated and varied between 0.49 and 0.90 ($\Omega(t_k)$ = 3.1 to 8.0) (Figure 2.3B).

The $SI(t_k)$ for forsterite (Mg_2SiO_4) remained relatively constant and was negative throughout the experiment, thus indicating conditions that promote olivine dissolution (Figure 2.3D). Between day 14 and 35, DSi concentrations dropped below the detection limit (0.36 µmol L^{-1}) thus providing anomalous $SI(t_k)$ values in the controls. The $SI(t_k)$ for amorphous ferrihydrite was negative for the seawater control and close to 0 for the olivine treatments throughout the experiment (Figure 2.3C). However, these $SI(t_k)$ values should be interpreted with caution since high dissolved Fe concentration in olivine treatments (Supplementary Figure B.3D) suggest sampling of nanoparticulate $Fe(OH)_3$. The $SI(t_k)$ for sepiolite was relatively constant in the rotation treatments and remained at an elevated values ($SI(t_k)$ = 1.5 to 7.8 or $\Omega(t_k)$ = 32 to 6.3E+07) throughout the experiment (Figure 2.3E), thus signifying the potential of sepiolite formation. The $SI(t_k)$ values of talc ($Mg_3Si_4O_{10}(OH)_2$), chrysotile ($Mg_3Si_2O_5(OH)_4$), calcite ($CaCO_3$) and amorphous silica ($SiO_2(am)$) are shown in Supplementary Figure B.2.1.
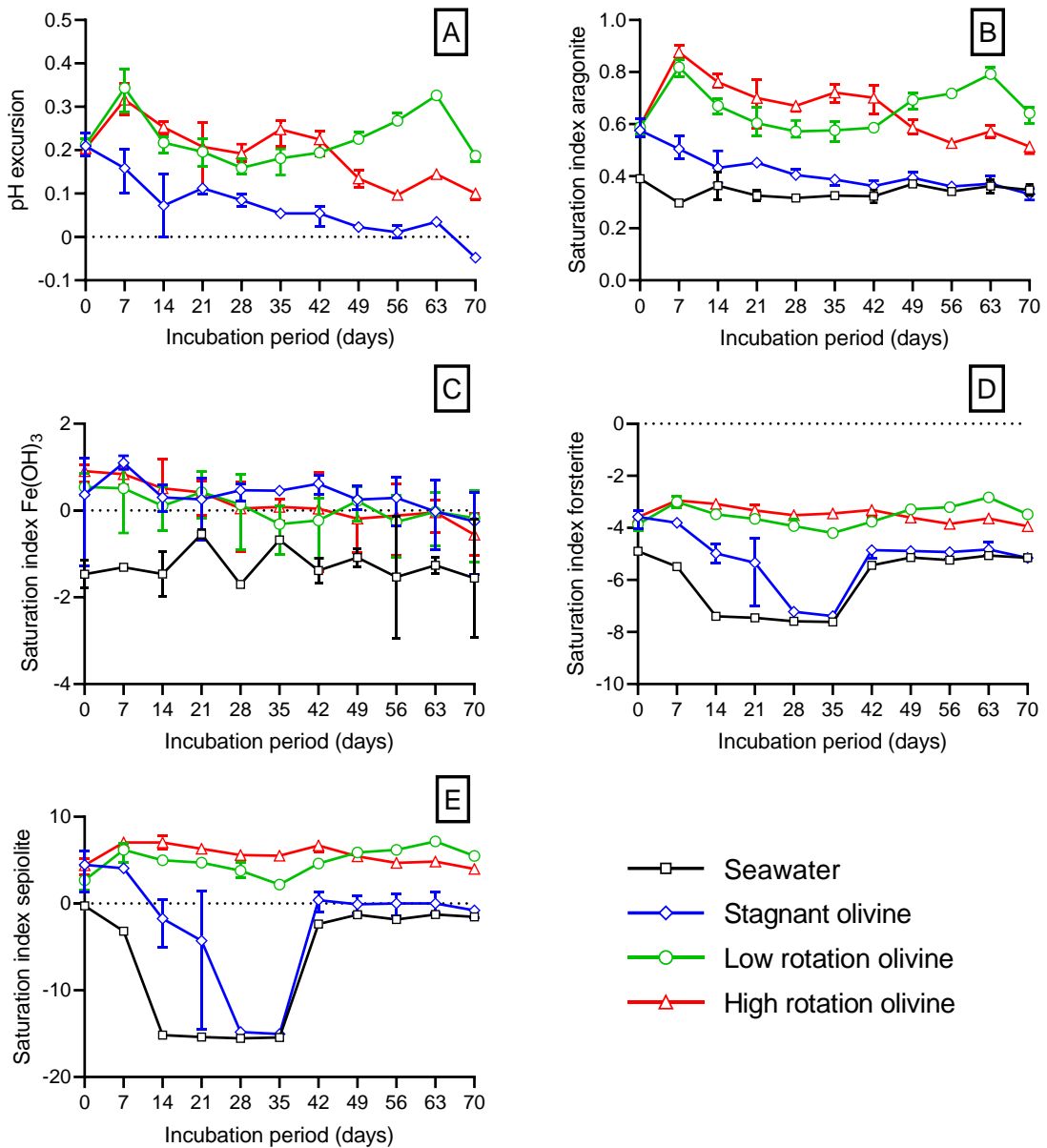
Figure 2.3: Weekly excursion of (A) seawater pH, and temporal evolution of (B) aragonite, (C) Fe(OH)$_3$, (D) forsterite (Mg$_2$SiO$_4$), and (E) sepiolite saturation indices calculated from experimental data in PHREEQC V3 using the LNLL database. Mean values with range for olivine treatments (N = 3) and seawater control (N = 2) are shown.

2.3.3 Grain scale dissolution features

The olivine surface Mg/Si ratio was analysed to assess the presence of cation depleted layers which could significantly reduce mineral reactivity (Meysman and Montserrat, 2017; Oelkers et al., 2018). The Mg/Si ratio on individual olivine grains showed considerable variation, ranging between 1.0 and 3.1 in all olivine treatments (Figure 2.4A). The median Mg/Si ratio was significantly higher in the stagnant (2.26, $P < 0.001$), and high rotation (2.25, $P = 0.0071$) treatment, but not the low rotation treatment (2.16, $P = 0.23$) compared to fresh olivine (2.12) (Figure 2.4A). It is important to note that differences in median Mg/Si ratios were relatively small, even though they were found to be statistically significant. Fresh olivine grains analysed via SEM-EDX showed smooth/featureless grain surfaces, angular edges, and a large variation in grain shapes (ranging from rod-like to spherical) (Supplementary Figure B.8A – C). The fresh olivine also showed a small amount of alteration products (possibly hydrous minerals like serpentine, chlorite, or amphibole), which likely developed during natural long-term weathering before the dunite was mined (Supplementary Figure B.9) (Jung et al., 2020; Jung et al., 2021). Some of the fresh olivine grains exhibited cracks and damaged grain edges, which may originate from the mechanical crushing process during dunite sand production (Supplementary Figure B.9). Olivine grains that were retrieved from the rotation treatments at the end of the experiment showed an increase in surface dissolution features (e.g. etch pits and striation-like features) compared to fresh and stagnant olivine (Figure 2.4C – E and Supplementary Figure B.8 and B.9). Additionally, damaged grain edges and a higher abundancy of microcracks were observed inside some of the weathered olivine grains compared to fresh olivine grains (Figure 4B and Supplementary Figure B.9). Still, we could not establish a significant statistical difference in microcrack frequency or size between stagnant and rotation treatments (Supplementary Figure B.9).
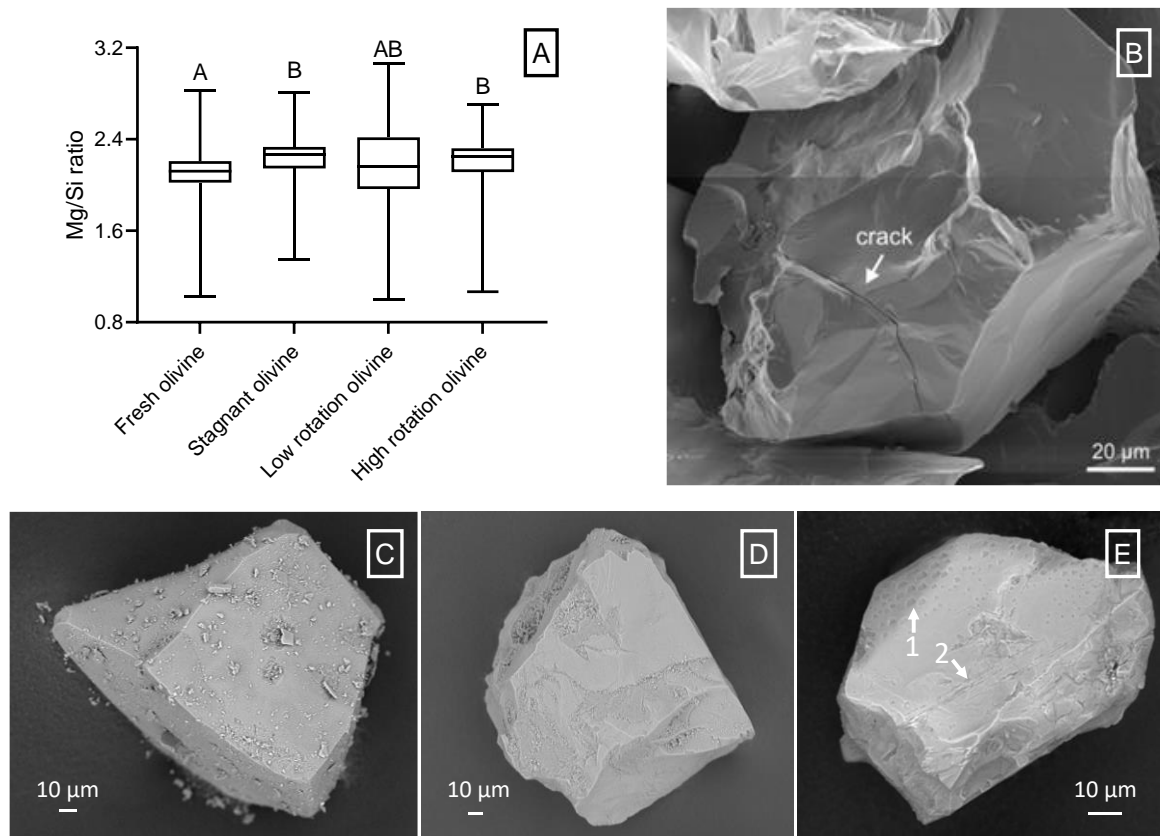
Figure 2.4: (A) Box and whisker plots of the magnesium to silicon (Mg/Si) ratio on the surface of fresh (N = 100 spots) and experimental olivine grains (N = 50 spots), and scanning electron microscopy (SEM) images of (B) a cracked olivine grain of the high rotation treatment, olivine grain of the (C) fresh, (D) stagnant, and (E) high rotation treatment. Note the presence of small adhering particles on fresh olivine (C) and etch pits (E-1) and striation-like features (E-2) on weathered olivine. Whiskers in (A) represent the minimum and maximum Mg/Si ratio.

SEM images of fresh olivine grains revealed the presence of small ($\leq$ 10 µm) adhering olivine particles on larger grains (Figure 2.4C and 2.5A). These small particles were absent on olivine recovered from stagnant and rotation treatments at the end of the experiment (Figure 2.4D-E and 2.5A). The median (*D50*) and 90th percentile (*D90*) grain diameter decreased significantly in the stagnant (*D50* = 133 µm, *P* = 0.049, *D90* = 210 µm, *P* =

0.010) and low rotation ($D50$ = 134 µm, P = 0.024, $D90$ = 210 µm, P = 0.0070) treatments compared to fresh olivine ($D50$ = 136 µm, $D90$ = 216 µm). For the 10th percentile grain diameter ($D10$), no significant differences among treatments were found (H(3) = 3.74, P = 0.29). No significant difference in $D10$, $D50$, or $D90$ was observed among recovered experimental olivine samples (Figure 2.5A).

Over time, a shift towards larger suspended sediment particles was observed in the high rotation treatment (Figure 2.5B). SEM-EDX analysis showed that suspended particles were mainly olivine (Figure 2.5C). Secondary minerals were not found, although they were possibly present in minor amounts given the supersaturated conditions (Figure 2.3). At day 0, water samples taken after stirring and subsequent settling for 20 s were dominated by olivine particles smaller than 16 µm (Figure 2.5B-C). The median suspended grain diameter increased from 10 µm at day 0 to 51 µm at day 70 (Figure 2.5B). Similar trends were observed for the stagnant and low rotation treatments and are discussed in supplementary section B.2.4. Loss of suspended particles during weekly sampling and water renewals likely explains the shift towards larger suspended grains. According to Stokes' law, all grains with a diameter smaller than 70 µm (6% of the total sediment volume) could have been removed during sampling (Supplementary section B.2.4). However, observed total loss of dunite mass was more limited (2.1 ± 0.44 wt%, Table B.3).
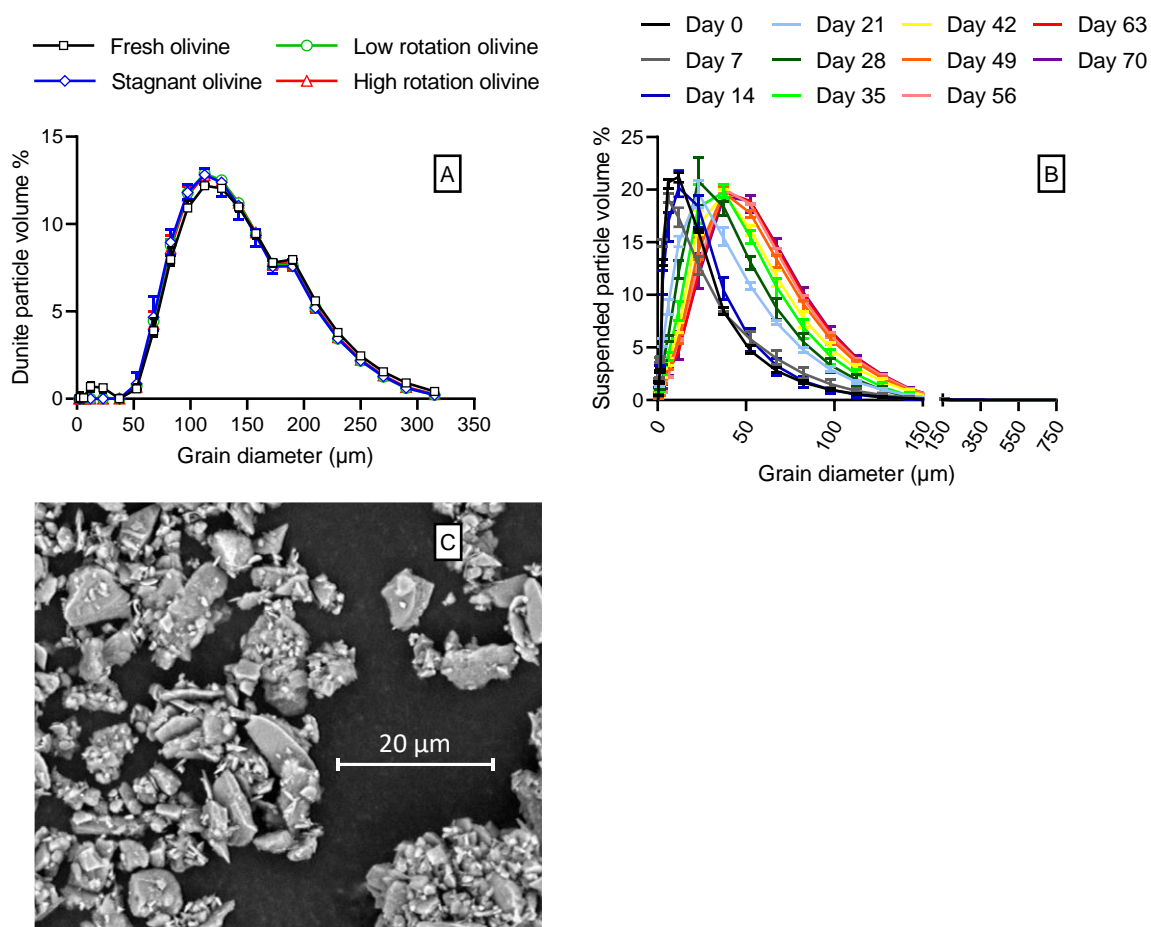
Figure 2.5: (A) Volumetric dunite grain size distribution of fresh (N = 5) and weathered (N = 6) dunite grains (mean and range). (B) Volumetric grain size distribution of suspended sediment for the high rotation treatment at different time points (Mean and range, N = 1 – 3). (C) scanning electron microscopy (SEM) image of representative grains from the suspended sediment in the high rotation treatment at day 7.

2.3.4 Trace metal release

A relatively constant weekly Ni accumulation was observed in the stagnant treatment ($\Delta \widehat{N}^{k}_{\text{DNi}}$ = 1.2 µmol mol^{-1} olivine; range 0.59 – 1.7 µmol mol^{-1} olivine) (Figure 2.6A). Until day 28, dissolved Ni accumulations did not differ significantly among olivine treatments (Figure 2.6A). Afterwards Ni accumulations were significantly higher in the rotation

treatments compared to the stagnant treatment, following a similar temporal trend as dissolved Si accumulations (Figure 2.2C).

Dissolved chromium (DCr) accumulation was approximately 10 times lower than DNi accumulation (Figure 2.6B). It was elevated, but variable at the start of the experiment, and then decreased, with no significant difference among olivine treatments ($\Delta \widehat{N}_{DCr}^{k}$= -0.017 – 0.31 µmol mol^{-1} olivine) (Figure 2.6B). From day 49 onwards, DCr concentrations remained below detection limit (0.38 nmol L^{-1}) in all treatments (Figure 2.6B). Results for other metals (Fe, Cu, Cd, Zn, Pb, and Mn) and major elements (Na, Mg, Ca, and K) can be found in supplementary information (section B.2.2).
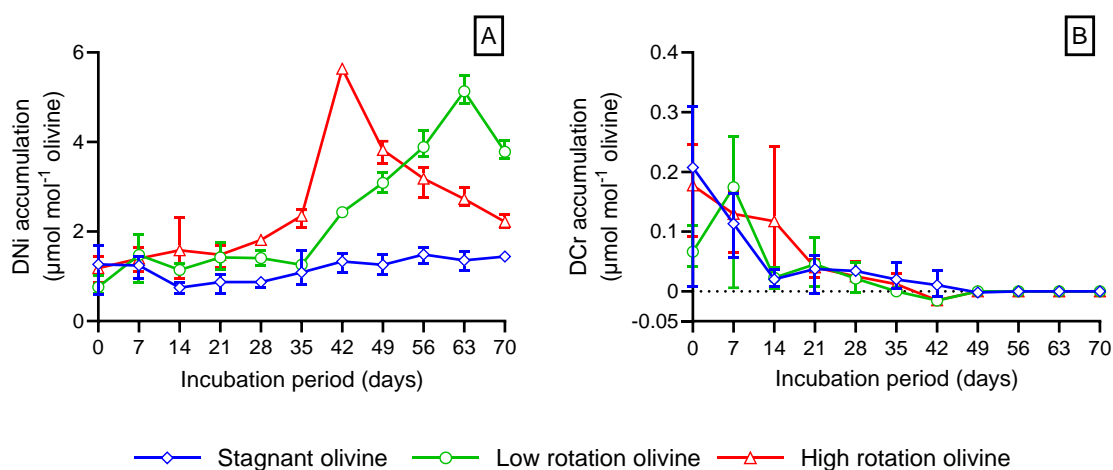
Figure 2.6: (A) Weekly evolution of dissolved (<0.2 µm) nickel (DNi) and (B) chromium (DCr) accumulation in natural filtered (<0.2 µm) seawater. Mean values with range (N = 3) are shown.

2.3.5 CO$_2$ sequestration

Our results showed that CO$_2$ was sequestered from the atmosphere in response to an increased TA accumulation. DIC accumulation in the stagnant treatment remained low throughout the experiment (Figure 2.7A). The limited DIC accumulation during the first

days of the experiment can be explained by the relatively slow CO_2 invasion in seawater given the reduced pCO_2 values in all olivine treatments compared to the seawater control (Figure 2.7C) (Kuss and Schneider, 2004; Sarmiento, 2013). DIC accumulations were significantly higher in the rotation treatments and peaked at day 7. The mean DIC accumulation was 457 µmol mol^{-1} olivine ($\Delta \widehat{N}_{\mathrm{DIC}}^{k}$ = 58 – 791 µmol mol^{-1} olivine) in the low rotation and 624 µmol mol^{-1} olivine ($\Delta \widehat{N}_{\mathrm{DIC}}^{k}$ = 67 – 1297 µmol mol^{-1} olivine) in the high rotation treatment (Figure 2.7A). Similar to the DSi and TA results, mean DIC accumulation was significantly higher in the high rotation compared to the low rotation treatment until day 42 (Figure 2.7A).

TA increases clearly resulted in DIC increases in the rotation treatments (Figure 2.7B). Theoretical CO_2 sequestration efficiency (γ_{CO_2}) at the experimental conditions, assuming a constant seawater CO_2 fugacity ($f\mathrm{CO_2}$) of 420 µatm, was on average 0.82 mol CO_2 mol^{-1} TA (dashed line in Figure 2.7B). This theoretical CO_2 sequestration efficiency matches the DIC to TA ratio as seen in the data (Figure 2.7B), suggesting that the seawater solutions equilibrated with the atmosphere ($pCO_2 \approx$ 420 µatm) during the rotation experiments. Equilibration of the seawater carbonate system with the atmosphere was confirmed by pCO_2 values that were only slightly lower in the olivine treatments (243 – 514 µatm, N = 99) compared to the seawater control (418 – 533 µatm, N = 22) on most sampling days (Figure 2.7C). Notably, the lowest pCO_2 values were observed in the low rotation treatment (Figure 2.7C).
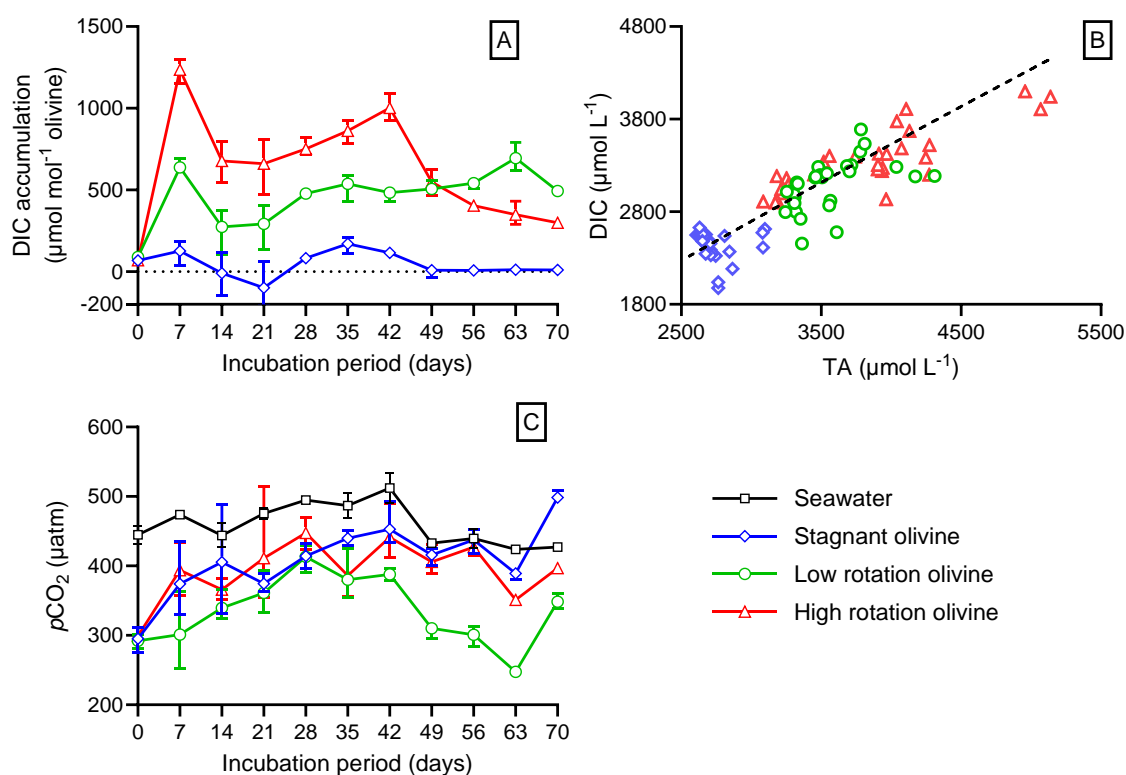
Figure 2.7: Weekly evolution of (A) dissolved (<0.2 µm) inorganic carbon (DIC) accumulation and (C) partial pressure of CO_2 (pCO_2) in natural filtered (<0.2 µm) seawater. Mean values with range for olivine treatments (N = 3) and seawater control (N = 2) are shown. (B) Theoretical (at fCO_2 = 420 µatm, black dashed line) and observed relationship between dissolved inorganic carbon (DIC) and total alkalinity (TA) concentrations.

2.3.6 Olivine dissolution rate constants

Dissolution rate constants k_i were derived for different olivine reaction products from observed weekly accumulations (as shown in Figure 2.8 and Supplementary Figure B.5). Olivine k_i values for DSi, TA and DIC were relatively similar within treatments suggesting stoichiometric olivine dissolution (Figure 2.8A). Olivine k_i values derived from DNi accumulations were considerably higher and showed more temporal variation than those

derived for TA, DIC and DSi, as was previously observed in the study by Montserrat et al. (2017) (Figure 2.8A).

Based on TA, DSi and DIC accumulations, median k_i values in the stagnant treatment (0.80 to 1.1 µmol m^{-2} d^{-1}) were ~8 to 14 times lower compared to the low rotation treatment (9.1 to 10.8 µmol m^{-2} d^{-1}), and ~12 to 19 times lower compared to the high rotation treatment (13.2 to 15.2 µmol m^{-2} d^{-1}). Therefore, continuous rotation increased olivine k_i values by a factor of 8 to 19 (Figure 2.8A). For the high rotation treatment, median k_i values were up to 1.7 times higher compared to the low rotation treatment (Figure 2.8A). In comparison to the average predicted k_i values by Rimstidt et al. (2012), observed median k_i values were 7 to 10 times lower in the stagnant treatment and 1.3 to 2.8 times higher in the rotation treatments (Figure 2.8A). Nevertheless, the range of observed k_i values overlap considerably with predictions by Rimstidt et al. (2012), indicating good agreement between values (Figure 2.8A).

Temporal changes in k_{TA} are displayed in Figure 2.8B, while k_{Si}, k_{DIC} and k_{Ni} values are shown in supplementary section B.2.3. In general, highest values for k_{TA} are observed in the first two accumulation sessions (Figure 2.8B), after which the value in the rotation treatments remains relatively constant (apart from the conspicuous baseline shift at day 42). The k_{TA} in the stagnant treatment gradually decreases over the successive accumulation sessions. A similar temporal trend was observed for k_{Si} and k_{DIC} (Supplementary Figure B.5).
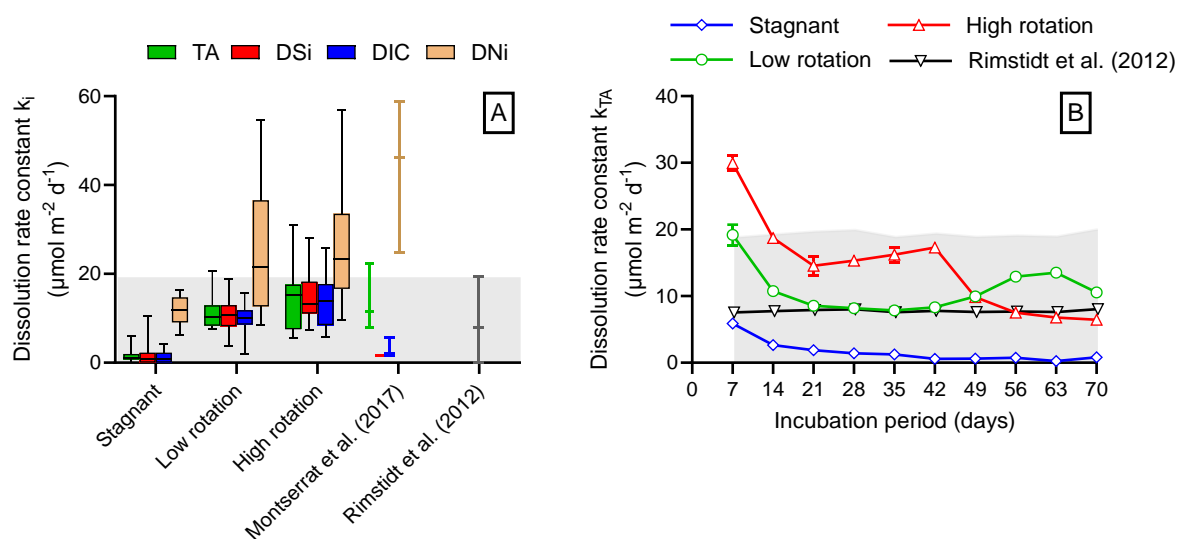
Figure 2.8: (A) Box and whisker plots of the olivine dissolution rate constants k_i (μmol m^{-2} d^{-1}) in natural filtered (<0.2 μm) seawater (N = 30) during the 70-day experiment (whiskers indicate the range). Values were derived from weekly accumulation of total alkalinity (TA, in green), dissolved silicon (DSi, in red), dissolved inorganic carbon (DIC, in blue), and dissolved nickel (DNi, in orange) normalized for reaction stoichiometry (supplementary section B.1.2). For comparison, olivine k_i values derived by Montserrat et al. (2017) (median and range, N = 4) and Rimstidt et al. (2012) (predicted values and propagated errors represented as a line and shading in grey) are shown. Values reported by Montserrat et al. (2017) were temperature normalized (to 15 °C) using the Arrhenius equation and activation energy (79.5 kJ mol^{-1}) provided by Wogelius and Walther (1992). (B) weekly evolution of olivine k_{TA} values in natural filtered (<0.2 μm) seawater. Mean and range values are shown (N = 3). Expected weekly olivine k_i values by Rimstidt et al. (2012) and propagated errors are shown in grey (line and shading).

2.3.7 Kinetic model simulations

Modelled TA and DSi accumulations reflect observed values reasonably well, although temporal fluctuations in the rotation treatments could not be accurately simulated

(dashed lines in Figure 2.2A and 2.2C). The model underestimated TA production in the high rotation treatment (Figure 2.2A) and overestimates DSi accumulation in the low rotation treatment (Figure 2.2C). At the end of the experiment the model predicted a total amount of dissolved olivine of 0.69, 2.32, and 2.84 mmol in the stagnant, low rotation, and high rotation treatments, respectively (indicating that 0.07%, 0.25%, and 0.31% of the initially present olivine was dissolved). The rate controlling pre-factor k_{rc} (Supplementary equation B.11) implemented in the rate equation by Rimstidt et al. (2012) that gave the best model fit to the data was 0.43 in the stagnant, 2.0 in the low rotation, and 2.3 in the high rotation treatment.

Our model simulations suggest limited secondary mineral precipitation. For all olivine treatments, 0.12 mol $Fe(OH)_3$ precipitation occurred per mol of dissolved olivine (Eq. (2.20 − 2.22)). In the low rotation treatment, formation of 0.086 mol chrysotile mol^{-1} olivine and 0.10 mol aragonite mol^{-1} olivine were simulated (Eq. 2.21). For the high rotation treatment this was 0.015 mol chrysotile mol^{-1} olivine and 0.22 mol aragonite mol^{-1} olivine (Eq. 2.22). In the stagnant treatment 0.069 mol mol^{-1} olivine chrysotile formation was modelled (Eq. 2.20). Overall, modelled secondary mineral precipitation resulted in an 11 to 19% decrease of the TA production by olivine dissolution. The reaction stoichiometry derived from modelled olivine dissolution and secondary mineral precipitation is as follows:

Stagnant olivine:

$$Mg_{1.87}Fe_{0.13}SiO_4 + 3.72H_2O + 0.03O_2 + 3.37CO_2 \rightarrow 0.12Fe(OH)_3 + 0.86Si(OH)_4 +$$
$$0.069\,Mg_3Si_2O_5(OH)_4 + 0.013Fe^{3+} + 1.66Mg^{2+} + 3.37HCO_3^- \qquad [2.20]$$

Low rotation olivine:

$$Mg_{1.87}Fe_{0.13}SiO_4 + 3.96H_2O + 0.033O_2 + 3.66CO_2 + 0.10Ca^{2+} \rightarrow 0.12Fe(OH)_3 + 1.00Si(OH)_4 + 0.10CaCO_3 + 0.000087\ Mg_3Si_2O_5(OH)_4 + 0.0073Fe^{3+} + 1.87Mg^{2+} + 3.56HCO_3^-$$

[2.21]

High rotation olivine:

$$Mg_{1.87}Fe_{0.13}SiO_4 + 3.77H_2O + 0.033O_2 + 3.45CO_2 + 0.22Ca^{2+} \rightarrow 0.12Fe(OH)_3 + 0.97Si(OH)_4 + 0.0076Fe^{3+} + 1.83Mg^{2+} + 0.22CaCO_3 + 0.015Mg_3Si_2O_5(OH)_4 + 3.23HCO_3^-$$

[2.22]
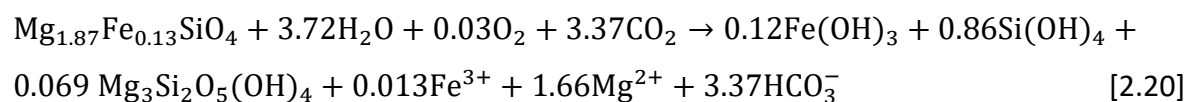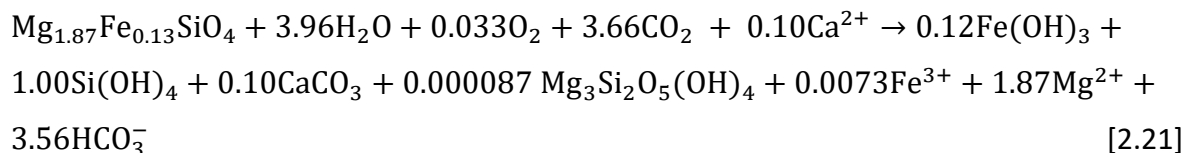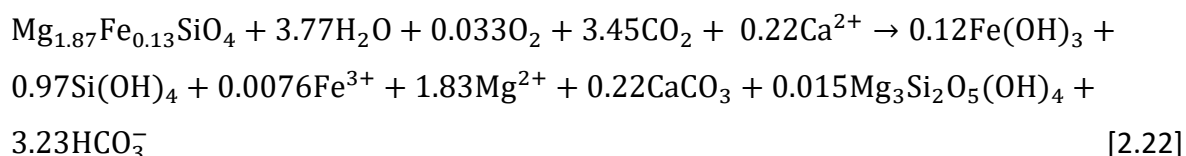
2.4 Discussion

2.4.1 Collision enhances olivine dissolution in seawater

We investigated the effect of continuous grain tumbling on olivine dissolution kinetics in seawater and hypothesized that increasing physical stress would enhance olivine dissolution through increased particle fragmentation. Significantly higher TA and DSi accumulation in the rotation treatments compared to the stagnant treatment (Figure 2.2A – D) confirm that continuous grain tumbling enhanced olivine dissolution. Derived olivine dissolution rate constants showed that continuously tumbled olivine dissolved approximately 8 to 19 times faster than stagnant olivine (Figure 2.8). Four processes can potentially explain this enhanced weathering in our study, namely (I) grain fragmentation induced by abrasion, (II) removal of passivating layers upon grain-grain collisions, (III) rate limiting air-seawater CO_2 exchange under stagnant conditions, and (IV) flushing of reaction products from the pore solution by sediment movement.

Grain fragmentation enhances olivine dissolution by increasing the effective surface area (Oelkers et al., 2018; Rigopoulos et al., 2018). However, no significant change in olivine grain size distribution was observed (Figure 2.5A), indicating that grain fragmentation was limited in our 70-day study. Previous studies have observed extensive olivine cracking and fragmentation at high temperature (200 °C) or low pH (pH = 1.5) solutions (Varadachari et al., 1994; Lafay et al., 2018). However, in our experiment, olivine dissolution took place at

seawater pH ≈ 8.2 and ambient temperature of ≈ 15 °C. Under these mild conditions, it is expected that internal micro cracks and grain fragmentation will only develop over time scales of years (Hangx and Spiers, 2009).

Continuous grain tumbling can also prevent formation of passivating layers on olivine grains, such as amorphous silica (SiO_2(am)) or iron hydroxides ($Fe(OH)_3$). These passivating layers slow down dissolution by decreasing the olivine-fluid interfacial area and increasing the diffusion distance towards the active dissolution zone (Béarat et al., 2006; Daval et al., 2011; Schuiling and De Boer, 2011; Maher et al., 2016; Griffioen, 2017; Meysman and Montserrat, 2017). Undersaturation of the bulk solution with regards to SiO_2(am) (Supplementary Figure B.2D) indicates that passivating SiO_2(am) layer formation was implausible. However, the pore water of the stagnant treatment could have been supersaturated with respect to SiO_2(am), resulting in thin passivating layer formation that could be undetectable with SEM. Nevertheless, removal of brittle SiO_2(am) layers during weekly water renewals likely prevented significant passivation of olivine surfaces (Béarat et al., 2006). A similar fate is expected for any $Fe(OH)_3$ crystals that inevitably formed given that they were not observed via SEM-EDX analysis. Preferential Mg release at pH ≤ 8.8 can lead to the rapid formation of cation depleted layers on olivine grains (Seyama et al., 1996; Pokrovsky and Schott, 2000b, 2000a; Montserrat et al., 2017). In our experiment, the olivine surface Mg/Si ratios differed only slightly between treatments (Figure 2.4A), indicating that extensive cation depleted layers were not formed. Nevertheless, a relatively large variation in Mg/Si ratio was observed on individual olivine grains, confirming spatial variability in composition and surface reactivity (Rimstidt et al., 2012; Oelkers et al., 2018). Overall, we assert that removal of passivating layers was not the prime enhancement factor of olivine dissolution in our experiment.

Waves and currents are essential for ocean mixing (Moum, 2021), which is a pivotal process for CESW since it drives transport of alkalinity enriched bottom water to the surface ocean for CO_2 uptake and equilibration (Bach et al., 2023). This CO_2 equilibration prevents high seawater pH excursions that could be harmful for marine biota and slow

down olivine dissolution (Bach et al., 2019). Here, seawater pCO$_2$ values were lowest in the low rotation treatment (Figure 2.7C) likely as a result of slower water movement compared to the high rotation treatment. Importantly, seawater pCO$_2$ values in the stagnant treatment were generally close to atmospheric pCO$_2$ (~420 µatm) and not significantly lower compared to the rotation treatments (Figure 2.7C), indicating that low olivine dissolution rates were not the result of slow CO$_2$ equilibration.

Finally, olivine dissolution can be impeded by saturation of the surrounding water, and so flushing of reaction products from the olivine-seawater interface could enhance dissolution (Meysman and Montserrat, 2017; Montserrat et al., 2017). Previous studies have shown that advective pore water flow can enhance solute fluxes to the overlying water by up to 50-fold compared to stagnant conditions (Precht and Huettel, 2003; Cook et al., 2007; Santos et al., 2012). Under stagnant conditions, molecular diffusion towards the grain interface can be rate controlling. We did not directly assess the concentration of reaction product accumulation and saturation indices in the pore water of the stagnant treatment. However, given limited particle fragmentation, implausible passivating layer formation, and no rate limiting seawater CO$_2$ influx, enhanced weathering in our rotation treatments appears to be mainly driven by pore water flushing. This conclusion is supported by previous studies which showed that silicate weathering rates are directly proportional to solute transport rates for systems with a water residence time longer than two days (Maher, 2010; Yu and Hunt, 2017).

2.4.2 Temporal variation in olivine dissolution rates

The rate of olivine dissolution was not constant with time in our 70-day experiment (Figure 2.8B). An immediate increase in seawater pH, TA and DSi accumulation was observed in all olivine treatments after adding the olivine to the seawater solution (Figures 2.2A, 2.2D, and 2.3A). This "dissolution spike" can be explained by the rapid (within minutes) exchange of Mg^{2+} or other divalent cations (e.g. Ni^{2+}, Fe^{2+}) for protons (H$^+$) in the first one or two monolayers of the olivine grain surfaces (Luce et al., 1972; Blum and Lasaga, 1988; Oelkers et al., 2018). However, in our experiment the "dissolution

spike" was sustained over a much longer period (first two weeks). We also noticed that fresh olivine grains were covered with fine adhering particles (≤ 10 μm), which likely are formed during crushing of olivine rich rocks for sand production (Figure 2.4C). Weathering of these fines likely explains the prolonged DSi accumulation and high TA, pH, and DIC accumulation within the first two weeks of the experiment (Figure 2.2A, 2.2D, 2.3A, and 2.7A).

A decreased olivine reactivity was observed from day 42 and 63 onwards in the high rotation and low rotation treatments, respectively (Figure 2.2A, C and 2.8B). Given that formation of passivating or cation-depleted layers was highly unlikely for rotated olivine grains, a decrease in surface reactivity could possibly explain the observed results (Grandstaff, 1978; Wogelius and Walther, 1992; Bandstra and Brantley, 2008; Rimstidt et al., 2012). Such a decrease in surface reactivity can be caused by variation in dissolution rates of distinct crystallographic planes (Grandstaff, 1978; Chung-Cherng and Pouyan, 1993; Oelkers et al., 2018). Upon inspection, etch pits were observed on some olivine grains (Figure 2.4E and Supplementary Figure B.8K), but not all. Furthermore, striation like features, cracked grain edges and surficial and internal micro-cracks were observed on weathered and fresh olivine grains (Figure 2.4B, 2.4E and Supplementary Figure B.9).

Our results suggest that stoichiometric olivine dissolution took place in the experiment. Average $\Delta \widehat{N}_{\text{TA}}^{k} / \Delta \widehat{N}_{\text{DSi}}^{k}$ ratios in the low rotation (4.3 mol TA mol^{-1} DSi) and high rotation treatment (3.7 mol TA mol^{-1} DSi) were close to the theoretical value of 3.73 mol TA mol^{-1} DSi, which accounts for full dissolution of olivine followed by Fe(OH)$_3$ precipitation (supplementary section B.1.2). In previous experiments on olivine weathering in seawater, Montserrat et al. (2017) and Fuhr et al. (2022) observed $\Delta N_{\text{TA}}^{k} / \Delta N_{\text{DSi}}^{k}$ ratios that deviated significantly from the theoretical value. Deviation of the $\Delta N_{\text{TA}}^{k} / \Delta N_{\text{Si}}^{k}$ ratio from the theoretical value can be explained by (1) incomplete olivine dissolution, (2) dissolution of other minerals in the dunite sand, or (3) precipitation of secondary phases (Fuhr et al., 2022). Therefore, a multiparameter approach, where DSi, TA, DNi and DIC are

conjointly measured, seems advised to monitor olivine dissolution and CO_2 sequestration rates under field conditions (Montserrat et al., 2017).

Experimental olivine dissolution rate constants are within the range of previously reported k_i values (Rimstidt et al., 2012; Montserrat et al., 2017). Yet, estimated k_i values are underestimations due to the loss of the finest olivine particles during weekly water renewals (discussed in supplementary section B.2.4). At the end of the experiment a loss of olivine mass (by 1.6 to 2.8 wt%, Supplementary Table B.3) and decrease in olivine A_{GEO} (from 0.0161 to 0.0145 m^2 g^{-1}, Supplementary Table B.4) was observed which could not be accurately accounted for in weekly k_i value derivation, resulting in an underestimation of derived values by up to 14%.

2.4.3 Minimal secondary mineral formation

Secondary mineral formation can significantly reduce net alkalinity production and resulting atmospheric CO_2 uptake during olivine weathering (Griffioen, 2017; Meysman and Montserrat, 2017; Montserrat et al., 2017; Oelkers et al., 2018). Previous studies have found contradictory results on the importance of secondary carbonate formation. Rigopoulos et al. (2018) observed only small TIC changes when dunite was weathered in artificial seawater (2 g dunite L^{-1} for 60 days). Similarly, Montserrat et al. (2017) did not observe a significant TIC increase or aragonite precipitation when olivine was weathered in natural and artificial seawater (8.7 – 29 g olivine L^{-1} for up to 137 days). In contrast, Fuhr et al. (2022) observed significant aragonite formation after reacting olivine rich (~75%) sand in artificial seawater (25 – 100 g ultramafic sand L^{-1} for 134 days).

Here, we observed no increase in olivine TIC content (Supplementary Figure B.10) or aragonite crystals on weathered olivine grains (Figure 2.4 and Supplementary Figure B.8) even though aragonite was supersaturated in the overlying seawater (Figure 2.3B). Under natural conditions, seawater is supersaturated with respect to $CaCO_3$, but precipitation does not occur due to the lack of mineral precipitation nuclei and presence of dissolved organic carbon, Mg^{2+} and phosphate which inhibit precipitation (Morse et al., 2007; Pan

et al., 2021; Moras et al., 2022). The threshold SI for aragonite precipitation in seawater is dependent on the availability of precipitation surfaces, being higher in their absence (Moras et al., 2022). In the absence of precipitation surfaces, homogeneous aragonite precipitation would occur at a SI of ~ 1.26 ($\Omega \approx$ 18) in 25 °C seawater (Sun et al., 2015). In the presence of colloids and organic particles, pseudo-homogenous precipitation of aragonite would be expected at a SI value of ~1.06 ($\Omega \approx$ 11.5) for the experimental seawater (salinity of 33 ‰ and temperature of 15 °C) (Marion et al., 2009). Furthermore, recently Moras et al. (2022) observed heterogeneous (i.e. on mineral phases) aragonite precipitation on CaO and $Ca(OH)_2$ particles smaller than 63 μm at a SI value of ~0.85 ($\Omega \approx$ 7) in 21 °C natural seawater (salinity of 35 ‰). This threshold is very close to SI peak values up to 0.9 observed on day 7 and 63 of our experiment, signifying potential heterogeneous aragonite precipitation. Overall, we can conclude that $CaCO_3$ precipitation was limited in our study given that aragonite SI values remained below critical thresholds on most sampling days (Figure 2.3B).

Secondary precipitation of iron(hydr)oxides inevitably occurred, although $Fe(OH)_3$ crystals were not observed through SEM analysis, possibly due to removal during weekly water renewals. The experimental olivine contains on average 6.6% fayalite, compared to 93.4% of forsterite (Supplementary Section B.1.2). Under oxic conditions, any Fe(II) released during dissolution will be rapidly oxidized to Fe(III) and precipitated as iron(III) (hydr)oxide (Millero, 1998; Griffioen, 2017; Meysman and Montserrat, 2017; Montserrat et al., 2017). This process hence reduced the total alkalinity production by 6.6% for the olivine employed here (Griffioen, 2017; Montserrat et al., 2017).

Finally, regarding phyllosilicates, seawater was supersaturated with respect to sepiolite, talc, and chrysotile on most sampling days in the olivine treatments (Figure 2.3E and Supplementary Figure B.2). However, similar to Montserrat et al. (2017), no phyllosilicate precipitates were observed on olivine grains (Figure 2.4B-E and Supplementary Figure B.8) and formation was expected to be low based on the best fitting models for the experimental data (Figure 2.2A and 2.2C). The combination of weekly water renewals and

slow formation kinetics could possibly explain the absence of Mg-silicate precipitates in our experiment (Baldermann et al., 2018).

2.4.4 Trace metal release

One of the environmental concerns of enhanced olivine weathering in marine conditions is the accumulation of Ni and Cr within the ecosystem (Montserrat et al., 2017; Flipkens et al., 2021). In the crystal structure of olivine, Ni^{2+} substitutes for other divalent cations (e.g. Mg^{2+} and Fe^{2+}) and is present at concentrations ranging from 0.1 to 0.5 wt% (here 0.25 wt%, Table 2.2) (Thompson et al., 1984; Santos et al., 2015; Lynn et al., 2017). Nickel is an essential trace element for macrophytes and microorganisms, but its essentiality for aquatic animals remains under debate (Muyssen et al., 2004; Blewett and Leonard, 2017). Exposure to elevated Ni concentrations can lead to toxicological effects including reduced growth, reproduction and survival as a result of oxidative stress, disruption of ion homeostasis and respiratory impairment (Blewett and Leonard, 2017; Gissi et al., 2020). We observed no significant difference in DNi accumulation among treatments until day 28 (Figure 2.6A), which is possibly explained by Ni adsorption to fine suspended olivine particles that were gradually removed during sampling (Kleiv and Thornhill, 2004). Minimal (<1.5%) Ni adsorption to precipitated $Fe(OH)_3$ particles was expected according to PHREEQC diffuse double layer surface-complexation models assuming $Fe(OH)_3$ specific surface area (600 m^2 g^{-1}) and binding site availability (0.005 and 0.2 mol/mol for strong and weak sites, respectively) according to Dzombak and More (1990). From day 35 onwards, high non stoichiometric Ni release was observed (Figure 2.6A and Figure 2.8A). In general, our findings are in line with the results of Montserrat et al. (2017), suggesting preferential release of metal cations (Ni^{2+} and Mg^{2+}) compared to Si at seawater pH although this was not evident from Mg/Si ratios on weathered olivine grains (Figure 2.4A). Therefore the reason for the high Ni release remains uncertain and requires further research.

Chromium (III) is heterogeneously distributed in olivine containing dunite grains, mainly in the form of chromite ($FeCr_2O_4$) inclusions (Santos et al., 2015; Bell, 2021), and hence not

part of the olivine silicate matrix. Upon olivine dissolution, chromite nanoparticles could be released, which can interact with Mn(IV) oxides resulting in the dissolution of chromite and subsequent oxidation to Cr(VI) or precipitation as Cr(III) hydroxides (Ivarsson et al., 2011; McClenaghan and Schindler, 2022). However, Mn(IV) oxides were likely not present in significant amounts in our experiment since their formation is mainly microbially driven (Tebo et al., 2004). Furthermore, under oxic conditions, Cr(III) released during dissolution could be converted to Cr(VI) as indicated by the high Cr(VI) concentrations found in streams and rivers near chromite and Ni mines (Gunkel-Grillon et al., 2014; Das et al., 2021). While Cr(VI) is considered as a highly mobile human carcinogen, Cr(III) is comparatively less toxic and relatively immobile (Aharchaou et al., 2018). Although the Cr content of the experimental olivine was relatively high (0.30 wt.%, Table 2.2), dissolved Cr accumulation was low in all treatments (Figure 2.6B), confirming that most Cr remained in a particulate form.

Overall, our results confirm that Ni is the trace metal of most concern for future CESW applications due to its release as a soluble compound (Montserrat et al., 2017; Flipkens et al., 2021). Low aqueous solubility of Cr^{3+} infers lower bioavailability compared to Ni (Flipkens et al., 2021), but potential oxidation to Cr^{6+} or accumulation of Cr^{3+} nanoparticles in marine sediment could still pose a risk to marine biota (Gunkel-Grillon et al., 2014; Kanakalakshmi et al., 2017; Das et al., 2021).

2.4.5 Implications for natural and enhanced marine silicate weathering

The carbonate-silicate geochemical cycle plays a pivotal role in regulating Earth's climate over geological time scales (Penman et al., 2020). Coastal enhanced silicate weathering aims to accelerate this process to help mitigate human-induced climate change (Meysman and Montserrat, 2017). A thorough understanding of factors controlling silicate weathering kinetics under marine conditions is crucial to comprehend the natural carbon cycle and quantify the CDR potential of CESW (Meysman and Montserrat, 2017; Sun et al., 2019). In this regard, our results show that pore water exchange rates can significantly affect silicate mineral dissolution rates in seawater. Hence, hydrodynamic

conditions should be considered when quantifying natural silicate weathering rates to obtain a more comprehensive understanding of the Earth's carbon cycle (Maher, 2010; Yu and Hunt, 2017). Additionally, these findings highlight that olivine should ideally be supplied in coastal areas with high bed shear stress and pore water exchange rates such as near shore zones, where the seafloor is impacted by wave action and longshore currents (Jong et al., 2020). This ensures enhanced mineral dissolution and effective CO_2 sequestration.

The present study should be seen as a step towards future experimental olivine weathering studies in flume and mesocosm set-ups that mimic natural conditions more closely. Furthermore, marine olivine toxicity tests are needed to accurately assess environmental impacts of coastal enhanced olivine weathering (Flipkens et al., 2021). If the environmental risk is acceptable larger-scale scale field trials could be set up to generate field data needed for the more realistic assessment of the CO_2 sequestration potential and scalability of CESW.

2.5 Conclusions

Coastal enhanced olivine weathering has been put forward as a way to remove atmospheric CO_2 for climate change mitigation. However, the efficiency and environmental impacts of the technique remain to be assessed, since data on olivine dissolution in natural seawater conditions is scarce. Here, we investigated the effect of continuous grain-grain collisions on olivine dissolution and trace metal release kinetics in natural seawater. Olivine dissolution was complete and stoichiometric, while secondary mineral precipitation and passivating layer formation were restricted. Olivine dissolution rate constants were 8 to 19 times higher for rotated olivine compared to stagnant olivine. Seawater CO_2 equilibration was not significantly rate limiting, and grain size distribution analysis suggests that minimal particle fragmentation occurred. Therefore, we infer that advective pore water flushing was the main process enhancing olivine dissolution during this experiment. The presence of micro cracks inside olivine grains suggests that physical

agitation could potentially enhance olivine dissolution over longer time scales. Overall, this study shows that coastal hydrodynamics could enhance silicate weathering in a marine environment, which is of importance for both the natural silicon cycle and coastal enhanced olivine weathering. Therefore, olivine should ideally be supplied in dynamic coastal areas with high bed shear stress and pore water exchange rates (e.g. nearshore zones). However, the question remains how olivine dissolution rates in this laboratory agitation experiment compare to actual rates in coastal ocean settings with complex hydrodynamical conditions and presence of biological processes (e.g. bioturbation and microbial acidification).

2.6 Supplementary information

Dunite chemical composition, olivine reaction stoichiometry, specific surface area, and mass added to the experimental bottles are provided in Appendix B. Furthermore, North Sea water chemical composition, salinity, and measured trace element (Zn, Cu, Cd, Fe, and Mn) and major element (Na, Mg, Ca and K) concentrations are shown. To visualize temporal trends in olivine reactivity, the cumulative dissolved olivine and weekly k_i values are given. A detailed description of model calculation and input data are provided together with $SI(t_k)$ values for several secondary phases. Finally, weekly grain size distribution of the suspended olivine and grain scale changes of the weathered olivine are illustrated.

2.7 Acknowledgements

Chapter 3   Effects of current on olivine dissolution kinetics in permeable marine sediment: a flume experiment

Flowing seawater   Stagnant seawater

Olivine + sediment   Olivine + sediment

equally low olivine dissolution rate

Based on:

Abstract

Gigaton-scale atmospheric carbon dioxide (CO_2) removal (CDR) is needed to keep global warming below 2 °C. Ocean alkalinity enhancement (OAE) via coastal enhanced olivine ($Mg_xFe_{2-x}SiO_4$) weathering is a proposed strategy to increase the ocean carbon sink for climate change mitigation. However, the CO_2 sequestration potential and ecological effects of the technique remain poorly resolved due to a scarcity of environmentally relevant experimental data. Here, we conducted a 175-day flume experiment to assess the effects of water currents on forsterite olivine dissolution in natural permeable beach sediment. Continuous flow stimulated natural alkalinity release from the sediment. However, overall accumulation of total alkalinity (TA) and dissolved silicate (DSi) in the overlying natural seawater was limited, suggesting that olivine dissolution was more than one order of magnitude slower than expected based on previous laboratory findings. Air-seawater CO_2 exchange was not rate limiting and passivating layer formation was not observed. Pore water saturation effects and the formation of secondary minerals could not be resolved conclusively due to the lack of pore water chemistry data and a variety and abundance of mineral phases originally present in the marine sediment. Overall, olivine reactivity in permeable marine sediment was significantly lower than expected and could not be explained, highlighting the need for additional research on olivine dissolution rates under natural marine conditions to assess the efficacy of coastal enhanced olivine weathering as a CDR technique.

Keywords: olivine, ocean alkalinity enhancement, silicate weathering, climate change mitigation

3.1 Introduction

Rapid and substantial reductions in carbon dioxide (CO_2) emissions as well as large scale carbon dioxide removal (CDR) are both needed to keep global warming well below the goals set out in the 2015 Paris agreement (UNFCC, 2015; Rueda et al., 2021). Ocean alkalinity enhancement (OAE) via coastal enhanced silicate weathering (CESW) has attracted attention as a potential CDR technology (Schuiling and De Boer, 2011; Meysman and Montserrat, 2017; Montserrat et al., 2017; Rigopoulos et al., 2018; Fuhr et al., 2022). The chemical weathering of silicate minerals, either on land or in the ocean, regulates atmospheric CO_2 concentrations over geological time scales (Penman et al., 2020). Dissolution of silicate minerals in coastal environments increases seawater alkalinity, which drives uptake of atmospheric CO_2 by the surface ocean (Eq. 3.1 and 3.2) (Meysman and Montserrat, 2017; Montserrat et al., 2017). To accelerate this natural process, finely ground silicate rock can be distributed in dynamic coastal environments, where biological and physical factors will potentially enhance silicate dissolution (Meysman and Montserrat, 2017). Magnesium rich olivine (i.e. forsterite $Mg_xFe_{2-x}SiO_4$) has received most attention for CESW because of its global abundance and relatively fast weathering rate (Hangx and Spiers, 2009; Schuiling and De Boer, 2011; Hartmann et al., 2013; Meysman and Montserrat, 2017; Montserrat et al., 2017; Fuhr et al., 2022; Fuhr et al., 2023).

The dissolution rate of olivine has traditionally been studied in laboratory settings, employing small-scale shaking devices and idealized aqueous solutions (Grandstaff, 1980; Blum and Lasaga, 1988; Awad et al., 2000; Pokrovsky and Schott, 2000b; Olsen and Rimstidt, 2008) or filtered seawater (Montserrat et al., 2017; Rigopoulos et al., 2018; Fuhr et al., 2022; Flipkens et al., 2023a). These studies show that solution pH and temperature are the main factors driving olivine reactivity (see reviews by Oelkers et al. (2018) and Rimstidt et al. (2012)). However, studies on olivine weathering kinetics under more natural marine conditions are limited (Fuhr et al., 2023). Fuhr et al. (2023) conducted an incubation experiment with organic rich Baltic Sea sediments amended with calcite ($CaCO_3$) or finely ground dunite rock. Their results indicated that microbial activity was

the main driver of $CaCO_3$ dissolution by lowering pore water pH, but strong natural background fluxes of silicic acid prevented the evaluation of olivine dissolution (Fuhr et al., 2023). Next to microbial metabolism, processes such as macro-faunal bioturbation and advective pore water flushing could potentially enhance olivine reactivity (Meysman and Montserrat, 2017; Montserrat et al., 2017). The importance of these processes has received little research attention, but is crucial to better estimate *in situ* olivine dissolution rates and assess the CDR potential of CESW (Meysman and Montserrat, 2017; Flipkens et al., 2023a).

Waves and currents could potentially enhance olivine reactivity via bedload transport and increased grain-grain collisions (Schuiling and De Boer, 2011; Meysman and Montserrat, 2017; Flipkens et al., 2023a). Grain abrasion during advective transport can result in the development of cracked mineral surfaces and ultimately grain fragmentation, which could increase olivine dissolution rates by enhancing the reactive mineral surface area (Oelkers et al., 2018; Madhavaraju et al., 2021; Ramos-Vázquez and Armstrong-Altrin, 2021). Additionally, grain abrasion could prevent the development of cation depleted layers or secondary surface precipitates that would passivate olivine surfaces (Béarat et al., 2006; Meysman and Montserrat, 2017; Oelkers et al., 2018). Once olivine becomes mixed in the surface sediment, the build-up of reaction products (e.g. dissolved Si (DSi) and alkalinity) could lead to porewater saturation, which would reduce olivine reactivity. Advective pore water flushing induced by currents and waves could counteract such saturation effects (Meysman and Montserrat, 2017; Flipkens et al., 2023a) and also prevent the formation of secondary mineral phases that scavenge alkalinity (Table 3.1) (Montserrat et al., 2017; Fuhr et al., 2022). Finally, waves and currents induce turbulence, which aids in the transportation of alkalinity enriched bottom water to the ocean surface for atmospheric CO_2 uptake and equilibration (Bates et al., 2001; Bach et al., 2023).

Table 3.1: Relevant chemical reactions for coastal enhanced olivine weathering. The olivine dissolution, acid-base dissociation reactions of the seawater carbonate system, and possible secondary mineral formation reactions are given.

Olivine dissolution	$Mg_xFe_{2-x}SiO_4 + 4H^+ \rightarrow xMg^{2+} + (2-x)Fe^{2+} + H_4SiO_4$	[3.1]
Seawater acid-base equilibrium	$CO_2(aq) + H_2O \rightleftharpoons HCO_3^- + H^+ \rightleftharpoons CO_3^{2-} + 2H^+$	[3.2]
	Potential secondary mineral formation	
Aragonite/calcite	$Ca^{2+} + 2HCO_3^- \rightarrow CaCO_3 + CO_2 + H_2O$	[3.3]
Iron hydroxide	$Fe^{2+} + 0.25O_2 + 3H_2O \rightarrow Fe(OH)_3 + 2H^+ + 0.5H_2O$	[3.4]
Sepiolite	$2Mg^{2+} + 3H_4SiO_4 \rightarrow Mg_2Si_3O_{7.5}(OH)(H_2O)_3 + 4H^+ + 0.5H_2O$	[3.5]
Chrysotile	$3Mg^{2+} + 2H_4SiO_4 + H_2O \rightarrow Mg_3Si_2O_5(OH)_4 + 6H^+$	[3.6]

Two crucial, but understudied aspects of CESW are the extent of secondary mineral precipitation and ecosystem risks of Ni and Cr release during olivine weathering (Flipkens et al., 2021; Fuhr et al., 2022). Recently, Fuhr et al. (2022) observed significant formation of calcium carbonates, phyllosilicates and iron (hydr)oxides during weathering of olivine rich (~75%) sand in artificial seawater (at 21 to 23.9 °C and 35 ‰) for 134 days. Formation of these minerals consumes alkalinity (Table 3.1) and can thus significantly reduce the CO_2 sequestration efficiency of CESW (Griffioen, 2017; Fuhr et al., 2022). However, the mechanisms and kinetics of their formation remain relatively poorly understood, which prevents accurate assessment of the CO_2 sequestration potential of CESW (Fuhr et al., 2022; Moras et al., 2022; Hartmann et al., 2023). Additionally, the acceptability of coastal olivine spreading could potentially be limited by accumulation of Ni and Cr to toxic levels in the marine environment (Montserrat et al., 2017; Flipkens et al., 2021). However, uncertainties regarding *in situ* trace metal release rates, environmental fate, bioavailability, and toxicity prevent derivation of accurate environmentally safe coastal olivine application guidelines (Flipkens et al., 2021).

To bridge the gap between laboratory experiments and complex field studies, we conducted a 175-day flume experiment with permeable marine sediments, in which the effect of water current and pore water advection on the dissolution and trace metal release rate of olivine was investigated. We hypothesized that advective pore water

flushing would enhance olivine dissolution and minimize secondary mineral formation by preventing porewater saturation. Regarding trace metals, we expected an elevated export of trace metals from the sediment to the water column under high flow conditions due to increased pore water flushing (Huettel et al., 1998; Flipkens et al., 2023a).

3.2 Material and Methods

3.2.1 Flume experimental design

A 175-day flume experiment was conducted at the Mesodrome facility of the University of Antwerp (Belgium) from October 2021 until April 2022 to investigate the effect of water current on the dissolution kinetics of forsterite in natural marine sediment. The experiment took place at ambient temperature (water temperature = 6.7 – 20.6 °C) and pressure (~1 atm) conditions. Four racetrack flumes (LxHxW = 395x75x121 cm) were filled with 630 kg (~ 16.4 ± 1.1 cm sediment layer) of commercial North Sea beach sediment (Handelsonderneming Hoogerheide, The Netherlands) (Figure 3.1). Subsequently, 20 kg of VANGUARD dunite sand (Sibelco, Norway) was homogenously mixed in the sediment of two flumes resulting in a dunite concentration of 3.1% w/w. The other two flumes serves as controls without dunite addition. Dunite sand will be referred to as olivine throughout the text. The mineralogical, textural, and chemical composition of the dunite and beach sediment are given in Table 3.2.

Table 3.2: Geochemical properties of the dunite and beach sediment used in the experiment. Mineralogical composition (XRD-analysis), element composition (ICP-OES), and textural composition including grain size quantiles, geometric specific surface area, mineral density and bulk density are given. Details about the geochemical analyses are given in Supplementary Section C.1 and C.2. N.A. = not available, ND = not detected.

Mineralogical composition (*N* = 1)	Dunite	Beach sediment
Ferroan-forsterite (wt%)	83	ND
Enstatite (wt%)	8	ND

	Dunite	Beach sediment
Chlorite (wt%)	2	ND
Quartz (wt%)	1	88
Antigorite (wt%)	2	ND
Talc (wt%)	1	ND
Hornblende (wt%)	2	ND
Feldspar (wt%)	ND	6
Calcite (wt%)	ND	3
Others (wt%)	1	3
Textural composition (*N* = 4)	**Dunite**	**Beach sediment**
D10 (μm)	93 ± 6	202 ± 3
D20 (μm)	122 ± 6	236 ± 3
D50 (μm)	189 ± 5	329 ± 3
D80 (μm)	279 ± 5	454 ± 3
D90 (μm)	332 ± 5	523 ± 3
Geometric specific surface area ($m^2 \, g^{-1}$)	0.013 ± 0.0013	0.0074 ± 0.00008
Mineral density ($g \, cm^{-3}$)	3.3	2.65
Bulk density ($g \, cm^{-3}$)	N.A.	1.6 ± 0.020
Sediment organic matter (wt%)	0.099 ± 0.0065	0.52 ± 0.14
Total inorganic carbon (wt%)	0.0047 ± 0.0010	0.64 ± 0.09
Chemical composition (*N* = 5)	**Dunite**	**Beach sediment**
MgO (wt%)	39.9	0.062
SiO_2 (wt%)	41.8[a]	100[a]
Fe_2O_3 (wt%)	5.8	0.22
NiO (wt%)	0.29	0.00022
Al_2O_3 (wt%)	0.33	0.49
Cr_2O_3 (wt%)	0.18	0.00037
MnO (wt%)	0.084	0.0045
CoO (wt%)	0.016	0.00012
ZnO (wt%)	0.0056	0.00041

[a]concentrations of SiO_2 were obtained from the manufacturer for dunite and the beach sediment was assumed to be entirely comprised of quartz (i.e. 100% SiO_2).

At the start of the experiment, approximately 1111 ± 19 L of North Sea water was pumped into all flumes resulting in a 19 to 21 cm layer of water on top of the sediment with a porosity of 39 to 41% (Figure 3.1B). The seawater was collected from the North Sea coast (Sea Life, Blankenberge, Belgium) and transported to Antwerp with a tank truck. To prevent algal growth, the flumes were covered with a black weed mat and white tarp for blocking and reflecting the sunlight, respectively (Figure 3.1C). Finally, a current velocity of 0.40 ± 0.13 m s^{-1} (mean ± S.D., N = 44) was imposed in two flumes (one with olivine and one control). No flow was induced in the other two flumes. Reynolds number calculations indicated highly turbulent flow conditions (Supplementary Section C.4). Oceanic bottom current velocities usually range from 0.01 to 0.2 m s^{-1}, but can be as high as 3 m s^{-1} (Shanmugam, 2020). Hence, the current velocity used in our experiment can be considered realistic for a dynamic coastal environment. Flow velocity was measured with a Model 801 Electromagnetic flowmeter (Valeport) at different locations and heights above the sediment bed at day 128 (Supplementary Section C.4). Sediment bed topography was measured at day 105 to determine bed shear stress (Supplementary Section C.4 and C.5). Overall, the flumes represented four treatments which will be referred to as the "stagnant sand", "stagnant olivine", "flow sand", and "flow olivine" throughout the text.

After a couple weeks with minimal TA accumulation in the overlying seawater across all treatments, the seawater was pumped out of the flumes on day 112. Subsequently, on day 119, 1213 ± 2 L of fresh seawater (~23 cm overlying water layer) was added to initiate a second measurement series. This was done to investigate the reproducibility of results due to lack of experimental unit replication. The seawater for the second series was collected from the North Sea by the RV Simon Stevin (Flanders Marine institute, Belgium) at station 330 (51.43N , 2.808E) and transported to Antwerp in black cubitainers. Prior to addition, the seawater was equilibrated to atmospheric conditions for six days with continuous aeration during the first three days (discussed in supplementary section C.6). This equilibration period explains the 7-day time gap between the removal of the seawater from the first measurement series and addition of new seawater to the flumes.
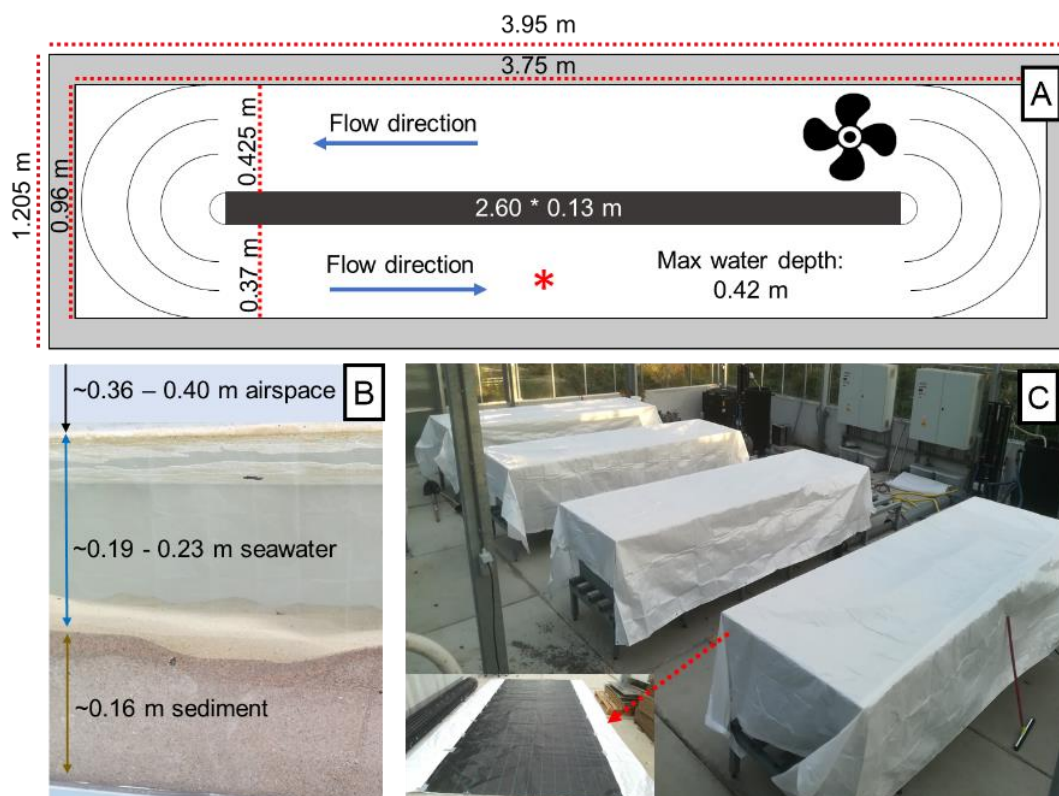
Figure 3.1: (A) Schematic top view of the experimental racetrack flumes. Red asterisk indicates sampling location, where samples were collected ~6 cm below the water surface. (B) Flume side view showing the respective depth of the sediment, seawater and airspace above. (C) Flumes were covered with black weed mat and white tarp for sunlight obscuration.

3.2.2 Seawater geochemical analyses

Overlying seawater samples for analysis of pH, conductivity, dissolved inorganic carbon (DIC), total alkalinity (TA), turbidity and dissolved metal(loid)s were collected in triplicate with 20 mL syringes (Beckton Dickinson) at various timepoints. Samples were always collected at the same location (red asterisk Figure 3.1A) and depth (~6 cm below water surface) in the flumes.

Seawater pH and salinity were measured using a HQ30D portable multi-meter (Hach) equipped with a PHC101 pH and CDC401 conductivity electrode. The pH electrode was

calibrated at the start of each sampling day with three NIST buffers (pH 4.0, 7.0, and 10.01). Seawater pH results were converted to the total hydrogen ion concentration scale based on the readings of a TRIS (2-amino-2-hydroxy-1,3-propanediol) and AMP (2-aminopyridine) buffer prepared according to Dickson et al. (2007). The relative standard deviation (RSD) was smaller than 0.14% for all samples. Calibration of the conductivity electrode was performed with NIST 50 and 12.88 mS/cm conductivity standards (VWR International) before each use. Measured conductivity values deviated from certified values by maximally 4% and the RSD was smaller than 0.55% for all samples.

Water samples for DIC and TA analysis were filtered through 0.2 µm filters (Chromafil XTRA PES-20/25, Macherey-Nagel) and stored in 50 mL Falcon tubes without headspace at 4 °C. To stop biological activity, 90 µl of mercury chloride solution (7 g L^{-1}) was added to the DIC samples before storage (Dickson et al., 2007). DIC samples were analyzed with a Shimadzu Total Organic Carbon Analyzer (TOC-VCPH). For quality control, an ultrapure MQ water sample and 50 mg L^{-1} TIC standard (Bernd Kraft) were included at the start and end of the analysis. The RSD was better than 5.1% for all samples. Seawater TA was analyzed via an open cell automated potentiometric titration with 0.1 M HCl using an automated titrator setup (888 Titrando, Metrohm). A non-linear least-squares approach was used to derive seawater total alkalinity from the titration data (Dickson et al., 2007). RSD values lower than 1.0% were obtained for all samples.

For dissolved metal(loid)s, 10 ml water samples were filtered through 0.2 µm cellulose acetate filters filter (OE66, Whatman) and acidified to 1.4% V/V nitric acid (HNO_3) with TraceMetal™ Grade 67-69% HNO_3 (Fisher Scientific) before storage at -20 °C. Samples were diluted 20 times with 2% V/V HNO_3 before analysis by HR-ICP-MS (Element XR, Thermo Scientific). Procedural blanks (2% V/V HNO_3) and NIST SRM 1640a reference samples (Merck) were included in the analysis to check for sample contamination and accuracy of the analytical results, respectively. A maximum RSD of 5% was allowed for the measurements.

Unfiltered seawater samples for turbidity analysis were analyzed with a Hach DR 2000 spectrophotometer by measuring light absorption at a wavelength of 450 nm (Hach method 8237). On each measurement day, a two-fold serial dilution (1.56 to 400 FTU) was made from a 4000 NTU formazin turbidity standard (VWR International) for calibration ($R^2 \geq 0.9997$). For quality control, a 100 NTU formazin turbidity standard and ultrapure Milli-Q (MQ) water (Merck) blank were measured after every 12 samples. A maximal RSD of 66% was obtained for the lower turbidity (<6 FTU) samples and 12% for higher turbidity (>6 FTU) samples.

3.2.3 Saturation state calculations

Based on the measured seawater chemistry, mineral saturation states as a function of time ($\Omega(t)$) were calculated using PHREEQC Interactive (version 3.7.3-15968) and its LLNL database (Parkhurst and Appelo, 2013). Mineral saturation states correspond to the ratio of the actual ion activity product and the solubility product. Subsequently, mineral saturation indices ($SI(t)$) were calculated as $SI(t) = \log10(\Omega(t))$ (undersaturation occurs at $SI(t) < 0$, supersaturation at $SI(t) > 0$). Seawater temperature, density, TA, pH, and total dissolved concentrations for a range of chemical species (Ca, Mg, Cd, Pb, V, Al, Cr, Mn, Co, Fe, Ni, Cu, Zn, Si, K, Na, Cl, SO_4, and Li) were given as input data for the calculations of ($\Omega(t)$) values. Seawater Na, Cl, and SO_4 concentrations were not analyzed but derived from the chemical composition of natural seawater assuming a fixed ratio with measured K concentrations (Hem, 1985).

3.2.4 Solid phase analyses

At the start of the experiment, beach sediment and olivine were sampled for grain size distribution, elemental, and sediment organic matter (SOM) analysis (Table 3.2). Grain size distribution was analyzed with a Mastersizer 2000 laser diffraction particle analyzer (Malvern Panalytical) according to standard operating procedures (SOPs) without chemical pre-treatment. Beach sediment samples were sieved through a 1 mm mesh size sieve prior to analysis to remove large shell fragments. Elemental composition was

determined via ICP-OES (iCAP 6300 Duo, Thermo Scientific) after microwave-assisted acid digestion according to a modified chromite ore protocol described in Supplementary Section C.2 (CEM Corporation, 1999).

Sediment organic matter (SOM) content of olivine and beach sediment (expressed in % w/w) was determined via loss on ignition according to the protocol by Wang et al. (2012). Briefly, 5.011 ± 0.025 g of olivine or beach sediment was dried at 105 °C for 12 hours to constant weight. Subsequently, organic matter was combusted in a muffle furnace (B180, Nabertherm) at 375 °C for 17 hours. SOM was calculated as the dry weight loss 375 °C (d.w.$_{375}$) compared to 105 °C (d.w.$_{105}$) as follows:

$$\text{SOM} = \frac{(\text{d.w.}_{105} - \text{d.w.}_{375})}{\text{d.w.}_{105}} 100 \qquad [3.7]$$

Unfiltered seawater samples for analysis of suspended solids were collected at each sampling day in 50 mL Falcon tubes and centrifuged at 2773 g for 1 min before decanting the supernatant seawater. The remaining pellet was subsequently rinsed twice with ultrapure MQ water and dried at 60 °C for 48 hours. The dried samples were analysed via both scanning electron microscopy with energy dispersive X-ray analysis (SEM-EDX) and Raman spectroscopy. For SEM-EDX analysis, dried samples were fixed on aluminium pin stubs with double sided carbon tape and analyzed with a Tescan MIRA3 SEM equipped with a Field Emission Gun (FEG) and energy dispersive spectrometer (EDS) capability. For Raman spectroscopy, a Renishaw inVia Qontor confocal Raman microscope equipped with 30 mW 405 nm and a charged-coupled device array detector was used for analysis of 20 random points in each sample. For all measurements a 2400 line mm^{-1} grating was used. The laser power at the sample surface was adjusted to approximately 1.8 mW. The laser beam was focused onto the sample surface through a Leica HC PL Fluotar 100x and 0.9 NA objective, resulting in a spatial resolution of 275 nm. Prior to the analysis the energy was calibrated and verified using an internal silicon standard with a Raman shift at 520.2 ± 0.5 cm^{-1}. The spectral range was set to 93-2390 cm^{-1} for all samples. All data acquisition was performed using the Renishaw WiRE v.5.6 software package. Cosmic rays

were manually removed with the ZAP function and the background was subtracted using least squares polynomial fitting. Obtained spectra were compared to the Renishaw library for inorganic materials and the RRUFF database.

At the end of the experiment, sediment cores were taken to investigate olivine depth distribution, secondary mineral formation, olivine dissolution features, sediment bulk density, and sediment total inorganic carbon (TIC) content. Sediment cores for bulk density and porosity derivation were taken in the stagnant sand and stagnant olivine treatment at the end of the experiment. Kopecky rings (Ø 53 mm) were inserted in the top 5 cm (= height Kopecky ring) of the sediment. The cores were transferred to pre-weighed polypropylene containers and weighed on an analytical balance before and after drying at 60 °C for 72 h to calculate the bulk density (ρ_b in kg m^{-3}) according to following equation:

$$\rho_b = \frac{m_s}{V_s}$$ [3.8]

In which m_s is the dry weight of the sediment (kg) and V_s is the volume of the sediment (1.1E-04 cm³). The porosity (φ in %) of the sediment was then calculated using the particle density of quartz (ρ_p = 2650 kg m^{-3}) according to following equation:

$$\varphi = 1 - \frac{\rho_b}{\rho_p}$$ [3.9]

Sediment cores to assess the olivine depth distribution could not be taken using conventional sediment corers (e.g. liner sampler) due to sandy North Sea beach sediment. Therefore, PVC tubes (Ø = 1 cm, height = 30 cm) were gently inserted in the beach sediment and taken out using a gauging trowel. Cores were transported to the lab upright and stored frozen at -20 °C until analysis via micro computed tomography (micro-CT). Scanning was performed for one core of the flow olivine and stagnant olivine treatment using the XRE CoreTOM (Tescan) instrument with a voxel size of 3 µm. Both samples were scanned using the same scanning parameter of 100 kV accelerating voltage, 10 W power,

225 ms exposure time and 0.5 mm aluminium filter mounted at the source. Radiographs then were reconstructed using Panthera software by Tescan. The 3D images then were processed using Avizo 2022.2. The image was filtered using non-local means, segmented using interactive thresholding, and touching particles were separated by a morphology operation. Subsequently, the particles were individually labelled and analyzed. Since the grey values for $CaCO_3$ and olivine were similar, particles were differentiated based on the assumption that olivine particles would be more rounded than $CaCO_3$ particles, having a sphericity larger than 0.6. The analysis procedure and results of sediment TIC content are given in Supplementary Section C.2.

Finally, the upper 10 cm of the sediment was sampled with a modified (top cut off) 100 mL syringe (Plastipak, Becton Dickinson) and deposited minerals on the flume walls were collected at the end of the experiment to investigate the presence of olivine dissolution features and secondary mineral formation. Sediment samples were divided in an upper (0-5 cm) and lower (5-10 cm) section, carefully rinsed with ultrapure MQ, and dried at 60 °C before SEM-EDX analysis. Mineral deposits on the flume walls were rinsed with ultrapure MQ, and dried at 60 °C before analysis via SEM-EDX and Raman spectroscopy.

3.2.5 Total dissolved olivine

The amount of dissolved olivine was monitored based on the concentration difference of specific compounds (i = TA, DIC, DSi, DNi) in the overlying seawater of olivine treatments compared to beach sediment treatments. The accumulation ΔN_i (expressed in mmol) of a give compound i at time t (days) was calculated as:

$$\Delta N_i(t) = \left[C_{ol,i}(t) - C_{bs,i}(t)\right]V_{total}(t) \qquad [3.10]$$

Where $C_{ol,i}(t)$ and $C_{bs,i}(t)$ represent the concentration (expressed in mmol L^{-1}) of compound i at time t (days) in an olivine treatment (ol) or beach sediment (bs) treatment, respectively. $V_{total}(t)$ is the total seawater volume (expressed in L) in the flumes at time t, which was calculated from the total height (sediment + overlying water) at time t ($h_{total}(t)$,

expressed in m), flume surface area (A_{flume} = 3.097 m²), sediment volume (V_{sed} = 0.39 or 0.42 m³ for *bs* and *ol* treatments, respectively) and sediment porosity (Φ = 0.39 and 0.41 for *bs* and *ol* treatments, respectively) according to

$$V_{total}(t) = (h_{total}(t)A_{flume} - V_{sed}(1 - \Phi))1000 \qquad\qquad [3.11]$$

The sediment volume V_{sed} was derived from the total sediment mass (m_{total} = 630 or 650 kg for *bs* and *ol* treatments, respectively) and sediment bulk density (V_{sed} = m_{total}/ρ_b). Subsequently, the amount of dissolved olivine $N_{ol,i}(t)$ at time t could be calculated using the theoretical stoichiometric coefficient ν_i (expressed in mmol mmol^{-1} olivine) for a specific compound i in the experimental olivine ($\nu_{TA} = 3.73, \nu_{DIC} = 3.13, \nu_{Si} = 1, \nu_{DNi} = 0.0055$; Supplementary Section C.1 provides details on the derivation of stoichiometric coefficients) via

$$N_{ol,i}(t) = \frac{\Delta N_i(t)}{\nu_i} \qquad\qquad [3.12]$$

Please note that in Eq. 3.10, we make the assumption that concentrations of olivine reaction products are equal in the overlying water and pore water. It is important to recognize that this assumption is not valid for the stagnant olivine treatment due to slow reaction product efflux from the sediment in the absence of water current. However, since reaction product concentrations were not measured in pore water, adjustments cannot be made to account for this discrepancy. Consequently, the calculated amount of dissolved olivine is likely to be underestimated, particularly for the stagnant treatment.

For comparison to laboratory enhanced olivine weathering experiments, the olivine dissolution rate constant ($k_{ol}(t)$, expressed in mol m^{-2} s^{-1}) for the seawater temperature (T, expressed in K) and pH at a given sampling day was derived from the rate equation by Rimstidt et al. (2012)

$$k_{ol} = 10^{4.07 - 0.256pH(t) - \frac{3465}{T}} \qquad\qquad [3.13]$$

Finally, the estimated amount of dissolved olivine $N_{ol}(t)$ (mmol) at time t (s) was calculated with the dunite geometric specific surface area A_{GEO} (0.013 m² g⁻¹), mass m_{dunite} (20000 g), and its olivine fraction φ_{ol} (0.83) according to

$$N_{ol}(t) = 1000 k_{ol}(t) m_{dunite} \varphi_{ol} A_{GEO} t \qquad [3.14]$$

3.3 Results

3.3.1 Seawater chemistry changes

During the first three weeks of the experiment significant changes were observed in seawater pH, TA, and DIC (Figure 3.2A-C). A low seawater pH of 7.7 and high DIC concentration (around 2580 µmol L⁻¹) were measured in all flumes at the start of the experiment (Figure 3.2A and 3.1C). Seawater pH rose to approximately 8.05 after 2 days in the flow treatments and 17 days in the stagnant treatments (Figure 3.2A). Simultaneously, DIC concentrations decreased by approximately 300 µmol L⁻¹ (to 2200 µmol L⁻¹) after 7 days in the flow treatments and 21 days in the stagnant treatments (Figure 3.2C). A slow and steady increase in TA from 2787 µmol L⁻¹ to around 2865 µmol L⁻¹ was observed for the stagnant treatments, while TA concentrations first decreased from 2787 µmol L⁻¹ at day 0 to approximately 2625 µmol L⁻¹ at day 7 in the flow treatments before increasing on subsequent sampling days (Figure 3.2B).

From day 21 until day 112, seawater pH varied from 7.92 to 8.19 in all treatments (Figure 3.2A). On day 70 and 91 onwards, seawater pH was substantially elevated (by 0.15 – 0.26) in the flow treatments compared to the stagnant treatments (Figure 3.2A). Differences in pH between the olivine and control treatments were limited (up to ± 0.04) for both the stagnant and flow conditions (Figure 3.2A). Seawater TA continued to slowly increase in the stagnant treatments to reach approximately 3035 µmol L⁻¹ at day 112. TA concentrations increased to 3265 µmol L⁻¹ in the flow sand and 3354 µmol L⁻¹ in the flow olivine treatment at day 81 after which no further increase was observed (Figure 3.2B). DIC concentrations steadily increased to 2870 µmol L⁻¹ in the stagnant and 3150 µmol L⁻¹

in the flow treatments at day 81 (Figure 3.2C). Afterwards, DIC concentrations remained stable until day 112 (Figure 3.2C).

After water renewal on day 119, seawater TA and DIC increased until day 129 in all treatments (Figure 3.2B-C). From day 129 onwards, TA concentrations steadily increased in the stagnant treatments and remained stable in the flow treatment to reach similar concentrations (2707 – 2772 µmol L^{-1}) at day 175 (Figure 3.2B). Seawater DIC concentrations remained stable in the stagnant treatments and steadily decreased in the flow treatments to reach similar concentrations (2191 – 2290 µmol L^{-1}) at day 175 (Figure 3.2C).

Both DSi and DCa concentrations varied considerably throughout the experiment, but no clear temporal trends or differences between treatments were observed (Figure 3.2D-E). DSi concentrations ranged from 33 to 60 µmol L^{-1}, while DCa concentrations ranged from 6.6 to 11.8 mmol L^{-1} (Figure 3.2D-E). Concentrations of dissolved magnesium (DMg) and dissolved potassium (DK) showed similar temporal variation compared to DCa (Supplementary Figure C.15).
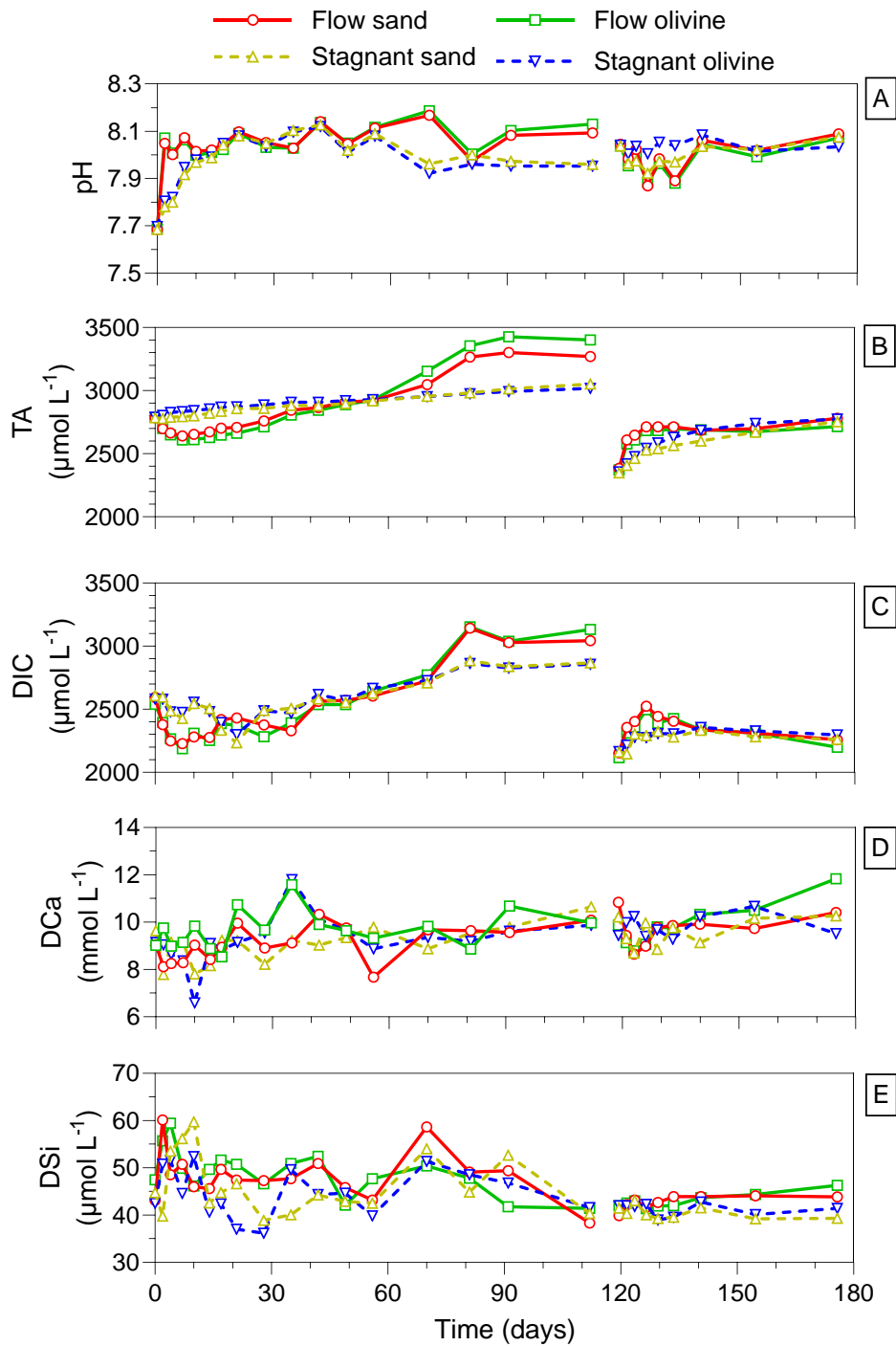
Figure 3.2: Temporal evolution of (A) seawater pH, (B) total alkalinity (TA), (C) dissolved (<0.2 μm) inorganic carbon (DIC), (D) dissolved calcium (DCa), and (E) dissolved silicon (DSi) during the 175-day flume experiment.

3.3.2 Potential of secondary mineral precipitation

The $SI(t)$ for forsterite (Mg_2SiO_4) and several secondary minerals observed in previous laboratory marine olivine weathering experiments (Rigopoulos et al., 2018; Fuhr et al., 2022) are shown in Figure 3.3. Similar trends were observed for the forsterite, aragonite, and chrysotile $SI(t)$ throughout the first measurement series (Figure 3.3A-C). At day 2, the $SI(t)$ of these minerals rapidly increased in the flow treatments and remained elevated until day 7 (Figure 3.3A-C). From day 10 to 56 the $SI(t)$ of aragonite and chrysotile remained positive and relatively stable, while the seawater remained undersaturated with respected to forsterite (Figure 3.3A-C). From day 70 until day 112 significant temporal variation was observed with elevated $SI(t)$ in the flow treatments compared to the stagnant treatments (Figure 3.3A-C). The $Fe(OH)_3$ $SI(t)$ was negative on most sampling days with no clear differences among treatments (Figure 3.3D).

After water renewal on day 119, $SI(t)$ fluctuations until day 133 were observed followed by a continuous increase in the $SI(t)$ of forsterite and all considered secondary minerals until the end of the experiment (Figure 3.3). The seawater was supersaturated with respect to aragonite (Figure 3.3B) and undersaturated with forsterite (Figure 3.3A) on all sampling days. The amorphous ferrihydrite $SI(t)$ was close to equilibrium and the seawater was supersaturated with respect to chrysotile on most sampling days (Figure 3.3C-D). Overall, the $SI(t)$ of $Fe(OH)_3$, aragonite and chrysotile was positive at the end of the experiment, elevated under flow conditions on some sampling days, but not significantly different between olivine and sand treatments (Figure 3.3B-D).
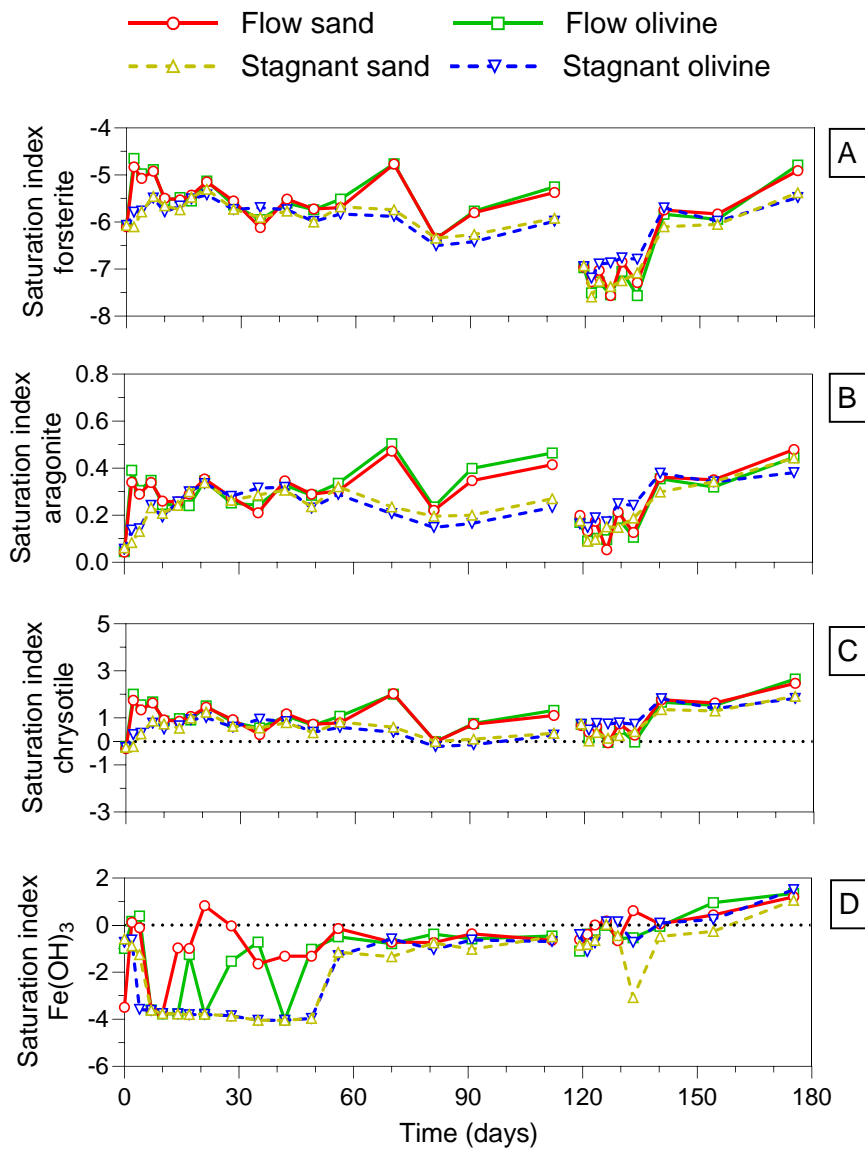
Figure 3.3: Temporal evolution of seawater (A) forsterite, (B) aragonite, (C) chrysotile, and (D) Fe(OH)$_3$ saturation indices calculated from the experimental data in PHREEQC V3 using the LLNL database.

3.3.3 Composition of suspended and deposited phases

Significant amounts of particles were suspended at the start of the experiment in the flumes with current as indicated by the high seawater turbidity of 98 FTU in the flow sand

and 127 FTU in the flow olivine treatment at day 2 (Figure 3.4). Seawater turbidity remained low (0.5 to 7 FTU) in the stagnant sand and stagnant olivine treatment throughout the 175-day experiment (Figure 3.4). Seawater turbidity decreased logarithmically on subsequent sampling days and levelled off at 13 FTU in the flow sand and 68 FTU in the flow olivine treatment at day 112 (Figure 3.4). An elevated seawater turbidity of 34 FTU and 85 FTU was observed in the flow sand and flow olivine treatment two days after seawater renewal (day 121) (Figure 3.4). Subsequently, seawater turbidity decreased logarithmically to reach 10 FTU and 31 FTU on day 175 in the flow sand and flow olivine treatment, respectively (Figure 3.4).
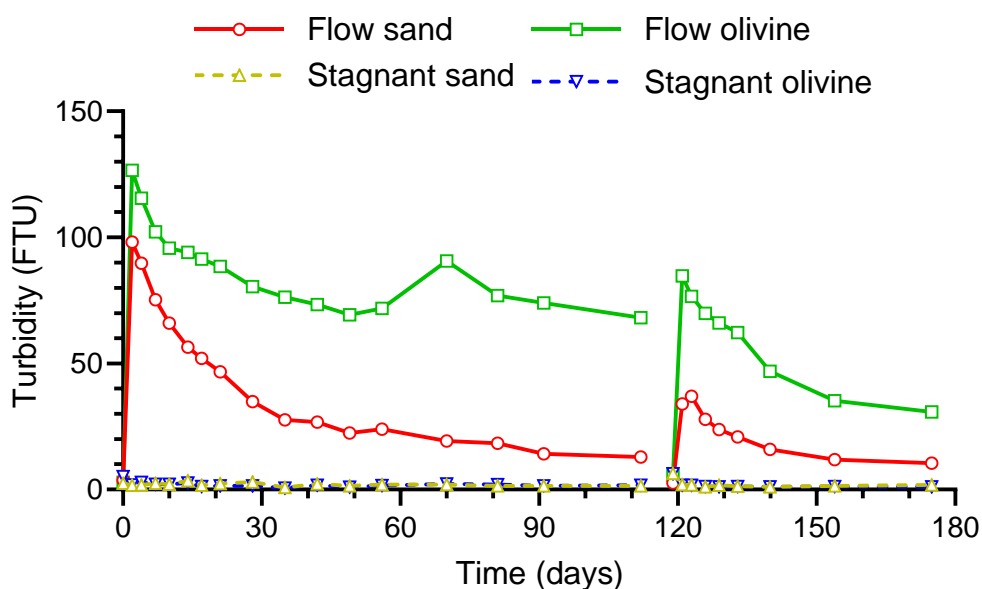
Figure 3.4: Temporal evolution of seawater turbidity (FTU) during the 175-day flume experiment.

The suspended mineral matrix was primarily composed of amorphous material containing a range of elements (O, Mg, K, Si, Al, Ca, Fe) (Figure 3.5C1-C2). These elements could not be definitively attributed to specific minerals through SEM-EDX analysis. Similarly, Raman spectroscopy did not yield specific mineral identifications. However, a clear peak at

approximately 1600 cm^{-1} suggested the presence of amorphous carbon (Dychalska et al., 2015) (Figure C.10-C.11), indicating that the predominant component of the suspended material matrix was organic in nature. The nature of the suspended particles did not differ significantly between flow treatments (Figure 3.5) or sampling days. Next to the amorphous organic material, some olivine and quartz particles were identified (Figure 3.5C6). Moreover, iron rich particles containing Cr, Ni and S were observed, indicating the possible presence of chromite, iron sulphides (probably pyrite), and iron (hydr)oxides. Finally, considerable amounts of rod-shaped calcium carbonate ($CaCO_3$) particles (likely aragonite) were observed (Figure 3.5C4 and 3.5C5).
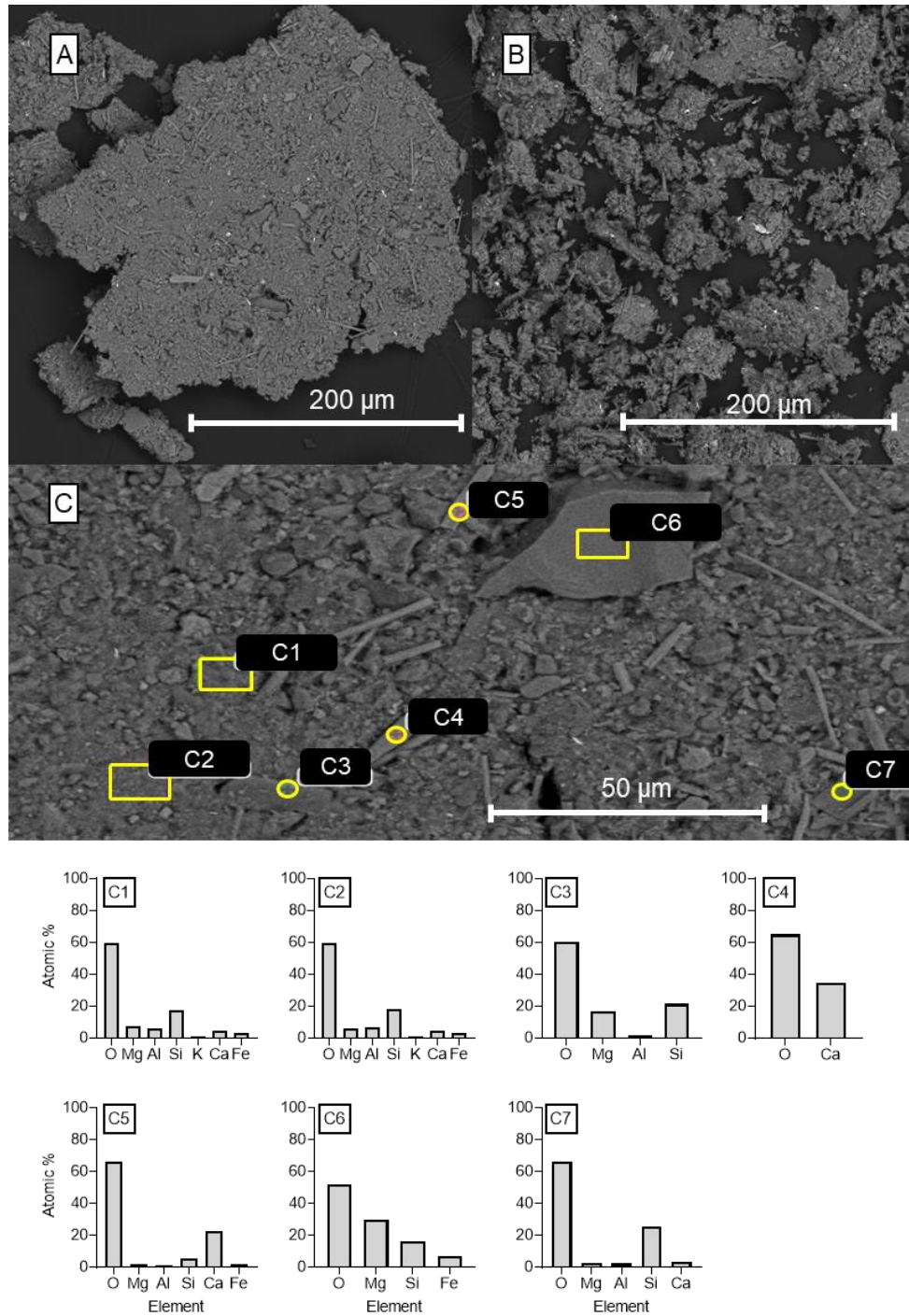
Figure 3.5: Backscattered electron (BSE) scanning electron microscopy (SEM) images of suspended particles from the (A, C) flow olivine and (B) flow sand treatment on day 2 of the experiment. (C1-C7) Elemental composition of the suspended particles in (C) measured via SEM-EDS analysis.

Deposited particles on the flume walls at the end of the experiment were brown to black in colour (Figure 3.6A) and consisted mainly of fine (<10 μm) particles with different elemental compositions (Figure 3.6B-D). Particles on the flume walls were visually observed to be more abundant and darker in colour in the flow treatments compared to the stagnant treatments. No clear difference in mineral composition of the wall deposits could be identified between the olivine and sand treatments via SEM-EDX and Raman spectroscopy. Similar to the suspended matter, the bulk mineral matrix was comprised of a range of elements (including O, Al, Si, Na, Zn, Cr, and Fe) and organic in nature as indicated by the distinct amorphous carbon peaks at approximately 1600 cm^{-1} in the Raman spectra (Figure C.12-C.13). A considerable amount of high atomic number particles (light coloured in BSE-SEM image) were present in the flow treatments which were rich in Fe and Cr according to SEM-EDS analysis (Figure 3.6D1, 3.6D4, and 3.6D5). Additionally, several particles also contained some S and Ni, suggesting that these iron rich phases could be chromite ($FeCr_2O_4$), nickel or iron sulphides, iron (hydr)oxides, or particles released from corrosion of the stainless steel flume. Moreover, particles rich in Ca were observed, which were likely $CaCO_3$ minerals that were flushed from the sediment and settled on the flume walls (Figure 3.6D3). Cubic NaCl crystals, that formed during sample drying, were also consistently present (Figure 3.6D6).
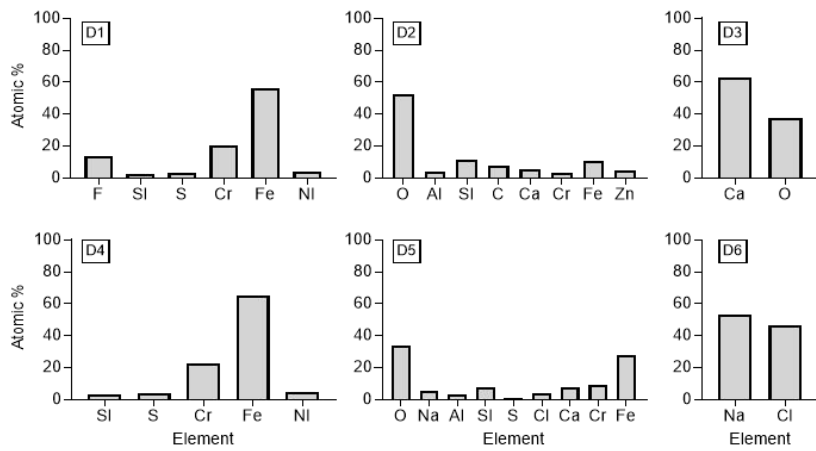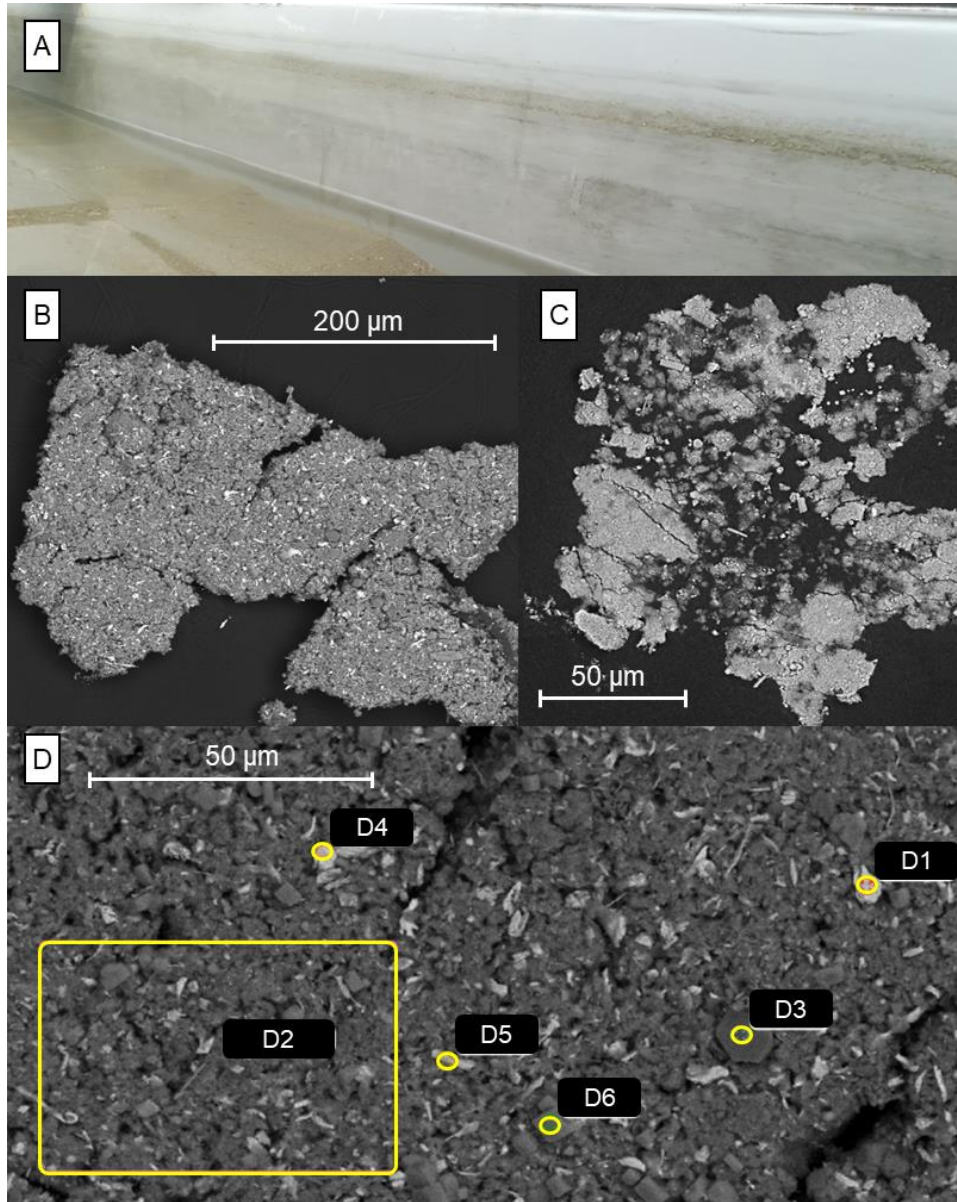
Figure 3.6: (A) Dark brown particles distributed across the walls of the flow olivine flume at the end of the experiment. Backscattered electron (BSE) scanning electron microscopy (SEM) images of wall precipitates from the (B, D) flow sand and (C) stagnant sand treatment. (D1-D6) Elemental composition of the wall precipitates in (D) measured via SEM-EDS analysis.

3.3.4 Olivine distribution and dissolution features

Olivine was relatively homogeneously distributed in the 1 cm wide sediment cores from the stagnant and flow olivine treatment according to micro-CT scans of sediment cores (Figure 3.7). However, the overall olivine concentrations of 7.5% V/V in the flow olivine treatment was significantly higher than the 1% V/V in the stagnant olivine treatment (Figure 3.7). No clear trend was observed for the $CaCO_3$ concentration as a function of sediment depth in the stagnant olivine treatment (Figure 3.7A). Conversely, $CaCO_3$ was more abundant at a depth of 5 cm (Figure 3.7B), which is supported by visual observations of large amounts of shell fragments in the top sediment layer from the flow treatments.
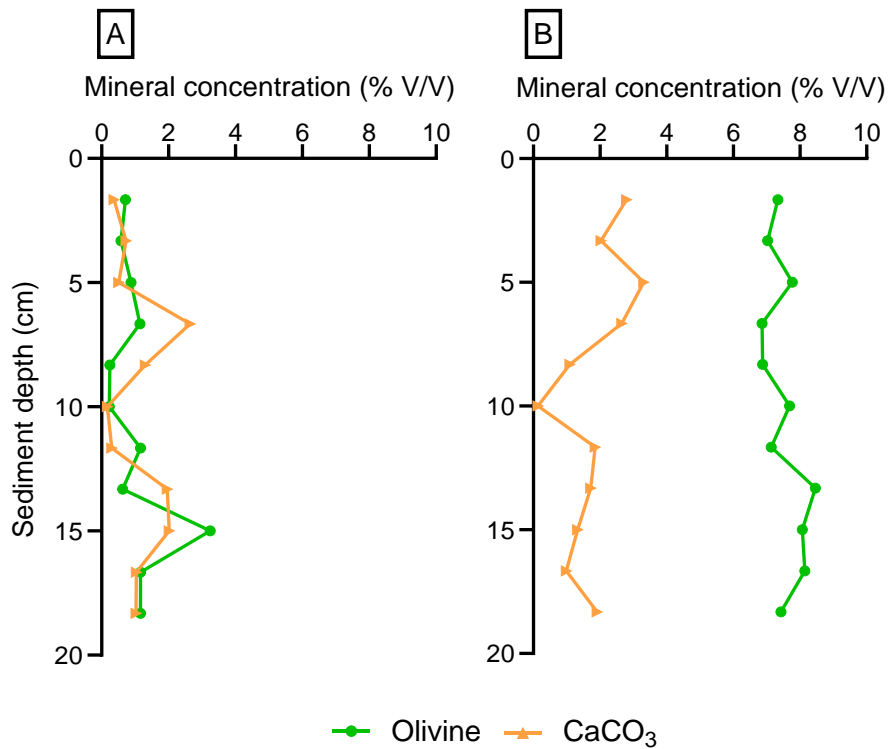
Figure 3.7: Depth profile of the olivine and CaCO3 concentration (% V/V) in the (A) stagnant olivine and (B) flow olivine treatment derived from micro-CT scans of sediment cores collected at the end of the 175-day flume experiment.

Fresh olivine consisted of angular grains of various shapes with sharp edges (Figure 3.8A). Furthermore, pristine grains were covered with fine (<10 μm) olivine particles, likely originating from the industrial grinding process (Figure 3.8A). At the end of the 175-day experiment, olivine collected from the top 5 cm of the sediment exhibited a notable reduction in surface fines in case of the stagnant treatment and virtually no surface fines in case of the flow treatment (Figure 3.8B-C). Furthermore, these grains did not show a clear increase in surface dissolution features (e.g. etch pits or surface fractures) or rounded grain edges compared to fresh olivine (Figure 3.8B-C). Finally, no secondary mineral coatings were observed on weathered olivine grains (Figure 3.8B-C).
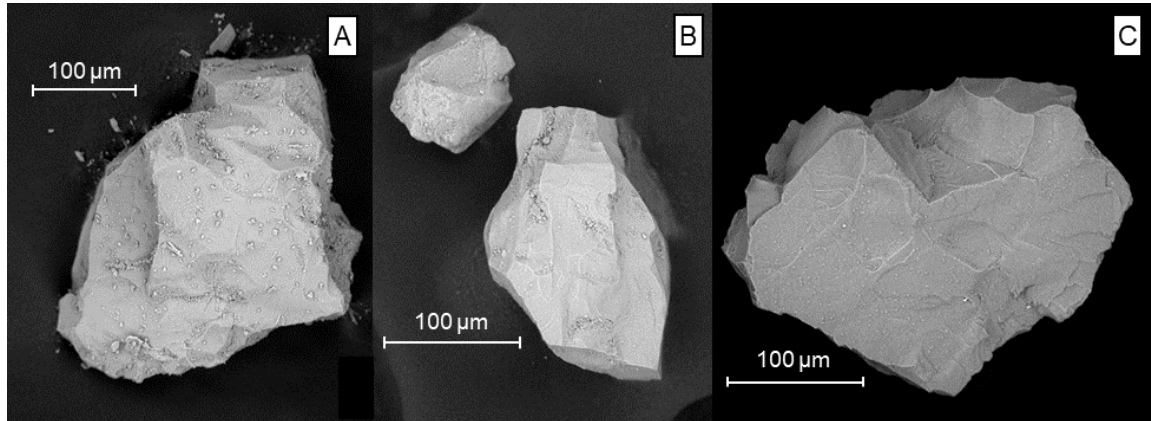
Figure 3.8: Scanning electron microscope (SEM) images of representative grains of (A) fresh olivine and weathered olivine from (B) the stagnant and (C) the flow treatment recovered from the top 5 cm of the sediment at the end of the 175-day flume experiment.

3.3.5 Trace metal accumulation

Dissolved Ni concentrations in the stagnant treatments remained below the detection limit (0.34 nmol L^{-1}) until day 70 (Figure 3.9A). Afterwards, concentrations increased up to 0.46 µmol L^{-1} in the stagnant sand and 1.2 µmol L^{-1} stagnant olivine treatment, respectively (Figure 3.9A). For the flow treatments DNi concentrations increased from below the detection limit at day 0 to approximately 0.85 µmol L^{-1} within three weeks (Figure 3.9A). Subsequently, DNi concentrations proceeded to increase up to 1.6 µmol L^{-1} in the flow sand and 5.4 µmol L^{-1} in the flow olivine treatment (Figure 3.9A). After water renewal on day 119, DNi concentrations ranged between 0.13 and 0.28 µmol L^{-1} (Figure 3.9A). In the stagnant sand and stagnant olivine treatment concentrations gradually increased to 0.82 and 0.34 on day 175, respectively (Figure 3.9A). For the flow sand treatment Ni concentrations increased to 1.2 µmol L^{-1} after one week (day 126) and remained relatively stable (1.2 to 1.6 µmol L^{-1}) until the end of the experiment. For the flow olivine treatment, a rapid increase to 2.2 µmol L^{-1} was observed within two days (day 121) followed by a further increase up to 3.3 µmol L^{-1} on day 133. Afterwards, dissolved Ni concentrations gradually decreased to 2.3 µmol L^{-1} on day 175 (Figure 3.9A).

Dissolved Cr concentrations were significantly lower than dissolved Ni concentrations for all treatments throughout the experiment (Figure 3.9B). For the stagnant sand and olivine treatments, concentrations decreased from approximately 0.020 µmol L^{-1} at day 0 to below detection limit (<0.38 nmol L^{-1}) until day 70 (Figure 3.9B). From day 70 until day 112 varying concentrations up to 0.047 µmol L^{-1} were observed with no clear difference between treatments (Figure 3.9B). For the flow sand and flow olivine treatment, an initial increase in DCr concentration up to 0.086 and 0.24 µmol L^{-1} was observed after 2 and 4 days, respectively (Figure 3.9B). Subsequently, DCr concentrations fluctuated until day 112 from below detection limit to 0.28 µmol L^{-1} in the flow sand and 0.026 to 0.21 µmol L^{-1} in the flow olivine treatment (Figure 3.9B). After water renewal, DCr concentrations ranged from below detection limit to 0.023 µmol L^{-1} in the stagnant treatments (Figure 3.9B). For the flow sand treatment, concentrations ranged from below the detection limit to 0.051 µmol L^{-1} with a sudden increase to 0.34 µmol L^{-1} on day 175 (Figure 3.9B). Dissolved Cr concentrations in the flow olivine treatment were higher compared to the flow sand treatment on most sampling days ranging between 0.011 and 0.12 µmol L^{-1} (Figure 3.9B).
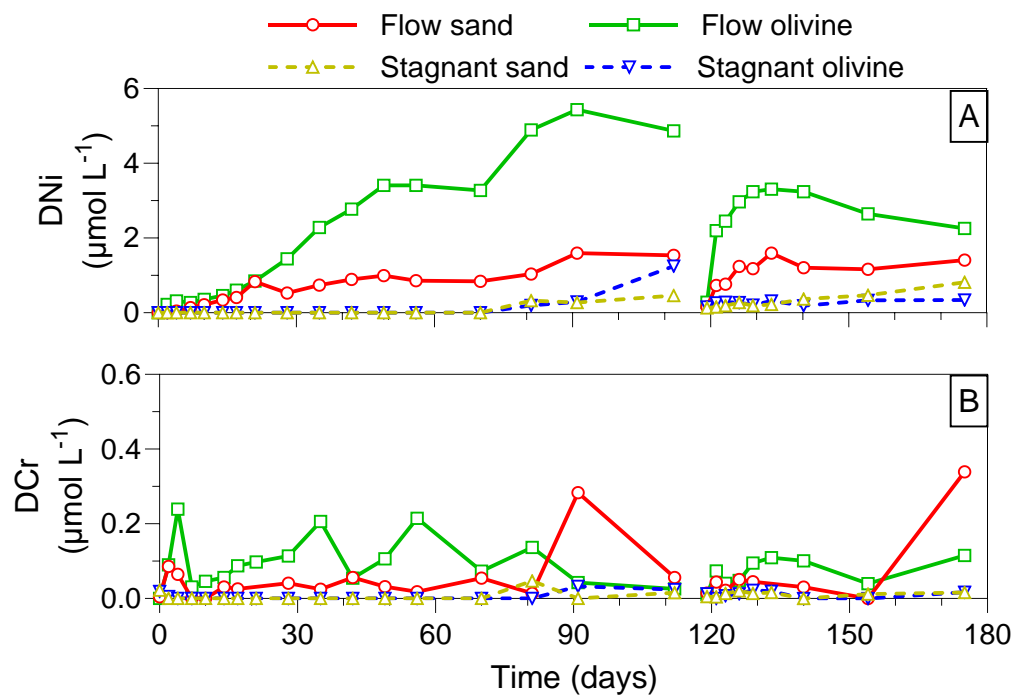
Figure 3.9: Temporal evolution of dissolved (<0.2 μm) nickel (DNi) and chromium (DCr) concentrations (μmol L^{-1}) during the 175-day flume experiment.

3.3.6 Total dissolved olivine

The amount of dissolved olivine based on accumulation of TA, DIC, and DSi were low during both measurement series for the stagnant and flow olivine treatment (Figure 3.10). For the stagnant olivine a total amount of -10 to 1.1 mmol would have dissolved during the first measurement series (112 days) and 1.5 to 14 mmol during the second measurement series (day 119 to 175) (Figure 3.10B). For the flow olivine treatment 1.5 to 37 mmol of olivine would have dissolved at day 112 and -23 to 2.4 mmol at the end of the second measurement series (day 175) (Figure 3.10B). Please note that negative values for the amount of dissolved olivine indicate that concentrations of TA, DIC, and/or DSi were overall higher in the sand control compared to the olivine treatment. These negative values should not be interpreted as precipitation of olivine.

The amount of dissolved olivine derived from DNi accumulation was significantly higher compared to TA, DIC and DSi derived amounts and elevated in the flow olivine treatment compared to the stagnant olivine treatment (Figure 3.10). At total amount of 158 mmol olivine would have dissolved until day 112 and -104 mmol from day 119 to 175 based on DNi accumulation for the stagnant olivine treatment (Figure 3.10A). For the flow olivine treatment, 641 mmol of olivine would have dissolved during the first measurement series and 185 mmol during the second measurement series (Figure 3.10B). Importantly, porewater concentrations from the first measurement series were not measured and could therefore not be subtracted from measured overlying water concentration in the second measurement series. Therefore, the amount of dissolved olivine from day 119 to day 175 is an overestimation.

The average amount of dissolved olivine after 112 days based on the rate equation by Rimstidt et al. (2012) is equal to 136 mmol (-66 to 338 mmol) for the stagnant olivine treatment and 132 mmol (-64 to 327 mmol) for the flow olivine treatment (Figure 3.10A). At the end of the second measurement series (day 175), the expected amount of dissolved olivine would be equal to 121 mmol (-57 to 300 mmol) for the stagnant and 124 mmol (-58 to 306 mmol) for the flow olivine treatment (Figure 3.10B).
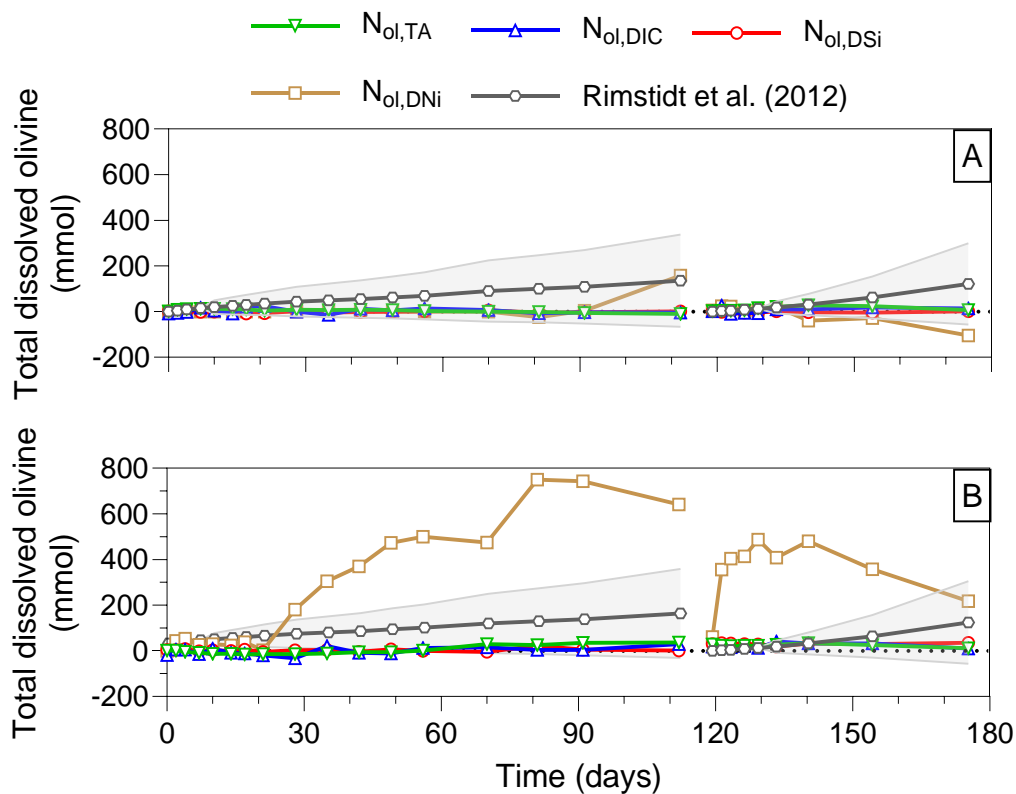
Figure 3.10: Temporal evolution of total dissolved olivine $N_{ol,i}$ (mmol) in the (A) stagnant, and (B) flow treatment derived from weekly concentrations of seawater total alkalinity (TA), dissolved inorganic carbon (DIC), dissolved silicon (DSi), or dissolved nickel (DNi). Additionally, the estimated amount of total dissolved olivine (grey line) and associated propagated errors (grey shading) based on the rate equation by Rimstidt et al. (2012) is shown.

3.4 Discussion

3.4.1 Low olivine dissolution rates

We investigated the effect of water current on olivine dissolution kinetics in natural seawater and hypothesized that advective pore water flushing and bedload transport would enhance olivine dissolution by preventing porewater saturation and the formation of secondary coatings on mineral grains (Meysman and Montserrat, 2017). Although

water current enhanced alkalinity release from marine sediment (Figure 3.2B), olivine addition did not result in significant seawater TA, DIC, and DSi increases compared to the beach sediment control under both stagnant and flow conditions (Figure 3.2). Consequently, the total amount of dissolved olivine derived from TA, DIC and DSi accumulations for both stagnant (maximally 9.6 mmol) and flow (maximally 16 mmol) treatment was significantly lower than expected based on estimates from the empirical rate equation by Rimstidt et al. (2012) (around 255 mmol) (Figure 3.10). Four processes could potentially explain the apparently low olivine dissolution in our study, namely (I) rate limiting air-seawater CO_2 exchange, (II) pore water saturation, (III) reduced olivine reactive surface area through for example passivating layer formation, and (IV) secondary mineral formation.

Olivine dissolution generates alkalinity enriched (i.e. CO_2 deficient) seawater that needs to be transported from the seafloor to the surface ocean for CO_2 uptake to occur via atmospheric CO_2 equilibration (Bach et al., 2023). This process, which is enhanced by currents and waves (Wanninkhof, 2014), is also necessary to prevent high seawater pH increases that could adversely affect marine biota and reduce olivine reactivity (Bach et al., 2019). Here, seawater pCO$_2$ values were not significantly different among treatments and relatively close to atmospheric pCO$_2$ levels ($\approx$ 420 µatm) on most sampling days (Figure C.4). At the start of the experiment seawater pCO$_2$ was high (1229 ± 18 µatm , N = 4) in all treatments (Figure C.4), which can be explained by the pressurized seawater transfer from the tank truck to the flumes which resulted in low seawater pH and high DIC concentrations (Figure 3.2A and 3.2C). Outgassing of CO_2 occurred significantly faster in the flow treatments (within 2 days) compared to the stagnant treatments (roughly 17 days) (Figure C.4 and Figure 3.2C). Overall, seawater pCO$_2$ values indicate that air-seawater CO_2 exchange rates did not limit olivine dissolution during our experiment.

Upon olivine dissolution in a coastal seabed, increases in pore water pH and build-up of reaction products could reduce olivine reactivity (Meysman and Montserrat, 2017; Montserrat et al., 2017). However, porewater flushing by means of burrowing macrofauna (i.e. bio-irrigation) and advection by waves and currents could remove olivine dissolution products more quickly than they are generated (Meysman and Montserrat, 2017). A number of mechanisms drive pore water flow in permeable sediments exposed to continuous currents, including flow-and topography-induced pressure gradients, ripple migration, and fluid shear (Santos et al., 2012). Results of a two-dimensional numerical model approach by (Shum, 1992) indicated that the zone of advection is limited to a few ripple heights below the ripple surface under a range of different wave and sediment characteristics. Based on an average measured ripple height of approximately 2.5 cm in the flow treatments, olivine dissolution possible slowed down in deeper parts of the sediment due to pore water saturation. However, due to a lack of pore water data, this hypothesis cannot be confirmed.

The reactive surface area of olivine, interacting with the porewater solution, may have been considerably lower than the total olivine surface area due to grain-to-grain contact and the development of passivating mineral coatings (Oelkers et al., 2018). Unfortunately, the area of touching grain surfaces could not be confidently estimated from sediment core micro-CT scans due to the difficulty in distinguishing olivine from $CaCO_3$ particles. Thin passivating amorphous Si layers have been observed to reduce olivine dissolution by several orders of magnitude in previous experiments conducted at elevated pCO_2 (10 – 247 atm) and temperature (25 – 185 °C) conditions (Béarat et al., 2006; Daval et al., 2011; Wang and Giammar, 2013; Johnson et al., 2014). Additionally, precipitation of Fe(III) hydroxide phases can reduce reactivity of mineral grain surfaces (Schott and Berner, 1985), although its importance during forsterite olivine dissolution remains uncertain (Oelkers et al., 2018). Nevertheless, undersaturation of the overlying seawater with respect to amorphous SiO_2 (Figure C.8C) and current-induced pore water flushing should have prevented passivating layer formation in the flow olivine treatment. Although supersaturation of the pore water with respect to amorphous SiO_2 cannot be ruled out

for the stagnant treatment, no surface precipitates were observed via SEM-EDX analysis on recovered olivine grains (Figure 3.8B-C). Yet, these surface layers could have been too thin (≤ 50 nm) to observe via SEM-EDX (Béarat et al., 2006; Daval et al., 2011) or any loosely adhering surface precipitates could have potentially been washed of during rinsing of the sediment with ultrapure MQ water before analysis. Overall, passivation of mineral grain surfaces can likely not explain the low olivine dissolution rates in the flow olivine treatment and its importance for the stagnant treatment cannot be confidently inferred.

Finally, secondary mineral precipitation can significantly reduce the net alkalinity production and subsequent CO_2 removal during olivine dissolution in seawater (Table 3.1) (Griffioen, 2017; Meysman and Montserrat, 2017; Fuhr et al., 2022). In our 175-day experiment, various mineral phases were observed via SEM-EDX analysis on the flume walls and in the suspended particulate matter of the flow treatments (Figure 3.5 and 3.6). Iron (hydr)oxides, inevitably formed under oxic conditions, reduced the net TA production by up to 6.8% for the olivine used in this study (Griffioen, 2017; Montserrat et al., 2017). We also observed deposited Cr and Fe rich particles on the flume walls of the flow treatments at the end of the experiment (Figure 3.6D1 and 3.6D4), which likely originate from corrosion of the stainless steel flume (further discussed in section 3.4.2) rather than olivine dissolution, as they were also present in the flow sand treatment.

Next to Fe-rich phases, multiple phyllosilicate minerals can form during olivine weathering (Delvigne et al., 1979; Hövelmann et al., 2011; Hellmann et al., 2012; Sissmann et al., 2013; Griffioen, 2017; Rigopoulos et al., 2018; Fuhr et al., 2022). In our study, seawater was supersaturated with respect to chrysotile on most sampling days (Figure 3.3C-D), while supersaturation for sepiolite only occurred in the flow treatments on a couple of sampling days (Figure C.8B). However, no phyllosilicate minerals were found via SEM-EDX analysis (Figure 3.5 and 3.6) or Raman spectroscopy (Supplementary section C.8), possibly due to their slow formation kinetics under the experimental conditions (Baldermann et al., 2018).The absence of a clear increasing trend in DSi

concentrations during the experiment (Figure 3.2E) may therefore be due to DSi uptake by marine silicifiers (e.g. diatoms) (Struyf et al., 2009), despite our efforts to limit their growth by conducting the experiment in dark conditions (Figure 3.1C).

Finally, loss of alkalinity through $CaCO_3$ formation, notably the morphotype aragonite, has been observed in several laboratory OAE experiments (Rigopoulos et al., 2018; Fuhr et al., 2022; Moras et al., 2022; Hartmann et al., 2023). Seawater is naturally supersaturated with respect to $CaCO_3$, but precipitation does not occur due to the absence of precipitation nuclei and inhibition by dissolved Mg^{2+}, orthophosphate and organic matter (Morse et al., 2007; Marion et al., 2009). The critical saturation state threshold for $CaCO_3$ precipitation is dependent on various factors including salinity, temperature, and the concentration and lattice compatibility of (in)organic particles that can act as nucleation sites (Moras et al., 2022; Hartmann et al., 2023; Schulz et al., 2023). Notably, $CaCO_3$ precipitation will occur at any saturation index above 0 ($\Omega > 1$) in the presence of $CaCO_3$ seed particles due to perfect lattice compatibility (Zhong and Mucci, 1989; Moras et al., 2022). Consequently, the abundant rod-shaped $CaCO_3$ particles observed in the suspended particulate matter from day 2 onwards (Figure 3.5C), signify the possibility of aragonite precipitation during our study, even at the relatively low saturation levels we observed (Figure 3.3B). However, the relatively high $CaCO_3$ background concentration (5.4% w/w, as derived from TIC content in Table 3.2) prevented the identification of any secondary $CaCO_3$ minerals that might have formed during the 175-day experiment.

3.4.2 Trace metal accumulation

The accumulation of Ni and Cr in the marine environment could be a potential risk for marine biota during large scale coastal olivine applications (Montserrat et al., 2017; Flipkens et al., 2021; Guo et al., 2022). At low concentrations, Ni is an essential element for microorganisms and macrophytes (Muyssen et al., 2004; Nielsen, 2021). However, elevated Ni exposure can result in a range of adverse effects in marine organisms (Blewett and Leonard, 2017; Gissi et al., 2020). No significant DNi accumulation was observed in the overlying water of the stagnant olivine treatment compared to the

stagnant sand treatment (Figure 3.9A), possibly due to limited olivine dissolution and Ni binding to the sediment matrix (e.g. organic matter, carbonates, Mn-oxides) (Yu et al., 2001; Fuhr et al., 2022). Elevated DNi concentrations in the flow sand treatment were unexpected given the low Ni content of the experimental beach sediment (Table 3.2), but are possibly explained by weathering of the stainless steel flume as a result of sediment abrasion and seawater corrosion. This hypothesis is supported by the high dissolved Zn accumulation in all flumes (Figure C.14A) and presence of Cr and Fe-rich particles on the walls of the flow sand flume (Figure 3.4D). Concentrations of DNi were significantly higher in the flow olivine treatment compared to flow sand treatment (Figure 3.9A) and higher than expected based on TA, DIC and DSi accumulation (Figure 3.10B). High non stoichiometric Ni release was previously also observed by Montserrat et al. (2017) and Flipkens et al. (2023a) during laboratory olivine weathering experiments in seawater and was possibly explained by preferential Ni compared to Si release. In our study, increased abrasion of the metal flume as a result of the higher seawater turbidity in the flow olivine compared to flow sand treatment (Figure 3.4) possibly contributed to the elevated DNi concentrations (Figure 3.9A). SEM-EDX results show that secondary mineral phases scavenged some of the DNi through adsorption or coprecipitation (Figure 3.5 and 3.6) (Lakshtanov and Stipp, 2007; Lazarevic et al., 2010; Alvarez et al., 2021; Fuhr et al., 2022). Overall, the difference in Ni accumulation between the flow olivine and flow sand treatment cannot be confidently assigned to olivine weathering, excluding Ni as a reliable proxy to determine olivine dissolution rates in our study.

Chromium is present in the form of Cr(III)-bearing chromite in dunite rock (Santos et al., 2015). Trivalent Cr is an essential micronutrient which forms complexes with low aqueous solubility and bioavailability in a marine environment (Pettine, 2000; Das et al., 2021). Nevertheless, Cr(III) can be oxidized to the highly bioavailable and toxic Cr(VI) in the presence of Mn(IV) oxides (Ivarsson et al., 2011; McClenaghan and Schindler, 2022). Here, Mn oxidation and scavenging by secondary minerals occurred given the low dissolved Mn concentrations in all treatments throughout the experiment (Figure C.14I) (Yavuz et al., 2003; Anschutz et al., 2005; Son et al., 2019). DCr concentrations were elevated in the

141

flumes with current compared to the stagnant flumes and highest in the flow olivine treatment on most sampling days (Figure 3.9B). However, DCr concentrations remained relatively low (<0.38 – 339 nmol L^{-1}, N = 102) compared to DNi concentrations, indicating that most Cr was present in a particulate form (Figure 3.9B). Weathering of the metal flume could have accounted for some DCr input given the elevated DCr concentrations and presence of Cr rich particles (Figure 3.6D) in the flow sand treatment.

3.4.3 Considerations for future research

Results from the current flume experiment, which bridged the gap between poorly realistic laboratory tests and complex field studies, showed that olivine dissolution kinetics in permeable marine sediment were more than one order of magnitude lower than anticipated based on previous laboratory findings. Unfortunately, the reason for this discrepancy could not be confidently identified with the available data. Additional large scale flume and mesocosm experiments in combination with field deployments are therefore crucially needed to further assess the CDR potential of CESW. These follow-up investigations should adhere to best practice guidelines for ocean alkalinity enhancement research (Cyronak et al., 2023; Dupont and Metian, 2023; Riebesell et al., 2023; Schulz et al., 2023; Steenkamp and Webb, 2023) to ensure that the acquired results are accurate and provide valuable insight into the efficacy and ecological impacts of OAE via CESW. Pore water chemistry analysis, using discrete sampling and/or micro profiling, depending on the required spatial resolution, is essential to gain a comprehensive understanding of the biogeochemical processes occurring in the sediment (Cyronak et al., 2023; Fuhr et al., 2023; Riebesell et al., 2023).

Regarding dissolved trace metals, the results in the overlying seawater followed the previously observed trend of high non-stoichiometric Ni and low Cr accumulation (Montserrat et al., 2017; Flipkens et al., 2023a; Flipkens et al., 2023b). However, it is important to note that corrosion of the stainless steel flumes prevented the drawing of meaningful conclusions about trace metal release rates during olivine dissolution in permeable marine sediment. To address this issue, future work should consider using

flumes or mesocosms constructed from inert materials to avoid leaching or active adsorption of substances (Riebesell et al., 2023). Additionally, stable isotope compositions for elements such as Ni ($\delta^{60/58}$Ni) and Si (δ^{30}Si) could potentially be used to distinguish olivine dissolution from other biogeochemical processes (Ratié et al., 2015; Geilert et al., 2020). However, experimental verification of this approach is still needed. Lastly, it is advisable to measure factors that influence metal bioavailability in sediment (e.g. acid volatile sulphides and organic matter content) (Zhang et al., 2014), and overlying water (e.g. dissolved organic carbon content) (Sherman et al., 2021) to gain a better understanding of trace metal environmental fate and possible toxicological risks associated with CESW (Flipkens et al., 2021).

3.5 Conclusions

Coastal enhanced olivine weathering is a proposed ocean alkalinity enhancement method for climate change mitigation. However, its CO_2 sequestration efficiency and environmental safety remain uncertain due to the paucity of experimental data on the rates of olivine dissolution, trace metal release, and secondary mineral formation in seawater. Furthermore, the importance of natural processes such as bioturbation and hydrodynamics on olivine reactivity in seawater have not been assessed. Therefore, we conducted a 175-day flume experiment to investigate the effects of water current on olivine dissolution in natural beach sediment. We hypothesized that advective porewater flushing would enhance olivine dissolution and minimize secondary mineral formation by preventing porewater saturation. Water current stimulated alkalinity release from permeable marine sediment, but olivine addition (at a concentration of 3% w/w) did not result significant accumulation of alkalinity or DSi in the overlying seawater. Consequently, the estimated amount of dissolved olivine was more than one order of magnitude slower than expected from previous laboratory findings. Unfortunately, this discrepancy could not be explained based on the available data. Nickel accumulation in seawater was greater than Cr accumulation and was enhanced under continuous current conditions. However, Ni incorporation in secondary phases and potential release from

weathering of the metal flume excluded its use as a suitable proxy to derive olivine dissolution rates. Overall, the low olivine reactivity in the current study highlights the need for additional olivine weathering experiments that consider the complexity of natural marine systems to better constrain the CO_2 sequestration potential and ecosystem impacts of coastal enhanced olivine weathering.

3.6 Supplementary information

Dunite and beach sand physicochemical properties, olivine reaction stoichiometry, specific surface area, and North Sea water chemistry are provided in Appendix C. Furthermore, Seawater hydrodynamics, sediment topography, temporal evolution in secondary mineral saturation indices, and Raman spectra of the suspended and deposited mineral phases are given.

3.7 Acknowledgements

Chapter 4 Deriving nickel (Ni(II)) and chromium (Cr(III)) based environmentally safe olivine guidelines for coastal enhanced silicate weathering

Published as:

Abstract

Enhanced silicate weathering (ESW) by spreading finely ground silicate rock along the coastal zone to remove atmospheric carbon dioxide (CO_2) is a proposed climate change mitigation technique. The abundant and fast dissolving mineral olivine has received most attention for this application. However, olivine contains nickel (Ni) and chromium (Cr), which may pose a risk to marine biota during a gigaton-scale ESW application. Herein we derive a first guideline for coastal olivine dispersal based on existing marine environmental quality standards (EQS) for Ni and Cr. Results show that benthic biota are at highest risk when olivine and its associated trace metals are mixed in the surface sediment. Specifically, depending on local sedimentary Ni concentrations, 0.059 − 1.4 kg olivine m^{-2} of seabed could be supplied without posing risks for benthic biota. Accordingly, globally coastal ESW could safely sequester only 0.51 to 37 Gt of CO_2 in the 21st century. Based on current EQS, we conclude that adverse environmental impacts from Ni and Cr release could reduce the applicability of olivine in coastal ESW. Our findings call for more in-depth studies on the potential toxicity of olivine towards benthic marine biota, especially in regard to bioavailability and metal mixture toxicity.

4.1 Introduction

Achieving the goals set in the 2015 Paris agreement to limit global warming to well below 2 °C will require drastic reductions in anthropogenic greenhouse gas emissions during the coming decades (Haszeldine et al., 2018). Additionally, carbon dioxide (CO_2) will also need to be captured from the atmosphere by so-called negative emission technologies (NETs) (Minx et al., 2018). These NETs are needed to be able to achieve net zero CO_2 emissions by the year 2050 and net negative CO_2 emissions during the second half of the 21st century (Gasser et al., 2015; Detz and van der Zwaan, 2019). One of the proposed NETs is coastal enhanced silicate weathering (CESW). This technique aims to artificially speed up the natural CO_2-consuming chemical weathering of a silicate mineral by supplying gigatons of finely ground source rock to the dynamic coastal environment (Meysman and Montserrat, 2017).

The mineral olivine ($Mg_{2x}Fe_{2(1-x)}SiO_4$) is a prime candidate for CESW because of its relatively fast dissolution rate and widespread abundance (Hangx and Spiers, 2009; Hartmann et al., 2013; Meysman and Montserrat, 2017). Billions of tonnes of olivine are globally present in mafic and ultramafic igneous rocks and yearly approximately 8 Mt is mined from dunite (rock containing >90% olivine) or serpentinite (metamorphosed olivine-rich ultramafic rock) deposits for metallurgical use (Harben and Smith jr., 2006; Kremer et al., 2019; Scott et al., 2021). Relatively low energy costs and low CO_2 emissions associated with grinding olivine source rock to 100 μm particles make this a desirable grain size for use in CESW (Hangx and Spiers, 2009). However, several studies indicate that grain sizes of 10 μm or smaller might be needed to ensure significant olivine dissolution and CO_2 uptake in the coming decades (Hangx and Spiers, 2009; Renforth, 2012; Hartmann et al., 2013).

During olivine dissolution, protons are consumed (Eq. 4.1) which leads to a shift in the equilibrium of the acid-base reactions of the seawater carbonate system (Eq. 4.2) to the right. Consequently, seawater total alkalinity (TA) will increase, and additional CO_2 can be

taken up from the atmosphere (Eq. 4.3) (Meysman and Montserrat, 2017). This artificial seawater TA increase to drive atmospheric CO_2 removal is called ocean alkalinity enhancement (OAE) (Ilyina et al., 2013; Bach et al., 2019).

$$Mg_{2\times}Fe_{2(1-\times)}SiO_4 + 4H^+ \rightarrow 2\times Mg^{2+} + 2(1-\times)Fe^{2+} + H_4SiO_4 \qquad [4.1]$$

$$CO_2(aq) + H_2O \rightleftharpoons HCO_3^- + H^+ \rightleftharpoons CO_3^{2-} + 2H^+ \qquad [4.2]$$

$$CO_2(atm) \rightleftharpoons CO_2(aq) \qquad [4.3]$$
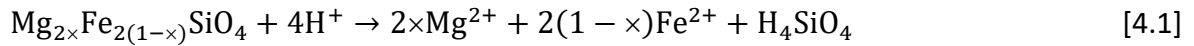
Combining these reactions gives the overall dissolution reaction of olivine (Eq. 4.4), from which we can derive that theoretically 4 mol of CO_2 is sequestered in the form of bicarbonate (HCO_3^-) per mol of dissolved olivine (Montserrat et al., 2017).

$$Mg_{2\times}Fe_{2(1-x)}SiO_4 + 4H_2O + 4CO_2 \rightarrow 2\times Mg^{2+} + 2(1-\times)Fe^{2+} + H_4SiO_4 + 4HCO_3^- \quad [4.4]$$
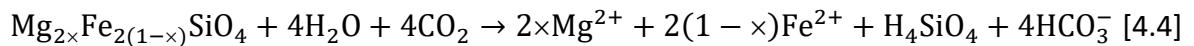
In addition to CO_2 sequestration, the proton consumption during dissolution could counteract ocean acidification. Furthermore, the released iron (Fe) and silicon (Si) are necessary nutrients for phytoplankton growth and could therefore result in additional atmospheric CO_2 uptake and increased abundance of silicifiers (e.g. diatoms), but these aspects remain to be investigated (Meysman and Montserrat, 2017; Bach et al., 2019). In contrast to these associated benefits, olivine also contains chromium (Cr) and nickel (Ni), which are toxic to marine organisms above certain threshold concentrations (Edwards et al., 2017; Meysman and Montserrat, 2017).

Nickel is a transition metal that is mainly used in the production of stainless steel and other Ni alloys (Brix et al., 2017). In the crystal structure of olivine, Ni^{2+} is homogeneously distributed in the M1 octahedral binding sites, substituting for other divalent cations such as Mg^{2+} or Fe^{2+}, thereby forming a nickel silicate (Ni_2SiO_4) (Bish, 1981; Santos et al., 2015). The Ni content in olivine ranges from 2.4 to 12 mmol Ni mol^{-1} of olivine depending on the site of origin (Keefner et al., 2011; Santos et al., 2015; Montserrat et al., 2017). Nickel is

an essential component of nine enzymes associated with carbon, nitrogen and oxygen cycling in marine microorganisms (Mulrooney and Hausinger, 2003; Ho, 2013). However, for other marine biota Ni essentiality has not been recognized and the uptake mechanisms are not well known (Blewett and Leonard, 2017). Exposure to elevated concentrations of Ni can lead to toxicological effects as a consequence of three main toxicity mechanisms: (1) ionoregulatory disruption (mainly Ca^{2+}, Mg^{2+} and $Fe^{2+/3+}$), (2) respiratory toxicity as a result of an allergic type reaction of respiratory epithelia, and (3) reactive oxygen species-induced oxidative stress (Blewett and Leonard, 2017; Brix et al., 2017). However, the relative importance of the different toxicity mechanisms is not well known for marine organisms (Blewett and Leonard, 2017).

In contrast to nickel, chromium is not homogeneously distributed in olivine, but rather present in iron (Fe) rich areas, likely as Cr^{3+} in the form of water-insoluble chromite ($FeCr_2O_4$) (Santos et al., 2015). Reported Cr concentrations in olivine from the Norwegian Åheim mine (the largest exploited olivine source) vary considerably, ranging from 0.19 mmol mol^{-1} olivine to 6.6 mmol mol^{-1} olivine (Keefner et al., 2011; Kleiv and Thornhill, 2011; Santos et al., 2015; Shur and Perchuk, 2015; Montserrat et al., 2017). In the marine environment Cr occurs in two stable oxidation states: Cr^{3+} and Cr^{6+}, which differ significantly in their environmental and biological behaviour (Aharchaou et al., 2018). Hexavalent Cr occurs as chromate (CrO_4^{2-}) or dichromate ($Cr_2O_7^{2-}$) anions in aquatic systems, which can easily cross biological membranes via non-specific anion channels and are therefore considered highly bioavailable and potentially very toxic (Dayan and Paine, 2001; Aharchaou et al., 2018; Bakshi and Panigrahi, 2018). After entering the cell, Cr(VI) is reduced to Cr(III). This reduction is accompanied by the production of reactive oxygen species (ROS) which can damage cell membranes, proteins and DNA when in excess of antioxidant molecules (Wang et al., 1997a; Dayan and Paine, 2001). In contrast, trivalent chromium is predominantly present as $Cr(OH)_3$ or $Cr(OH)_2^+$ in the marine environment, which are chemical species of less ecotoxicological concern compared to Cr(VI) species due to their low aqueous solubility (Pettine, 2000; Aharchaou et al., 2018).

A body of literature is available on the acute and chronic toxicity of Ni^{2+} and Cr^{3+}/Cr^{6+} towards marine biota (Reish, 1981; Frey et al., 1983; Missimer et al., 1989; Bielmyer et al., 2005; Urrutia et al., 2008; Gissi et al., 2018; Panneerselvam et al., 2018; Wang et al., 2020). Most of the data has been derived from laboratory studies that exposed single biological species to single metal ions (e.g. Ni^{2+} or Cr^{3+}) under optimal conditions (e.g. constant pH and temperature). Using various approaches, e.g. species sensitivity distributions (SSDs), these data are used to derive marine metal environmental quality standards (EQS), which are threshold metal concentrations in seawater or sediment that are considered to be sufficiently protective for the aquatic environment (Wang et al., 2014). These EQS are used by industries, the government, and environmental agencies as a guidance tool in the setting of regulations (Gissi et al., 2016).

It has been predicted that, depending on the weathering rate and the water residence time, CESW may cause accumulation of Cr and Ni in coastal waters to levels that are well above the background (Edwards et al., 2017; Meysman and Montserrat, 2017). Currently, possible negative ecosystem impacts of CESW are unknown since no marine toxicity tests have yet been conducted with olivine. However, for Ni and Cr considered individually, marine EQS do exist. Therefore, this study aimed to derive a maximum amount of olivine that could be supplied to the coastal seas without exceedance of the Ni or Cr EQS. This olivine guideline provides a first indication of the environmental safety and applicability of the mineral for employment in global scale CESW.

4.2 Material and methods

All calculations were performed in Microsoft Excel (2016) and figures were constructed in GraphPad Prism version 9.01 for Windows (GraphPad Software, La Jolla California USA).

4.2.1 Global coastal Ni and Cr concentrations

Data on Ni and Cr concentrations in coastal seawater and sediment was compiled from primary literature. Coastal waters were defined as those with a water depth up to 200 m, located on the continental or insular shelves (Mackenzie and Lerman, 2006). Data was included when the water depth at the sampling location was ≤ 200 m or when it was specified that the sampling was conducted in bays, lagoons, estuaries, near-shore banks, harbours, or coastal zones (Mackenzie and Lerman, 2006). For Ni and Cr in seawater, only data on dissolved metal concentrations (meaning water samples filtered through ≤0.45 μm pore-size filters) was collected. For sediment, metal concentrations on a dry weight (dry wt) basis measured after microwave-assisted acid mixture digestion of sieved or unsieved sediment were included. Data collected on a transect along a coastline (e.g. on a cruise or along an expected pollution gradient) or at different time points or depths on the same location were summarized using descriptive statistics (supplementary Tables D.4-D.7 and Figures D.1-D.4). The mean concentrations for each location were then summarized in the same way to derive median values and percentiles of Ni and Cr in the coastal environment around the globe.

4.2.2 Deriving a Ni-based guideline for olivine application in coastal systems

The occurrence of most Cr in olivine as water-insoluble $FeCr_2O_4$ implies low bioavailability and lower ecotoxicological concern compared to Ni (Santos et al., 2015). Therefore, the following calculations were made under the assumption that Ni release from olivine weathering is the factor of highest concern for the health of marine biota during a gigaton-scale olivine application in the world's coastal seas (Hartmann et al., 2013; Meysman and Montserrat, 2017). The corresponding calculations for Cr are given and discussed in the supplementary material (Supplementary Section D.6).

Based on the environmental quality standards for Ni in marine water and sediment, the expected maximum amount of olivine that could be supplied to the coastal zone without

adverse effects for marine biota was calculated. Calculations were made assuming the two limiting application scenarios being; all metals released during weathering end up in either (I) the water column or (II) the sediment.

4.2.2.1 **(I) All Ni ends up in the water column**

The maximum amount of olivine, m_{app}, that could be applied per m² of seabed (kg m⁻²) without exceeding the Ni marine EQS was calculated from:

$$m_{\text{app}} = \frac{c_{\text{max}}V_w}{k_{\text{diss}}At} \qquad [4.5]$$

where c_{max} is the maximum allowed concentration of olivine (mol l⁻¹) based on the European seawater Ni EQS (0.147 μmol l⁻¹) (Tyle and Scott-Fordsmand, 2008), V_w is the water volume per m² of seabed (l m⁻²), A is the reactive surface area of olivine (m² kg⁻¹), t is the water residence time (s) and k_{diss} is the olivine dissolution rate constant (mol m⁻² s⁻¹). The dissolution of olivine was modelled for two grain sizes, 100 μm and 10 μm grain diameter, for both a temperate (15 °C) and a tropical (25 °C) coastal system. For all further calculations, the dissolution rate constants for olivine were considered to be 5.19×10⁻¹¹ mol m² s⁻¹ and 1.58×10⁻¹⁰ mol m⁻² s⁻¹ for the 15 °C and 25 °C scenario, respectively as derived by Hangx and Spiers (2009) A more detailed description of how seawater Ni EQS based olivine guidelines were derived is provided in the supplementary material (section D.1).

4.2.2.2 **(II) All Ni remains in the sediment**

For sediment, the maximum amount of olivine, m_{app}, that could be supplied per m² of seabed (kg m⁻²) without exceeding the marine Ni EQS for sediment was calculated from:

$$m_{\text{app}} = C_{\text{max}}V_s\rho_s(1 - \Phi)M_{\text{olivine}} \qquad [4.6]$$

where C_{max} is the maximum allowed amount of olivine (mmol kg⁻¹ dry wt) based on a sediment Ni EQS (0.729 mmol kg⁻¹ dry wt) (Macdonald et al., 1996), V_s is the volume of

the sediment in which olivine is mixed per m² of seabed (m³ m⁻² seabed), ρ_s is the specific density of marine sediment (2650 kg m⁻³), $M_{olivine}$ is the molecular weight of olivine (kg mol⁻¹), and Φ is the porosity of the sediment. The application of common forsterite olivine with a molar Mg-to-Fe ratio of 0.94:0.06 ($Mg_{1.88}Fe_{0.12}SiO_4$) was assumed, resulting in a molecular weight of 0.144 kg mol⁻¹ (Montserrat et al., 2017). The porosity of marine surface sediment was assumed to be 0.60 based on the predicted global coastal sediment porosity ranging from approximately 0.50 to 0.85 (Martin et al., 2015). To estimate the global maximum amount of olivine that could be distributed, the global continental shelf was assumed to have a surface area of 28×10^6 km² for all further calculations (Mackenzie and Lerman, 2006).

4.2.3 Implications of the olivine guideline for CO_2 sequestration potential

Based on the derived olivine guideline value for CESW, the associated CO_2 uptake during the 21st century was calculated to investigate if Ni release would limit the potential of coastal enhanced olivine weathering as a NET. Under the assumption that olivine grains are spherical, olivine is not expected to dissolve linearly over the coming decades, but according to a shrinking core model (Hangx and Spiers, 2009). The volume fraction of dissolved olivine $X(t)$ at time t can be expressed as:

$$X(t) = \frac{d_0^3 - (d_0 - 2k_{diss}V_m t)^3}{d_0^3}$$

[4.7]

where d_0 is the starting olivine grain diameter (m); k_{diss} is the dissolution rate constant of olivine (mol m⁻² s⁻¹), and V_m is the molar volume of olivine (4.38×10^{-5} m³ mol⁻¹). The dissolution of olivine was modelled for two grain sizes, 100 μm and 10 μm grain diameter, for both a temperate (15 °C) and a tropical (25 °C) coastal system. A weekly application of 9.615 Mt of olivine along the global continental shelf was assumed. This would equate to 500 Mt of olivine spread along the coast every year, which was estimated to be logistically feasible by Hangx and Spiers (2009) assuming significant expansion of the cargo-ship fleet

size and olivine mining industry. The amount of olivine dissolved as a function of time is calculated from:

$$m_{\text{oa}} = \sum_{t=0}^{n} X(t)S \quad \text{with } n = \text{the duration of olivine application (weeks)} \qquad [4.8]$$

where m_{oa} is the amount of olivine (Mt) weathered at time t (weeks), $X(t)$ is the fraction of olivine dissolved at time t (weeks) and S is the supply rate of olivine (9.615 Mt week^{-1}) for an n-week application. In a typical application scenario, the olivine supply will be stopped after n-weeks, i.e. once the global continental shelf has been covered in olivine and the expected maximum environmentally safe amount of olivine has been reached. The weekly amount of dissolved olivine for the next 4160-n weeks (i.e. after olivine application has stopped) can then be expressed as:

$$m_{\text{os}} = \sum_{i=1}^{4160-n} \sum_{t=0}^{n} X(t+i)S \quad \text{with } n = \text{the duration of olivine application (weeks)} \qquad [4.9]$$

where m_{os} is the amount of olivine weathered (Mt) at time $t+i$ (weeks) from the moment olivine supply was halted onwards, i is the index for each week after olivine supply was stopped, $X(t+i)$ is the fraction of olivine dissolved at time $t+i$ (weeks) and S is the supply rate of olivine (9.615 Mt week^{-1}), for an n-week application. Subsequently, the associated weekly CO_2 uptake was calculated from:

$$m_{\text{CO}_2} = \gamma_{\text{CO}_2} m_{\text{oa/os}} \qquad [4.10]$$

Where m_{CO_2} is the amount of CO_2 sequestered via olivine dissolution (Mt), γ_{CO_2} is the net CO_2-sequestration efficiency, which represents the net amount of CO_2 that is withdrawn from the atmosphere upon dissolution of 1 kg of olivine, which was taken to be 1 kg of CO_2 based on upper limits of expected values (Meysman and Montserrat, 2017; Montserrat et al., 2017). Finally, $m_{\text{oa/os}}$ is the amount of olivine dissolved during the period of application (m_{oa}) or after olivine supply was stopped (m_{os}), respectively.

4.3 Results and discussion

4.3.1 Global coastal Ni concentrations

A literature search was conducted to obtain globally occurring coastal Ni and Cr concentrations for the derivation of an olivine application guideline. A summary of the Ni concentrations globally occurring in coastal waters and sediment is shown in Table 4.1. A summary for Cr and data from individual studies is shown in Supplementary Tables D.1 and D.4-D.7 and Figures D.1-D.4. The median dissolved Ni concentration in seawater for the 30 coastal locations was 3.92 nmol l^{-1}. This value is similar to the reported dissolved Ni concentration in open ocean seawater of the Southern Ocean (6.2 ± 0.3 nmol l^{-1}) (Wang et al., 2019) and total Ni concentrations offshore in the North-East Atlantic Ocean (3.9 ± 1.6 nmol l^{-1}) (Danielsson et al., 1985). Dissolved Ni concentrations ranged from 0.92 nmol l^{-1} in 2002 at the Bay of Bengal in India to 5290 nmol l^{-1} in 2003 at the Alang–Sosiya ship scrapping yard in the Gulf of Cambay, India (Reddy et al., 2005; Rejomon et al., 2008). Generally, human-impacted coastal waters and sediments tend to have elevated and more variable Ni concentrations than offshore locations due to nearshore mining or industrial activities (Arikibe and Prasad, 2020; Yunus et al., 2020).

Total recoverable Ni concentrations in 50 coastal sediments ranged from 0.06 mmol kg^{-1} dry wt measured along the Eastern Gulf of Mexico , USA (Steffy et al., 2013) to 5.44 mmol kg^{-1} dry wt around the thermal power plant on the Tuticorin coast in India (Srikanth et al., 2014). The median sediment Ni concentration was 0.52 mmol kg^{-1} dry wt. These relatively high concentrations show that the sediment serves as a sink for metals in the marine environment (Partheeban et al., 2021).

Table 4.1: Summary of dissolved (≤0.45 µm) nickel (Ni) concentrations (nmol l^{-1}) in seawater and total Ni concentrations (mmol kg^{-1} dry wt) in sediment for coastal systems (water depth ≤ 200 m) around the world.[a]

	Dissolved seawater [Ni] (nmol l^{-1}) (n = 30)	Total sediment [Ni] (mmol kg^{-1} dry wt) (n = 50)
Median	3.92	0.52
P25 – P75	2.81 – 36.2	0.29 – 0.70
P5 – P95	1.24 – 373	0.14 – 3.46
Min – Max	0.92 – 5290	0.06 – 5.44

^{a}Number of locations (n), median, percentiles (P), and range (Min – Max) are provided to illustrate the distribution of the data. Results for Cr and mean data of the individual locations are provided in supplementary Tables D.1 and D.4-D.7.

4.3.2 Deriving a Ni-based guideline for olivine application in coastal systems

The expected maximum amount of olivine that can be supplied to the coastal zone without exceedance of existing marine Ni EQS was derived for the two limiting olivine application scenarios in which all Ni released during olivine weathering ends up in either (I) the water column or (II) the sediment.

4.3.2.1 (I) All Ni ends up in the water column

The maximum amount of olivine that can be distributed in coastal waters without exceedance of the European Ni EQS for seawater (0.147 µM) (Tyle and Scott-Fordsmand, 2008) assuming an olivine Ni concentration of 7.5 mmol mol^{-1} olivine is shown in Figure 4.1. A seawater Ni background concentration of 3.92 nmol l^{-1} was considered. As indicated by the study of Hangx & Spiers (2009), based on the Arrhenius equation and an olivine dissolution activation energy of 79.5 kJ mol^{-1} in seawater conditions (Wogelius and Walther, 1992), the dissolution rate of olivine is expected to be approximately three times higher in tropical (25 °C) compared to temperate (15 °C) coastal waters (Hangx and Spiers, 2009). Furthermore, assuming that the olivine grains are spherical, grains with a diameter of 10 µm are expected to dissolve approximately 10 times faster than grains with a diameter of 100 µm according to basic geometry (see Eq. D.4 in supplementary section

D.1) (Hangx and Spiers, 2009). If all Ni released during olivine weathering is being homogeneously mixed in the overlying water, then Ni concentrations will be 10 times lower at a location with a water depth of 100 m compared to a location with a 10 m water depth with the same water residence time.

From these assumptions, we can derive that for continental shelf seas with a short water residence time of two weeks, such as the East Brazil shelf in the South Atlantic Ocean or the California Current in the Pacific Ocean (Liu et al., 2019), relatively high quantities of olivine (in the order of $5 - 1.7 \times 10^3$ kg m^{-2} depending on water depth, temperature, and olivine grain size) can be distributed without exceedance of the European Ni EQS. For coastal waters with a relatively long residence time of approximately one year, such as the North Sea or the East China Sea (Liu et al., 2019), the amount of olivine that can be distributed is approximately 26 times lower than that for seas with a residence time of two weeks assuming total coverage of the continental shelf with olivine.

We note that these results were derived from average, laboratory-based olivine dissolution rate constants for seawater (Hangx and Spiers, 2009). However, when supplied to the coastal zone, the rate and extent of olivine dissolution could be enhanced or reduced by several biotic (e.g. bioturbation) and abiotic (e.g. wave induced pore water flushing or burial by sediment) processes (Meysman and Montserrat, 2017). Furthermore, in deeper parts of continental shelf seas, released trace metals might not be homogeneously mixed in the water column due to presence of seasonal or permanent pycnoclines (boundaries between two water layers of different density) or other oceanic processes (de Boyer Montégut et al., 2004). Moreover, an olivine Ni concentration of 7.5 mmol mol^{-1} olivine was assumed (Montserrat et al., 2017), while concentrations can vary from 2.4 to 12 mmol Ni mol^{-1} of olivine depending on the origin of the source rock (Santos et al., 2015). Additionally, a low Ni background concentration (3.92 nmol l^{-1}) was considered, while concentrations of up to three orders of magnitude higher have been observed (Reddy et al., 2005). Finally, the European seawater Ni EQS of 0.147 µmol l^{-1} was used to derive the olivine guideline, but different EQS values are implemented in other

regions (see Supplementary Table D.2) and Ni concentrations as low as 0.102 µmol l⁻¹ have been recently recommended to ensure protection of marine biota (Gissi et al., 2020).

These sources of variation can significantly affect the olivine application guideline and should therefore be taken into account in the best way possible on a local scale when determining the amount of olivine that can be supplied to a specific coastal area. Especially the *in situ* olivine dissolution and metal release rate remain unknown and require additional research efforts (Meysman and Montserrat, 2017).
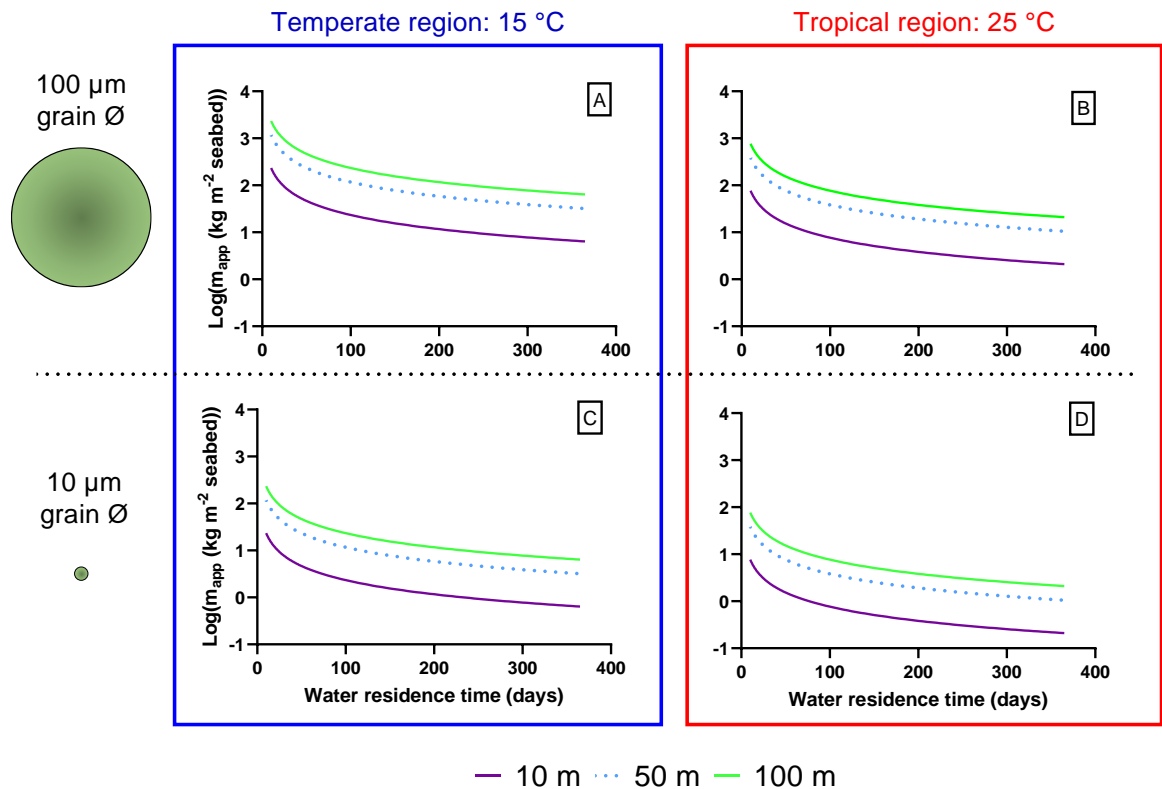
Figure 4.1: Maximum amount of olivine (kg m⁻² seabed) on a logarithmic scale that can be distributed without exceedance of the European nickel (Ni) environmental quality standard (0.147 µM) as a function of coastal water residence time (days). Scenarios for coastal waters with an average water depth of 10, 50 or 100 m located in a 15 °C temperate region (A, C) or 25 °C tropical region (B, D) are shown. The maximum

application of olivine with a uniform grain diameter of 100 μm (A, B) or 10 μm (C, D) is given. A seawater Ni background concentration of 3.92 nmol l^{-1} and Ni concentration in olivine of 7.5 mmol mol^{-1} olivine were assumed. As derived by Hangx & Spiers (2009), olivine dissolution rate constants of 5.19×10^{-11} and 1.58×10^{-10} mol m^{-2} s^{-1} were used for the temperate (15 °C) and tropical (25 °C) scenario, respectively.

4.3.2.2 (II) All Ni ends up in the sediment

In addition to Ni EQS for seawater, there are also sediment Ni EQS values, of which the threshold effect level (TEL) and probable effect level (PEL) derived by the Florida Department of Environmental Protection (FDEP) (supplementary Table D.3) are among the most widely used (Macdonald et al., 1996; Hübner et al., 2009). The TEL was derived to represent the pollutant concentration below which adverse biological effects rarely occur, while the PEL corresponds to the pollutant concentrations above which adverse biological effects are frequently expected. In the context of CESW, a conservative approach would be to halt olivine deposition when future Ni release is expected to exceed TEL (Macdonald et al., 1996; Hübner et al., 2009). However, 76% of the collected coastal sedimentary Ni concentrations are above the TEL of 0.271 mmol Ni kg^{-1} dry wt. Furthermore, in the biological effects database for sediments, adverse biological effects were only observed in 9.4% of cases where sedimentary Ni concentrations exceeded the PEL, whereas for other metals these percentages were a lot higher (e.g. 56% for copper) (Macdonald et al., 1996). Moreover, Chapman et al. (1999) and Bakke et al. (2010) derived sediment Ni EQS at which biological effects were unlikely of 0.68 mmol kg^{-1} dry wt and 0.78 mmol kg^{-1} dry wt, respectively. Therefore, the PEL of 0.729 mmol Ni kg^{-1} dry wt is a more suitable threshold concentration for deriving an olivine application guideline.
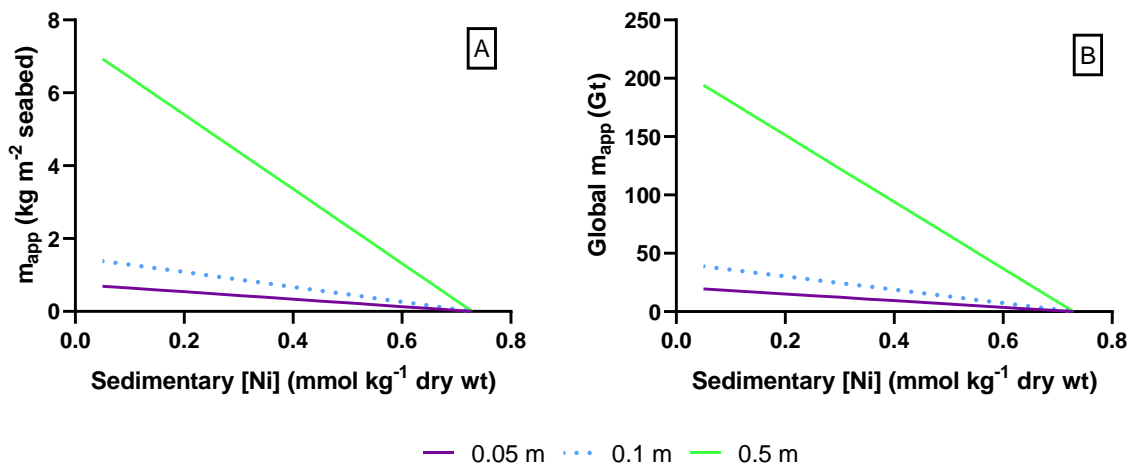
Figure 4.2: Maximum amount of olivine, m_{app}, that can locally (A) or globally (B) be distributed without exceedance of the nickel (Ni) probable effect level (PEL) for marine biota (0.729 mmol kg^{-1} dry wt) as a function of sedimentary Ni concentrations (mmol kg^{-1} dry wt) for different olivine mixing depths (0.05, 0.1 and 0.5 m). The global continental shelf was assumed to have a surface area of 28×10^6 km² and the olivine was assumed to have a nickel concentration of 7.5 mmol Ni mol^{-1} olivine. The worst-case scenario is shown for which all the nickel released from olivine weathering is assumed to stay inside the sediment.

The maximum amount of olivine that can be distributed in coastal waters without future exceedance of the PEL derived for Florida coastal sediments (0.729 mmol kg^{-1} dry wt) is shown in Figure 4.2. For the scenario where olivine remains in the upper 5 cm of the sediment, a maximum amount of 0.69 kg m^{-2} and minimum amount of 0.029 kg m^{-2} seabed can be dispersed without exceedance of the PEL if sedimentary Ni concentrations are 0.05 or 0.7 mmol Ni kg^{-1} dry wt, respectively (Figure 4.2A). In case the olivine gets mixed to greater depths by wave action or bioturbation in a site with average sedimentary Ni concentrations of 0.52 mmol Ni kg^{-1} dry wt, double (0.42 kg m^{-2}) or 10 times (2.1 kg m^{-2}) the amount of olivine can be spread out on the seafloor for a 10 cm or 50 cm mixing depth scenario (Figure 4.2A).

Importantly, in these calculations the sediment Ni EQS derived for Florida waters was used while guidelines for a range of locations have been derived in the past ~30 years ranging from 0.27 to 0.75 mmol kg^{-1} dry wt to protect local marine biota (Birch, 2018). Furthermore, marine sediments were considered a static sink for metals, while in reality metals are constantly exchanged between the sediment and the overlying water column (Frogner-Kockum et al., 2016). Metal efflux from the sediment is mainly driven by molecular diffusion but can be significantly enhanced by bioturbation and advection (Van Cappellen and Wang, 1995; Frogner-Kockum et al., 2016; van de Velde and Meysman, 2016). To take these metal effluxes into consideration when deriving an olivine application guideline, accurate data on local biological and physicochemical processes in the sediment would be required. However, in literature these data are scarce and can show significant temporal and spatial variation (Frogner-Kockum et al., 2016; Solan et al., 2019). Furthermore, the olivine mixing depth and weathering rate as a function of sediment depth and time need to be well defined, since they would have a large effect on the magnitude of the metal influx and efflux. Currently these data are lacking (Meysman and Montserrat, 2017). Therefore, olivine sediment EQS based guidelines were only derived under the conservative assumption that all trace metals released during olivine weathering remain in the sediment.

Collectively, the calculations show that benthic marine biota are at highest risk from Ni release during a large-scale coastal olivine application in the case where all the released Ni stays in the sediment. Assuming a mixing depth of 10 cm and a sedimentary Ni concentration of 0.52 mmol kg^{-1} dry wt, the maximum amount of olivine that can be distributed without future exceedance of the Ni guidelines is 0.42 kg m^{-2}. When comparing this amount to the amount needed to surpass the Ni water quality guidelines, only in the case that very fine-grained olivine (10 µm grain diameter) is dispersed in tropical (25° C) or shallow temperate (15 °C, 10 m water depth) coastal areas with a water residence time of more than half a year (>181 days), Ni water quality guidelines can be exceeded by dispersing lower amounts of olivine (Fig. 1D). Therefore, for most locations

around the world the maximum amount of olivine that can be dispersed should be based on the local sedimentary Ni concentrations.

4.3.3 Implications of the olivine guideline for CO_2 sequestration potential

To investigate the potential of CESW as a NET in the 21st century, the dissolution of an environmentally safe amount of olivine derived from the FDEP sediment Ni EQS and associated CO_2 sequestration are shown in Figure 4.3. A CO_2-sequestration efficiency of 1 ton of CO_2 per ton of supplied olivine was assumed (Montserrat et al., 2017). A conservative environmentally safe olivine application of 1.7 to 39 Gt, spread over a period of 3.4 to 78 years was calculated based on an olivine mixing depth of 10 cm and the assumption that all trace metals released during weathering remain in the sediment (Figure 4.2B). This mixing depth was based on the zone in the sediment where most benthic fauna is present (Simpson and Batley, 2016; Solan et al., 2019). For the larger 100 μm olivine grains, 0.51 Gt (~30%) to 6.4 Gt (~16%) of the supplied olivine would have dissolved by the end of the 21st century in a temperate (15 °C) region (Figure 4.3A) and 1.2 Gt (~71%) to 16 Gt (~42%) in a tropical (25 °C) region (Figure 4.3B). Alternatively, if 10 μm grain-sized olivine would be distributed, 1.7 Gt (100%) to 31 Gt (~80%) and 1.7 Gt (100%) to 37 Gt (~95%) of the supplied olivine would be dissolved at the end of the 21st century for a temperate or tropical zone, respectively (Figure 4.3C and 4.3D). These results highlight that olivine would have to be ground to very small grain sizes to dissolve fast enough to achieve significant CO_2 withdrawal from the atmosphere during the coming decades (Hangx and Spiers, 2009; Renforth, 2012).
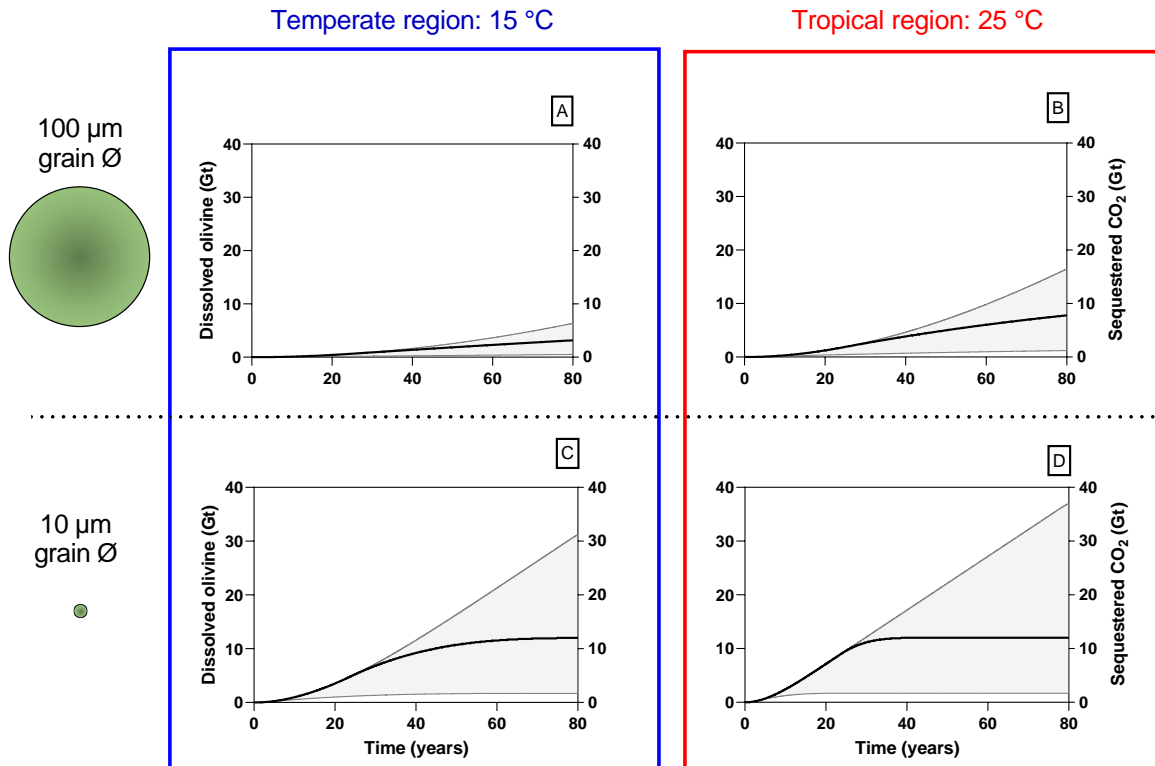
Figure 4.3: Amount of dissolved olivine (Gt) and associated CO_2 sequestration (Gt) as a function of time (years) for a 1.7 to 39 Gt global coastal enhanced olivine weathering scenario. A constant olivine supply rate (S) of 9.615 Mt per week for a period of 3.4 to 78 years was assumed based on a sedimentary Ni concentration of 0.05 to 0.7 mmol kg^{-1} dry wt. The solid black line shows the scenario where 12 Gt of olivine is supplied to an average coastal sediment (0.52 mmol Ni kg^{-1} dry wt) for a period of 24 years. Scenarios for a 15 °C temperate region (A, C) and 25 °C tropical region (B, D) are shown for olivine with a uniform grain diameter of 100 μm (A, B) or 10 μm (C, D). Olivine dissolution was assumed to occur according to a core shrinking model with olivine dissolution rate constants of 5.19×10^{-11} and 1.58×10^{-10} mol m^{-2} s^{-1} and activation energy of 79.5 kJ mol^{-1} (Wogelius and Walther, 1992) for the 15 °C and 25 °C scenarios, respectively. The CO_2-sequestration efficiency was taken to be 1 ton of CO_2 sequestered for each ton of dispersed olivine.

Based on the environmentally safe amount of olivine that could be applied to the global continental shelf, a maximum net amount of ~0.51 to 37 Gt CO_2 could be removed from the atmosphere during the 21st century using coastal enhanced olivine weathering.

Narrowing this result down based on the median coastal sedimentary Ni concentration (0.52 mmol kg^{-1} dry wt), 3.2 to 12 Gt of CO_2 could be sequestered in the coming 80 years depending on the olivine grain size, application location, and net CO_2-sequestration efficiency. The latter is estimated to vary between 0.50 to 1.0 ton of CO_2 sequestered per ton of dispersed olivine (Moosdorf et al., 2014; Meysman and Montserrat, 2017). The net CO_2-sequestration efficiency is dependent on the mineral composition of the source rock, potential secondary mineral formation during olivine dissolution, and CO_2 emissions from mining, grinding and transportation of the olivine from its source to the coastal zone (Hangx and Spiers, 2009; Renforth, 2012; Moosdorf et al., 2014; Meysman and Montserrat, 2017).

To keep global warming below 1.5 °C, all NETs would need to collectively capture approximately 150 to 1180 Gt of CO_2 during the 21st century, depending on the rate of conventional mitigation (Rueda et al., 2021). Therefore, a total CO_2 capture potential of 0.51 to 37 Gt via coastal enhanced olivine weathering is relatively low. Hence, this first olivine application guideline shows that additional research on the environmental safety of the technique is needed.

4.3.4 Future perspectives: the need for site-specific olivine guidelines

Overall, our results show that Ni and Cr release could limit the potential safe usage of the mineral olivine in coastal enhanced silicate weathering on a global scale. As explained in more detail in supplementary section D.6, the release of Cr is expected to be of lower concern compared to Ni. However, the potential of some released Cr^{3+} to be oxidized to Cr^{6+}, which forms anionic complexes in seawater that are highly bioavailable and potentially synergistically toxic with Ni^{2+} implies that Cr^{3+} release during olivine weathering cannot be disregarded in the risk assessment of CESW (Verriopoulos and Dimas, 1988; Pettine, 2000; Dayan and Paine, 2001; Aharchaou et al., 2018).

Ecological risk assessment of olivine in CESW is still at a very early stage. Data on olivine toxicity in marine environments and accurate predictions on *in situ* olivine dissolution rates and mixing depths are still lacking (Meysman and Montserrat, 2017). In a coastal environment, organisms will be exposed to Ni and Cr released in the water (porewater or overlying water) or in their gastrointestinal tract after ingestion of sediment particles and/or contaminated food (Adams et al., 2011). The degree of metal uptake will depend on the exposure concentration and duration, metal speciation, competition with other ions for uptake, abiotic variables (such as temperature, pH and organic carbon) and the organism's physiology (Adams et al., 2011; Adams et al., 2020). Toxicological effects will occur when metal concentrations in an organism's biologically active metal compartments exceed certain threshold values (Adams et al., 2011).

Biotic ligand models (BLMs) have been used to account for site- and species-specific metal bioavailability in the derivation of the European freshwater Ni EQS and have been recently validated for Australian freshwater species (Peters et al., 2018; Stauber et al., 2021). However, for marine systems additional research on the interactions between seawater chemistry, Ni bioavailability, and toxicity is needed to derive bioavailability based EQS (Blewett and Leonard, 2017; Sherman et al., 2021).

Differences in biogeochemical processes among coastal sites necessitate the derivation of site-specific olivine application guidelines. The risk assessment should be based on multiple lines of evidence (laboratory toxicity testing and field-based studies) to determine implications of coastal olivine spreading for ecosystem health (Simpson and Batley, 2016). Potential benefits (counteracting ocean acidification and global warming) of olivine spreading should also be considered to decide how much olivine will ultimately be dispersed in a specific coastal sea (Meysman and Montserrat, 2017).

To conclude, we recommend that future studies try to fill in the data gap on olivine toxicity to marine biota and *in situ* olivine dissolution rates by conducting (I) laboratory flume experiments, (II) olivine toxicity tests for a range of (benthic) marine organisms

(algae, invertebrates, and fish) and (III) monitoring campaigns at natural olivine beaches (e.g. Papakōlea beach, Hawaii) before conducting large-scale field trials. Our work provides a first conservative coastal olivine application guideline and highlights the need for additional research to perform an accurate site-specific risk assessment of coastal enhanced olivine weathering.

4.4 Supplementary information

A more detailed description on how the olivine guidelines were derived based on seawater EQS for Ni and Cr is provided. Additionally, globally occurring Cr concentrations in coastal seawater and sediment are shown. Moreover, tables with all literature data used to derive a summary on global coastal Ni and Cr concentrations are given. Finally, Cr EQS-based olivine guidelines are shown and discussed.

4.5 Acknowledgments

Chapter 5 Olivine avoidance behaviour by marine gastropods (*Littorina littorea* L.) and amphipods (*Gammarus locusta* L.) within the context of ocean alkalinity enhancement

Picture *Littorina littorea*: © WoRMS, Claude Nozères

Abstract

Gigaton scale atmospheric carbon dioxide (CO_2) removal (CDR) is needed to keep global warming below 1.5 °C. Coastal enhanced olivine weathering is a CDR technique that could be implemented in coastal management programmes, but its CO_2 sequestration potential and environmental safety remain uncertain. Large scale olivine spreading would change the surficial sediment characteristics, which could potentially reduce habitat suitability and ultimately result in community composition changes. To test this hypothesis, we investigated the avoidance response of the marine gastropod *Littorina littorea* (Linnaeus, 1758) and marine amphipod *Gammarus locusta* (Linnaeus, 1758) to relatively coarse (83 – 332 µm) olivine and olivine-sediment mixtures during short-term choice experiments. Pure olivine was significantly avoided by both species, while no significant avoidance was observed for sediment with 3% or 30% w/w olivine. For *L. littorea*, aversion of the light green colour of pure olivine (i.e. positive scototaxis) was the main reason for avoidance. Moreover, olivine was not significantly avoided when it was 7.5 cm (45%) closer to a food source/darker microhabitat (*Ulva sp.*) compared to natural sediment. The amphipod *G. locusta* possibly avoided pure olivine to reduce Ni and Cr exposure. Yet, a significant increase in whole body Ni concentrations was observed after 79 h of exposure in the 30% and 100% w/w olivine treatments compared to the sediment control, likely as a result of waterborne Ni uptake. Overall, our results are significant for ecological risk assessment of coastal enhanced olivine weathering as they show that *L. littorea* and *G. locusta* will not avoid sediments with up to 30% w/w relatively coarse olivine added and that the degree of olivine avoidance is dependent on local environmental factors (e.g. food or shelter availability).

5.1 Introduction

Limiting global warming to 1.5°C requires fast reductions of anthropogenic greenhouse gas emissions to net zero by 2050 (IPCC, 2022b). This primarily requires a shift from fossil fuels to renewable energy sources and improved energy conservation and efficiency (Yousefi et al., 2019; IPCC, 2022b). Furthermore, atmospheric carbon dioxide (CO_2) removal (CDR) is needed on a gigaton scale to compensate for carbon budget overshoot and greenhouse gas emissions from sectors that are challenging to decarbonize (e.g. aviation, shipping, industrial processes) (Minx et al., 2018; IPCC, 2022b). Ocean alkalinity enhancement (OAE) is a proposed CDR technique that relies on the increase in seawater alkalinity after addition of alkaline substances (e.g. olivine, calcite, lime) to drive atmospheric CO_2 drawdown and enhance the ocean carbon sink (Renforth and Henderson, 2017). Spreading finely ground fast weathering silicate rock in dynamic coastal environments has been put forward as a promising OAE method due the abundance of suitable source rock, technological readiness, and possible co-benefits including promotion of primary production and counteracting ocean acidification (Meysman and Montserrat, 2017; Montserrat et al., 2017; Bach et al., 2019; Caserini et al., 2022). The silicate mineral olivine ($Mg_xFe_{2-x}SiO_4$) has received most attention for use in coastal enhanced silicate weathering (CESW) due to its abundance and relatively fast dissolution kinetics (Meysman and Montserrat, 2017). However, the CO_2 sequestration potential and environmental safety of CESW remain uncertain (Montserrat et al., 2017; Flipkens et al., 2021; Fuhr et al., 2022).

Spreading large amounts of finely ground olivine rich rock in coastal environments could alter the local habitat of marine organisms. The impacts could resemble those seen in beach nourishment, encompassing smothering of marine organisms and alterations in both the physical (such as sediment density, grain size, shape, and colour) and chemical (including contaminant and organic carbon content) properties of the surficial sediment (Speybroeck et al., 2006). Freshly ground forsterite olivine sand is typically composed of green, angular grains with sharp edges (Montserrat et al., 2017). The grain size of olivine

that would ideally be distributed remains uncertain. Very fine (≤ 10 µm) grains dissolve and sequester CO_2 faster than coarser grains (≥ 100 µm), but cost more energy to produce, are more difficult to transport, and could pose a higher environmental risk (Hangx and Spiers, 2009; Flipkens et al., 2021; Duan et al., 2022; Foteinis et al., 2023). Nickel (Ni) and chromium (Cr) concentrations in olivine are typically significantly higher than in natural marine sediment and could result in toxic effects depending on their release rate during olivine dissolution and subsequent accumulation by marine biota (Flipkens et al., 2021).

The effects of olivine exposure on marine biota have only been subject to limited research, as indicated by a handful of recent studies (Ren et al., 2021; Flipkens et al., 2023b; Guo et al., 2023; Hutchins et al., 2023). Ren et al. (2021) observed an increase in the abundance of biofilm forming particle-attached microbes following a 10-day exposure to 1% w/w olivine in natural seawater. In the study by Hutchins et al. (2023), six phytoplankton species exposed to synthetic olivine leachates with Ni(II) and Cr(VI) concentrations up to 0.13 and 0.12 µmol L^{-1} exhibited neutral to positive physiological responses. Guo et al. (2023) reported an increase in the abundance of several small (<20 µm) phytoplankton taxa and the dinoflagellate *Noctiluca scintillans* ((Macartney) Kofoid & Swezy, 1921) after 21 days of olivine exposure in natural seawater. However, ctenopods (*Penilia sp.*) and tunicates (*Oikopleura sp.*) reduced in number, possibly due to impaired feeding in the presence of suspended olivine particles (at a concentration of 1.9 g L^{-1}) (Guo et al., 2023). Finally, Flipkens et al. (2023b) found significant grain size-dependent metal accumulation in the marine amphipod *G. locusta* (Linnaeus, 1758) during acute olivine exposures lasting 24 to 72 hours. Additionally, chronic exposure to olivine for 35 days reduced the survival, growth, and reproduction of juvenile *G. locusta* at concentrations of 10% w/w and higher, likely due to metal toxicity. Overall, these findings highlight the critical need for further research on olivine exposure effects on marine biota to ensure that coastal enhanced olivine weathering can be scaled sustainably in the future for climate change mitigation.

Avoidance of olivine-rich sediment patches could possibly occur to reduce Ni and Cr exposure or escape unpreferred substrate types (Araújo et al., 2016). A range of studies have reported dose dependent avoidance of contaminated sediments by various aquatic invertebrates and fish (Araújo et al., 2016). Additionally, coarse substrates, which often have a lower food content in the form of organic material compared to fine substrates, were significantly avoided by various marine organisms (Moles et al., 1994; Hellou et al., 2005; Boos et al., 2010). Overall, avoidance of coastal olivine application sites could lead to changes in local biodiversity, which could severely impact ecosystem structure and functioning (Lopes et al., 2004; Araújo et al., 2016). Therefore, the behavioural responses of marine organisms to olivine exposure should be considered in ecological risk assessment of CESW.

Amphipods and to a lesser extent gastropods have been frequently used as test organisms in sediment avoidance assays (Araújo et al., 2016). The gastropod *L. littorea* (Linnaeus, 1758) and amphipod *G. locusta* are widespread along shorelines of the Northeast Atlantic. They occur in the intertidal and subtidal zone on a range of substrate types, although *L. littorea* has preferences for rocky substrates and *G. locusta* is mostly found at sheltering structures (e.g. macroalgae and stones) (Costa and Costa, 2000; Carlson et al., 2006). Both species shape intertidal communities by extensive algae grazing and are an important food source for higher trophic levels (e.g. fish and aquatic birds) (Anderson and Underwood, 1997; Costa and Costa, 2000; Andersson et al., 2009).

In this study, we investigated the avoidance response of the periwinkle *L. littorea* and amphipod *G. locusta* to relatively coarse (83 – 332 µm) olivine and olivine-sediment mixtures. These investigations were conducted during several short-term choice experiments aimed at evaluating the potential impact of coastal olivine spreading on the habitat suitability for these two benthic macroinvertebrate species. In addition to the response to equidistant substrates, we investigated whether the degree of pure olivine avoidance in *L. littorea* was dependent on the distance to a food source. Finally, the importance of colour preference on substrate avoidance was assessed for both species.

We hypothesized that substrates with a high olivine concentration would be avoided by *G. locusta* and *L. littorea* due to their elevated Ni and Cr content. Additionally, we hypothesized that the distance to a food source could affect the degree of pure olivine avoidance *in L. littorea* since movement is likely driven by food availability in this species (Seuront et al., 2007).

5.2 Material and methods

5.2.1 Test organisms

Adult *L. littorea* (shell height: 21.4 ± 1.3 mm, shell width: 18.2 ± 1.1 mm, *N* = 632) originating from Ireland were obtained from a commercial supplier in the Netherlands. All data henceforth are presented as mean ± standard deviation (S.D.), unless stated otherwise. *Littorina littorea* were housed at a temperature of 15 ± 1 °C and photoperiod of 12 h light and 12 h dark (12L:12D) in a 210 L polyethylene (PE) tank (NORAH Plastics) filled with 200 L of artificial seawater (ASW). The ASW was made by adding 7.15 kg of seasalt (hw-Marinemix®) to ultrapure water (Eurowater DPRO B1 – 1/1) and aerating the solution for at least 24 h before use. *Littorina littorea* were fed *Ulva sp. ad libitum*. A trickling filter was used and 30 to 50% water changes were conducted on a weekly basis to ensure good water quality. Seawater temperature (15 ± 1 °C), pH (8.00 ± 0.08), salinity (33.4 ± 1.1 ‰), and concentrations of dissolved oxygen (DO) (7.95 ± 0.20 mg L^{-1}) were measured weekly with a HQ30D portable multimeter (Hach). Approximate concentrations of nitrate (NO_3^-), nitrate (NO_2^-) and total ammonia (NH_3/NH_4^+) were determined with commercial test kits (Tetra). The pH and conductivity electrode were calibrated before each with standard pH (pH 4.00, 7.00, and 10.01) and conductivity (12.9 and 50 mS cm^{-1}) solutions (VWR international). The oxygen probe (Intellical LDO101, Hach) was used with factory calibration settings.

Amphipods were collected by hand in the Eastern Scheldt estuary (51°27'31.6"N 4°04'50.4"E, Krabbendijke, the Netherlands) during low tide and transported to the laboratory in clean HDPE buckets filled with ASW. A subsample of 10 amphipods were

identified microscopically as *G. locusta* using the key of Vader and Tandberg (2019). The animals were maintained in a 210 L PE tank filled with ASW and a 1 cm layer of control sediment (Section 5.2.2) and stones from the collection site. Amphipods were fed *Ulva sp. ad libitum* and Sera Micron Nature (1 mg individual^{-1}) three times per week. A trickling filter and protein skimmer were set up and weekly 15 to 30% water changes were conducted. Seawater temperature (18.6 ± 1.1 °C), pH (8.04 ± 0.07), salinity (33.6 ± 0.7 ‰), dissolved oxygen (7.37 ± 0.25 mg L^{-1}) and nitrogenous waste products were measured before each water change.

5.2.2 Sediment collection and characterization

Surficial (< 10 cm depth) North Sea sediment was collected from the intertidal zone at the Belgian coast (51°14'28.1"N 2°56'01.0"E, Ostend, Belgium) with a shovel and wet sieved *in situ* through a 1 mm screen to remove macrofauna. Sediment was brought to the laboratory in clean, sealed HDPE buckets and stored at 4 °C before use in the olivine avoidance assays with *L. littorea*. For the experiments with *G. locusta*, surficial control sediment was collected at the amphipod collection site and wet sieved through a 500 μm screen before storage at 4 °C until experimental use. Norwegian dunite sand was obtained from Sibelco's Aheim site. This dunite sand consists mainly (83 − 86 wt%) of forsterite-rich olivine ($Mg_{1.87}Fe_{0.13}SiO_4$) and will be referred to as olivine throughout the text. The mineral characterization of dunite sand is provided in Supplementary Section E.1.

Experimental sediments were characterized for their sediment organic matter (SOM) content, grain size distribution and trace metal concentrations. The loss on ignition method according to Heiri et al. (2001) was used to determine SOM content. Grain size distribution was measured with a Mastersizer 2000 particle size analyzer (Malvern) according to standard operating procedures without chemical pre-treatment. The elemental composition was determined via ICP-OES (iCAP 6300 Duo, Thermo Scientific). Sediment samples were acid digested according to a modified chromite ore digestion protocol (CEM Corporation, 1999). Briefly, 1.4 mL of Ultrapure sulphuric acid (≥96%,

Merck) and 2.6 mL of orthophosphoric acid (85%, Honeywell Chemicals) were added to 0.1 g of dry sediment and subsequently heated at 240 °C for 30 min in a Discover SP-D 80 microwave digestion system (CEM Corporation). Afterwards, 2 mL of 67-69% nitric acid (Fisher Scientific) was added and samples were heated again at 240 °C for 15 min. After digestion, samples were diluted 8.3 times with ultrapure Milli-Q (MQ) water. Finally, the supernatant of the samples was collected after centrifugation at 1600 g for 5 min for ICP-OES analysis. For quality control, certified reference material (SARM-6 NIM-D dunite, MINTEK) and procedural blanks were included during analysis. Average elemental recoveries were acceptable for all elements (72 to 93%) except Si due to the insolubility of silicate in HNO_3 (~0.4%).

5.2.3 *Littorina littorea* olivine avoidance assays

Novel choice experiments were conducted on square Nunc® bioassay dishes (L x W × H = 24.5 × 24.5 × 2.5 cm) to assess which substrate adult *L. littorea* avoided to reach a food source (*Ulva sp.*) and whether this avoidance was distance or substrate colour dependent. All experiments were conducted at controlled temperature (15 ± 1 °C) and light (12L:12D) conditions and bioassay dishes were cleaned with 2% V/V HCl (VWR International) and ultrapure MQ before use. A similar experimental setup was used for all seven experiments. Namely, dishes were filled with 200 mL of ASW (~6 mm layer) and a ~3 mm thick circular or rectangular band of different substrates (experiment specific) surrounded by a ~2 cm wide band (50.0 ± 0.04 g) of *Ulva sp.* (Figure 5.1). The number of dishes was equal to the amount of substrate patches and dishes were rotated by 360/*i* degrees, with *i* equal to the dish number, in order to exclude the possible effect of directional preference on test results. Substrate weights for all experiments are provided in Supplementary Section E.2.2.

At the start of an experimental trial, adult *L. littorea* were individually placed in the centre of the dishes with the apex of the shell pointing southeastwards. Subsequently, *L. littorea* could move around freely for 10 min after which the first substrate crossed to reach the *Ulva sp.* was recorded. Blinding researchers from the experimental substrates was

unfeasible due to the distinctive morphology of the control sediment and olivine sand. Next, approximately 95% of the ASW was removed with a syringe and dishes were wiped with paper towel to remove any mucus trails which could affect the path of subsequent *L. littorea* (Erlandsson and Kostylev, 1995). Afterwards, the substrate patches were rearranged if needed and 200 mL of fresh ASW was added to the dishes to start a new trial. A total of 20 trials were conducted for each experiment. A light diffuser (Bresser TR-4) was installed 80 cm above the experimental setup to create soft lighting conditions and experiments were recorded with a digital camera (Fujifilm FinePix XP60).

In a first experiment, six substrate types including pure (100% w/w) North Sea sediment, 3%, 30%, and 100% w/w olivine, copper (Cu) tape, and a blank patch were put in a circular band with an inner diameter of 14.5 cm and width of 1.5 cm on the dishes (Figure 5.1A). The Cu tape served as a positive control since it is known to be avoided by most gastropod species (Barnes and Hill, 2022), while the blank patch was included in case sandy substrates would be avoided. For the second experiment, the first experimental setup was replicated without Cu tape as a substrate (Figure 5.1B), since Cu release could affect periwinkle behaviour (Barnes and Hill, 2022). This experiment was also repeated with the substrate band and 200 mL ASW on a second dish beneath the original dish containing the circular band of 50 g *Ulva sp.* and 200 mL ASW to assess if sediment avoidance was colour based (Figure 5.1C).

The width of the circular substrate band was increased from 1.5 to 6.5 cm (decreasing the inner circle diameter to 5 cm) during the fourth experiment to examine whether the size of the sediment patch would affect the choice of *L. littorea* (Figure 5.1D). Only pure North Sea sediment, pure olivine and a blank patch were included as substrate types in this experiment. This setup was also replicated with the substrate band in a separate dish below the original dish, similar to the third experiment, to assess whether *L. littorea* exhibited colour preference (Figure 5.1E). During the sixth and seventh experiment, substrates were positioned in a rectangular formation of different size to assess whether sediment avoidance was affected by the distance to the food source (Figure 5.1F-G). The

distance from the periwinkle to the two olivine patches was either half (7.5 cm, Figure 5.1F) or equal to (15 cm, Figure 5.1E) the distance to a 100% w/w North Sea sediment and blank patch. The width of the sediment patches was equal to 1.5 cm in both experiments (Figure 5.1F-G). Pictures of the experimental set ups are shown in Supplementary Figure E.2.

Seawater pH (8.18 ± 0.07), temperature (14.8 ± 0.4 °C), salinity (33.2 ± 1.1 ‰), DO (8.09 ± 0.16 mg L^{-1}), and nitrogenous waste concentrations were measured at the start of each experiment. Furthermore, water samples for dissolved metal analysis were collected with a syringe from all dishes at the end of the first trial and last trial of each experiment. Water samples were filtered through 0.2 µm pore size filters (Chromafil XTRA PES-20/25, Macherey-Nagel) and diluted 20 times with 2% V/V TraceMetalTM Grade nitric acid (Fisher Scientific) before analysis via HR-ICP-MS (Element XR™, Thermo Scientific™). Procedural blanks (2% V/V HNO_3) and certified reference material (1643f, NIST) were included in the analysis for quality control. Dissolved metal results are provided in Supplementary Section E.2.3.
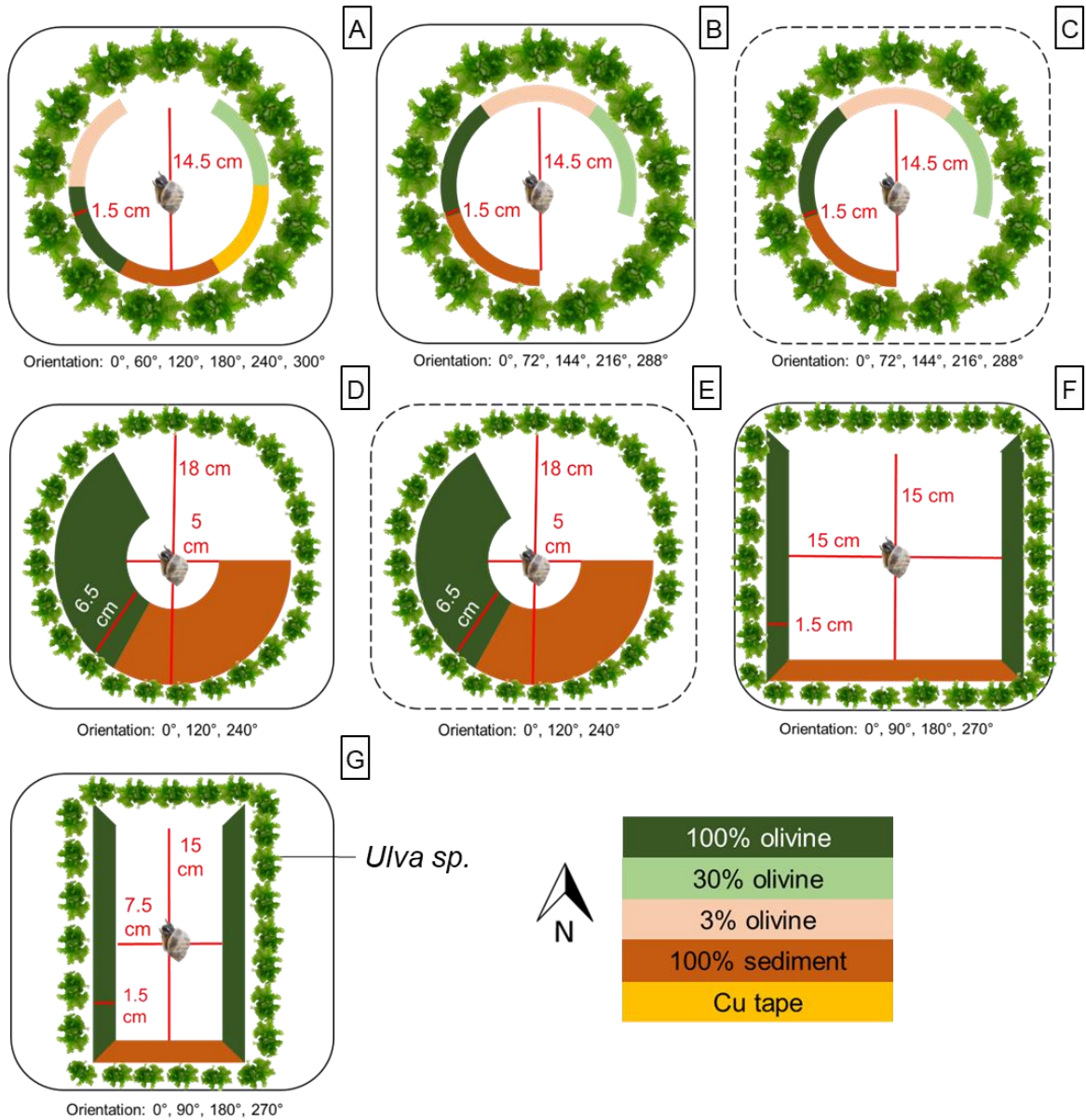
Figure 5.1: Schematic representation of the olivine avoidance assays with L. littorea. (A – G) Square bioassay dishes were filled with 200 mL ASW and a circular or rectangular band of various substrates (listed in the figure) surrounded by a band of Ulva sp. (details provided in text). Dotted lines in (C) and (E) indicate that the substrate was put underneath the dish to assess colour preference. Each set up consisted of three to six replicates which were rotated (values below subfigures) to avoid that directional preference would affect the test results. Pictures: Ulva lactuca © Jiří Novák, Littorina littorea © WoRMS, Claude Nozères.

5.2.4 *Gammarus locusta* olivine avoidance assays

A bi-compartmented system according to De Lange et al. (2006) was used with minor modifications to assess olivine avoidance in the marine amphipod *G. locusta* (Figure 5.2 and Supplementary Figure E.4). A total of 25 glass aquariums (L x W x H = 30 x 20 x 15 cm) representing 5 treatments were rinsed with 2% V/V HCl, ultrapure MQ and set up in a temperature controlled room (18.6 ± 1.1 °C) with a fixed photoperiod (12L:12D). For four treatments, aquariums were divided in two equal sections (L x W = 15 x 15 cm) which were filled with a 5 mm layer (175.6 ± 0.007 g, *N* = 20) of wet control sediment on one side, and a 5 mm layer of control sediment, 3% w/w, 30% w/w, or 100% w/w olivine on the other side (Figure 5.2). For the remaining treatment a 5 mm layer of control sediment and 5 mm layer of 100% w/w olivine was put underneath the five replicate aquariums to assess if olivine avoidance was colour based (Figure 5.2). Aquariums were rotated (0, 90, 180, 180, and 270°) to have the sediments face different directions. Sediment weights are provided in Supplementary Table E.4. Subsequently, 6 L of ASW was added to each aquarium and continuously aerated with aeration lines fitted with plastic tips positioned 8 cm above the sediment surface. The sediment was then left to settle for 2 days and a 50% water changed was conducted 24 h before 10 adult amphipods (70 – 80% males) were added to each aquarium. Survival and position of the amphipods was then recorded three times per day for three consecutive days. Afterwards, surviving amphipods were collected to examine whole body trace metal concentrations.

Amphipods for whole body metal analysis were individually rinsed with ultrapure MQ and dried at 60 °C for 24 h in preweighed 5 mL tubes. Standard reference material (SRM-2976, NIST) and procedural blanks were included during sample preparation and analysis. Sample dry weight was recorded with an ultra-microbalance (Sartorius SE2). Next, samples were digested in 400 µL of TraceMetal™ Grade nitric acid (67 – 69% V/V, Fisher Scientific) at room temperature for at least 12 h. Afterwards, digestion was continued at 105 °C for 15 min in a SC154 HotBlock® (Environmental Express) (Van Ginneken et al., 2015; Flipkens et al., 2023b). Subsequently, 50 µL of 30 – 32% W/W H_2O_2 (Fisher

179

Scientific) was added and samples were left to incubate at room temperature for 10 min. Finally, the samples were heated at 105 °C for 15 min and subsequently diluted with ultrapure MQ to a final acid concentration of 2.2% V/V. Elemental concentrations were analysed via HR-ICP-MS (Element XR, Thermo Fischer Scientific). Certified reference material (1643f, NIST) was measured every 20 to 22 samples for analytical quality control. The recoveries of Ni and Cr for SRM-2976 were 80.1 ± 7.6% (N = 8) and 49.3 ± 11.3% (N = 8), respectively. The lower Cr recoveries may be attributed to both the relatively low certified value of 0.5 µg g^{-1} for SRM-2976 and the potential small variations during sample preparation and analysis. Measured whole body Cr concentrations for *G. locusta* were not adjusted to account for the lower SRM-2976 Cr recoveries.

Seawater pH (8.12 ± 0.04), temperature (18.4 ± 0.1 °C), and salinity (32.7 ± 0.3 ‰) were measured at the start of the experiment and after 48 and 72 h in all aquariums. Simultaneously, DO (7.7 ± 0.1 mg L^{-1}) and nitrogenous waste concentrations (NO$_3^-$ < 12.5 mg L^{-1}, NO$_2^-$ < 0.3 mg L^{-1}, and NH$_3$/NH$_4^+$ ≤ 0.25 mg L^{-1}) were measured in one replicate of each treatment. A 50% water change was conducted after 48 h of exposure and 10 mL water samples for dissolved metal analysis were collected from all aquariums on each experimental day.
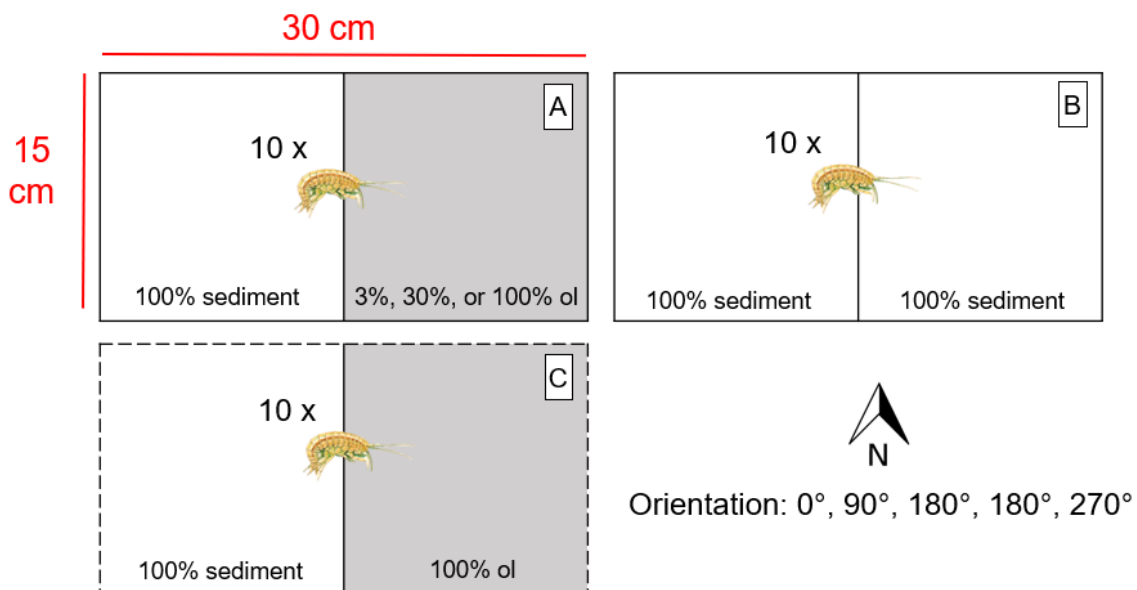
Figure 5.2: Schematic representation of the olivine avoidance assays with G. locusta. Glass aquariums (9 L, represented by large rectangles) were filled with 6 L ASW and divided in two equal compartments with a 5 mm layer of 100% w/w sediment on one side (shown in white) and (A) 3%, 30%, or 100% w/w olivine (ol, shown in grey) or (B) 100% w/w sediment on the other side. (C) To assess colour preference, 100% w/w sediment and 100% w/w ol were put underneath the aquarium (indicated by dotted lines). Five aquariums with 10 amphipods were used for each treatment and rotated by 0°, 90°, 180°, 180°, or 270° (orientation) to exclude the effect of possible directional preference on the experimental results.

5.2.5 Statistical analyses

Statistical analyses were conducted in RStudio (version 2022.12.0+353) using R version 4.2.1 (R Core Team, 2022) and figures were constructed in GraphPad Prism version 9.5.1 for Windows. For the *L. littorea* olivine avoidance assays, Pearson chi-square tests were performed to test whether observed frequencies deviated significantly from expected frequencies under the null hypothesis that *L. littorea* did not show substrate avoidance. Subsequently, squared standardized residuals were used to determine which substrate types were significantly avoided with the pchisq() function.

For the *G. locusta* olivine avoidance bioassays, differences in amphipod survival between treatments were assessed via one-way ANOVA. A binomial generalized linear mixed model (GLMM) was fit by maximum likelihood (Laplace approximation) to assess the main and interactive effect of time (fixed factor with four levels) and treatment (fixed factor with five levels) on the fraction of amphipods in the control compartment. Aquarium ID and repeated daily observations were included as random factors (25 and three levels, respectively) in the model. Aquarium ID was nested in treatment and observations were nested in time. ANOVA tests were performed to simplify the model by removal of a non-significant (p-value < 0.05) interaction term and explanatory variables. The model was found to not be overdispersed by comparing the sum of squared Pearson residuals to the residual degrees of freedom. Furthermore, normality and homoscedasticity of the model

residuals were visually assessed via quantile-quantile and residuals plots, respectively and found to be acceptable. The conditional and marginal R^2 values of the GLMM were estimated using the "r.squaredGLMM" function of the "MuMIn" package using the delta method (Nakagawa et al., 2017).

Differences in amphipod whole body metal concentrations among treatments were investigated with a GLMM using the R package "nlme". Treatment was considered a fixed factor and aquarium ID a random factor (25 levels) nested in treatment. Statistical differences in ASW dissolved metal concentrations among experiments with *L. littorea* were analysed similarly. Here, experiment was considered a fixed factor and trial a random factor (two levels). Normality and homoscedasticity of model residuals were assessed as described previously. Data were not transformed after violation of the normality assumption due to the robustness of GLMMs to deviation of model residuals from a normal distribution (Schielzeth et al., 2020). In case of heteroscedasticity, a weights argument was added to the model to differentially weight the data of different treatments. The object containing the weights was created using the "varIdent" function. Post hoc multiple comparisons were performed with the "emmeans" package" to identify significant differences among treatments. Adjustment of p-values was done using Tukey's method.

5.3 Results and discussion

5.3.1 Sediment characteristics

A low average SOM content was observed for the control sediment (0.44% w/w) and pure olivine (0.28% w/w) used in the avoidance assays with *L. littorea* (Table 5.1). Both olivine and control sediment were sandy substrates, but the olivine (D10 − D90 = 83 − 214 µm) was finer than the control sediment (D10 − D90 = 180 − 385 µm). The average Ni and Cr concentrations of pure olivine (42 and 58 µmol g^{-1} d.w., respectively) were 1150 and 138 times higher those of the control sediment (0.037 and 0.42 µmol g^{-1} d.w., respectively) (Table 5.1).

For the avoidance assays with *G. locusta*, the average SOM content was also low for both the control sediment (1.0% w/w) and pure olivine (0.29% w/w) (Table 5.1). The olivine used in these tests was slightly coarser (D10 − D90 = 93 − 332 µm) than the control sediment (71 − 222 µm) and had average Ni and Cr concentrations (38 and 23 µmol g^{-1} d.w., respectively) that were 1078 and 26 times higher than those of the control sediment (0.036 and 0.90 µmol g^{-1} d.w., respectively). The 60% lower Cr concentration of the different olivine batch used in the avoidance assays with *G. locusta* compared to *L. littorea* can likely be explained by the heterogeneous distribution of chromite ($FeCr_2O_4$) in dunite rock (Santos et al., 2015). The concentrations of Mg, Fe, Al, Mn, Co, and Zn for the different experimental sediments are provided in Supplementary Table E.2.

Table 5.1: Geochemical properties of the sediments in the olivine avoidance assays with L. littorea and G. locusta. Mean and S.D. (N = 3 − 5) are given for the sediment organic matter content (SOM), volumetric effective grain sizes (D) and sediment nickel (Ni) and chromium (Cr) concentrations (µmol g^{-1} d.w.). The grain size distribution of the 3% and 30% w/w olivine was not measured (N.A.) for the olivine avoidance assays with G. locusta.

L. littorea olivine avoidance assays				
Treatment	100% sediment	3% olivine	30% olivine	100% olivine
SOM (%)	0.44 ± 0.029	0.44[a]	0.39[a]	0.28 ± 0.0066
D10 (µm)	180 ± 2.0	174 ± 1.6	131 ± 2.5	83 ± 0.7
D50 (µm)	263 ± 2.6	261 ± 2.4	236 ± 0.9	135 ± 1.0
D90 (µm)	385 ± 10	391 ± 3.5	404 ± 9.3	214 ± 1.4
Ni (µmol g^{-1} d.w.)	0.037 ± 0.0047	1.3[a]	13[a]	42 ± 0.8
Cr (µmol g^{-1} d.w.)	0.42 ± 0.080	2.2[a]	18[a]	58 ± 3.4
G. locusta olivine avoidance assays				
Treatment	100% sediment	3% olivine	30% olivine	100% olivine
SOM (%)	1.0 ± 0.087	1.0[a]	0.81[a]	0.29 ± 0.0072
D10 (µm)	71 ± 0.80	N.A.	N.A.	93 ± 6.9
D50 (µm)	126 ± 2.8	N.A.	N.A.	189 ± 5.4

D90 (μm)	222 ± 8.1	N.A.	N.A.	332 ± 5.5
Ni (μmol g^{-1} d.w.)	0.036 ± 0.018	1.2[a]	12[a]	38 ± 0.87
Cr (μmol g^{-1} d.w.)	0.90 ± 0.16	1.6[a]	7.8[a]	23 ± 0.85

[a]The SOM content and concentrations of Ni and Cr for the 3% and 30% w/w olivine were not analytically determined, but derived from the measured concentrations in the 100% w/w sediment and 100% w/w olivine treatment.

5.3.2 *Littorina littorea* olivine avoidance

Littorina littorea showed clear avoidance and preference of certain substrate types to reach a food source (Figure 5.3). The number of *L. littorea* that crossed the patch without substrate to reach *Ulva sp.* was 20% higher than expected in case of no substrate preference (X^2 (5, N = 104) = 24.6, p < 0.001) for the experiment with Cu tape and 26% higher (X^2 (4, N = 93) = 32.0, p < 0.001) in the replicated experiment without Cu tape (Figure 5.3A-B). Based on the eye anatomy, *L. littorea* are expected to have relatively good vision underwater allowing them to clearly resolve objects of approximately 2 cm in size up to 72 cm away (SEYER, 1992). Hence, *L. littorea* could possibly see that no foreign substrate had to be crossed in order to reach *Ulva sp.* via the blank patch, which could explain the higher choice for this substrate type in the current experimental set up. Conversely, Cu tape was only crossed by 2% of the *L. littorea*, indicating significant avoidance (X^2 (5, N = 104) = 13.6, p = 0.019) (Figure 5.3A). Previous studies have reported that terrestrial and aquatic gastropods prevent crossing Cu barriers, although the reason for avoidance remains unknown (Barnes and Hill, 2022).

Littorina littorea did not significantly avoid 100% w/w sediment or sediment with 3% w/w or 30% w/w olivine in both experiments (Figure 5.3A-B). However, 100% w/w olivine was significantly avoided, with only 1.9% of the individuals crossing pure olivine in the experiment with Cu tape (X^2 (5, N = 104) = 13.6, p = 0.019) and 1.1% in the experiment without Cu tape (X^2 (4, N = 93) = 16.7, p = 0.0023) (Figure 5.3A-B). A number of reasons can possibly explain pure olivine avoidance by *L. littorea* including high trace metal concentrations, low sediment organic matter content (food quantity and quality), and

differences in olivine morphology (grain shape, edge sharpness, size, and colour) compared to natural sediment (Araújo et al., 2016). The SOM content of olivine and control sediment was low and not significantly different (Table 5.1). Hence, olivine avoidance is likely not the result of differences in substrate SOM content. Furthermore, during the experiment most *L. littorea* (initially not located on pure olivine) immediately moved towards a substrate different from 100% w/w olivine, indicating that pure olivine was likely not avoided due to its smaller, less rounded grains compared to natural beach sand (Supplementary Figure E.1A-D). Therefore, olivine avoidance was likely driven by chemical cues or substrate colour.
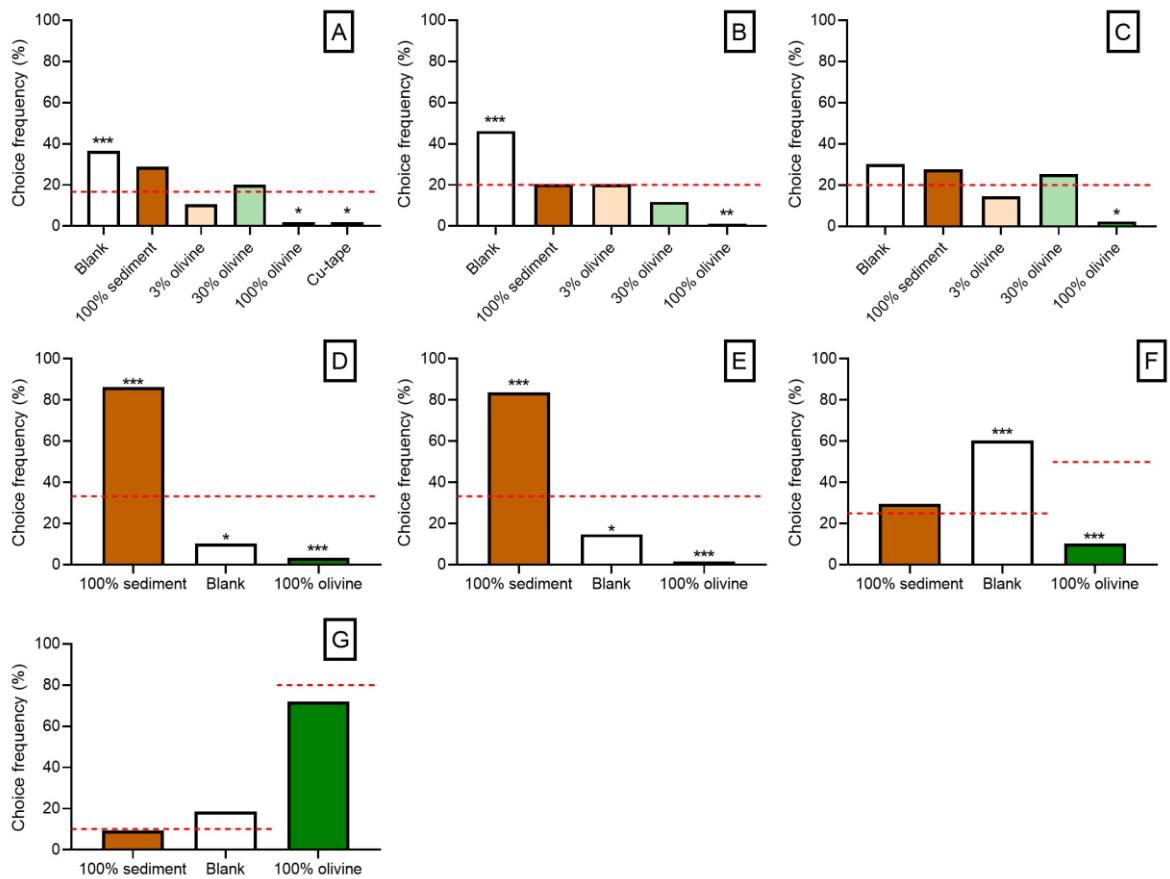
Figure 5.3: Substrate preference of L. littorea during acute olivine avoidance assays. Choice frequency (%) of different substrates that were first crossed by L. littorea to reach a

*food source (Ulva sp.) are shown for the experimental setups displayed in Figure 5.1. Subfigure numbers correspond to subfigure numbers in Figure 5.1. Significance compared to the expected frequency in case of no avoidance (red dotted line): * = p < 0.05, ** = p < 0.01, *** = p < 0.001.*

Significant avoidance of 100% w/w olivine (X^2 (2, N = 58) = 15.5, p < 0.001) was also observed when the width of the substrate bands was increased from 1.5 to 6.5 cm (Figure 5.3D). In contrast to previous results, significant preference of the 100% w/w sediment patch (X^2 (2, N = 58) = 48.6, p < 0.001) and avoidance of the blank patch (X^2 (2, N = 58) = 9.20, p = 0.010) was observed (Figure 5.3D). These findings are in line with positive scototaxis (attraction to dark shapes) previously observed in *L. littorea* (Moisez and Seuront, 2020) given the relatively dark colour of the natural sediment and light colour of the 100% w/w olivine and blank patch (Supplementary Figure E.2). This behaviour is likely important for *L. littorea* in its natural environment (typically rocky shores) to find dark crevices where they are safe from predation, desiccation, and thermal stress (Seuront et al., 2018; Moisez and Seuront, 2020). The scototactic response is dependent on the dimensions of the dark shape (Moisez and Seuront, 2020), which could explain why no significant preference of the 100% w/w sediment was observed when the patch was only 1.5 cm wide (Figure 5.3A-C).

When substrates were put underneath the bioassay dishes, 100% w/w olivine was still significantly avoided in both the experiment with the wider substrate circle (X^2 (2, N = 93) = 15.5, p < 0.001) (Figure 5.3E) and smaller substrate circle (X^2 (4, N = 83) = 12.84, p = 0.012) (Figure 5.3C). The relative number of *L. littorea* that crossed 100% w/w olivine was very similar in these experiments (1.6 – 2.4%) compared to the previous experiments (1.1 – 3.4%, Figure 5.3A-B and 5.3D). Therefore, we can conclude that pure olivine avoidance was mainly a positive scototactic response due to the significantly lighter colour of 100% w/w olivine compared natural sediment (see Supplementary Figure E.2).

Finally, distance towards the food source significantly affected the substrate choice of *L. littorea* (Figure 5.3F-G). Similar to previous experiments with 1.5 cm wide substrate patches, olivine was significantly avoided (X^2 (2, N = 78) = 24.6, *p* < 0.001) and the blank patch was preferred (X^2 (2, N = 78) = 38.8, *p* < 0.001) when the distance between the *L. littorea* and the *Ulva sp.* was equal (15 cm) for all substrate types (Figure 5.3F). However, no significant avoidance of pure olivine was observed when the distance between the *L. littorea* and the *Ulva sp.* was 45% smaller via the olivine patches (9 cm) compared to the blank or 100% sediment patch (16.5 cm) (X^2 (2, N = 75) = 0.60, *p* = 0.74) (Figure 5.3G). Hence, we can infer that distance to a food source or darker microhabitat (*Ulva sp.* in this case) could significantly affect the degree of pure olivine avoidance in *L. littorea* (Seuront et al., 2007; Moisez and Seuront, 2020).

5.3.3 *Gammarus locusta* avoidance assays

5.3.3.1 Avoidance behaviour

Average amphipod survival ranged between 84 to 90% and was not significantly different among treatments (*F*(4, 20) = 0.24, *p* = 0.91). Overall, control preference was close to 50% throughout the experiment in the 100% w/w sediment control (average values ranging between 31 and 53%, *N* = 12), indicating that amphipods did not exhibit significant directional preference (Figure 5.4). No significant effect of exposure day (X^2 = 2.22, Df = 3, *p* = 0.53) or the interaction between treatment and exposure day (X^2 = 8.76, Df = 12, *p* = 0.72) was observed on amphipod control preference. Therefore, these terms were removed from the binomial GLMM. No significant preference for the control compartment was observed in the 3% w/w (β = 0.060, z = 0.14, *p* = 0.89) and 30% w/w (β = -0.0033, z = -0.008, *p* = 0.99) olivine treatments (Figure 5.4). However, pure olivine was significantly avoided (β = 2.67, z = 5.07, *p* < 0.001) by amphipods throughout the experiment (Figure 5.4).

Pure olivine avoidance was not significantly driven by colour preference (β = 0.095, z = 0.20, *p* = 0.84, Figure 5.4) in contrast to our findings for *L. littorea*. Differences in food availability (sediment organic carbon) can also likely not explain the observed 100% w/w

olivine avoidance, since SOM concentrations were low in all treatments (Table 5.1) and olivine avoidance occurred within hours (Figure 5.4) while amphipods were fed prior to the experiment. Furthermore, *G. locusta* inhabits a wide variety of sediment types (from gravel to mud) along its natural distribution (Costa and Costa, 2000), and its survival under laboratory conditions was not significantly affected by the fraction of fine (<63 μm) particles in the sediment during a 10-day exposure (Costa et al., 1996). Therefore, the limited difference in grain size distribution between pure olivine and control sediment (Table 5.1) also likely does not explain the observed 100% w/w olivine avoidance. However, various studies have shown that amphipods significantly avoid contaminated sediments in a concentration dependent manner (Hellou et al., 2005; De Lange et al., 2006; Szczybelski et al., 2018). Therefore, *G. locusta* possibly avoided pure olivine due to its high Ni (38 μmol g^{-1} d.w.) and Cr (23 μmol g^{-1} d.w.) content (Table 5.1) in order to reduce trace metal exposure (Araújo et al., 2016).
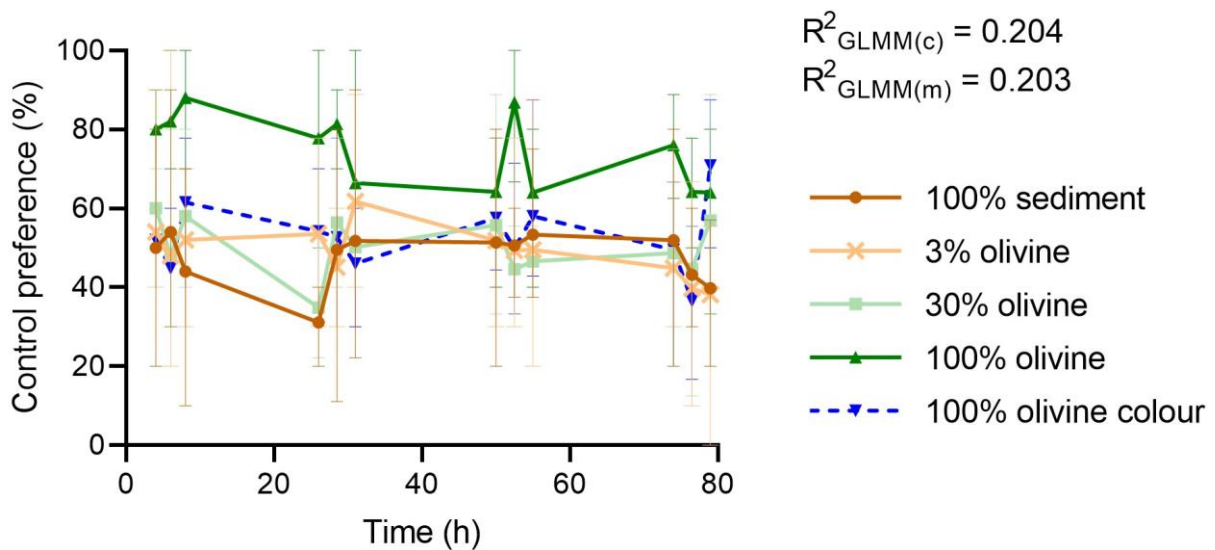
Figure 5.4: Control sediment preference (%) of G. locusta as a function of time (h) during the three day bi-compartmented olivine avoidance assays. Mean and range values (N = 5) are shown for the 100% w/w sediment control and various olivine treatments (3, 30, and 100% w/w olivine) including a pure olivine treatment where the substrate was put

underneath the aquariums to investigate colour preference (100% olivine colour). The conditional ($R^2_{GLMM(c)}$) and marginal ($R^2_{GLMM(m)}$) coefficients of determination (R^2) are also given.

5.3.3.2 Trace metal accumulation

Whole body Ni concentrations were significantly elevated in amphipods of the 30% w/w olivine treatment (mean ± S.D. = 0.18 ± 0.13 µmol g^{-1} d.w., range = 0.05 – 0.57 µmol g^{-1} d.w., N = 20) and 100% w/w olivine treatment (mean ± S.D. = 0.30 ± 0.27 µmol g^{-1} d.w., range = 0.08 – 1.16 µmol g^{-1} d.w., N = 18) compared to the 100% w/w sediment control (mean ± S.D. = 0.063 ± 0.022 µmol g^{-1} d.w, range = 0.04 – 0.13 µmol g^{-1} d.w., N = 20) at the end of the experiment (Figure 5.5A). This increase in whole body Ni concentrations can be the result of waterborne Ni uptake and dietary Ni uptake via the ingestion of olivine grains (Adams et al., 2011). However, the number of olivine grains that were ingested by experimental amphipods was likely limited, since no significant increase in whole body Cr ($F(4,20)$ = 2.26, p = 0.099) or Fe ($F(4,20)$ = 1.03, p = 0.42) concentrations was observed (Figure 5.5B and Supplementary Figure E.6A). Hence, the observed Ni accumulation was mainly the result of waterborne Ni uptake.

Dissolved Ni concentrations in the ASW were elevated in the 100% w/w olivine (112 – 174 nmol L^{-1}, N = 10) and 100% olivine colour (107 – 122 nmol L^{-1}, N = 15) treatment compared to the sediment control (42 – 64 nmol L^{-1}, N = 10) (Figure 5.5C). Elevated Ni concentrations in the 100% w/w olivine treatment are the result of olivine weathering (Montserrat et al., 2017), while potential impurities in the sea salt could explain higher concentrations in the 100% olivine colour treatment which was tested separately from the other treatments. Reported waterborne Ni uptake rate constants vary between 0.0052 and 0.24 L g^{-1} d^{-1} for different aquatic invertebrates exposed to dissolved Ni concentrations ranging between 0.26 and 767 nmol L^{-1} (Hédouin et al., 2007; Urien et al., 2017). Given these Ni uptake rate constants and the observed Ni concentrations in the ASW, a whole body Ni concentration between 0.090 and 0.18 µmol g^{-1} d.w. would be expected in amphipods of the 100% w/w olivine treatment (calculations provided in

Supplementary Section E.3.4), which was exceeded in 61% of the exposed amphipods (Figure 5.5A). Exposure to elevated Ni concentrations in the porewater compared to the overlying water and interindividual differences in the amount of time spent on the olivine 100% w/w olivine compartment could possibly explain the high and variable whole body Ni concentrations (Figure 5.5A) (Simpson and Batley, 2007).

Whole body Cr concentrations (<0.34 − 827 nmol g^{-1} d.w., N = 84) were generally lower than whole body Ni concentrations and did not differ significantly between treatments (F(4,20) = 2.26, p = 0.099) (Figure 5.5B). The large variation in whole body Cr concentrations in the 100% olivine colour treatment was unexpected and the cause remains unknown. Dissolved Cr concentrations in ASW were not significantly elevated in the olivine treatments (2.2 − 36 nmol L^{-1}, N = 40) compared to the sediment control (2.6 − 4.6 nmol L^{-1}, N = 10) (Figure 5.5D). The lack of Cr accumulation in the ASW of the olivine treatments can be explained by low water solubility of chromite ($FeCr_2O_4$), which is the dominant Cr-bearing phase in dunite rock (Santos et al., 2015).
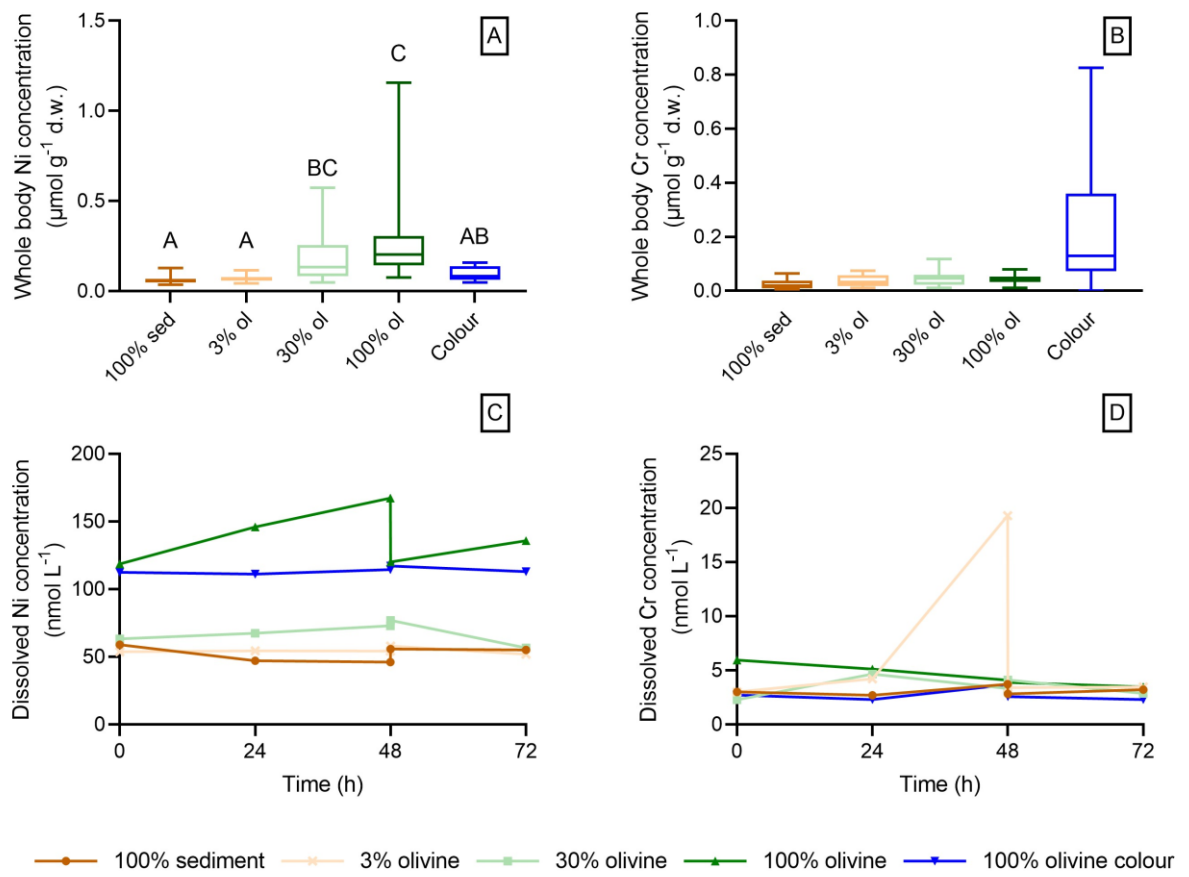
Figure 5.5: Metal accumulation in G. locusta and artificial seawater during olivine avoidance assays. Box and whisker plots of the whole body (A) nickel (Ni) and (B) chromium (Cr) concentrations (µmol g^{-1} d.w.) in G. locusta (N = 10 – 20) at the end of the three day olivine avoidance assays. Results are shown for the sediment (sed) control and different olivine (ol) treatment including the 100% w/w olivine treatment to test colour preference (Colour). Temporal evolution of average dissolved (C) Ni and (D) Cr concentrations (nmol L^{-1}) in artificial seawater (N = 2 or 3).

5.3.4 Implications for coastal enhanced olivine weathering

Changes in the physicochemical properties of the surficial sediment (e.g. metal and SOM content, grain size distribution) after large scale coastal olivine spreading for climate change mitigation could possibly alter habitat suitability for marine biota and

subsequently lead to avoidance of olivine rich sediment patches (Araújo et al., 2016). Here we found that *L. littorea* and *G. locusta* significantly avoided 100% w/w olivine sand. Under the current experimental designs, olivine was avoided due to its light colour (positive scototaxis) by *L. littorea* and possibly its high metal content by *G. locusta*. However, olivine was not significantly avoided when it was mixed with natural marine sediment at concentrations of 3% w/w and 30% w/w olivine. Therefore, these benthic macroinvertebrates will likely not avoid olivine-rich sediment patches after large-scale coastal deployments of relatively coarse olivine. Nevertheless, an olivine deployment method suitable for the local beach conditions should be adopted to avoid short-term disturbance and mortality (e.g. by burial) of marine biota (Speybroeck et al., 2006) in addition to long term adverse effects (e.g. possible trace metal toxicity and changes in community composition) (Bach et al., 2019; Flipkens et al., 2021).

For beach nourishment practices, olivine characteristics (e.g. grain size, metal content) in addition to the scale, timing, and method of deployment likely play an important role to minimize ecological impacts (Speybroeck et al., 2006). A number of smaller olivine deployments are generally preferred over a single large deployment, although this would reduce the net CO_2 sequestration efficiency of CESW as a result of higher transport associated CO_2 emissions (Speybroeck et al., 2006; Hangx and Spiers, 2009). Furthermore, olivine spreading is preferably done in periods of low biological activity and the type of deployment (classic, foreshore, or backshore nourishment) should be chosen based on local biodiversity taking into account social and political acceptance (Speybroeck et al., 2006; Low et al., 2022). Ideally, olivine with a similar grain size distribution as that of the local sediment would be dispersed to minimize ecological impacts, although finer grain sizes are possibly preferred from a climate change mitigation perspective due to their faster dissolution and CO_2 sequestration rate (Speybroeck et al., 2006; Hangx and Spiers, 2009; Foteinis et al., 2023). The distribution of fine-grained olivine (<63 μm) could affect the particle-attached microbial community composition (Ren et al., 2021) and sediment siltation could have adverse impacts on various marine biota including shellfish, mangroves, and corals (Erftemeijer et al., 2012; Noor et al., 2015; Poirier et al., 2021).

Finally, the positive (e.g. improved calcification and phytoplankton growth) and negative effects (e.g. Ni and Cr toxicity) of olivine dissolution products on marine biota and contribution to climate change mitigation should be considered to assess the scale at which olivine could be safely deployed in coastal waters (Bach et al., 2019; Flipkens et al., 2021; Hutchins et al., 2023). Hence, additional studies on olivine exposure effects for various marine organisms are needed to accurately determine the most suitable, location specific, olivine deployment strategy for atmospheric CO_2 removal.

5.4 Conclusions

Coastal enhanced olivine weathering has been proposed as a large scale atmospheric CO_2 removal technique for climate change mitigation. However, changes in the surficial sediment physicochemistry after olivine addition could possibly alter the habitat suitability and result in avoidance of olivine rich substrates by some marine species. To test this hypothesis, we conducted several short-term choice experiments to assess the avoidance response of the marine gastropod *L. littorea* and the marine amphipod *G. locusta* to both pure olivine and olivine mixed with natural sediment. Pure olivine was significantly avoided by both organisms, while 3% w/w and 30% w/w olivine mixtures with natural sediment were not. In contrast to our hypothesis, *L. littorea* avoided pure olivine due to its light colour rather than its high trace metal content as a result of an innate attraction to dark shapes (i.e. positive scototaxis). As hypothesized, the degree of avoidance was dependent on the distance to a food source, since pure olivine was not significantly avoided when it was 7.5 cm (45%) closer to *Ulva sp.* than natural sediment. The amphipod *G. locusta* did not avoid pure olivine due to its colour, but possibly to reduce Ni and Cr exposure. Nevertheless, a significant increase in whole body Ni concentrations was observed in *G. locusta* of the 30% and 100% olivine treatments compared to the sediment control after 79 h of exposure. Overall, our results indicate that *G. locusta* and *L. Littorea* would not significantly avoid coastal zones with relatively coarse olivine mixed in the surficial sediment up to concentrations of 30% w/w olivine. However, additional research on the effects of long-term olivine exposure on various

marine biota is needed to accurately determine the scale and suitable deployment strategy of coastal olivine spreading to maximize the benefits and minimize the ecological risks.

5.5 Supplementary information

Pictures of the experimental setups, substrate weights, and measured and expected metal accumulation are given in Appendix E.

5.6 Acknowledgements

Chapter 6 **Acute bioaccumulation and chronic toxicity of olivine in the marine amphipod *Gammarus locusta***
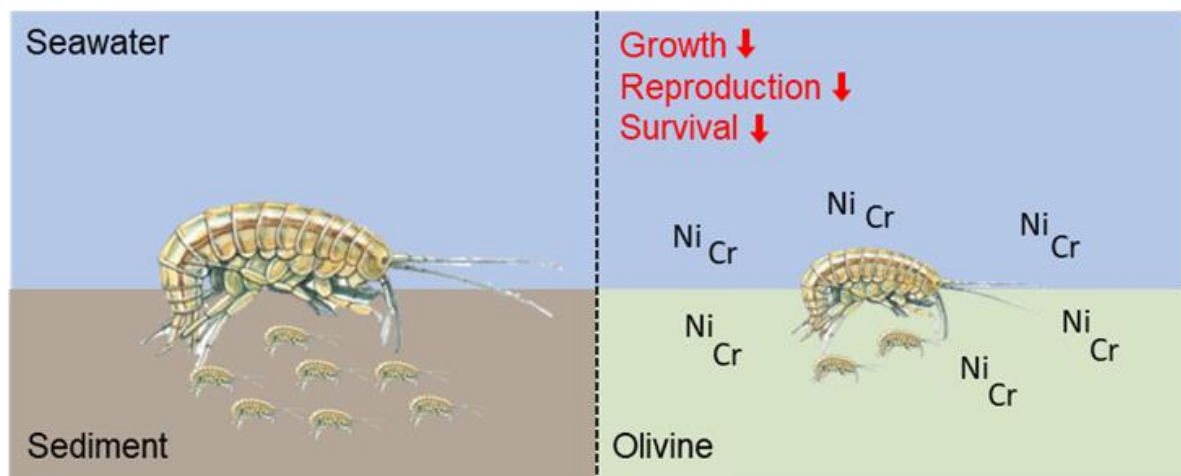
Published as:

Abstract

Active atmospheric carbon dioxide removal (CDR) is needed at a gigaton scale in the next decades to keep global warming below 1.5 °C. Coastal enhanced silicate weathering (CESW) aims to increase natural ocean carbon sequestration via chemical weathering of finely ground olivine ($Mg_xFe_{(1-x)}SiO_4$) rich rock dispersed in dynamic coastal environments. However, the environmental safety of the technique remains in question due to the high Ni and Cr content of olivine. Therefore, we investigated the short term bioaccumulation and chronic toxicity of olivine in the marine amphipod *Gammarus locusta*. Acute 24-h olivine exposure resulted in significant grain size dependent olivine ingestion and subsequent Ni and Cr accumulation in tissues. Thousands of small (mainly $\leq$ 10 μm) olivine grains were ingested by *G. locusta*, but their importance for trace metal bioaccumulation requires additional research. Most olivine grains were egested within 24 h. Chronic 35-day olivine (3 – 99 μm) exposure reduced amphipod survival, growth, and reproduction, likely as a result of metal induced oxidative stress and disturbance of major cation homeostasis. Amphipod reproduction was significantly reduced at olivine concentrations of 10% w/w and higher. In the context of ecological risk assessment, application of an arbitrary assessment factor of 100 to the highest no observed effect concentration of 1% w/w olivine yields a very low predicted no-effect concentration (PNEC) of 0.01% w/w olivine. This low PNEC value highlights the urgent need for additional marine olivine toxicity data to accurately assess the environmentally safe scale of coastal enhanced weathering for climate change mitigation.

6.1 Introduction

Limiting global warming to 1.5 °C requires gigaton scale atmospheric carbon dioxide (CO_2) removal (CDR) in the next decades (Minx et al., 2018). Ocean alkalinization (OA) via coastal enhanced silicate weathering (CESW) has been proposed as a scalable CDR strategy to help stabilize global temperatures and minimize adverse effects on natural ecosystems and human societies (Meysman and Montserrat, 2017). This technique aims to accelerate natural chemical weathering of silicate minerals by distributing suitable finely ground source rock in dynamic coastal areas. During silicate mineral dissolution, total alkalinity in seawater increases via the consumption of protons, which drives atmospheric CO_2 drawdown (Meysman and Montserrat, 2017). The relatively fast weathering kinetics (Rimstidt et al., 2012) and abundance (Caserini et al., 2022) of olivine ($Mg_xFe_{(1-x)}SiO_4$) rich rock (i.e. dunite) make it an attractive option for CESW. Possible co-benefits of CESW include counteracting ocean acidification and enhanced primary production of silicifiers (e.g. diatoms) via proton consumption and supply of iron (Fe) and silicon (Si), respectively (Bach et al., 2019). In contrast to these benefits, coastal enhanced olivine weathering could have adverse ecosystem impacts as a result of both geophysical environmental changes (e.g. sediment siltation and pore space clogging) (Schlacher et al., 2012) and nickel (Ni) and chromium (Cr) accumulation to potentially toxic levels (Flipkens et al., 2021).

A recent modelling study showed that relatively low olivine applications ($0.059 - 1.4$ kg m$^-$^{2} seabed) could potentially lead to sediment Ni concentrations that exceed existing environmental quality standards and pose a toxicological threat to benthic marine biota (Flipkens et al., 2021). Furthermore, smaller olivine particles could potentially be more toxic than larger ones due to their faster weathering rate and easier ingestion by various marine organisms (Duan et al., 2022). However, due to the paucity of data on olivine exposure effects on aquatic biota, currently limited to microorganisms (Ren et al., 2021; Hutchins et al., 2023; Xie et al., 2023), accurate ecological risk assessment of coastal enhanced olivine weathering remains impossible.

Therefore, we investigated the acute 24 to 96 h bioaccumulation and chronic 35-day toxicity of olivine in the benthic marine amphipod *Gammarus locusta*. This species has been reported as the most sensitive European marine *Gammarus* spp. to environmental disturbance (e.g. hypoxia and temperature fluctuations) and contaminant exposure (e.g. oil spills and trace metals) (Costa and Costa, 2000), making it a suitable test species to examine olivine bioaccumulation and toxicity. Based on the ingestion of 500 x 20 μm polyamide fibers by the freshwater *Gammarus fossarum* we hypothesized that olivine grains of comparable dimensions or smaller could be ingested (Blarer and Burkhardt-Holm, 2016). Furthermore, we expected olivine dose and grain size dependent metal accumulation and toxic effects (Flipkens et al., 2021; Duan et al., 2022). Finally, we hypothesized lower bioavailability of Cr compared to Ni due to the low aqueous solubility of chromite, which is the dominant Cr-bearing phase in dunite rock (Flipkens et al., 2021).

6.2 Material and methods

6.2.1 Amphipod collection and housing

Amphipods were collected from the relatively uncontaminated Eastern Scheldt estuary (51°27'31.6"N 4°04'50.4"E, Krabbendijke, the Netherlands) during low tide where they were abundantly present on sea lettuce (*Ulva* sp.) (den Otter et al., 2023). Amphipods were microscopically identified as *G. locusta* in the laboratory (Supplementary Section F.1). Amphipods were cultured and experiments were conducted under controlled temperature (experiment specific) and light conditions (12:12 h light:dark cycle). Amphipods were housed in a 210 L polyethylene tank filled with artificial seawater (ASW), a 1 cm layer of control sediment (see Section 6.2.2.) and stones from the sampling location. To prepare ASW, seasalt (hw-Marinemix®, 35.75 g L^{-1}) was added to ultrapure water (Eurowater DPRO B1 – 1/1) and aerated for at least 24 h. Amphipods were fed *Ulva* sp. *ad libitum* and commercial fish food (Sera Micron Nature, 1 mg amphipod^{-1}) three times per week (Neuparth et al., 2002). A protein skimmer and trickling filter were

installed, and weekly 15 to 30% water changes were conducted. Before water renewal, nitrogenous waste concentrations were measured with commercial test kits (Tetra) and seawater temperature, pH, dissolved oxygen (DO) and conductivity were measured with a HQ30D portable multimeter (Hach). The conductivity cell and pH electrode were calibrated before each use with NIST conductivity standards (12880 µS cm^{-1} and 50000 µS cm^{-1}, VWR international) and pH buffers (pH 4.00, 7.00, and 10.01, VWR international), respectively. The pH of a TRIS (2-amino-2-hydroxy-1,3-propanediol) and AMP (2-aminopyridine) buffer were measured to calibrate pH measurements to the appropriate total pH scale for seawater (Dickson et al., 2007).

6.2.2 Sediment collection and geochemical analyses

Surficial (<10 cm depth) control sediment was collected with a shovel at the amphipod collection site. In the laboratory, sediment was wet sieved through a 500 µm screen to remove macrofauna before storage in a clean HDPE bucket at 4 °C until experimental use. VANGUARD refractory grade dunite sand from Åheim (Norway) was obtained from Sibelco. This sand is composed of 69 to 86 wt% olivine, of which 93.2 – 93.4% is forsterite and 6.6 – 6.8% is fayalite (characterization procedure in Supplementary Section F.2) and will be referred to as olivine throughout the text.

For sediment characterization, organic matter (SOM) content was determined via loss on ignition according to protocol by Heiri et al. (2001). Grain size distribution was analysed with a laser diffraction particle analyzer (Mastersizer 2000, Malvern Panalytical) according to standard operating procedures without chemical pre-treatment. Different sizes of olivine sand will be referred to by their volume-based effective grain size D10 and D90 throughout the text (e.g. 3 – 99 µm olivine). Finally, the elemental composition was determined via ICP-OES (iCAP 6300 Duo, Thermo Scientific) after microwave-assisted acid digestion following a modified chromite ore digestion protocol that is provided in Supplementary Section F.2 (CEM Corporation, 1999).

6.2.3 Acute exposure to different olivine sizes

6.2.3.1 Experimental set-up

For the accumulation phase, adult amphipods (metasomatic length (ML) = 9 – 17 mm) were individually exposed for 24 h in high-density polyethylene (HDPE) beakers filled with 400 mL ASW and 25 ± 0.03 g (~4 mm layer) of different olivine grain sizes (3 – 99 μm, 93 – 332 μm, and 208 – 488 μm) (Figure 6.1A). Beakers were randomly assigned to treatments and rinsed with 2% V/V HCl and ultrapure water before use. Seven replicate beakers, each comprising one individual (overall total of 3 males and 4 females or vice versa) were set up for each olivine treatment and an ASW control (400 mL ASW) and continuously aerated with aeration lines fitted with plastic tips positioned 6 cm above the sediment. Olivine was allowed to settle for 24 h and amphipods were starved for 24 h prior to exposure. Amphipods were photographed on 1 mm graph paper for sex and ML determination. The ML is the distance between the anterior end of the rostrum and the posterior end of the last metasomatic segment and was measured in ImageJ using the segmented line tool (Supplementary Figure F.2). A clear difference in gnathopod morphology allowed sex identification of adult *G. locusta* (Supplementary Figure F.3). For the depuration phase, adult amphipods exposed to different olivine grain sizes for 24 h (as described above) were rinsed with ASW and transferred to clean HDPE beakers filled with 400 mL ASW (Figure 6.1A). Depuration lasted 24 hours with 7 experimental replicates (3 males and 4 females or vice versa) (Figure 6.1A). Amphipods were collected at the end of the accumulation and depuration phase for metal analysis as described in Section 6.2.3.2.

Seawater temperature (17.5 ± 0.6 °C), salinity (33 ± 0.4 ‰), pH (8.1 ± 0.06), dissolved oxygen (7.7 ± 0.1 mg L^{-1}), and nitrogenous waste concentrations (NO_3^- = 12.5 mg L^{-1}, NO_2^- ≤ 0.3 mg L^{-1}, NH_3/NH_4^+ = 0.25 mg L^{-1}) were measured in fresh ASW and experimental beakers after the 24 h exposure and 24 h depuration (individual values provided in Supplementary Section F.3.1). Simultaneously, 0.2 μm filtered (Chromafil XTRA PES-20/25, Macherey-Nagel) seawater samples were collected for dissolved metal analysis. After collection, samples were diluted 20 times with 2% V/V TraceMetal™ Grade nitric

acid (Fisher Scientific) to minimize matrix effects during analysis via HR-ICP-MS (Element XR, Thermo Fisher Scientific). Procedural blanks (2% V/V HNO$_3$) and certified reference material (1643f, NIST) was measured for quality control.

6.2.3.2 Amphipod elemental analysis

Amphipods collected for whole body element analysis were rinsed with ultrapure water and dried in preweighed 5 mL tubes at 60 °C for 48 h. Standard reference material (SRM-2976 mussel tissue, NIST) and procedural blanks (empty 5 ml tubes) were included for quality control. Sample dry weight was measured with an ultra-microbalance (Sartorius SE2). Subsequently, 400 μL of concentrated (67 – 69%) TraceMetal™ Grade nitric acid (Fisher Scientific) was added to the samples to digest at room temperature for at least 12 h. Next, the samples were heated at 105 °C for 15 min in an SC154 HotBlock® (Environmental Express). Subsequently, 50 μL of 30 - 32% W/W H$_2$O$_2$ (Fisher Scientific) was added and samples were incubated at room temperature for 10 min before additional heating at 105 °C for 15 min. After digestion, samples were diluted to 2.2% V/V HNO$_3$ with ultrapure water before elemental analysis via HR-ICP-MS. Certified reference material (1643f, NIST) was included for analytical quality control. In the different experiments (*N* = 3) average element recoveries for the SRM-2976 ranged between 60 and 85% for Ni and 20 to 66% for Cr.

6.2.4 Acute 3 – 99 μm olivine uptake and elimination

6.2.4.1 Experimental set-up

For the accumulation phase, clean HDPE beakers were filled with 25 g (~ 2 mm layer) of dry 3 – 99 μm olivine and 800 mL ASW (Figure 6.1B). Beakers were randomly assigned to treatments and continuously aerated as described previously. Olivine was allowed to settle and adult amphipods were not fed for 24 h before exposure. Adult amphipods (ML = 8 – 16 mm) were photographed before exposure for length and sex determination as described previously. During the accumulation phase, amphipods were not fed and

exposed to 3 – 99 µm olivine for 0, 1, 3, 6, 24, 48, and 72 hours with 11 replicate beakers, each comprising one individual (7 males and 4 females) per exposure time (Figure 6.1B). for the depuration phase, adult amphipods were exposed to olivine for 72 h as described above and subsequently transferred to clean HDPE beakers with 800 mL ASW and 100 mg *Ulva* sp. (Figure 6.1B). Before transfer, amphipods were rinsed with ASW. Depuration lasted 0, 2, 4, 6, 24, 48, or 96 hours with 12 replicate beakers, each comprising one individual (7 males and 5 females) for each depuration period (Figure 6.1B). *Ulva* sp. was provided *ad libitum* during the depuration phase.

Seawater temperature (19.1 ± 0.4 °C) and pH (8.2 ± 0.2) were measured at each sampling time during the accumulation and depuration experiment (Supplementary Figure F.6). Furthermore, amphipod survival was monitored and samples for dissolved metal analysis were collected. Seawater salinity (33 ± 0.8 ‰), dissolved oxygen (7.5 ± 0.1 mg L^{-1}) and concentrations of nitrate (≤ 12.5 mg L^{-1}), nitrite (< 0.3 mg L^{-1}) and ammonium (≤ 0.25 mg L^{-1}) were measured at the start and end of the experiment in at least three replicates (Supplementary Figure F.6). Surviving amphipods were sampled at each timepoint to determine whole body metal accumulation (6 to 8 individuals) and ingested olivine grain sizes (1 to 3 individuals). Temporal differences in the ingested olivine grain size distribution were not investigated due to limited amount of samples per timepoint.

6.2.4.2 Ingested olivine size analysis

Amphipods collected for ingested olivine size analysis were rinsed with ultrapure water, euthanized with 70% V/V ethanol, and dissected under a stereomicroscope to collect ingested olivine particles. Then, olivine samples were washed with ultrapure water and dried at 60 °C for 12 h. Afterwards, dry olivine grains were mounted on aluminium pin stubs with double sided carbon tape for imaging at 1600x magnification with a Phenom ProX scanning electron microscope (SEM). The particle size distribution was determined in ImageJ. First, the image was calibrated using the SEM image scale. Afterwards, a gaussian blur (sigma = 1.5) was applied and the image was thresholded (default option, Auto threshold). Then, touching particles were separated using the watershed algorithm

for irregular features (erosion cycle number = 12) before analysis using the "Analyze Particles" command. Particles on the edge of the image were excluded and interior holes in grains were filled. Finally, the Feret's diameter and equivalent sphere diameter were derived for comparison to laser diffraction data.

6.2.5 Chronic 3 – 99 µm olivine toxicity test

6.2.5.1 Experimental set-up

A chronic 35-day olivine toxicity test was conducted according to the study by Neuparth et al. (2005) with minor modifications. Twenty-four clean HDPE buckets were filled with a 1 cm layer of wet control sediment manually mixed with different concentrations of dry 3 – 99 µm olivine (0, 1, 10, 25, 50, or 100% dry w/w, Supplementary Section F.5.1). Four replicates were used for each olivine treatment and the sediment control. Subsequently, samples for geochemical analysis (Section 6.2.2.) were collected and 5 small stones (~8 cm³ in size) were added to provide shelter. Buckets were slowly filled with 8 L of ASW and aerated as described previously. The sediment was left to equilibrate for 7 days before amphipod addition.

The chronic bioassay started when 1 g of *Ulva* sp. and 35 juvenile amphipods (ML = 1.3 – 4.5 mm) were carefully added to the experimental buckets with a Pasteur pipette. Amphipod survival and food availability were checked daily. *Ulva* sp. was provided *ad libitum* in portions of 1 g and commercial fish food (Sera Micron Nature, 0.5 mg amphipod^{-1}) was provided once a week. Seawater temperature (19.8 ± 0.4 °C), pH (8.10 ± 0.06), DO (7.1 ± 0.1 mg L^{-1}), salinity (33 ± 0.5 ‰), and nitrogenous waste concentrations (NO_3^- ≤ 12.5 mg L^{-1}, NO_2^- ≤ 0.3 mg L^{-1}, NH_3/NH_4^+ ≤ 0.25 mg L^{-1}) were measured twice a week before conducting a 50% water renewal (Supplementary Figure F.8). Furthermore, seawater samples for dissolved metal and dissolved organic carbon (DOC) analysis were collected once a week before and after water change. Additionally, seawater total alkalinity (TA) was measured on day 14 and 35. Methods and results of DOC and TA analysis are provided in Supplementary Section F.5.2.

At the end of the experiment, the contents of the buckets was sieved through 1000 and 250 μm mesh sieves to collect surviving adults and juveniles, respectively. The juveniles were counted and all adult amphipods were photographed on 1 mm graph paper for size and sex determination. Afterwards, adult males and non-gravid females were rinsed with ultrapure water and pooled (1 – 4 pools) for metal analysis (4 – 13 individuals, 28 – 166 mg w.w.) and thiobarbituric acid reactive substances (TBARS) determination (3 – 6 individuals, 45 – 171 mg w.w.). Pooled amphipods for TBARS measurements were immediately frozen in liquid nitrogen and stored at -80 °C until analysis. Gravid females were preserved in 70% V/V ethanol (VWR International) at 4 °C to study reproductive endpoints within a week.
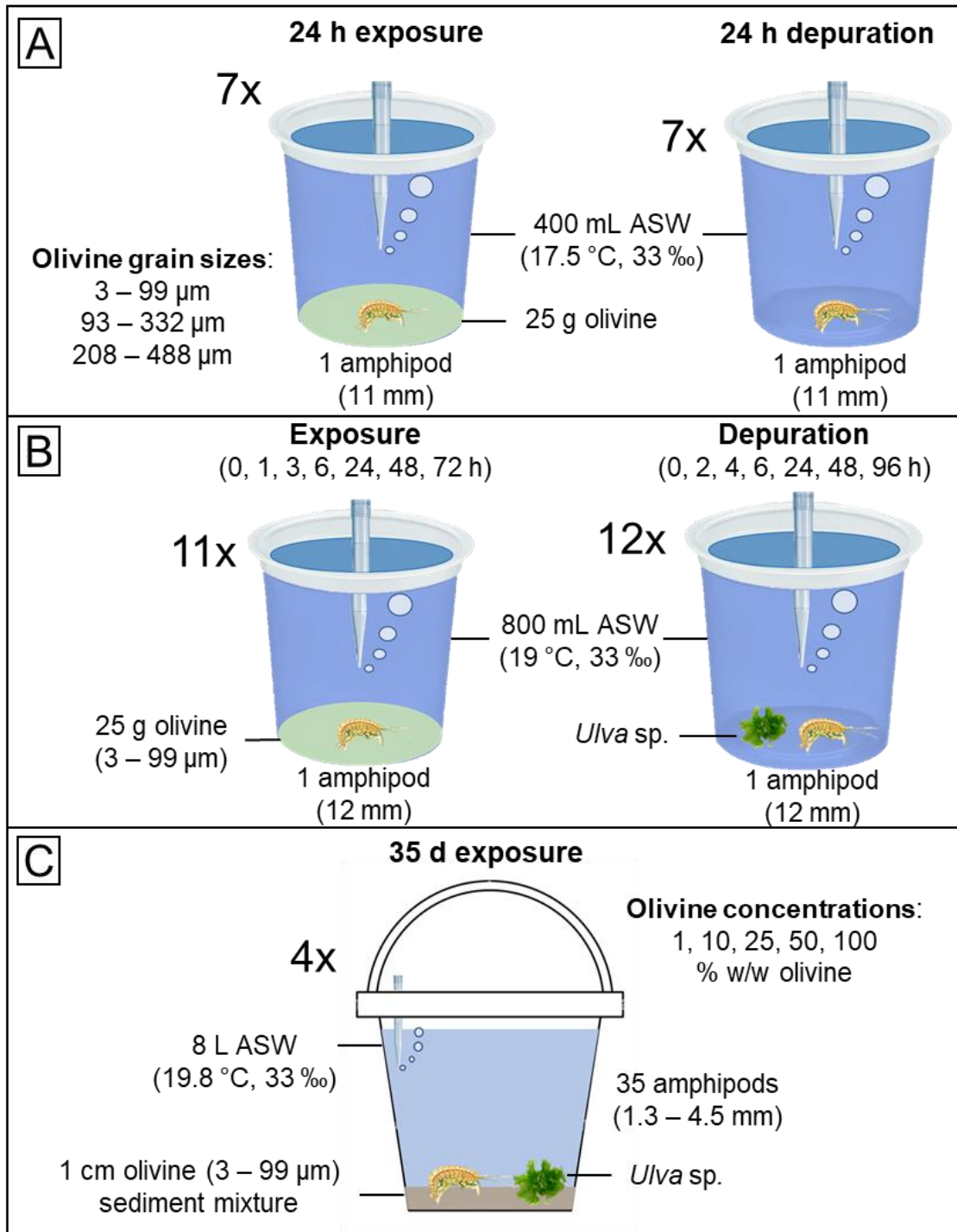
Figure 6.1: Schematic representation of the (A) acute grain size experiment, (B) uptake and elimination experiment and (C) chronic toxicity test are shown. ASW = artificial seawater. Pictures: pipette tip © CliniveX, Ulva lactuca © Jiří Novák, bucket © Jemastock.

6.2.5.2 Biological endpoints

Several biological endpoints were determined at the end of the 35-day experiment, including amphipod survival, sex ratio, growth, reproductive traits, whole body trace metal and major cation concentrations, and lipid peroxidation. The sex ratio was determined by dividing the number of surviving males by the number of surviving females for each replicate. The individual growth was determined as the ML of the surviving amphipods. The number of gravid females was divided by the total number of females in each replicate to derive the percentage gravid females. The number of juveniles and embryos in the brood pouch of gravid females was counted to determine the total juvenile and embryo production. Whole body metal (Ni, Cr, Fe, Cu, Zn, Cd, Mn) and major cation (Na, K, Ca, Mg) concentrations were measured for pooled amphipods of each replicate as described previously (Section 6.2.3.2). The TBARS content was quantified using a thiobarbituric acid reactive substances (TBARS) assay (Cayman Chemical) following the manufacturer's guidelines for tissue homogenates. The TBARS levels were determined spectrophotometrically at a wavelength of 530 nm with a multimode microplate reader (Spark, Tecan). TBARS concentrations were calculated from an malondialdehyde (MDA) colorimetric standard curve and expressed per gram of sample wet weight (μmol TBARS g^{-1} w.w.).

6.2.6 Statistical analyses

Kruskal-Wallis analysis of variance (ANOVA) was performed on data of the acute experiments to investigate differences in metal accumulation between olivine treatments and timepoints. A non-parametric test was conducted since model residuals were not normally distributed according to QQ plots and Shapiro-Wilk tests. Homoscedasticity of model residuals was assessed via residual plots and Levene's tests. Relevant post hoc pairwise comparisons were made using Dunn's test with "holm" p value adjustment method.

One-way ANOVA and Dunnett's Tests were conducted to investigate differences in amphipod survival, reproduction, trace metal accumulation and major ion concentrations

between treatments and the control after 35-day exposure. Model assumptions were assessed and non-parametric tests were conducted if model residuals were not normally distributed as described in the previous paragraph. Robust standard errors were used to correct for unequal residual variance (i.e. heteroscedasticity) using the vcov="sandwich" argument from the 'sandwich' package. A linear mixed effects model (lmerTest package) was fit to investigate the effect of chronic olivine exposure on amphipod growth. Bucket ID was included as a random effects term and nested in treatment. T-tests using the Satterthwaite's method were performed to investigate differences between treatments and the control.

The relationship between experimental endpoints and whole body Ni concentrations was assessed via simple linear regressions and Kendall correlation coefficients to investigate if adverse effects could be empirically linked to metal toxicity. Kendall rank-based correlation tests were used since data were not normally distributed according to QQ plots and Shapiro-Wilk tests. Whole body Cr concentrations were not included in the linear regressions due to multicollinearity issues. Diagnostic plots were constructed to assess model assumptions. If needed, the whole body Ni concentrations were log transformed to improve linearity of the model residuals and robust linear regression was used to deal with influential outliers (Cook's distance > 0.5). Results were considered statistically significant when *p* value < 0.05. Statistical analyses were conducted in RStudio (version 2022.12.0+353) using R version 4.2.1 and figures were constructed in GraphPad Prism version 9.5.1 for Windows.

6.3 Results and discussion

6.3.1 Sediment characteristics

The geochemical properties of Eastern Scheldt control sediment and olivine treatments are provided in Table 6.1. Overall, the average SOM content of control sediment (1%) and olivine (0.15 – 1.5%) were relatively low compared to the broad range of total organic carbon concentrations reported for estuarine sediments (0.3 – 23%) (Ouyang et al., 2006;

Chakraborty et al., 2015). Average concentrations of Cr were 24 to 33 times higher in olivine (22 – 30 µmol g^{-1} d.w.) compared to control sediment (0.9 µmol g^{-1} d.w.), while average olivine Ni concentrations (36 – 41 µmol g^{-1} d.w.) were approximately 1000 times higher than control sediment (0.036 µmol g^{-1} d.w.). Additionally, significantly higher Mg and Fe concentrations are found in olivine (respectively 9043 and 652 µmol g^{-1} d.w.) compared to control sediment (respectively 80 and 85 µmol g^{-1} d.w.) (Supplementary Table F.2). However, low aqueous solubility of Fe, high background Mg concentrations in seawater, and essentiality of both elements infer that these metals are of low ecotoxicological concern compared to Ni and Cr (Meysman and Montserrat, 2017). Concentrations of Mg, Fe, Al, Mn, Co, and Zn in olivine and control sediment are provided in Supplementary Section F.2.

Table 6.1: Geochemical properties of the experimental sediments. Sediment organic matter content (SOM, expressed in %), volumetric effective grain sizes (D, expressed in µm) and nickel (Ni) and chromium (Cr) concentrations (µmol g^{-1} d.w.) of control sediment and different olivine (ol) sizes. Data for the different 3 – 99 µm olivine concentrations (% w/w) of the chronic experiment are also provided. Mean ± S.D. values are shown (N = 4 – 5).

Sediment type	SOM (%)	D10 (µm)	D50 (µm)	D90 (µm)	Ni (µmol g^{-1} d.w.)	Cr (µmol g^{-1} d.w.)
Control	1.0±0.04	71±1	126±3	222±8	0.036±0.018	0.90±0.16
3 – 99 µm ol						
1% w/w	1.01±0.03	69±0.5	125±0.8	220±2	0.40[a]	1.2[a]
10% w/w	1.14±0.03	33±14	116±3	217±3	3.7[a]	3.8[a]
25% w/w	1.36±0.03	12±2	99±2	206±2	9.1[a]	8.1[a]
50% w/w	1.34±0.04	5.8±0.2	62±3	175±3	18[a]	15[a]
100% w/w	1.53±0.19	3.23±0.06	24±0.2	99±2	36±2	30±2
93 – 332 µm ol	0.29±0.04	93±7	189±5	332±5	38±0.9	23±0.9

| 208 – 488 µm ol | 0.15±0.04 | 208±3 | 320±5 | 488±7 | 41±0.4 | 22±3 |

[a]Concentrations of Ni and Cr for the 1% w/w to 50% w/w 3 – 99 µm olivine were not analytically determined, but derived from the measured concentrations in the control sediment and 100% w/w 3 – 99 µm olivine.

6.3.2 Acute exposure to different olivine sizes

All amphipods survived the acute bioaccumulation experiment. However, olivine exposure resulted in a significant grain size dependent increase of whole body Ni and Cr concentrations (Figure 6.2A and 6.2B). Median whole body Ni concentrations were significantly elevated in the 93 – 332 µm (0.55 µmol g^{-1} d.w., p = 0.011) and 3 – 99 µm (2.3 µmol g^{-1} d.w., p < 0.001) olivine treatments compared to the ASW control (0.13 µmol g^{-1} d.w.) after 24 h exposure (Figure 6.2A). Median dissolved Ni concentrations were higher for smaller grain sizes and were significantly elevated (p = 0.029) in the 3 – 99 µm treatment (0.76 µmol L^{-1}) compared to the seawater control (0.050 µmol L^{-1}) (Figure 6.2C). Higher dissolved Ni for smaller olivine grain sizes can be explained by the larger reactive olivine surface area, which enhances olivine dissolution and trace metal release (Rimstidt et al., 2012). After 24 h depuration, median Ni concentrations remained significantly elevated in amphipods exposed to 3 – 99 µm olivine (0.83 µmol g^{-1} d.w., p = 0.0011) compared to ASW control amphipods (0.10 µmol g^{-1} d.w.) (Figure 6.2A). Dissolved Ni concentrations in ASW did not differ significantly between treatments (0.029 – 0.079 µmol L^{-1}, N = 12) at the end of the depuration phase (Figure 6.2C).

Median whole body Cr concentrations were significantly elevated in all olivine treatments (median values of 0.098 to 0.39 µmol g^{-1} d.w.) compared to the ASW control (0.011 µmol g^{-1} d.w.) after 24 h exposure (Figure 6.2B). The median Cr accumulation was 3 to 8 times lower than the median Ni accumulation (Figure 6.2B), which can partly be explained by the 1.2 to 1.9 times lower Cr compared to Ni content of the experimental olivine (Table 6.1). Furthermore, dissolved Cr concentrations remained below the detection limit (0.38 nmol L^{-1}) in all treatments except the 3 – 99 µm olivine treatment (median = 0.048 µmol L^{-1}) (Figure 6.2D). After 24 h depuration, the median Cr body burden was still significantly

elevated in amphipods exposed to 3 – 99 μm olivine (94 nmol g^{-1} d.w., *p* = 0.046) compared to ASW control amphipods (0.015 nmol g^{-1} d.w.) (Figure 6.2B) and dissolved Cr concentrations remained below the detection limit (Figure 6.2D).

Limited Cr accumulation in ASW is likely explained by the low aqueous solubility of chromite ($FeCr_2O_4$), which is the dominant Cr-bearing phase in dunite rock (Flipkens et al., 2021). Hence, elevated whole body Cr concentrations can be mainly ascribed to olivine grains in the guts of exposed amphipods. Given the Cr content of the ingested olivine sizes (Figure 6.4A), more than 450,000 olivine grains would have to be ingested (~3.6% of gut volume) to result in the Cr concentrations observed in the 3 – 99 μm olivine treatment (Figure 6.2B) (Supplementary Section F.3.3). Based on the potential dissolution rate of ingested olivine, a dietary Cr exposure rate of 0.17 nmol g^{-1} d.w. d^{-1} was derived (Supplementary Section F.3.4), which was significantly lower than the estimated waterborne Cr uptake rate between 1.4 and 4.1 nmol g^{-1} d.w. d^{-1} (Wang et al., 1997b). A similar conclusion can be drawn for Ni (Supplementary Section F.3.4). However, after 24 h depuration median whole body Ni (0.83 μmol g^{-1} d.w.) and Cr (0.094 μmol g^{-1} d.w.) accumulations were approximately 28 and 20 to 59 (depending on the Cr oxidation state) times higher than expected assuming the calculated metal uptake rates. Uncertainties regarding the number of ingested grains, olivine dissolution rate, and waterborne metal uptake rate likely explain this discrepancy between observed and predicted Ni and Cr bioaccumulation. Hence, further research is required to assess the importance of olivine ingestion as a trace metal exposure pathway in marine biota.
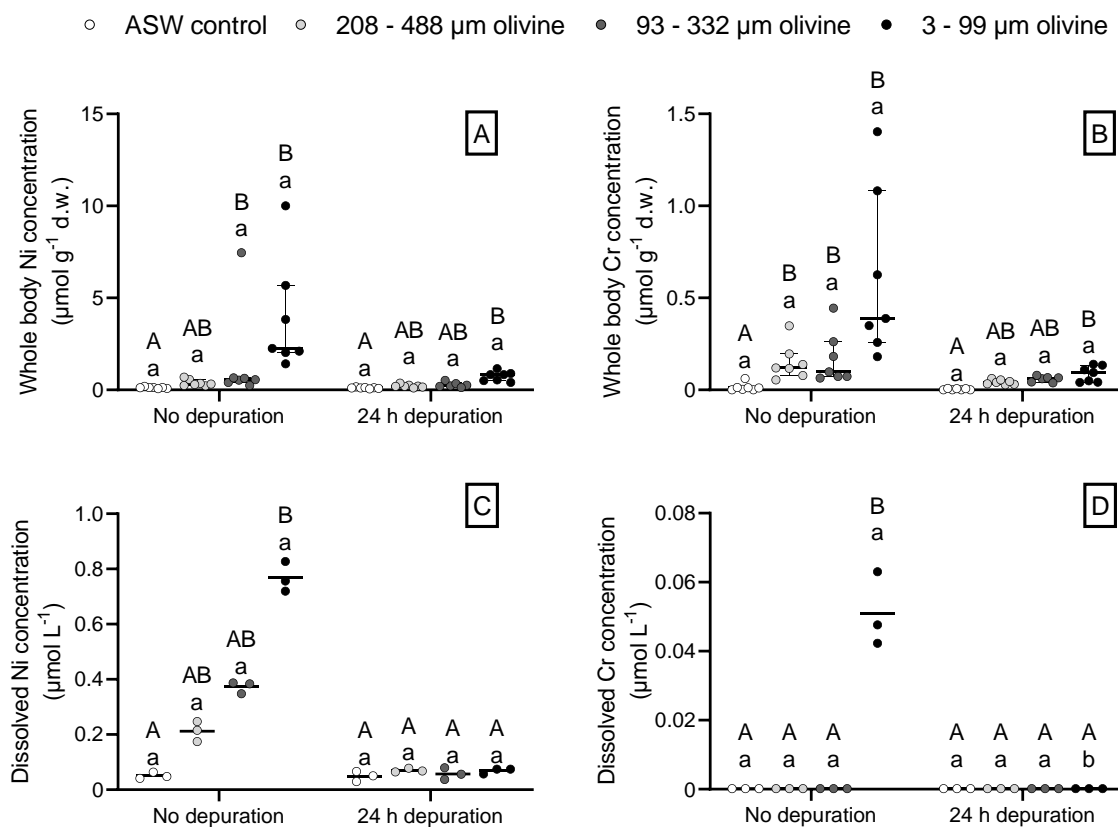
Figure 6.2: Whole body concentration (µmol g⁻¹ dry weight) of (A) nickel (Ni) and (B) chromium (Cr) in amphipods exposed to various olivine sizes for 24 h and subsequently not depurated or depurated for 24 h before analysis. Median and IQR are shown (N = 6 or 7). Dissolved concentrations (µmol L⁻¹) of (C) Ni and (D) Cr in artificial seawater at the end of the accumulation and depuration phase (Mean, N = 3). Lower case letters indicate significant differences (p < 0.05) between experimental phases and capital letters indicate significant differences (p < 0.05) between olivine treatments within an experimental phase.

6.3.3 Acute 3 – 99 µm olivine uptake and elimination

6.3.3.1 Trace metal accumulation and depuration

Most amphipods survived acute 72-h exposure to 3 – 99 µm olivine (93%) and depuration in ASW (88%). However, lethargic behaviour was observed after 24 h of exposure. Median

amphipod whole body Ni concentrations rapidly increased upon olivine exposure and remained stable around 1.0 to 1.4 µmol g^{-1} d.w. after 24 hours of exposure (Figure 6.3A). Median dissolved Ni concentrations were elevated at the start of the experiment (0.64 µmol L^{-1}) and further increased up to 1.0 µmol L^{-1} after 72 h as a result of olivine dissolution (Figure 6.3C). Considerable variation in whole body trace metal accumulation was observed, likely due to differences in olivine ingestion among individuals.

Median whole body Ni concentrations decreased by approximately 60% from 1.0 to 0.42 µmol g^{-1} d.w. after 6 h of depuration which was still elevated compared to 0.033 µmol g^{-1} d.w. in unexposed amphipods (Figure 6.3A). Afterwards, whole body Ni concentrations remained stable and varied little among individuals, suggesting that most olivine grains were egested within 24 hours (Figure 6.3A). Olivine egestion was confirmed via microscopic examination, although some olivine grains were still present in the guts after 96 h of depuration, suggesting a long gut passage time or possible reingestion of egested grains. Dissolved Ni concentrations remained stable (0.056 – 0.20 µmol L^{-1}, *N* = 18) throughout the depuration phase (Figure 6.3C). Previous studies with *Gammarus* spp. have reported considerable variation in gut passage time from 0.5 h to more than 64 h depending on the ingested particle type (Willoughby and Earnshaw, 1982; Straub et al., 2017). Overall, the observed olivine egestion rate was within the range of egestion rates reported for other particle types in *Gammarus* spp. Cr concentrations in amphipods (Figure 6.3B) and ASW (Figure 6.3D) followed the same temporal trends as Ni concentrations, although lower accumulation was observed similar to the results of the acute exposure to different olivine grain sizes (Section 6.3.2).
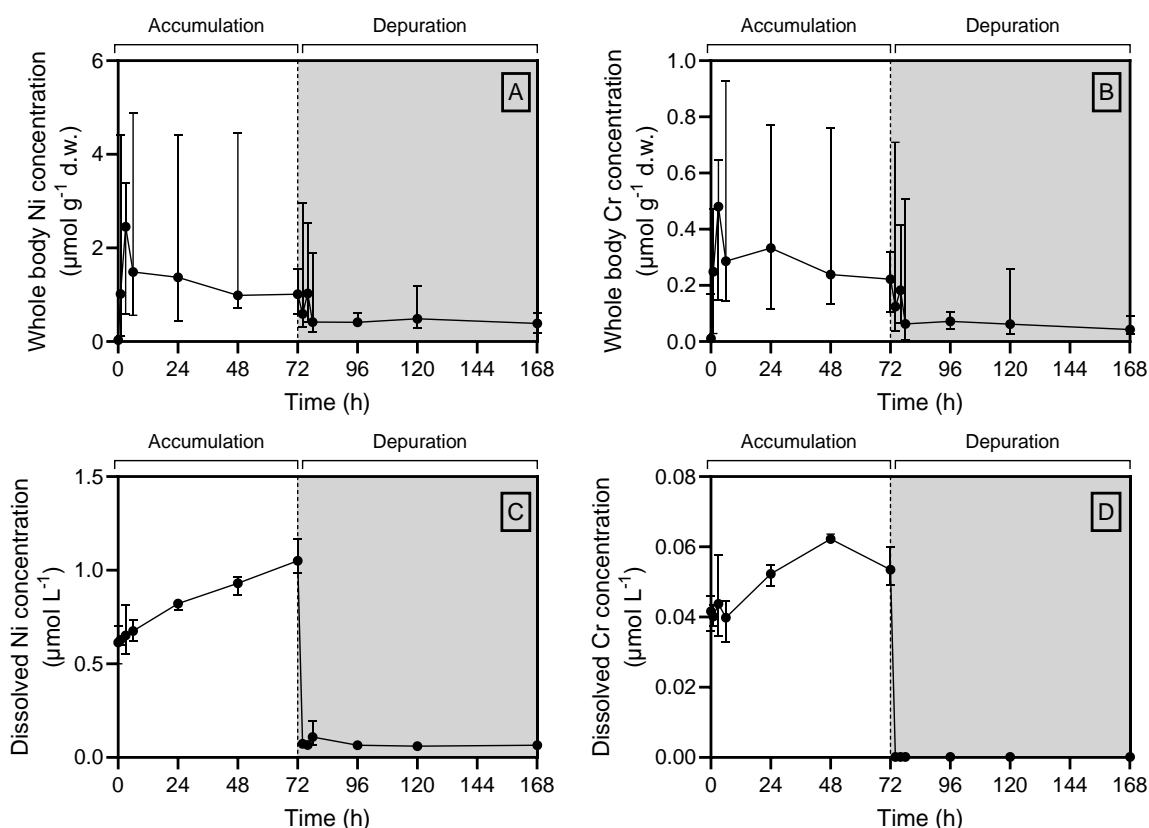
Figure 6.3: Temporal evolution of nickel (Ni) and chromium (Cr) concentrations in amphipods (A, B) and artificial seawater (C, D) during 72 h pure olivine exposure (white area) and 96 h depuration (grey area). Median and range are shown for concentrations in amphipods (N = 7 or 8) and mean and range for concentrations in ASW (N = 3).

6.3.3.2 Ingested olivine size distribution

Thousands of olivine grains of various sizes were ingested by *G. locusta* during the 96-h exposure experiment (Figure 6.4B). Ingested olivine grains had a Feret diameter ranging from 0.1 to 185 μm and grains with a diameter between 0.3 and 8 μm were most abundant (89% of all particles) (Figure 6.4A). The bulk olivine was comprised mostly (91%) of very small particles with a diameter between 0.3 and 1 μm, which were 64% less abundant in the guts of exposed amphipods (Figure 6.4A). *G. locusta* mainly feeds on

macroalgae and sediment detritus close to the seafloor in the lower intertidal and subtidal zone (Costa and Costa, 2000), which could explain the lower ingestion of very fine particles which would be suspended in the water column. Several microplastic exposure studies have also reported low ingestion rate of 1.0 to 1.6 µm (in diameter) particles in *Gammarus* spp. (Blarer and Burkhardt-Holm, 2016; Scherer et al., 2017). Overall, large amounts of small (mainly ≤ 10 µm) olivine particles were observed in the guts of exposed amphipods.
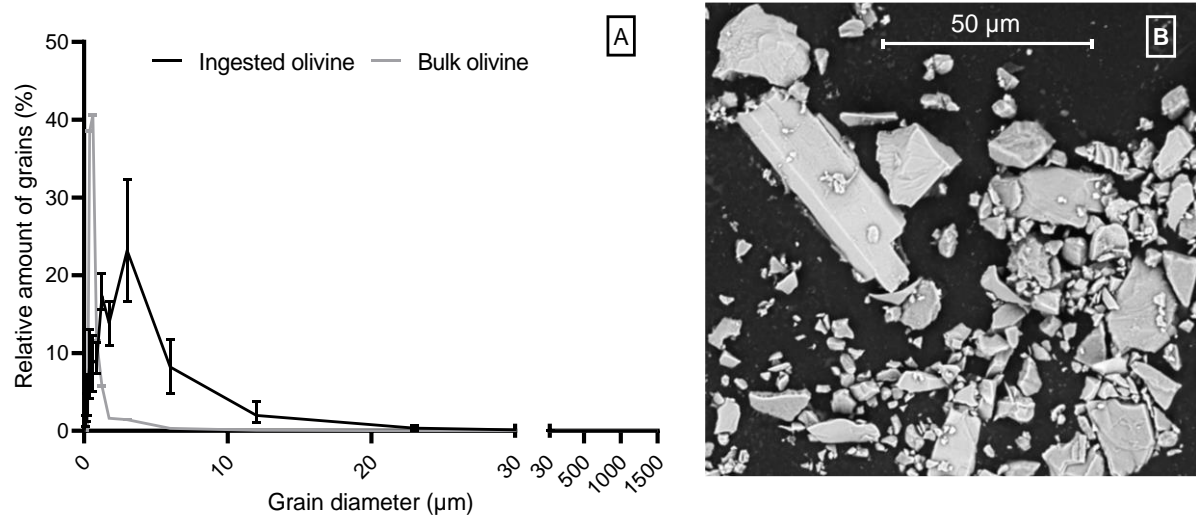
Figure 6.4: Ingested olivine grains by G. locusta. (A) Number based particle size distribution for bulk 3 – 99 µm olivine (grey, N = 4) and ingested olivine in the guts of amphipods (black, N = 9 amphipods, 53206 particles measured) exposed for various times (2 – 72 h). The relative amount of grains (%) for different grain diameters (µm) is shown as median and range values. (B) Scanning electron microscope image of olivine grains present in the guts of an amphipod exposed to 3 – 99 µm olivine for 24 h.

6.3.4 Chronic 3 – 99 μm olivine toxicity test

6.3.4.1 Survival rate

Chronic exposure to 3 – 99 μm olivine reduced median amphipod survival by half in the 100% w/w treatment (21%, $p < 0.001$) compared to the control (44%) (Figure 6.5A). A significant negative relationship was observed between amphipod survival and whole body Ni concentrations (τ = -0.51, R^2 = 0.51, $F(1, 22)$ = 23, $p < 0.001$) (Figure 6.5B), suggesting that metal-induced toxic effects involving oxidative damage (Figure 6.10) and disruption of major cation homeostasis (Figure 6.9) were likely the main reason for decreased amphipod survival in the 100% w/w treatment (Blewett and Leonard, 2017; DesMarias and Costa, 2019). A slightly higher median survival rate in the 1% w/w treatment (50%) compared to the control (44%) could be explained by stimulation of biological processes at low stress levels (i.e. hormesis), although the difference in survival rate was not statistically significant (p = 0.92) (Figure 6.5A) (Rix et al., 2022).
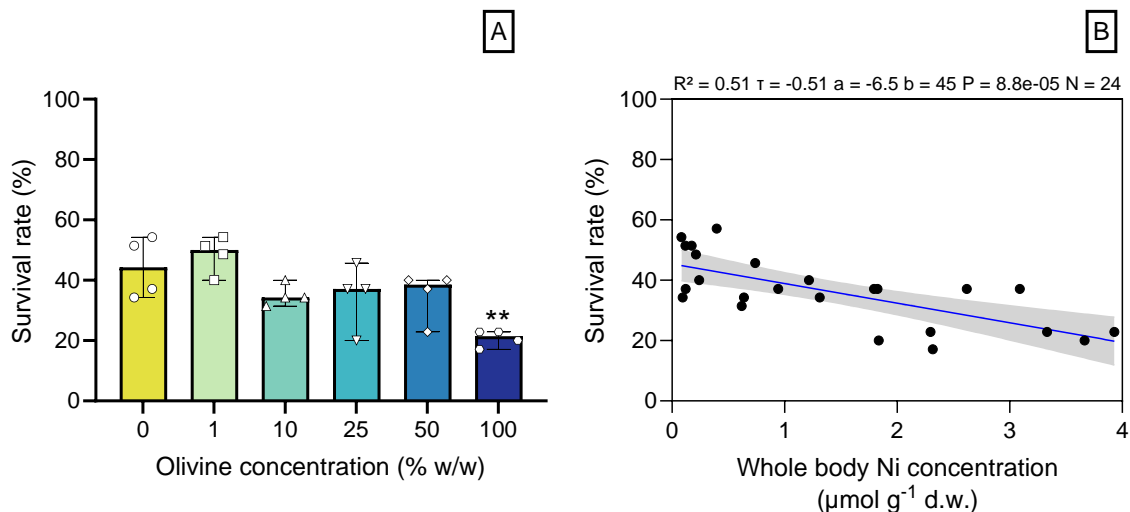
Figure 6.5: (A) Survival rate (%) of G. locusta exposed to natural sediment mixed with various amounts of 3 – 99 μm olivine (expressed in % w/w) for 35 days. Median and range are shown (N = 4). Significance compared to 0% w/w olivine: * = p < 0.05, ** = p < 0.01,

*** = p < 0.001. (B) Linear regression between G. locusta survival rate and whole body Ni concentration (µmol g^{-1} d.w.). Regression line (blue) with 95% confidence interval (dark grey shading) is shown. The coefficient of determination (R²), Kendall correlation coefficient (τ), sample size (N), and regression line slope (a), intercept (b), and p value (P) are given.*

Similar to our study, low control survival rates around 50% have been observed in other chronic laboratory experiments with *G. locusta* (Costa et al., 2005). This can be explained by cannibalism (Costa et al., 2005) and the relatively short maximum life span of around 16 weeks at 20 °C and 33 ‰ (Neuparth et al., 2002). Neuparth et al. (2002) reported an increase in amphipod life expectancy by at least 4 weeks at a temperature of 15 °C compared to 20 °C. However, for standardizing tests and reducing costs, Neuparth et al. (2002) recommended a temperature of 20 °C for routine chronic sediment toxicity testing. Furthermore, 20 °C represents typical summer water temperatures in the Eastern Scheldt estuary (Rios-Yunes et al., 2023), which would likely coincide with the period of highest toxicological risk following olivine spreading. This is due to faster olivine dissolution and trace metal release during warmer temperatures (Rimstidt et al., 2012).

6.3.4.2 Individual growth
Surviving amphipods from the 25, 50, and 100% w/w olivine treatments were respectively 16 (*p* = 0.013), 27 (*p* = 0.0015) and 32% (*p* < 0.001) smaller (median ML: 6.6 – 8.1 mm) compared to control amphipods (median ML: 9.7 mm) (Figure 6.6A). A difference in food availability cannot explain reduced growth, since sediment SOM concentrations did not differ substantially among treatments (Table 6.1) and food (*Ulva* sp.) was provided *ad libitum*. Furthermore, limited stress is expected from differences in sediment grain size distribution among treatments, since *G. locusta* inhabits a wide range of sediment types and can tolerate exposure to sandy and silty sediments under laboratory conditions (Costa and Costa, 2000). Therefore, significant metal accumulation (Figure 6.8A and 6.8B)

likely resulted in oxidative stress (Figure 6.10) and increased energy demand for detoxification and maintaining ion homeostasis which led to reduced individual growth (Brix et al., 2017). Amphipods did not compensate for reduced metabolic energy by increasing their feeding rate (Figure 6.6B). In a natural ecosystem, a reduction in amphipod growth could have both population and community-level consequences via the reduction in reproductive output and lower food availability for higher trophic levels (e.g. fish and shorebirds), respectively (Sibley et al., 1997). Additionally, the important role of amphipods in nutrient recycling by detritus consumption and shaping of coastal landscapes through grazing on macroalgae could be compromised (Costa and Costa, 2000).
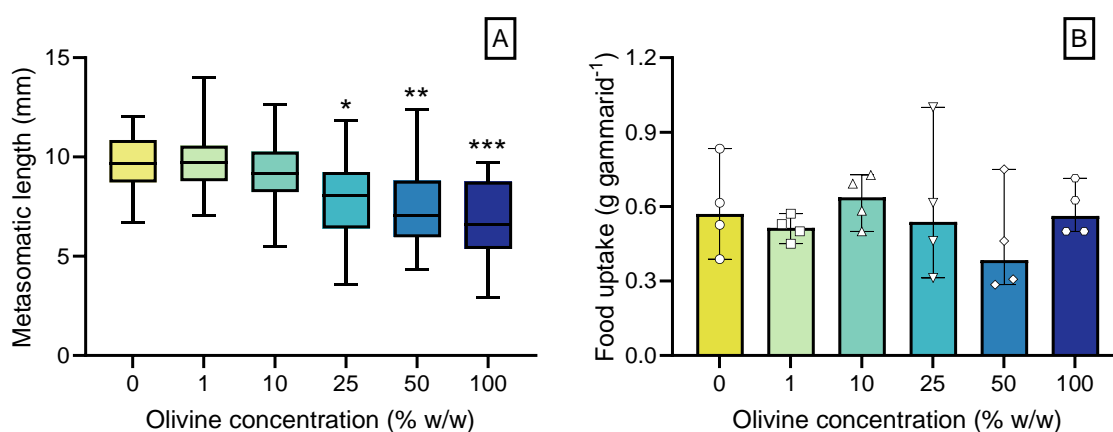
*Figure 6.6: (A) Box and whisker plots of the metasomatic length (mm) (N = 29 − 68 amphipods), and (B) bar plots of the food uptake (g gammarid^{-1}) (median and range, N = 4) for G. locusta exposed to natural sediment mixed with various amounts of 3 − 99 μm olivine (expressed in % w/w) for 35 days. Whiskers in (A) represent the minimum and maximum length. Significance compared to 0% w/w olivine: * = p < 0.05, ** = p < 0.01, *** = p < 0.001.*

6.3.4.3 **Reproductive traits**

Chronic olivine exposure resulted in significant reproductive impairment in *G. locusta* at olivine concentrations of 10% w/w and higher (Figure 6.7A – 6.7C). The median percentage of gravid females was significantly reduced from 100% in the control to 58 (*p* = 0.048), 33 (*p* < 0.001), and 20% (*p* < 0.001) in the 10, 50, and 100% w/w olivine treatments, respectively (Figure 6.7A). Consequently, the median total number of embryos was only 8 (range: 0 – 35) in the 50% w/w (*p* = 0.010) and 5 (range: 0 – 35) in the 100% w/w (*p* = 0.0090) olivine treatment compared to a significantly higher 123 (range: 14 – 159) in the control (Figure 6.7B). The median total number of juveniles was significantly reduced from 46 (range: 29 – 57) in the control to between 0 and 14 (median values) in treatments with olivine concentrations of 10% w/w and higher (Figure 6.7C). From the significant negative relationship observed between reproductive endpoints and whole body Ni concentrations (Supplementary Figure F.15A and F.16), we infer that metal toxicity was the driver for reproductive impairment in *G. locusta*.
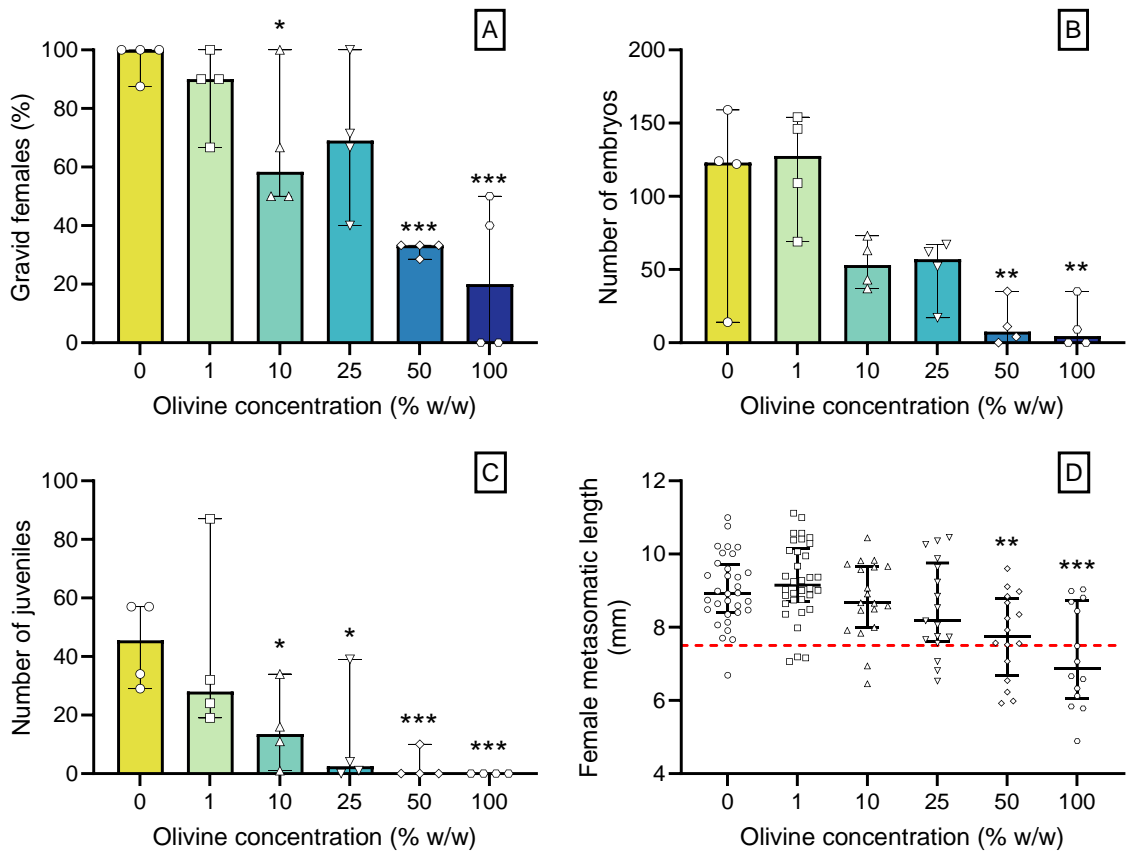
*Figure 6.7: (A) Percentage of gravid females, and total number of (B) embryos and (C) juveniles for G. locusta exposed to natural sediment mixed with various amounts of 3 – 99 μm olivine (expressed in % w/w) for 35 days. Median and range are shown (N = 4). (D) The metasomatic length of surviving females is shown as individual values, median, and IQR (N = 14 – 34 amphipods). Red dotted line in (D) represents the size of sexual maturity in G. locusta (7.5 mm) according to Neuparth et al. (2002). Significance compared to 0% w/w olivine: * = p < 0.05, ** = p < 0.01, *** = p < 0.001.*

Female *G. locusta* need to reach a size of approximately 7.5 to 8.3 mm (ML) to reproduce, and their brood size is positively correlated with body size (Neuparth et al., 2002). In our study, approximately 97% of the surviving females in the control reached the estimated size of sexual maturity (>7.5 mm), while only 90, 82, 69, and 36% of the females in the 10,

25, 50, and 100% w/w olivine treatments reached this size (Figure 6.7D). Hence, stunted growth can at least partly explain the lower percentage of gravid females in treatments with an olivine concentration of 10% w/w and higher. However, only 3.2% of the females larger than 7.5 mm were not gravid in the control while this was 29, 55, and 60% in the 10, 50, and 100% w/w olivine treatments. This can potentially be explained by increased brood abortion to preserve energy for individual fitness (Maltby and Naylor, 1990), or a reduction in pairing behaviour as a result of contaminant exposure (Love et al., 2020). Results for the number of embryos and juveniles per female are discussed in Supplementary Section F.5.4.

6.3.4.4 Trace metal accumulation

Olivine-exposed amphipods showed significantly ($p < 0.001$) elevated whole body Ni (0.17 – 3.7 µmol g^{-1} d.w., N = 24) and Cr (0.049 – 0.65 µmol g^{-1} d.w., N = 24) concentrations compared to control amphipods (0.083 – 0.12 µmol Ni g^{-1} d.w. and 0.0059 – 0.017 µmol Cr g^{-1} d.w., N = 4) after 35 days of exposure (Figure 6.8A and 6.8B). Whole body metal accumulation was dose dependent and Cr accumulation was generally lower than Ni accumulation, indicating lower Cr bioavailability (Figure 6.8A and 6.8B). Amphipods were not depurated before analysis, so ingested olivine grains could have contributed significantly to the observed metal concentrations. However, since SOM concentrations in sediment (Table 6.1) and DOC concentrations in ASW (Supplementary Figure F.8E) were low, higher trace metal bioavailability is expected (Blewett and Leonard, 2017).
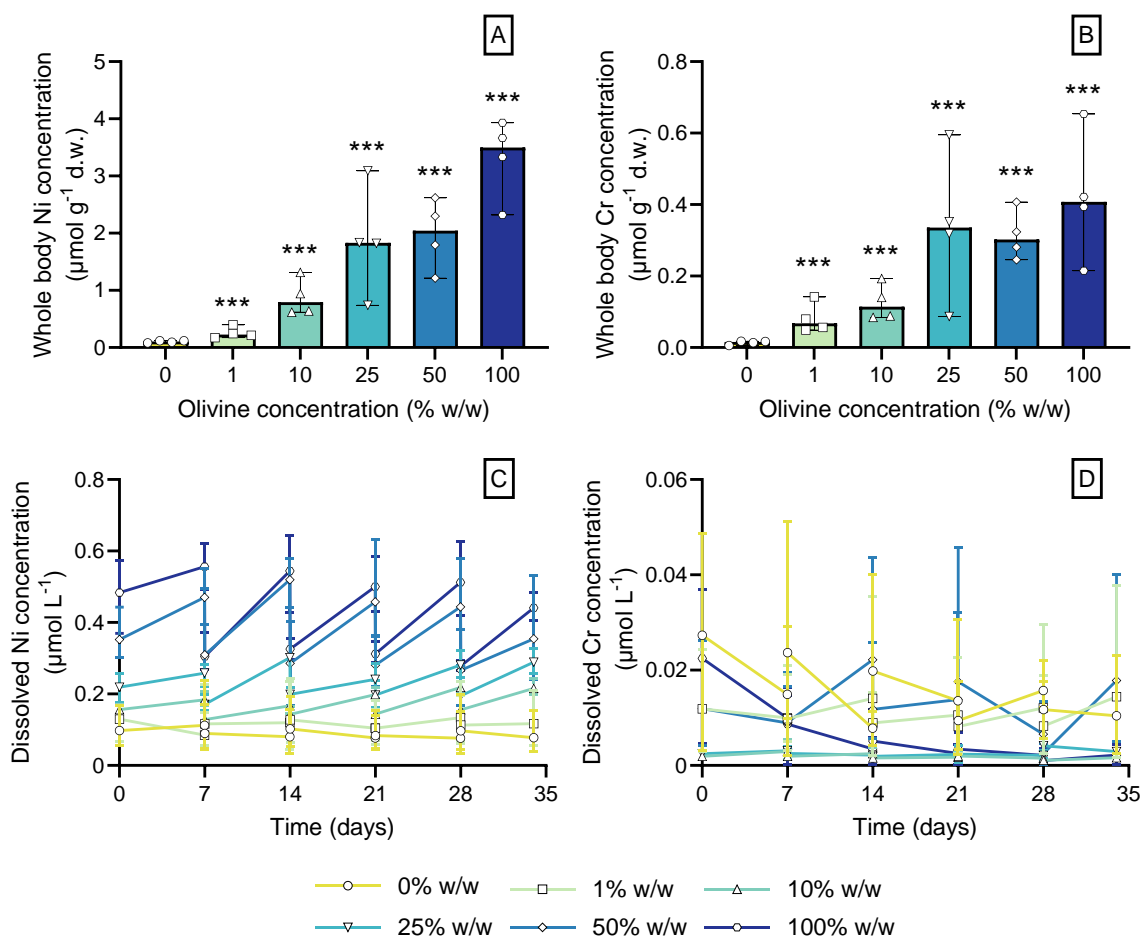
Figure 6.8: Whole body concentration (µmol g^{-1} dry weight) of (A) nickel (Ni), and (B) chromium (Cr) in pooled G. locusta exposed to natural sediment mixed with various amounts of 3 – 99 µm olivine (expressed in % w/w) for 35 days. Median and range are shown (N = 4). Significance compared to 0% w/w olivine: * = p < 0.05, ** = p < 0.01, *** = p < 0.001. Temporal evolution of dissolved (C) Ni and (D) Cr concentrations (µmol L^{-1}) in artificial seawater during the 35 day experiment. Mean and range (N = 2 or 3) are shown.

Dissolved Ni concentrations were relatively stable in the control (0.034 – 0.24 µmol L^{-1}, *N* = 30) and increased dose dependently in the olivine treatments with concentrations up to 0.64 µmol L^{-1} in the 50% w/w and 100% w/w treatment (Figure 6.8C). Dissolved Cr concentrations (<0.39 – 51 nmol L^{-1}, *N* = 180) did not differ significantly among

treatments or sampling days (Figure 6.8D). However, measured dissolved Ni and Cr concentrations were significantly elevated compared to typical concentrations (<10 nmol L^{-1}) for coastal waters (Flipkens et al., 2021). Nevertheless, observed dissolved Ni concentrations could potentially be reached under realistic 1 to 10% w/w coastal 3 – 99 μm olivine applications in shallow (10 m water depth) temperate (15 °C) coastal seas with a water residence time of more than one month (Supplementary Section F.5.3) and thus represent possibly realistic exposure concentrations for *G. locusta*.

6.3.4.5 Whole body major cation content

Chronic exposure to 100% w/w olivine resulted in a significant 16 to 21% reduction of whole body Ca, Na, and K concentrations compared to the control (Figure 6.9A – 6.9C). Whole body Mg concentrations were significantly elevated in amphipods exposed to olivine concentrations of 25% w/w and higher, likely as a result of olivine ingestion (Figure 6.9D). Disruption of Ca, Mg, Na, and K ionoregulation has been previously observed in marine invertebrates exposed to Ni concentrations ranging from 0.14 to 51 μmol L^{-1} via ion mimicry and inhibition of ion transporters such as the Ca^{2+}- and Na^+/K^+-ATPases (Blewett and Leonard, 2017; Brix et al., 2017). Furthermore, both Ni and Cr can induce oxidative stress, which can cause oxidative degradation of cell membranes (Section 6.3.4.6.) and thus disrupt the activity of transmembrane ion transporters (Lushchak, 2011). Therefore, disruption of ion homeostasis is likely the result of Ni and Cr toxicity in amphipods exposed to 100% w/w olivine.
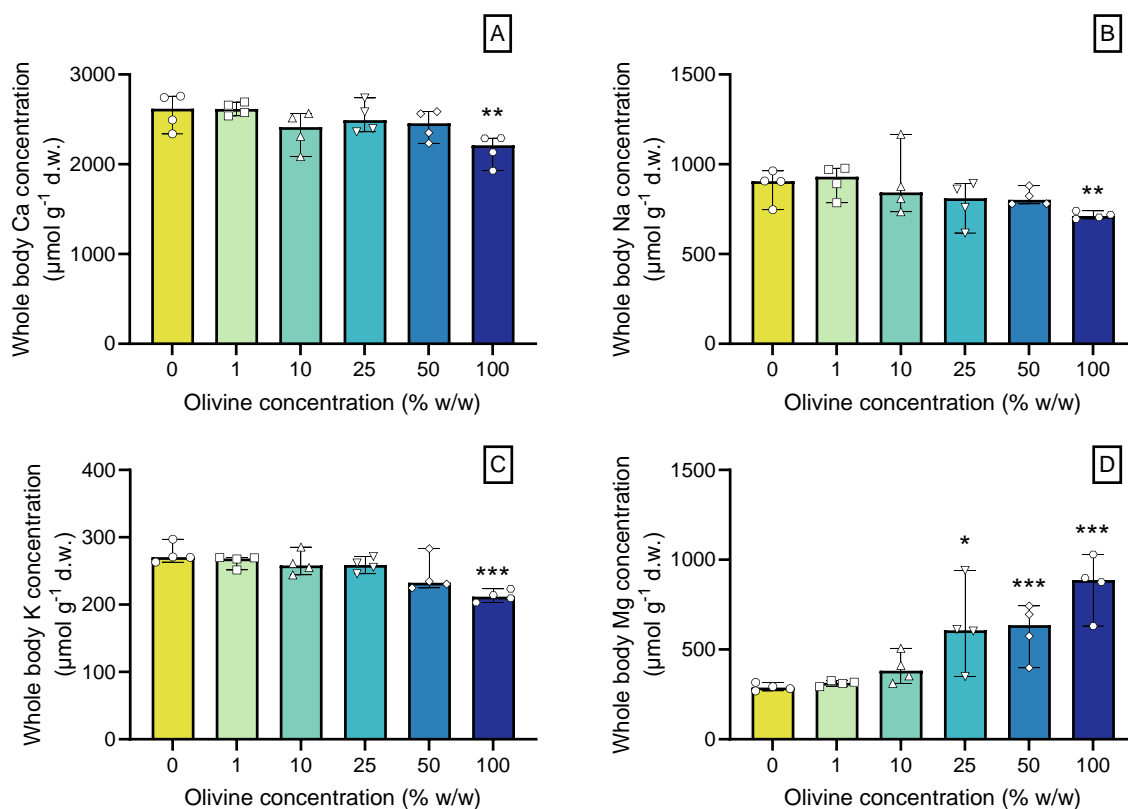
Figure 6.9: Whole body concentration (μmol g⁻¹ dry weight) of (A) calcium (Ca), (B) sodium (Na), (C) potassium (K), and (D) magnesium (Mg) in pooled G. locusta exposed to natural sediment mixed with various amounts of 3 – 99 μm olivine (expressed in % w/w) for 35 days. Median and range are shown (N = 4). Significance compared to 0% w/w olivine: * = p < 0.05, ** = p < 0.01, *** = p < 0.001.

6.3.4.6 Lipid peroxidation

TBARS concentrations were approximately 1.5 times higher in the 10% w/w olivine treatment (median = 1.08 μmol g⁻¹ w.w.) and doubled in the 100% w/w treatment (1.54 μmol g⁻¹ w.w.) compared to the control (median = 0.74 μmol g⁻¹ w.w.) (Figure 6.10A). A significant positive relationship (τ = 0.69, R^2 = 0.71, $F(1, 11)$ = 27, $p < 0.001$) was observed between TBARS concentrations and whole body Ni concentrations (Figure 6.10B), suggesting metal-induced oxidative damage.
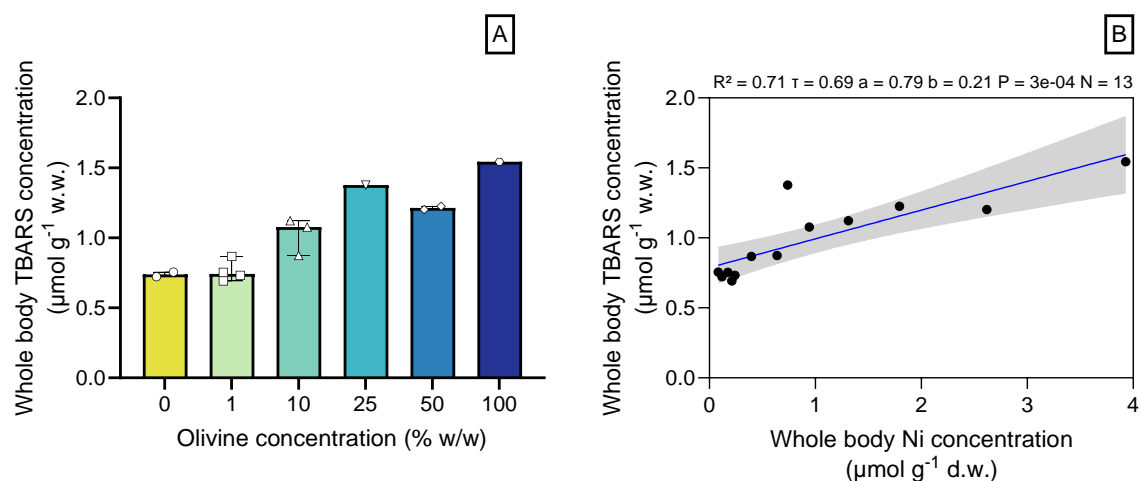
Figure 6.10: (A) Whole body thiobarbituric acid reactive substances (TBARS) concentration ($\mu mol\ g^{-1}$ w.w.) in pooled G. locusta exposed to natural sediment mixed with various amounts of 3 – 99 \mu m olivine (expressed in % w/w) for 35 days. Median and range are shown (N = 4). Significance compared to 0% w/w olivine: * = p < 0.05, ** = p < 0.01, *** = p < 0.001. (B) Linear regression between whole body TBARS concentration and whole body Ni concentration ($\mu mol\ g^{-1}$ d.w.) in pooled G. locusta. Regression line (blue) with 95% confidence interval (dark grey shading) is shown. The coefficient of determination (R^2), Kendall correlation coefficient (τ), sample size (N), and regression line slope (a), intercept (b), and p value (P) are given.

Nickel could cause oxidative stress by substituting for Fe^{2+} in the reactive oxygen species (ROS) producing Fenton/Haber Weiss reactions, inhibiting antioxidant enzyme activity such as catalase, or by decreasing the ROS scavenging potential of compounds like glutathione by complex formation (Blewett and Leonard, 2017; Brix et al., 2017). In previous studies, significant changes in antioxidant enzyme activities and MDA levels have been observed in *Tigriopus japonicus* and *Mytilus galloprovincialis* exposed to Ni concentrations of 2.1 and 13 $\mu mol\ L^{-1}$ during a 12 and 4-day exposure, respectively (Wang and Wang, 2010; Attig et al., 2014). Additionally, Cr(VI) exposure resulted in lipid peroxidation at concentrations as low as 0.019 $\mu mol\ L^{-1}$ in gills of *Venus verrucosa*

exposed for 7 days (Chaâbane et al., 2020). Reduction of Cr(VI) to Cr(III) after cellular uptake is accompanied by significant ROS production resulting in oxidative stress if antioxidant responses are inadequate (DesMarias and Costa, 2019). Although Cr is present as less toxic Cr(III) in chromite associated with dunite, release and oxidation of chromite nanoparticles could result in elevated Cr(VI) exposure, accumulation and potential toxicity (Das et al., 2021; Flipkens et al., 2021). Overall, olivine exposure resulted in oxidative stress, likely as a result of significant Ni and Cr accumulation (Figure 6.8A and 6.8B).

6.3.4.7 Implications for coastal enhanced olivine weathering

Olivine exposure effects on aquatic biota remain scarcely studied (Ren et al., 2021; Hutchins et al., 2023; Xie et al., 2023), preventing accurate assessment of the environmentally safe CDR scale of coastal enhanced olivine weathering. An increase in the abundance of biofilm forming particle attached microbes was observed 10 days after 1% w/w olivine addition to natural seawater (Ren et al., 2021). Furthermore, Mg release from olivine dissolution promoted the growth of the freshwater green microalgae *Chlamydomonas reinhardtii* and *Chlorella pyrenoedosa* during a 9 day exposure 8 g of olivine L^{-1} (Xie et al., 2023). Finally, positive and neutral growth responses were observed for two marine diatom species, one marine coccolithophore, and three marine cyanobacteria grown in synthetic olivine leachates with Ni(II) and Cr(VI) concentrations up to 0.13 and 0.12 µmol L^{-1} for a maximum of 10 days (Hutchins et al., 2023).

In contrast to the overall neutral to positive effects of olivine exposure reported by previous studies, we observed reduced survival, growth, and reproduction of *G. locusta* chronically exposed to fine-grained olivine. The percentage of gravid females and juvenile production were significantly reduced at 10% w/w olivine and higher after 35 days of exposure (Figure 6.7A and 6.7C), resulting in a highest no observed effect concentration (NOEC) for 1% w/w olivine. Additionally, a 10% effect concentrations (EC10) of 0.99% (0 – 4.4%) w/w olivine for juvenile production and 5.5% (0 – 17%) w/w olivine for percentage of gravid females were obtained (Supplementary Section F.5.7). In regards to chemical

risk assessment, an arbitrary assessment factor of 100 would be applied to the lowest NOEC or EC10 value when only one chronic marine sediment toxicity test was conducted, resulting in a predicted no effect concentration (PNEC) of 0.01% w/w olivine (ECHA, 2008). This PNEC value is very low, even compared to the conservative olivine application guideline of 0.059 – 1.4 kg olivine m^{-2} or 0.056 to 1.3% w/w derived by Flipkens et al. (2021) based on existing Ni sediment quality guidelines. Hence, these findings highlight the need for additional olivine toxicity data for a range of marine species to derive accurate olivine PNEC values. Research should especially be focused on those species which are known to be sensitive to Ni exposure (e.g. sea urchin early life stages) (Gissi et al., 2020). Moreover, molecular endpoints (e.g. antioxidant enzyme expression and activity levels) should be considered in future olivine toxicity tests to advance the understanding of molecular mechanisms that drive Ni and Cr toxicity in marine biota. Furthermore, the effect of grain size on olivine toxicity should also be explored, since larger grains might be less toxic because they lead to lower metal bioaccumulation (Figure 6.2A-B). Finally, research on the environmental safety of alternative silicates with a lower trace metal content compared to dunite, such as basalt, kimberlite, or wollastonite for use in coastal enhanced weathering seems advised.

6.4 Conclusions

Coastal enhanced olivine weathering is a proposed atmospheric CO_2 removal strategy for climate change mitigation. However, uncertainties regarding the CO_2 sequestration potential and environmental safety prevent fast upscaling of the technique from laboratory studies to field trials. This study investigated acute 24 to 96 h bioaccumulation and chronic 35-day bioaccumulation and toxicity of olivine in the marine amphipod *G. locusta*. Acute olivine exposure resulted in significant grain size dependent olivine ingestion as well as whole body and tissue trace metal accumulation in *G. locusta*. The tissue bioaccumulation of Ni was 3 to 8 times higher compared to Cr, and limited Cr accumulation was observed in the seawater dissolved phase, suggesting lower Cr bioavailability. Thousands of small olivine grains (mainly 0.3 to 8 μm in size) were

observed in the guts of exposed amphipods, but further experimental evidence is needed to assess their significance as a trace metal exposure pathway. Chronic 35-day exposure of juvenile amphipods to 3 – 99 μm olivine resulted in significant adverse effects on survival, growth, and reproduction, likely as a result of metal induced oxidative stress and disruption of Ca^{2+}, Na^+, and K^+ homeostasis. The total juvenile production and percentage of gravid females was significantly reduced at an exposure concentration of 10% w/w olivine. From this first sediment olivine toxicity test, application of arbitrary risk assessment protocols yields a very low PNEC of 0.01% w/w olivine (3 – 99 μm), highlighting the need for additional marine olivine toxicity data to strengthen the derived olivine application guideline. Furthermore, the CO_2 sequestration potential and ecosystem effects of silicates with a lower Ni and Cr content (e.g. basalt, kimberlite, and wollastonite) should be investigated to assess the scale at which these rocks could be safely used for coastal enhanced silicate weathering.

6.5 Supplementary information

Gammarus species, sex, and size determination details, sediment and olivine geochemical properties, and additional results from the different olivine exposure experiments with *G. locusta* can be found in the Appendix F. Research data is accessible through the Marine Data Archive at https://doi.org/10.14284/614.

6.6 Acknowledgments

Chapter 7   General discussion and future perspectives

Olivine, the green and revolutionary
mitigator of climate change?

Climate change has detrimental effects on humankind and natural ecosystems primarily due to sea level rise, ocean warming and acidification, and increased frequency and intensity of extreme weather events (IPCC, 2022a). Without substantial reductions in anthropogenic CO_2 emissions, global temperature rise could already exceed the Paris Agreement targets of 1.5 °C by around 2030 and 2 °C by approximately 2050 (Liu et al., 2022). Therefore, strong greenhouse gas emission cuts are urgently needed to avoid severe and potentially irreversible impacts of climate change. Additionally, atmospheric CO_2 removal is needed on a gigaton scale to compensate for any carbon budget overshoot and residual CO_2 emissions from sectors that are difficult to decarbonize (e.g. aviation and shipping) (Minx et al., 2018). Ocean alkalinity enhancement (OAE) via coastal enhanced olivine weathering is a proposed carbon dioxide removal (CDR) technique that can be readily implemented in existing coastal management programmes. However, the CO_2 sequestration potential and ecosystem impacts of the technique remain poorly constrained due to the scarcity of experimental data under environmentally relevant conditions (Meysman and Montserrat, 2017).

This body of research aimed to advance the understanding of olivine dissolution and CO_2 sequestration in seawater, with a focus on the impact of hydrodynamics on the kinetics of these processes. Additionally, existing marine Ni and Cr ecotoxicity data and environmental quality standards were consulted and effects of olivine exposure on two benthic marine invertebrates were empirically assessed to provide an initial indication of the ecosystem risks of coastal enhanced olivine weathering. In this concluding chapter, the main experimental findings are discussed and recommendations for future research are provided.

7.1 Impact of hydrodynamics on olivine dissolution rates

The reactivity of olivine in aqueous solutions has been extensively studied under laboratory conditions in the past decades due to its relatively simple and consistent dissolution mechanism, and increasing interest with regards to carbon storage and

weathering of the surface of Mars (Oelkers et al., 2018). Schuiling and Krijgsman (2006) proposed that olivine could be used in enhanced weathering for cheap and effective atmospheric CO_2 drawdown. As a response, Hangx and Spiers (2009) critically analyzed the concept and concluded that coastal enhanced olivine weathering was not a viable method for large scale atmospheric CO_2 removal due to the slow dissolution rate of olivine in seawater. Schuiling and De Boer (2010) subsequently commented that the CO_2 sequestration potential was grossly underestimated by Hangx and Spiers (2009), since the possible enhancement of olivine dissolution by biological and physical processes was not considered in their assessment.

Waves and currents could potentially enhance olivine dissolution in various ways as described in detail in Chapter 3 and 4. Briefly, grain abrasion from bedload transport could prevent passivating layer formation on mineral grains and also result in particle fragmentation, which would enhance the reactive mineral surface area and thus the dissolution rate (Béarat et al., 2006; Schuiling and De Boer, 2011; Oelkers et al., 2018). Additionally, advective pore water flow induced by waves and currents would limit the accumulation of reaction products which would slow down olivine dissolution and promote the formation of secondary minerals that scavenge alkalinity. (Meysman and Montserrat, 2017).

The effect of continuous grain-grain collisions on olivine reactivity in natural filtered seawater was experimentally assessed in Chapter 3 using bench top rock tumblers. The accumulation of reaction products in the overlying seawater revealed that olivine subjected to different degrees of continuous physical agitation dissolved 8 to 19 times faster than olivine in stagnant seawater. Olivine dissolution was found to occur stoichiometrically, given that similar olivine dissolution rate constants were derived from the accumulation of different dissolution products (i.e. TA, DIC, and DSi) with the exception of Ni (discussed in section 7.3). The median olivine dissolution rate constants for the agitated olivine derived from the TA, DIC, and DSi accumulations (9.1 to 15.2 μmol m^{-2} d^{-1}) were similar to those previously derived from the same parameters in agitated

seawater media (0.80 to 22.3 μmol m^{-2} d^{-1}) by Montserrat et al. (2017). Furthermore, observed dissolution rate constants were relatively close to the average values between 6.9 and 8.6 μmol m^{-2} d^{-1} predicted from the rate equation by Rimstidt et al. (2012). The latter rate equation was derived based on 125 forsterite olivine dissolution rate constants observed in various aqueous solutions with a pH greater than 5.6 and temperature between 0 and 150 °C (Rimstidt et al., 2012). In our study, limited secondary mineral formation occurred, no passivating layers were observed on olivine grains, and air-seawater CO_2 exchange was not rate limiting for the stagnant olivine treatment. Although development of microcracks was observed inside weathered olivine grains, no significant changes in the olivine grain size distribution were observed at the end of the 70-day experiment, indicating minimal particle fragmentation on this timescale. Therefore, we concluded that olivine dissolution was primarily enhanced through continuous mixing which prevented the accumulation of reaction products at the grain surface. These findings highlight that olivine should ideally be supplied in coastal areas with high bed shear stress and pore water exchange rates, such as nearshore zones, to enhance mineral dissolution.

An additional factor contributing to the low olivine reactivity in the stagnant treatment, not addressed in Chapter 3, might be the diminished reactive mineral surface area resulting from grain-to-grain contact. For future studies, micro-CT scanning of mineral grain packs could potentially provide valuable insights on the extent of grain-to-grain contact, providing information on the surfaces that may display reduced reactivity.

A 175-day large scale flume experiment was subsequently conducted to investigate the effect of current on the dissolution kinetics of olivine in permeable marine sediment (Chapter 4). Based on previous findings, we hypothesized that advective pore water flushing would enhance olivine dissolution and minimize secondary mineral precipitation by preventing pore water saturation. Results showed that continuous flow stimulated alkalinity release from natural permeable sediment. However, limited accumulation of TA and DSi was observed in the flume with olivine and current, suggesting that olivine

dissolution was minimal or that substantial secondary mineral formation occurred. No passivating layers were observed on recovered olivine grains and possible formation of secondary minerals could not be confirmed due to the lack of pore water chemistry data, and high background concentration of $CaCO_3$ and other phases in the beach sediment. Furthermore, the extent of grain-to-grain contact could not be estimated from sediment core micro-CT scans due to the difficulty in confidently identifying olivine particles in the sediment matrix. Finally, potential pore water saturation could not be confirmed due to a lack of pore water chemistry data. Consequently, the exact cause for the limited accumulation of olivine reaction products in the overlying water cannot be confidently identified from the available data. Therefore, additional flume, mesocosm, and small field experiments that follow best practice guidelines (Cyronak et al., 2023; Dupont and Metian, 2023; Riebesell et al., 2023; Steenkamp and Webb, 2023) are required to further assess the impact of hydrodynamics on the efficacy of olivine dissolution under natural seafloor conditions. The effect of biological processes on *in situ* olivine dissolution kinetics should also be explored. Benthic macrofauna such as the lugworm *Arenicola marina* could stimulate olivine dissolution through bioirrigation (Rao et al., 2014) and olivine transit through its acidic gut environment with high gut enzymatic activity (Mayer et al., 1997; Jansen and Ahrens, 2004; Needham et al., 2004). Additionally, organic matter decomposition by benthic microorganisms acidifies the pore water solution through production of CO_2 and organic acids (Lin et al., 2022). This process has been shown to enhance carbonate dissolution and could potentially also stimulate silicate dissolution (Rao et al., 2012; Cyronak and Eyre, 2016).

7.2 CO₂ sequestration potential of CESW

The potential contribution of coastal enhanced silicate weathering (CESW) to climate change mitigation during the 21st century remains unclear due to its poorly constrained CO_2 sequestration potential under environmentally relevant conditions. As described in previous chapters (detailed description in Section 1.6), the CO_2 sequestration potential is dependent on the net CO_2 sequestration efficiency $\gamma_{CO_2}^{net}$ and the olivine dissolution rate.

The current understanding of olivine reactivity in seawater was discussed in the previous section (Section 7.1), while state-of-the-art knowledge and our experimental findings regarding the $\gamma_{CO_2}^{net}$ will be reviewed in the following paragraphs.

The net CO_2 sequestration efficiency is dependent on the seawater CO_2 sensitivity $(\delta DIC/\delta TA)_{pCO_2}$, alkalinity release during olivine dissolution, and CO_2 emissions associated with mining, grinding and transportation of the source rock. According to the reaction stoichiometry, dissolution of 1 mol of olivine produces 4 moles of alkalinity and sequesters the same amount of CO_2 (Eq. 7.1). However, the seawater CO_2 sensitivity $(\delta DIC/\delta TA)_{pCO_2}$ which defines the amount of CO_2 that is taken up from the atmosphere for each mole of alkalinity added is typically between 0.8 and 0.9 mol DIC mol^{-1} TA due to buffering by the carbonate and borate buffer systems in seawater (Hoffmann et al., 2012; Montserrat et al., 2017; Bertagni and Porporato, 2022). Hence, the actual CO_2 uptake during olivine dissolution in seawater would be 10 to 20% lower than that expected from the chemical weathering equation depending on the seawater temperature, salinity and chemical composition at the deployment site (Hofmann et al., 2009; Bertagni and Porporato, 2022). This buffering effect was visible for our 70-day weathering experiment (Chapter 3), where the average observed seawater CO_2 sensitivity of 0.79 mol DIC mol TA^{-1} for the rotation treatments matched the expected average value of 0.82 mol DIC mol TA^{-1} for the experimental conditions quite well.

$$(Mg, Fe)_2SiO_4 + 4H_2O + 4CO_2 \rightarrow 2(Mg, Fe)^{2+} + 4HCO_3^- + H_4SiO_4 \qquad [7.1]$$
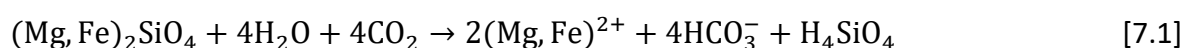
Olivine-rich rock first needs to be mined and ground to the desired grain size before it can be transported to the coastal deployment site of choice for atmospheric CO_2 drawdown (Hangx and Spiers, 2009; Foteinis et al., 2023). These different steps in the life cycle of this CDR technique are accompanied by CO_2 emissions and environmental impacts that need to be considered to determine the $\gamma_{CO_2}^{net}$ and sustainability of the technique (Foteinis et al., 2023). Small olivine grains are generally assumed to dissolve and drawdown CO_2 faster than large olivine grains due to the larger reactive surface area (Hangx and Spiers,

2009; Foteinis et al., 2023). However, grinding source rock to a very fine grain size of, for example, 10 μm would require several energy intensive grinding steps that result in significant CO_2 emissions when fossil fuel generated electricity is used. Overall, the mining and grinding steps to acquire 10 μm grain sized material would reduce $\gamma_{CO_2}^{net}$ by between 5 and 11% depending on the fossil fuel source. For grain sizes larger than 40 μm no ultra-fine grinding is needed which significantly reduces the energy costs and decrease of $\gamma_{CO_2}^{net}$ to less than 2% (Hangx and Spiers, 2009). The use of renewable electricity in the future would undoubtedly reduce the environmental footprint of this energy intensive grinding process (Foteinis et al., 2023). Transportation of ground olivine to the coastal zone could be executed by ships, trains, and trucks. This transport is estimated to result in a further decrease of the net CO_2 sequestration efficiency by 0.1 to 1% per 100 km (Hangx and Spiers, 2009). Hence, the mode of transport and distance between the mining site and deployment location should be carefully considered to limit transport-associated CO_2 emissions and maximize environmental sustainability (Hangx and Spiers, 2009; Foteinis et al., 2023). Environmental impacts associated with mining, such as vibration, dust and noise pollution, local deforestation, soil Ni and Cr enrichment, and loss of fertile surface soil layers (Manoj and Prasannakumar, 2002; Guevara et al., 2021) are also important to consider in the life cycle assessment and ecological risk assessment of CESW (Foteinis et al., 2023). Overall, production and transport related CO_2 emissions and seawater CO_2 sensitivity at a certain coastal site can be relatively accurately quantified before deployment (Meysman and Montserrat, 2017).

One process that could significantly reduce the CO_2 sequestration efficiency of coastal enhanced olivine weathering, but remains poorly understood, is the formation of secondary minerals (Griffioen, 2017; Fuhr et al., 2022). Geochemical thermodynamic equilibrium modelling (Griffioen, 2017) and limited experimental studies (Rigopoulos et al., 2018; Fuhr et al., 2022) have shown that iron (hydr)oxides, calcium carbonates (predominantly aragonite), and phyllosilicate minerals (e.g. sepiolite and chrysotile) could potentially form during enhanced olivine weathering in seawater. The formation of these

minerals is undesirable since it consumes alkalinity and therefore reduces the potential CO_2 drawdown (Fuhr et al., 2022).

The formation of iron (hydr)oxides during fayalite dissolution under oxic conditions is inevitable (Griffioen, 2017; Meysman and Montserrat, 2017). Fayalite typically represents 7 to 20% of the olivine present in ultramafic rocks such as dunite and other peridotites (Griffioen, 2017). The oxidation of Fe(II) released during fayalite dissolution and subsequent precipitation as iron(III) (hydr)oxides would reduce the total alkalinity production by 7 to 20% depending on the fayalite content (Griffioen, 2017; Montserrat et al., 2017). The ratio between TA and DSi accumulation in the seawater of the rotation treatments from our 70-day weathering experiment reflects this iron (hydr)oxide formation as it matched the expected TA/DSi ratio of 3.73 for the experimental Fo$_{93}$ olivine reasonably well (Chapter 3). Hence, olivine-rich rock with a low iron content should be used where possible to maximize ocean alkalinity enhancement and subsequent atmospheric CO_2 drawdown (Griffioen, 2017).

Seawater is naturally supersaturated with $CaCO_3$, but precipitation does not occur due to absence of precipitation nuclei, and inhibition by dissolved Mg, orthophosphate, and organic matter (Morse et al., 2007; Marion et al., 2009). The precipitation rate of $CaCO_3$ in seawater is dependent on the degree of supersaturation with respect to $CaCO_3$ and abundance and quality of precipitation nuclei (Moras et al., 2022; Hartmann et al., 2023). The saturation state threshold for $CaCO_3$ formation is expected to be lowest in the presence of mineral phases (i.e. heterogeneous precipitation) with a large surface area of high quality (Moras et al., 2022; Hartmann et al., 2023). However, this threshold for heterogenous $CaCO_3$ precipitation remains poorly constrained (Marion et al., 2009; Moras et al., 2022). Moras et al. (2022) recently observed aragonite precipitation on fine (<63 μm) CaO and Ca(OH)$_2$ particles at a *SI* of ~0.85 ($\Omega \approx 7$) in natural seawater (at 21 °C and 35 ‰). Furthermore, so-called "runaway precipitation" was observed during which $CaCO_3$ formation removed more alkalinity than was initially added (Moras et al., 2022). Fuhr et al. (2022) already observed significant aragonite formation at a *SI* as low as 0.48 ($\Omega \approx 3$)

during weathering of olivine rich (~75%) sand, but this occurred in artificial seawater (at 21.5 – 23.9 °C and 35 ‰) where inhibitory orthophosphates and organic matter are absent.

During our 70-day laboratory olivine weathering experiment in natural seawater, olivine TIC content did not increase and no aragonite crystal formation was observed via SEM-EDX analysis (Chapter 3). Furthermore, the relationship between DIC and TA concentrations was as expected in the absence of $CaCO_3$ precipitation, and the critical SI of ~0.85 derived by Moras et al. (2022) was not exceeded on most sampling days. Hence, collectively these results indicate that minimal $CaCO_3$ precipitation occurred. This same conclusion cannot be drawn for the 175-day flume experiment (Chapter 4). Although the threshold SI of ~0.85 was not reached in the overlying seawater during the experiment (maximum SI value of 0.48), significant amounts of rod shaped $CaCO_3$ particles were observed in the suspended matter of the flow treatments via SEM-EDX analysis from day 2 onwards. Furthermore, olivine addition did not result in significant increases of seawater TA, DSi or DIC compared to the beach sand control, signifying possible secondary mineral formation. However, as stated in section 7.1, it cannot be proven that the observed $CaCO_3$ particles were newly formed since the 630 kg of original beach sand already contained a significant amount (~5.4%) of $CaCO_3$. Under the assumption that all alkalinity generated from olivine dissolution (following the rate equation by Rimstidt et al. (2012)) would have been consumed via $CaCO_3$ and $Fe(OH)_3$ precipitation, only an undetectable amount of ~48 mg of $CaCO_3$ would have formed. Hence, results from the current flume experiment cannot provide new insights about the possible kinetics of $CaCO_3$ formation during olivine dissolution in permeable marine sediment.

Finally, phyllosilicates such as sepiolite, talc and chrysotile have been observed to form in relatively small amounts during previous olivine weathering studies in seawater (Rigopoulos et al., 2018; Fuhr et al., 2022). In our weathering experiments, seawater supersaturation with respect to these silicate phases was observed. Nevertheless, no phyllosilicates were observed via SEM-EDX analysis on recovered sediment for both

experiments. Additionally, Raman spectroscopy did not reveal any phyllosilicates in the suspended matter or wall precipitates of the 175-day flume experiment. Hence, phyllosilicate formation was likely limited in both experiments, which could be explained by the slow precipitation kinetics at ambient temperature compared to carbonate minerals (Griffioen, 2017; Baldermann et al., 2018).

Overall, kinetics and critical saturation state thresholds for secondary mineral precipitation in seawater during OAE remain poorly constrained (Fuhr et al., 2022; Moras et al., 2022; Hartmann et al., 2023). Hence, additional dedicated experiments on this topic (similar to Hartmann et al. (2023) and Moras et al. (2022)) are needed to accurately assess the CO_2 sequestration efficiency and model the global CDR potential of CESW (Hartmann et al., 2023). Furthermore, detailed knowledge on the hydrodynamics and atmospheric CO_2 exchange rates are crucial to determine the *in situ* dilution potential of alkalinity-enriched seawater and air-seawater CO_2 influx (Bach et al., 2023; Hartmann et al., 2023). Finally, the potential reduction of natural alkalinity generation (by biogenic carbonate mineral dissolution) as a response to anthropogenic alkalinity addition should be considered and mitigated (Bach, 2023).

7.3 Possible adverse ecosystem impacts of CESW

Large scale coastal olivine deployments would lead to chemical and physical alterations of the local marine environment. The impact of these changes on marine biota are currently poorly constrained, preventing accurate assessment of the scale at which coastal enhanced olivine weathering could be safely implemented for climate change mitigation (Hartmann et al., 2013; Köhler et al., 2013; Meysman and Montserrat, 2017; Bach et al., 2019). The possible ecosystem effects that have presently been recognized are reviewed in the general introduction (Chapter 1). The novel insights we acquired about potential adverse effects and recommended directions for future work will be provided in the following paragraphs.

The potential concern of Ni and Cr accumulation to toxic levels during coastal enhanced olivine weathering has been raised in several previous studies (Hartmann et al., 2013; Köhler et al., 2013; Meysman and Montserrat, 2017; Montserrat et al., 2017). Marine organisms will be exposed to these trace metals via the water (overlying and pore water) and via ingestion of contaminated food or sediment particles (Adams et al., 2011; Simpson and Batley, 2016). Metals will be present in various physicochemical forms (i.e. chemical species) with different bioavailability (Blewett and Leonard, 2017). Free Ni^{2+} ions released during olivine dissolution can for example form complexes with inorganic (e.g. SO_4^{2-}, Cl^-, HCO_3^-) or organic (e.g. fulvic and humic acids) ligands that potentially reduce Ni bioavailability and toxicity (Blewett and Leonard, 2017; Adams et al., 2020).

Chemical speciation under different OAE scenarios with olivine was estimated in Visual MINTEQ (ver. 3.1) using the default settings for DOC (Nica-Donnan model) and the water chemistry data provided in Supplementary Table G.1. The dominant (≥ 1% of total dissolved concentration) Ni species in seawater (34.6 ‰) with various olivine reaction products (Ni, Cr, and TA) and dissolved organic carbon (DOC) concentrations are shown in in Figure 7.1. The free Ni^{2+} concentration represents 25 to 55% of the total Ni species, depending on the total dissolved Ni, TA, and DOC concentration (Figure 7.1). The remaining Ni species mainly consist of complexes with DOC (0 – 55%) and anions such as SO_4^{2-} (15 – 34%), Cl^- (1.3 – 2.9%), CO_3^{2-} (1.8 – 7.3%), and HCO_3^- (1.6 – 6.3%). Significant increases in seawater total alkalinity (from 2350 to 4544 µmol L^{-1}) only marginally reduce the free Ni^{2+} fraction (from 55 to 51%) due to $NiCO_3$ and $NiHCO_3^-$ formation (Figure 7.1A). Similarly, at elevated dissolved Ni concentrations, Ni-DOC complexes only represent a relatively small fraction of the total Ni species (Figure 7.1B-C). Consequently, these speciation calculations suggest that the protective effect of ocean alkalinity enhancement and elevated DOC concentrations on marine Ni toxicity is potentially limited. However, the metal speciation would also be dependent on the type of DOC (here assumed to be 100% fulvic acid), active fraction of dissolved organic matter to DOC (here equal to 1.65), and variations in seawater pH and salinity (Brown, 1987; Carder et al., 1989; Blewett and Leonard, 2017; Zhang et al., 2018). Additionally, experimental studies have shown that

the relationship between Ni toxicity and seawater DOC concentrations is complex and does not align well with these model predictions (Nadella et al., 2009; Blewett et al., 2016). This highlights the need for additional work on the factors that influence Ni toxicity in marine environments.
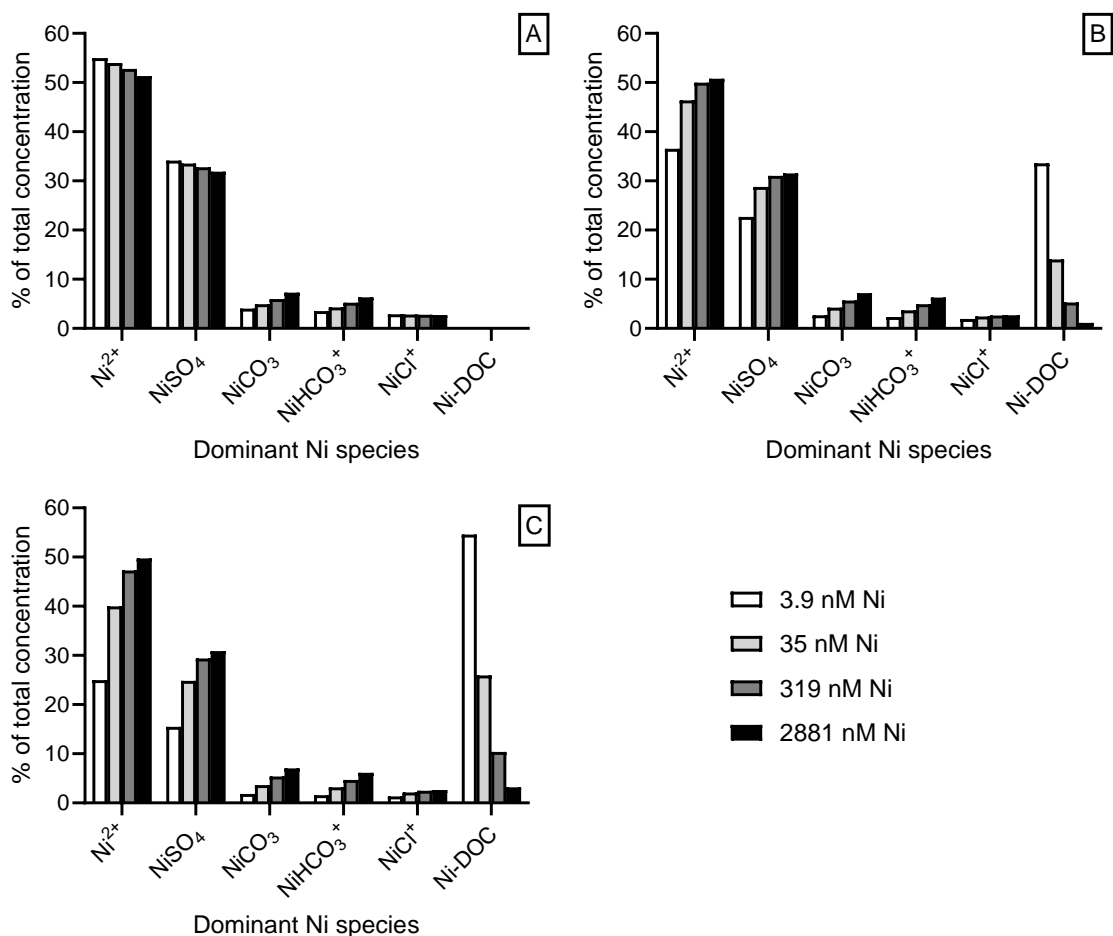
Figure 7.1: Speciation of Ni in seawater (34.6 ‰) with various Ni, Cr, and TA concentrations in the presence of (A) 0 mg L^{-1}, (B) 4 mg L^{-1}, or (C) 8 mg L^{-1} DOC. Chemical speciation was modelled in Visual MINTEQ using the default DOC settings (Nica-Donnan model). Water chemistry data is shown in Supplementary Table G.1.

In sediment, metals can sorb or bind to several phases (e.g. organic matter, oxides, sulfides, carbonates, and carbonate or clay minerals), which vary in abundance within and among coastal sites (Zhang et al., 2014). The uptake and internal accumulation of metals will only lead to toxic effects in marine biota when concentrations in metabolically active compartments exceed critical thresholds (Adams et al., 2011). To avoid adverse effects on aquatic biota, protective values for aquatic life have been used by regulatory agencies for several decades (Adams et al., 2011; Kwok et al., 2014).

To provide a first indication of the environmental safety of global-scale coastal enhanced olivine weathering, we derived the maximum amount of olivine that could be supplied to coastal oceans without exceedance of existing Ni and Cr seawater environmental quality standards (EQS) and sediment quality guidelines (Chapter 2). Calculations were made for the two end-member scenarios where all trace metals released during olivine dissolution would either remain in the sediment or end up in the overlying water column. An intermediate, more realistic, scenario was not considered due to the lack of knowledge on trace metal environmental fate during olivine dissolution. Additionally, considerable variation in physicochemical conditions among coastal sites (Frogner-Kockum et al., 2016; Solan et al., 2019) necessitates the derivation of site-specific olivine application guidelines. Low aqueous solubility of chromite (Gunkel-Grillon et al., 2014) and higher EQS for Cr^{3+} compared to Ni^{2+} suggest that Ni is the main metal of concern during coastal enhanced olivine weathering. Nevertheless, results showed that the large dilution effect would allow substantial amounts of olivine to be supplied to coastal areas without exceedance of the European seawater Ni^{2+} EQS (0.147 µmol L^{-1}). However, under the assumption that olivine would get mixed and dissolve in the upper 10 cm of the sediment, only 0.059 to 1.4 kg of olivine per m² of seabed (or 1.7 to 39 Gt globally) could be supplied without future exceedance of the probable effect level (PEL) derived by the Florida Department of Environmental Protection (FDEP). Overall, these findings indicate that sedimentary Ni and Cr accumulation could limit the safe usage of olivine in CESW. Hence, benthic organisms will possibly be at higher risk of metal toxicity compared to pelagic species. In conclusion, more in-depth studies on the Ni and Cr release rate, environmental

fate, bioavailability, and potential mixture toxicity are needed to derive accurate site-specific olivine application guidelines.

The rate of Ni and Cr release during olivine dissolution in seawater has been scarcely investigated (Montserrat et al., 2017; Fuhr et al., 2022; Guo et al., 2023), but is crucial for accurate risk assessment of coastal enhanced olivine weathering. During our 70-day olivine weathering experiment, high non-stoichiometric Ni release was observed from day 35 onwards. Specifically, DNi accumulation was 1.8 to 3.4 times higher than that expected based on DSi accumulation. Similarly, for the chronic 35-day olivine toxicity test with *G. locusta*, DNi accumulation was on average 2.5 times higher than that expected based on DSi accumulation. This discrepancy between observed and expected DNi accumulation was even larger (7.3 to 12 times difference) during the acute 24-h olivine bioaccumulation test with *G. locusta*. Finally, high DNi accumulation was also observed during the 175 day flume experiment, but this could not be confidently ascribed to olivine weathering due to possible Ni release from stainless steel parts of the flumes. Overall, Ni release was consistently higher than expected based on the dissolution reaction stoichiometry. This was also observed by Montserrat et al. (2017) and was explained by preferential leaching of metal cations compared to Si based on the observed significant decrease in Mg-to-Si ratios on the surface of olivine grains weathered in natural or artificial seawater. During our 70-day weathering experiment, this decrease in mineral surface Mg-to-Si ratios was not observed, indicating that additional research is needed to confidently explain the high non-stoichiometric Ni release. Regardless of the reason, these findings highlight that model predictions of trace metal accumulation during CESW need to take into account preferential Ni release and cannot simply assume stoichiometric olivine dissolution. Additionally, this non-stoichiometric behaviour questions the reliable use of Ni as proxy for olivine dissolution rate monitoring under *in situ* conditions (Montserrat et al., 2017; Fuhr et al., 2022).

In contrast to DNi, DCr accumulation was significantly lower than stoichiometrically expected in all experiments. These findings were expected given that Cr is predominantly

241

present in the form of relatively insoluble Cr-bearing spinel minerals (e.g. chromite and Cr-magnetite) in dunite rock (Oze et al., 2004; Santos et al., 2015; Chrysochoou et al., 2016). The negligible leaching of Cr(III) from chromite is of little ecotoxicological concern due to the low bioavailability and toxicity of Cr(III) species (Aharchaou et al., 2018). However, biogenic Mn(IV) oxides could dissolve chromite nanoparticles under *in situ* conditions, resulting in the oxidation of Cr(III) to Cr(VI) or precipitation as Cr(III) hydroxides (Ivarsson et al., 2011; McClenaghan and Schindler, 2022). Hexavalent Cr (VI) is a highly mobile and toxic chemical species that is recognized as a human carcinogen (Aharchaou et al., 2018). Therefore, seawater and sediment Cr speciation analysis (Unceta et al., 2010; Davidson et al., 2020) in follow-up experiments is essential to further unravel the bioavailability and toxicity of Cr released during olivine dissolution.

The effects of olivine exposure on aquatic biota currently remains poorly studied (Ren et al., 2021; Guo et al., 2023; Hutchins et al., 2023; Xie et al., 2023). Addition of 1% w/w fine grained (D50 = 30 μm) olivine to natural seawater increased the abundance of biofilm forming particle-attached microbes after 10 days of incubation (Ren et al., 2021). Furthermore, Xie et al. (2023) observed increased growth of the freshwater green microalgae *Chlamydomonas reinhardtii* and *Chlorella pyrenoedosa* exposed to 8 g of olivine per liter for 9 days as a result of Mg^{2+} addition through mineral dissolution. Moreover, Hutchins et al. (2023) observed neutral to positive physiological responses in 6 phytoplankton species exposed to synthetic olivine leachates with Ni(II) and Cr(VI) concentrations up to 0.13 and 0.12 μmol L^{-1}, respectively. Finally, Guo et al. (2023) observed changes in the abundance of several coastal phyto- and zooplankton species after exposure to 1.9 g forsterite olivine (D10 – D90 = 22 – 228 μm) per liter of natural seawater for 21 days. Specifically, several small (<20 μm) phytoplankton taxa and the dinoflagellate *Noctiluca scintillans* increased in abundance, while ctenopods (*Penilia sp.*) and tunicates (*Oikopleura sp.*) reduced in number (Guo et al., 2023). The authors hypothesized that the elevated seawater turbidity from suspended olivine particles adversely affected zooplankton feeding, resulting in reduced abundance of these primary

consumers and increased abundance of their food source (small phytoplankton taxa) (Guo et al., 2023).

Next to these more realistic mixture exposures, two recent studies have also specifically investigated Ni exposure effects on phytoplankton species in light of ocean alkalinity enhancement with dunite rock (Guo et al., 2022; Xin et al., 2023). Guo et al. (2022) observed limited growth or photo-physiological effects in 11 marine phytoplankton species exposed to dissolved Ni concentrations ranging from 0.07 to 50000 nmol L^{-1}. Limited Ni effects were explained by the use of nitrate as a nitrogen source the presence of a high concentration of the synthetic organic ligand (100 µmol L^{-1} EDTA) in the growth medium, which greatly reduced Ni bioavailability through chelation. Finally, Xin et al. (2023) observed adverse effects of dissolved (< 0.2 µm) Ni concentrations up to 81 µmol L^{-1} (in a medium with 12 µmol L^{-1} EDTA) on the growth of the marine coccolithophore *Emiliania huxleyi*, dinoflagellate *Amphidinium carterae* and diatom *Thalassiosira weissflogii* during a 6 day exposure. *Thalassiosira weissflogii* was found to be most sensitive to Ni with an IC50 of 63.9 µmol L^{-1}, while the IC50 for the other two species exceeded the highest exposure concentration (of 81 µmol L^{-1}). Overall, previous studies showed that olivine addition could alter the community composition of marine phyto- and zooplankton. Hence, caution is required with application of Ni-rich source rock to avoid exceedance of critical Ni toxicity or turbidity thresholds that could perturb the base of the marine food web (Guo et al., 2022; Xin et al., 2023).

Our conservative estimates of the maximum amount of olivine that could be supplied to coastal areas without exceedance of existing Ni environmental quality standards highlighted that benthic organisms are possibly at higher risk of trace metal toxicity compared to pelagic organisms (see Chapter 2). To advance the understanding of olivine exposure effects on benthic marine biota, we assessed the avoidance of pure olivine and olivine-sediment mixtures by the marine amphipod *Gammarus locusta* and gastropod *Littorina littorea* during several short term choice experiments (Chapter 5). Additionally,

24 h to 96 h bioaccumulation tests and a 35-day toxicity test were conducted with the marine amphipod *G. locusta* (Chapter 6).

Changes in surficial sediment physicochemistry (e.g. metal and organic matter content, grain size distribution) after olivine application could potentially alter habitat suitability for certain marine species and ultimately result in community composition changes (Saengsupavanich et al., 2023). Short term choice experiments showed that *G. locusta* and *L. littorea* significantly avoided pure olivine (83 – 332 µm), but not realistic olivine-sediment mixtures with 3 or 30% w/w olivine. Relatively coarse olivine was avoided due to its light colour (positive scototaxis) by *L. littorea* and likely its high metal content by *G. locusta*. Olivine was not significantly avoided by *L. littorea* when it was 7.5 cm (45%) closer to *Ulva sp.* than natural sediment, highlighting the positive scototaxic behaviour and food availability driven movement in this species (Seuront et al., 2007; Moisez and Seuront, 2020). Importantly, these experiments show that *L. littorea* and *G. locusta* will likely not avoid sediments with up to 30% w/w relatively coarse olivine added and that the degree of avoidance is dependent on other environmental factors (e.g. food or shelter availability). From a climate change mitigation perspective, finer ground olivine, known for its accelerated dissolution and CO_2 sequestration (Hangx and Spiers, 2009; Foteinis et al., 2023), is preferred. Yet, adhering to best practice guidelines for beach nourishment, olivine with a grain size akin to native beach sand should be dispersed to limit ecological impacts and alterations in beach morphodynamics (Benedet et al., 2004; Speybroeck et al., 2006).

Acute (24 to 72 h) exposure of *G. locusta* to olivine resulted in rapid ingestion of mineral grains and significant grain size dependent metal accumulation. For all experiments, accumulation of Ni was higher than Cr in both seawater and olivine-exposed amphipods, confirming that most Cr remained in a particulate form with low bioavailability. Metal bioaccumulation in *G. locusta* acutely (24 h) exposed to 3-99 µm olivine was significantly higher than expected based on estimated waterborne and dietary metal uptake. Hence, waterborne and/or dietary metal uptake rates were underestimated. A lack of Cr

bioaccumulation and better agreement between predicted waterborne Ni uptake and observed Ni bioaccumulation in *G. locusta* at the end of the short term (78 h) 93 – 332 µm olivine avoidance test suggest that dietary metal uptake from ingestion of larger olivine particles was limited. Overall, bioaccumulation results are in line with the hypothesis by Duan et al. (2022) that smaller particles will be more toxic than larger ones due to their faster trace metal release rate and easier ingestion by marine biota. A combination of waterborne exposures to olivine reaction product mixtures (similar to Hutchins et al. (2023)) and olivine exposures as conducted here could be performed by future studies to further assess the importance of olivine ingestion as a trace metal exposure pathway for a range of marine biota.

Chronic 35-d exposure to natural marine sediment mixed with various concentrations of 3-99 µm (D10 – D90) olivine resulted in dose dependent whole body Ni and Cr accumulation and reduced survival, growth, and reproduction in *G. locusta*. Adverse effects were likely the result of metal toxicity given the elevated whole body thiobarbituric acid reactive substances concentration and disruption of whole body major cation (i.e. Na^+, K^+, and Ca^{2+}) homeostasis (Blewett and Leonard, 2017; Brix et al., 2017). A predicted no effect concentration of 0.01% w/w olivine was derived from the 1% w/w no observed effect concentration (and 10% effect concentration) value for juvenile production by applying an arbitrary assessment factor of 100 (ECHA, 2008). This very low predicted no effect concentration (PNEC) highlights the need for additional chronic olivine toxicity data to derive environmentally safe olivine concentrations.

A variety of species from different trophic levels and functional feeding groups should be tested under a broad range of representative environmental conditions that could affect trace metal bioavailability (e.g. pH, dissolved and total organic carbon (DOC and TOC), acid volatile sulfide (AVS) concentrations) (Schlekat et al., 2016; Simpson et al., 2016). Metal exposure conditions in the solid and aqueous (i.e. porewater and overlying water) phase and other key sediment and water chemistry parameters should be thoroughly characterized (Schlekat et al., 2016). A species sensitivity distribution (SSD) approach

could be employed to derive an olivine PNEC value if high quality olivine toxicity data are available for a minimum of 8 species from at least 4 taxonomic groups (Warne et al., 2014). The need to incorporate bioavailability in ecological risk assessment of metals in water and sediment is broadly recognized (Schlekat et al., 2016; Väänänen et al., 2018; Adams et al., 2020). When data on key bioavailability-controlling water and sediment chemistry parameters are available, bioavailability normalization is possible through model approaches (e.g. biotic ligand models and linear regression models) (Schlekat et al., 2016; Peters et al., 2018; Stauber et al., 2021). Importantly, these bioavailability models should adhere to four key principles: (I) they need to be constructed based on a comprehensive understanding of metal toxicity mechanisms, (II) they should ideally be relatively user-friendly, (III) validation (via mesocosm and/or field experiments) and application should be conducted within the relevant range of water and sediment chemistry, and (IV) clear rationale for the selection of a specific model needs to be provided (Schlekat et al., 2016; Adams et al., 2020). Overall, this bioavailability normalization approach would require a greater amount of data compared to the use of generic EQS; however, it would enable the derivation of robust site-specific olivine application guidelines designed to effectively protect local marine biodiversity, ecosystem functioning and ecosystem services (Väänänen et al., 2018).

Risk assessment frameworks are currently still primarily based on individual metal assessments while organisms often face metal mixtures in their natural environment (Meyer et al., 2015; Nys et al., 2018; Väänänen et al., 2018). The combined toxicity of metals in such mixtures can be roughly equal to (i.e. additive), larger than (i.e. synergistic), or smaller than (i.e. antagonistic) the sum of the individual metal toxicities (Nys et al., 2017). Although synergistic interactions are relatively rare (Nys et al., 2018), previous studies have reported synergism between Ni(II) and Cr(VI) in the freshwater fish *Cirrhinus mrigala* and marine copepod *Tisbe holothuriae* (Verriopoulos and Dimas, 1988; Palaniappan and Karthikeyan, 2009). Therefore, it is crucial to explore the interaction between Ni and Cr released during marine olivine dissolution via dedicated chronic laboratory experiments. These experiments could expose marine organisms to individual

metals and binary mixtures under realistic environmental conditions (Nys et al., 2017). Experimental findings could enhance our mechanistic understanding of marine olivine toxicity and enable the proper consideration of interaction effects in ecological risk assessment of coastal enhanced olivine weathering. This could for example be achieved through a tiered approach that considers bioavailability-normalized SSDs (Nys et al., 2018) or via the application of multi-metal biotic ligand models (Santore and Ryan, 2015).

Studies on trace metal cycling and biodiversity richness in ultramafic soils, as well as the environmental consequences of ultramafic rock mining, can offer valuable insights for assessing the ecological risks associated with CESW. Ultramafic soils are naturally rich in trace metals (e.g. Cr, Ni, Mn, and Co), possess a low calcium (Ca) to magnesium (Mg) ratio, and are deficient in nutrients and organic matter (Kumar and Maiti, 2013; Vithanage et al., 2019; Kierczak et al., 2021). In line with our findings, these soils exhibit a substantially higher bioavailable fraction of Ni (0.1 – 13 mmol kg^{-1}) compared to Cr (0.0004 – 0.3 mmol kg^{-1}) (Vithanage et al., 2019). However, under oxidizing conditions, chromite weathering in these soils could be a significant source of the highly mobile and toxic Cr(VI) to the environment (Pattnaik and Equeenuddin, 2016; Vithanage et al., 2019; Kierczak et al., 2021). The activity of soil enzymes, which play a vital role in organic matter decomposition and nutrient cycling, decreased in proximity to chromite mining sites and was significantly inversely correlated with total concentrations of metals in the soil (Pattnaik and Equeenuddin, 2016). Moreover, ultramafic soils often exhibit a low productivity, yet they can support endemic extremophile plant species and diverse bacterial communities that have adapted to thrive in these metal-rich environments (Kumar and Maiti, 2013; Vithanage et al., 2019; Kierczak et al., 2021; Lu et al., 2022). Nonetheless, the accumulation of metals in food crops and water sources could pose a chronic risk to human health (Vithanage et al., 2019; Naz et al., 2020; Kierczak et al., 2021).

While previous studies on ultramafic soils and mining sites have primarily focused on various plant species to assess their potential for phytomining via hyperaccumulation

(Vithanage et al., 2019), Søndergaard (2013) monitored metal bioaccumulation in lichens (*Flavocetraria nivalis*), seaweeds (*Fucus vesiculosus*), mussles (*Mytilus edulis*) and fish (*Myoxocephalus Scorpius*) at various distances (0 to 17 km) from the open pit olivine mine at Seqi in Southwest Greenland, both before (2004), during (2005 – 2009), and after (2009 – 2011) its operation. Results showed that lichens up to 5 km from the mining site exhibited significantly elevated metal concentrations (especially Ni, Cr, Fe, and Co) relative to pre-mining levels, with increases up to 130 times caused by dust dispersion. Concentrations of Ni and Cr were also moderately elevated in seaweeds and mussels (up to a factor of 7) in close vicinity (<1 km) of the mine. In contrast, fish did not show significant metal accumulation. After the mine closed, significant decreases in metal concentrations were observed in lichens, seaweeds and mussels. By 2011, metal concentrations were only significantly elevated compared to pre-mining levels in lichens close (<1 km) to the mining site. Overall, Søndergaard (2013) concluded that the environmental impact of the olivine mine at Seqi was relatively low compared to other mining operations in Greenland (e.g. Pb-Zn mine in Maarmorilik) where significant contamination of the marine environment persisted for decades after mine closure. collectively, these studies illustrate the long-term effects of ultramafic rock weathering on natural ecosystems, potential risk to human health, and underscore the importance of a comprehensive examination of the ecological impacts associated with CESW.

The climate change mitigation and ecosystem benefits from coastal enhanced olivine weathering should ideally also be taken into account when setting olivine application guidelines. The determination of the optimal olivine grain size and concentration should be site-specific, considering the significant variation in physical, chemical, and biological conditions among coastal sites. Therefore, a comprehensive characterization of the olivine application area before deployment, coupled with a profound understanding of olivine's environmental fate and ecological effects, is essential for deriving robust, site-specific olivine application guidelines.

Overall, our work provides valuable insights in the possible adverse ecological impacts of coastal enhanced olivine weathering and highlights the need for additional data (discussed throughout section 7.3) to derive accurate site-specific olivine application guidelines. A portfolio of CDR techniques will be needed to achieve the gigaton scale atmospheric CDR that is needed to keep global warming below the Paris agreement target of 2°C, ideally 1.5 °C (Minx et al., 2018; Rueda et al., 2021). Therefore, research on the CO_2 sequestration potential and environmental safety of silicates other than dunite (e.g. basalt and wollastonite) for coastal enhanced silicate weathering seems advised. Finally, it is important to reiterate that CDR techniques are too slow, expensive and technically uncertain to replace the urgent need for comprehensive and rapid decarbonization (Smith et al., 2016). Therefore, the primary focus for limiting global warming must remain on immediate and aggressive reductions in CO_2 emissions, with the implementation of CDR techniques as a secondary, albeit necessary, measure.

7.4 Overall conclusions and future possibilities

Coastal enhanced olivine weathering is a considered scalable atmospheric CO_2 removal technique for climate change mitigation. However, its efficiency and ecological impacts remain uncertain due to limited experimental data. In this work, we investigated how hydrodynamic processes affect the CO_2 sequestration potential and evaluated possible adverse ecological effects of olivine and its associated trace metals on marine biota. Our weathering experiments clearly demonstrated the significant enhancement of alkalinity release from marine sediment through advective pore water flushing. Calculated dissolution rate constants for continuously rotated olivine in seawater were consistent with previous studies and 8 to 19 times higher than those obtained under stagnant conditions. The observed CO_2 sequestration efficiency aligned with theoretical estimates for the experimental conditions, indicating equilibrium of the seawater carbonate system with the atmosphere and limited secondary mineral precipitation, primarily as iron(hydr)oxides which inevitably form during fayalite dissolution under oxic conditions. However, when olivine was mixed with marine sediment and subjected to continuous

current, mineral dissolution and associated CO_2 sequestration were unexpectedly low. Unfortunately, we could not definitively identify the cause for the low olivine reactivity based on the available data. Therefore, additional large-scale studies are imperative to further assess marine olivine reactivity and potential CO_2 sequestration under conditions that closely mimic natural coastal systems.

The accumulation of trace metals in marine systems during large-scale coastal enhanced olivine weathering raises potential toxicological concerns, but has received little research attention. We concluded that sedimentary metal accumulation could restrict the environmentally safe olivine application concentration based on existing marine environmental quality standards for Ni and Cr. However, the conclusion drawn from this preliminary risk assessment involves considerable uncertainty due to lack of information on *in situ* olivine Ni and Cr release rates, environmental fate, bioavailability, and potential mixture toxicity. Hence, in-depth experimental studies are warranted.

In all our olivine experiments, Ni accumulation in the seawater dissolved phase exceeded stoichiometric expectations, while dissolved Cr accumulation consistently fell below anticipated levels, likely due to its release in a particulate form with low bioavailability. This lower Cr compared to Ni bioavailability was confirmed during acute (24 to 72 h) and chronic (35 d) exposures of the marine amphipod *Gammarus locusta* to different olivine grain sizes and concentrations. Amphipods ingested large amounts of olivine grains and accumulated trace metals in a grain size and concentration dependent manner. The importance of olivine ingestion as a trace metal exposure pathway could not be clearly resolved and requires additional research as specified in section 7.3.

Changes in surficial sediment physicochemistry may lead to certain species avoiding olivine-rich sediment patches, potentially impacting coastal species richness in the long term. Our experiments with the marine amphipod *G. locusta* and gastropod *Littorina littorea* revealed significant avoidance of pure olivine (83 – 332 µm) due to positive scototaxis and possible trace metal exposure avoidance, respectively. However, relatively

coarse olivine mixed with natural sediment at realistic coastal application concentrations (3 and 30% w/w olivine) did not result in significant avoidance. Overall, experimental findings suggest that olivine application sites are unlikely to be avoided by *G. locusta* and *L. littorea* and that avoidance is influenced by local environmental parameters such as food and shelter availability.

Chronic exposure to various concentrations of fine-grained (3 – 99 µm) olivine mixed with natural marine sediment resulted in reduced amphipod survival, growth, and reproduction, likely due to metal-induced oxidative stress and disruption of major cation (Ca^{2+}, Na^+, K^+) homeostasis. A very low PNEC of 0.01% w/w olivine was derived from the highest no observed effect concentration of 1% w/w olivine for reproduction, using an arbitrary assessment factor of 100. This low PNEC value underscores the need for additional marine olivine toxicity data to improve ecological risk assessment of coastal enhanced olivine weathering. Finally, it is important to consider factors such as trace metal bioavailability, potential mixture toxicity, and ecosystem benefits from olivine spreading when establishing robust, site-specific olivine application guidelines.

Supplementary information

Appendix A: Chapter 1

Table A1: Chronic marine nickel (Ni) toxicity data (NOEC and EC10 values) for ecologically relevant endpoints used to construct a species sensitivity distribution. N.R. = not reported.

Taxon	Species	Life stage	Duration	Toxicity measure	Ni concentration (μmol L^{-1})	Ni concentration in SSD (μmol L^{-1})	Reference
Crustaceans	*Acartia danae*	Adult	4 d	NOEC (survival)	5.74	5.74	(Panneerselvam et al., 2018)
Crustaceans	*Acartia sinijensis*	Larvae	3 d	EC10 (development)	0.094	0.094	(Gissi et al., 2018)
Cnidaria	*Acropora digitifera*	Gametes	5 h	NOEC (fertilization)	16.0	24.7	(Gissi et al., 2017)
		Gametes	5 h	EC5 (fertilization)	28.6		
		Gametes	5 h	EC10 (fertilization)	34.1		
Cnidaria	*Aiptasia pulchella*	Adult	28 d	EC10 (juvenile production)	1.12	2.10	(Howe et al., 2014)
		Adult	28 d	EC10 (offspring production)	4.51		
		Adult	28 d	NOEC (juvenile production)	4.48		

		Adult	28 d	NOEC (offspring production)	4.48		
Crustaceans	*Americamysis bahia*	N.R.	7 d	NOEC (survival)	3.63	1.04	ECOTOX Knowledgebase (Gentile et al., 1982)
		Juvenile	36 d	NOEC (reproduction)	1.04		
Crustaceans	*Amphibalanus amphitrite*	Nauplii	4 d	EC10 (metamorphosis)	1.14	1.14	(Gissi et al., 2018)
Fish	*Atherinops affinis*	Larvae	40 d	NOEC (survival)	55.2	58.2	(Hunt et al., 2002)
		Larvae	40 d	EC10 (survival)	61.3		
Algae	*Ceratoneis closterium*	-	3 d	EC10 (growth rate)	104	52.3	(Gissi et al., 2016)
		-	3 d	EC10 (growth rate)	49.4		
		-	3 d	NOEC (growth rate)	67.6		(Gissi et al., 2018)
		-	3 d	EC10 (growth rate)	55.4		
		-	3 d	NOEC (growth rate)	27.4		
		-	3 d	EC10 (growth rate)	43.3		
Algae	*Champia parvula*	Adult	10 d	EC10 (reproduction)	2.45	2.45	(DeForest and Schlekat, 2013)
Algae	*Coscinodiscus centralis*	-	4 d	NOEC (growth rate)	2.04	2.04	(Panneerselvam et al., 2018)

Molluscs	*Crassostrea gigas*	Embryo	2 d	EC10 (development)	7.3	7.3	(DeForest and Schlekat, 2013)
Algae	*Cryothecomonas armigera*	-	24 d	EC10 (growth rate)	20.8	20.8	(Koppel et al., 2017)
Bacteria	*Cyanobium sp.*	-	3 d	EC10 (growth rate)	63.0	63.0	(Alquezar and Anastasi, 2013)
Fish	*Cyprinodon variegatus*	Larvae	28 d	EC10 (growth)	354	354	(DeForest and Schlekat, 2013)
Echinodermata	*Dendraster excentricus*	Embryo	2 d	EC10 (development)	3.3	3.3	(DeForest and Schlekat, 2013)
Echinodermata	*Diadema antillarum*	Embryo	40 h	EC10 (development)	0.049	0.049	(Bielmyer et al., 2005)
Echinodermata	*Diadema savignyi*	Embryo	2 d	NOEC (development)	0.40	0.40	(Rosen et al., 2015)
Algae	*Dunaliella tertiolecta*	-	3 d	EC10 (growth rate)	306	306	(DeForest and Schlekat, 2013)
Algae	*Glenodinium halli*	-	"chronic"	NOEC (growth rate)	0.68	0.68	(NIVA, 2007)
Algae	*Gracilaria tenuistipitata*	-	4 d	NOEC (growth rate)	37.5	37.5	(Haglund et al., 1996)
Molluscs	*Haliotis rufescens*	Embryo	22 d	EC10 (metamorphosis)	0.62	0.37	(Hunt et al., 2002)

		Juvenile	14 d	NOEC (shell growth)	0.37		
Crustaceans	*Idotea balthica*	-	>21 d	EC0 (survival)	25.6	25.6	(El-Nady and Atta, 1996)
Algae	*Isochrysis galbana*	-	"chronic"	NOEC (growth rate)	0.68	0.68	(NIVA, 2007)
Algae	*Isochrysis sp.*	-	3 d	EC10 (growth rate)	55.2	55.2	(Gissi et al., 2016)
Algae	*Macrocystis pyrifera*	Zoospores	2 d	EC10 (germination)	8.4	1.6	(DeForest and Schlekat, 2013)
		Zoospores	2 d	EC10 (growth)	1.6		
Crustaceans	*Melita plumulosa*	Adult	4 d	NOEC (survival)	73.4	14.7	(King et al., 2006)
		Juvenile	4 d	NOEC (survival)	14.7		
		Adult	10 d	NOEC (survival)	36.3		
Fish	*Menidia beryllina*	-	7 d	NOEC (survival)	128	128	ECOTOX Knowledgebase
Molluscs	*Monodonta labio*	Juvenile	30 d	EC10 (survival)	0.97	0.46	(Wang et al., 2020)
		Juvenile	30 d	EC10 (growth rate)	0.58		
		Juvenile	30 d	EC10 (shell length growth)	1.6		
		Juvenile	30 d	NOEC (growth rate)	0.37		
		Juvenile	30 d	NOEC (shell length growth	0.92		

Crustaceancs	*Mysidopsis intii*	Juvenile	28 d	NOEC (growth)	0.17	0.35	(Hunt et al., 2002)
		Juvenile	28 d	EC10 (growth)	0.77		
Molluscs	*Mytilus galloprovincialis*	Embryo	2 d	EC10 (development)	4.6	4.6	(DeForest and Schlekat, 2013)
Molluscs	*Mytilus trossolus*	Embryo	2 d	EC10 (development)	1.0	1.0	(Nadella et al., 2009)
Molluscs	*Nassarius dorsatus*	Larvae	4 d	EC10 (growth)	1.1	1.1	(Gissi et al., 2018)
Annelida	*Neanthes arenaceodentata*	Juvenile	90 d	EC10 (reproduction)	0.38	0.38	(DeForest and Schlekat, 2013)
Algae	*Odontella mobiliensis*	-	4 d	NOEC (growth rate)	0.27	0.27	(Panneerselvam et al., 2018)
Crustaceans	*Oithona similis*	Adult	4 d	NOEC (survival)	8.0	8.0	(Panneerselvam et al., 2018)
Fish	*Oryzias melastigma*	Juvenile	21 d	EC10 (survival)	28.3	20.1	(Wang et al., 2020)
		Embryo	25 d	NOEC (survival)	179		(Liu et al., 2021)
		Embryo	25 d	NOEC (development)	20.1		
		Larvae	5 d	NOEC (survival)	142		
Echinodermata	*Paracentrotus lividus*	Embryo	3 d	EC10 (shell development)	2.4	1.42	(Novelli et al., 2003)

		Embryo	3 d	EC10 (development)	1.5		
		Embryo	1 h	NOEC (reproduction)	8.5		
		Embryo	3 d	NOEC (development)	0.85		
Algae	*Phaeocystis antarctica*	-	20 d	NOEC (growth rate)	18.2	18.2	(Gissi et al., 2015)
Cnidaria	*Platygyra daedalea*	Gametes	5 h	NOEC (reproduction)	15.7	15.7	(Gissi et al., 2017)
Algae	*Skeletonema costatum*	-	3 d	EC10 (growth rate)	4.5	5.0	(DeForest and Schlekat, 2013)
				EC10 (growth rate)	3.2		
				EC10 (growth rate)	13.2		
				EC10 (growth rate)	2.1		
				EC10 (growth rate)	11.3		
Echinodermata	*Strongylocentrotus purpuratus*	Embryo	2 d	EC10 (development)	5.7	5.7	(DeForest and Schlekat, 2013)
Algae	*Symbiodinium sp*	-	3 d	NOEC (growth rate)	5.3	5.3	(Gissi, 2019)
Crustaceans	*Tigriopus japonicus*	whole life-cycle	4 d	Survival	39.7	0.64	(Wang et al., 2020)
		Nauplii	20 – 30 d	EC10 (survival)	8.2		
		Maturation	20 – 30 d	EC10 (survival)	0.75		

	stage				
	Whole life-cylce	20 – 30 d	EC10 (population growth)	0.49	
	Nauplii	20 – 30 d	NOEC (survival)	1.7	
	Maturation stage	20 – 30 d	NOEC (survival)	0.85	
	Whole life-cylce	20 – 30 d	NOEC (population growth)	0.85	
Algae	*Tisochrysis lutea*	-	3 d	NOEC (growth rate)	4.3	(Gissi, 2019)
		-	3 d	EC10 (growth rate)	5.6	

Table A2: Chronic marine hexavalent chromium (Cr(VI)) toxicity data (NOEC and EC10 values) for ecologically relevant endpoints used to construct a species sensitivity distribution. N.R. = not reported.

Taxon	Species	Life stage	Duration	Toxicity measure	Cr(VI) concentration (μmol L^{-1})	Cr(VI) concentration in SSD (μmol L^{-1})	Reference
Crustaceans	*Acartia tonsa*	Egg	5 d	NOEC (development)	6.80	6.80	(Andersen et al., 2001)
Crustaceans	*Allorchestes*	Juvenile	40 d	NOEC (growth)	4.8	4.8	(Ahsanullah and

	compressa						Williams, 1991)
		Juvenile	40 d	NOEC (mortality)	4.8		
		Juvenile	40 d	NOEC (reproduction)	4.8		
Crustaceans	*Americamysis bahia*	Juvenile	7 d	NOEC (growth)	30.8	1.7	(Jop, 1989)
		Juvenile	7 d	NOEC (reproduction)	30.8		
		Juvenile	7 d	NOEC (survival)	30.8		
		Juvenile	7 d	NOEC (reproduction)	30.8		
		Juvenile	7 d	NOEC (survival)	11.5		
		Juvenile	7 d	NOEC (growth)	11.5		
		Juvenile	7 d	NOEC (reproduction)	8.1		(Goodfellow and Rue, 1989)
		Juvenile	7 d	NOEC (reproduction)	6.2		
		Post-larvae	38 d	NOEC (survival)	17.5		(Lussier et al., 1985)
		Post-larvae	38 d	NOEC (reproduction)	1.7		
Echinodermata	*Arbacia punctulata*	Gametes	1 h	NOEC (fertilization)	2404	2859	(Jop, 1989)
		Gametes	1 h	NOEC (fertilization)	4808		
		Gametes	1 h	NOEC (fertilization)	2404		
		Gametes	1 h	NOEC (fertilization)	2404		

Crustaceans	*Artemia salina*	7 d Nauplii	15 d	NOEC (growth)	10.0	10.0	(Umarani et al., 2012)
Annelida	*Capitella capitata*	Larvae	150 d	NOEC (survival)	0.96	0.96	(Reish, 1981)
		Larvae	150 d	NOEC (reproduction)	0.96		
Algae	*Champia parvula*	-	2 d	NOEC (reproduction)	0.0019	0.019	(Jop, 1989)
		-	2 d	NOEC (reproduction)	0.19		
Molluscs	*Chlamys asperrima*	Larvae	2 d	NOEC (development)	10.2	10.2	(Krassoi et al., 1997)
Ascidiacea	*Ciona intestinalis*	Larvae	70 h	NOEC (development)	78.8	78.8	(Bellas et al., 2004)
		Gametes	20 h	NOEC (development)	158		
Bacteria	*Cyanobium sp.*	-	3 d	EC5 (growth)	34.0	36.5	(Yamagishi et al., 2016)
		-	3 d	EC10 (growth)	42.1		
		-	3 d	NOEC (growth)	33.8		
Fish	*Cyprinodon variegatus*	Larvae	7 d	NOEC (survival)	271	74.2	(Jop, 1989)
		Larvae	7 d	NOEC (growth)	48.1		
		Larvae	7 d	NOEC (survival)	144		(McCulloch and Rue, 1989)
		Larvae	7 d	NOEC (survival)	346		
		Larvae	7 d	NOEC (growth)	71.2		

		Larvae	7 d	NOEC (growth)	144		
		Larvae	7 d	NOEC (growth)	62.5		
		Larvae	7 d	NOEC (survival)	298		
		Larvae	7 d	NOEC (survival)	346		(Hutchinson et al., 1994)
Annelida	*Dinophilus gyrociliatus*	Juvenile	7 d	NOEC (reproduction)	1.9	1.9	(Jop, 1989)
		Juvenile	7 d	NOEC (survival)	19.2		
		Juvenile	7 d	NOEC (survival)	19.2		
Algae	*Ecklonia radiata*	Zoospore	2 d	NOEC (germination)	287	152	(Bidwell et al., 1998)
		Zoospore	2 d	NOEC (growth)	152		
Algae	*Gracilaria tenuistipitata*	-	4 d	NOEC (growth rate)	6.5	6.5	(Haglund et al., 1996)
Echinodermata	*Heliocidaris tuberculata*	Larvae	3 d	NOEC (development)	8.8	8.8	(Doyle CJ 1999)
Crustaceans	*Idotea balthica*	N.R.	>21 d	EC0 (survival)	28.8	28.8	(El-Nady and Atta, 1996)
Annelida	*Neanthes arenaceodentata*	30-40 segments	>45 d	NOEC (reproduction)	0.32	0.32	(Oshida and Word, 1982)
Algae	*Olisthodiscus*	-	10 d	NOEC (growth)	0.96	0.96	(Mahoney, 1982)

	luteus						
Fish	*Oncorhynchus kisutch*	Juvenile	3 d	NOEC (survival)	612	342	(Holland, 1960)
		Juvenile	5 d	NOEC (survival)	342		
		Juvenile	11 d	NOEC (survival)	342		
Algae	*Skeletonema costatum*	-	2 d	NOEC (growth rate)	3.8	3.8	(Missimer et al., 1989)
		-	3 d	NOEC (growth rate)	3.8		
		-	4 d	NOEC (growth rate)	15.4		
Algae	*Thalassiosira pseudona*	-	15 d	NOEC (growth rate)	0.19	0.19	(Frey et al., 1983)
Crustaceans	*Tisbe battagliai*	Adult	8 d	NOEC (survival)	19.2	6.2	(Hutchinson et al., 1994)
		Adult	8 d	NOEC (reproduction)	6.2		
		Nauplii	8 d	NOEC (survival)	6.2		
Crustaceans	*Tisbe holothuriae*	F2 females	22.5 d	NOEC (survival)	9.6	9.6	(Verriopoulos and Dimas, 1988)

263

Appendix B: Chapter 2

B.1 ADDITIONAL METHODS

B.1.1 Elemental composition of dunite sand

The elemental composition for the forsterite dunite sand used in the experiments is shown in Table B.1. The elemental composition was determined in three different ways: the composition provided by the manufacturer, and also obtained by digestion and ICP-OES analysis following two separate protocols.

Table B.1: Molar elemental concentrations (mol mol^{-1} olivine) of the experimental olivine. Concentrations provided by the manufacturer (Sibelco) and analysed by ICP-OES after digestion via an alkali fusion (N = 1) or chromite ore protocol (N = 5, mean ± S.D.) are provided. Element concentrations for dunite sand digested according to the chromite ore digestion protocol were used for calculations in the main text (Table 2.2) and were calculated assuming a Si concentration of 1.03 mol mol^{-1} olivine.

Digestion protocol	Chromite ore (N = 5)	Alkali fusion	Manufacturer
Element	Molar concentration (mol mol^{-1} olivine)		
Mg	1.79 ± 0.04	1.70	1.76
Si	N.A.	1.03	1.00
Fe	0.130 ± 0.002	0.13	0.13
Cr	0.0083 ± 0.0004	0.0070	0.010
Ni	0.0061 ± 0.0002	0.0065	0.0062
Al	0.0043 ± 0.0002	0.023	0.012
Mn	0.0018 ± 0.00004	0.0019	N.A.
K	N.A.	0.00094	N.A.
Ca	0.00065 ± 0.00010	0.0050	N.A.
Co	0.00045 ± 0.00001	N.A.	N.A.
Ti	N.A.	0.00018	N.A.
Zn	0.00014 ± 0.000002	N.A.	N.A.

Protocol 1. A modified chromite ore microwave-assisted acid digestion procedure was followed (CEM Microwave Sample Preparation Note 5OS-47). Briefly, 0.1 g of dried (48 h at 60 °C) sand was weighed and added to 80 mL quartz pressure vessels (CEM Corporation). Next, 2.6 mL of Ultrapure ~85% orthophosphoric acid (Honeywell Chemicals) and 1.4 mL of ≥96% sulfuric acid (Merck) were added. Subsequently the vessels were heated at 240 °C for 30 minutes in a Discover SP-D 80 microwave (CEM Corporation). Afterwards, the vessels were allowed to cool down and 2 mL of TraceMetal™ Grade 67-69% nitric acid (Fisher Scientific) was added. Next the vessels were heated at 240 °C for 15 minutes. Afterwards the solution was transferred into 50 mL polypropylene (PP) vials and ultrapure Milli-Q water was added up to the 50 mL mark. The vials were centrifuged for 5 minutes at 3000 rpm and the supernatant was subsequently transferred to new 50 mL tubes before analysis via ICP-OES (iCAP 6300 Duo, Thermo Scientific). For quality control, reference NIM-D dunite (SARM-6, MINTEK) and procedural blanks were included during processing and analysis of the samples. Element recoveries (ranging from 72 to 93%) were acceptable for all certified elements except Si (~0.4%). A maximum relative standard deviation (RSD) of 5% was allowed for the measurements.

Protocol 2. Dunite sand was dissolved via a modified alkaline fusion method (ISO 14869-2:2002). Briefly, about 0.4 g of dried milled (<0.4 mm) sample was weighted and transferred into a platinum (Pt) crucible. The crucible was placed in a furnace and pre-ignited at 850 °C for 30 minutes. After the crucible cooled down to room temperature, the ignited sample was thoroughly mixed with 2 g of lithium metaborate and fused for 15 minutes at 950 °C in a pre-heated muffle furnace. The melt was allowed to cool down for 12 hours after which the crucible was immersed in a 100 ml beaker containing 70-80 ml of 4% nitric acid. The solution was stirred with a magnetic stirrer for 3 to 4 hours until the solid phase dissolved. Afterwards, the solution was made up to 100 ml, filtered through prewashed (with 10% HNO_3) 0.45 μm pore size filter paper and stored for analysis via ICP-OES (720-ES, Agilent).

Calculation of elemental concentrations. Concentrations C (µg L^{-1}) obtained via ICP-OES were converted to elemental concentrations C_m expressed in wt% as follows

$$C_m = \frac{CV}{m_{\text{dunite}}} 10^{-4}$$
[B.1]

Where V is total sample volume (L), m_{dunite} is the mass of digested dunite sand (g), and 10000 is the factor to convert from µg g^{-1} to wt%.

Calculation of metal oxide concentrations. Conversion of elemental concentrations C_m (wt%) to metal oxide concentration C_{mo} (wt%) was done via

$$C_{mo} = \frac{C_m}{\frac{M_m}{M_m + M_O}}$$
[B.2]

In this, M_m and M_O represent the molar masses (g mol^{-1}) of the metal atoms and oxygen atoms present in the considered metal oxide. The metal oxide concentration C_{mo} (wt%) could be converted to a molar oxide concentration C_{MO} (mol oxide g^{-1} olivine) based on the metal oxide molar mass M_{MO} (g mol^{-1}) ($C_{MO} = C_{mo}/M_{MO}$).

Finally, the molar oxide concentrations C_{MO_i} (mol oxide g olivine^{-1}) for a given metal i could be converted to a molar elemental concentrations C_{M_i} (mol mol^{-1} olivine) via

$$C_{M_i} = \frac{4 C_{MO_i} N_{C_i}}{\sum_{i=1}^{n} C_{MO_i} N_{O_i}}$$
[B.3]

Where N_{C_i} is the amount (mol) of metal cations for a given metal oxide i, n is the total amount of metal oxides for olivine, 4 is the theoretical amount of oxygen atoms in one mole of olivine (mol O mol^{-1} olivine), and N_{O_i} is the amount (mol) of oxygen atoms for a given metal oxide.

B.1.2 Stoichiometric model of olivine

Stoichiometric coefficients ν_i (expressed in µmol µmol^{-1} olivine) are calculated below and provided in Table B.2. Mineralogical composition of the dunite sand was analysed using the TIMA software of the Tescan SEM (Hrstka et al., 2018). The system operated in high-vacuum mode at 25 kV and a beam current of 22 nA. Data were collected using high resolution mapping with 5 µm pixel spacing. Dunite sand was composed of 90.54 wt% olivine and 9.46 wt% other minerals of which enstatite was the most abundant (6.02 wt%) (Table 2.2). Forsterite (Mg_2SiO_4) content Fo (%) of the olivine was calculated from the molar elemental concentrations C_{M_i} (mol mol^{-1} olivine) of Fe and Mg as

$$Fo = \frac{C_{M_{Mg}}}{(C_{M_{Mg}}+C_{M_{Fe}})} 100 \qquad [B.4]$$

Which resulted in a forsterite content of 93.4%. The fayalite (Fe_2SiO_4) content Fa (%) could then be calculated by subtracting the Fo from 100% (Fa = 100% – Fo), resulting in a fayalite content of 6.6%.

Table B.2: Stoichiometric coefficients ν_i (µmol µmol^{-1} olivine) for various compounds i (TA, DIC, DSi, and DNi) of the experimental olivine. The ν_i values were derived from the elemental and mineralogical data as described in the text.

Compound	Stoichiometric coefficient ν_i (µmol µmol^{-1} olivine)
TA	3.73
DIC	3.06
DSi	1.00
DNi	0.0061

Based on the idealized complete dissolution reaction of olivine, 4 µmol of alkalinity are released upon dissolution of 1 µmol of olivine (i.e. through consumption of 4 µmol of protons).

$$\text{Mg}_x\text{Fe}_{2-x}\text{SiO}_4 + 4\text{H}^+ \rightarrow x\text{Mg}^{2+} + (2-x)\text{Fe}^{2+} + \text{H}_4\text{SiO}_4 \qquad\qquad [\text{B.5}]$$
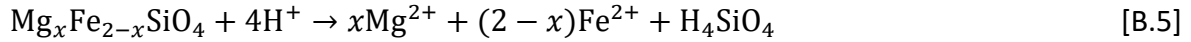
Yet, under oxic conditions, ferrous iron will likely be immediately oxidized (Eq. B.6) resulting in the consumption of 2 μmol of TA (i.e. production of 2 μmol of protons) upon precipitation of 1 μmol iron(III) (hydr)oxide.

$$\text{Fe}^{2+} + 0.25\text{O}_2 + 1.5\text{H}_2\text{O} \rightarrow FeOOH + 2\text{H}^+ \qquad\qquad [\text{B.6}]$$
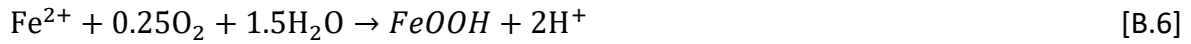
As a result, for olivine with a fayalite fraction of 2 - x = 0.133 (Eq. B.5), the TA production reduces to $v_{\text{TA}} = 4 - 2(2 - x) = 3.73$ μmol μmol^{-1} olivine.

The stoichiometric accumulation rate of dissolved Inorganic carbon (DIC) is defined as

$$v_{\text{DIC}} = (\delta DIC/\delta TA)_{pCO_2} v_{\text{TA}} \qquad\qquad [\text{B.7}]$$

The seawater CO_2 sequestration efficiency $(\delta DIC/\delta TA)_{pCO_2}$ specifies the increase in seawater DIC for each mol of TA increase. It is dependent on the atmospheric partial CO_2 pressure (pCO$_2$), salinity, temperature, and chemical composition of the seawater (Hofmann et al., 2009). The theoretical CO_2 sensitivity for our experimental conditions (T = 15 °C, S = 33.0 ‰, TA = 2550 − 5170 μmol L^{-1}, and pCO$_2$ = 420 ppmv) computed using the AquaEnv R package is equal to 0.82 ± 0.016 (Hofmann et al., 2010). Therefore, the expected amount of CO_2 sequestered upon dissolution of 1 μmol of olivine is v_{DIC} = 0.82 * 3.73 = 3.06 μmol DIC released per μmol of olivine dissolved.

The stoichiometric coefficients v_i for DNi and DSi are equal to the molar elemental concentrations (Table B.1) derived from the chromite ore protocol (v_{DNi} = 0.0061 μmol Ni μmol^{-1} olivine) and manufacturer (v_{Si} = 1 μmol Si μmol^{-1} olivine), respectively.

B.1.3 Dunite mass loss and specific surface area

Table B.3: Initial dunite mass (g) added to the experimental bottles at day 0, and recovered dunite mass at day 70 for the different olivine treatments : stagnant (SO), low rotation (LRO), and high rotation (HRO) (numbers 1-2-3 indicate different replicates). Absolute (g) mass loss and relative (%) mass loss at the end of the experiment are also shown.

Treatment – replicate	Dunite mass day 0 (g)	Dunite mass day 70 (g)	Absolute mass loss (g)	Relative mass loss (%)
SO – 1	149.5303	146.9229	2.6074	1.75
SO – 2	149.5313	147.1311	2.4002	1.61
SO – 3	149.5279	147.1113	2.4166	1.62
LRO – 1	149.5262	145.8547	3.6715	2.46
LRO – 2	149.5305	146.4817	3.0488	2.04
LRO – 3	149.5260	146.4282	3.0978	2.07
HRO – 1	149.5292	145.8775	3.6517	2.44
HRO – 2	149.5272	145.3903	4.1369	2.77
HRO – 3	149.5310	145.6556	3.8754	2.59

Table B.4: Geometric and B.E.T specific surface area (A_{GEO} and A_{BET}, expressed in $m^2\,g^{-1}$) of dunite from the stagnant, low rotation, and high rotation treatment. Mean ± standard deviation (N = 5) values for the fresh (day 0) and weathered (day 70) dunite are shown.

Treatment	A_{GEO} day 0 ($m^2\,g^{-1}$)	A_{GEO} day 70 ($m^2\,g^{-1}$)	A_{BET} day 0 ($m^2\,g^{-1}$)	A_{BET} day 70 ($m^2\,g^{-1}$)
Stagnant olivine	0.0161 ± 0.0016	0.0146 ± 0.00025	0.9 ± 0.1	N.A.
Low rotation olivine		0.0145 ± 0.00011		N.A.

High rotation olivine	0.0144	±	0.33 ± 0.03	
	0.00019			

The geometric surface area A_{GEO} (m² g⁻¹) of the experimental dunite sand is shown in Table B.4. It was calculated from the different grain diameter classes i (n = 22, between 1.5 and 330 μm grain diameter) of the volumetric particle size distribution (Figure 2.5A) as

$$A_{\text{GEO}} = \Sigma_{i=1}^{n} \left(\frac{\frac{\varphi_i * V_{\text{dunite}}}{V_{\text{grain}_i}} * A_{\text{grain}_i}}{m_{\text{dunite}}} \right) \quad [\text{B.8}]$$

Where φ_i is the volume fraction of olivine of a certain grain diameter class i (e.g. 180 – 200 μm), V_{dunite} (cm³) the total olivine volume in the HDPE bottles calculated from the olivine mass m_{dunite} (g) and the mineral density ρ_{dunite} (g cm⁻³) (V_{dunite} = $M_{\text{dunite}}/\rho_{\text{dunite}}$). V_{grain_i} and A_{grain_i} are the volume (cm³) and surface area (m²) of a single olivine grain calculated from the average grain diameter of a certain grain diameter class (e.g 190 μm for 180 – 200 μm) assuming perfect spherical particles.

B.1.4 North Sea water chemical composition and salinity
Table B.5: Chemical composition of filtered (<0.2 μm) North Sea water in the rock tumbler experiment. The mass concentrations were derived by HR-ICP-MS analysis (N = 4, mean ± standard deviation (S.D.)).

Major element	Molar mass (g mol⁻¹)	Mass concentration (mg L⁻¹)	Molar concentration (mmol L⁻¹)
Na	22.99	10298 ± 264	448 ± 11
Mg	24.31	1178 ± 38	49 ± 1.6
Ca	40.08	417 ± 15	10 ± 0.37
K	39.10	369 ± 10	9.4 ± 0.27
Si	28.09	0.93 ± 0.17	0.035 ± 0.0061

Fe	55.85	0.029 ± 0.0063	0.52 ± 0.11
Cl (#)	35.45	18635 ± 478	526 ± 28
SO$_4$ (#)	96.06	2648 ± 68	28 ± 0.7
Minor element	**Molar mass (g mol^{-1})**	**Mass concentration (µg L^{-1})**	**Molar concentration (µmol L^{-1})**
Ni	58.69	4.6 ± 2.3	0.078 ± 0.040
Cr	52.00	13 ± 9.1	0.25 ± 0.18
Mn	54.94	72 ± 26	1.3 ± 0.47
Cu	63.55	0.18 ± 0.085	0.0028 ± 0.0013
Cd	112.4	2.8 ± 0.23	0.025 ± 0.0021
Zn	65.38	15 ± 3.8	0.23 ± 0.057
Pb	207.2	0.19 ± 0.13	0.00089 ± 0.00065

Chloride (Cl) and sulphate (SO$_4$) concentrations were not analytically determined, but derived from the chemical composition of natural seawater (Hem, 1985) based on measured Na concentrations.
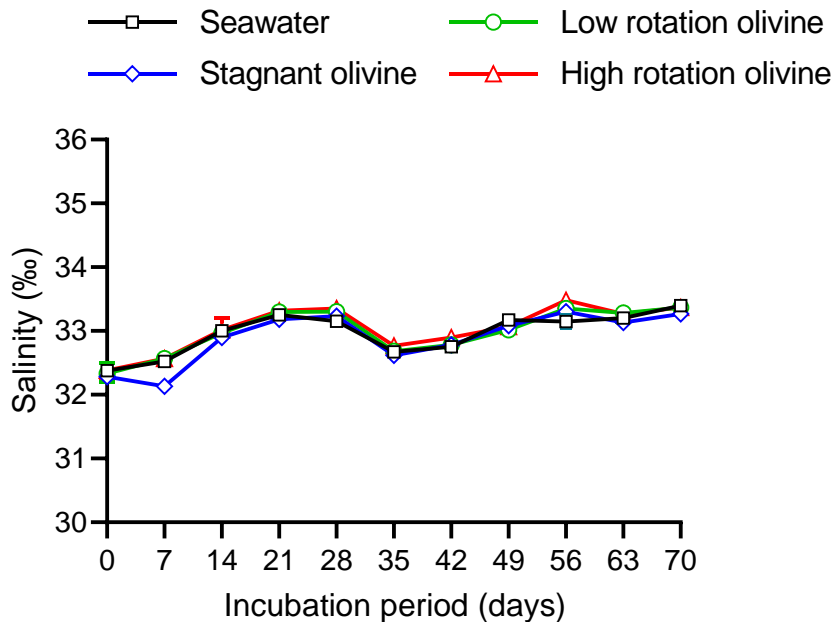
Figure B.1: Weekly evolution of seawater salinity in the rock tumbler experiment. Mean values with range for the olivine treatments (N = 3) and seawater control (N = 2) are shown.

B.1.5 Kinetic box model information

Olivine dissolution, secondary mineral formation and temporal evolution of dissolved Mg, Si, Ca, Fe, and TA were modelled according to the kinetic box model by Fuhr et al. (2022). All relevant equations used for the model calculations can be found below. Changes in chemical species were calculated using differential equations:

$$\frac{dC}{dt} = \varphi_{ol} r_{ol} - \sum_i \varphi_{m_i} r_{m_i} - r_s (C - C_{in})$$ [B.9]

Where C is the dissolved concentration of the considered species (µmol L^{-1}), t is the tumbling time (d), φ_{ol} is the species abundance in olivine (ol) expressed in µmol µmol^{-1} olivine, r_{ol} is the olivine dissolution rate (µmol L^{-1} d^{-1}), r_{mi} is the precipitation rate of secondary mineral i (µmol L^{-1} d^{-1}) and φ_{mi} is the species abundance in the respective secondary mineral (µmol µmol^{-1} olivine). Weekly water renewal was considered by the sampling rate (r_s, in L d^{-1}) and concentration difference between the sample (C) and the fresh natural seawater (C_{in}). The sampling rate was calculated as:

$$r_s = \frac{v_s}{t_s} \sum \left(\frac{1}{1+e^{\frac{t-i-t_s}{0.0001}}} - \frac{1}{1+e^{\frac{t-i}{0.0001}}} \right)$$ [B.10]

With v_s the sample volume (set to 2.1 L to indicate complete water renewal), t_s the sampling duration set to $\frac{1}{24*30} d$ or 2 minutes, t the tumbling time (d) and i the sampling days.

The olivine dissolution rate constant (k_{ol}, mol m^{-2} s^{-1}) was modelled with the seawater pH, temperature (T, expressed in K), according to the rate equation by Rimstidt et al. (2012) with implementation of a rate controlling pre-factor k_{rc}:

$$k_{\mathrm{ol}} = k_{rc}10^{4.07-0.256pH(t)-\frac{3465}{T}}$$ [B.11]

The k_{ol} value was converted to a daily dissolution rate (r_{ol}, µmol L^{-1} d^{-1}) via:

$$r_{\mathrm{ol}} = \frac{10^6 k_{\mathrm{ol}} A_{\mathrm{GEO}}(t)86400}{V}$$ [B.12]

Where V is the seawater volume in the plastic bottles (0.7 L) and $A_{\mathrm{GEO}}(t)$ is the geometric specific surface area (m²) at time t (d). Fresh olivine was assumed to have an enhanced reactive surface area resulting from fine adherent particles (Fuhr et al., 2022). The temporal decrease in reactive surface area was accounted for according to:

$$A_{\mathrm{GEO}}(t) = 0.9 A_{\mathrm{GEO}}\left(1 + \varepsilon_{1surf}2^{(-\varepsilon_{2surf}*t)}\right)$$ [B.13]

Where A_{GEO} is the geometric specific surface area (m²) calculated from the weathered olivine volumetric grain size distribution and starting weight, 0.9 the forsterite olivine fraction in the dunite sand, ε_{1surf} the surface area enhancement factor, and ε_{2surf} the factor considering the speed of convergence between $A_{\mathrm{GEO}(t)}$ and A_{GEO}. Tuning factor values are provided in Supplementary Table B.6.

The secondary mineral precipitation rate (r_{mi}, µmol L^{-1} d^{-1}) was calculated from the PHREEQC derived saturation state ($\Omega_i(t)$):

$$r_{m_i} = \varepsilon_{pre1_i}Unitstep(\Omega_i(t) - 1)|\Omega_i(t) - 1|^{\varepsilon_{pre2_i}}$$ [B.14]

UnitStep expresses a function that returns 0 for arguments smaller than or equal to 0 and 1 for all arguments larger than 0. Therefore, precipitation could only occur in case the seawater was oversaturated with regards to the considered mineral ($\Omega_i(t) > 1$). The reaction order was defined by ε_{pre2_i} and ε_{pre1_i} was derived from:

$$\varepsilon_{pre1_i} = k_{pre_i}\left(1 - \frac{1}{1+e^{\frac{t-\alpha_i}{\beta_i}}}\right)\left(2^{-k2_{pre_i}t}\right) \qquad \text{[B.15]}$$

Where k_{pre_i} is the precipitation rate constant (μmol L^{-1} d^{-1}), α is the time delay until the precipitation starts (days) and β determines the speed with which the precipitation starts (days). $k2_{pre_i}$ is a negative constant. Thus, with the combination of the two terms the model can simulate precipitation that occurs only over a certain time of the experiment. Reaction rates were determined by tuning the unknown rate parameters until a minimum misfit between measured and modelled Mg, Si, Ca and TA concentrations was obtained. Tuning parameters are given in Table B.6. The squared errors summed over time and all species was employed as merit function where the errors for each species were normalized using the mean concentration of the respective species ($C_i(mean)$):

$$ssr = \frac{(C_i(t) - C_i(t_m))^2}{C_i(mean)^2} \qquad \text{[B.16]}$$

Where $C_i(t)$ and $C_i(t_m)$ represent the modelled and measured concentration of a species (i), respectively. Ferrous iron oxidation was simulated according to the kinetic rate for abiotic iron oxidation (Millero et al., 1987). Olivine dissolution and secondary mineral precipitation were assumed to occur to following chemical equations:

Olivine: $(Mg_{0.935}Fe_{0.065})_2SiO_4 + 4H^+ \rightarrow 1.87Mg^{2+} + 0.13Fe^{2+} + H_4SiO_4$ $\qquad$ [B.17]

Chrysotile: $3Mg^{2+} + 2H_4SiO_4 + H_2O \rightarrow Mg_3Si_2O_5(OH)_4 + 6H^+$ $\qquad$ [B.18]

Sepiolite: $2Mg^{2+} + 3H_4SiO_4 \rightarrow Mg_2Si_3O_{7.5}(OH)(H_2O)_3 + 4H^+ + 0.5H_2O$ $\qquad$ [B.19]

Talc: $3Mg^{2+} + 4H_4SiO_4 + 4H_2O \rightarrow Mg_3Si_4O_{10}(OH)_2 + 6H^+$ $\qquad$ [B.20]

Fe(OH)$_3$: $Fe^{3+} + 3H_2O \rightarrow Fe(OH)_3 + 3H^+$ $\qquad$ [B.21]

Aragonite: $Ca^{2+} + 2HCO_3^- \rightarrow CaCO_3 + CO_2 + H_2O$ [B.22]

Oxidation of Fe^{2+} to Fe^{3+}: $Fe^{2+} + 0.25O_2 + H^+ \rightarrow Fe^{3+} + 0.5H_2O$ [B.23]
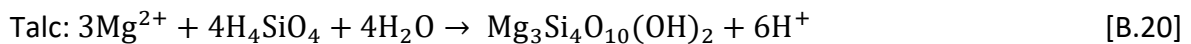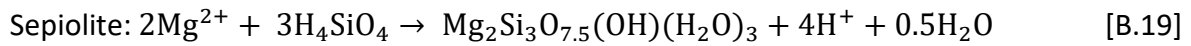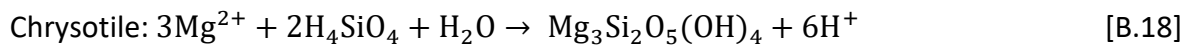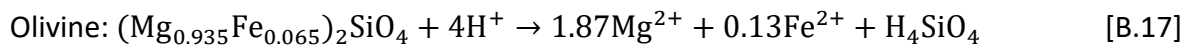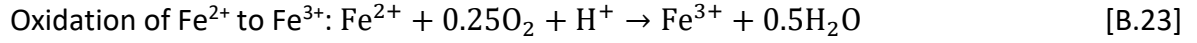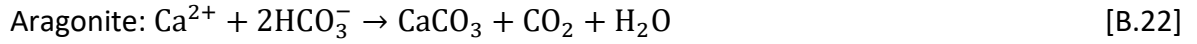
Table B.6: Tuning parameter (TP) values of the best fitting models for the stagnant olivine (SO), low rotation olivine (LRO), and high rotation olivine (HRO) treatment.

Parameter	Symbol	SO	LRO	HRO	Unit
First TP for olivine surface	ε_{1surf}	8	1.5	2	-
Second TP for olivine surface	ε_{2surf}	0.46	0.25	0.26	d^{-1}
TP for olivine dissolution	k_{pre}	0.429	2.0	2.292	-
First TP for sepiolite precipitation	$k_{pre_{sep}}$	0	0	0	$\mu mol\, l^{-1}d^{-1}$
Second TP for sepiolite precipitation	$\varepsilon_{pre2_{sep}}$	0.04	0.04	0.04	-
Third TP for sepiolite precipitation	$k2_{pre_i}$	0	0	0	-
First TP for chrysotile precipitation	$k_{pre_{chr}}$	4	0.3	252	$\mu mol\, l^{-1}d^{-1}$
Second TP for chrysotile precipitation	$\varepsilon_{pre2_{chr}}$	0.04	0.04	0.04	-
Third TP for chrysotile precipitation	$k2_{pre_i}$	-0.18	-0.18	-0.18	-
First TP for talc precipitation	$k_{pre_{talc}}$	0	0	0	$\mu mol\, l^{-1}d^{-1}$
Second TP for talc precipitation	$\varepsilon_{pre2_{talc}}$	0.04	0.04	0.04	-
Third TP for talc precipitation	$k2_{pre_i}$	0	0	0	-
First TP for aragonite precipitation	$k_{pre_{ara}}$	0	12.6	10	$\mu mol\, l^{-1}d^{-1}$
Second TP for aragonite precipitation	$\varepsilon_{pre2_{ara}}$	2.75	2.75	2.75	-
Third TP for aragonite precipitation	$k2_{pre_i}$	-1.3	-0.37	-0.2	-
Delay of sepiolite precipitation	α_{sep}	0	0	0	d
Delay of sepiolite precipitation	β_{sep}	0	0	0	d
Delay of chrysotile precipitation	α_{chr}	40	18	55	d
Delay of chrysotile precipitation	β_{chr}	0.2	5	1	d
Delay of talc precipitation	α_{talc}	0	0	0	d
Delay of talc precipitation	β_{talc}	0	0	0	d
Delay of aragonite precipitation	α_{ara}	0	35	55	d

Delay of aragonite precipitation	β_{ara}	0	1.9	1.2	d

B.2 ADDITIONAL RESULTS

B.2.1 Talc, chrysotile, calcite and amorphous SiO₂ saturation indices
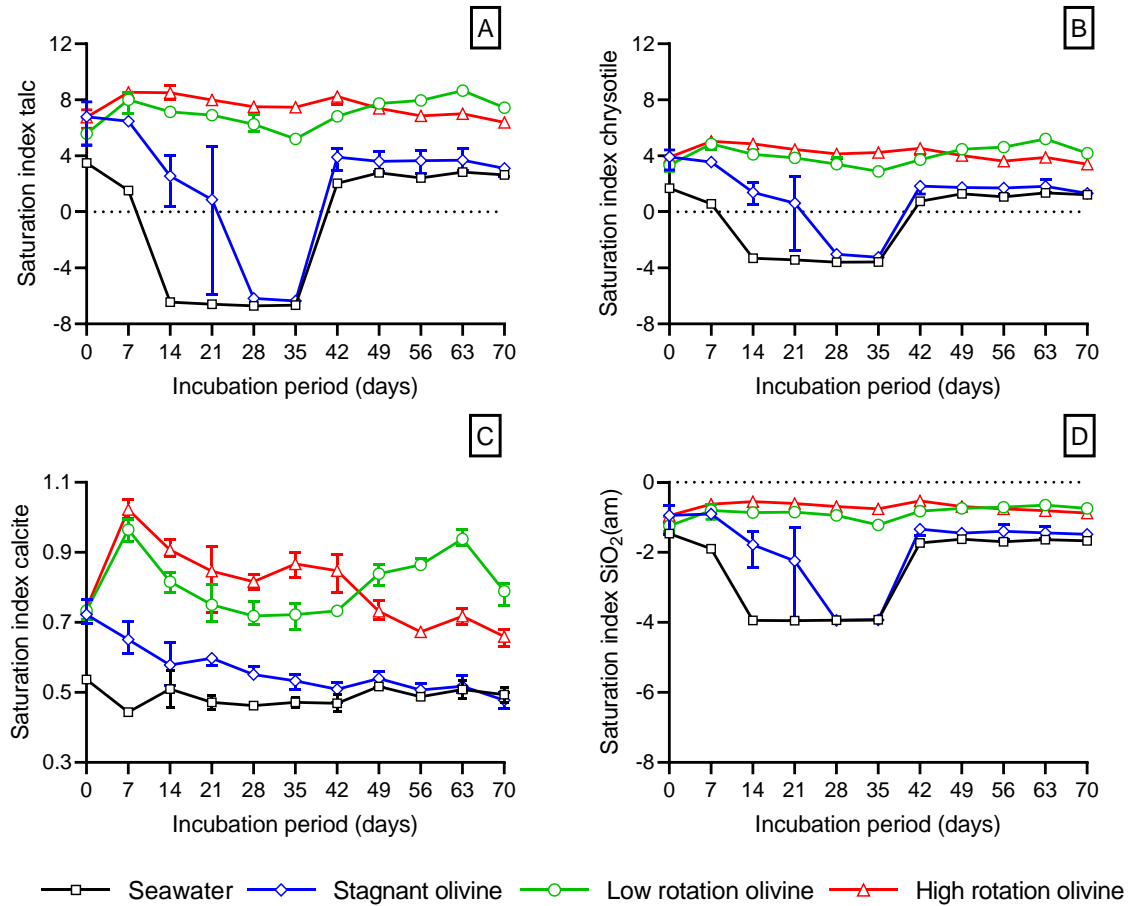
Figure B.2: Weekly evolution of (A) talc, (B) chrysotile, (C) calcite, and (D) amorphous silica (SiO₂(am)) saturation indices calculated from the experimental data in PHREEQC V3 using the LNLL database. Mean values with range for the olivine treatments (N = 3) and seawater control (N = 2) are shown.

B.2.2 Seawater elemental concentrations
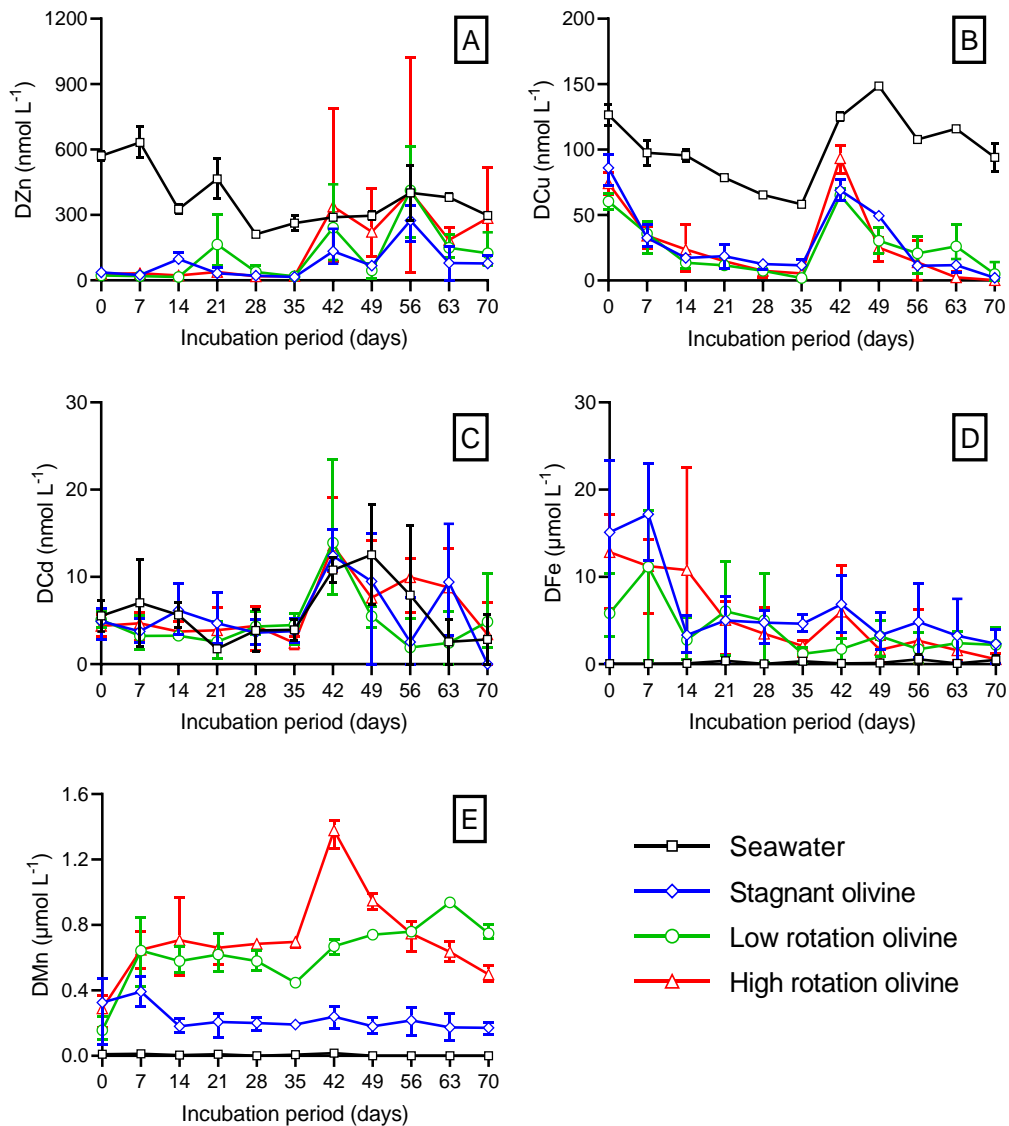
Figure B.3: Weekly evolution of dissolved (<0.2 μm) (A) zinc (DZn), (B) copper (DCu), (C) cadmium (DCd), (D) iron (DFe) and (E) manganese (DMn) concentrations in natural filtered (<0.2 μm) seawater. Mean values with range for the olivine treatments (N = 3) and seawater control (N = 2) are shown. Note that concentrations are given in nmol L⁻¹ for DZn, DCu and DCd (A, B, and C) and μmol L⁻¹ for DFe and DMn (D and E).
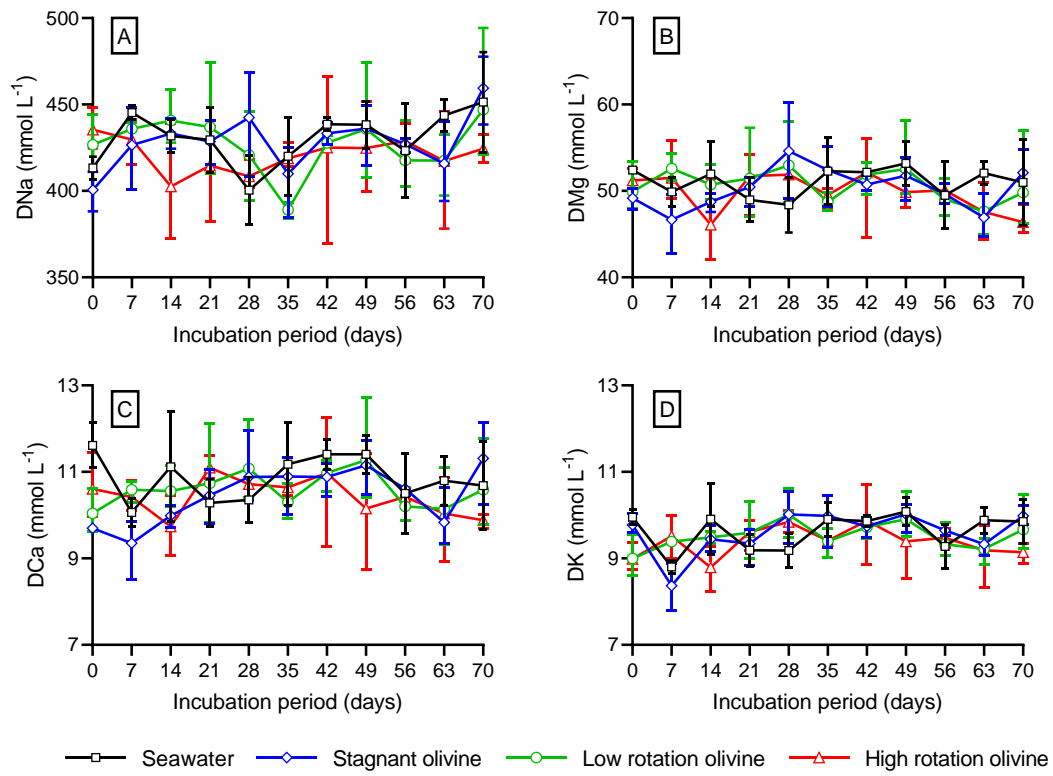
Figure B.4: Weekly evolution of dissolved (<0.2 µm) (A) sodium (DNa), (B) magnesium (DMg), (C) calcium (DCa), and (D) potassium (DK) concentrations in natural filtered (<0.2 µm) seawater. Mean values with range for the olivine treatments (N = 3) and seawater control (N = 2) are shown.

B.2.3 Predicted and observed olivine dissolution
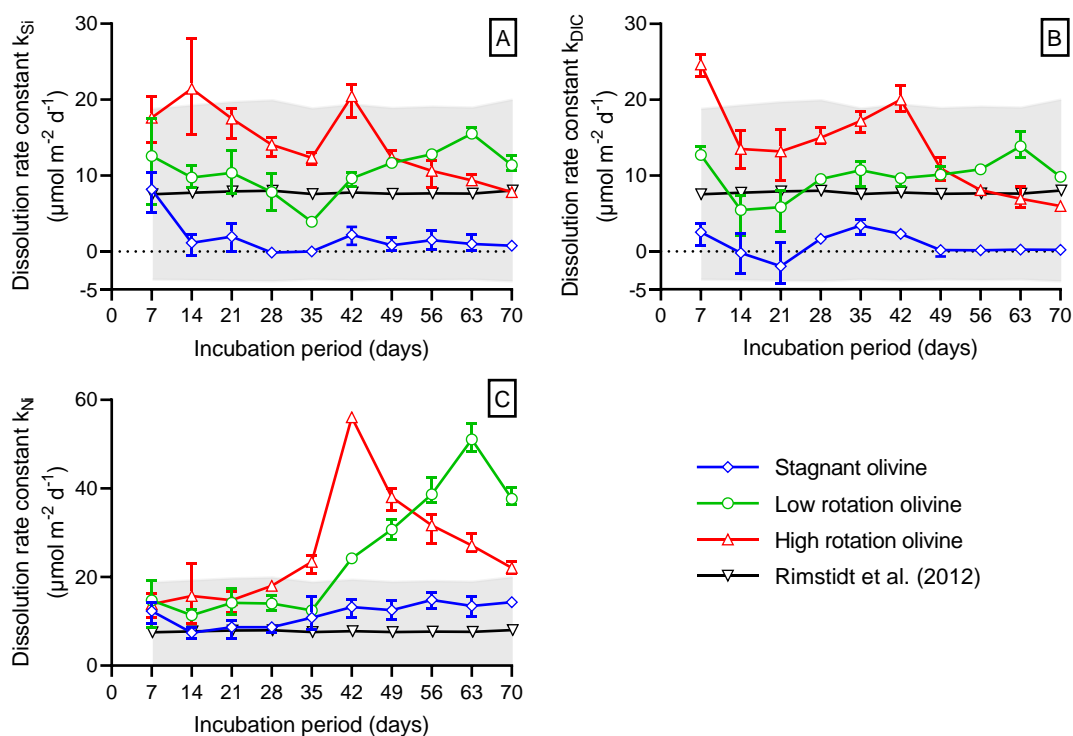
Figure B.5: Weekly evolution of olivine dissolution rate constants (k_i, µmol m^{-2} d^{-1}) in natural filtered (<0.2 µm) seawater. Values were derived from the weekly accumulation of (A) dissolved Si, (B) dissolved inorganic carbon (DIC), and (C) dissolved Ni normalized for reaction stoichiometry (supplementary section B.1.2). Mean and range values are shown (N = 3). Expected weekly olivine k_i values by Rimstidt et al. (2012) are shown in grey (line and grey shading).
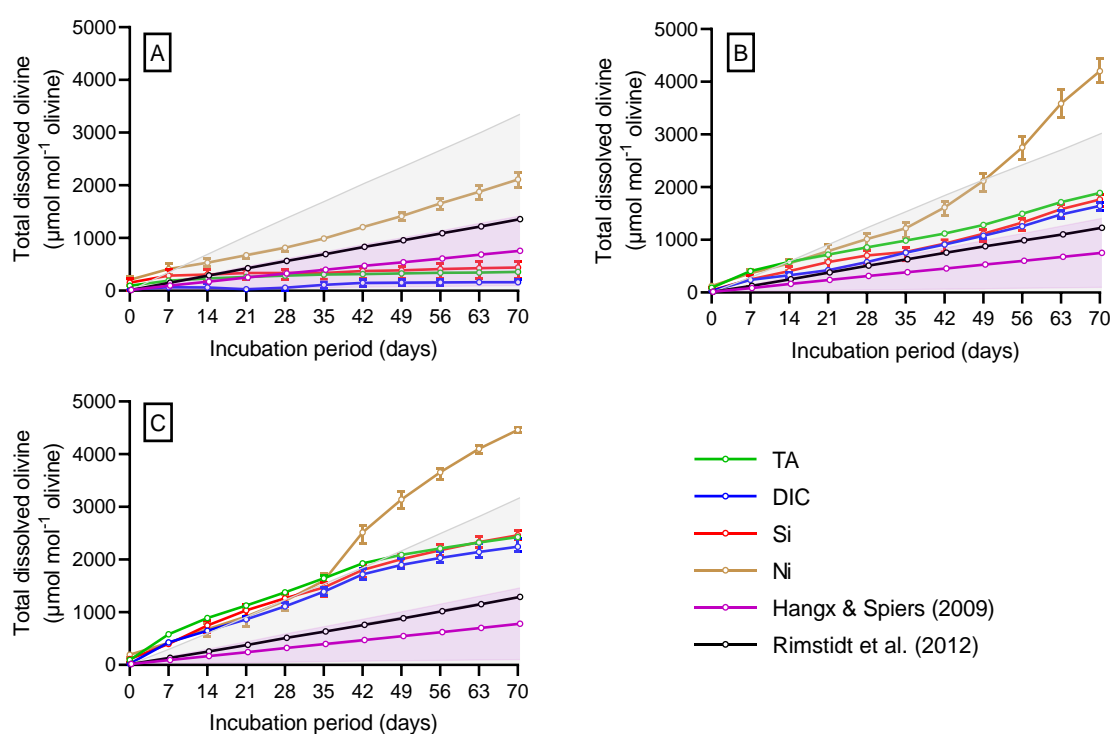
Figure B.6: Predicted and observed weekly evolution of total dissolved olivine (μmol) in the rock tumbler experiment. Observed amounts were derived from the measured seawater total alkalinity (TA, in green), dissolved silicon (Si, in red), dissolved inorganic carbon (DIC, in blue), and dissolved nickel (Ni, in orange) based on the reaction stoichiometry (Section B.1.2). Modelled amounts were derived based on the olivine dissolution rate equation by Rimstidt et al. (2012) (in grey), and the temperature corrected olivine dissolution rate at seawater (pH = 8.2) derived by Hangx and Spiers (2009)(in purple). Mean and range (N = 3) are shown for the stagnant (A), low rotation (B), and high rotation (C) olivine treatments.

B.2.4 Grain size distributions of suspended olivine particles
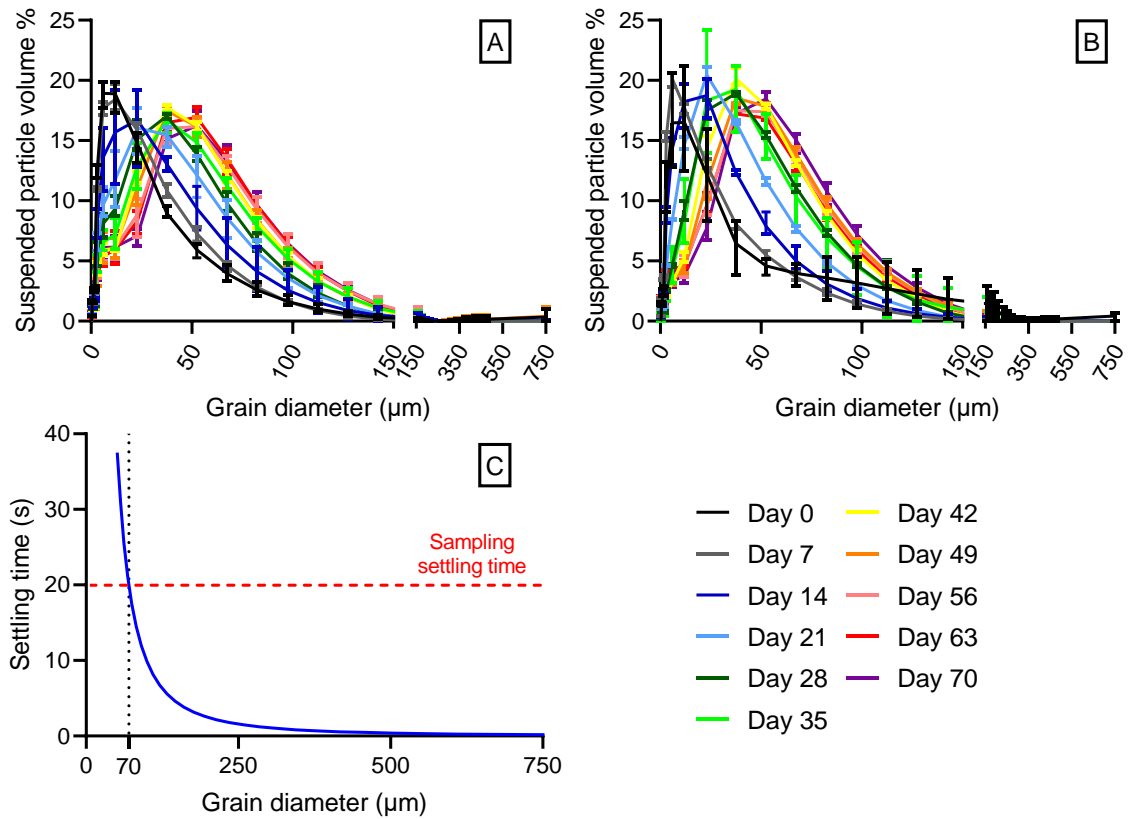
Figure B.7: Weekly volumetric grain size distribution of suspended sediment grains for the stagnant (A), and low rotation (B) treatment. Results for the high rotation treatment are shown in Figure 2.5B of the main text. Mean and range are shown (N = 1 − 3). Expected settling time of spherical olivine particles in a 0.1 m stagnant 15 °C seawater water column according to the stokes' law (C) is shown. Red dashed line (C) represents the settling time (20 s) before sampling.

According to the Stokes' law the gravimetric settling velocity of a spherical particle in solution is equal to:

$$v = \frac{gd^2(\rho_p - \rho_s)}{18\eta} \qquad \text{[B.24]}$$

where g is the acceleration of gravity (9.81 m² s^{-1}), d is the particle diameter (m), ρ_p is the density of the particle (3300 kg m^{-3}), ρ_s is the density of the solution (1024 kg m^{-3} for 33 ‰ seawater at 15 °C), and η is the dynamic viscosity of the solution (0.0012 kg m^{-1} s^{-1}). Seawater density and dynamic viscosity were derived using the "swRho" and "swViscosity" function of the "oce" package in R.

Assuming spherical olivine particles, all grains larger than 70 µm should have sunk 10 cm during 20 s (Figure B.7C). Therefore, given the grainsize distribution of the starting olivine (Figure 2.5A), ~94 ± 0.46% of the total particle volume would not be sucked up during sampling. However, small (<70 µm) olivine particles could have been easily removed during sampling which was observed both visually (decreasing sample turbidity as a function of time) and from the grain size distribution results of the remaining olivine (Figure 2.5A). Overall, the loss of dunite sand during sampling was minimal (2.1 ± 0.44%, Table B.3), but removal of small particles (<70 µm) occurred and decreased the derived olivine dissolution rates (discussed in section 4.2 of the main text).

B.2.5: Olivine weathering at the grain scale
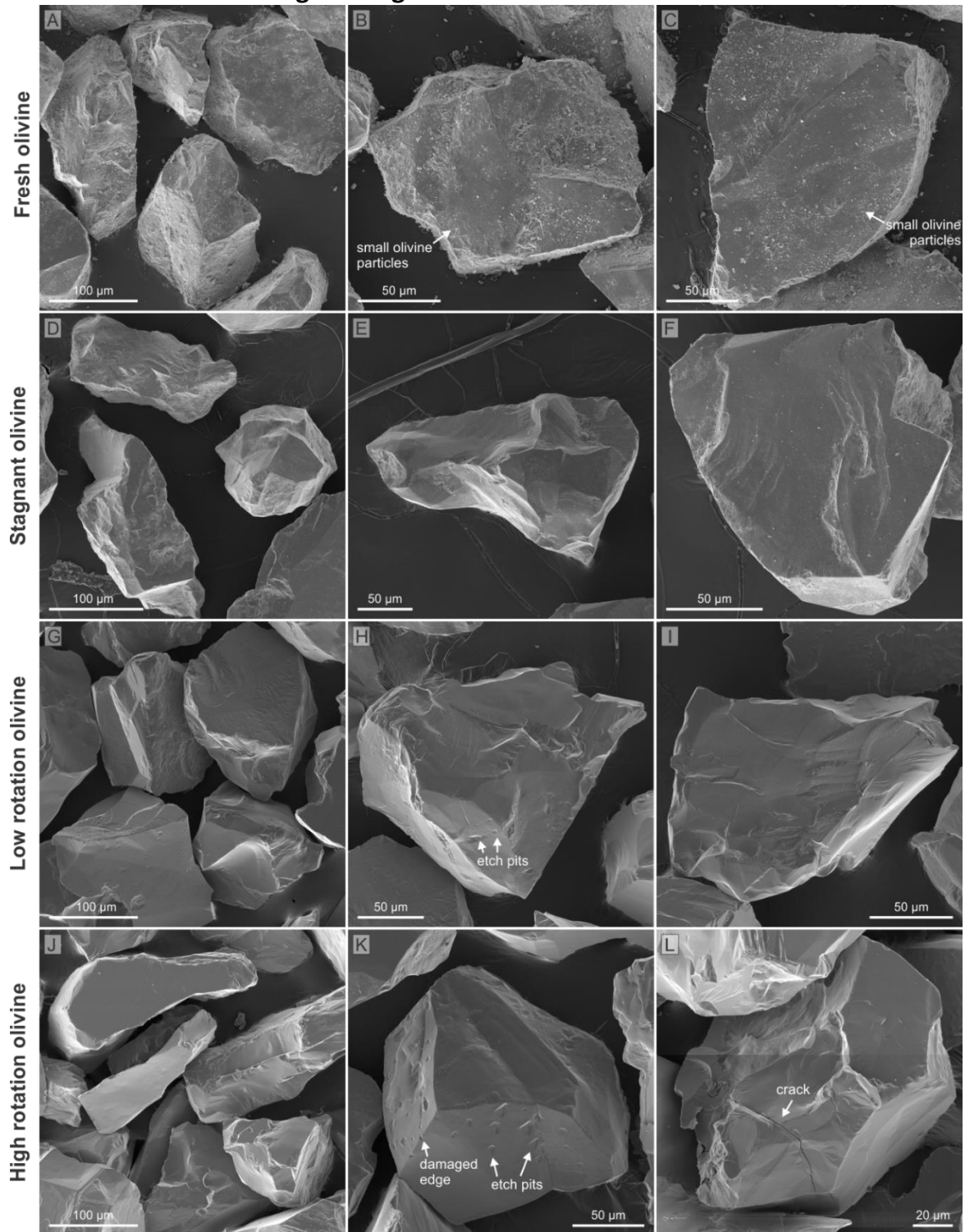
Figure B.8: Scanning electron microscope (SEM) images of surface features before and after the experiments. (A, B, C) fresh olivine, (D, E, F) stagnant treatment, (G, H, I) low rotation treatment and (J, K, L) high rotation treatment. The fresh olivine is covered by fine

adhering olivine particles (A-C), of which very few appear in the stagnant treatment (D-F), and none in the low and high rotation treatment (G-L). Note occurrence of etch pits (H, K), damaged edges (K) and cracking (L) in olivine grains from the low and high rotation treatment.
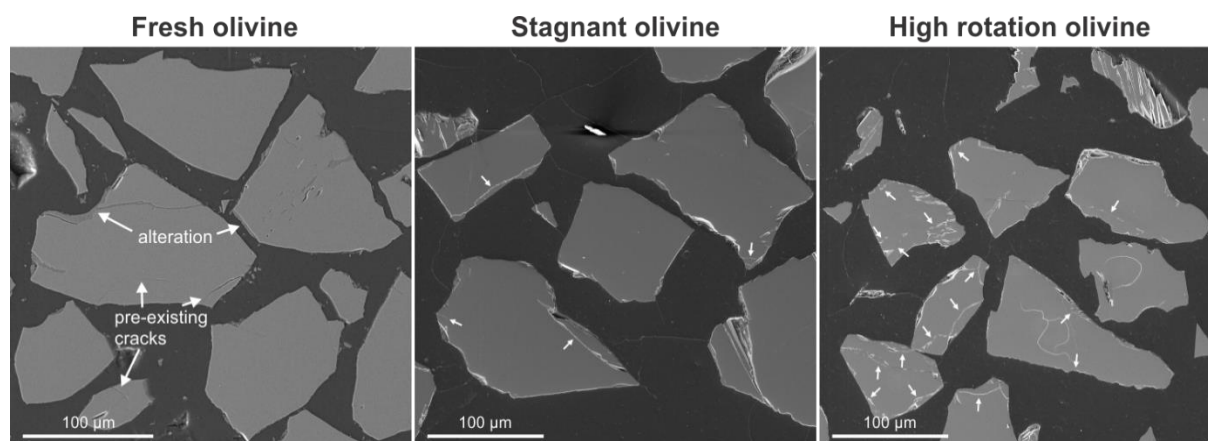
Figure B.9: Scanning electron microscope (SEM) images of polished cross sections through fresh and reacted olivine grains from the stagnant and high rotation treatment. Note the presence of pre-existing cracks and alterations in the fresh olivine grains. Cracking (white arrows) appears to be more prominent in the high rotation treatment compared to the fresh olivine and olivine from the stagnant treatment.
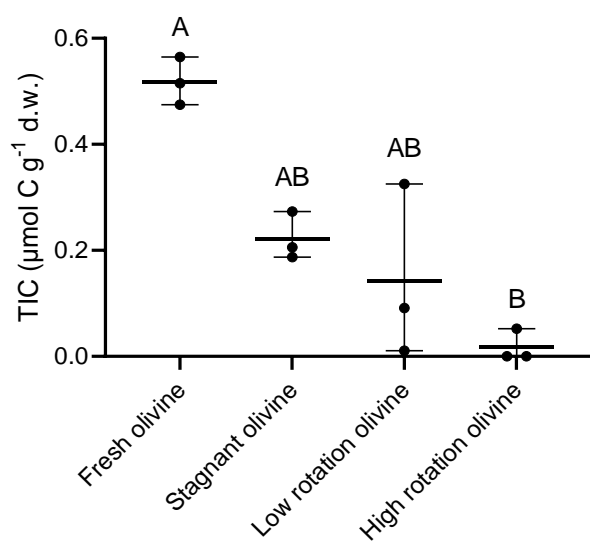
Figure B.10: Total inorganic carbon (TIC, μmol g^{-1} d.w.) concentration of the fresh and recovered experimental olivine. Individual data points and mean and range (N = 3) are shown.

Appendix C: Chapter 3

C.1 Stoichiometric model of olivine

Stoichiometric coefficients ν_i (expressed in µmol µmol^{-1} olivine) are calculated below and provided in Table C.1. The stoichiometric coefficients ν_i for DNi and DSi are equal to the molar elemental concentrations 0.0055 µmol Ni µmol^{-1} olivine and 1 µmol Si µmol^{-1} olivine, respectively.

Mineralogical composition of the dunite sand was determined via X-ray diffraction (XRD) analysis with a Bruker D8 ECO Advance equipped with a Cu-anode (40 kV, 25 mA) and an energy-dispersive position sensitive LynxEye XE detector. The incoming beam was collimated to a fixed beam length of 17 mm. Before analysis, samples were first pulverized to a grain size smaller than 500 µm and subsequently micronized (<10 µm grain diameter) by wet grinding with ethanol using a McCrone Micronizing mill. Afterwards, the slurry was dried for XRD-analysis. For each sample, a 2 g aliquot mixed with 5% zincite was included for analysis to serve as internal standards. Phases were identified using the DIFFRAC.EVA suite. The spectra were interpreted semi quantitatively using the BGMN Rietveld method with Profex version 5.0 as user interface (Bergmann et al., 1998; Doebelin and Kleeberg, 2015). The Norwegian dunite sand consisted mainly of ferroan-forsterite (83 wt%) and enstatite (8 wt%). The forsterite (Mg_2SiO_4) content *Fo* (%) was derived from the molar concentration C_{M_i} (mol mol^{-1} olivine) of Fe and Mg as

$$Fo = \frac{C_{M_{Mg}}}{(C_{M_{Mg}} + C_{M_{Fe}})} 100 \qquad\qquad [C.1]$$

From which a forsterite content of 93.2% and fayalite content *Fa* (%) of 6.8% was derived (*Fa* = 100% - *Fo*).

During complete olivine dissolution without secondary mineral precipitation, 4 µmol of alkalinity would be produced per µmol of dissolved olivine via proton consumption (Eq. C.2).

$$Mg_xFe_{2-x}SiO_4 + 4H^+ \rightarrow xMg^{2+} + (2-x)Fe^{2+} + H_4SiO_4 \qquad\qquad [C.2]$$
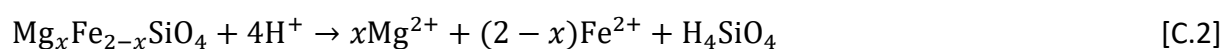
However, ferrous iron oxidation and subsequent precipitation under oxic conditions (Eq. C.3) would consume 2 µmol of TA per µmol of precipitated iron(III) hydroxide.

$$Fe^{2+} + 0.25O_2 + 3H_2O \rightarrow Fe(OH)_3 + 2H^+ + 0.5H_2O \qquad \text{[C.3]}$$
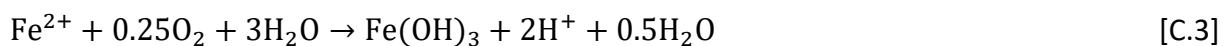
This would result in a 6.8% reduction of the TA production to ν_{TA} = 3.73 µmol µmol^{-1} olivine during Fo93 olivine dissolution.

The stoichiometric coefficient for dissolved inorganic carbon (DIC) can be calculated as

$$\nu_{DIC} = (\delta DIC/\delta TA)_{pCO_2} \nu_{TA} \qquad \text{[C.4]}$$

Where the seawater CO_2 sequestration efficiency $(\delta DIC/\delta TA)_{pCO_2}$ gives the increase in seawater DIC for each mol of TA increase. It is dependent on the atmospheric partial CO_2 pressure (pCO_2), salinity, temperature, and chemical composition of the seawater (Hofmann et al., 2009). The theoretical CO_2 sensitivity for our experimental conditions (T = 6.7 - 20 °C, S = 29.7 - 35.0 ‰, TA = 2278 − 3344 µmol L^{-1}, and pCO_2 = 420 ppmv) computed using the AquaEnv R package is equal to 0.84 ± 0.0053 (Hofmann et al., 2010). Therefore, the expected amount of CO_2 sequestered upon dissolution of 1 µmol of Fo93 olivine is ν_{DIC} = 0.84 * 3.73 = 3.13 µmol DIC released per µmol of olivine dissolved.

Table C.1: Stoichiometric coefficients ν_i (µmol µmol^{-1} olivine) for various compounds i (TA, DIC, DSi, and DNi) of the experimental Fo93 olivine. The ν_i values were derived from the elemental and mineralogical data as described in Section C.1.

Compound	Stoichiometric coefficient ν_i (µmol µmol^{-1} olivine)
TA	3.73
DIC	3.13
DSi	1.00
DNi	0.0055

C.2 Olivine and beach sand physicochemical properties

Elemental composition of the experimental beach sand and dunite was determined via ICP-OES (iCAP 6300 Duo, Thermo Scientific) after microwave-assisted acid digestion according to

a modified chromite ore protocol (CEM Corporation, 1999). Briefly, 0.1 g of dried (48 h at 60 °C) olivine and beach sand was added to 80 mL quartz pressure vessels (CEM Corporation). Next, 2.6 mL of Ultrapure ~85% orthophosphoric acid (Honeywell Chemicals) and 1.4 mL of ≥96% sulfuric acid (Merck) were added and the vessels were heated at 240 °C for 30 minutes in a Discover SP-D 80 microwave (CEM Corporation). After cooling down, 2 mL of TraceMetal™ Grade 67-69% nitric acid (Fisher Scientific) was added. Subsequently, samples were heated at 240 °C for 15 minutes. Afterwards, samples were transferred to 50 mL polypropylene vials and diluted to the 50 mL mark with ultrapure Milli-Q water (Merck). The vials were centrifuged for 5 minutes at 1600 g and the supernatant was subsequently transferred to new 50 mL tubes before analysis via ICP-OES. For quality control, reference NIM-D dunite (SARM-6, MINTEK) and procedural blanks were included during analysis of the samples. Element recoveries (ranging from 72 to 93%) were acceptable for all certified elements except Si (~0.4%). A maximum relative standard deviation (RSD) of 5% was allowed for the measurements. Elemental concentrations are given in Table 3.2 of the main text.
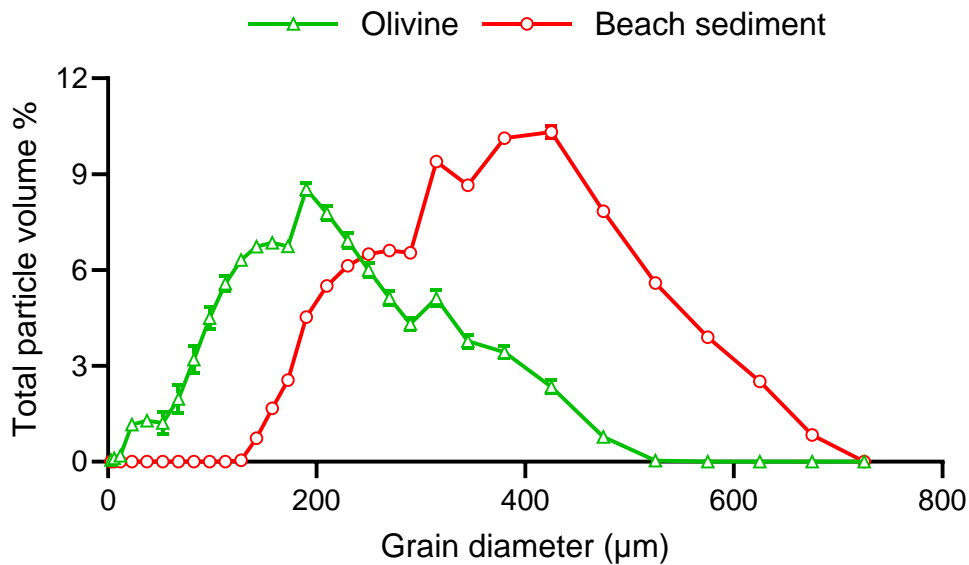
Figure C.1: Volumetric grain size distribution of the experimental dunite and beach sediment at the start of the experiment (N = 4, mean ± S.D.).

Table C.2: Bulk density and porosity of the top 5 cm of the sediment in the stagnant sand and stagnant olivine treatment at the end of the flume experiment (N = 6, mean ± S.D.).

Treatment	Bulk density (g cm^{-3})	Porosity (%)
Stagnant sand	1.6 ± 0.020	39 ± 0.75
Stagnant olivine	1.56 ± 0.039	41 ± 1.5

Total inorganic carbon (TIC) content of 63 ± 9 mg (N = 54) fresh beach sediment, and surficial (0 – 5 cm) weathered beach sediment from the various flumes was analyzed in triplicate with an elemental analyzer (Flash 2000 CN Soil Analyser, Interscience). Beach sediment samples were homogenized by manual mortar and pestle grinding before analysis. To combust organic carbon, samples were dried at 105 °C for 12 h and ignited in a muffle furnace at 375 °C for 17 h prior to TIC determination (Wang et al., 2012). Results were expressed in function of the sample dry weight (105 °C) and are shown in Figure C.2.
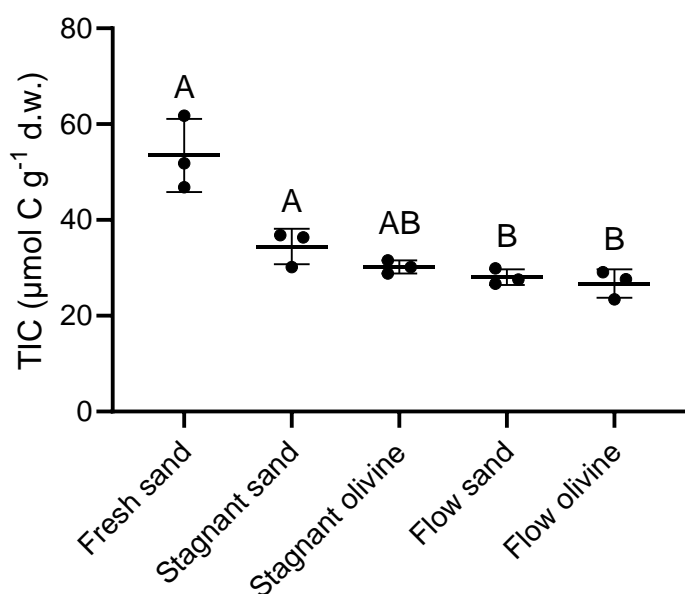
Figure C.2: Total inorganic carbon (TIC, µmol g^{-1} d.w.) concentration of the fresh beach sediment and recovered sediment from the different experimental treatments at the end of the 175-day flume experiment. Individual data points, mean, and standard deviation (N = 3) are shown.

C.3 North Sea water chemistry, temperature, and *p*CO₂

Table C.3: Chemical composition of filtered (<0.2 µm) North Sea water used in the first and second measurement series of the racetrack flume experiment. Concentrations were

determined by HR-ICP-MS (mean ± standard deviation (S.D.)). (#) Concentrations for Na, Cl and SO₄ were not analytically determined but derived from measured potassium (K) concentrations using the conservative element ratios in natural seawater reported by Hem (1985). BQL = below the quantification limit, which was 0.1 μg L⁻¹ for Al and 0.02 μg L⁻¹ for the other trace elements.

Major element	Molar concentration (mmol L⁻¹) series 1 (N = 3)	Molar concentration (mmol L⁻¹) series 2 (N = 4)
Mg	52 ± 2.8	41 ± 4.8
Ca	12 ± 0.58	9.1 ± 0.93
K	11 ± 0.20	8.6 ± 1.1
Si	0.085 ± 0.0045	0.0052 ± 0.00011
Fe	BQL	0.00080 ± 0.00028
Na (#)	508 ± 9.6	402 ± 52
Cl (#)	592 ± 11	469 ± 61
SO₄ (#)	31 ± 0.58	24 ± 3.1
Minor element	Molar concentration (μmol L⁻¹) series 1	Molar concentration (μmol L⁻¹) series 2
Ni	BQL	0.18 ± 0.032
Cr	0.066 ± 0.034	0.013 ± 0.0038
Mn	0.46 ± 0.0038	0.071 ± 0.078
Cu	BQL	0.49 ± 0.15
Cd	0.0051 ± 0.0014	0.019 ± 0.0066
Zn	0.087 ± 0.0044	0.62 ± 0.12
Pb	0.0020 ± 0.0017	0.0022 ± 0.00098
Li	127 ± 16	26 ± 3.5
Al	BQL	BQL
V	BQL	0.041 ± 0.0040
Sc	BQL	BQL
Ti	BQL	0.27 ± 0.18
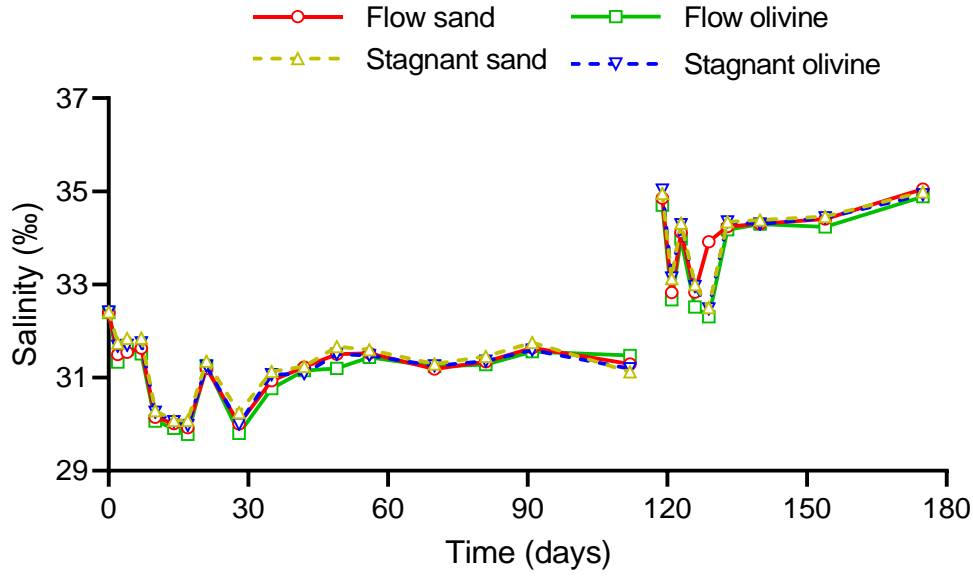
Figure C.3: Temporal evolution of seawater salinity (‰) during the 175-day flume experiment.
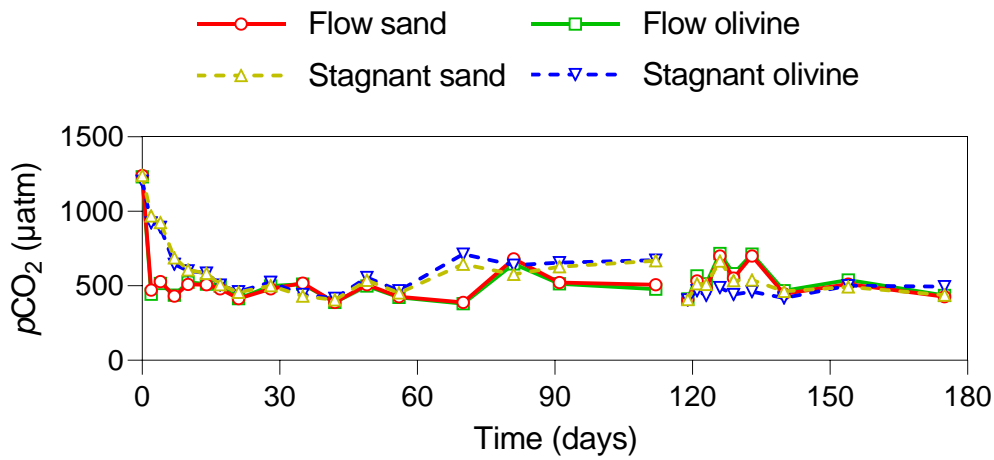
Figure C.4: Temporal evolution of seawater partial CO_2 pressure pCO_2 (μatm) during the 175-day flume experiment. pCO_2 values were derived with the carb function in R using the measured seawater pH, TA, temperature, salinity, hydrostatic pressure (0 bar), and DSi as input values.

C.4 Seawater hydrodynamics

Flow velocity was measured at different locations (Figure C.5) and depths in the flow sand flume at day 128 using an electromagnetic flow meter (EMF; Valeport model 801, Totnes,

UK). Flow velocities were measured at a frequency of 1 Hz for 60 s. Average velocities ranged from 0.1 to 0.62 m s^{-1} with an average value of 0.40 m s^{-1} (Table C.4).
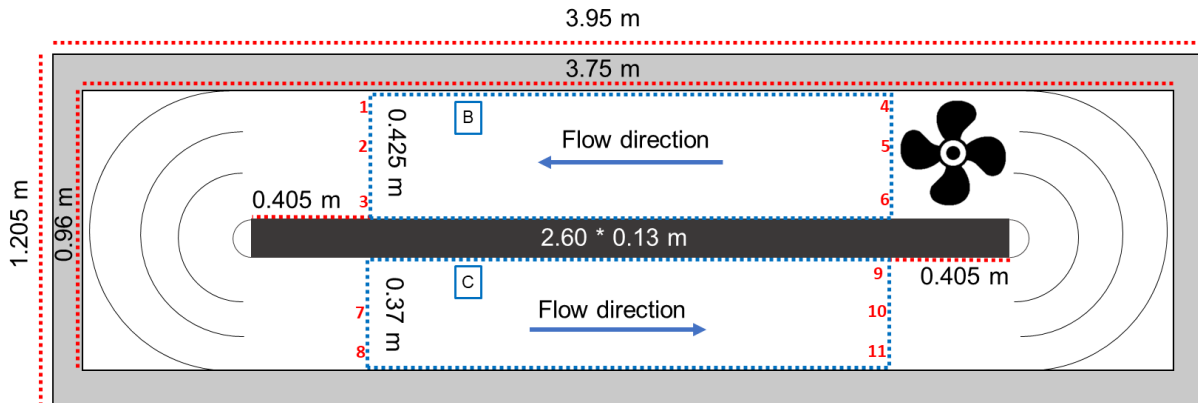
Figure C.5: Schematic representation of the experimental race track flumes with sediment height measurement areas shown as dotted blue rectangles. Letters B and C match with subplot labels of Figure C.6. Numbers (1 to 12) represent flow velocity measurement locations. Flow velocity was measured at 5 cm depth intervals.

Table C.4: Flow velocity (m s^{-1}) measured at various locations (shown in Figure C.5) and heights above the sediment (cm) in the flow sand flume at day 128. Mean ± S.D. values of 60 measurements (f = 1 Hz) are shown. Flow velocities could not be measured at the same number of depths in all locations in the flow sand flume due to differences in sediment topography (see Section C.5).

Location	Flow velocity (m s^{-1}) at height above the sediment (cm)						
	5	10	15	20	25	30	35
1	0.27	0.32	0.34	0.27	0.27	0.28	0.27
	± 0.025	± 0.011	± 0.007	± 0.009	± 0.010	± 0.010	± 0.013
2	0.25	0.16	0.10	0.26	0.20		
	± 0.05	± 0.047	± 0.03	± 0.015	± 0.030	/	/
3	0.35	0.31	0.28	0.25			
	± 0.01	± 0.006	± 0.007	± 0.010	/	/	/
4	0.40	0.38	0.33	0.38			
	± 0.008	± 0.011	± 0.024	± 0.011	/	/	/
5	0.28	0.32	0.38	0.43			
	± 0.020	± 0.021	± 0.009	± 0.005	/	/	/
6	0.45	0.45	0.44	0.45	/	/	/

	± 0.006	± 0.006	± 0.009	± 0.008			
7	0.48	0.44	0.43				
	± 0.006	± 0.010	± 0.009	/	/	/	/
8	0.50	0.57					
	± 0.015	± 0.006	/	/	/	/	/
9	0.50	0.57	0.57				
	± 0.015	± 0.006	± 0.006	/	/	/	/
10	0.56	0.62	0.59				
	± 0.033	± 0.007	± 0.003	/	/	/	/
11	0.56	0.60	0.58				
	± 0.01	± 0.006	± 0.007	/	/	/	/

The current-induced bed shear stress τ_c (N m^{-2}) was subsequently derived according to

$$\tau_c = \rho u_*^2 \qquad \text{[C.5]}$$

Where ρ is the seawater density (1026 kg m^{-3} at day 129), and u_* is the friction velocity (m s^{-1}) which can be expressed as follows for steady currents:

$$u_* = \frac{\kappa U(z)}{\ln\left(\frac{z}{z_0}\right)} \qquad \text{[C.6]}$$

Where κ is the von Karman's constant (0.40), $U(z)$ is the horizontal current velocity (m s^{-1}) at height z above the sediment (m), and z_0 is the characteristic roughness length (m) (Belliard et al., 2019). The roughness length z_0 was taken to be equal to one tenth of the average current ripple height (of approximately 0.025 m) (Garratt, 1992).

To determine whether the flow was laminar or turbulent, the dimensionless Reynolds number *Re* was calculated according to

$$Re = \frac{v d_{charac}}{\nu} \qquad \text{[C.9]}$$

Where v is the flow velocity (m s^{-1}), d_{charac}, is the characteristic length (m), and ν is the kinematic viscosity (m² s^{-1}) (Silinski et al., 2016). The kinematic viscosity was derived by dividing the seawater viscosity η (0.0013 kg m^{-1} s^{-1} at day 129) by the seawater density ρ (1026 kg m^{-3} at day 129) ($\nu = \eta/\rho$), which were calculated using the "swViscosity" and "swRho" function in R. The characteristic length was considered to be equal to the hydraulic diameter d_h , which is defined as

$$d_{charac} = d_h = \frac{4A}{P}$$ [C.10]

Where A is cross-sectional area of the channel (m²), *and P* is the wetted perimeter (m) (Lewis, 1992). Subsequently, considering the gravitation acceleration g (9.81 m s⁻²), the dimensionless Froude number *Fr* was derived according to Eq. C.11 to distinguish between subcritical and hypercritical flow.

$$Fr = \frac{v}{\sqrt{gd_{charac}}}$$ [C.11]

Table C.5: Average current induced bed shear stress (N m⁻²) at various locations (shown in Figure C.5) and heights above the sediment (cm) in the flow sand flume at day 128.

Location	Current induced bed shear stress (N m⁻²) at height above the sediment (cm)						
	5	10	15	20	25	30	35
1	1.35	1.22	1.13	0.62	0.56	0.55	0.49
2	1.14	0.32	0.098	0.58	0.31	/	/
3	2.25	1.13	0.76	0.55	/	/	/
4	2.85	1.77	1.06	1.25	/	/	/
5	1.46	1.26	1.38	1.60	/	/	/
6	3.70	2.43	1.91	1.71	/	/	/
7	4.18	2.31	1.81	/	/	/	/
8	4.59	3.88	/	/	/	/	/
9	4.59	3.88	3.18	/	/	/	/
10	5.80	4.64	3.40	/	/	/	/
11	5.67	4.28	3.28	/	/	/	/

The average current-induced bed shear stress in the flow sand treatment ranged from 0.097 to 5.8 N m⁻² (N = 42) with a median value of 1.7 N m⁻² (Table C.5). Current-induced bed shear stress can vary largely in natural coastal systems (0.001 – 10 N m⁻²) depending on the flow conditions, bed roughness, and topography (Dufois et al., 2008; Mitchell et al., 2010; Dalyander et al., 2013; Ward et al., 2015; Johnson and Cowen, 2017). Overall, a relatively high force was exerted on the sediment bed in our experiment, indicating significant sediment transport in the flumes with current as shown by the relatively high seawater turbidity (Figure 3.4).

Table C.6: Average Reynolds number at various locations (shown in Figure C.5) and heights above the sediment (cm) in the flow sand flume at day 128.

Location	Reynolds number at height above the sediment (cm)						
	5	10	15	20	25	30	35
1	5.8E+04	6.7E+04	7.2E+04	5.7E+04	5.7E+04	5.9E+04	5.8E+04
2	5.0E+04	3.3E+04	2.0E+04	5.2E+04	3.9E+04	/	/
3	7.9E+04	6.9E+04	6.3E+04	5.7E+04	/	/	/
4	1.1E+05	1.1E+05	9.3E+04	1.1E+05	/	/	/
5	8.9E+04	1.0E+05	1.2E+05	1.4E+05	/	/	/
6	1.4E+05	1.4E+05	1.4E+05	1.4E+05	/	/	/
7	9.7E+04	8.9E+04	8.7E+04	/	/	/	/
8	1.1E+05	1.2E+05	/	/	/	/	/
9	9.4E+04	1.1E+05	1.1E+05	/	/	/	/
10	1.1E+05	1.2E+05	1.1E+05	/	/	/	/
11	1.1E+05	1.1E+05	1.1E+05	/	/	/	/

Very high Reynolds numbers were calculated for different locations in the flow sand flume ranging from 2.0E+04 to 1.4E+05 (N = 42) (Table C.6), which indicate highly turbulent flow conditions (Raghavan and Bernitsas, 2011).

Table C.7: Average Froude number at various locations (shown in Figure C.6) and heights above the sediment (cm) in the flow sand flume at day 128.

Location	Froude number at height above the sediment (cm)						
	5	10	15	20	25	30	35
1	0.17	0.19	0.21	0.17	0.17	0.17	0.17
2	0.16	0.10	0.063	0.17	0.13	/	/
3	0.21	0.18	0.17	0.15	/	/	/
4	0.21	0.20	0.17	0.20	/	/	/
5	0.14	0.16	0.19	0.22	/	/	/
6	0.23	0.22	0.22	0.22	/	/	/
7	0.30	0.27	0.27	/	/	/	/
8	0.30	0.34	/	/	/	/	/
9	0.33	0.37	0.37	/	/	/	/
10	0.36	0.40	0.38	/	/	/	/

| 11 | 0.36 | 0.39 | 0.37 | / | / | / | / |

Froude numbers ranged from 0.06 to 0.40 (N = 42) in the flow sand treatment on day 129 (Table C.7), indicating subcritical flow conditions (Silinski et al., 2016).

1 **C.5 Sediment topography**
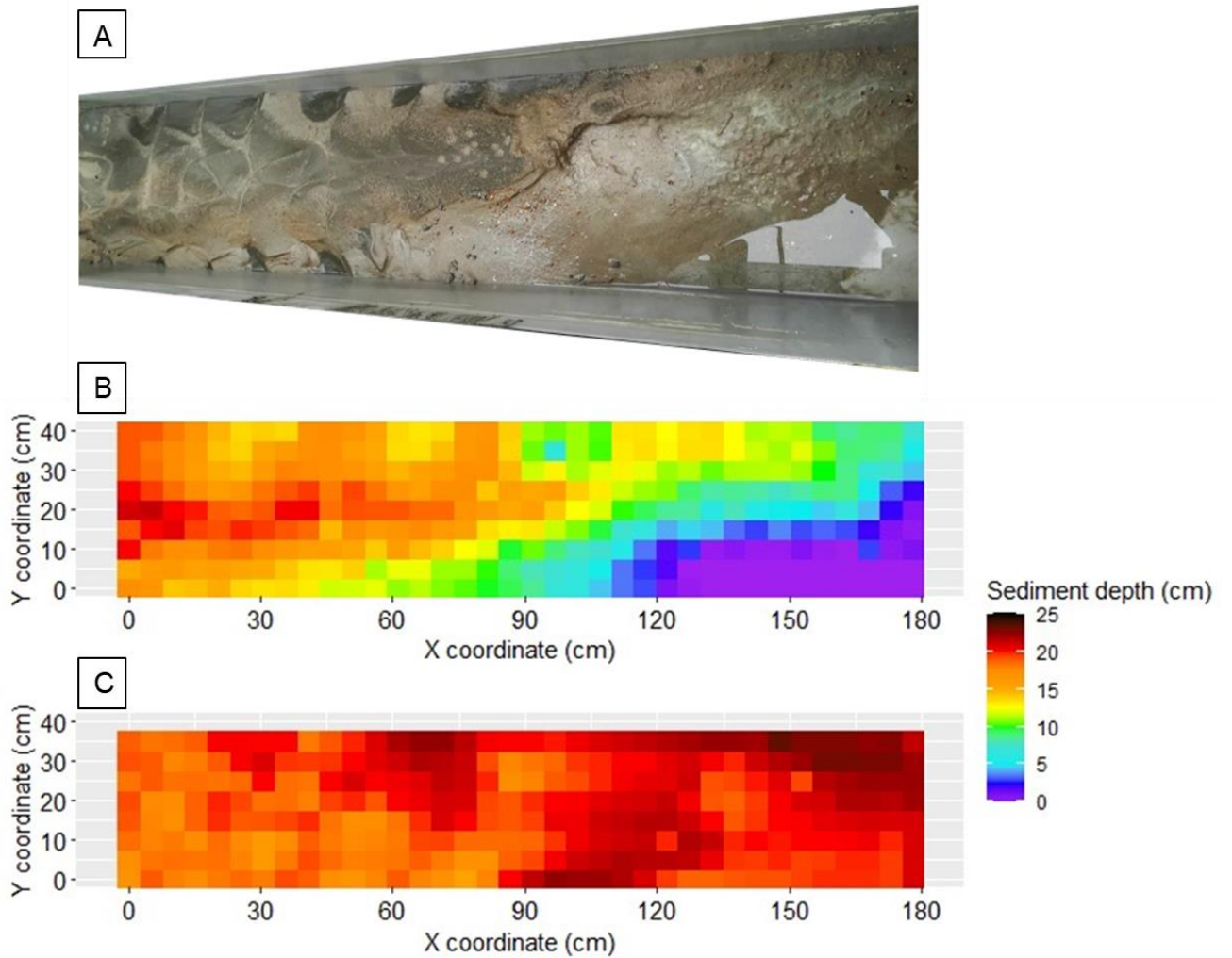
2

3 *Figure C.6: (A) picture of sediment topography in the top section of the flow olivine flume at*

4 *day 116. Note the presence of sediment ripples, dark brown precipitates, and match with*

5 *manual sediment depth measurements in (B). Raster plots of the sediment depth (cm) at*

6 *different locations in the straight sections of the flow sand flume at day 103. Subplot labels B*

7 *and C match with indicated areas in Figure C.5. Sediment depth was manually measured with*

8 *a 5 cm spatial resolution.*

9   **C.6 North Sea water equilibration**
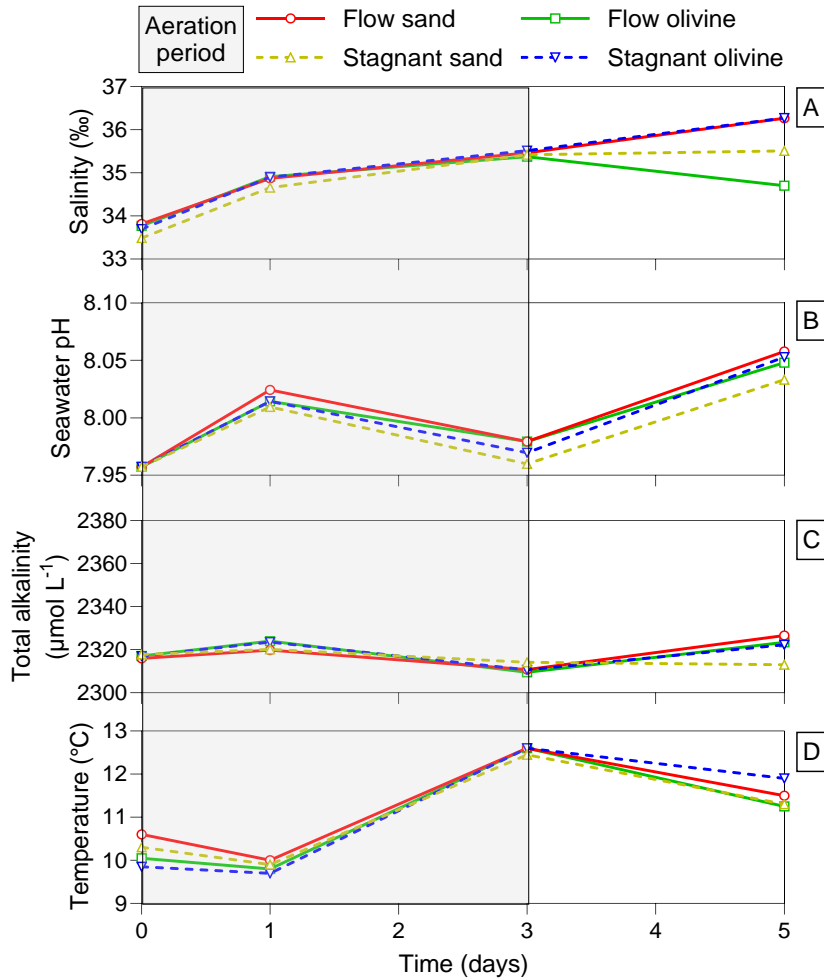
Figure C.7: Temporal evolution of seawater salinity, pH, total alkalinity and temperature during the equilibration period of the North Sea water before use in the second measurement series (day 119 – 175) of the 175-day flume experiment. Seawater was continuously aerated for three days after arrival (grey shading).

C.7 Calcite, sepiolite and amorphous SiO₂ saturation indices
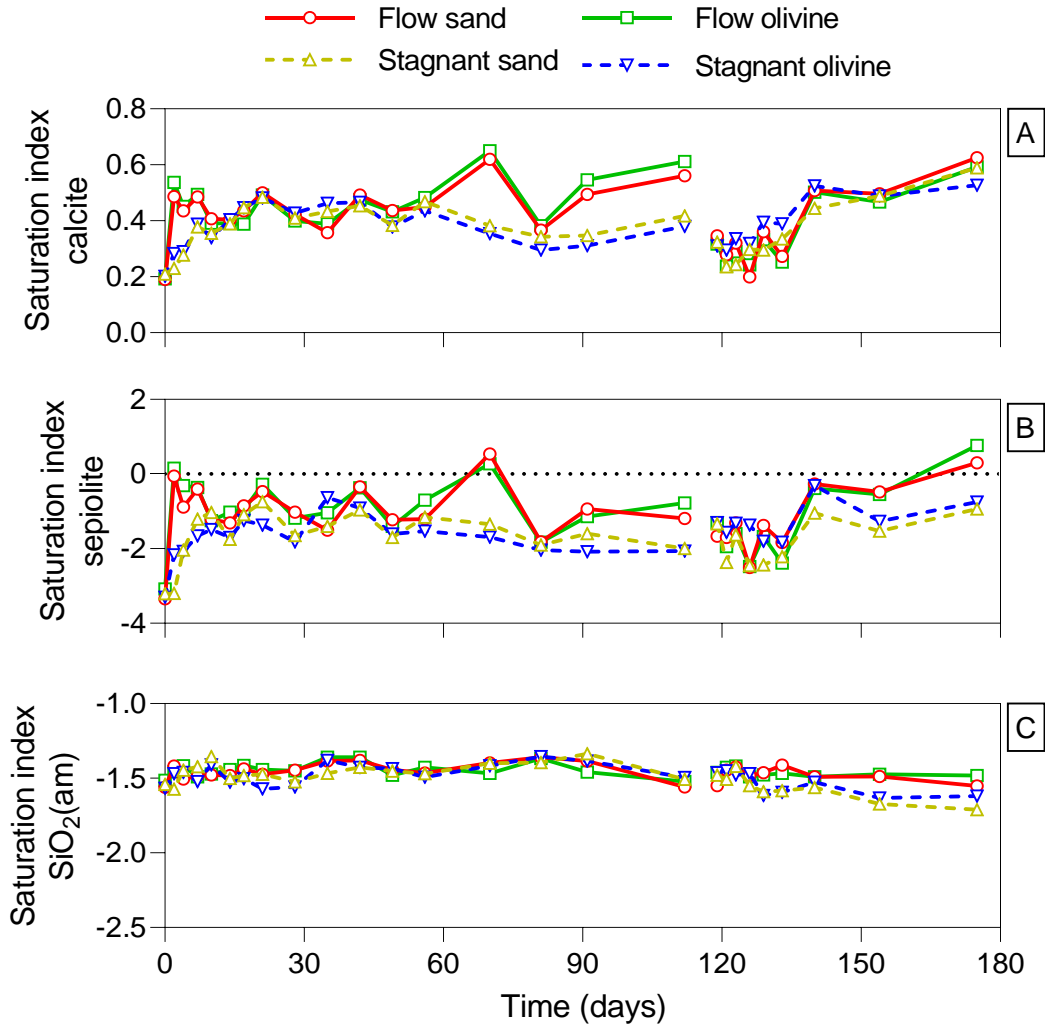
Figure C.8: Temporal evolution of (A) calcite, (B) sepiolite, and (C) amorphous silica (SiO₂(am)) saturation indices during the 175-day flume experiment calculated from the experimental data in PHREEQC V3 using the LLNL database.

C.8 Raman spectra of suspended and deposited mineral phases
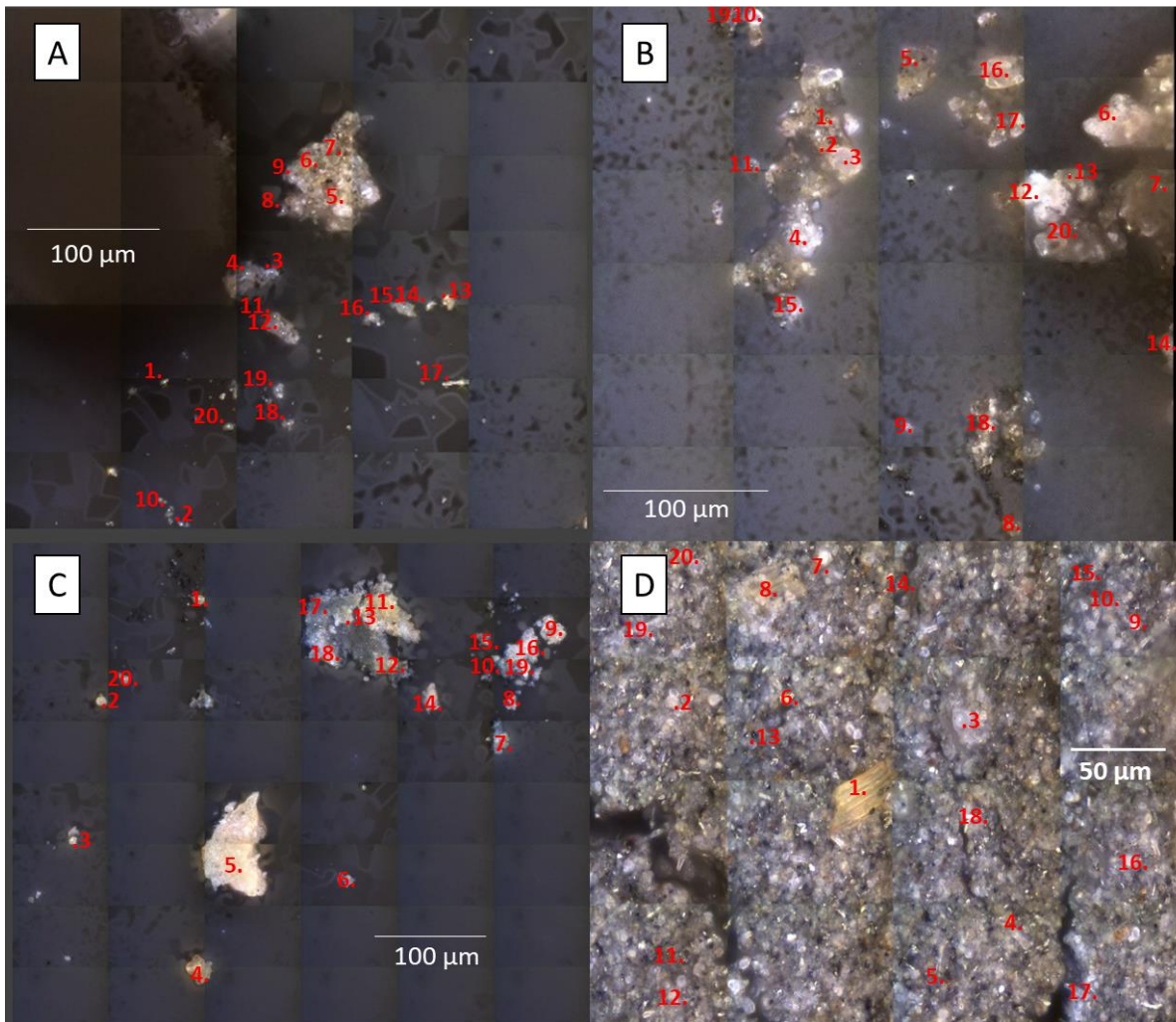
Figure C.9: Confocal Raman microscopy images of the suspended particulate matter in (A) the flow olivine treatment, and (B) the flow sand treatment at day 4. Flume wall deposits in the (C) stagnant sand, and (D) flow sand treatment at the end of the 175-day experiment. The composition of 20 random points (in red) was analyzed and the corresponding Raman spectra are given in Figure C.10-C13.
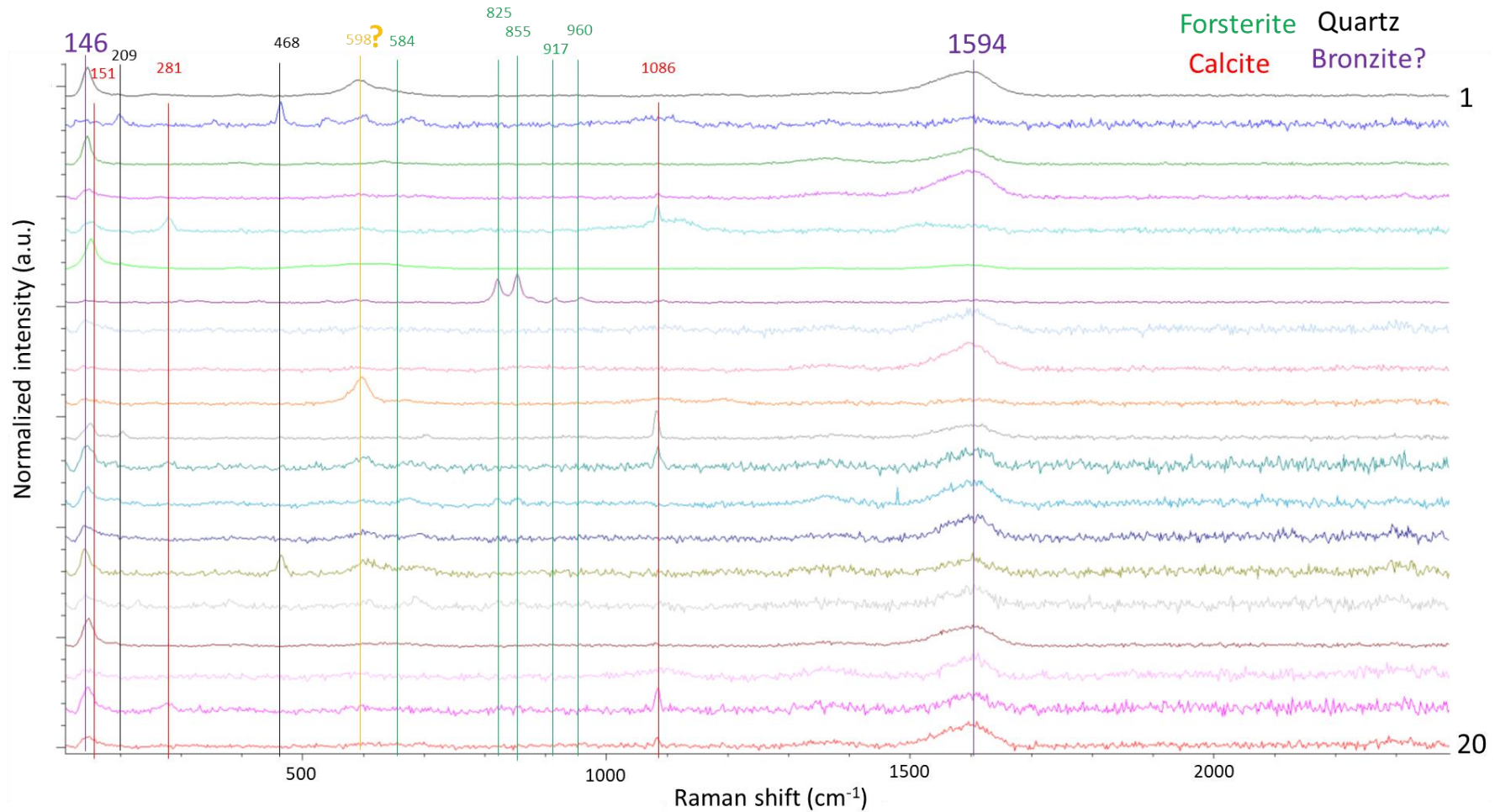
Figure C.10: Normalized and stacked Raman spectra for the 20 point measurements of the suspended particulate matter in the flow olivine treatment at day 4. Position of the point measurements are shown in Figure C.9A. Vertical lines represent characteristic wavelengths for phases given in the top right of the figure. Question marks indicate uncertain mineral identification.
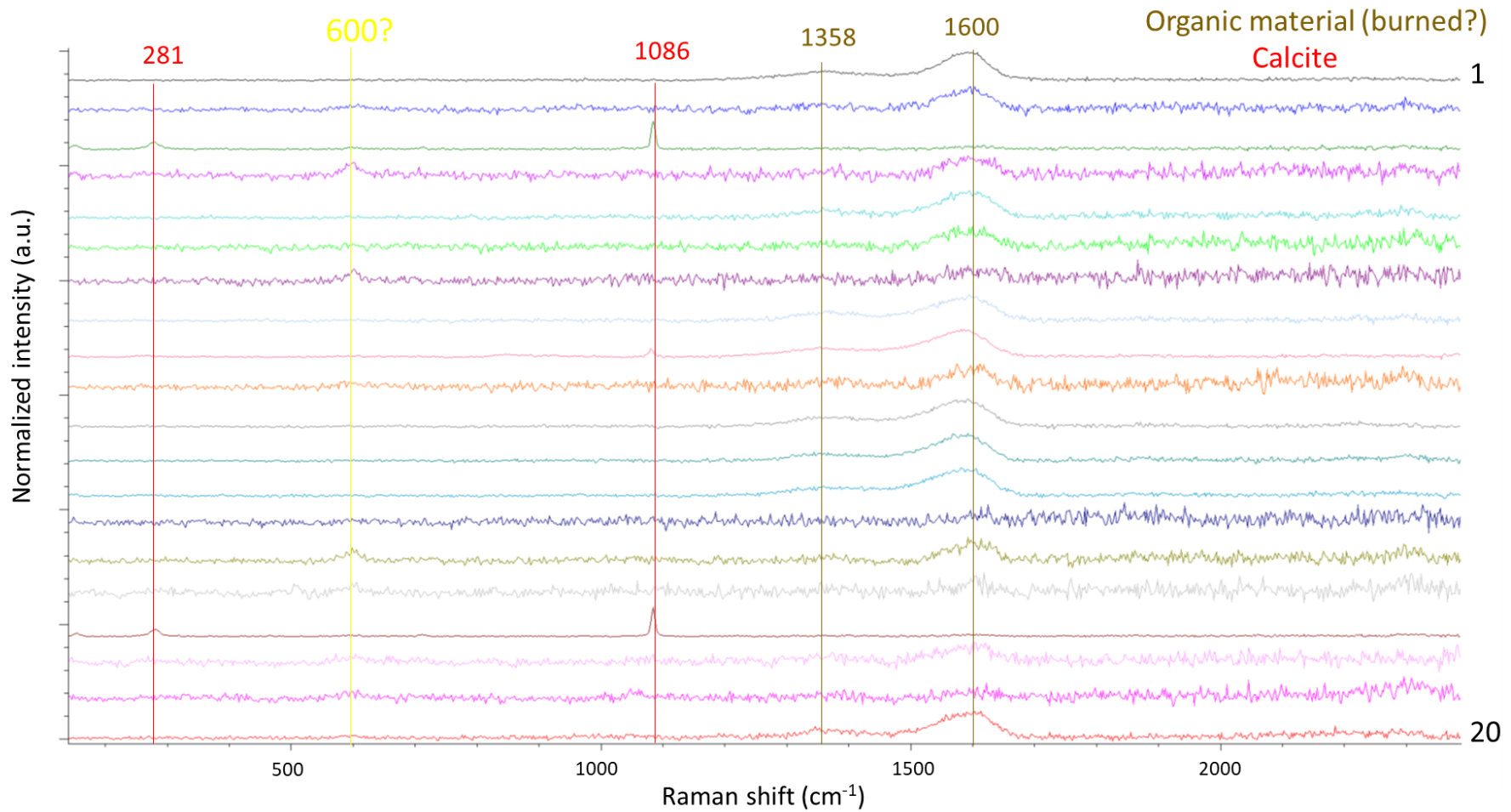
Figure C.11: Normalized and stacked Raman spectra for the 20 point measurements of the suspended particulate matter in the flow sand treatment at day 4. Position of the point measurements are shown in Figure C.9B. Vertical lines represent characteristic wavelengths for phases given in the top right of the figure. Question marks indicate uncertain mineral identification.
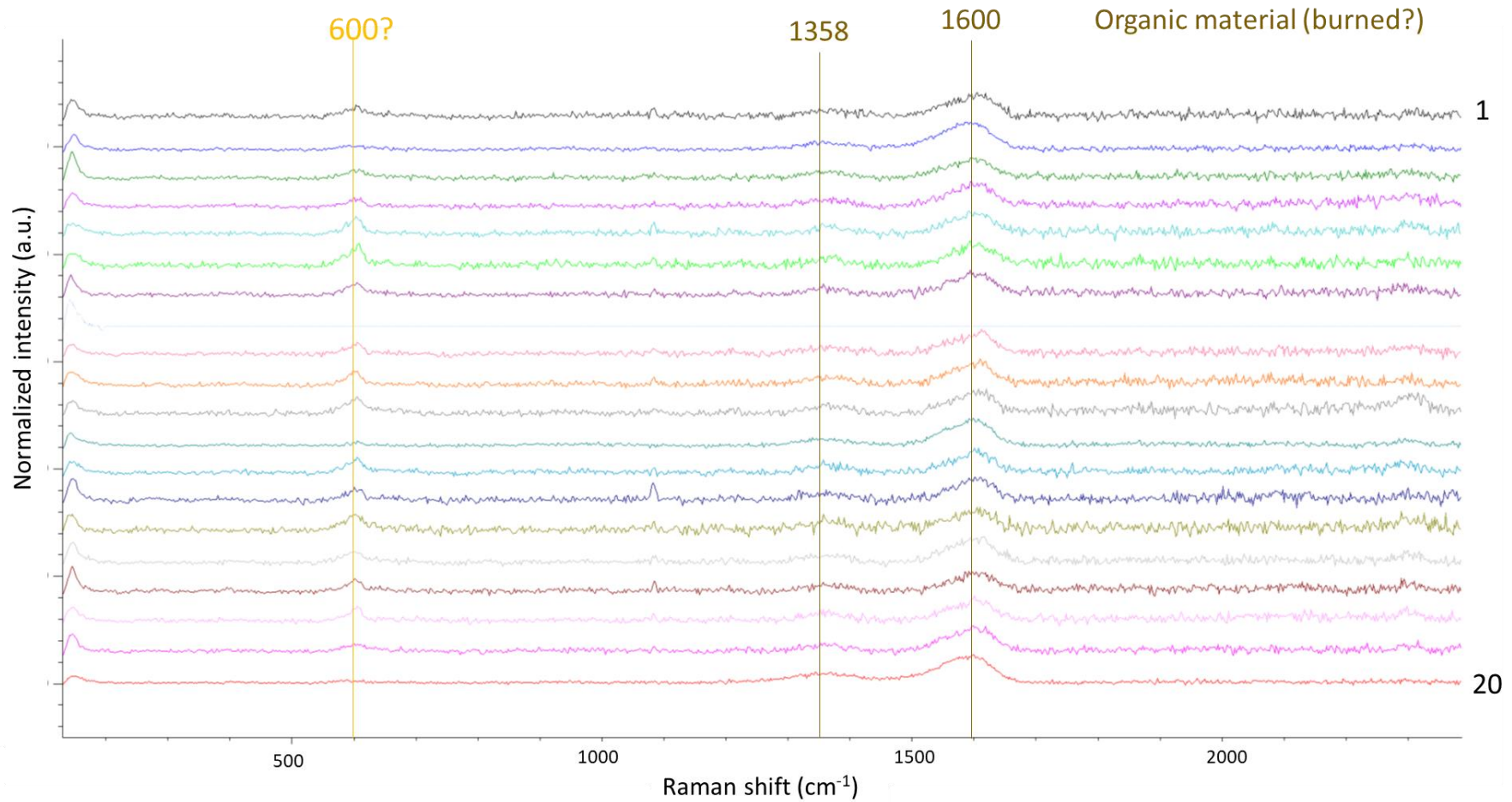
Figure C.12: Normalized and stacked Raman spectra for the 20 point measurements of the flume wall deposits in the stagnant sand treatment at the end of the 175-day experiment. Position of the point measurements are shown in Figure C.9C. Vertical lines represent characteristic wavelengths for phases given in the top right of the figure. Question marks indicate uncertain mineral identification.
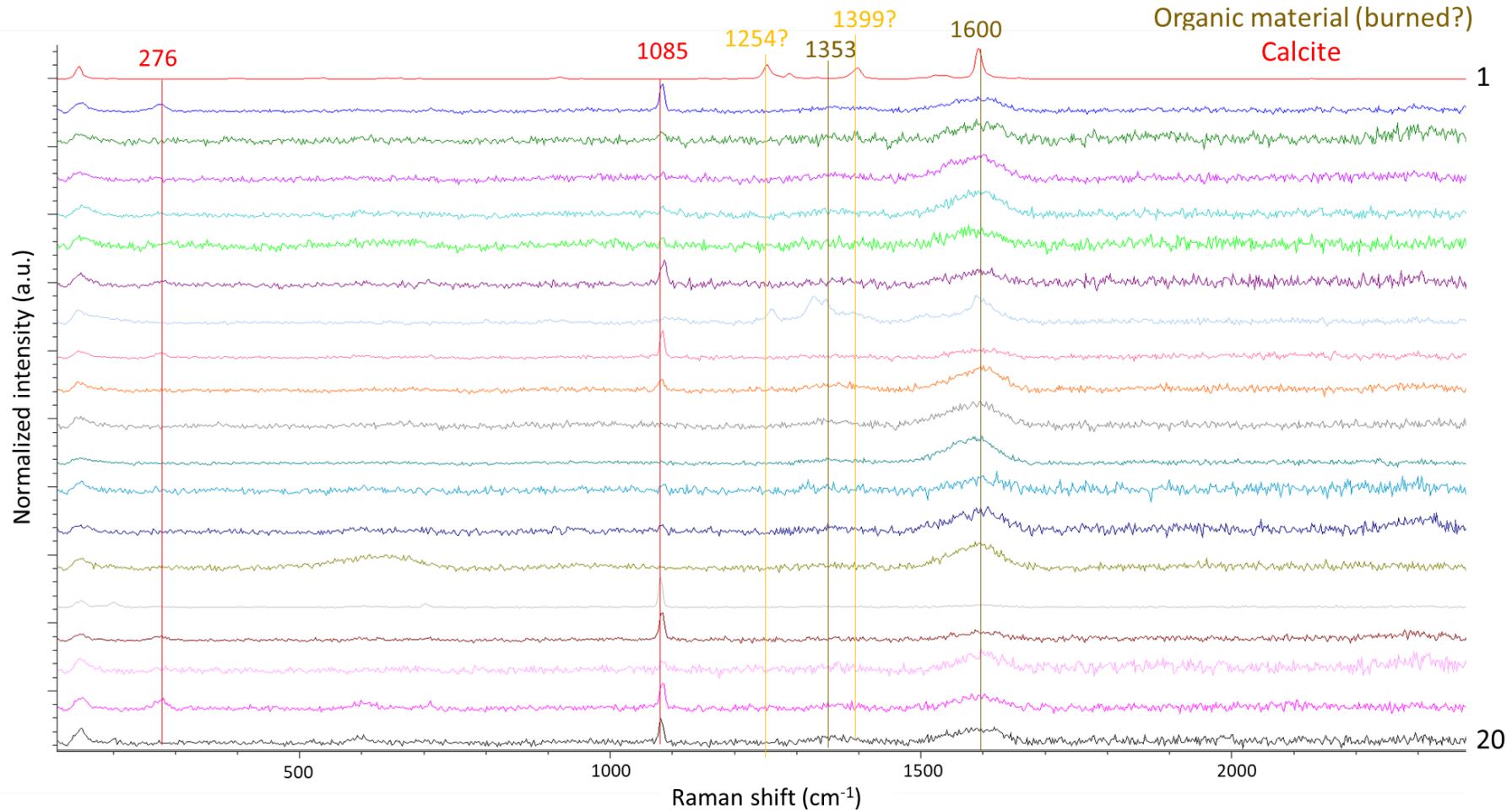
Figure C.13: Normalized and stacked Raman spectra for the 20 point measurements of the flume wall deposits in the flow sand treatment at the end of the 175-day experiment. Position of the point measurements are shown in Figure C.9D. Vertical lines represent characteristic wavelengths for phases given in the top right of the figure. Question marks indicate uncertain mineral identification.

C.9 Dissolved element concentrations
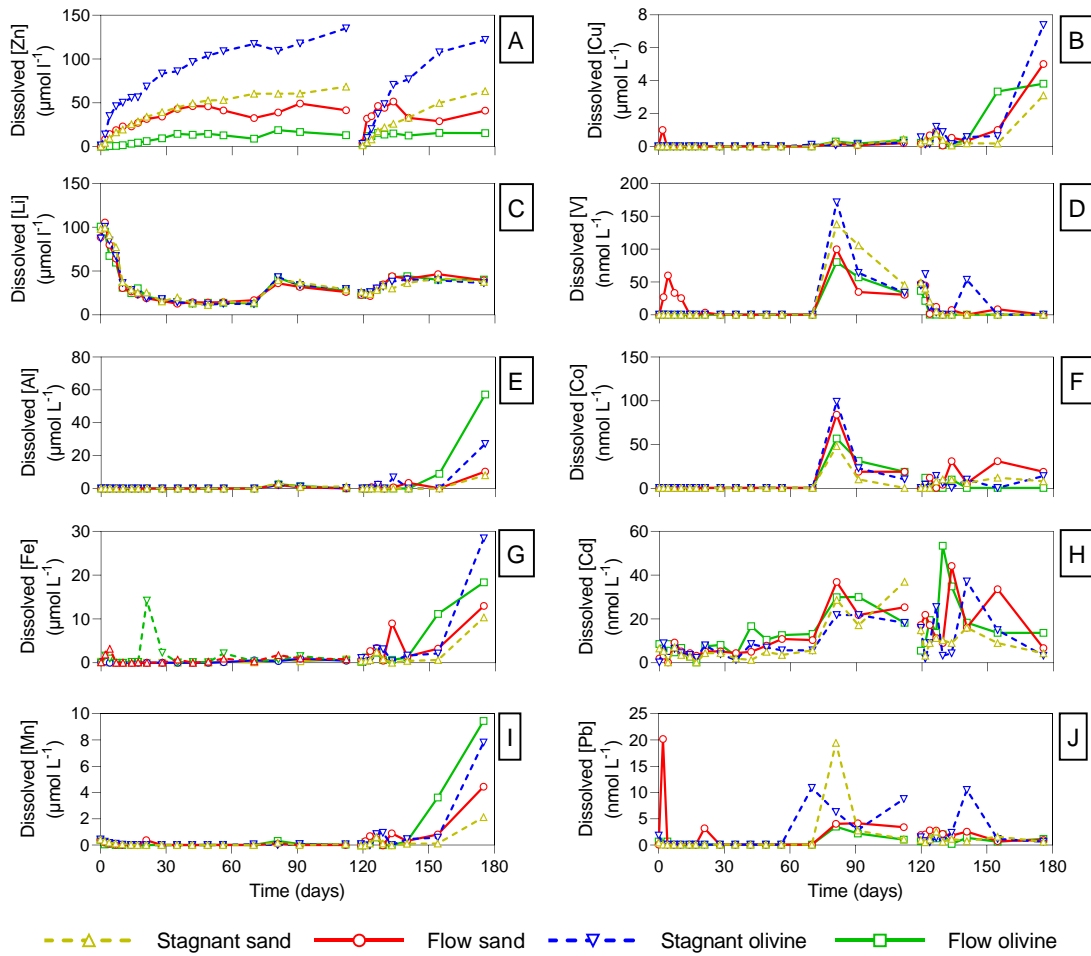
Figure C.14: Temporal evolution of dissolved (<0.2 μm) (A) Zn, (B) Cu, (C) Li, (D) V, (E) Al, (F) Co, (G) Fe, (H) Cd, (I) Mn, and (J) Pb during the 175-day flume experiment. Note that concentrations for Zn, Cu, Li, Al, Fe, and Mn are given in μmol L^{-1}, while concentrations for V, Co, Cd, and Pb are given in nmol L^{-1}.
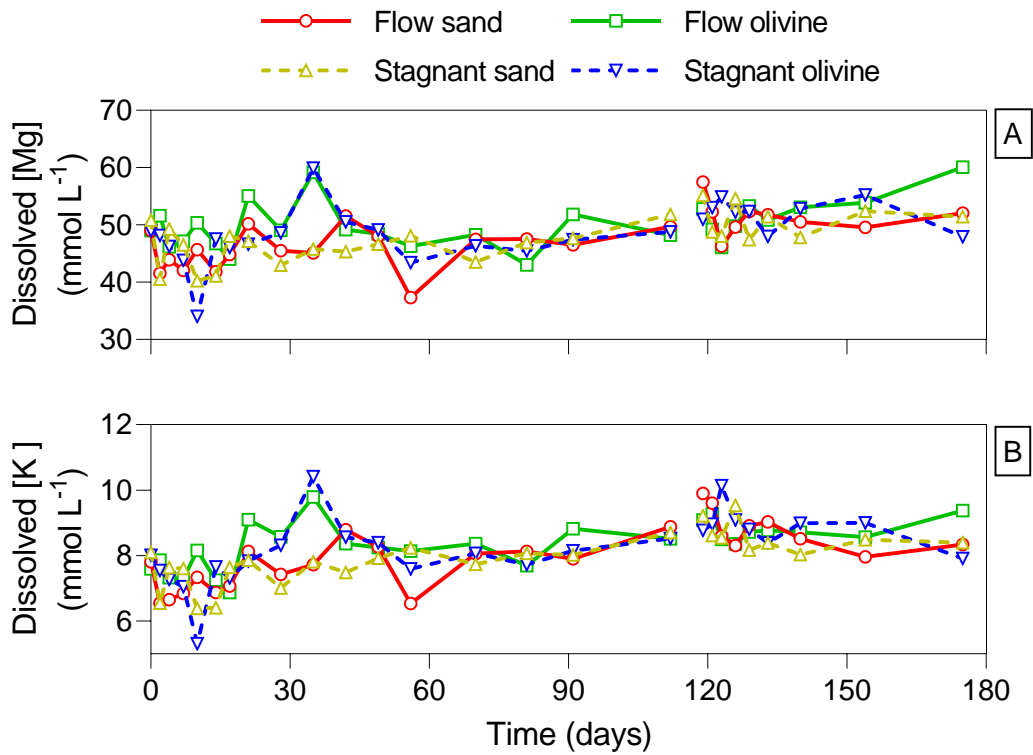
Figure C.15: Temporal evolution of (A) dissolved magnesium (Mg), and (B) potassium (K) concentrations (mmol L^{-1}) during the 175-day flume experiment.

Appendix D: Chapter 4

D.1 Methodology of deriving a seawater metal EQS based olivine guideline

The expected maximum amount of olivine that could be supplied to the coastal zone without adverse effects for marine biota was calculated based on existing seawater environmental quality standards. First, the maximum environmentally safe dissolution rate of olivine, R_{max} (mol s^{-1} m^{-2} seabed) was calculated from:

$$R_{\text{max}} = \frac{C_{\text{max}} V_{\text{w}}}{t}$$
[D.1]

With $C_{\text{max}} = \dfrac{C_{\text{EQS}} - C_{\text{bg}}}{\chi}$
[D.2]

Where C_{max} is the maximum allowed concentration of olivine (mol l^{-1}), V_w is the water volume per m^2 of seabed (l m^{-2}), t is the water residence time (s), C_{EQS} is the environmental quality standards for Ni or Cr^{3+} in seawater (mol l^{-1}), C_{bg} is the background concentration (mol l^{-1}) of Ni or Cr^{3+} in seawater and χ is the concentration of Ni or Cr^{3+} in olivine (7.5 or 6.57 mmol mol^{-1} olivine, respectively).(Santos et al., 2015; Montserrat et al., 2017) Generally, the dissolution rate of olivine, R (mol s^{-1} m^{-2} seabed), is expressed as:

$$R = k_{\text{diss}} A m_{app}$$
[D.3]

with $A = \dfrac{4\pi r^2}{\frac{4}{3}\pi r^3 \rho_{\text{olivine}}}$
[D.4]

where k_{diss} is the dissolution rate constant of olivine (mol m^{-2} s^{-1}), A is the specific surface area of the mineral grains (m^2 kg^{-1}), m_{app} is the amount of olivine applied to the seabed (kg m^{-2} of seabed), r is the radius of the olivine grains (m), and $\rho_{olivine}$ is the density of olivine (3300 kg m^{-3}) (Montserrat et al., 2017). Based on the preceding equations, the maximum amount of olivine, m_{app}, that could be supplied per m^2 meter of seabed (kg m^{-2}) without exceeding Ni or Cr^{3+} seawater EQS was calculated by substituting the dissolution rate, R (eq 3) into eq 1 and solving for m_{app}, to give:

$$m_{app} = \frac{C_{max} * V_w}{k_{diss} * A * t}$$ [D.5]

D.2 Summarized global coastal Cr concentrations

A summary of Cr concentrations globally occurring in coastal waters and sediment is shown in Table D.1. Summarized data from individual studies is shown in Table D.5 and D.7. Chromium can exist in two stable oxidation states in the aquatic environment: trivalent (Cr^{3+}) or hexavalent (Cr^{6+}) chromium. Typically, Cr^{6+} is the dominant species for well oxygenated coastal waters, which is confirmed by collected data showing a median dissolved Cr^{3+} concentration of 0.84 nmol l^{-1} and Cr^{6+} concentrations of 2.42 nmol l^{-1} (Table D.1). Based on several studies, it was shown that the Cr^{6+}/Cr^{3+} ratio can range from <1 to >100 depending on the local redox conditions (Pettine, 2000).

Total Cr concentrations in coastal sediment ranged from 0.03 mmol kg^{-1} dry wt at the Tuzla Aydinli Bay in Turkey to 9.73 mmol kg^{-1} dry wt at the East Outfall Site of the Seaplane Lagoon in the San Francisco Bay, California (O'Day et al., 2000; Baysal and Akman, 2018). This latter location is known to be polluted with several metals due to its military and industrial history (O'Day et al., 2000). The median total recoverable Cr concentration in the surface sediments was 1.37 mmol kg^{-1} dry wt.

Table D.3: Summary of dissolved chromium ($Cr^{3+/6+}$) concentrations (nmol l^{-1}) in seawater and total Cr concentrations (mmol kg^{-1} dry wt) in sediment for coastal systems (water depth ≤ 200 m) around the world. Number of locations (n)median, percentiles (P) and range (Min – Max) are provided to illustrate the distribution of the data.

	Dissolved seawater [Cr^{3+}] (nmol l^{-1}) (*n* = 15)	Dissolved seawater [Cr^{6+}] (nmol l^{-1}) (*n* = 12)	Total [Cr] in sediment (mmol kg^{-1} dry wt) (*n* = 46)
Median	0.84	2.42	1.46
P25 – P75	0.48 – 1.49	1.82 – 2.63	0.53 – 1.95
P5 – P95	0.26 – 1.99	0.86 – 3.35	0.13 – 7.53

Min – Max	0.08 – 2.47	0.23 – 3.83	0.03 – 9.73

D.3 Coastal Ni and Cr environmental quality standards (EQS)

Marine EQS for Ni, Cr^{3+} and Cr^{6+} in water and sediment are shown in Table D.2 and D.3, respectively. In different countries/regions specific metals are prioritized in risk assessment based on the local risk they pose to the marine environment (Tyle and Scott-Fordsmand, 2008). Furthermore, some seawater EQS are based on total metal concentrations (e.g. Canadian EQS) (CCME, 1999), while others are based on dissolved metal concentrations (e.g. USA EQS) (USEPA, 1995). For Ni, the recently derived EQS of 0.102 µmol l^{-1} by Gissi et al. (2020) is also shown, which was obtained using a species sensitivity distribution (SSD) approach that combined chronic no-effect or negligible effect (≤20% of individuals affected) data for temperate and tropical species (Gissi et al., 2020). Exceedance of EQS can lead to a range of toxicological effects in marine biota that are sensitive to Ni, e.g. sea urchins, copepods, polychaete worms, gastropods and mysid shrimp (Gissi et al., 2020).

For sediment, only one of the most widely used guidelines as derived by the Florida department of environmental protection (FDEP) are shown (Table D.3) (Macdonald et al., 1996; Hübner et al., 2009). In their approach, a Threshold Effect Level (TEL) below which adverse effects on biota are rare and a Probable Effect Level (PEL) above which adverse effects occur frequently are derived from the Biological Effects Database for Sediments containing thoroughly screened reports on the concentration-effect relationships for marine biota (Macdonald et al., 1996; Hübner et al., 2009). Unlike for water quality guidelines, sediment EQS should be used as a preliminary screening tool; meaning that if total metal concentrations in the sediment exceed the guidelines, further risk assessment should be conducted by examining the metal bioavailability and site-specific sediment toxicity (Hübner et al., 2009; Simpson and Batley, 2016).

Table D.2: Chronic marine environmental quality standards (EQS) for nickel (Ni) and chromium (Cr^{6+}/Cr^{3+}) in seawater. Nickel EQS as derived by Gissi et al. (2020) which incorporated recently obtained marine Ni toxicity data is also shown. Metal concentrations are expressed in μmol l^{-1}. References are given in parentheses in superscript.

Country/region/study	Ni EQS (μmol l^{-1})	Cr^{6+} EQS (μmol l^{-1})	Cr^{3+} EQS (μmol l^{-1})
Europe	0.147	/	/
USA	0.140	0.962	/
Canada	/	0.029	1.077
Australia and New Zealand	0.119	0.085	0.192
Gissi et al. (2020)	0.102	/	/

Table D.3: Sediment environmental quality standards (EQS) for nickel (Ni) and chromium (Cr) as derived by the Florida department of environmental protection (FDEP) (Macdonald et al., 1996). Threshold effect level (TEL) below which adverse effects are rarely expected and probable effect level (PEL) above which adverse effects frequently occur are shown for both metals expressed in mmol kg^{-1} dry wt.

Metal	TEL (mmol kg^{-1} dry wt)	PEL (mmol kg^{-1} dry wt)
Ni	0.271	0.729
Cr	1.006	3.077

D.4 Global Ni and Cr$^{3+/6+}$ concentrations in coastal seawater

Table D.4: Dissolved nickel (Ni) concentrations (nmol l^{-1}) in coastal seawater collected from primary literature. The location, sampling depth, number of samples taken at each site and reference to the study are given. Data from a single location were summarized using descriptive statistics (mean ± standard deviation (S.D.), median and range) where possible.

Location	Sampling depth (m)	Sample size (n)	Mean ± S.D. [Ni] (nmol l^{-1})	Median [Ni] (nmol l^{-1})	Min – Max [Ni] (nmol l^{-1})	Pore size filter (µm)	Reference
Menai straits, Irish Sea, Liverpool Bay (UK)	0 (Surface)	3	8.9 ± 3	7.5	7.2 - 12	0.45	(Van den Berg and Nimmo, 1987)
Irish Sea, Liverpool Bay (UK)	0 (Surface)	/	3.2	/	/	0.45	(Van den Berg and Nimmo, 1987)
The English Channel (UK)	40	/	3.7	/	/	0.45	(Van den Berg and Nimmo, 1987)
South San Francisco Bay (USA)	1	2	54 ± 5	54	50 – 58	0.45	(Donat et al., 1994)
Northern Great Barrier Reef (Australia)	0.1	8	1.47 ± 0.2	1.45	1.19 – 1.70	0.45	(Denton and Burdon-Jones, 1986)
Central Great Barrier Reef (Australia)	0.1	8	1.98 ± 0.5	2.04	1.19 – 2.73	0.45	(Denton and Burdon-Jones, 1986)
Southern Great Barrier Reef	0.1	8	1.38 ± 0.3	1.36	1.02 – 1.7	0.45	(Denton and Burdon-

(Australia)							Jones, 1986)
Hawaii (USA)	1	9	4.64 ± 0.8	5.02	3.35 – 5.83	0.2	(Bienfang et al., 2009)
Oahu (USA)	1	6	5.71 ± 1.9	5.21	3.74 – 8.63	0.2	(Bienfang et al., 2009)
Kauai (USA)	1	3	3.79 ± 0.7	3.96	3.61 – 4.87	0.2	(Bienfang et al., 2009)
Southern Caspian Sea coast (Iran)	0 (Surface)	/	169	/	/	0.45	(Abadi et al., 2018)
Gorgan bay at Caspian Sea (Iran)	0 (Surface)	/	172	/	/	0.45	(Abadi et al., 2018)
Southern Caspian Sea estuaries (Iran)	0 (Surface)	/	80.6	/	/	0.45	(Abadi et al., 2018)
Chabahar, Oman (Iran)	0.5	6	173 ± 90	192	49 – 263	/	(Mirzaei et al., 2016)
Darwin Harbour (Australia)	0.5	16	3.95	/	2.52 – 5.61	0.45	(Munksgaard and Parry, 2001)
Bing Bong coast (Australia)	0.5	29	2.81	/	2.52 – 3.19	0.45	(Munksgaard and Parry, 2001)
Karumba Offshore (Australia)	0.5	12	2.66	/	1.98 – 3.66	0.45	(Munksgaard and Parry, 2001)
northwestern Bay of Bengal (India)	0 (Surface)	/	/	/	24.88 – 60.66	0.45	(Srichandan et al., 2016)

Bay of Bengal (India)	0 (Surface)	12	0.92 ± 0.7	0.605	0.36 – 2.11	0.45	(Rejomon et al., 2008)
western Bay of Bengal (India)	0 - 75	28	9.18 ± 13	1.09	0.58 – 33.7	0.45	(Rejomon et al., 2010)
Eastern Red sea, Jeddah (Saudi Arabia)	0.5	44	3.92 ± 5.4	2.45	1.30 – 28.1	0.45	(Al-Farawati et al., 2011)
southern Bohai Sea (China)	Surface + bottom	7	33.9 ± 14	42.3	14.3 – 49.6	0.2	(Li et al., 2015)
Tuticorin coast (India)	0 (Surface)	2	840 ± 259	803	571 – 1180	0.4	(Srikanth et al., 2014)
Gulf of Mannar (India)	bottom	15	42.4 ± 3.9	/	/	0.4	(Rao et al., 2007)
western coast of the Gulf of Suez, Red Sea (Egypt)	2	14	38.4 ± 11	35.9	23.2 – 62.2	/	(Hamed and Emara, 2006)
Saemangeum coastal area, Buan (South Korea)	0 (Surface)	6	20.2 ± 25	11.6	4.94 – 71.4	0.4	(Kim et al., 2010)
Alang–Sosiya ship scrapping yard, Gulf of Cambay (India)	1	9	5290 ± 5407	3360	477 - 16100	0.45	(Reddy et al., 2005)
San Francisco Bay estuary (USA)	1	62	29.39 ± 11	26.38	9.77 – 69.36	0.45	(Flegal et al., 1991)
Western basin Mediterranean	/	8	3.34 ± 0.9	3.27	2.14 – 4.5	0.4	(Achterberg and Van

Sea, Mallorca (Spain)							Den Berg, 1997)
Strait of Gibraltar (Spain and Morocco)	/	8	3.10 ± 1.1	3.11	1.67 – 4.54	0.4	(Achterberg and Van Den Berg, 1997)
Strait of Sicily (Italy)	/	8	3.23 ± 0.9	3.32	2.11 – 4.2	0.4	(Achterberg and Van Den Berg, 1997)

Dissolved nickel (Ni) concentrations (nmol/l) in coastal waters

Ni concentration (nmol/l)
- 1 - 5
- 5 - 20
- 20 - 102
- 102 - 1000
- \>1000
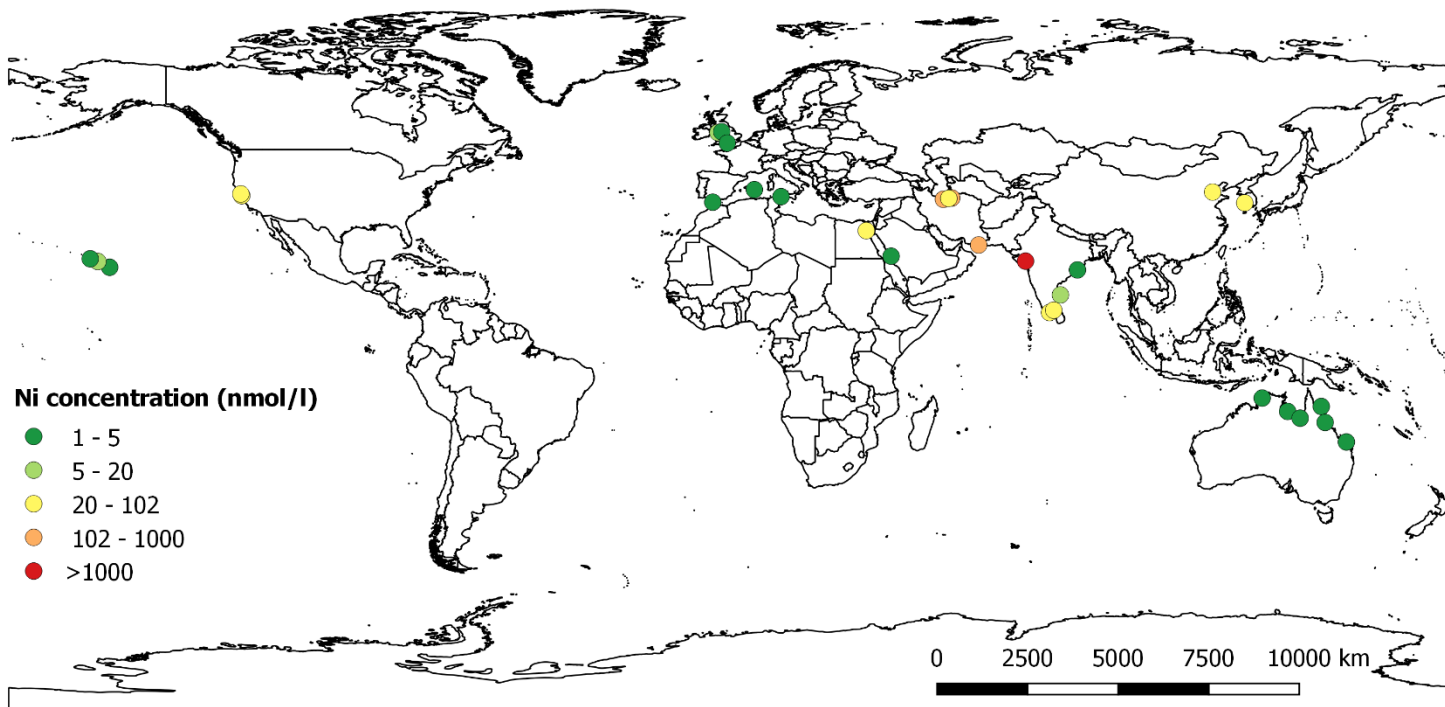
Figure D.1: Dissolved nickel (Ni) concentrations (nmol l^{-1}) in coastal seawater collected from primary literature. Locations where dissolved Ni concentrations exceed the guideline proposed by Gissi et al. (2020) are shown in orange and red. Individual datapoints are shown in Supplementary Table D.4. This map was made in QGIS Desktop version 2.16.3.

Table D.5: Dissolved chromium (Cr^{3+}/Cr^{6+}) concentrations (nmol l^{-1}) in coastal seawater collected from primary literature. The location, sampling depth, number of samples taken at each site and reference to the study are given. Data from a single location were summarized using descriptive statistics (mean ± standard deviation (S.D.), median and range) where possible.

Location	Sampling depth (m)	Sample size (n)	Mean ± S.D. [Cr] (nmol l^{-1})	Median [Cr] (nmol l^{-1})	Min – Max [Cr] (nmol l^{-1})	Pore size filter (μm)	Oxidation state (Cr^{6+}/Cr^{3+}/Total)	Reference
Saanich Inlet, oxic zone (Canada)	/	/	1.5 ± 0.3	/	/	/	Cr^{6+}	(Cranston and Murray, 1978)
Saanich Inlet, oxic zone (Canada)	/	/	0.08 ± 0.08	/	/	/	Cr^{3+}	(Cranston and Murray, 1978)
Saanich Inlet, anoxic zone (Canada)	/	/	0.23 ± 0.1	/	/	/	Cr^{6+}	(Cranston and Murray, 1978)

Saanich Inlet, anoxic zone (Canada)	/	/	0.84 ± 0.2	/	/	/	Cr^{3+}	(Cranston and Murray, 1978)
Columbia river estuary (Canada)	/	/	2.4 ± 0.7	/	/	/	Cr^{6+}	(Cranston and Murray, 1978)
Columbia river estuary (Canada)	/	/	0.32 ± 0.4	/	/	/	Cr^{3+}	(Cranston and Murray, 1978)
Coast of Baja (Mexico)	/	/	/	/	1.1 - 6	0.4	Cr^{6+}	(Murray et al., 1983)
Concarneau, South Britanny (France)	0 (Surface)	/	1.38 ± 0.07	/	/	0.2	Cr^{3+}	(Jeandel and Minster, 1984)
Concarneau, South Britanny (France)	0 (Surface)	/	2.7 ± 0.1	/	/	0.2	Total	(Jeandel and Minster, 1984)
Perros Guirec, North Britanny (France)	0 (Surface)	/	1.81 ± 0.03	/	/	0.2	Cr^{3+}	(Jeandel and Minster, 1984)
Locquirec, North Britanny (France)	0 (Surface)	3	2.47 ± 0.1	2.42	2.4 – 2.59	0.2	Cr^{3+}	(Jeandel and Minster, 1984)
Northwestern Mediterranean Sea (Spain/France)	Surface to bottom	17	0.34 ± 0.5	0.1	0 – 1.2	0.4	Cr^{3+}	(van den Berg et al., 1994)
Northwestern	Surface to	17	3.83 ±	4.05	2.7 – 4.5	0.4	Cr^{6+}	(van den Berg et

Mediterranean Sea (Spain/France)	bottom		0.6					al., 1994)
San Francisco Bay Estuary (USA)	1	27	3.16 ± 1.9	2.2	1.7 – 8.3	0.4	Total	(Abu-Saba and Flegal, 1995)
San Francisco Bay Estuary (USA)	1	27	1.11 ± 1.8	0.2	0 – 6.7	0.4	Cr^{3+}	(Abu-Saba and Flegal, 1995)
San Francisco Bay Estuary (USA)	1	27	2.06 ± 6.7	2	0.6 – 4.7	0.4	Cr^{6+}	(Abu-Saba and Flegal, 1995)
Western basin Mediterranean Sea, Mallorca (Spain)	/	4	3 ± 0.3	3.04	2.69 – 3.24	0.4	Total	(Achterberg and Van Den Berg, 1997)
Strait of Gibraltar (Spain and Morocco)	/	4	2.87 ± 0.3	2.94	2.51 – 3.09	0.4	Total	(Achterberg and Van Den Berg, 1997)
Strait of Sicily (Italy)	/	4	3.05 ± 0.3	3.08	2.61 – 3.41	0.4	Total	(Achterberg and Van Den Berg, 1997)
Western basin Mediterranean Sea, Mallorca (Spain)	/	4	2.51 ± 0.3	2.39	2.35 – 2.91	0.4	Cr^{6+}	(Achterberg and Van Den Berg, 1997)

317

Strait of Gibraltar (Spain and Morocco)	/	4	2.44 ± 0.2	2.46	2.15 – 2.7	0.4	Cr^{6+}	(Achterberg and Van Den Berg, 1997)
Strait of Sicily (Italy)	/	4	2.54 ± 0.5	2.42	2.15 – 3.18	0.4	Cr^{6+}	(Achterberg and Van Den Berg, 1997)
Western basin Mediterranean Sea, Mallorca (Spain)	/	4	0.49 ± 0.2	0.42	0.33 – 0.8	0.4	Cr^{3+}	(Achterberg and Van Den Berg, 1997)
Strait of Gibraltar (Spain and Morocco)	/	4	0.43 ± 0.2	0.46	0.16 – 0.63	0.4	Cr^{3+}	(Achterberg and Van Den Berg, 1997)
Strait of Sicily (Italy)	/	4	0.51 ± 0.3	0.47	0.24 – 0.86	0.4	Cr^{3+}	(Achterberg and Van Den Berg, 1997)
Western Harbour, Alexandria (Egypt)	0 (Surface)	10	55.62 ± 47	46.54	3.85 – 145.59	0.45	Total	(Abdallah, 2014)
Saanich Inlet, British Columbia (Canada)	0 – 200	5	2.21 ± 0.2	2.32	1.92 – 2.47	0.2	Total	(Davidson et al., 2020)
Saanich Inlet, British	0 – 200	5	1.38 ±	1.5	0.41 –	0.2	Cr^{6+}	(Davidson et al.,

Location	Depth	n	Mean ± SD		Range		Form	Reference
Columbia (Canada)			0.9		2.38			2020)
Saanich Inlet, British Columbia (Canada)	0 – 200	5	0.83 ± 0.8	0.48	0.09 – 1.9	0.2	Cr^{3+}	(Davidson et al., 2020)
Humber estuary (UK)	0 (surface)	3	3.91 ± 0.7	3.85	3.27 – 4.62	0.45	Total	(Gardner and Ravenscroft, 1996)
Humber estuary (UK)	0 (surface)	3	0.96 ± 0.2	0.96	0.77 – 1.15	0.45	Cr^{3+}	(Gardner and Ravenscroft, 1996)
Humber estuary (UK)	0 (surface)	3	2.95 ± 0.6	2.69	2.5 – 3.65	0.45	Cr^{6+}	(Gardner and Ravenscroft, 1996)
Hiroshima Bay of the Seto Inland Sea (Japan)	0 – 20	6	2.81 ± 0.3	2.69	2.63 – 3.33	0.4	Total	(Hirata et al., 2000)
Hiroshima Bay of the Seto Inland Sea (Japan)	0 – 20	6	1.92 ± 0.2	1.89	1.65 – 2.31	0.4	Cr^{6+}	(Hirata et al., 2000)
Hiroshima Bay of the Seto Inland Sea (Japan)	0 – 20	6	0.89 ± 0.1	0.92	0.65 – 1.01	0.4	Cr^{3+}	(Hirata et al., 2000)
Northern Pacific Ocean, Southern California (USA)	0 (Surface)	14	4.60 ± 2.6	3.94	1.73 – 113.47	0.4	Total	(Jan and Young, 1978)
Northern Pacific Ocean, Southern California	0 (Surface)	14	2.9 ± 0.3	2.88	2.31 – 3.46	0.4	Cr^{6+}	(Jan and Young, 1978)

(USA)						
Northern Pacific Ocean, Southern California (USA)	0 (Surface)	14	1.83 ± 1.4	1.33	0.56 – 4.81	0.4	Cr^{3+}	(Jan and Young, 1978)
lagoon of New Caledonia (New Caledonia)	5	12	4.22 ± 3.3	2.93	1.33 – 11.29	0.2	Total	(Migon et al., 2007)
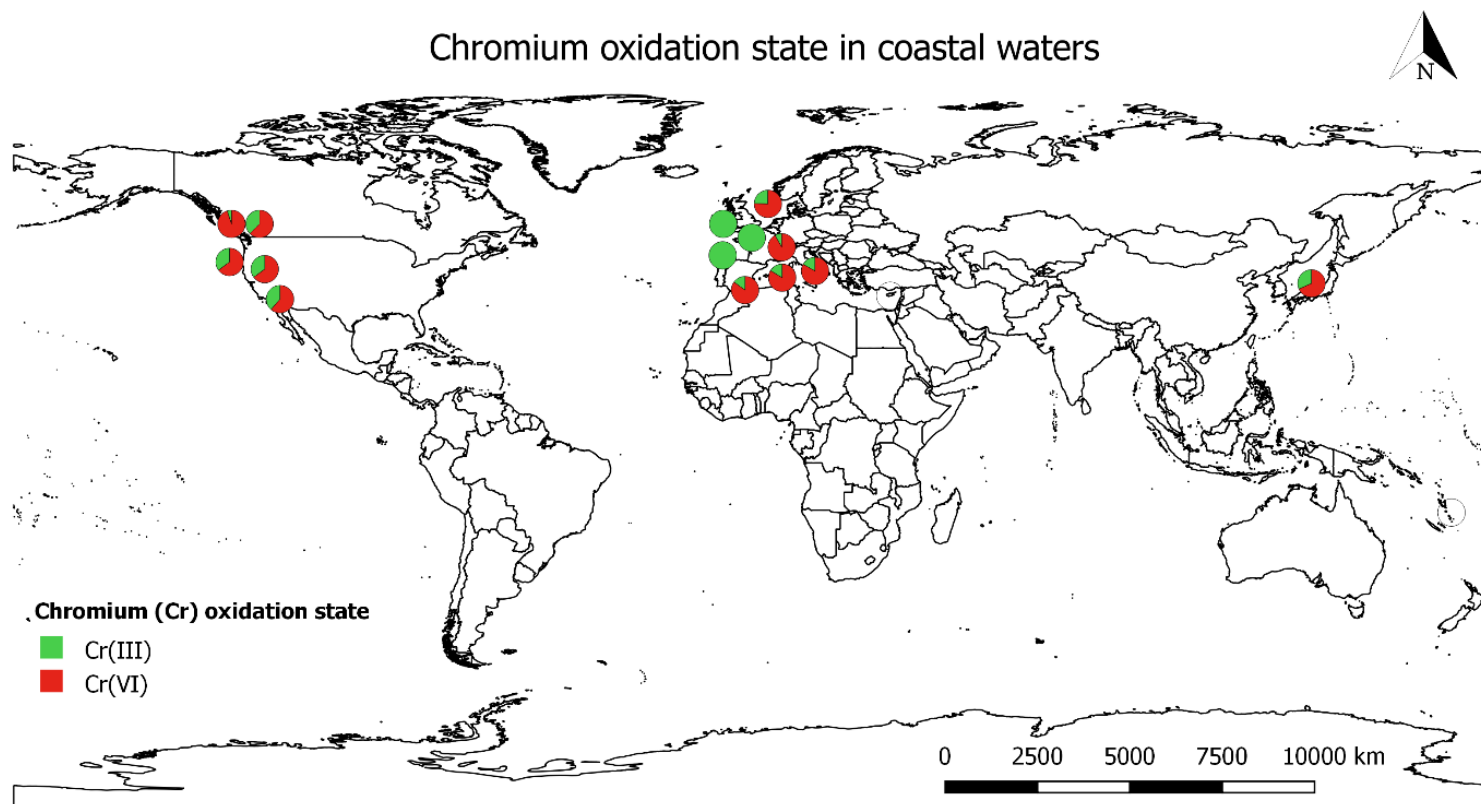
Figure D.2: Chromium (Cr) oxidation state (Cr^{3+} or Cr^{6+}) in coastal seawater collected from primary literature. Individual datapoints are shown in Supplementary Table D.5. This map was made in QGIS Desktop version 2.16.3.

D.5 Global Ni and Cr concentrations in coastal sediment

Table D.6: Total recoverable nickel (Ni) concentrations (mmol kg^{-1} dry weight) in coastal sediment collected from primary literature. The location, sampling depth, number of samples taken at each site, chemical(s) used for metal extraction from the sediment and reference to the study are given. Data from a single locations were summarized using descriptive statistics (mean ± standard deviation (S.D.), median and range) where possible.

Location	Sample size (n)	Sampling depth (m)	Sediment fraction	Mean ± S.D. [Ni] (mmol kg^{-1} dry wt)	Median [Ni] (mmol kg^{-1} dry wt)	Min – Max [Ni] (mmol kg^{-1} dry wt)	Chemical(s) used for metal extraction	Reference
Berre Lagoon, Marseille (France)	17	0 (surface)	Bulk	0.63 ± 0.2	0.60	0.31 – 0.95	HNO$_3$, H$_2$O$_2$ and HF	(Accornero et al., 2008)
Thames Estuary (UK)	28	0 (surface)	<63 µm	0.36 ± 0.1	/	/	HNO$_3$ and H$_2$O$_2$	(Attrill and Thomes, 1995)
North Sea (Belgium)	16	0 (Surface)	Bulk	0.23 ± 0.1	0.22	0.043 – 0.46	HNO$_3$, HF and HClO$_4$	(Van Alsenoy et al., 1993)
North Sea (Belgium)	16	0 (Surface)	<63 µm	0.36 ± 0.1	0.34	0.22 – 0.65	HNO$_3$, HF and HClO$_4$	(Van Alsenoy et al., 1993)
Baltic proper, Baltic Sea (Sweden)	59	0 – 10	<63 µm	0.78 ± 0.5	/	/	HNO$_3$, HF and HClO$_4$	(Hallberg, 1991)

Vistula Lagoon (Poland)	25	0 (Surface)	<63 μm	0.66 ± 0.1	0.65	0.47 – 0.82	HNO_3, HF and $HClO_4$	(Szefer et al., 1999)
Gei wai 13, Mai Po Marshes (China)	3	0 – 0.08	<63 μm	0.56	/	0.53 – 0.59	H_2SO_4 and HNO_3	(Lau and Chu, 1999)
Tees estuary (UK)	11	0 – 0.05	Bulk	0.68 ± 0.1	0.70	0.36 – 0.83	HNO_3, HF and $HClO_4$	(Jones and Turki, 1997)
Atlantic Ocean (Spain)	15	0 – 0.03	<63 μm	0.34 ± 0.2	0.29	0.17 – 0.85	HNO_3 and $HClO_4$	(Morillo et al., 2004)
Ferrol Ria (Spain)	35	0 (Surface)	<63 μm	0.55 ± 0.2	/	/	HNO_3 and HF	(Cobelo-García and Prego, 2004)
Ria de Vigo (Spain)	34	0 (Surface)	Bulk	0.58 ± 0.1	/	/	HNO_3, HF and $HClO_4$	(Rubio et al., 2000)
Medway Estuary, Kent (UK)	8	0 (Surface)	Bulk	0.55 ± 0.1	0.55	0.39 – 0.65	HNO_3, HF and $HClO_4$	(Spencer, 2002)
Mersey Estuary (UK)	19	0 – 0.02	Bulk	4.39 ± 10	0.9	0.59 – 34.6	*Aqua regia*	(Harland et al., 2000)
Boston Harbor (USA)	88	0 - 1.74	Bulk	0.46 ± 0.4	0.44	0.14 – 3.25	HNO_3, HF and $HClO_4$	(Bothner et al., 1998)
Jurujuba Sound (Brazil)	64	0 – 0.05	<63 μm	0.99 ± 0.2	/	0.75 – 1.35	*Aqua regia*	(Neto et al., 2000)

Gulf of Venice (Italy)	102	0 (Surface)	<63 µm	0.39 ± 0.1	0.38	0.21 – 0.87	HNO_3, HF and $HClO_4$	(Donazzolo et al., 1981)
Ensenada de San Simón (inner Ría de Vigo), Galicia, (Spain)	29	0 (Surface)	Bulk	0.39 ± 0.2	0.44	0.034 – 0.55	HNO_3, HF and $HClO_4$	(Evans et al., 2003)
Guanabara Bay, (Brazil)	4	0 – 0.05	Bulk	0.16 ± 0.04	0.16	0.10 – 0.20	HNO_3 and $HClO_4$	(Machado et al., 2002)
Jinzhou Bohai (China)	14	0 (Surface)	<63 µm	0.51 ± 0.2	0.53	0.25 – 0.70	HNO_3 and $HClO_4$	(Fan et al., 2002)
NE Chukchi Sea, Alaska (Canada)	31	0 (Surface)	Bulk	0.38 ± 0.1	0.41	0.17 – 0.65	HNO_3 and HF	(Naidu et al., 1997)
Taranto Gulf, Ionian Sea (Italy)	19	0 – 0.05	Bulk	0.91 ± 0.07	0.89	0.82 – 1.04	*Aqua regia* and HF	(Buccolieri et al., 2006)
Ligurian Sea between Arenzano and Capo Noli (Italy)	56	0 – 0.05	Bulk	4.48 ± 2.0	4.12	0.20 – 10.15	HF, $HClO_4$ and HCl	(Cosma et al., 1979)
Gulf of Suez, Red Sea (Egypt)	14	0 – 0.05	<0.75 mm	0.55 ± 0.2	0.55	0.29 – 0.85	HNO_3, $HClO_4$ and HF	(Hamed and Emara, 2006)
Saemangeum region, Yellow Sea (South Korea)	35	0 (Surface)	Bulk	0.18	/	0.049 – 0.34	*Aqua regia* and HF	(Kim et al., 2010)

Tuticorin coast (India)	9	0 (Surface)	<63 µm	5.44 ± 1.4	/	4.14 – 7.16	HNO_3, $HClO_4$ and HF	(Srikanth et al., 2014)
Gulf of Mannar, Tuticorin coast (India)	32	0 (Surface)	Bulk	0.41 ± 0.2	0.36	0.24 – 0.99	*Aqua regia* and HF	(Jonathan et al., 2004)
Jiaozhou Bay, Qingdao (China)	10	0 – 0.1	<125 µm	0.22 ± 0.1	0.20	0.046 – 0.39	HNO_3 and H_2O_2	(Wang et al., 2007)
Bay of Bengal (India)	21	0 (Surface)	Bulk	0.66	/	0.34 – 0.91	$HClO_4$ and HF	(Raj and Jayaprakash, 2008)
Jordan Gulf of Aqabe, Red sea (Jordan)	44	0 – 0.02	Bulk	0.57 ± 0.3	0.46	0.17 – 1.29	HNO_3, $HClO_4$ and HF	(Abu-Hilal, 1987)
Palos Verdes Peninsula, Los angeles (USA)	44	0 – 0.05	Bulk	1.06 ± 0.6	0.83	0.27 – 2.28	HNO_3 and HCl	(Hershelman et al., 1981)
Halifax bay (Australia)	34	0 – 0.1	Bulk	0.19	0.20	/	HNO_3, $HClO_4$ and HF	(Knauer, 1977)
Cleveland bay (Australia)	34	0 – 0.1	Bulk	0.15	0.16	/	HNO_3, $HClO_4$ and HF	(Knauer, 1977)
Tokyo Bay (Japan)	7	0 – 0.025	Bulk	0.52 ± 0.2	0.54	0.28 – 0.75	*Aqua regia* and $HClO_4$	(Fukushima et al., 1992)

Bombay coast (India)	11	0 – 0.8	Bulk	0.87 ± 0.09	0.87	0.72 – 1.00	HNO_3, $HClO_3$ and HF	(Dilli, 1986)
Victoria harbour, Hong Kong (China)	8	0 (Surface)	Bulk	0.98 ± 0.9	0.62	0.42 – 3.01	H_2O_2, HNO_3, $HClO_3$ and HF	(Wong et al., 1995)
Seaplane Lagoon, California (USA)	3	0 – 0.05	Bulk	2.33 ± 0.3	2.32	2.04 – 2.64	HF and HCl	(O'Day et al., 2000)
Gulf of Suez (Egypt)	18	0 (Surface)	Bulk	1.14 ± 0.2	1.04	0.76 – 1.65	HNO_3, $HClO_4$ and HF	(Khaled et al., 2006)
Gulf of Chabahar (Iran)	10	0.05 – 0.1	Bulk	0.30 ± 0.1	0.28	0.14 – 0.49	HNO_3, $HClO_4$ and HF	(Bazzi, 2014)
Tuzla Aydinli Bay, Istanbul (Turkey)	32	0 – 0.2	<2 mm	0.13 ± 0.07	0.12	0.022 – 0.34	*Aqua regia*	(Baysal and Akman, 2018)
Bohai bay (China)	42	0 (Surface)	Bulk	0.69	/	0.40 – 0.90	HNO_3, $HClO_4$ and HF	(Gao and Chen, 2012)
Persian Gulf (Iran)	10	0 – 0.05	Bulk	1.04 ± 0.7	0.79	0.29 – 2.28	*Aqua regia*	(Jafarabadi et al., 2017)
Eastern Gulf of Mexico, Florida (USA)	3	0 – 0.15	Bulk	0.061 ± 0.04	0.045	0.033 – 0.10	HNO_3 and H_2O_2	(Steffy et al., 2013)
Hainan Island (China)	140	0 (Surface)	<74 µm	0.43	/	0.12 – 0.73	HNO_3 and HF	(Cai et al., 2021)
Quintero Bay (Chili)	14	0 – 0.15	<63 µm	0.20 ± 0.07	0.19	0.12 – 0.36	HNO_3, $HClO_4$ and	(Parra et al.,

							HF	2015)
Chabahar Bay (Oman)	9	0 (Surface)	<63 µm	0.69 ± 0.4	0.85	0.23 – 1.38	*Aqua regia*	(Agah et al., 2016)
Admiralty Bay, King George Island (Antarctica)	4	0 (Surface)	Bulk	0.15 ± 0.05	0.15	0.080 – 0.21	HNO_3 and H_2O_2	(Trevizani et al., 2016)
Mar Menor coastal lagoon (Spain)	3	0 (Surface)	<0.5 mm	0.37 ± 0.02	/	/	HNO_3, $HClO_4$ and H_2O_2	(Serrano et al., 2019)
Coramandal Coast of Bay of Bengal (India)	24	0 (Surface)	Bulk	0.27	/	0.13 – 0.48	*Aqua regia* and HF	(Anbuselvan and Sridharan, 2018)
Gorgan Bay, Caspian Sea (Iran)	12	0 (Surface)	<63 µm	0.28 ± 0.07	0.28	0.13 – 0.36	*Aqua regia*	(Gholizadeh and Patimar, 2018)
Yanbu coast, Red Sea, (Saudi Arabia)	14	0 – 0.10	<63 µm	1.10 ± 1.1	0.73	0.47 – 4.12	*Aqua regia* and HF	(Alharbi et al., 2019)
Great Australian Bight (Australia)	6	0 – 0.05	<250 µm	0.12 ± 0.1	0.11	0.0048 – 0.27	*Aqua regia*	(Chakraborty and Owens, 2014)

Nickel concentrations (mmol/kg dw) in coastal sediments
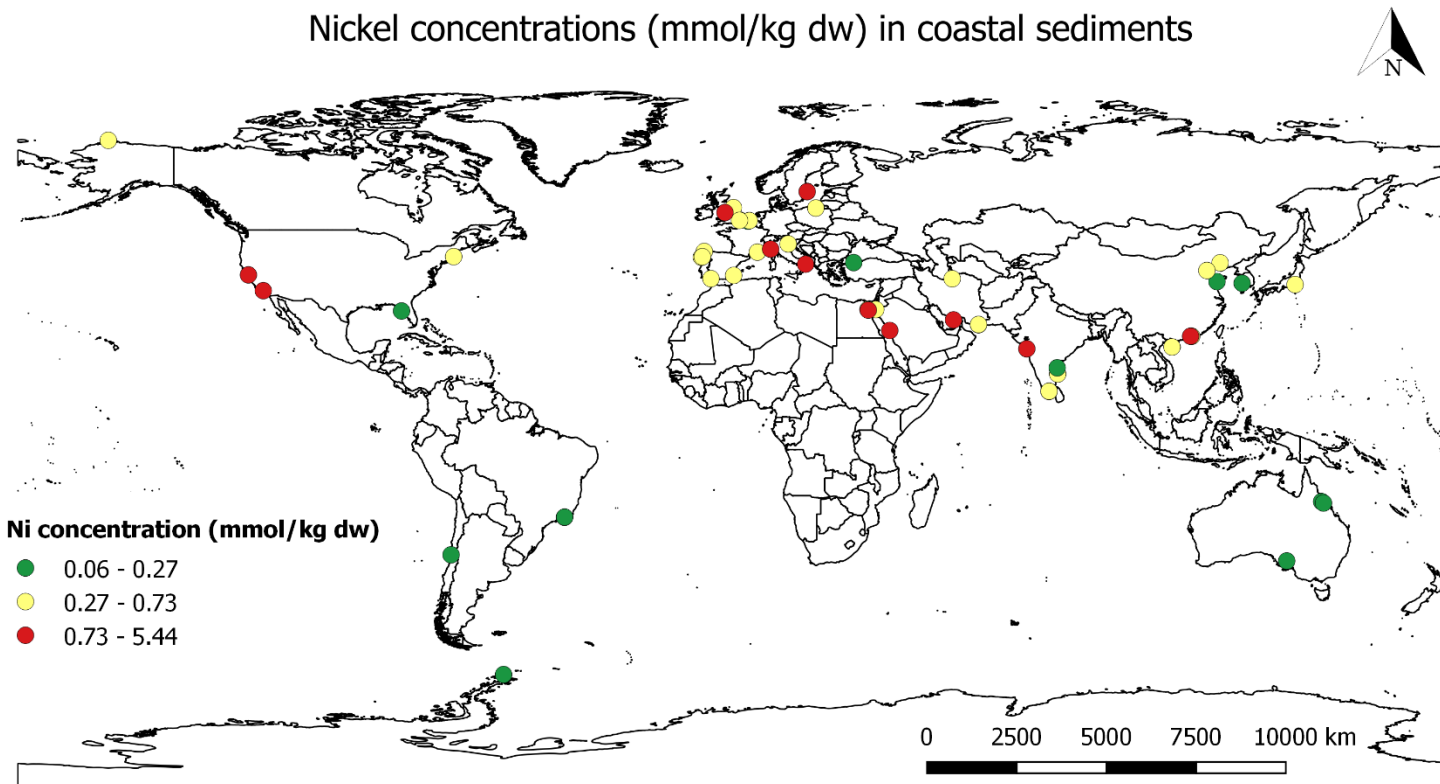
Figure D.3: Total recoverable nickel (Ni) concentrations (mmol/kg dry weight) in coastal sediment collected from primary literature. Locations where Ni concentrations exceed the threshold or probable effect level derived by the Florida department of environmental protection (FDEP) are shown in yellow or red, respectively. Individual datapoints are shown in Supplementary Table D.6. This map was made in QGIS Desktop version 2.16.3.

Table D.7: Total recoverable chromium (Cr) concentrations (mmol kg^{-1} dry weight) in coastal sediment collected from primary literature. The location, sampling depth, number of samples taken at each site, chemical(s) used for metal extraction from the sediment and reference to the study are given. Data from a single locations were summarized using descriptive statistics (mean ± standard deviation (S.D.), median and range) where possible.

Location	Sample size (n)	Collection depth (m)	Sediment fraction	Mean ± S.D. [Cr] (mmol kg^{-1} dry wt)	Median [Cr] (mmol kg^{-1} dry wt)	Min – Max [Cr] (mmol kg^{-1} dry wt)	Chemical(s) used for metal extraction	Reference
Berre Lagoon, Marseille (France)	17	0 (surface)	Bulk	1.97 ± 1.8	1.40	0.73 – 8.23	HNO$_3$, H$_2$O$_2$ and HF	(Accornero et al., 2008)
Thames estuary, North Sea (UK)	28	0 (Surface)	<63 µm	0.69 ± 0.2	/	/	HNO$_3$ and H$_2$O$_2$	(Attrill and Thomes, 1995)
North Sea (Belgium)	9	0 (Surface)	Bulk	1.94 ± 0.4	1.98	1.33 – 2.25	HNO$_3$, HF and HClO$_4$	(Van Alsenoy et al., 1993)
Vistula Lagoon (Poland)	25	0 (Surface)	<63 µm	1.76 ± 0.5	1.69	1.31 – 3.67	HNO$_3$, HF and HClO$_4$	(Szefer et al., 1999)
Atlantic Ocean (Spain)	15	0 – 0.03	<63 µm	1.14 ± 0.3	1.21	0.62 – 1.78	HNO$_3$ and HClO$_4$	(Morillo et al., 2004)
Ferrol Ria (Spain)	35	0 (Surface)	<63 µm	1.73 ± 0.6	/	/	HNO$_3$ and HF	(Cobelo-García

								and Prego, 2004)
Ria de Vigo (Spain)	34	0 (Surface)	Bulk	1.01 ± 0.6	/	/	HNO_3, HF and $HClO_4$	(Rubio et al., 2000)
Bay of Cadiz (Spain)	6	0 (Surface)	>200 µm	4.32 ± 1.0	4.67	2.48 – 5.35	Aqua regia and HF	(Carrasco et al., 2003)
Medway estuary (UK)	8	0 (Surface)	Bulk	1.75 ± 0.3	1.84	1.27 – 2.15	HNO_3, HF and $HClO_4$	(Spencer, 2002)
Mersey estuary (UK)	17	0 – 0.02	Bulk	0.53 ± 0.1	0.50	0.36 – 0.73	Aqua regia	(Harland et al., 2000)
Boston Harbour (USA)	88	0 - 1.74	Bulk	2.70 ± 1.5	2.61	0.75 – 5.62	HNO_3, HF and $HClO_4$	(Bothner et al., 1998)
Jurujuba Sound, (Brazil)	64	0 – 0.05	<63 µm	1.71 ± 1.1	/	0.19 – 4.29	Aqua regia	(Neto et al., 2000)
Sepetiba Bay (Brazil)	37	0 (Surface)	<63 µm	1.62	/	0.46 – 2.32	HCl, HNO_3 and $HClO_4$	(De Lacerda et al., 1987)
Gulf of Venice (Italy)	102	0 (Surface)	<63 µm	0.28 ± 0.3	0.20	0.071 – 2.31	HNO_3, HF and $HClO_4$	(Donazzolo et al., 1981)
Ensenada de San Simon (Spain)	29	0 (Surface)	Bulk	0.81 ± 0.3	0.88	0.038 – 1.17	HNO_3, HF and $HClO_4$	(Evans et al., 2003)
Caribbean Sea,	4	0 (Surface)	<250 µm	0.46 ± 0.1	0.44	0.35 – 0.61	Aqua regia	(Bastidas et al.,

Parque Nacional Morrocoy (Venezuela)							1999)
Macau, Pearl River estuary (China)	13	0 – 0.1	Bulk	0.54 ± 0.2	0.58	0.077 – 0.74	*Aqua regia*	(Ferreira et al., 1996)
NE Chukchi See, Alaska (Canada)	31	0 (Surface sediment)	Bulk	1.64 ± 0.5	1.60	0.73 – 2.71	HNO_3 and HF	(Naidu et al., 1997)
Taranto Gulf, Ionian Sea (Italy)	19	0 – 0.05	Bulk	1.59 ± 0.3	1.61	0.58 – 1.98	*Aqua regia* and HF	(Buccolieri et al., 2006)
Ligurian Sea between Arenzano and Capo Noli (Italy)	56	0 – 0.05	Bulk	8.60 ± 6.8	6.48	2.13 – 34.56	HF, $HClO_4$ and HCl	(Cosma et al., 1979)
Gulf of Suez, Red Sea (Egypt)	14	0 – 0.05	<0.75 mm	0.13 ± 0.05	0.12	0.048 – 0.25	HNO_3, $HClO_4$ and HF	(Hamed and Emara, 2006)
Saemangeum region, Yellow Sea (South Korea)	35	0 (Surface)	Bulk	0.66 ± 0.05	/	0.14 – 1.09	*Aqua regia* and HF	(Kim et al., 2010)

Gulf of Mannar, Tuticorin coast, (India)	32	0 (Surface)	Bulk	3.41 ± 3.6	2.26	1.37 – 18.52	*Aqua regia* and HF	(Jonathan et al., 2004)
Jiaozhou Bay, Qingdao (China)	10	0 – 0.1	<125 µm	0.43 ± 0.3	0.38	0.096 – 0.98	HNO_3 and H_2O_2	(Wang et al., 2007)
Bay of Bengal (India)	21	0 (Surface)	Bulk	3.75	/	2.86 – 4.68	$HClO_4$ and HF	(Raj and Jayaprakash, 2008)
Jordan Gulf of Aqabe, Red sea (Jordan)	44	0 – 0.02	Bulk	0.80 ± 1.0	0.43	0.085 – 3.58	HNO_3, $HClO_4$ and HF	(Abu-Hilal, 1987)
Palos Verdes Peninsula, Los Angeles (USA)	44	0 – 0.05	Bulk	9.19 ± 8.5	4.88	1.00 – 28.46	*Aqua regia*	(Hershelman et al., 1981)
Tokyo Bay (Japan)	7	0 – 0.025	<65 µm	1.37 ± 0.7	1.15	0.56 – 2.42	*Aqua regia* and $HClO_4$	(Fukushima et al., 1992)
Bombay coast (India)	11	0 – 0.8	Bulk	2.15 ± 0.2	2.17	1.96 – 2.51	HNO_3, $HClO_3$ and HF	(Dilli, 1986)
Victoria harbour, Hong Kong (China)	8	0 (Surface)	Bulk	3.31 ± 3.4	2.28	1.11 – 11.56	H_2O_2, HNO_3, $HClO_3$ and HF	(Wong et al., 1995)

Seaplane Lagoon, California (USA)	3	0 – 0.05	Bulk	9.73 ± 5.0	9.83	4.67 – 14.7	HF and HCl	(O'Day et al., 2000)
Gulf of Suez (Egypt)	18	0 (Surface)	Bulk	0.61 ± 0.4	0.48	0.31 – 1.65	HNO_3, $HClO_4$ and HF	(Khaled et al., 2006)
Gulf of Chabahar (Iran)	10	0.05 – 0.1	Bulk	0.59 ± 0.2	0.51	0.048 – 0.86	HNO_3, $HClO_4$ and HF	(Bazzi, 2014)
Tuzla Aydinli Bay, Istanbul (Turkey)	32	0 – 0.2	<2 mm	0.031 ± 0.02	0.028	0.0096 – 0.10	*Aqua regia*	(Baysal and Akman, 2018)
Bohai bay (China)	42	0 (Surface)	Bulk	1.95	/	1.16 – 4.32	HNO_3, $HClO_4$ and HF	(Gao and Chen, 2012)
Bay of Bengal (Bangladesh)	10	0 – 0.1	<160 µm	0.014 ± 0.001	/	0.012 – 0.015	*Aqua regia*	(Khan et al., 2017)
Persian Gulf (Iran)	10	0 – 0.05	Bulk	0.14 ± 0.09	0.11	0.033 – 0.28	*Aqua regia*	(Jafarabadi et al., 2017)
Eastern Gulf of Mexico, Florida (USA)	3	0 – 0.15	Bulk	0.13 ± 0.03	0.12	0.11 – 0.17	HNO_3 and H_2O_2	(Steffy et al., 2013)
Hainan Island (China)	140	0 (Surface)	<74 µm	1.55	/	0.50 – 2.87	HNO_3 and HF	(Cai et al., 2021)
Quintero Bay (Chili)	14	0 – 0.15	<63 µm	0.88 ± 0.3	0.77	0.54 – 1.54	HNO_3, $HClO_4$ and HF	(Parra et al., 2015)

Chabahar Bay (Oman)	9	0 (Surface)	<63 µm	3.56 ± 1.8	2.88	1.67 – 7.69	*Aqua regia*	(Agah et al., 2016)
Admiralty Bay, King George Island (Antarctica)	4	0 (Surface)	Bulk	0.22 ± 0.06	0.22	0.16 – 0.29	HNO_3 and H_2O_2	(Trevizani et al., 2016)
Mar Menor coastal lagoon (Spain)	3	0 (Surface)	<0.5 mm	0.44 ± 0.008	/	/	HNO_3, $HClO_4$ and H_2O_2	(Serrano et al., 2019)
Coramandal Coast of Bay of Bengal (India)	24	0 (Surface)	Bulk	1.64	/	0.98 – 1.87	*Aqua regia* and HF	(Anbuselvan and Sridharan, 2018)
Gorgan Bay, Caspian Sea (Iran)	12	0 (Surface)	<63 µm	0.34 ± 0.08	0.36	0.17 – 0.44	*Aqua regia*	(Gholizadeh and Patimar, 2018)
Yanbu coast, Red Sea, (Saudi Arabia)	14	0 – 0.10	<63 µm	1.67 ± 1.7	0.98	0.29 – 5.56	*Aqua regia* and HF	(Alharbi et al., 2019)
Great Australian Bight (Australia)	6	0 – 0.05	<250 µm	0.51 ± 0.5	0.46	0.067 – 1.33	*Aqua regia*	(Chakraborty and Owens, 2014)

Chromium concentrations (mmol/kg dw) in coastal sediments

Cr concentration (mmol/kg dw)
- 0.01 - 1.01
- 1.01 - 3.08
- 3.08 - 9.73
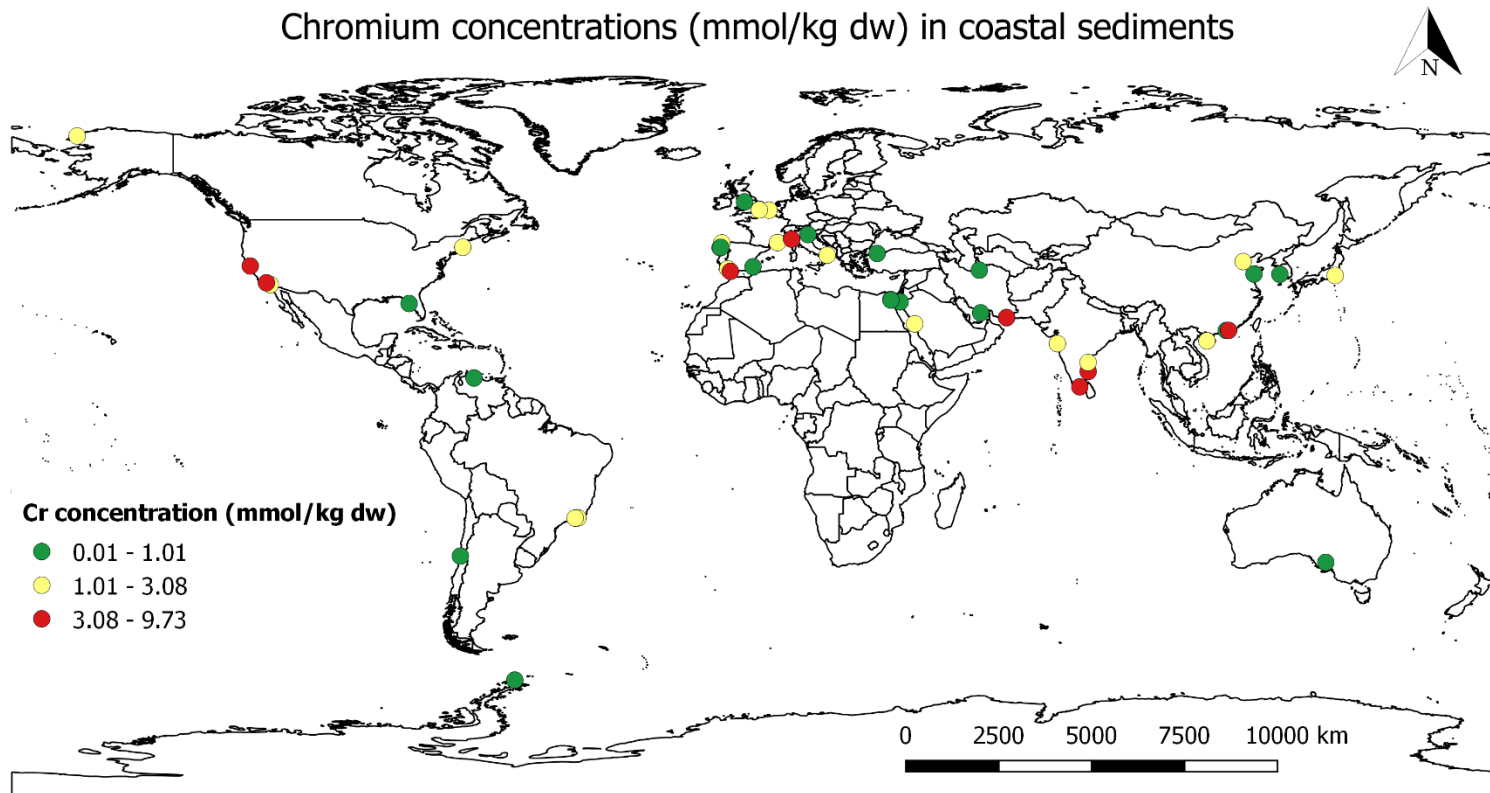
Figure D.4: Total recoverable chromium (Cr) concentrations (mmol/kg dry weight) in coastal sediment collected from primary literature. Locations where Cr concentrations exceed the threshold or probable effect level derived by the Florida department of environmental protection (FDEP) are shown in yellow or red, respectively. Individual datapoints are shown in Supplementary Table D.7. This map was made in QGIS Desktop version 2.16.3.

D.6 Deriving a Cr-based guideline for olivine application in coastal systems

The maximum amount of olivine that can be supplied to the coastal environment without health risks for marine biota was calculated based on the existing Cr^{3+} environmental quality standard (EQS) for seawater and marine sediment. Calculations were made assuming the two limiting application scenarios being; all metals released during weathering remain in either (I) the water column or (II) the sediment.

D.6.1 All Cr ends up in the water column

The maximum amount of olivine that can be distributed in coastal waters without exceedance of the Australian seawater Cr^{3+} EQS (0.192 µmol l^{-1}) (ANZECC and ARMCANZ, 2000), assuming a Cr concentration of 6.57 mmol mol^{-1} olivine (Santos et al., 2015), is shown in Figure D.5. The obtained environmentally safe amounts of olivine that can be distributed are 1.5 times higher than those derived based on the European seawater EQS for Ni (main text, Figure 4.1).

Figure D.5: Maximum amount of olivine (kg m⁻² seabed) on a logarithmic scale that can be distributed without exceedance of the Australian trivalent chromium (Cr³⁺) environmental quality standard (0.192 µmol l⁻¹) as a function of coastal water residence time (days). Scenarios for coastal w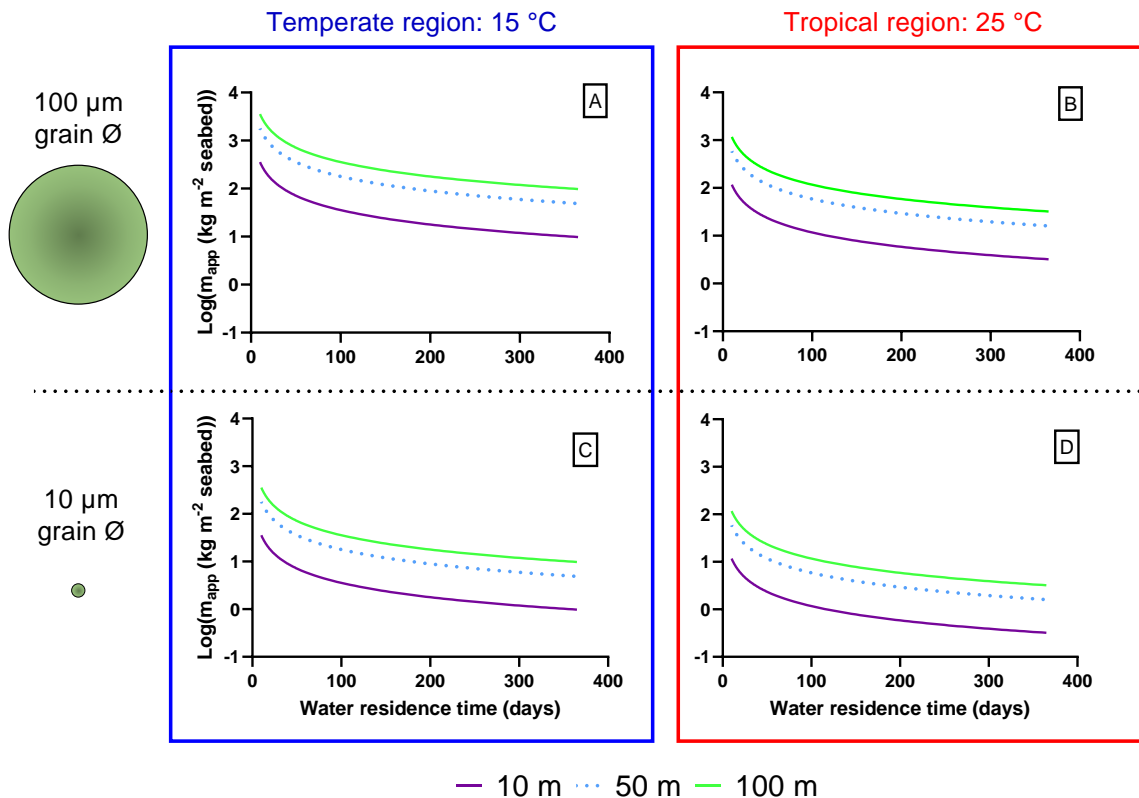aters with an average water depth of 10, 50 or 100 m located in a 15 °C temperate region (A, C) or 25 °C tropical region (B, D) are shown. The maximum application of olivine with a uniform grain diameter of 100 µm (A, B) or 10 µm (C, D) is given. A seawater Cr³⁺ background concentration of 0.84 nmol l⁻¹ and Cr concentration in olivine of 6.57 mmol mol⁻¹ olivine were assumed. As derived by Hangx & Spiers (2009), olivine dissolution rate constants of 5.19×10⁻¹¹ and 1.58×10⁻¹⁰ mol m⁻² s⁻¹ were used for the temperate (15 °C) and tropical (25 °C) scenario, respectively.

For these results, it should be noted that a worst-case scenario is shown, where a relatively high olivine Cr concentration (6.57 mmol mol⁻¹ olivine) and the strict Australian Cr³⁺ EQS (0.192 µmol l⁻¹; see Table D.2) were used for the calculations of the olivine guideline. Therefore, the amount of olivine that could be safely distributed based on expected Cr³⁺ release could be higher, depending on the application site and Cr concentration in the olivine that is supplied. However, some of the dissolved Cr³⁺ could be oxidized to Cr⁶⁺ in well oxygenated coastal waters (Pettine, 2000). Hexavalent Cr forms anionic complexes in seawater that are highly bioavailable and potentially toxic (Dayan and Paine, 2001; Aharchaou et al., 2018). Furthermore, a synergistic interaction (more than additive toxicity) between Ni²⁺ and Cr⁶⁺ has been observed in several organisms exposed to its binomial mixture, with one study using the marine copepod species *Tisbe holothuriae* (Verriopoulos and Dimas, 1988; Dive et al., 1989; Palaniappan and Karthikeyan, 2009; Karthikeyan, 2014; Gupta and Karthikeyan, 2016). Therefore, more in-depth studies on the Cr release kinetics, redox chemistry, bioavailability and mixture toxicity are needed to derive an accurate prediction on the amount of olivine that can safely be supplied to the coastal oceans.

D.6.2 All Cr remains in the sediment
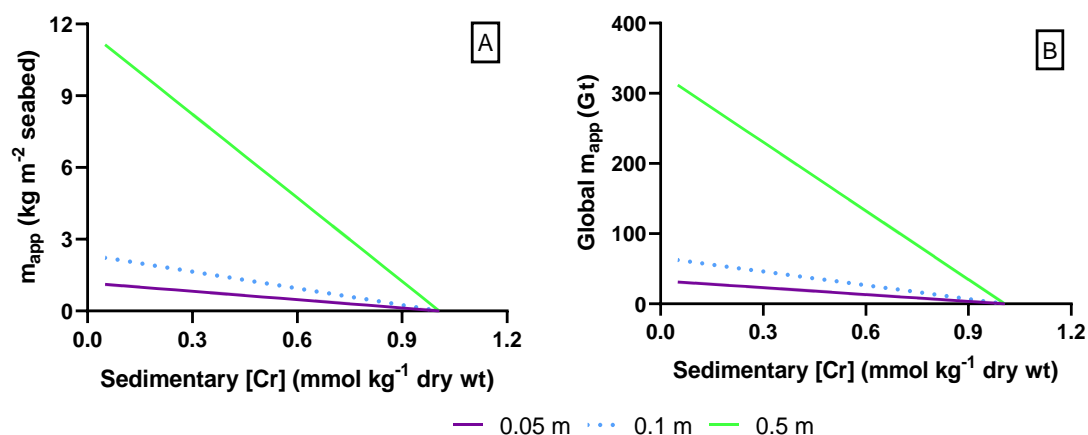
Figure D.6: Maximum amount of olivine that can locally (A) or globally (B) be distributed without exceedance of the chromium (Cr) Threshold effect level (TEL) for marine biota (1.006 mmol kg dry wt^{-1}) as a function of sedimentary Cr concentrations (mmol kg dry wt^{-1}) for different olivine mixing depths (0.05, 0.1 and 0.5 m). The global continental shelf was assumed to have a surface area of 28×10^6 km² and the olivine was assumed to have a Cr concentration of 6.57 mmol Cr mol^{-1} olivine. The worst-case scenario is shown for which all the Cr released from olivine weathering is assumed to stay inside the sediment.

Appendix E: Chapter 5

E.1 Marine sediment and olivine characteristics

Mineralogical composition of the dunite sand was determined via X-ray diffraction (XRD) analysis with a Bruker D8 ECO Advance equipped with a Cu-anode (40 kV, 25 mA) and an energy-dispersive position sensitive LynxEye XE detector. The incoming beam was collimated to a fixed beam length of 17 mm. Before analysis, samples were first pulverized to a grain size smaller than 500 μm and subsequently micronized (<10 μm grain diameter) by wet grinding with ethanol using a McCrone Micronizing mill. Afterwards, the slurry was dried for XRD-analysis. For each sample, a 2 g aliquot mixed with 5% zincite was included for analysis to serve as internal standards. Phases were identified using the DIFFRAC.EVA suite. The spectra were interpreted semi quantitatively using the BGMN Rietveld method with Profex version 5.0 as user interface (Bergmann et al., 1998; Doebelin and Kleeberg, 2015).

The Norwegian dunite sand used in the olivine avoidance assays with *L. littorea* and *G. locusta* was composed of 83 and 86 wt% ferroan-forsterite, respectively (Table E.1). The forsterite (Mg_2SiO_4) content of the olivine *Fo* (%) was calculated from the molar Fe and Mg concentration c_{M_i} (mol mol^{-1} olivine) as

$$Fo = \frac{c_{M_{Mg}}}{(c_{M_{Mg}} + c_{M_{Fe}})} 100 \qquad \qquad \text{[E.1]}$$

And was found to be 93.3% and 93.2% for the olivine used in the *L. littorea* and *G. locusta* olivine avoidance assays, respectively. Subsequently, the fayalite (Fe_2SiO_4) content *Fa* (%) defined as 100% − *Fo* was equal to 6.7% and 6.8%, respectively.

Table E.1: Mineralogical composition of Norwegian dunite sand used in the olivine avoidance assays with Littorina littorea and Gammarus locusta.

Mineral	*L. littorea* assays	*G. locusta* assays
Ferroan-forsterite (wt%)	86	83
Enstatite (wt%)	7	8
Chlorite (wt%)	1	2
Antigorite (wt%)	2	2
Hornblende (wt%)	1	2
Talc (wt%)	N.A.	1
Quartz (wt%)	1	N.A.
Magnetite (wt%)	1	N.A.
Others (wt%)	1	2

Table E.2: Elemental composition of experimental sediments. Concentrations ($\mu mol\ g^{-1}$ d.w.) of magnesium (Mg), iron (Fe), aluminium (Al), manganese (Mn), cobalt (Co), and zinc (Zn) for the different substrates of the L.littorea and G. locusta olivine avoidance assays. Mean ± S.D. values are shown (N = 4 – 5). Concentrations of Cd and Pb remained below the detection limit ($0.0044\ nmol\ g^{-1}$ d.w. Cd and $0.0024\ nmol\ g^{-1}$ d.w. Pb).

L. littorea olivine avoidance assays			
Treatment	100% sediment	3% olivine	30% olivine	100% olivine
Mg	31 ± 4.1	405[a]	3775[a]	12512 ± 491
Fe	54 ± 4.5	79[a]	305[a]	891 ± 28
Al	156 ± 21	152[a]	118[a]	30 ± 1.1
Mn	2.5 ± 0.4	2.8[a]	5.5[a]	12 ± 0.2
Co	0.073 ± 0.007	0.19[a]	1.2[a]	3.9 ± 0.05
Zn	0.069 ± 0.022	0.097[a]	0.35[a]	1.0 ± 0.017
G. locusta olivine avoidance assays			
Treatment	100% sediment	3% olivine	30% olivine	100% olivine
Mg	80 ± 1.9	375[a]	3027[a]	9901 ± 469
Fe	85 ± 2.3	104[a]	276[a]	721 ± 33
Al	370 ± 50	361[a]	278[a]	65 ± 2.6

Mn	2.2 ± 0.18	2.5[a]	5.1[a]	12 ± 0.3
Co	0.15 ± 0.008	0.25[a]	1.2[a]	3.6 ± 0.08
Zn	0.29 ± 0.009	0.31[a]	0.41[a]	0.69 ± 0.011

[a]Elemental concentrations for the 3% w/w and 30% w/w olivine treatments were not analytically determined, but derived from the measured concentrations in the control sediment and 100% w/w olivine.
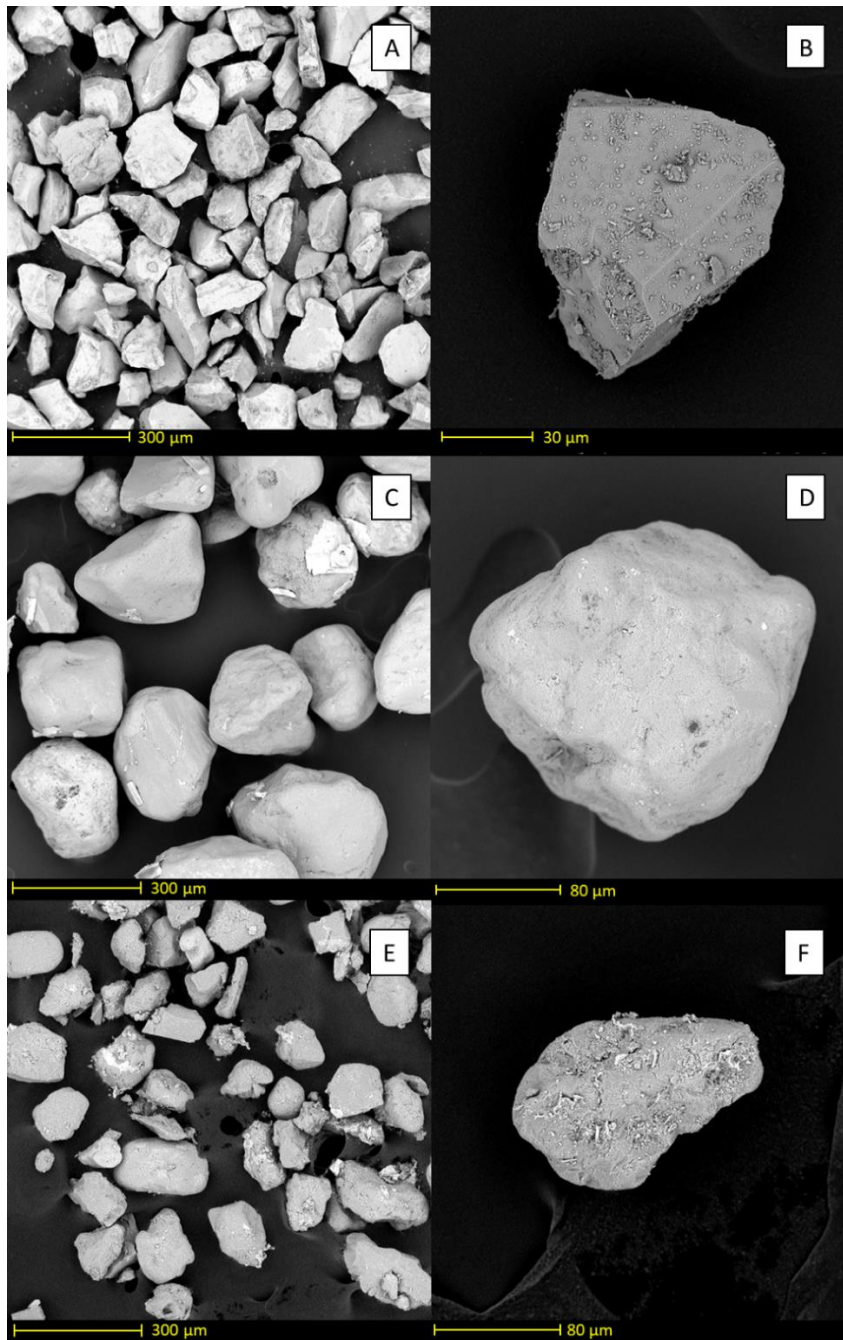
Figure E.1: Scanning electron microscopy (SEM) images of the (A, B) experimental olivine (C, D) North Sea sediment, and (E, F) Eastern Scheldt sediment. Note the scale differences since the images were not all taken at the same magnification. SEM images of olivine (A, B) are from the avoidance assays with L. Littorina. Olivine images for the G. locusta avoidance assays are not shown since grains were similar in shape and size.

E.2 *Littorina littorea* olivine avoidance assays

E.2.1 Pictures experimental set ups
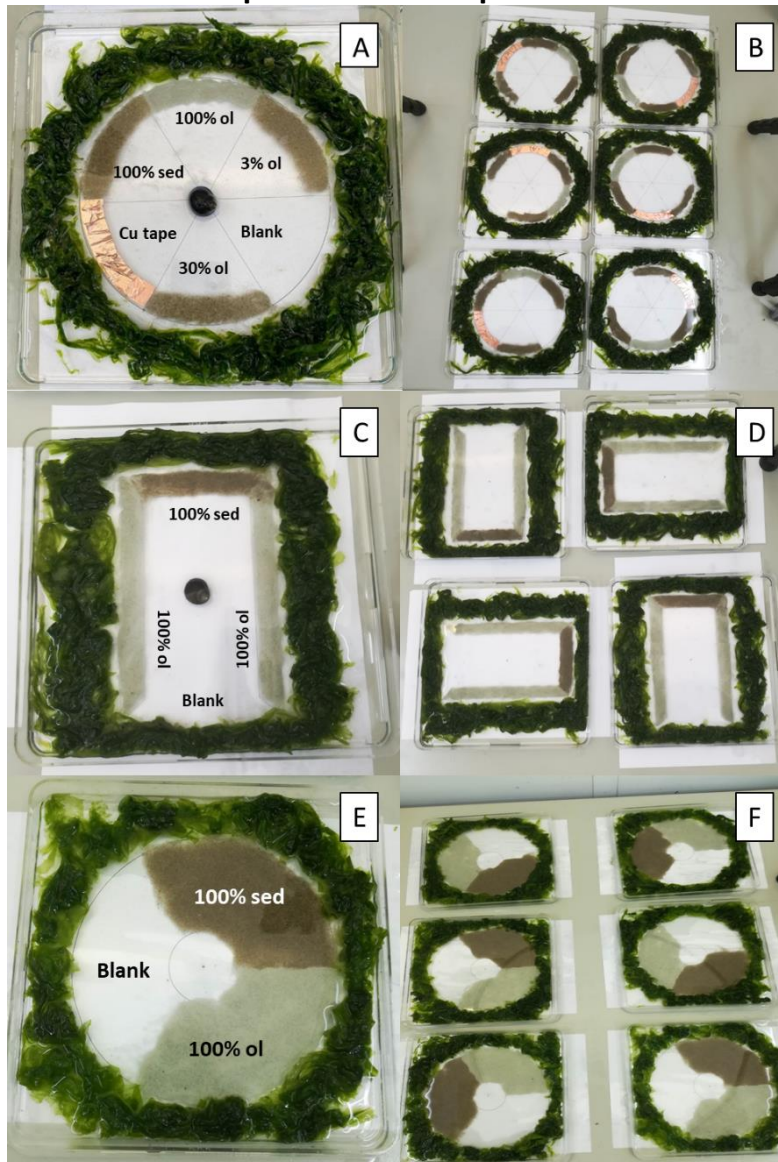
Figure E.2: Pictures of the olivine avoidance assays with L. littorea (A-F). Experimental set-ups correspond to the schematic representations shown in (A, B) Figure 5.1A, (C,E) Figure 5.1G, and (E,F) Figure 5.1E of the main text. Sed = sediment, ol = olivine.

E.2.2 Substrate weights

The sediment weights of the different olivine avoidance assays with *L. littorea* are shown in Table E.3. For olivine-sediment mixtures, dry olivine sand was manually mixed with wet North Sea sediment. Sediment water content W (%) was calculated from the weight loss after drying at 60 °C for 72 h via

$$W = \frac{m_{wet} - m_{dry}}{m_{wet}} 100 \qquad\qquad [E.2]$$

Where m_{wet} and m_{dry} represent the sediment wet weight (g w.w.) and dry weight (g d.w.), respectively. The water content (21.2 ± 2.2%, N = 10), was used to determine the weight of dry olivine m_{ol} (g d.w.) needed to obtain an olivine concentration c_{ol} of 3% w/w ol or 30% w/w ol on a dry weight basis after mixing with a given weight of wet sediment m_{sed} (g w.w.) via

$$m_{ol} = m_{sed}\left(1 - \frac{W}{100}\right)\frac{c_{ol}}{100} \qquad\qquad [E.3]$$

Table E.3: Substrate weights (shown as mean ± S.D.) of the olivine avoidance assays with L. littorea. North Sea sediment (sed) wet weight (mg) and olivine (ol) dry weight (mg) for the different treatments (100% sed, 3%, 30%, and 100% ol) of the seven olivine avoidance assays with L. littorea. Experiments are indicated by letters that correspond with the set-ups shown in Figure 5.1 of the main text. The number of bioassay dishes per experiment (N) is given.

Experiment	100% w/w sed	3% w/w ol	30% w/w ol	100% w/w ol
A (N = 6)	3000 ± 0.5 mg sed	70.9 ± 0.01 mg ol	709 ± 0.05 mg ol	1600±0.1 mg ol
		2910 ± 0.4 mg sed	2100 ± 0.3 mg sed	

B ($N = 5$)	3600 ± 3 mg sed	85.5 ± 0.4 mg ol 3492 ± 5 mg sed	851 ± 0.7 mg ol 2528 ± 4 mg sed	2160 ± 0.2 mg ol
C ($N = 5$)	3602 ± 5 mg sed	85.6 ± 0.6 mg ol 3490 ± 3 mg sed	851 ± 0.2 mg ol 2521 ± 4 mg sed	2160 ± 0.3 mg ol
D ($N = 6$)	25001 ± 4 mg sed	NA	NA	13009 ± 7 mg ol
E ($N = 6$)	25013 ± 4 mg sed	NA	NA	13010 ± 8 mg ol
F ($N = 4$)	7513 ± 0.6 mg sed	NA	NA	4102 ± 1 mg ol each patch
G ($N = 4$)	4100 ± 1 mg sed	NA	NA	3901 ± 0.8 mg ol each patch

E.2.3 Dissolved metal concentrations
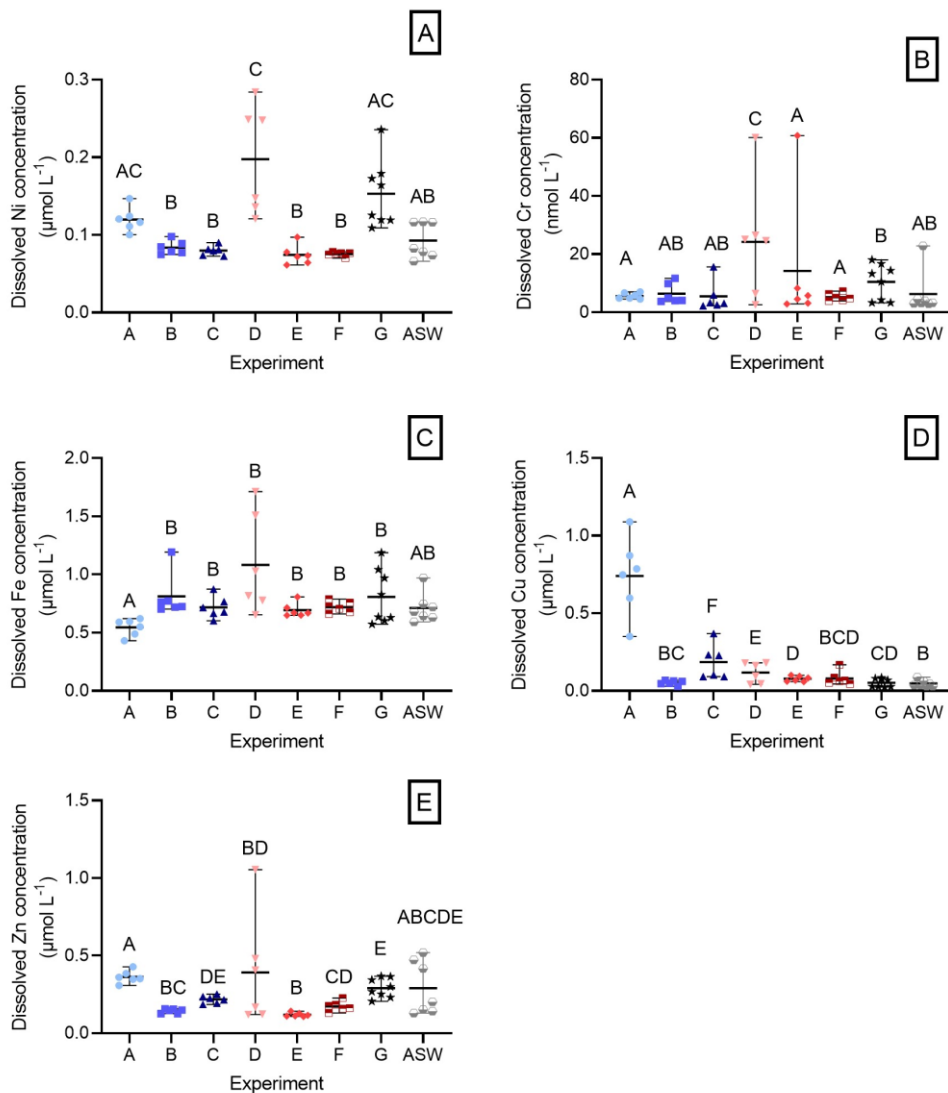
Figure E.3: Dissolved (A) nickel (Ni), (B) chromium (Cr), (C) iron (Fe), (D) copper (Cu), and (E) zinc (Zn) in artificial seawater of the different experiments with L. littorea depicted in Figure 5.1. Note that dissolved Cr concentrations are given in nmol L^{-1}, while other concentrations are given in µmol L^{-1}. Experimental letters correspond to subfigure numbers in Figure 5.1. Concentrations in fresh artificial seawater (ASW) are also given. Individual data points, mean, and range are shown (N = 6 − 8). Capital letters indicate significant differences (p < 0.05) between experiments.

E.3 *Gammarus locusta* olivine avoidance assays

E.3.1 Pictures experimental set ups
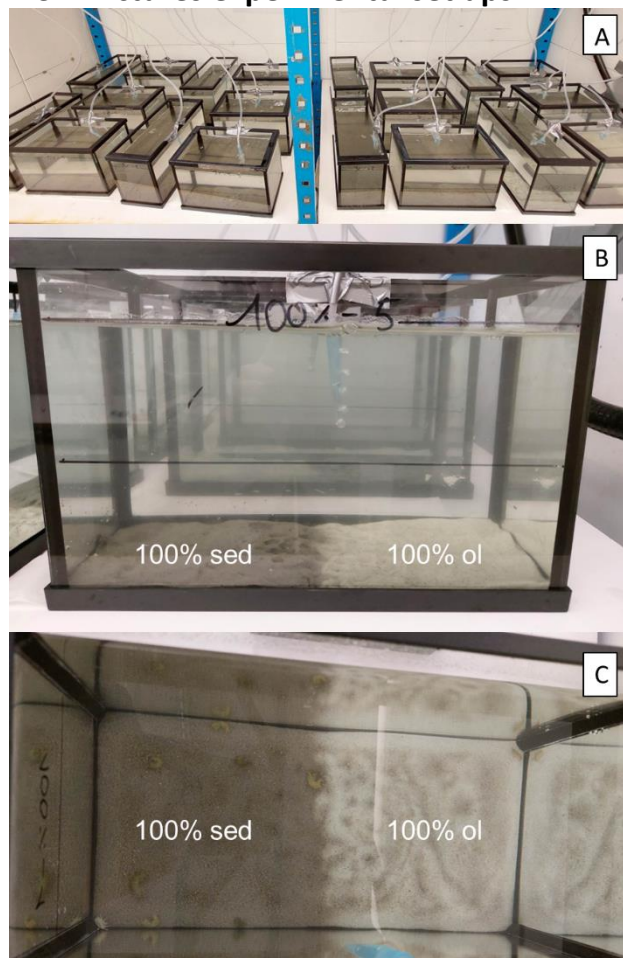
Figure E.4: Pictures of the olivine avoidance assays with G. locusta (A-C). (A) Overview of the experimental set-up and individual experimental aquarium (L x W x H = 30 x 20 x 15 cm) viewed from (B) the side and (C) above. Sed = sediment, ol = olivine.

E.3.2 Substrate weights

Table E.4: Substrate weights (shown as mean ± S.D.) of the olivine avoidance assays with G. locusta. Eastern Scheldt sediment (sed) wet weight (g) and olivine (ol) dry weight (g) for the different treatments (100% sed, 3%, 30%, 100% ol, and 100% ol colour) of the avoidance assays with G. locusta. The amount of dry olivine for the 3% and 30% w/w ol treatment was calculated based on the water content of the Eastern Scheldt sediment (mean ± S.D. = 25.6 ± 0.9%, N = 15) according to supplementary equation E.2 and E.3.

Treatment	100% w/w sed patch (*N* = 5)	Treatment patch (*N* = 5)
100% w/w sed	175.626 ± 0.005 g sed	175.626 ± 0.005 g sed
3% w/w ol	175.626 ± 0.005 g sed	3.906 ± 0.005 g ol
		170.368 ± 0.004 g sed
30% w/w ol	175.632 ± 0.008 g sed	39.194 ± 0.009 g ol
		122.938 ± 0.008 g sed
100% w/w ol	175.630 ± 0.007 g sed	130.642 ± 0.008 g ol
100% w/w ol colour	175.634 ± 0.003 g sed	130.646 ± 0.001 g ol

E.3.3 Trace metal accumulation
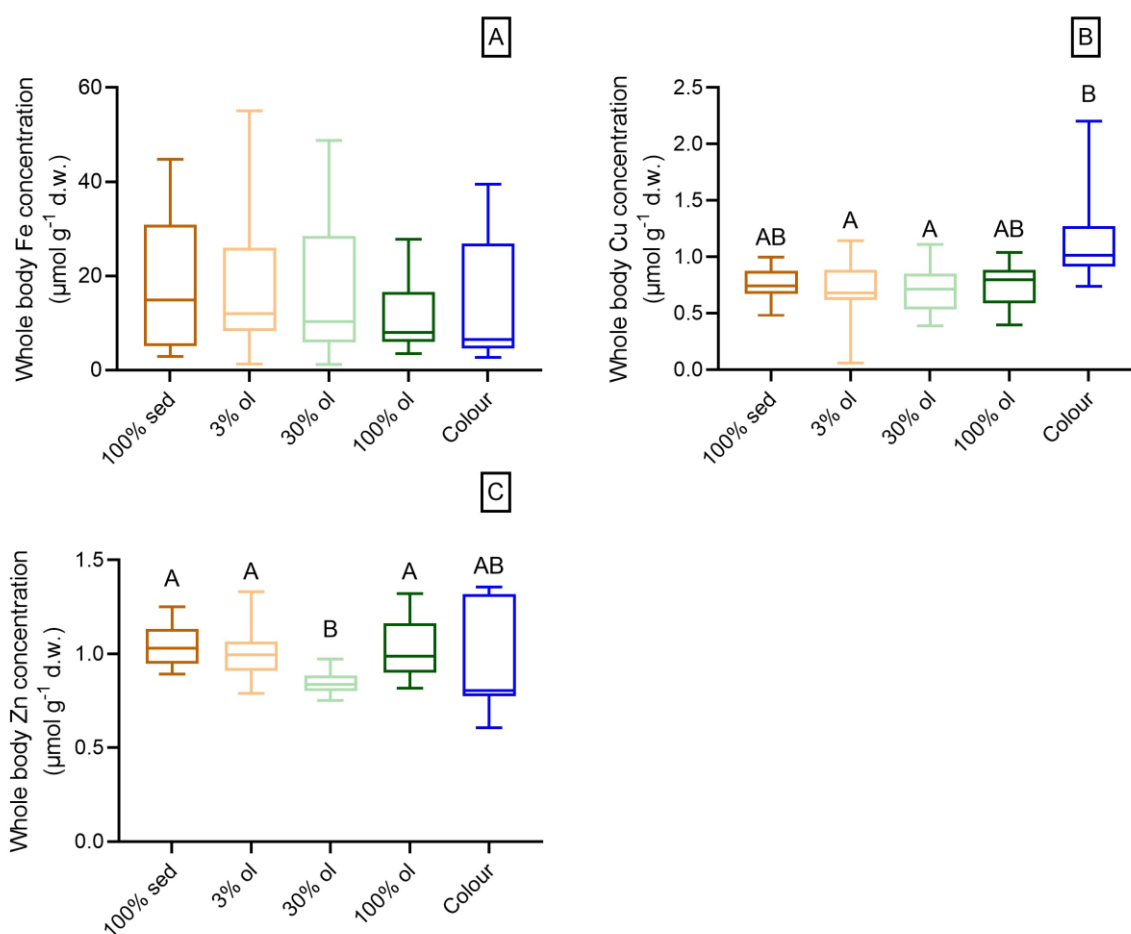
Figure E.5: Box and whisker plots of the whole body (A) iron (Fe), (B) copper (Cu), and (C) zinc (Zn) concentrations (μmol g^{-1} d.w.) in G. locusta (N = 10 – 20) at the end of the three day olivine avoidance assays. Results are shown for the sediment (sed) control and different olivine (ol) treatment including the 100% w/w olivine treatment to test colour preference (Colour).
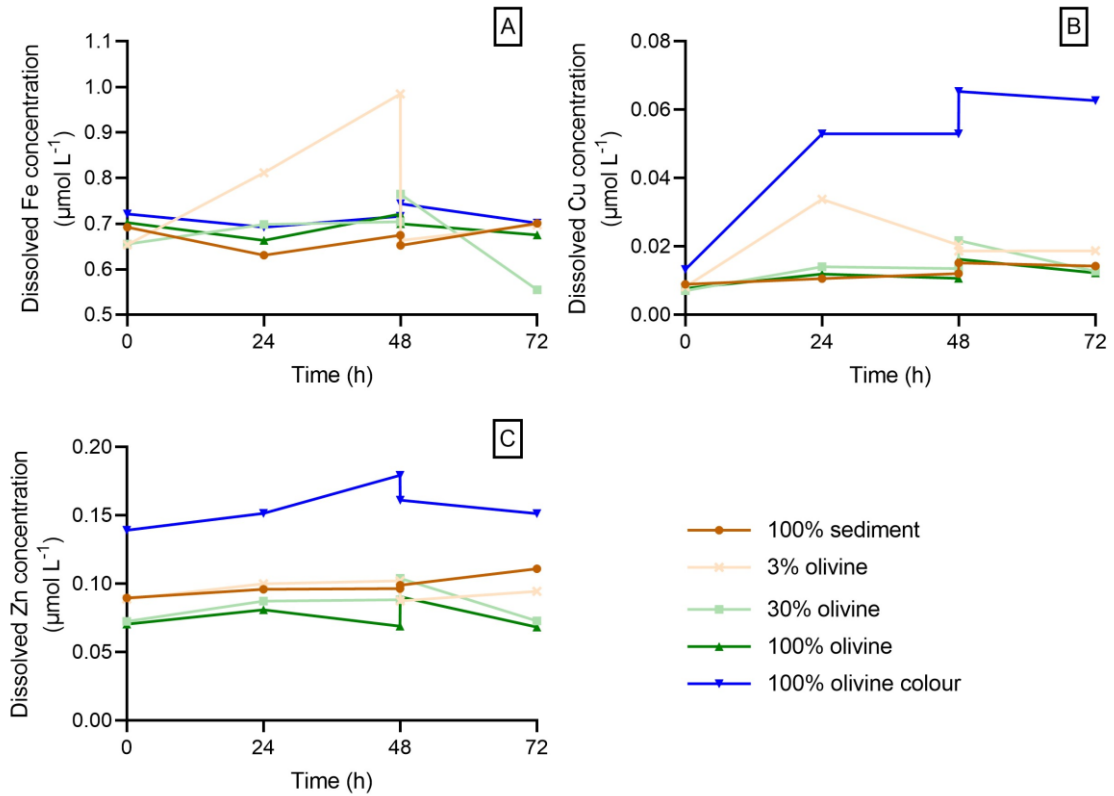
Figure E.6: Temporal evolution of average dissolved (A) iron (Fe), (B) copper (Cu) and (C) zinc (Zn) concentrations (µmol L⁻¹) in artificial seawater (N = 2 or 3) of the G. locusta olivine avoidance assays.

E.3.4 Expected whole body Ni concentrations

The expected range of whole body Ni concentrations in *G. locusta*, c_{Ni} (µmol g⁻¹ d.w.), at the end of the 79 h olivine avoidance assays was derived based on the lowest (0.000217 L g⁻¹ h⁻¹) and highest (0.01 L g⁻¹ h⁻¹) waterborne Ni uptake rate constant, k_u (L g⁻¹ h⁻¹), for aquatic invertebrates reported in previous studies (Hédouin et al., 2007; Urien et al., 2017) according to

$$c_{Ni} = \frac{m_{Ni,bg} + \sum_{i=0}^{79} k_u(t_i - t_{i-1})c_{Ni,ASW_i}m_{amp}}{m_{amp}} \qquad \text{[E.4]}$$

Where $m_{Ni,bg}$ (µg) represents the minimum (0.014 µg) or maximum (0.13 µg) background whole body Ni content in *G. locusta* which was assumed to be equal to the minimum and maximum whole body Ni concentration in amphipods from the 100% w/w sediment treatment. The possible daily waterborne Ni uptake was calculated from the literature derived k_u values, the measured dissolved Ni concentration in the water c_{Ni,ASW_i} (µg L^{-1}) at each sampling time t_i (h) (Figure 5.5C) and the minimum (0.0028 g) and maximum (0.037 g) amphipod dry weight.

Appendix F: Chapter 6

F.1 *Gammarus* species, sex, and size determination
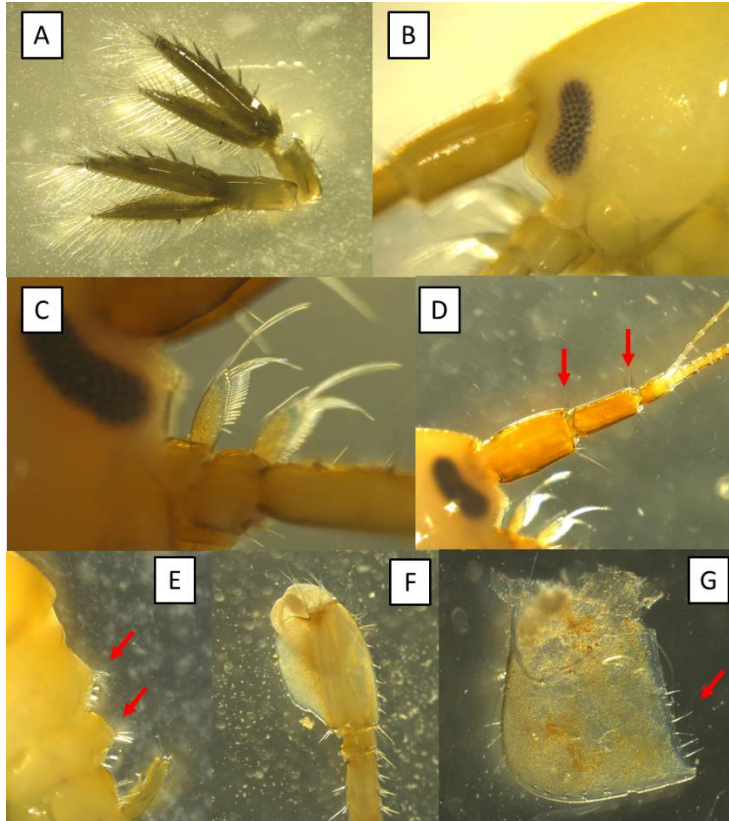
Figure F.1: Morphological identification features of Gammarus locusta according to Vader and Tandberg (2019). (A) U3 outer ramus with 2 articles, inner ramus of similar length compared to outer ramus first article. (B) Eyes are kidney shaped, clearly more than two times higher than wide. (C) All setae on the ventral margin of the third article of the mandibular palp are of similar length, forming a comb-shaped structure with gradually longer setae towards the tip of the article. (D) One or two setae groups on article 1 and article 2 of the A1 peduncle. (E) Urosome segments have clear "humps". (F) Posterodistal margin of P7 article 2 with both setae and spines, P7 basis more than 1.5 times longer than wide. (G) Ep3 has several setae along its hind margin.

Figure F.2: Amphipod metasomatic length measurement in ImageJ using the segmented line tool (yellow line) with 1 mm graph paper as scale. The metasomatic length is the distance between the anterior end of the rostrum and the posterior end of the last metasomatic segment (DeWitt et al., 1992).

Figure F.3: Sexual differences in gnathopod morphology of Gammarus locusta according to Lincoln (1979). (A) Female gnathopod 1 propodus is suboval with oblique palm and gnathopod 2 propodus is of similar size compared to 1, but elongate rectangular with transverse palm. (B) Male gnathopod 1 propodus is pear shaped with sinuous palm. Male gnathopod 2 propodus much broader than 1 and palm is less oblique. Differences in setae and spine coverage on male gnathopods are described by Lincoln (1979), but were not used for Gammarus sex identification.

F.2 Sediment and olivine geochemical properties

The sediment elemental composition was determined via ICP-OES (iCAP 6300 Duo, Thermo Scientific) after microwave-assisted acid digestion following a modified chromite ore digestion protocol (CEM Corporation, 1999). Briefly, 0.1 g of dried sediment was digested with 2.6 mL of 85% ultrapure orthophosphoric acid and 1.4 mL ≥96% sulphuric acid at 240 °C for 30 min in a Discover SP-D 80 microwave (CEM Corporation). Next, 2 mL of 67 − 69% nitric acid was added and samples were heated at 240 °C for 15 min. Afterwards, samples were diluted 8.3 times with ultrapure water and centrifuged for 5 min at 1600 g. The supernatant was used for elemental analysis. For quality control, reference NIM-D dunite (SARM-6, MINTEK) and procedural blanks were included during analysis. Average element recoveries (ranging from 72 to 93%) were acceptable for all certified elements except Si (~0.4%) due to the insolubility of silicate in HNO_3.

Mineralogical composition of the dunite sand was determined via X-ray diffraction (XRD) analysis with a Bruker D8 ECO Advance equipped with a Cu-anode (40 kV, 25 mA) and an energy-dispersive position sensitive LynxEye XE detector. The incoming beam was collimated to a fixed beam length of 17 mm. Before analysis, samples were first pulverized to a grain size smaller than 500 μm and subsequently micronized (<10 μm grain diameter) by wet grinding with ethanol using a McCrone Micronizing mill. Afterwards, the slurry was dried for XRD-analysis. For each sample, a 2 g aliquot mixed with 5% zincite was included for analysis to serve as internal standards. Phases were identified using the DIFFRAC.EVA suite. The spectra were interpreted semi quantitatively using the BGMN Rietveld method with Profex version 5.0 as user interface (Bergmann et al., 1998; Doebelin and Kleeberg, 2015).

Norwegian dunite sand was composed of 69 − 86 wt% ferroan-forsterite and 31 - 14 wt% other minerals of which enstatite (5 − 8 wt%) and chlorite (2 − 9 wt%) were the most abundant (Table F.1). Forsterite (Mg_2SiO_4) content, *Fo* (%), of the olivine was calculated from the molar elemental concentrations C_{M_i} (mol mol^{-1} olivine) of Fe and Mg as

$$Fo = \frac{C_{M_{Mg}}}{(C_{M_{Mg}}+C_{M_{Fe}})} 100 \qquad\qquad [F.1]$$

which resulted in a forsterite content ranging between 93.2 and 93.4% for the different olivine grain sizes. The fayalite (Fe_2SiO_4) content, *Fa* (%), could then be calculated by subtracting the *Fo* from 100% (*Fa* = 100% – *Fo*), resulting in a fayalite content between 6.6 and 6.8%.

Table F.1: Mineralogical composition of the different experimental olivine (ol) sizes based on XRD analysis.

Mineral	3 – 99 µm ol	93 – 332 µm ol	208 – 488 µm ol
Ferroan-forsterite (wt%)	69	83	86
Enstatite (wt%)	5	8	6
Chlorite (wt%)	9	2	4
Antigorite (wt%)	6	2	1
Hornblende (wt%)	2	2	1
Talc (wt%)	7	1	N.A.
Quartz (wt%)	1	N.A.	N.A.
Others (wt%)	1	2	2

Table F.2: Concentrations (µmol g^{-1} d.w.) of aluminium (Al), cobalt (Co), zinc (Zn), magnesium (Mg), iron (Fe), and manganese (Mn) for control sediment and different olivine (ol) sizes. Data for the different 3 – 99 µm olivine concentrations (% w/w) of the chronic experiment are also provided. Mean ± S.D. values are shown (N = 4 – 5).

Sediment type	Al	Co	Zn	Mg	Fe	Mn
Control sediment	370±50	0.15±0.0077	0.30±0.0095	80±2	85±2	2.2±0.18
3 – 99 µm ol						

1% w/w	367[a]	0.18[a]	0.30[a]	171[a]	90[a]	2.3[a]
10% w/w	345[a]	0.47[a]	0.34[a]	977[a]	142[a]	3.1[a]
25% w/w	307[a]	0.94[a]	0.40[a]	2321[a]	227[a]	4.5[a]
50% w/w	245[a]	1.7[a]	0.50[a]	4562[a]	368[a]	6.7[a]
100% w/w	120±3	3.3±0.22	0.70±0.045	9043±488	652±16	11±0.7
93 – 332 μm ol	65±3	3.6±0.080	0.69±0.011	9901±469	721±33	12±0.3
208 – 488 μm ol	90±5	3.7±0.034	0.74±0.018	10130±768	712±52	12±0.07

[a]Elemental concentrations for the 1% w/w to 50% w/w 3 – 99 μm olivine were not analytically determined, but derived from the measured concentrations in the control sediment and 100% w/w 3 – 99 μm olivine.

Concentrations of Cd and Pb remained below the detection limit (0.0044 nmol g^{-1} d.w. Cd and 0.0024 nmol g^{-1} d.w. Pb) in all sediment types.

F.3 Acute exposure to different olivine sizes

F.3.1 Seawater chemistry changes
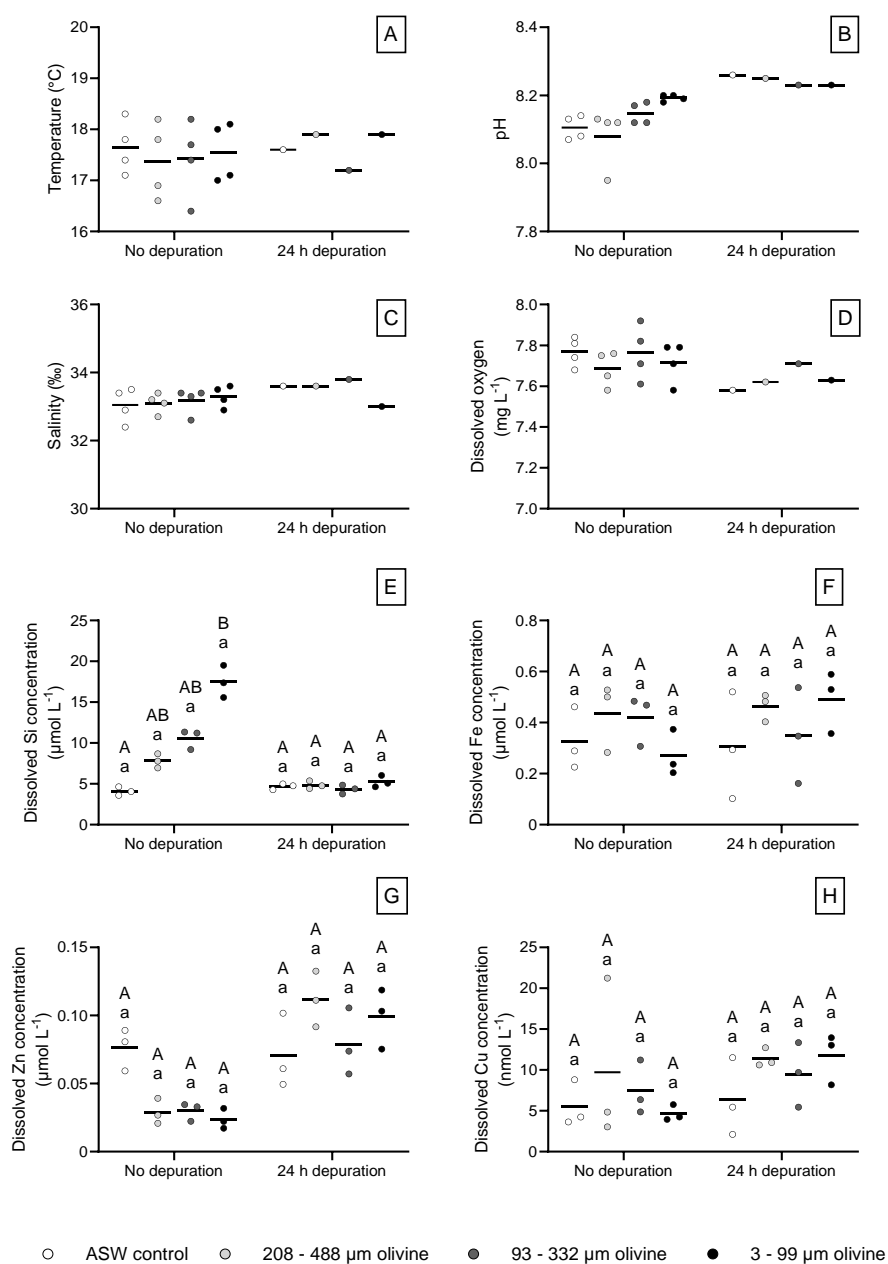
Figure F.4: Artificial seawater (A) temperature (°C), (B) pH, (C) salinity (‰), (D) dissolved oxygen concentrations (mg L^{-1}) and dissolved (< 0.2 µm) concentrations (µmol L^{-1}) of (E) silicon (Si), (F) iron (Fe), (G) zinc (Zn), and (H) copper (Cu) for various olivine grain size treatments at the end of the accumulation and depuration phase (Mean, N = 1 – 4). Lower

case letters indicate significant differences (p < 0.05) between experimental phases and capital letters indicate significant differences (p < 0.05) between treatments within an experimental phase.

F.3.2 Trace metal bioaccumulation
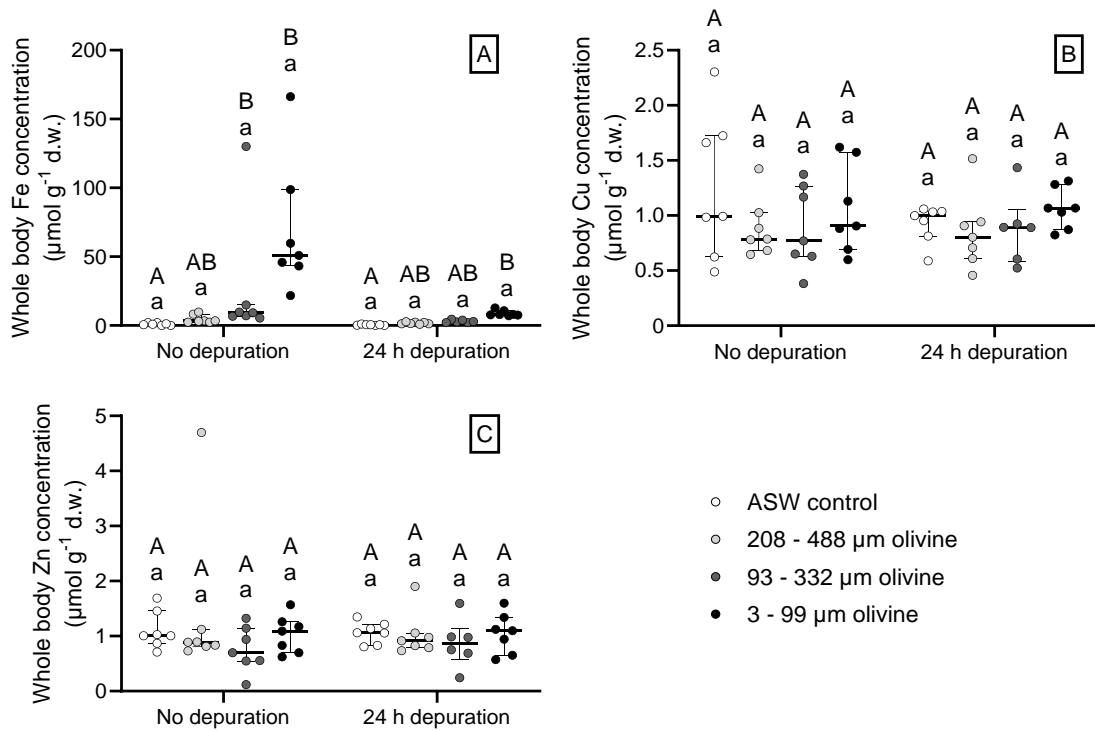
Figure F.5: Whole body concentration (µmol g^{-1} dry weight) of (A) iron (Fe), (B) copper (Cu), and (C) zinc (Zn) in amphipods exposed to various olivine sizes for 24 h and subsequently depurated for 0 or 24 h before analysis. Median and IQR are shown (N = 6 or 7).

F.3.3 Deriving the number of ingested olivine grains

The number of ingested olivine grains N_{ol} (Supplementary Table F.3) was derived from the whole body Cr or Ni concentration of exposed amphipods C_{exp} (µg g^{-1} d.w.) via

$$N_{ol} = \frac{C_{bg}m_{amp} - C_{exp}m_{amp}}{C_{exp}m_{ol} - m_{M,ol}}$$ [F.2]

Where c_{bg} is the median whole body Cr or Ni concentration of control amphipods (0.55 µg Cr g^{-1} d.w. and 7.6 µg Ni g^{-1} d.w.), m_{amp} is the median dry weight of an experimental amphipod (0.008 g), m_{ol} is the weighted average weight of an ingested olivine grain (2.3E-10 g), and $m_{M,ol}$ is the weighted average Cr or Ni content of an ingested olivine grain (3.5E-07 µg Cr or 4.9E-07 µg Ni). The m_{ol} was calculated as

$$m_{ol} = \sum_{i=1}^{n} m_i x_i \qquad\qquad\qquad [F.3]$$

Where m_i is the average weight of an olivine grain (g) within a certain grain size class i and x_i is its relative abundance in the ingested grain size distribution (Figure 6.4A). The m_i was calculated from the specific density of olivine ρ_{ol} (3.3E+06 g m^{-3}) and the volume of an olivine grain V_i (m³) within a certain grain size class i ($m_i = \rho_{ol} V_i$). Similarly, the $m_{M,ol}$ was calculated from

$$m_{M,ol} = \sum_{i=1}^{n} m_{M,ol_i} x_i \qquad\qquad\qquad [F.4]$$

where m_{M,ol_i} is the average Cr or Ni content of an olivine grain (µg) within a certain grain size class i and x_i is its relative abundance in the grain size distribution (Figure 6.4A). The m_{M,ol_i} was derived from the molar Cr or Ni concentration of olivine C_M (30 µmol Cr g^{-1} d.w. or 36 µmol Ni g^{-1} d.w., Table 6.1), the molar weight M_M of Cr (52.0 g mol^{-1}) or Ni (58.7 g mol^{-1}) and m_i ($m_{M,ol_i} = C_M m_i M_M$).

Note that Eq. F.2 assumes that the increase in whole body Ni and Cr concentration is entirely the result of olivine ingestion and does not consider waterborne metal uptake. Furthermore, complete dissolution of ingested olivine grains is assumed, which might not be the case given that Ni (85 ± 21%) and Cr (59 ± 3%) recoveries in the mussel reference material were smaller than 100%. Hence the derived amount of ingested olivine grains should be seen as a best estimate given the available data.

The relative guts volume occupied by ingested grains V_{rel} (%; Supplementary Table F.3) was derived by dividing the total ingested particle volume V_{tot} (m³) by the average amphipod guts volume V_{guts} (8.8E-10 m³) and multiplying by 100 ($V_{rel} = V_{tot}/V_{guts}100$). The V_{guts} was derived from the average guts length h_{guts} (1.1E-02 m) and guts diameter d_{guts} (3.1E-04 m) assuming that the guts were perfectly cylindrical in shape and had a length equal to the metasomatic length (ML). The V_{tot} was derived from the number of ingested olivine grains N_{ol} and the weighted average volume of an ingested olivine grain V_{ol} (6.9E-17 m³) ($V_{tot} = N_{ol}V_{ol}$). The V_{ol} was calculated as

$$V_{ol} = \sum_{i=1}^{n} V_i x_i \qquad\qquad [F.5]$$

Where V_i is the average volume of an olivine grain (m³) within a certain grain size class i and x_i is its relative abundance in the ingested grain size distribution (Figure 6.4A). The volume of an olivine grain V_i (m³) within a certain grain size class i was derived assuming that olivine were perfectly spherical.

F.3.4 Deriving dietary metal exposure rates

Amphipod dietary Cr and Ni exposure rates φ_{ol} (µmol g^{-1} d.w. d^{-1}, Supplementary Table F.3) via the ingestion of olivine particles were derived from the olivine dissolution rate R_{ol} (mol d^{-1}), molar mass of Fo93 olivine M_{ol} (144.8 g mol^{-1}), C_M (30 µmol Cr g^{-1} d.w. or 36 µmol Ni g^{-1} d.w., Table 6.1), and m_{amp} (0.008 g) via

$$\varphi_{ol} = \frac{R_{ol}M_{ol}C_M}{m_{amp}} \qquad\qquad [F.6]$$

The R_{ol} (mol d^{-1}) was derived from the rate equation

$$R_{ol} = N_{ol}A_{ol}k_{ol}(1-\Omega) \qquad\qquad [F.7]$$

Where N_{ol} is the calculated number of ingested olivine grains (see Eq. F.2), A_{ol} is the weighted average surface area of an individual olivine grain (2.65E-11 m²), Ω is the

mineral saturation state (assumed to be <<1), and k_{ol} is the olivine dissolution rate constant (mol m^{-2} d^{-1}) according to the following empirical rate equation by Rimstidt et al. (2012)

$$k_{ol} = 10^{4.07 - 0.256\text{pH} - \frac{3465}{T}} 86400 \qquad [F.8]$$

where pH and T represent the expected pH (6.5) and temperature (17.5 °C) in the gut environment of the experimental amphipods (Martin, 1966; Monk, 1977) and 86400 is the amount of seconds in a day. Finally, the A_{ol} was derived from the average surface area of an olivine grain A (m²) within a certain grain size class i and the relative abundance of that grain size x_i within the grain size distribution (Figure 6.4A) according to

$$A_{avg} = \sum_{i=1}^{n} A_i x_i \qquad [F.9]$$

Table F.3: Expected number of ingested olivine grains N_{ol} in amphipods exposed to 3 – 99 μm olivine for 24 h based on measured whole body Ni and Cr concentrations assuming no waterborne metal uptake. Estimated relative guts space occupied by ingested grains V_{rel} (%), and (C) possible dietary Ni and Cr exposure rates φ_{ol} (μmol g^{-1} d.w. d^{-1}).

Element	Ni	Cr
N_{ol}	2,196,168	450,899
V_{rel} (%)	17.3	3.56
φ_{ol} (μmol g^{-1} d.w. d^{-1})	1.00E-03	1.69E-04

F.4 Acute 3 – 99 µm olivine uptake and elimination

F.4.1 Seawater chemistry changes

Figure F.6: Temporal evolution of artificial seawater (A) temperature (°C), (B) pH, (C) salinity (‰), (D) dissolved oxygen concentration (mg L^{-1}) and dissolved (< 0.2 µm)

concentrations (μmol L^{-1}) of (E) silicon (Si), (F) iron (Fe), (G) zinc (Zn), and (H) copper (Cu) during a 72 h pure olivine exposure (white area) and 96 h depuration (grey area) period. Mean and range are shown (N = 3 – 11).

F.4.2 Trace metal bioaccumulation
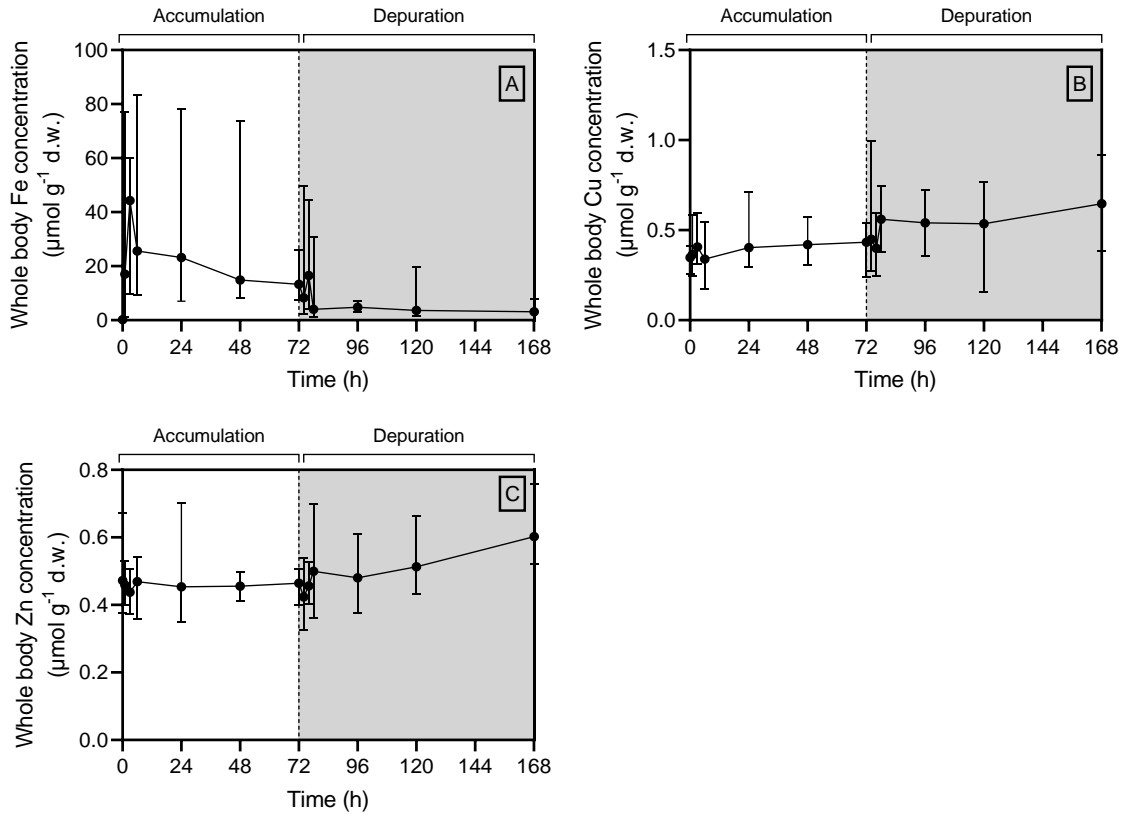
Figure F.7: Temporal evolution of whole body (A) iron (Fe), (B) copper (Cu), and (C) zinc (Zn) concentrations (μmol g^{-1} d.w.) in amphipods during 72 h pure olivine exposure (white area) and 96 h depuration (grey area). Median and range are shown (N = 7 or 8).

F.5 Chronic 3 – 99 μm olivine toxicity test

F.5.1 Sediment and olivine weight

The weight of olivine (g d.w.) and natural Eastern Scheldt sediment (g w.w.) that was manually mixed to obtain the different experimental treatments is shown in Table F.4. Water content, W (%), of Eastern Scheldt sediment was determined from the weight loss after drying at 60 °C for 72 h as

$$W = \frac{m_{wet} - m_{dry}}{m_{wet}} 100 \qquad\qquad [F.10]$$

Where m_{wet} and m_{dry} represent the sediment wet weight (g) and dry weight (g), respectively. The water content of the Eastern Scheldt sediment (23.77 ± 1.32%) was used to determine the amount of wet sediment needed for each experimental treatment to obtain the set concentration of olivine expressed in % w/w on a dry weight basis.

Table F.4: Weight of olivine (g dry weight) and control sediment (g wet weight) used for the different experimental treatments of the 35-day 3 – 99 μm olivine toxicity test. Mean and standard deviation values are shown (N = 4).

Treatment	3 – 99 μm olivine (g d.w.)	Control sediment (g w.w.)
0% w/w	0	712.43 ± 0.025
1% w/w	5.51 ± 0.21	705.33 ± 0.013
10% w/w	54.30 ± 0.005	641.18 ± 0.005
25% w/w	135.77 ± 0.025	534.35 ± 0.013
50% w/w	271.54 ± 0.029	356.24 ± 0.010
100% w/w	543.09 ± 0.0058	0

F.5.2 Temporal changes in water chemistry

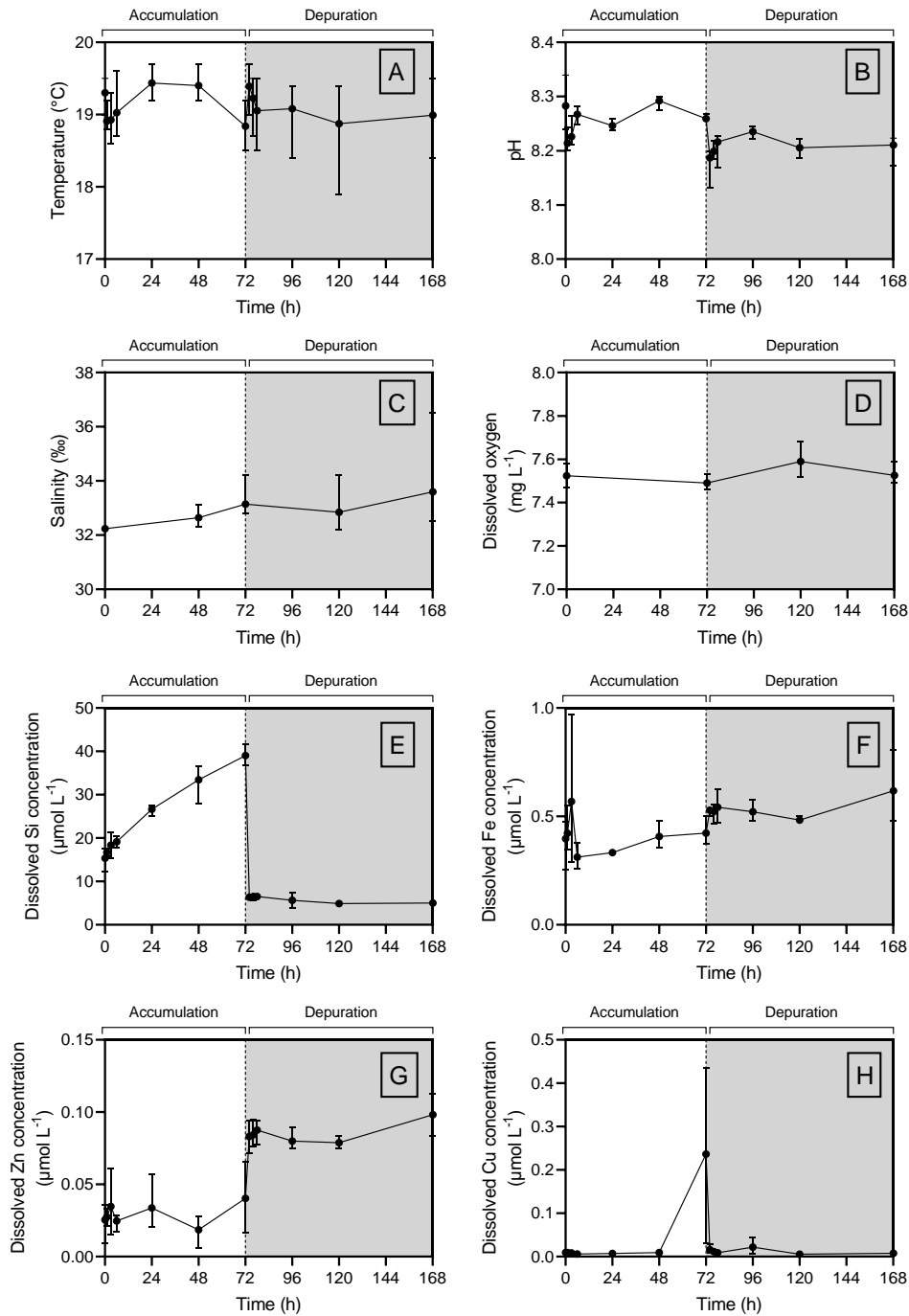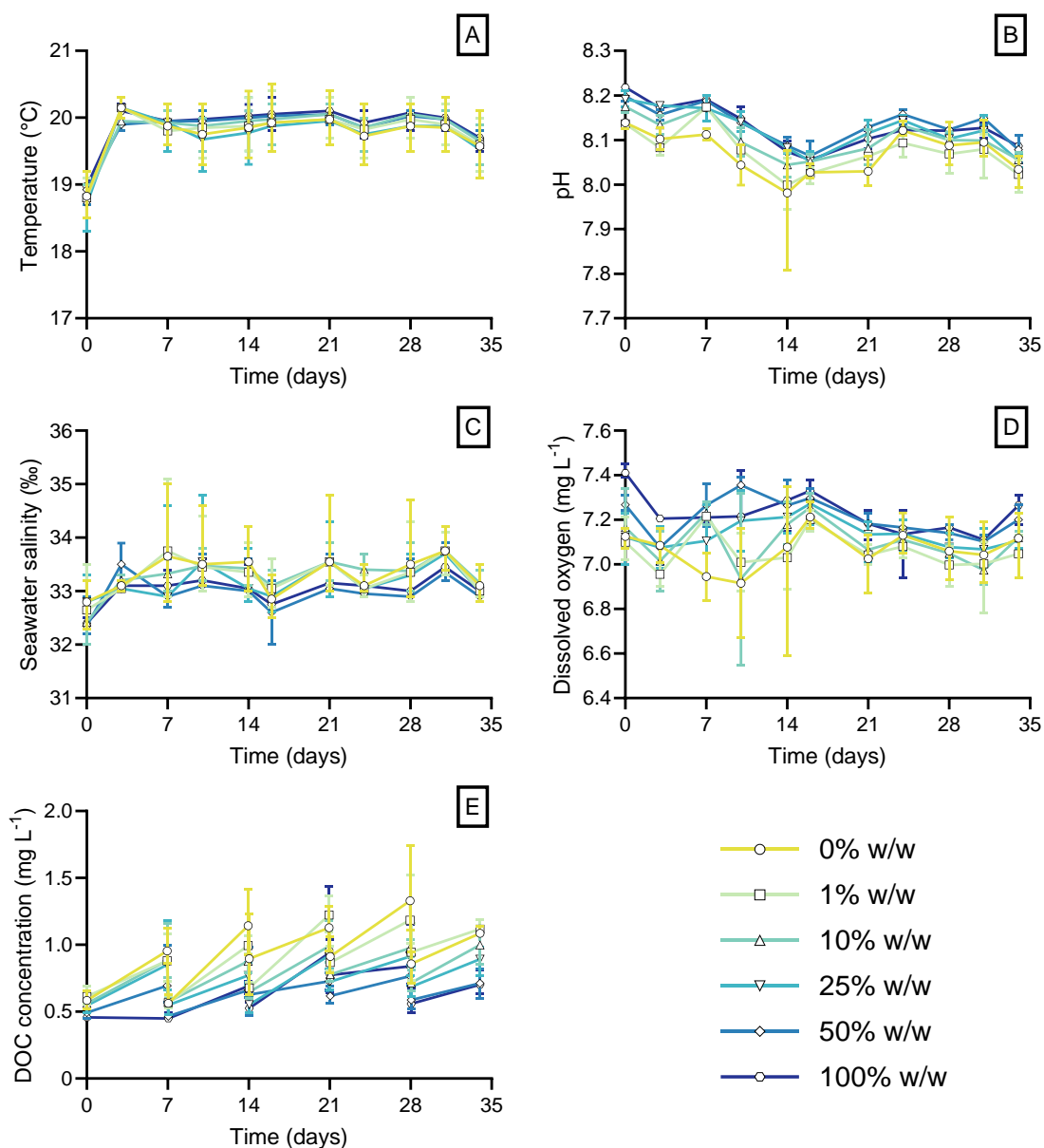*Figure F.8: Temporal evolution of artificial seawater (A) temperature (°C), (B) pH, (C) salinity (‰), (D) dissolved oxygen concentration (mg L^{-1}), and (E) dissolved organic carbon (DOC) concentration (mg L^{-1}). Mean and range values (N = 2 – 4) are shown.*

Filtered (Chromafil XTRA PES-20/25, Macherey-Nagel) ASW were collected at day 14 and 35 for total alkalinity (TA) measurements. An open cell potentiometric titration with 0.1 M HCl was conducted using an automated titrator setup (888 Titrando, Metrohm) and TA was derived from the titrant volume and pH measurements using a non-linear least-

squares method according to Dickson et al. (2007). Total alkalinity results are shown in Figure F.9.
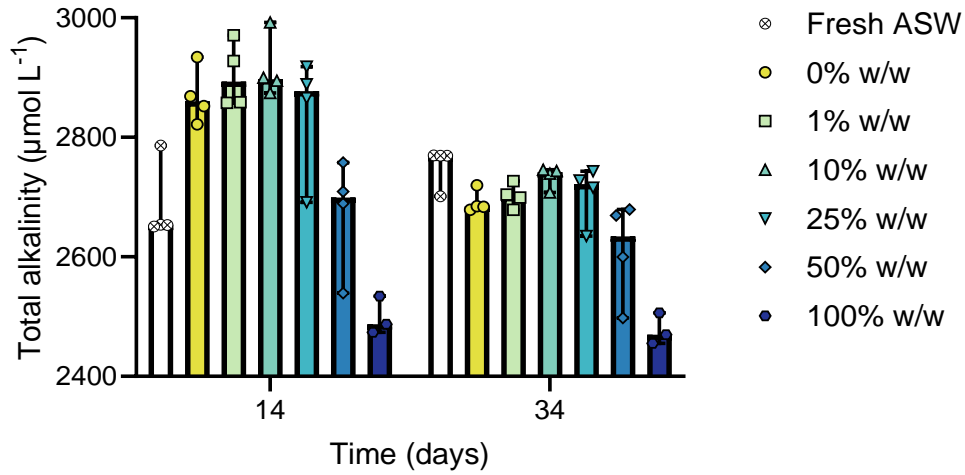
Figure F.9: Artificial seawater (ASW) total alkalinity (µmol L^{-1}) in different olivine treatments (% w/w) and fresh ASW at day 14 and 34 of the chronic 3 − 99 µm olivine toxicity test. Median and range values are shown (N = 3 or 4).
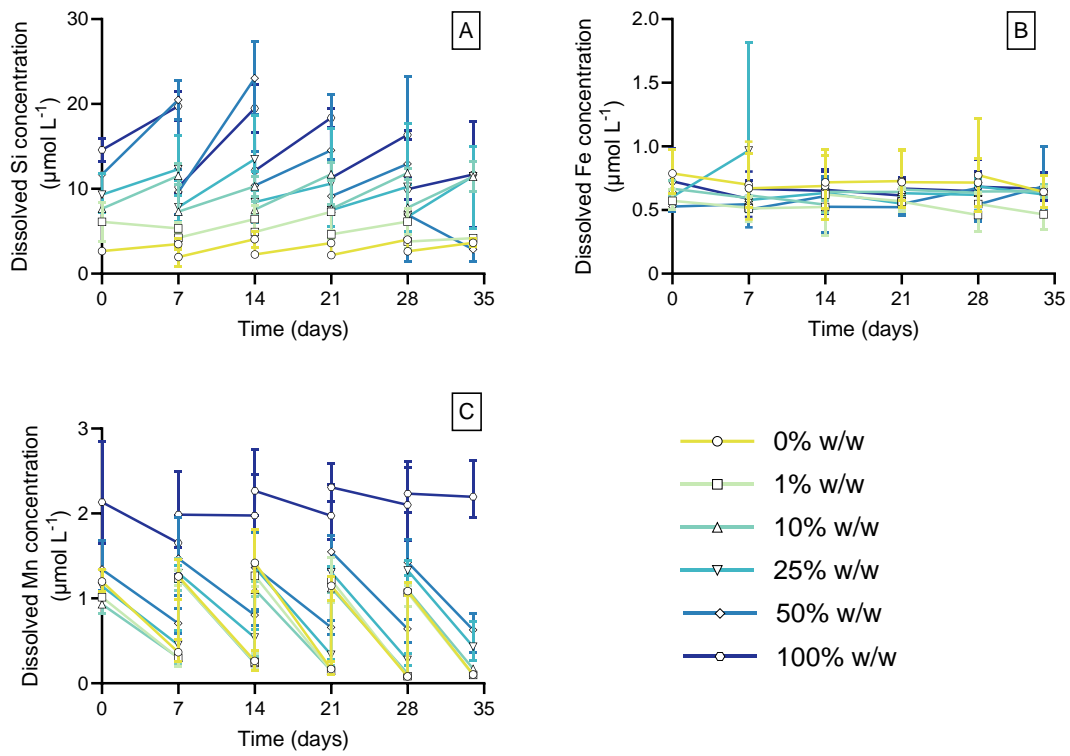
Figure F.10: Temporal evolution of dissolved (A) silicon (Si), (B) iron (Fe), and (C) manganese (Mn) concentrations (µmol L^{-1}) in artificial seawater. Mean and range (N = 2 or 3) are shown.
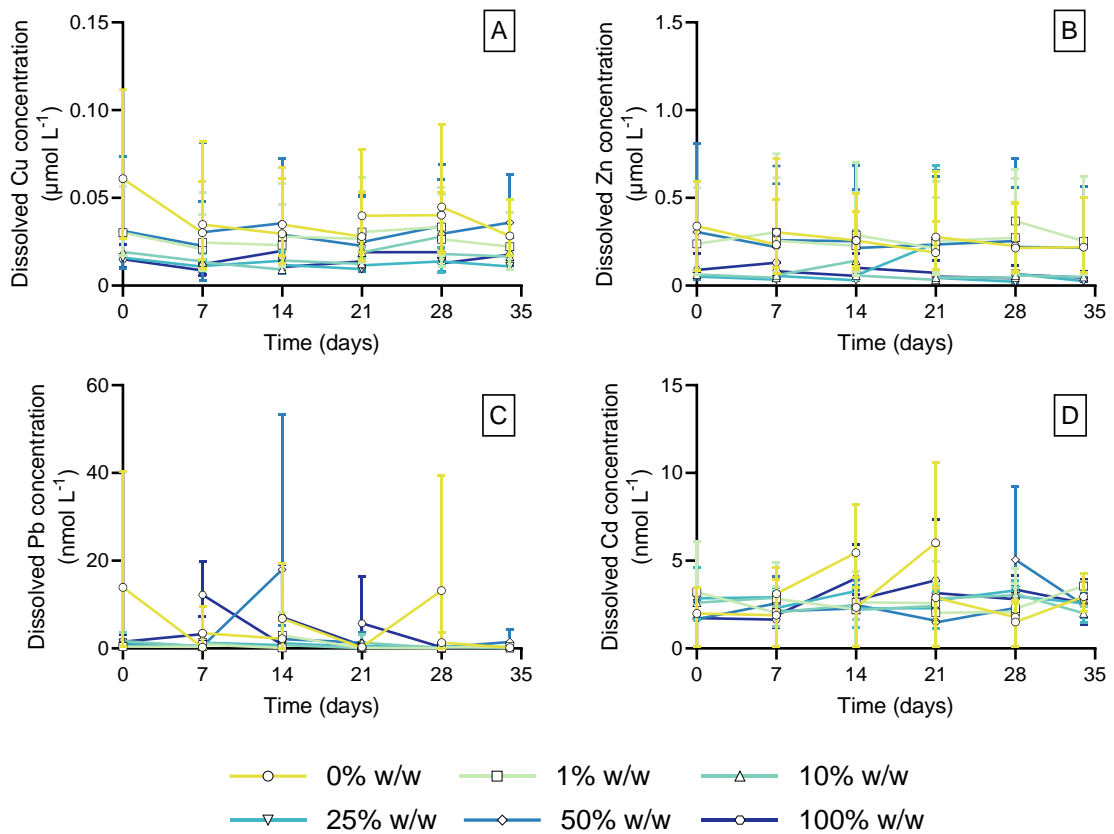
Figure F.11: Temporal evolution of dissolved (A) copper (Cu), (B) zinc (Zn), (C) lead (Pb), and (D) cadmium (Cd) in artificial seawater. Note that concentrations for Cu and Zn are expressed in µmol L⁻¹, while Pb and Cd concentrations are expressed in nmol L⁻¹. Mean and range (N = 2 or 3) are shown.

F.5.3 Possible Ni accumulation in coastal waters

The potential seawater dissolved Ni concentration in the water column C_{Ni} (µmol L⁻¹) after application of various amounts m_{ol} (g) of the experimental 3 - 99 µm olivine to a coastal seafloor was calculated under the assumption that all Ni ends up in the water column (Flipkens et al., 2021) via

$$C_{\text{Ni}} = \frac{C_{bg}V_w + R_{ol}t C_M M_{ol}}{V_w} \qquad \text{[F.11]}$$

Where V_w is the water volume per square meter of seabed (L), t is the water residence time (d), C_M is the Ni concentration of the experimental $3 - 99$ μm olivine (36.2 μmol g^{-1}, Table 6.1), M_{ol} is the molecular weight of Fo93 olivine (144.8 g mol^{-1}), C_{bg} is the background Ni concentration in seawater assumed to be 3.92 nmol L^{-1} based on a previous literature review (Flipkens et al., 2021), and R_{ol} is the olivine dissolution rate (mol d^{-1}). The R_{ol} was calculated from

$$R_{ol} = k_{ol}m_{ol}A_{GEO}(1 - \Omega) \qquad \text{[F.12]}$$

Where k_{ol} is the olivine dissolution rate constant (mol m^{-2} d^{-1}) according the empirical rate equation by Rimstidt et al. (2012) assuming a seawater pH of 8.1 (Eq. F.8), A_{GEO} is the geometric surface area (0.25 m^2 g^{-1}) derived from the volumetric grain size distribution, Ω is the mineral saturation state (assumed to be <<1), and m_{ol} is the olivine weight (g) applied to the coastal seabed. The m_{ol} was derived from the experimental olivine concentrations C_{ol} (% w/w) via

$$m_{ol} = V_s\rho_s(1 - \Phi)\left(\frac{C_{ol}}{100}\right) \qquad \text{[F.13]}$$

Where V_s is the sediment volume for 1 m^2 of seafloor assuming an olivine mixing depth of 10 cm (V_s = 0.1 m^3), ρ_s is the specific density of marine sediment (2650 kg m^{-3}), and Φ is the sediment porosity assumed to be 0.60 based on a predicted coastal sediment porosity ranging from 0.50 to 0.85 (Martin et al., 2015).
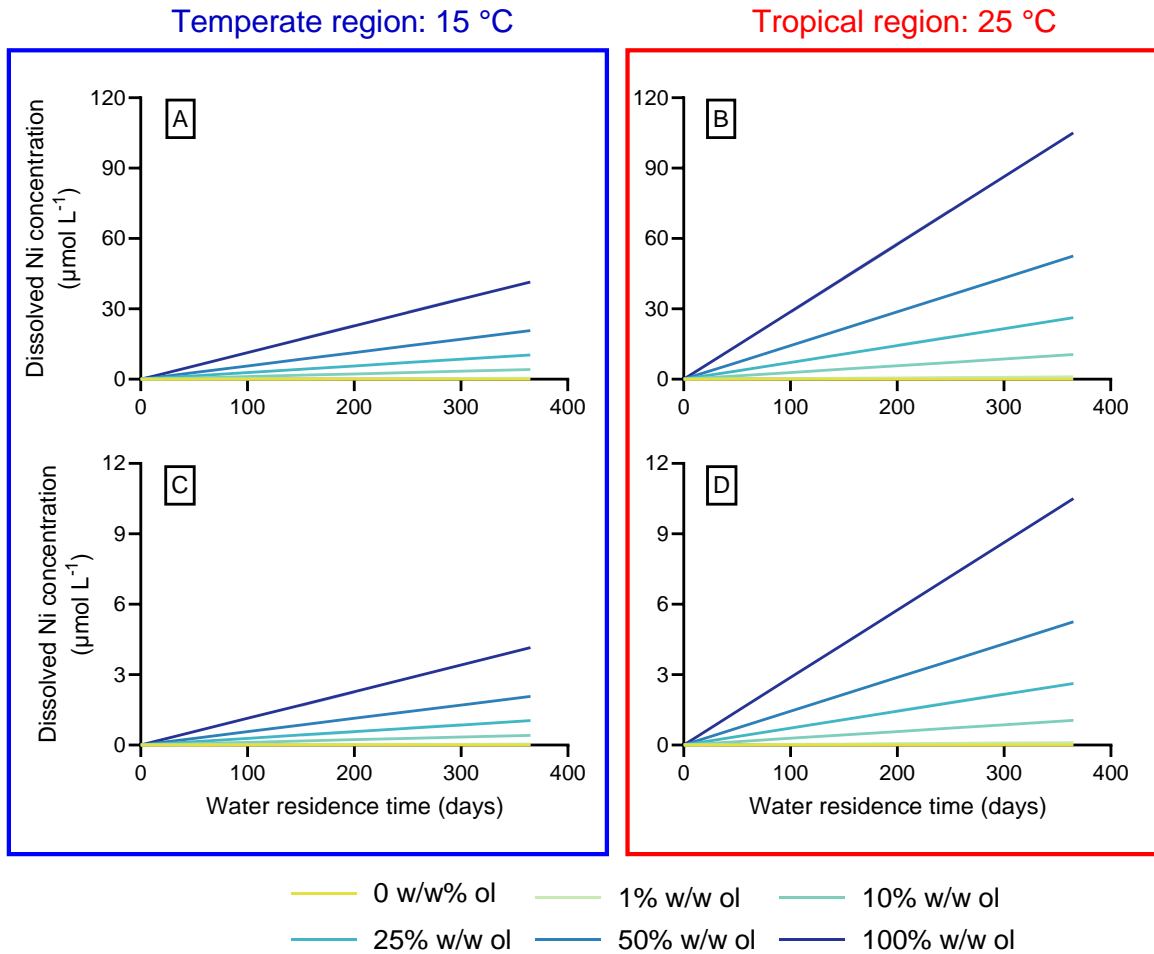
Figure F.12: Possible dissolved nickel (Ni) concentration (μmol L^{-1}) in seawater as a function of water residence time (days) after application of different amounts of the experimental 3 – 99 μm olivine (0 – 100% w/w) to the upper 10 cm of a coastal seafloor. Scenarios for a (A,C) temperate (15 °C) and (B,D) tropical (25 °C) deployment site with a water depth of (A,B) 10 or (C,D) 100 m are shown assuming a background dissolved Ni concentration of 3.92 nmol L^{-1} and an olivine Ni concentration of 5.2 mmol mol^{-1} olivine (Table 6.1). Note the difference in scale between the 10 m and 100 m water depth scenarios. Olivine dissolution rates were derived using the empirical rate equation of Rimstidt et al. (2012) based on a seawater pH of 8.1 and olivine geometric surface area of 0.25 m² g^{-1}.

F.5.4 Amphipod sex ratio and reproduction
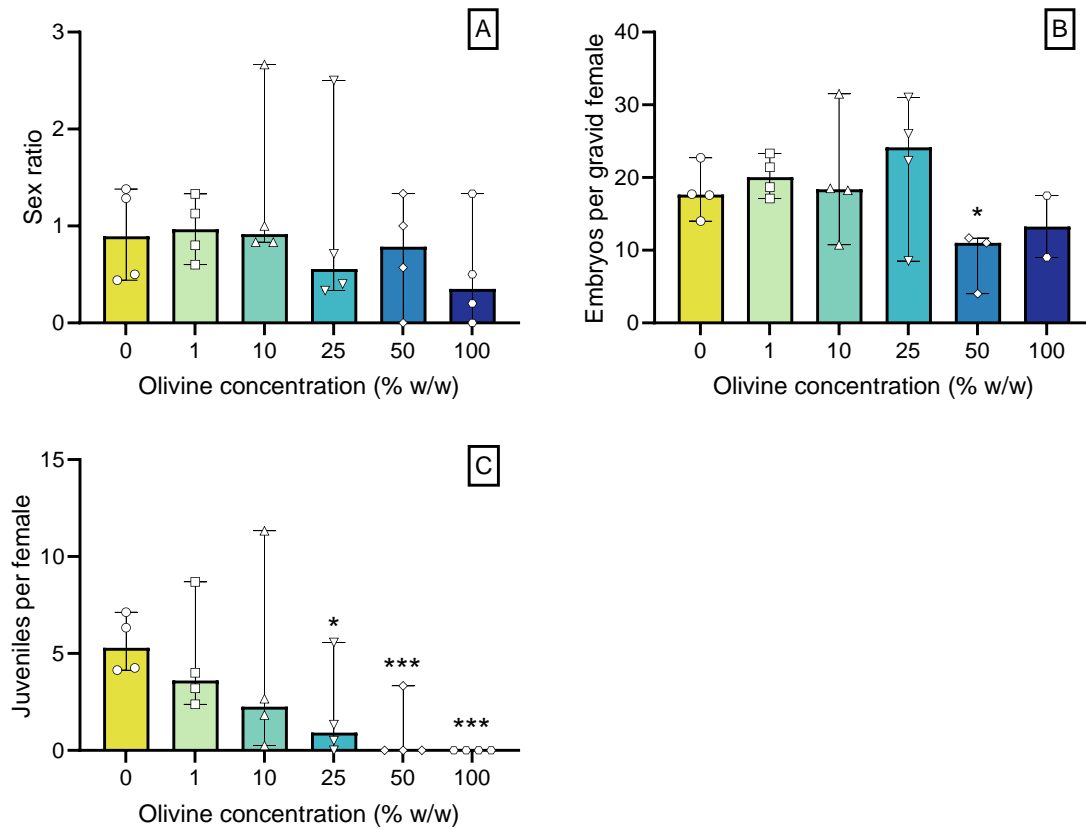
*Figure F.13: (A) sex ratio, (B) number of embryos per gravid female, and (C) number of juveniles per surviving female for amphipods exposed to natural sediment mixed with various amounts of 3 – 99 μm olivine (expressed in % w/w) for 35 days. Median and range (N = 2 – 4) are shown. Significance compared to 0% w/w olivine: * = p < 0.05, ** = p < 0.01, *** = p < 0.001.*

F.5.5 Trace metal(loid) bioaccumulation
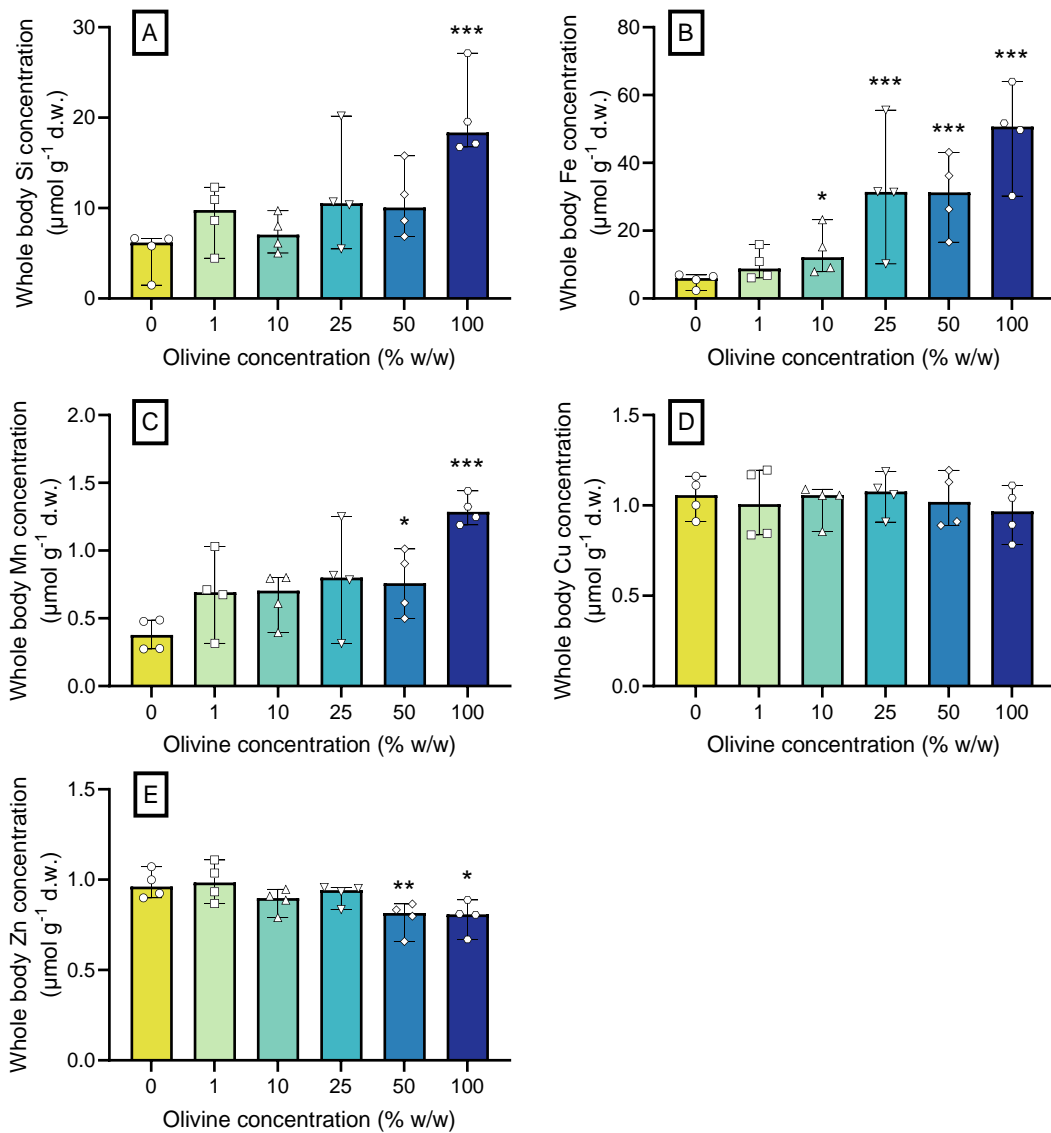
*Figure F.14: Whole body concentration (μmol g^{-1} dry weight) of (A) silicon (Si), (B) iron (Fe), (C) manganese (Mn), (D) copper (Cu), and (E) zinc (Zn) in pooled amphipods exposed to natural sediment mixed with various amounts of 3 – 99 μm olivine (expressed in % w/w) for 35 days. Median and range are shown (N = 4). Significance compared to 0% w/w olivine: * = p < 0.05, ** = p < 0.01, *** = p < 0.001.*

F.5.6 Relationship between endpoints and whole body Ni concentrations
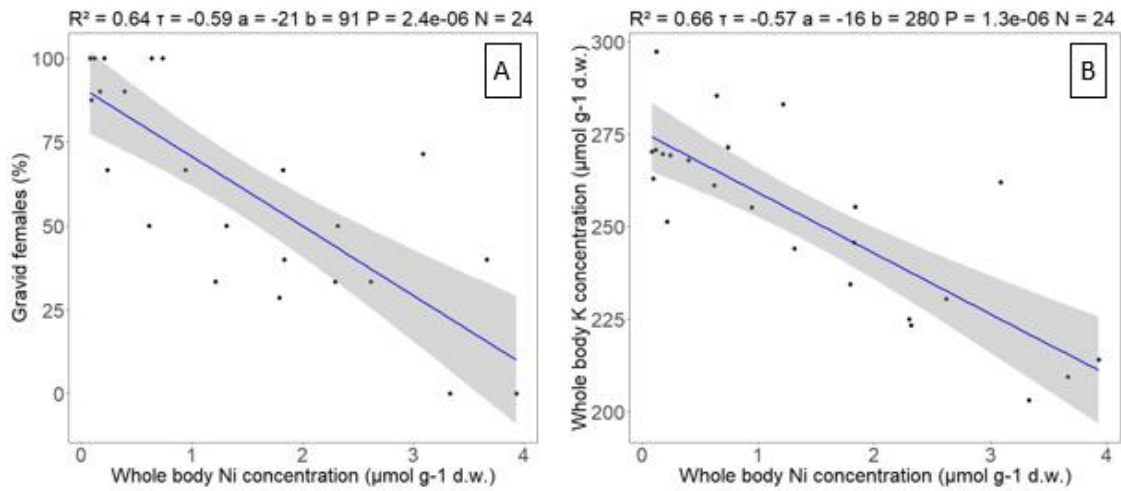
Figure F.15: Linear regression between experimental endpoints and whole body Ni concentration (μmol g^{-1} d.w.) in pooled G. locusta. Regression lines (blue) with 95% confidence intervals (dark grey shading) are shown for (A) gravid females (%) and (B) whole body potassium (K) concentration (μmol g^{-1} d.w.). The coefficient of determination (R²), Kendall correlation coefficient (τ), sample size (N), and regression line slope (a), intercept (b), and p value (P) are given above each plot.
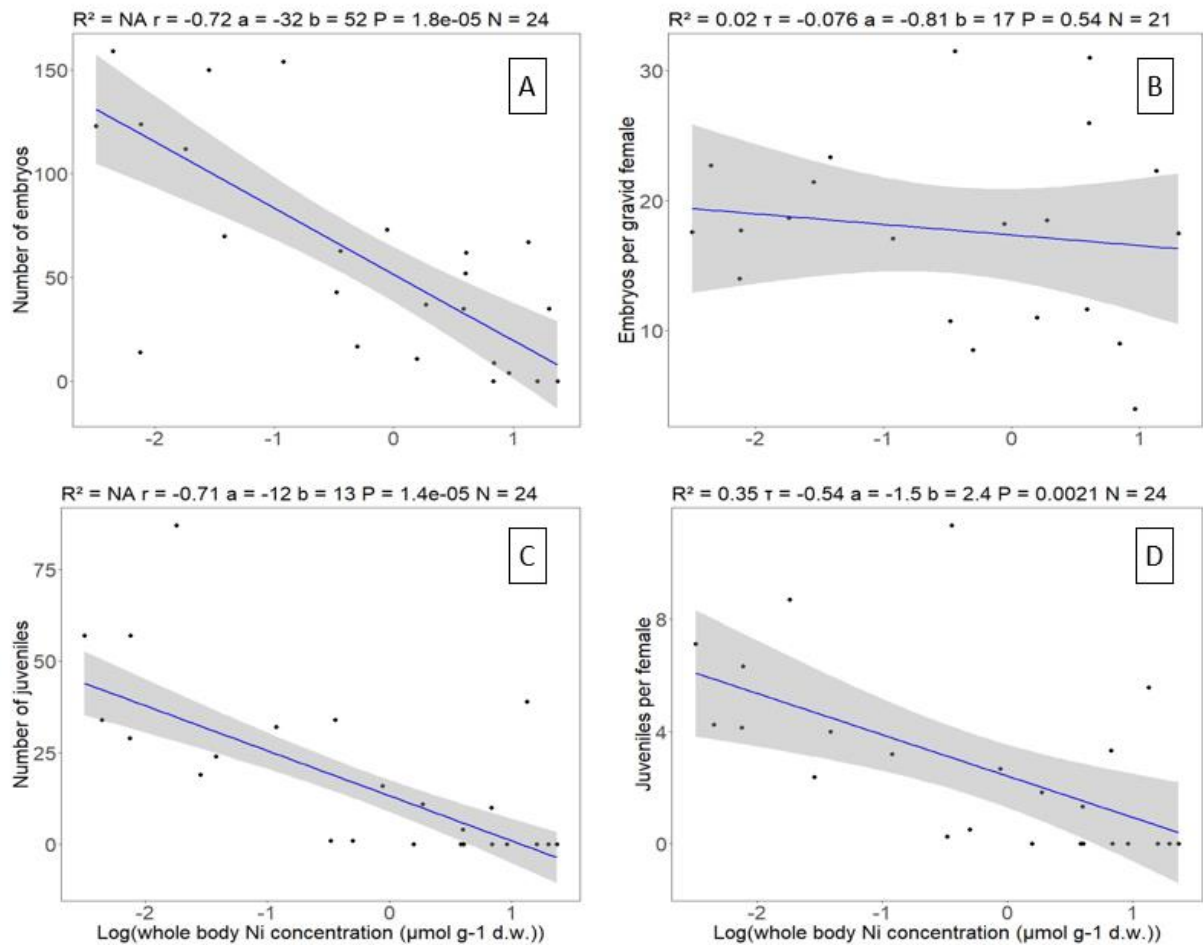
Figure F.16: Linear regression between experimental endpoints and log transformed whole body Ni concentration (μmol g^{-1} d.w.) in pooled G. locusta. Robust linear regression lines (blue) are shown for total number of (A) embryos, and (C) juveniles, while simple linear regression lines are shown for (B) embryos per gravid female, and (D) juveniles per female. The 95% confidence intervals (dark grey shading) are given for all regression lines. The coefficient of determination (R²), Kendall correlation coefficient (τ), sample size (N), and regression line slope (a), intercept (b), and p value (P), are given above each plot.

F.5.7 Dose response curves

Dose response curves were constructed for the chronic toxicity data using the "drm" function of the "drc" package in R (Ritz et al., 2015). A 3 parameter log logistic model was selected for the different effect data based on the AIC value (Figure F.17). The 5% and 10% effective concentrations (EC5 and EC10, respectively) and their confidence intervals were derived using the "ED" function with the delta method and are shown in Supplementary Table F.5. Wide confidence intervals were obtained for most effects due to the low number of replicates, variation among replicates and limited amount of exposure concentrations.
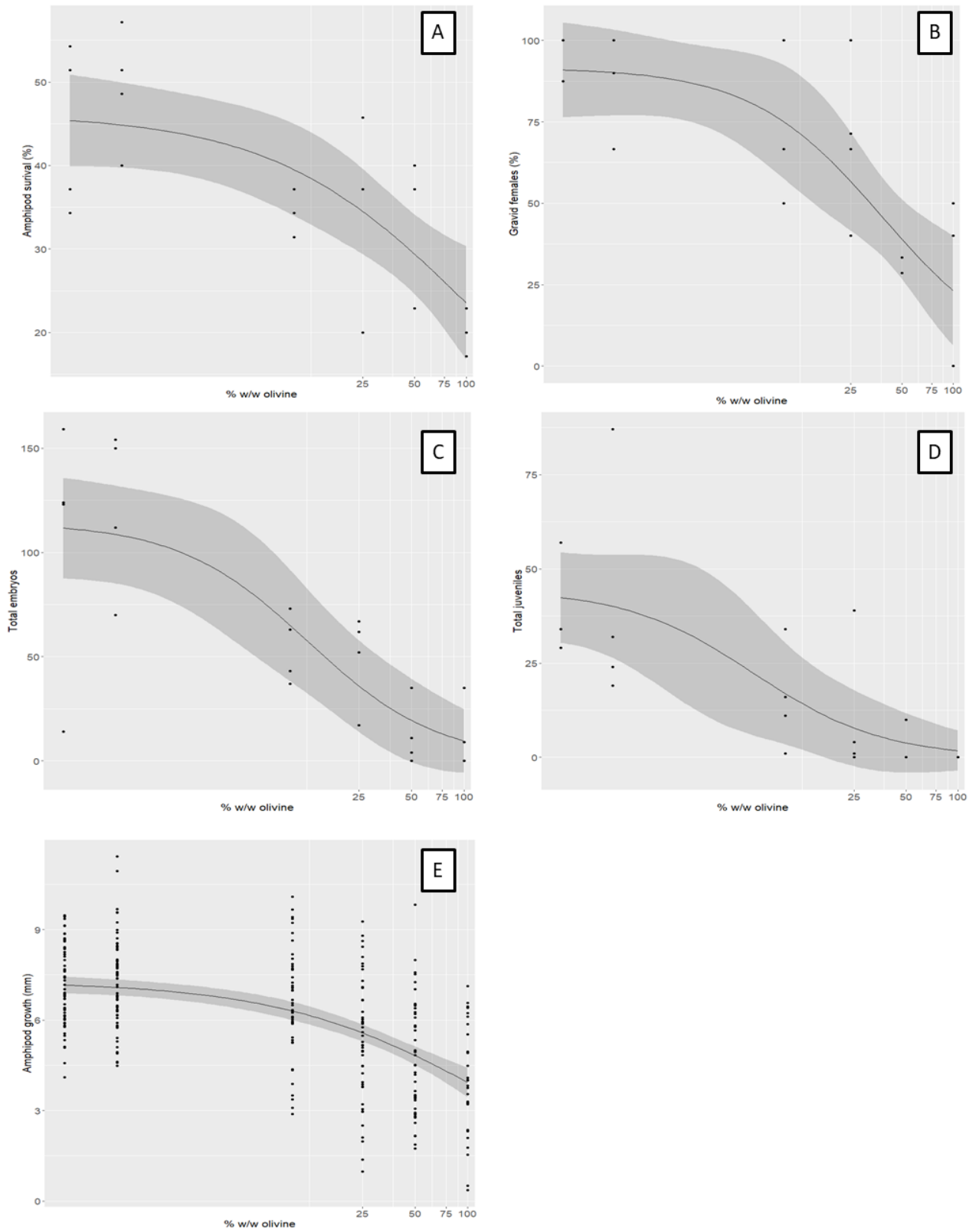
Figure F.17: Three parameter log logistic dose response curves (black line) with confidence intervals (dark grey shading) for amphipod (A) survival (%), (B) percentage of gravid females (%), (C) total embryos, (D) total juveniles, and (E) amphipod growth (mm).

Table F.5: Chronic highest no observed effect concentrations (NOEC), 5% effect (EC5) and 10% (EC10) effect concentrations (% w/w) for survival and several sublethal effects in Gammarus locusta exposed to 3 – 99 μm olivine for 35 days.

Effect	NOEC (% w/w)	EC5 (% w/w)	EC10 (% w/w)
Survival	50	2.1 (0 – 8.9)	5.7 (0 – 19)
Gravid females	1	2.8 (0 – 10)	5.4 (0 – 17)
Total juveniles	1	0.52 (0 – 2.7)	0.99 (0 – 4.4)
Total embryos	25	1.0 (0 – 3.5)	1.9 (0 – 5.7)
Growth	10	2.3 (0 – 4.9)	6.3 (1.2 – 12)

Appendix G: Chapter 7

Table G.1: Potential seawater chemistry after application of 10% w/w fine-grained (3-99 µm, see Table 6.1) olivine in shallow (10 m) tropical (25°C) coastal waters with various water residence times. Seawater composition reported by (Hem, 1985) is shown with potential Ni, Cr, and HCO₃⁻ concentrations as calculated in Supplementary Section F.5.3. Note that Ni and Cr concentrations are given in nmol L⁻¹ while concentrations for other elements and compounds are given in mmol L⁻¹.

Water residence time (days)	0 (background)	1.1	11	100
pH	8.1	8.1	8.1	8.1
Temperature (°C)	25	25	25	25
Na (mmol L^{-1})	457	457	457	457
Mg (mmol L^{-1})	55.5	55.5	55.5	55.5
K (mmol L^{-1})	10	10	10	10
Ca (mmol L^{-1})	10.2	10.2	10.2	10.2
Cl (mmol L^{-1})	536	536	536	536
SO$_4$ (mmol L^{-1})	28	28	28	28
HCO$_3^-$ (mmol L^{-1})	2.35	2.93	3.65	4.54
Ni (nmol L^{-1})	3.9	35	319	2881
Cr (nmol L^{-1})	0.84	12	167	2356
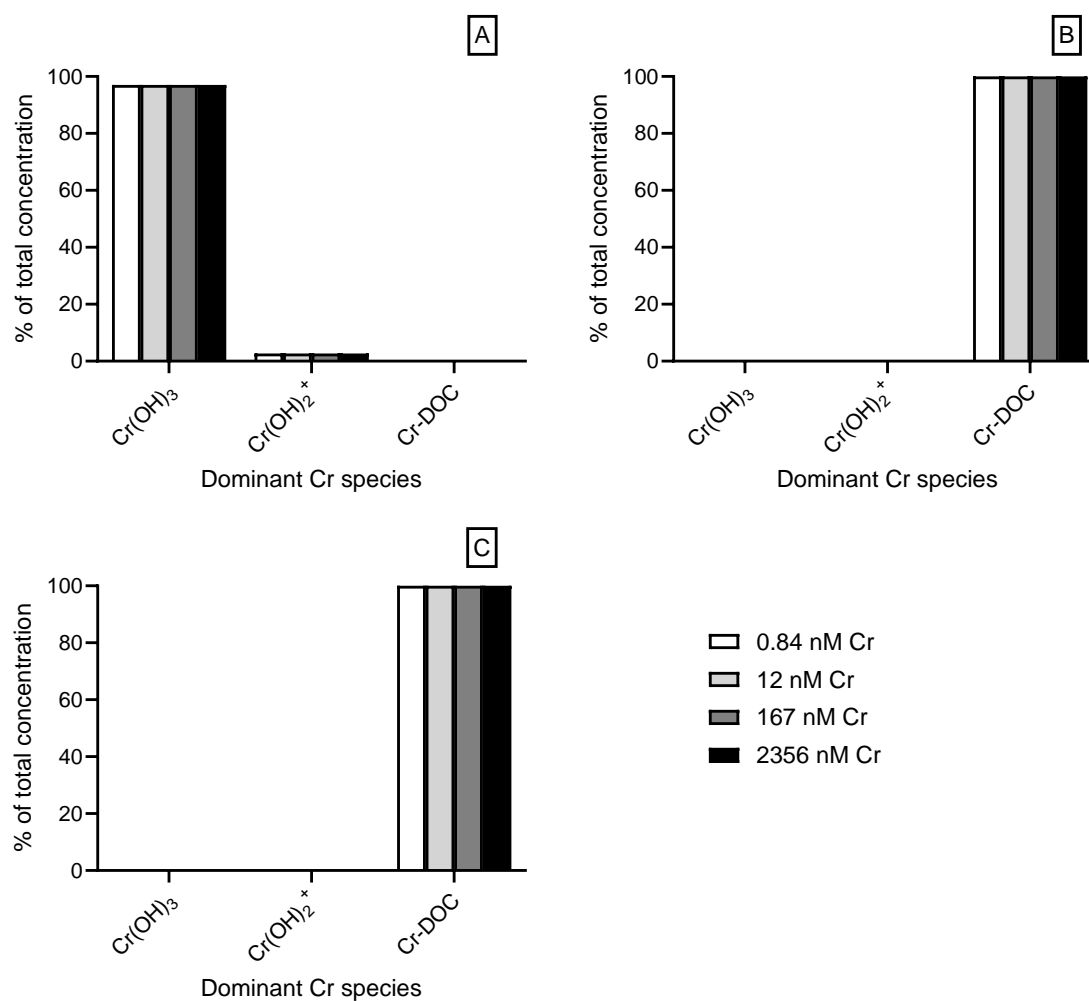
Figure G.1: Speciation of Cr^{3+} in seawater (34.6 ‰) with various Ni, Cr, and TA concentrations in the presence of (A) 0 mg L^{-1}, (B) 4 mg L^{-1}, or (C) 8 mg L^{-1} DOC. Chemical speciation was modelled in Visual MINTEQ using the default DOC settings (Nica-Donnan model). Water chemistry data is shown in Supplementary Table G.1.

Bibliography

Abadi, M., Zamani, A., Parizanganeh, A., Khosravi, Y., Badiee, H., 2018. Heavy metals and arsenic content in water along the southern Caspian coasts in Iran. Environ. Sci. Pollut. Res. 25 (24), 23725-23735.

Abdallah, M. A. M., 2014. Chromium geochemistry in coastal environment of the Western Harbour, Egypt: water column, suspended matter and sediments. J Coast Conserv. 18 (1), 1-10.

Abu-Hilal, A. H., 1987. Distribution of trace elements in nearshore surface sediments from the Jordan Gulf of Aqaba (Red Sea). Mar. Pollut. Bull. 18 (4), 190-193.

Abu-Saba, K. E., Flegal, A. R., 1995. Chromium in San Francisco Bay: superposition of geochemical processes causes complex spatial distributions of redox species. Mar. Chem. 49 (2-3), 189-199.

Accornero, A., Gnerre, R., Manfra, L., 2008. Sediment concentrations of trace metals in the Berre lagoon (France): an assessment of contamination. Arch Environ Contam Toxicol. 54 (3), 372-385.

Achterberg, E. P., Van Den Berg, C. M., 1997. Chemical speciation of chromium and nickel in the western Mediterranean. Deep Sea Res. Part II Top. Stud. Oceanogr. 44 (3-4), 693-720.

Adams, W., Blust, R., Dwyer, R., Mount, D., Nordheim, E., Rodriguez, P. H., Spry, D., 2020. Bioavailability Assessment of Metals in Freshwater Environments: A Historical Review. Environ Toxicol Chem. 39 (1), 48-59.

Adams, W. J., Blust, R., Borgmann, U., Brix, K. V., DeForest, D. K., Green, A. S., Meyer, J. S., McGeer, J. C., Paquin, P. R., Rainbow, P. S., Wood, C. M., 2011. Utility of tissue residues for predicting effects of metals on aquatic organisms. Integr. Environ. Assess. Manag. 7 (1), 75-98.

Agah, H., Bastami, K. D., Fumani, N. S., 2016. Ecological risk, source and preliminary assessment of metals in the surface sediments of Chabahar Bay, Oman Sea. Mar. Pollut. Bull. 107 (1), 383-388.

Aharchaou, I., Py, J. S., Cambier, S., Loizeau, J. L., Cornelis, G., Rousselle, P., Battaglia, E., Vignati, D. A., 2018. Chromium hazard and risk assessment: New insights from a detailed speciation study in a standard test medium. Environ. Toxicol. Chem. 37 (4), 983-992.

Ahsanullah, M., Williams, A., 1991. Sublethal effects and bioaccumulation of cadmium, chromium, copper and zinc in the marine amphipod Allorchestes compressa. Mar. Biol. 108 (1), 59-65.

Al-Farawati, R. K., Gazzaz, M. O., El Sayed, M. A., El-Maradny, A., 2011. Temporal and spatial distribution of dissolved Cu, Ni and Zn in the coastal waters of Jeddah, eastern Red Sea. Arab. J. Geosci. 4 (7-8), 1229-1238.

Al-Ghussain, L., 2019. Global warming: Review on driving forces and mitigation. Environ. Prog. Sustain. Energy. 38 (1), 13-21.

Albright, R., Caldeira, L., Hosfelt, J., Kwiatkowski, L., Maclaren, J. K., Mason, B. M., Nebuchina, Y., Ninokawa, A., Pongratz, J., Ricke, K. L., 2016. Reversal of ocean acidification enhances net coral reef calcification. Nature. 531 (7594), 362-365.

Alharbi, O. M., Khattab, R. A., Ali, I., Binnaser, Y. S., Aqeel, A., 2019. Assessment of heavy metals contamination in the sediments and mangroves (Avicennia marina) at Yanbu coast, Red Sea, Saudi Arabia. Mar. Pollut. Bull. 149, 110669.

Alquezar, R., Anastasi, A., 2013. The use of the cyanobacteria, Cyanobium sp., as a suitable organism for toxicity testing by flow cytometry. Bulletin of environmental contamination and toxicology. 90 (6), 684-690.

Alvarez, C. C., Quitté, G., Schott, J., Oelkers, E. H., 2021. Nickel isotope fractionation as a function of carbonate growth rate during Ni coprecipitation with calcite. Geochim. Cosmochim. Acta. 299, 184-198.

Anbuselvan, N., Sridharan, M., 2018. Heavy metal assessment in surface sediments off Coromandel Coast of India: Implication on marine pollution. Mar. Pollut. Bull. 131, 712-726.

Andersen, H. R., Wollenberger, L., Halling-Sørensen, B., Kusk, K. O., 2001. Development of copepod nauplii to copepodites—a parameter for chronic toxicity including endocrine disruption. Environ. Toxicol. Chem. 20 (12), 2821-2829.

Anderson, M., Underwood, A., 1997. Effects of gastropod grazers on recruitment and succession of an estuarine assemblage: a multivariate and univariate approach. Oecologia. 109, 442-453.

Andersson, S., Persson, M., Moksnes, P.-O., Baden, S., 2009. The role of the amphipod Gammarus locusta as a grazer on macroalgae in Swedish seagrass meadows. Mar. Biol. 156, 969-981.

Anschutz, P., Dedieu, K., Desmazes, F., Chaillou, G., 2005. Speciation, oxidation state, and reactivity of particulate manganese in marine sediments. Chem. Geol. 218 (3-4), 265-279.

ANZECC, ARMCANZ, 2000. Australian and New Zealand Guidelines for Fresh and Marine Water Quality. https://www.waterquality.gov.au/sites/default/files/documents/anzecc-armcanz-2000-guidelines-vol1.pdf (accessed 2023-08-08).

Araújo, C. V., Moreira-Santos, M., Ribeiro, R., 2016. Active and passive spatial avoidance by aquatic organisms from environmental stressors: A complementary perspective and a critical review. Environ. Int. 92, 405-415.

Arikibe, J. E., Prasad, S., 2020. Determination and comparison of selected heavy metal concentrations in seawater and sediment samples in the coastal area of Suva, Fiji. Mar. Pollut. Bull. 157, 111157.

Aschwanden, A., Fahnestock, M. A., Truffer, M., Brinkerhoff, D. J., Hock, R., Khroulev, C., Mottram, R., Khan, S. A., 2019. Contribution of the Greenland Ice Sheet to sea level over the next millennium. Science advances. 5 (6), eaav9396.

Attig, H., Kamel, N., Sforzini, S., Dagnino, A., Jamel, J., Boussetta, H., Viarengo, A., Banni, M., 2014. Effects of thermal stress and nickel exposure on biomarkers responses in Mytilus galloprovincialis (Lam). Mar. Environ. Res. 94, 65-71.

Attrill, M. J., Thomes, R. M., 1995. Heavy metal concentrations in sediment from the Thames Estuary, UK. Mar. Pollut. Bull. 30 (11), 742-744.

Au, D., Pollino, C., Wu, R., Shin, P., Lau, S., Tang, J., 2004. Chronic effects of suspended solids on gill structure, osmoregulation, growth, and triiodothyronine in juvenile green grouper Epinephelus coioides. Mar. Ecol. Prog. Ser. 266, 255-264.

Awad, A., Van Groos, A. K., Guggenheim, S., 2000. Forsteritic olivine: effect of crystallographic direction on dissolution kinetics. Geochim. Cosmochim. Acta. 64 (10), 1765-1772.

Bach, L. T., 2023. The additionality problem of Ocean Alkalinity Enhancement. Biogeosci. Disc. 2023, 1-25.

Bach, L. T., Gill, S. J., Rickaby, R. E., Gore, S., Renforth, P., 2019. CO2 removal with enhanced weathering and ocean alkalinity enhancement: Potential risks and co-benefits for marine pelagic ecosystems. Front. clim. 1, 7.

Bach, L. T., Ho, D. T., Boyd, P. W., Tyka, M. D., 2023. Toward a consensus framework to evaluate air–sea CO2 equilibration for marine CO2 removal. Limnol. Oceanogr. Lett.

Bach, L. T., Riebesell, U., Schulz, K. G., 2011. Distinguishing between the effects of ocean acidification and ocean carbonation in the coccolithophore Emiliania huxleyi. Limnol. Oceanogr. 56 (6), 2040-2050.

Bakke, T., Källqvist, T., Ruus, A., Breedveld, G. D., Hylland, K., 2010. Development of sediment quality criteria in Norway. J Soils Sediments. 10 (2), 172-178.

Bakshi, A., Panigrahi, A., 2018. A comprehensive review on chromium induced alterations in fresh water fishes. Toxicol. Rep. 5, 440-447.

Baldermann, A., Mavromatis, V., Frick, P. M., Dietzel, M., 2018. Effect of aqueous Si/Mg ratio and pH on the nucleation and growth of sepiolite at 25 C. Geochim. Cosmochim. Acta. 227, 211-226.

Bandstra, J. Z., Brantley, S. L., 2008. Surface evolution of dissolving minerals investigated with a kinetic Ising model. Geochim. Cosmochim. Acta. 72 (11), 2587-2600.

Barnes, A. J., Hill, J. M., 2022. Copper barriers can cause behavioral artifacts in experiments with marine snails. Mar. Ecol. Prog. Ser. 685, 127-136.

Bastidas, C., Bone, D., Garcia, E., 1999. Sedimentation rates and metal content of sediments in a Venezuelan coral reef. Mar. Pollut. Bull. 38 (1), 16-24.

Bates, N. R., Samuels, L., Merlivat, L., 2001. Biogeochemical and physical factors influencing seawater ƒCO2 and air-sea CO2 exchange on the Bermuda coral reef. Limnol. Oceanogr. 46 (4), 833-846.

Baysal, A., Akman, S., 2018. Assessment of chromium and nickel levels in surface sea waters and sediments from industrial marine area in Tuzla Aydinli Bay, Istanbul Turkey. Mar. Pollut. Bull. 130, 293-298.

Bazzi, A., 2014. Heavy metals in seawater, sediments and marine organisms in the Gulf of Chabahar, Oman Sea. J. Oceanogr. Mar. Sci. 5 (3), 20-29.

Béarat, H., McKelvy, M. J., Chizmeshya, A. V., Gormley, D., Nunez, R., Carpenter, R., Squires, K., Wolf, G. H., 2006. Carbon sequestration via aqueous olivine mineral carbonation: role of passivating layer formation. Environ. Sci. Technol. 40 (15), 4802-4808.

Behrenfeld, M. J., Westberry, T. K., Boss, E., O'Malley, R. T., Siegel, D. A., Wiggert, J. D., Franz, B., McClain, C., Feldman, G., Doney, S. C., 2009. Satellite-detected fluorescence reveals global physiology of ocean phytoplankton. Biogeosciences. 6 (5), 779-794.

Bell, A. S., 2021. Chromium Redox Systematics in Basaltic Liquids and Olivine, in: R. Moretti, Neuville, D.R. (Eds.), Magma Redox Geochemistry, pp. 165-176.

Bell, J. J., McGrath, E., Biggerstaff, A., Bates, T., Bennett, H., Marlow, J., Shaffer, M., 2015. Sediment impacts on marine sponges. Mar. Pollut. Bull. 94 (1-2), 5-13.

Bellas, J., Beiras, R., Vázquez, E., 2004. Sublethal effects of trace metals (Cd, Cr, Cu, Hg) on embryogenesis and larval settlement of the ascidian Ciona intestinalis. Arch Environ Contam Toxicol. 46 (1), 61-66.

Belliard, J.-P., Silinski, A., Meire, D., Kolokythas, G., Levy, Y., Van Braeckel, A., Bouma, T. J., Temmerman, S., 2019. High-resolution bed level changes in relation to tidal and wave forcing on a narrow fringing macrotidal flat: Bridging intra-tidal, daily and seasonal sediment dynamics. Mar. Geol. 412, 123-138.

Benedet, L., Finkl, C. W., Campbell, T., Klein, A., 2004. Predicting the effect of beach nourishment and cross-shore sediment variation on beach morphodynamic assessment. Coast. Eng. 51 (8-9), 839-861.

Bergmann, J., Friedel, P., Kleeberg, R., 1998. BGMN—a new fundamental parameters based Rietveld program for laboratory X-ray sources, its use in quantitative analysis and structure investigations. CPD Newsletter. 20 (5), 5-8.

Bertagni, M. B., Porporato, A., 2022. The Carbon-Capture Efficiency of Natural Water Alkalinization: Implications For Enhanced weathering. Sci. Total Environ. 838, 156524.

Bidwell, J. R., Wheeler, K. W., Burridge, T. R., 1998. Toxicant effects on the zoospore stage of the marine macroalga Ecklonia radiata (Phaeophyta: Laminariales). Mar. Ecol. Prog. Ser. 163, 259-265.

Bielmyer, G., Brix, K., Capo, T., Grosell, M., 2005. The effects of metals on embryo-larval and adult life stages of the sea urchin, Diadema antillarum. Aquat. Toxicol. 74 (3), 254-263.

Bienfang, P., De Carlo, E., Christopher, S., DeFelice, S., Moeller, P., 2009. Trace element concentrations in Coastal Hawaiian waters. Mar. Chem. 113 (3-4), 164-171.

Birch, G., 2017. Determination of sediment metal background concentrations and enrichment in marine environments–a critical review. Sci. Total Environ. 580, 813-831.

Birch, G. F., 2018. A review of chemical-based sediment quality assessment methodologies for the marine environment. Mar. Pollut. Bull. 133, 218-232.

Bish, D. L., 1981. Cation ordering in synthetic and natural Ni–Mg olivine. Am. Mineral. 66 (7-8), 770-776.

Blarer, P., Burkhardt-Holm, P., 2016. Microplastics affect assimilation efficiency in the freshwater amphipod Gammarus fossarum. Environ. Sci. Pollut. Res. 23, 23522-23532.

Blewett, T. A., Dow, E. M., Wood, C. M., McGeer, J. C., Smith, D. S., 2018. The role of dissolved organic carbon concentration and composition on nickel toxicity to early

life-stages of the blue mussel Mytilus edulis and purple sea urchin Strongylocentrotus purpuratus. Ecotoxicol. Environ. Saf. 160, 162-170.

Blewett, T. A., Glover, C. N., Fehsenfeld, S., Lawrence, M. J., Niyogi, S., Goss, G. G., Wood, C. M., 2015. Making sense of nickel accumulation and sub-lethal toxic effects in saline waters: Fate and effects of nickel in the green crab, Carcinus maenas. Aquat. Toxicol. 164, 23-33.

Blewett, T. A., Leonard, E. M., 2017. Mechanisms of nickel toxicity to fish and invertebrates in marine and estuarine waters. Environ. Pollut. 223, 311-322.

Blewett, T. A., Smith, D. S., Wood, C. M., Glover, C. N., 2016. Mechanisms of nickel toxicity in the highly sensitive embryos of the sea urchin Evechinus chloroticus, and the modifying effects of natural organic matter. Environ. Sci. Technol. 50 (3), 1595-1603.

Blum, A., Lasaga, A., 1988. Role of surface speciation in the low-temperature dissolution of minerals. Nature. 331 (6155), 431-433.

Boers, N., Rypdal, M., 2021. Critical slowing down suggests that the western Greenland Ice Sheet is close to a tipping point. Proc. Natl. Acad. Sci. U.S.A. 118 (21), e2024192118.

Boos, K., Gutow, L., Mundry, R., Franke, H.-D., 2010. Sediment preference and burrowing behaviour in the sympatric brittlestars Ophiura albida Forbes, 1839 and Ophiura ophiura (Linnaeus, 1758)(Ophiuroidea, Echinodermata). J. Exp. Mar. Biol. 393 (1-2), 176-181.

Bothner, M. H., Ten Brink, M. B., Manheim, F., 1998. Metal concentrations in surface sediments of Boston Harbor—changes with time. Mar. Environ. Res. 45 (2), 127-155.

Boyd, P. W., Ellwood, M. J., 2010. The biogeochemical cycle of iron in the ocean. Nat. Geosci. 3 (10), 675-682.

Bricelj, V., Malouf, R., De Quillfeldt, C., 1984. Growth of juvenile Mercenaria mercenaria and the effect of resuspended bottom sediments. Mar. Biol. 84, 167-173.

Brix, K. V., Schlekat, C. E., Garman, E. R., 2017. The mechanisms of nickel toxicity in aquatic environments: An adverse outcome pathway analysis. Environ. Toxicol. Chem. 36 (5), 1128-1137.

Brown, J. W., 1987. Studies of humic and fulvic acid dynamics in coastal marine waters of South Florida. Mar. Environ. Res. 21 (3), 163-174.

Buccolieri, A., Buccolieri, G., Cardellicchio, N., Dell'Atti, A., Di Leo, A., Maci, A., 2006. Heavy metals in marine sediments of Taranto Gulf (Ionian Sea, southern Italy). Mar. Chem. 99 (1-4), 227-235.

Cai, P., Cai, G., Chen, X., Li, S., Zhao, L., 2021. The concentration distribution and biohazard assessment of heavy metal elements in surface sediments from the continental shelf of Hainan Island. Mar. Pollut. Bull. 166, 112254.

Carder, K. L., Steward, R. G., Harvey, G. R., Ortner, P. B., 1989. Marine humic and fulvic acids: Their effects on remote sensing of ocean chlorophyll. Limnol. Oceanogr. 34 (1), 68-81.

Carlson, R. L., Shulman, M. J., Ellis, J. C., 2006. Factors contributing to spatial heterogeneity in the abundance of the common periwinkle Littorina littorea (L.). J. Molluscan Stud. 72 (2), 149-156.

Carrasco, M., Lopez-Ramırez, J., Benavente, J., López-Aguayo, F., Sales, D., 2003. Assessment of urban and industrial contamination levels in the bay of Cádiz, SW Spain. Mar. Pollut. Bull. 46 (3), 335-345.

Caserini, S., Storni, N., Grosso, M., 2022. The availability of limestone and other raw materials for ocean alkalinity enhancement. Glob. Biogeochem. Cycles. 36 (5), e2021GB007246.

CCME, 1999. Canadian Water Quality Guidelines for the Protection of Aquatic Life: Chromium — Hexavalent chromium and trivalent chromium. https://ccme.ca/en/res/chromium-en-canadian-water-quality-guidelines-for-the-protection-of-aquatic-life.pdf (accessed 2023-08-08).

CEM Corporation, 1999. Chromite Ore Microwave Sample Preparation Note: 5OS-47. http://www.uwm.edu.pl/kchemsr/MARS/OXIDSUL/Chromit.pdf (accessed 04/07/2022).

Cempel, M., Nikel, G., 2006. Nickel: A review of its sources and environmental toxicology. Pol J Environ Stud. 15 (3).

Chaâbane, M., Bejaoui, S., Trabelsi, W., Telahigue, K., Chetoui, I., Chalghaf, M., Zeghal, N., Soudani, N., 2020. The potential toxic effects of hexavalent chromium on oxidative stress biomarkers and fatty acids profile in soft tissues of Venus verrucosa. Ecotoxicol. Environ. Saf. 196, 110562.

Chakraborty, P., Sarkar, A., Vudamala, K., Naik, R., Nath, B. N., 2015. Organic matter—a key factor in controlling mercury distribution in estuarine sediment. Mar. Chem. 173, 302-309.

Chakraborty, S., Owens, G., 2014. Metal distributions in seawater, sediment and marine benthic macroalgae from the South Australian coastline. Int. J. Environ. Sci. Technol. (Tehran). 11 (5), 1259-1270.

Chapman, P. M., Allard, P. J., Vigers, G. A., 1999. Development of sediment quality values for Hong Kong special administrative region: a possible model for other jurisdictions. Mar. Pollut. Bull. 38 (3), 161-169.

Chapman, P. M., Fairbrother, A., Brown, D., 1998. A critical evaluation of safety (uncertainty) factors for ecological risk assessment. Environ. Toxicol. Chem. 17 (1), 99-108.

Cheung, S., Shin, P., 2005. Size effects of suspended particles on gill damage in green-lipped mussel Perna viridis. Mar. Pollut. Bull. 51 (8-12), 801-810.

Chrysochoou, M., Theologou, E., Bompoti, N., Dermatas, D., Panagiotakis, I., 2016. Occurrence, origin and transformation processes of geogenic chromium in soils and sediments. Curr. Pollut. Rep. 2, 224-235.

Chung-Cherng, L., Pouyan, S., 1993. Directional dissolution kinetics of willemite. Geochim. Cosmochim. Acta. 57 (1), 27-35.

Clarke, A., Morris, G. J., Fonseca, F., Murray, B. J., Acton, E., Price, H. C., 2013. A low temperature limit for life on Earth. PLoS One. 8 (6), e66207.

Cobelo-García, A., Prego, R., 2004. Influence of point sources on trace metal contamination and distribution in a semi-enclosed industrial embayment: the Ferrol Ria (NW Spain). Estuar. Coast. Shelf Sci. 60 (4), 695-703.

Cook, P. L., Wenzhöfer, F., Glud, R. N., Janssen, F., Huettel, M., 2007. Benthic solute exchange and carbon mineralization in two shallow subtidal sandy sediments: Effect of advective pore-water exchange. Limnol. Oceanogr. 52 (5), 1943-1963.

Cosma, B., Drago, M., Piccazzo, M., Scarponi, G., Tucci, S., 1979. Heavy metals in Ligurian Sea sediments: distribution of Cr, Cu, Ni, and Mn in superficial sediments. Mar. Chem. 8 (2), 125-142.

Costa, F., Costa, M., 2000. Review of the ecology of Gammarus locusta [L.]. Pol Arch Hydrobiol. 47 (3-4), 541-559.

Costa, F. O., Correia, A. D., Costa, M. H., 1996. Sensitivity of a marine amphipod to non-contaminant variables and to copper in the sediment. Ecologie. Brunoy. 27 (4), 269-276.

Costa, F. O., Neuparth, T., Correia, A. D., Costa, M. H., 2005. Multi-level assessment of chronic toxicity of estuarine sediments with the amphipod Gammarus locusta: II. Organism and population-level endpoints. Mar. Environ. Res. 60 (1), 93-110.

Cranston, R., Murray, J., 1978. The determination of chromium species in natural waters. Anal. Chim. Acta. 99 (2), 275-282.

Cripps, G., Widdicombe, S., Spicer, J. I., Findlay, H. S., 2013. Biological impacts of enhanced alkalinity in Carcinus maenas. Mar. Pollut. Bull. 71 (1-2), 190-198.

Cui, Y., Kump, L. R., Ridgwell, A. J., Charles, A. J., Junium, C. K., Diefendorf, A. F., Freeman, K. H., Urban, N. M., Harding, I. C., 2011. Slow release of fossil carbon during the Palaeocene–Eocene Thermal Maximum. Nat. Geosci. 4 (7), 481-485.

Cyronak, T., Albright, R., Bach, L., 2023. Field experiments in ocean alkalinity enhancement research. State Planet Discuss. 2023, 1-25.

Cyronak, T., Eyre, B. D., 2016. The synergistic effects of ocean acidification and organic metabolism on calcium carbonate ($CaCO_3$) dissolution in coral reef sediments. Mar. Chem. 183, 1-12.

Dalyander, P. S., Butman, B., Sherwood, C. R., Signell, R. P., Wilkin, J. L., 2013. Characterizing wave-and current-induced bottom shear stress: US middle Atlantic continental shelf. Cont. Shelf Res. 52, 73-86.

Danielsson, L.-G., Magnusson, B., Westerlund, S., 1985. Cadmium, copper, iron, nickel and zinc in the north-east Atlantic Ocean. Mar. Chem. 17 (1), 23-41.

Das, P. K., Das, B. P., Dash, P., 2021. Chromite mining pollution, environmental impact, toxicity and phytoremediation: a review. Environ. Chem. Lett. 19 (2), 1369-1381.

Das, R., 2014. Has industrialization benefited no one? Climate change and the non-identity problem. Ethical Theory Moral Pract. 17, 747-759.

Das, S., Mangwani, N., 2015. Ocean acidification and marine microorganisms: responses and consequences. Oceanologia. 57 (4), 349-361.

Daval, D., Sissmann, O., Menguy, N., Saldi, G. D., Guyot, F., Martinez, I., Corvisier, J., Garcia, B., Machouk, I., Knauss, K. G., 2011. Influence of amorphous silica layer formation on the dissolution rate of olivine at 90 °C and elevated pCO_2. Chem. Geol. 284 (1-2), 193-209.

Davidson, A. B., Semeniuk, D. M., Koh, J., Holmden, C., Jaccard, S. L., Francois, R., Crowe, S. A., 2020. A Mg (OH) 2 coprecipitation method for determining chromium speciation and isotopic composition in seawater. Limnol Oceanogr-Methods. 18 (1), 8-19.

Dayan, A., Paine, A., 2001. Mechanisms of chromium toxicity, carcinogenicity and allergenicity: review of the literature from 1985 to 2000. Hum. Exp. Toxicol. 20 (9), 439-451.

de Boyer Montégut, C., Madec, G., Fischer, A. S., Lazar, A., Iudicone, D., 2004. Mixed layer depth over the global ocean: An examination of profile data and a profile-based climatology. J. Geophys. Res. Oceans. 109 (C12).

De Hoog, J. C., Gall, L., Cornell, D. H., 2010. Trace-element geochemistry of mantle olivine and application to mantle petrogenesis and geothermobarometry. Chem. Geol. 270 (1-4), 196-215.

De Lacerda, L., Pfeiffer, W., Fiszman, M., 1987. Heavy metal distribution, availability and fate in Sepetiba Bay, SE Brazil. Sci. Total Environ. 65, 163-173.

De Lange, H. J., Sperber, V., Peeters, E. T., 2006. Avoidance of polycyclic aromatic hydrocarbon–contaminated sediments by the freshwater invertebrates Gammarus pulex and Asellus aquaticus. Environ. Toxicol. Chem. 25 (2), 452-457.

de Schipper, M. A., Ludka, B. C., Raubenheimer, B., Luijendijk, A. P., Schlacher, T. A., 2021. Beach nourishment has complex implications for the future of sandy shores. Nat. Rev. Earth Environ. 2 (1), 70-84.

DeForest, D. K., Schlekat, C. E., 2013. Species sensitivity distribution evaluation for chronic nickel toxicity to marine organisms. Integr. Environ. Assess. Manag. 9 (4), 580-589.

Deleebeeck, N. M., De Schamphelaere, K. A., Heijerick, D. G., Bossuyt, B. T., Janssen, C. R., 2008. The acute toxicity of nickel to Daphnia magna: Predictive capacity of bioavailability models in artificial and natural waters. Ecotoxicol. Environ. Saf. 70 (1), 67-78.

Deleebeeck, N. M., De Schamphelaere, K. A., Janssen, C. R., 2007. A bioavailability model predicting the toxicity of nickel to rainbow trout (Oncorhynchus mykiss) and fathead minnow (Pimephales promelas) in synthetic and natural waters. Ecotoxicol. Environ. Saf. 67 (1), 1-13.

Delvigne, J., Bisdom, E., Sleeman, J., Stoops, G., 1979. Olivines, their pseudomorphs and secondary products. Pedologie. 29 (3), 247-309.

den Otter, J., Pröfrock, D., Bünning, T., Strehse, J., van der Heijden, A., Maser, E., 2023. Release of Ammunition-Related Compounds from a Dutch Marine Dump Site. Toxics. 11 (3), 238.

Denton, G., Burdon-Jones, C., 1986. Trace metals in surface water from the Great Barrier Reef. Mar. Pollut. Bull. 17 (3), 96-98.

DesMarias, T. L., Costa, M., 2019. Mechanisms of chromium-induced toxicity. Curr. Opin. Toxicol. 14, 1-7.

Detz, R. J., van der Zwaan, B., 2019. Transitioning towards negative CO2 emissions. Energy Policy. 133, 110938.

DeWitt, T. H., Redmond, M., Sewall, J., Swartz, R. (1992). *Development of a chronic sediment toxicity test for marine benthic amphipods*. Retrieved from https://nepis.epa.gov/Exe/ZyPDF.cgi/50000MZ8.PDF?Dockey=50000MZ8.PDF

Dickson, A. G., 1981. An exact definition of total alkalinity and a procedure for the estimation of alkalinity and total inorganic carbon from titration data. Deep Sea Res. Part I Oceanogr. Res. Pap. 28 (6), 609-623.

Dickson, A. G., Sabine, C. L., Christian, J. R., 2007. Guide to best practices for ocean CO2 measurements, North Pacific Marine Science Organization, Sidney, British Columbia. 191pp. (PICES Special Publication 193; IOCCP Report 198).

Dilli, K., 1986. Geochronology and geochemistry of a sediment core from Bombay coast. Mahasagar. 19 (2), 87-95.

Dive, D., Gabriel, L., Hanssens, O., Benga-Bengomme, A., 1989. Studies on interactions between components of electroplating industry wastes: influence of nickel and calcium on interactions between cadmium, copper, chromium and zinc. Sci. Total Environ. 87-88, 355-364.

Doebelin, N., Kleeberg, R., 2015. Profex: a graphical user interface for the Rietveld refinement program BGMN. J. Appl. Crystallogr. 48 (5), 1573-1580.

Donat, J. R., Lao, K. A., Bruland, K. W., 1994. Speciation of dissolved copper and nickel in South San Francisco Bay: a multi-method approach. Anal. Chim. Acta. 284 (3), 547-571.

Donazzolo, R., Merlin, O. H., Vitturi, L. M., Orio, A. A., Pavoni, B., Perin, G., Rabitti, S., 1981. Heavy metal contamination in surface sediments from the Gulf of Venice, Italy. Mar. Pollut. Bull. 12 (12), 417-425.

Doney, S. C., Fabry, V. J., Feely, R. A., Kleypas, J. A., 2009. Ocean acidification: the other CO2 problem. Ann. Rev. Mar. Sci. 1, 169-192.

Doyle CJ 1999. Toxicity characterisation of contaminated sediment pore-water using the sea urchin Heliocidaris tuberculata. Honor thesis, University of Technology Sydney, New South Wales.

Duan, L., Song, J., Li, X., Yuan, H., Zhuang, W., 2022. Potential risks of CO2 removal project based on carbonate pump to marine ecosystem. Sci. Total Environ. 862, 160728.

Dufois, F., Garreau, P., Le Hir, P., Forget, P., 2008. Wave-and current-induced bottom shear stress distribution in the Gulf of Lions. Cont. Shelf Res. 28 (15), 1920-1934.

Dupla, X., Möller, B., Baveye, P. C., Grand, S., 2023. Potential accumulation of toxic trace elements in soils during enhanced rock weathering. Eur. J. Soil Sci., e13343.

Dupont, S., Metian, M., 2023. General considerations to experimental research on ocean alkalinity enhancement. State Planet Discuss. 2023, 1-11.

Dychalska, A., Popielarski, P., Franków, W., Fabisiak, K., Paprocki, K., Szybowicz, M., 2015. Study of CVD diamond layers with amorphous carbon admixture by Raman scattering spectroscopy. Mater. Sci.-Pol. 33 (4), 799-805.

Dzombak, D. A., More, F. M. M., 1990. Surface Complexation Modelling: Hydrous Ferric Oxide, John Wiley & Sons, New York. pp. 416.

Eastmond, D. A., MacGregor, J. T., Slesinski, R. S., 2008. Trivalent chromium: assessing the genotoxic risk of an essential trace element and widely used human and animal nutritional supplement. Crit. Rev. Toxicol. 38 (3), 173-190.

ECHA, 2008. Guidance on information requirements and chemical safety assessment Chapter R.10: Characterisation of dose [concentration]-response for environment. https://echa.europa.eu/documents/10162/13632/information_requirements_r10_en.pdf/bb902be7-a503-4ab7-9036-d866b8ddce69 (accessed 8 March 2023).

Edwards, D. P., Lim, F., James, R. H., Pearce, C. R., Scholes, J., Freckleton, R. P., Beerling, D. J., 2017. Climate change mitigation: potential benefits and pitfalls of enhanced rock weathering in tropical agriculture. Biology letters. 13 (4), 20160715.

El-Nady, F., Atta, M., 1996. Toxicity and bioaccumulation of heavy metals to some marine biota from the Egyptian coastal waters. J. Environ. Sci. Health A. 31 (7), 1529-1545.

Erftemeijer, P. L., Riegl, B., Hoeksema, B. W., Todd, P. A., 2012. Environmental impacts of dredging and other sediment disturbances on corals: a review. Mar. Pollut. Bull. 64 (9), 1737-1765.

Erlandsson, J., Kostylev, V., 1995. Trail following, speed and fractal dimension of movement in a marine prosobranch, Littorina littorea, during a mating and a non-mating season. Mar. Biol. 122, 87-94.

Evans, G., Howarth, R. J., Nombela, M., 2003. Metals in the sediments of Ensenada de San Simon (inner Ría de Vigo), Galicia, NW Spain. Appl. Geochem. 18 (7), 973-996.

Fakhraee, M., Li, Z., Planavsky, N. J., Reinhard, C. T., 2023. A biogeochemical model of mineral-based ocean alkalinity enhancement: impacts on the biological pump and ocean carbon uptake. Environ. Res. Lett. 18 (4), 044047.

Falkner, R., 2016. The Paris Agreement and the new logic of international climate politics. Int. Affairs. 92 (5), 1107-1125.

Fan, W., Wang, W.-X., Chen, J., Li, X., Yen, Y.-F., 2002. Cu, Ni, and Pb speciation in surface sediments from a contaminated bay of northern China. Mar. Pollut. Bull. 44 (8), 820-826.

Ferderer, A., Chase, Z., Kennedy, F., Schulz, K. G., Bach, L. T., 2022. Assessing the influence of ocean alkalinity enhancement on a coastal phytoplankton community. Biogeosci. Disc., 1-36.

Ferderer, A., Schulz, K. G., Riebesell, U., Baker, K. G., Chase, Z., Bach, L. T., 2023. Investigating the effect of silicate and calcium based ocean alkalinity enhancement on diatom silicification. Biogeosci. Disc. 2023, 1-28.

Ferreira, M. F., Chiu, W., Cheok, H., Cheang, F., Sun, W., 1996. Accumulation of nutrients and heavy metals in surface sediments near Macao. Mar. Pollut. Bull. 32 (5), 420-425.

Flegal, A., Smith, G., Gill, G., Sanudo-Wilhelmy, S., Anderson, L., 1991. Dissolved trace element cycles in the San Francisco Bay estuary. Mar. Chem. 36 (1-4), 329-363.

Flipkens, G., Blust, R., Town, R. M., 2021. Deriving nickel (Ni (II)) and chromium (Cr (III)) based environmentally safe olivine guidelines for coastal enhanced silicate weathering. Environ. Sci. Technol. 55 (18), 12362-12371.

Flipkens, G., Fuhr, M., Fiers, G., Meysman, F. J., Town, R. M., Blust, R., 2023a. Enhanced olivine dissolution in seawater through continuous grain collisions. Geochim. Cosmochim. Acta. 359, 84-99.

Flipkens, G., Horoba, K., Bostyn, K., Geerts, L. J., Town, R. M., Blust, R., 2023b. Acute bioaccumulation and chronic toxicity of olivine in the marine amphipod Gammarus locusta. Aquat. Toxicol. 262, 106662.

Foteinis, S., Campbell, J. S., Renforth, P., 2023. Life Cycle Assessment of Coastal Enhanced Weathering for Carbon Dioxide Removal from Air. Environ. Sci. Technol. 57 (15), 6169-6178.

Frey, B. E., Riedel, G. F., Bass, A. E., Small, L. F., 1983. Sensitivity of estuarine phytoplankton to hexavalent chromium. Estuar. Coast. Shelf Sci. 17 (2), 181-187.

Frogner-Kockum, P., Göransson, P., Åslund, H., Ländell, M., Stevens, R., Tengberg, A., Göransson, G., Ohlsson, Y., 2016. Metal contaminant fluxes across the sediment water interface. Mar. Pollut. Bull. 111 (1-2), 321-329.

Fuhr, M., Geilert, S., Schmidt, M., Liebetrau, V., Vogt, C., Ledwig, B., Wallmann, K., 2022. Kinetics of olivine weathering in seawater: an experimental study. Front. clim. 4:831587.

Fuhr, M., Wallmann, K., Dale, A. W., Diercks, I., Kalapurakkal, H. T., Schmidt, M., Sommer, S., Böhnke, S., Perner, M., Geilert, S., 2023. Disentangling artificial and natural benthic weathering in organic rich Baltic Sea sediments. Front. clim. 5, 1245580.

Fukushima, K., Saino, T., Kodama, Y., 1992. Trace metal contamination in Tokyo bay, Japan. Sci. Total Environ. 125, 373-389.

Fuss, S., Lamb, W. F., Callaghan, M. W., Hilaire, J., Creutzig, F., Amann, T., Beringer, T., de Oliveira Garcia, W., Hartmann, J., Khanna, T., 2018. Negative emissions—Part 2: Costs, potentials and side effects. Environ. Res. Lett. 13 (6), 063002.

Gao, X., Chen, C.-T. A., 2012. Heavy metal pollution status in surface sediments of the coastal Bohai Bay. Water Res. 46 (6), 1901-1911.

Gardner, M., Ravenscroft, J., 1996. Determination of chromium (III) and total chromium in marine waters. Fresenius J. Anal. Chem. 354 (5-6), 602-605.

Garratt, J. R., 1992. The atmospheric boundary layer, Cambridge University Press, Cambridge, UK.

Gasser, T., Guivarch, C., Tachiiri, K., Jones, C., Ciais, P., 2015. Negative emissions physically needed to keep global warming below 2 C. Nat. Commun. 6 (1), 1-7.

Gately, J. A., Kim, S. M., Jin, B., Brzezinski, M. A., Iglesias-Rodriguez, M. D., 2023. Coccolithophores and diatoms resilient to ocean alkalinity enhancement: A glimpse of hope? Sci. Adv. 9 (24), eadg6066.

Geilert, S., Grasse, P., Doering, K., Wallmann, K., Ehlert, C., Scholz, F., Frank, M., Schmidt, M., Hensen, C., 2020. Impact of ambient conditions on the Si isotope fractionation in marine pore fluids during early diagenesis. Biogeosciences. 17 (7), 1745-1763.

Genchi, G., Carocci, A., Lauria, G., Sinicropi, M. S., Catalano, A., 2020. Nickel: Human health and environmental toxicology. Int. J. Environ. Res. Public Health. 17 (3), 679.

Gentile, J., Gentile, S., Hairston, N., Sullivan, B. (1982). The use of life-tables for evaluating the chronic toxicity of pollutants to Mysidopsis bahia. In *Ecology of Mysidacea* (pp. 179-187): Springer.

Gholizadeh, M., Patimar, R., 2018. Ecological risk assessment of heavy metals in surface sediments from the Gorgan Bay, Caspian Sea. Mar. Pollut. Bull. 137, 662-667.

Gim, B. M., Hong, S., Lee, J. S., Kim, N. H., Kwon, E. M., Gil, J. W., Lim, H. H., Jeon, E. C., Khim, J. S., 2018. Potential ecotoxicological effects of elevated bicarbonate ion concentrations on marine organisms. Environ. Pollut. 241, 194-199.

Gissi, F., 2019. Biological effects of nickel on tropical marine biota to underpin the development of water quality guidelines for metals.

Gissi, F., Adams, M. S., King, C. K., Jolley, D. F., 2015. A robust bioassay to assess the toxicity of metals to the Antarctic marine microalga Phaeocystis antarctica. Environ. Toxicol. Chem. 34 (7), 1578-1587.

Gissi, F., Stauber, J., Reichelt-Brushett, A., Harrison, P. L., Jolley, D. F., 2017. Inhibition in fertilisation of coral gametes following exposure to nickel and copper. Ecotoxicol. Environ. Saf. 145, 32-41.

Gissi, F., Stauber, J. L., Binet, M. T., Golding, L. A., Adams, M. S., Schlekat, C. E., Garman, E. R., Jolley, D. F., 2016. A review of nickel toxicity to marine and estuarine tropical biota with particular reference to the South East Asian and Melanesian region. Environ. Pollut. 218, 1308-1323.

Gissi, F., Stauber, J. L., Binet, M. T., Trenfield, M. A., Van Dam, J. W., Jolley, D. F., 2018. Assessing the chronic toxicity of nickel to a tropical marine gastropod and two crustaceans. Ecotoxicol. Environ. Saf. 159, 284-292.

Gissi, F., Wang, Z., Batley, G. E., Leung, K. M., Schlekat, C. E., Garman, E. R., Stauber, J. L., 2020. Deriving a chronic guideline value for nickel in tropical and temperate marine waters. Environ. Toxicol. Chem. 39 (12), 2540-2551.

Godefroy, N., Le Goff, E., Martinand-Mari, C., Belkhir, K., Vacelet, J., Baghdiguian, S., 2019. Sponge digestive system diversity and evolution: filter feeding to carnivory. Cell Tissue Res. 377, 341-351.

Golubev, S. V., Pokrovsky, O. S., Schott, J., 2005. Experimental determination of the effect of dissolved CO_2 on the dissolution kinetics of Mg and Ca silicates at 25 C. Chem. Geol. 217 (3-4), 227-238.

Goodfellow, W., Rue, W. J. (1989). Evaluation of a chronic estimation toxicity test using Mysidopsis bahia. In *Aquatic Toxicology and Hazard Assessment: 12th Volume*: ASTM International.

Gore, S., Renforth, P., Perkins, R., 2019. The potential environmental response to increasing ocean alkalinity for negative emissions. Mitig. Adapt. Strateg. Glob. Chang. 24 (7), 1191-1211.

Grandstaff, D., 1978. Changes in surface area and morphology and the mechanism of forsterite dissolution. Geochim. Cosmochim. Acta. 42 (12), 1899-1901.

Grandstaff, D., 1980. The dissolution rate of forsteritic olivine from Hawaiian beach sand, in: S. M. Colman, Dethier, D. P. (Eds.), Rates of Chemical Weathering of Rocks and Minerals, Academic Press, Orlando, FL, pp. 41–59.

Grant, J., Thorpe, B., 1991. Effects of suspended sediment on growth, respiration, and excretion of the soft-shell clam (Mya arenaria). Can. J. Fish. Aquat. Sci. 48 (7), 1285-1292.

Griffioen, J., 2017. Enhanced weathering of olivine in seawater: The efficiency as revealed by thermodynamic scenario analysis. Sci. Total Environ. 575, 536-544.

Guevara, P., Pérez-Alberti, A., Carballo, R., Sánchez, M., López, I., Otero, X., 2021. Impact of serpentinized peridotite mine waste on the composition and quality of sediments in the Ría de Ortigueira (Galicia, NW Spain). Mar. Pollut. Bull. 163, 111963.

Gunkel-Grillon, P., Laporte-Magoni, C., Lemestre, M., Bazire, N., 2014. Toxic chromium release from nickel mining sediments in surface waters, New Caledonia. Environ. Chem. Lett. 12 (4), 511-516.

Guo, J. A., Strzepek, R., Willis, A., Ferderer, A., Bach, L. T., 2022. Investigating the effect of nickel concentration on phytoplankton growth to assess potential side-effects of ocean alkalinity enhancement. Biogeosciences. 19 (15), 3683-3697.

Guo, J. A., Strzepek, R. F., Swadling, K. M., Townsend, A. T., Bach, L. T., 2023. Influence of Ocean Alkalinity Enhancement with Olivine or Steel Slag on a Coastal Plankton Community in Tasmania. EGUsphere. 2023, 1-27.

Gupta, A. D., Karthikeyan, S., 2016. Individual and combined toxic effect of nickel and chromium on biochemical constituents in E. coli using FTIR spectroscopy and Principle component analysis. Ecotoxicol. Environ. Saf. 130, 289-294.

Gupta, J., 2010. A history of international climate change policy. Wiley Interdiscip. Rev. Clim. Change. 1 (5), 636-653.

Gutjahr, M., Ridgwell, A., Sexton, P. F., Anagnostou, E., Pearson, P. N., Pälike, H., Norris, R. D., Thomas, E., Foster, G. L., 2017. Very large release of mostly volcanic carbon during the Palaeocene–Eocene Thermal Maximum. Nature. 548 (7669), 573-577.

Haglund, K., Björklund, M., Gunnare, S., Sandberg, A., Olander, U., Pedersen, M. (1996). New method for toxicity assessment in marine and brackish environments using the macroalga Gracilaria tenuistipitata (Gracilariales, Rhodophyta). Paper presented at the Fifteenth International Seaweed Symposium

Hallberg, R. O., 1991. Environmental implications of metal distribution in Baltic Sea sediments. Ambio. 20 (7), 309-316.

Hallegraeff, G., 2003. Harmful algal blooms: a global overview. Manual on harmful marine microalgae. 33, 1-22.

Hamed, M. A., Emara, A. M., 2006. Marine molluscs as biomonitors for heavy metal levels in the Gulf of Suez, Red Sea. J. Mar. Syst. 60 (3-4), 220-234.

Hangx, S. J., Spiers, C. J., 2009. Coastal spreading of olivine to control atmospheric CO_2 concentrations: A critical analysis of viability. Int. J. Greenh. Gas Control. 3 (6), 757-767.

Harben, P. W., Smith jr., C., 2006. Olivine, in: J. E. Kogel, Trivedi, N. C., Barker, J. M., Krukowski, S. T. (Eds.), In *Industrial minerals & rocks: commodities, markets, and uses*, Society for Mining, Metallurgy, and Exploration, Inc., Colorado, pp. 679-683.

Harland, B., Taylor, D., Wither, A., 2000. The distribution of mercury and other trace metals in the sediments of the Mersey Estuary over 25 years 1974–1998. Sci. Total Environ. 253 (1-3), 45-62.

Hartmann, D., Ramanathan, V., Berroir, A., Hunt, G., 1986. Earth radiation budget data and climate research. Rev. Geophys. 24 (2), 439-468.

Hartmann, J., Jansen, N., Dürr, H. H., Harashima, A., Okubo, K., Kempe, S., 2010. Predicting riverine dissolved silica fluxes to coastal zones from a hyperactive region and analysis of their first-order controls. Int J Earth Sci. 99, 207-230.

Hartmann, J., Suitner, N., Lim, C., Schneider, J., Marín-Samper, L., Arístegui, J., Renforth, P., Taucher, J., Riebesell, U., 2023. Stability of alkalinity in ocean alkalinity enhancement (OAE) approaches–consequences for durability of CO 2 storage. Biogeosci. Disc. 20 (4), 781-802.

Hartmann, J., West, A. J., Renforth, P., Köhler, P., De La Rocha, C. L., Wolf-Gladrow, D. A., Dürr, H. H., Scheffran, J., 2013. Enhanced chemical weathering as a geoengineering strategy to reduce atmospheric carbon dioxide, supply nutrients, and mitigate ocean acidification. Rev. Geophys. 51 (2), 113-149.

Hashim, J. H., Hashim, Z., 2016. Climate change, extreme weather events, and human health implications in the Asia Pacific region. Asia Pac J Public Health. 28 (2_suppl), 8S-14S.

Haszeldine, R. S., Flude, S., Johnson, G., Scott, V., 2018. Negative emissions technologies and carbon capture and storage to achieve the Paris Agreement commitments. Philos Trans A Math Phys Eng Sci. 376 (2119), 20160447.

Hauck, J., Köhler, P., Wolf-Gladrow, D., Völker, C., 2016. Iron fertilisation and century-scale effects of open ocean dissolution of olivine in a simulated CO2 removal experiment. Environ. Res. Lett. 11 (2), 024007.

Hédouin, L., Pringault, O., Metian, M., Bustamante, P., Warnau, M., 2007. Nickel bioaccumulation in bivalves from the New Caledonia lagoon: seawater and food exposure. Chemosphere. 66 (8), 1449-1457.

Heinze, C., Meyer, S., Goris, N., Anderson, L., Steinfeldt, R., Chang, N., Le Quere, C., Bakker, D. C., 2015. The ocean carbon sink–impacts, vulnerabilities and challenges. Earth System Dynamics. 6 (1), 327-358.

Heiri, O., Lotter, A. F., Lemcke, G., 2001. Loss on ignition as a method for estimating organic and carbonate content in sediments: reproducibility and comparability of results. J. Paleolimnol. 25 (1), 101-110.

Hellmann, R., Wirth, R., Daval, D., Barnes, J.-P., Penisson, J.-M., Tisserand, D., Epicier, T., Florin, B., Hervig, R. L., 2012. Unifying natural and laboratory chemical weathering with interfacial dissolution–reprecipitation: A study based on the nanometer-scale chemistry of fluid–silicate interfaces. Chem. Geol. 294, 203-216.

Hellou, J., Cheeseman, K., Jouvenelle, M. L., Robertson, S., 2005. Behavioral response of Corophium volutator relative to experimental conditions, physical and chemical disturbances. Environ. Toxicol. Chem. 24 (12), 3061-3068.

Hem, J. D., 1985. Study and interpretation of the chemical characteristics of natural water, Third ed., Department of the Interior, US Geological Survey, Alexandria.

Henderson-Sellers, A., Meadows, A., 1977. Surface temperature of early Earth. Nature. 270 (5638), 589-591.

Henry, R. P., Lucu, Č., Onken, H., Weihrauch, D., 2012. Multiple functions of the crustacean gill: osmotic/ionic regulation, acid-base balance, ammonia excretion, and bioaccumulation of toxic metals. Front. Physiol. 3, 431.

Hershelman, G., Schafer, H., Jan, T.-K., Young, D., 1981. Metals in marine sediments near a large California municipal outfall. Mar. Pollut. Bull. 12 (4), 131-134.

Hirata, S., Honda, K., Shikino, O., Maekawa, N., Aihara, M., 2000. Determination of chromium (III) and total chromium in seawater by on-line column preconcentration inductively coupled plasma mass spectrometry. Spectrochim Acta Part B At Spectrosc. 55 (7), 1089-1099.

Ho, T.-Y., 2013. Nickel limitation of nitrogen fixation in Trichodesmium. Limnol. Oceanogr. 58 (1), 112-120.

Hoang, T. C., Tomasso, J. R., Klaine, S. J., 2004. Influence of water quality and age on nickel toxicity to fathead minnows (Pimephales promelas). Environ. Toxicol. Chem. 23 (1), 86-92.

Hoffmann, L. J., Breitbarth, E., Boyd, P. W., Hunter, K. A., 2012. Influence of ocean warming and acidification on trace metal biogeochemistry. Mar. Ecol. Prog. Ser. 470, 191-205.

Hofmann, A., Middelburg, J., Soetaert, K., Meysman, F., 2009. pH modelling in aquatic systems with time-variable acid-base dissociation constants applied to the turbid, tidal Scheldt estuary. Biogeosciences. 6 (8), 1539-1561.

Hofmann, A. F., Soetaert, K., Middelburg, J. J., Meysman, F. J., 2010. AquaEnv: An Aquatic Acid–Base Modelling Environment in R. Aquat. Geochem. 16 (4), 507-546.

Holland, G., 1960. Toxic effects of organic and inorganic pollutants on young salmon and trout. Res. Bull. Wash. Dep. Fish. No. 5. 278.

Holmén, K. (1992). 11 The Global Carbon Cycle. In *International Geophysics* (Vol. 50, pp. 239-262): Elsevier.

Hövelmann, J., Austrheim, H., Beinlich, A., Munz, I. A., 2011. Experimental study of the carbonation of partially serpentinized and weathered peridotites. Geochim. Cosmochim. Acta. 75 (22), 6760-6779.

Howe, P. L., Reichelt-Brushett, A. J., Clark, M. W., 2014. Effects of Cd, Co, Cu, Ni and Zn on asexual reproduction and early development of the tropical sea anemone Aiptasia pulchella. Ecotoxicology. 23 (9), 1593-1606.

Hrstka, T., Gottlieb, P., Skala, R., Breiter, K., Motl, D., 2018. Automated mineralogy and petrology-applications of TESCAN Integrated Mineral Analyzer (TIMA). J Geosci. 63 (1), 47-63.

Hübner, R., Astin, K. B., Herbert, R. J., 2009. Comparison of sediment quality guidelines (SQGs) for the assessment of metal contamination in marine and estuarine environments. J. Environ. Monit. 11 (4), 713-722.

Huettel, M., Ziebis, W., Forster, S., Luther Iii, G., 1998. Advective transport affecting metal and nutrient distributions and interfacial fluxes in permeable sediments. Geochim. Cosmochim. Acta. 62 (4), 613-631.

Hunt, J. W., Anderson, B. S., Phillips, B. M., Tjeerdema, R. S., Puckett, H. M., Stephenson, M., Tucker, D. W., Watson, D., 2002. Acute and chronic toxicity of nickel to marine organisms: implications for water quality criteria. Environ. Toxicol. Chem. 21 (11), 2423-2430.

Hutchins, D., Fu, F.-X., Zhang, Y., Warner, M., Feng, Y., Portune, K., Bernhardt, P., Mulholland, M., 2007. CO2 control of Trichodesmium N2 fixation, photosynthesis,

growth rates, and elemental ratios: Implications for past, present, and future ocean biogeochemistry. Limnol. Oceanogr. 52 (4), 1293-1304.

Hutchins, D. A., Fu, F.-X., Yang, S.-C., John, S. G., Romaniello, S. J., Andrews, M. G., Walworth, N. G., 2023. Responses of keystone phytoplankton groups to olivine dissolution products and implications for carbon dioxide removal via ocean alkalinity enhancement. bioRxiv.

Hutchinson, T. H., Williams, T. D., Eales, G. J., 1994. Toxicity of cadmium, hexavalent chromium and copper to marine fish larvae (Cyprinodon variegatus) and copepods (Tisbe battagliai). Mar. Environ. Res. 38 (4), 275-290.

Ilyina, T., Wolf-Gladrow, D., Munhoven, G., Heinze, C., 2013. Assessing the potential of calcium-based artificial ocean alkalinization to mitigate rising atmospheric CO2 and ocean acidification. Geophys. Res. Lett. 40 (22), 5909-5914.

IPCC. (2021). *Climate Change 2021: The Physcial Science Basis. Contribution of Working Group I to the Sixth Assessment Report of the Intergovernmental Panel on Climate Change*. Retrieved from https://report.ipcc.ch/ar6/wg1/IPCC_AR6_WGI_FullReport.pdf

IPCC. (2022a). *Climate Change 2022: Impacts, Adaptation, and Vulnerability. Contribution of Working Group II to the Sixth Assessment Report of the Intergovernmental Panel on Climate Change*. Retrieved from Cambridge, UK and New York, USA: https://report.ipcc.ch/ar6/wg2/IPCC_AR6_WGII_FullReport.pdf

IPCC. (2022b). *Climate Change 2022: Mitigation of Climate Change. Contribution of Working Group III to the Sixth Assessment Report of the Intergovernmental Panel on Climate Change*. Retrieved from https://www.ipcc.ch/report/ar6/wg3/downloads/report/IPCC_AR6_WGIII_FullReport.pdf

IPCC. (1990). *Climate Change: The IPCC Scientific Assessment*. Retrieved from Cambridge, GB, New York, USA, and Melbourne, Australia: https://archive.ipcc.ch/ipccreports/far/wg_I/ipcc_far_wg_I_full_report.pdf

Ivarsson, M., Broman, C., Holm, N. G., 2011. Chromite oxidation by manganese oxides in subseafloor basalts and the presence of putative fossilized microorganisms. Geochem. Trans. 12 (1), 1-10.

Jafarabadi, A. R., Bakhtiyari, A. R., Toosi, A. S., Jadot, C., 2017. Spatial distribution, ecological and health risk assessment of heavy metals in marine surface sediments and coastal seawaters of fringing coral reefs of the Persian Gulf, Iran. Chemosphere. 185, 1090-1111.

Jan, T.-K., Young, D. R., 1978. Chromium speciation in municipal wastewaters and seawater. J Water Pollut Control Fed. 50 (10), 2327-2336.

Jansen, H., Ahrens, M., 2004. Carbonate dissolution in the guts of benthic deposit feeders: A numerical model. Geochim. Cosmochim. Acta. 68 (20), 4077-4092.

Jeandel, C., Minster, J.-F., 1984. Isotope dilution measurement of inorganic chromium (III) and total chromium in seawater. Mar. Chem. 14 (4), 347-364.

Johannesson, K., Ekendahl, A., 2002. Selective predation favouring cryptic individuals of marine snails (Littorina). Biol. J. Linn. Soc. 76 (1), 137-144.

Johnson, E. D., Cowen, E. A., 2017. Estimating bed shear stress from remotely measured surface turbulent dissipation fields in open channel flows. Water Resour. Res. 53 (3), 1982-1996.

Johnson, N. C., Thomas, B., Maher, K., Rosenbauer, R. J., Bird, D., Brown Jr, G. E., 2014. Olivine dissolution and carbonation under conditions relevant for in situ carbon storage. Chem. Geol. 373, 93-105.

Jonathan, M., Ram-Mohan, V., Srinivasalu, S., 2004. Geochemical variations of major and trace elements in recent sediments, off the Gulf of Mannar, the southeast coast of India. Environ. Geol. 45 (4), 466-480.

Jones, B., Turki, A., 1997. Distribution and speciation of heavy metals in surficial sediments from the Tees Estuary, north-east England. Mar. Pollut. Bull. 34 (10), 768-779.

Jones, R., Bessell-Browne, P., Fisher, R., Klonowski, W., Slivkoff, M., 2016. Assessing the impacts of sediments from dredging on corals. Mar. Pollut. Bull. 102 (1), 9-29.

Jones, T. D., Lunt, D. J., Schmidt, D. N., Ridgwell, A., Sluijs, A., Valdes, P. J., Maslin, M., 2013. Climate model and proxy data constraints on ocean warming across the Paleocene–Eocene Thermal Maximum. Earth Sci Rev. 125, 123-145.

Jong, D., Bröder, L., Tanski, G., Fritz, M., Lantuit, H., Tesi, T., Haghipour, N., Eglinton, T. I., Vonk, J. E., 2020. Nearshore zone dynamics determine pathway of organic carbon from eroding permafrost coasts. Geophysical Research Letters. 47 (15), e2020GL088561.

Jop, K. M. (1989). Acute and rapid-chronic toxicity of hexavalent chromium to five marine species. In *Aquatic Toxicology and Hazard Assessment: 12th Volume*: ASTM International.

Jung, S., Jung, H., Austrheim, H., 2020. Microstructural evolution of amphibole peridotites in Åheim, Norway, and the implications for seismic anisotropy in the mantle wedge. Minerals. 10 (4), 345.

Jung, S., Yamamoto, T., Ando, J.-i., Jung, H., 2021. Dislocation Creep of Olivine and Amphibole in Amphibole Peridotites from Åheim, Norway. Minerals. 11 (9), 1018.

Kanakalakshmi, A., Janaki, V., Shanthi, K., Kamala-Kannan, S., 2017. Biosynthesis of Cr (III) nanoparticles from electroplating wastewater using chromium-resistant Bacillus subtilis and its cytotoxicity and antibacterial activity. Artif Cells Nanomed Biotechnol. 45 (7), 1304-1309.

Karthikeyan, S., 2014. Effect of heavy metals mixture nickel and chromium on tissue proteins of an edible fish Cirrhinus mrigala using FTIR and ICP-AES study. Rom. J. Biophys. 24 (2), 109-116.

Keefner, J., Mackwell, S., Kohlstedt, D., Heidelbach, F., 2011. Dependence of dislocation creep of dunite on oxygen fugacity: Implications for viscosity variations in Earth's mantle. J. Geophys. Res. Solid Earth. 116 (B5).

Kermani, S., Boutiba, M., Boutaleb, A., Fagel, N., 2016. Distribution of heavy and clay minerals in coastal sediment of Jijel, East of Algeria: indicators of sediment sources and transport and deposition environments. Arab. J. Geosci. 9, 1-18.

Khaled, A., El Nemr, A., El Sikaily, A., 2006. An assessment of heavy-metal contamination in surface sediments of the Suez Gulf using geoaccumulation indexes and statistical analysis. Chem Ecol. 22 (3), 239-252.

Khan, M., Hasan, M., Khan, M., Aktar, S., Fatema, K., 2017. Distribution of heavy metals in surface sediments of the Bay of Bengal Coast. J. Toxicol. 2017.

Kierczak, J., Pietranik, A., Pędziwiatr, A., 2021. Ultramafic geoecosystems as a natural source of Ni, Cr, and Co to the environment: A review. Sci. Total Environ. 755, 142620.

Kim, K.-H., Kabir, E., Ara Jahan, S., 2014. A review of the consequences of global climate change on human health. J. Environ. Sci. Health C Environ. Carcinog. Ecotoxicol. Rev. 32 (3), 299-318.

Kim, K. T., Kim, E. S., Cho, S. R., Park, J. K., Ra, K. T., Lee, J. M., 2010. Distribution of heavy metals in the environmental samples of the Saemangeum coastal area, Korea, in: A. Ishimatsu, Lie, H. J. (Eds.), In *Coastal environmental and ecosystem issues of the East China Sea*, TERRAPUB, Tokyo, pp. pp 71-90.

King, C., Gale, S., Stauber, J. L., 2006. Acute toxicity and bioaccumulation of aqueous and sediment-bound metals in the estuarine amphipod Melita plumulosa. Environ. Toxicol. 21 (5), 489-504.

Kjelland, M. E., Woodley, C. M., Swannack, T. M., Smith, D. L., 2015. A review of the potential effects of suspended sediment on fishes: potential dredging-related physiological, behavioral, and transgenerational implications. Environ. Syst. Decis. 35, 334-350.

Kleiv, R. A., Thornhill, M., 2004. Adsorptive retention of copper from acidic mine water at the disused sulphide mine at Løkken, central Norway—initial experiments using olivine. Miner. Eng. 17 (2), 195-203.

Kleiv, R. A., Thornhill, M., 2011. Dry magnetic separation of olivine sand. Physicochem. Probl. Miner. Process. 47 (47), 213-228.

Kleiv, R. A., Thornhill, M., 2008. Predicting the neutralisation of acid mine drainage in anoxic olivine drains. Miner. Eng. 21 (4), 279-287.

Knauer, G. A., 1977. Immediate industrial effects on sediment metals in a clean coastal environment. Mar. Pollut. Bull. 8 (11), 249-254.

Köhler, P., Abrams, J. F., Völker, C., Hauck, J., Wolf-Gladrow, D. A., 2013. Geoengineering impact of open ocean dissolution of olivine on atmospheric CO2, surface ocean pH and marine biology. Environ. Res. Lett. 8 (1), 014009.

Köhler, P., Hartmann, J., Wolf-Gladrow, D. A., 2010. Geoengineering potential of artificially enhanced silicate weathering of olivine. Proc. Natl. Acad. Sci. 107 (47), 20228-20233.

Kopp, R. E., Kirschvink, J. L., Hilburn, I. A., Nash, C. Z., 2005. The Paleoproterozoic snowball Earth: a climate disaster triggered by the evolution of oxygenic photosynthesis. Proc. Natl. Acad. Sci. U.S.A. 102 (32), 11131-11136.

Koppel, D. J., Gissi, F., Adams, M. S., King, C. K., Jolley, D. F., 2017. Chronic toxicity of five metals to the polar marine microalga Cryothecomonas armigera–Application of a new bioassay. Environ. Pollut. 228, 211-221.

Kozlova, T., Wood, C. M., McGeer, J. C., 2009. The effect of water chemistry on the acute toxicity of nickel to the cladoceran Daphnia pulex and the development of a biotic ligand model. Aquat. Toxicol. 91 (3), 221-228.

Krassoi, R., Anderson, I., Everett, D., 1997. Larval abnormalities in doughboy scallops Chlamys(mimachlamys) asperrima L. in response to test conditions and six reference toxicants. Australas. J. Ecotoxicol. 3 (1), 65-74.

Kremer, D., Etzold, S., Boldt, J., Blaum, P., Hahn, K. M., Wotruba, H., Telle, R., 2019. Geological mapping and characterization of possible primary input materials for the mineral sequestration of carbon dioxide in Europe. Minerals. 9 (8), 485.

Kumar, A., Maiti, S. K., 2013. Availability of chromium, nickel and other associated heavy metals of ultramafic and serpentine soil/rock and in plants. Int. j. emerg. technol. adv. eng. 3 (2), 256-268.

Kuss, J., Schneider, B., 2004. Chemical enhancement of the CO2 gas exchange at a smooth seawater surface. Mar. Chem. 91 (1-4), 165-174.

Kweku, D. W., Bismark, O., Maxwell, A., Desmond, K. A., Danso, K. B., Oti-Mensah, E. A., Quachie, A. T., Adormaa, B. B., 2018. Greenhouse effect: greenhouse gases and their impact on global warming. J. Sci. Res. Rep. 17 (6), 1-9.

Kwok, K. W., Batley, G. E., Wenning, R. J., Zhu, L., Vangheluwe, M., Lee, S., 2014. Sediment quality guidelines: challenges and opportunities for improving sediment management. Environ. Sci. Pollut. Res. 21 (1), 17-27.

Lafay, R., Montes-Hernandez, G., Renard, F., Vonlanthen, P., 2018. Intracrystalline reaction-induced cracking in olivine evidenced by hydration and carbonation experiments. Minerals. 8 (9), 412.

Lakshtanov, L., Stipp, S., 2007. Experimental study of nickel (II) interaction with calcite: Adsorption and coprecipitation. Geochim. Cosmochim. Acta. 71 (15), 3686-3697.

Lau, S., Chu, L., 1999. Contaminant release from sediments in a coastal wetland. Water Res. 33 (4), 909-918.

Lazarevic, S., Jankovic-Castvan, I., Djokic, V., Radovanovic, Z., Janackovic, D., Petrovic, R., 2010. Iron-modified sepiolite for Ni2+ sorption from aqueous solution: an equilibrium, kinetic, and thermodynamic study. J. Chem. Eng. Data. 55 (12), 5681-5689.

Lenton, T. M., Rockström, J., Gaffney, O., Rahmstorf, S., Richardson, K., Steffen, W., Schellnhuber, H. J., 2019. Climate tipping points—too risky to bet against. Nature. 575 (7784), 592-595.

Leonard, E. M., Barcarolli, I., Silva, K. R., Wasielesky, W., Wood, C. M., Bianchini, A., 2011. The effects of salinity on acute and chronic nickel toxicity and bioaccumulation in two euryhaline crustaceans: Litopenaeus vannamei and Excirolana armata. Comp. Biochem. Physiol. Part - C: Toxicol. Pharmacol. 154 (4), 409-419.

Lepper, P., 2005. Manual on the methodological framework to derive environmental quality standards for priority substances in accordance with Article 16 of the Water Framework Directive (2000/60/EC). Schmallenberg, Germany: Fraunhofer-Institute Molecular Biology and Applied Ecology. 15, 51-52.

Lewis, A. M., 1992. Measuring the hydraulic diameter of a pore or conduit. Am. J. Bot. 79 (10), 1158-1161.

Li, L., Liu, J., Wang, X., Shi, X., 2015. Dissolved trace metal distributions and Cu speciation in the southern Bohai Sea, China. Mar. Chem. 172, 34-45.

Lin, C. Y., Bradbury, H. J., Antler, G., Burdige, D. J., Bennett, T. D., Li, S., Turchyn, A. V., 2022. Sediment mineralogy influences the rate of microbial sulfate reduction in marine sediments. Earth Planet. Sci. Lett. 598, 117841.

Lincoln, R. J., 1979. British marine amphipoda: Gammaridea, British Museum (Natural History), 658 pp.

Liu, K., Song, J., Chi, W., Liu, H., Ge, S., Yu, D., 2021. Developmental toxicity in marine medaka (Oryzias melastigma) embryos and larvae exposed to nickel. Comp. Biochem. Physiol. C Toxicol. Pharmacol. 248, 109082.

Liu, X., Dunne, J. P., Stock, C. A., Harrison, M. J., Adcroft, A., Resplandy, L., 2019. Simulating Water Residence Time in the Coastal Ocean: A Global Perspective. Geophys. Res. Lett. 46 (23), 13910-13919.

Liu, Z., Deng, Z., Davis, S. J., Giron, C., Ciais, P., 2022. Monitoring global carbon emissions in 2021. Nat. Rev. Earth Environ. 3 (4), 217-219.

Lopes, I., Baird, D. J., Ribeiro, R., 2004. Avoidance of copper contamination by field populations of Daphnia longispina. Environ. Toxicol. Chem. 23 (7), 1702-1708.

Lopez, G. R., Levinton, J. S., 1987. Ecology of deposit-feeding animals in marine sediments. Q Rev Biol. 62 (3), 235-260.

Love, A. C., Crooks, N., Ford, A. T., 2020. The effects of wastewater effluent on multiple behaviours in the amphipod, Gammarus pulex. Environ. Pollut. 267, 115386.

Low, S., Baum, C. M., Sovacool, B. K., 2022. Taking it outside: exploring social opposition to 21 early-stage experiments in radical climate interventions. Energy Res. Soc. Sci. 90, 102594.

Lu, M., Wang, X., Li, Y., Liu, H., An, X., Lian, B., 2022. Soil microbial community structure and environmental effects of serpentine weathering under different vegetative covers in the serpentine mining area of Donghai County, China. Sci. Total Environ. 835, 155452.

Luce, R. W., Bartlett, R. W., Parks, G. A., 1972. Dissolution kinetics of magnesium silicates. Geochim. Cosmochim. Acta. 36 (1), 35-50.

Lushchak, V. I., 2011. Environmentally induced oxidative stress in aquatic animals. Aquat. Toxicol. 101 (1), 13-30.

Lussier, S., Gentile, J., Walker, J., 1985. Acute and chronic effects of heavy metals and cyanide on Mysidopsis bahia (Crustacea: Mysidacea). Aquat. Toxicol. 7 (1-2), 25-35.

Lynn, K. J., Shea, T., Garcia, M. O., 2017. Nickel variability in Hawaiian olivine: Evaluating the relative contributions from mantle and crustal processes. Am. Mineral. 102 (3), 507-518.

Macdonald, D. D., Carr, R. S., Calder, F. D., Long, E. R., Ingersoll, C. G., 1996. Development and evaluation of sediment quality guidelines for Florida coastal waters. Ecotoxicology. 5 (4), 253-278.

Machado, W., Silva-Filho, E., Oliveira, R., Lacerda, L., 2002. Trace metal retention in mangrove ecosystems in Guanabara Bay, SE Brazil. Mar. Pollut. Bull. 44 (11), 1277-1280.

Mackenzie, F. T., Lerman, A., 2006. Carbon in the Oceanic Coastal Margin, in: N. H. Landman, Douglas, J. S. (Eds.), In *Carbon in the Geobiosphere:-Earth's Outer Shell*, Springer, Dordrecht, pp. pp 255-288.

Madhavaraju, J., Armstrong-Altrin, J. S., James, R. A., Hussain, S., 2021. Palaeoenvironment and provenance signatures inferred from quartz grain surface features: A case study from Huatabampo and Altata beaches, Gulf of California, Mexico. J. S. Am. Earth Sci. 111, 103441.

Maher, K., 2010. The dependence of chemical weathering rates on fluid residence time. Earth Planet. Sci. Lett. 294 (1-2), 101-110.

Maher, K., Johnson, N. C., Jackson, A., Lammers, L. N., Torchinsky, A. B., Weaver, K. L., Bird, D. K., Brown Jr, G. E., 2016. A spatially resolved surface kinetic model for forsterite dissolution. Geochim. Cosmochim. Acta. 174, 313-334.

Mahoney, J., 1982. The effects of trace metals on growth of a phytoflagellate Olisthodiscus luteus, which blooms in lower New York Bay. Bull. NJ Acad. Sci. 27, 53-57.

Maltby, L., Naylor, C., 1990. Preliminary observations on the ecological relevance of the Gammarusscope for growth'assay: effect of zinc on reproduction. Funct. Ecol., 393-397.

Manoj, E., Prasannakumar, V., 2002. Environmental impact assessment and environmental management plan-a case study of magnesite and dunite mine, South India. Bol Parana Geocienc. 50, 21-25.

Marion, G., Millero, F., Feistel, R., 2009. Precipitation of solid phase calcium carbonates and their effect on application of seawater S A–T–P models. Ocean Sci. 5 (3), 285-291.

Martin, A., 1966. Feeding and digestion in two intertidal gammarids: Marinogammarus obtusatus and M. pirloti. J. Zool. 148 (4), 515-525.

Martin, K. M., Wood, W. T., Becker, J. J., 2015. A global prediction of seafloor sediment porosity using machine learning. Geophys. Res. Lett. 42 (24), 10,640-610,646.

Mayer, L. M., Schick, L. L., Self, R. F., Jumars, P. A., Findlay, R. H., Chen, Z., Sampson, S., 1997. Digestive environments of benthic macroinvertebrate guts: enzymes, surfactants and dissolved organic matter. J. Mar. Res. 55 (4), 785-812.

McClenaghan, N. W., Schindler, M., 2022. Release of chromite nanoparticles and their alteration in the presence of Mn-oxides. Am. Mineral. 107 (4), 642-653.

McCulloch, W. L., Rue, W. J. (1989). Evaluation of a seven-day chronic toxicity estimation test using Cyprinodon variegatus. In *Aquatic Toxicology and Hazard Assessment: 12th Volume*: ASTM International.

McInerney, F. A., Wing, S. L., 2011. The Paleocene-Eocene Thermal Maximum: A perturbation of carbon cycle, climate, and biosphere with implications for the future. Annu Rev Earth Planet Sci. 39, 489-516.

Meyer, J., Riebesell, U., 2015. Reviews and Syntheses: Responses of coccolithophores to ocean acidification: a meta-analysis. Biogeosciences. 12 (6), 1671-1682.

Meyer, J. S., Farley, K. J., Garman, E. R., 2015. Metal mixtures modeling evaluation project: 1. Background. Environ. Toxicol. Chem. 34 (4), 726-740.

Meysman, F. J. R., Montserrat, F., 2017. Negative CO2 emissions via enhanced silicate weathering in coastal environments. Biol. Lett. 13 (4), 20160905.

Middelburg, J. J., Soetaert, K., Hagens, M., 2020. Ocean alkalinity, buffering and biogeochemical processes. Rev. Geophys. 58 (3), e2019RG000681.

Migon, C., Ouillon, S., Mari, X., Nicolas, E., 2007. Geochemical and hydrodynamic constraints on the distribution of trace metal concentrations in the lagoon of Nouméa, New Caledonia. Estuar. Coast. Shelf Sci. 74 (4), 756-765.

Millero, F. J., 1998. Solubility of Fe (III) in seawater. Earth Planet. Sci. Lett. 154 (1-4), 323-329.

Millero, F. J., Sotolongo, S., Izaguirre, M., 1987. The oxidation kinetics of Fe (II) in seawater. Geochim. Cosmochim. Acta. 51 (4), 793-801.

Minx, J. C., Lamb, W. F., Callaghan, M. W., Fuss, S., Hilaire, J., Creutzig, F., Amann, T., Beringer, T., de Oliveira Garcia, W., Hartmann, J., 2018. Negative emissions—Part 1: Research landscape and synthesis. Environ. Res. Lett. 13 (6), 063001.

Mirzaei, M. R., Azini, M. R., Rad, T. A., 2016. Seasonal variation of heavy metal in seawater, sediment and hooded oyster, Saccostreacucullata, in Iranian southern waters (Chabahar coast). Research in Marine Sciences. 1 (1), 3-12.

Missimer, C. L., Lemarie, D. P., Rue, W. J., 1989. Evaluation of a chronic estimation toxicity test using Skeletonema costatum, in: (Eds.), In *Aquatic Toxicology and Hazard Assessment: 12th Volume*, ASTM International, Pennsylvania, pp. pp 345-354.

Mitchell, A. J., Uličný, D., Hampson, G. J., Allison, P. A., Gorman, G. J., Piggott, M. D., Wells, M. R., Pain, C. C., 2010. Modelling tidal current-induced bed shear stress and palaeocirculation in an epicontinental seaway: the Bohemian Cretaceous Basin, Central Europe. Sedimentology. 57 (2), 359-388.

Moisez, E., Seuront, L., 2020. Deciphering the known unknowns in the behavioural ecology of the intertidal gastropod Littorina littorea. J. Exp. Mar. Biol. Ecol. 524, 151313.

Moles, A., Rice, S., Norcross, B. L., 1994. Non-avoidance of hydrocarbon laden sediments by juvenile flatfishes. Neth J Sea Res. 32 (3-4), 361-367.

Monga, A., Fulke, A. B., Dasgupta, D., 2022. Recent developments in essentiality of trivalent chromium and toxicity of hexavalent chromium: implications on human health and remediation strategies. Journal of Hazardous Materials Advances. 7, 100113.

Monk, D., 1977. The digestion of cellulose and other dietary components, and pH of the gut in the amphipod Gammarus pulex (L.). Freshw. Biol. 7 (5), 431-440.

Montserrat, F., Renforth, P., Hartmann, J., Leermakers, M., Knops, P., Meysman, F. J., 2017. Olivine dissolution in seawater: implications for CO2 sequestration through enhanced weathering in coastal environments. Environ. Sci. Technol. 51 (7), 3960-3972.

Moosdorf, N., Renforth, P., Hartmann, J., 2014. Carbon dioxide efficiency of terrestrial enhanced weathering. Environ. Sci. Technol. 48 (9), 4809-4816.

Mor, S., Aneja, R., Madan, S., Ghimire, M., 2023. Kyoto Protocol and Paris Agreement: Transition from Bindings to Pledges–A Review. Millennial Asia. 0 (0).

Moras, C. A., Bach, L. T., Cyronak, T., Joannes-Boyau, R., Schulz, K. G., 2022. Ocean alkalinity enhancement–avoiding runaway $CaCO_3$ precipitation during quick and hydrated lime dissolution. Biogeosciences. 19 (15), 3537-3557.

Morillo, J., Usero, J., Gracia, I., 2004. Heavy metal distribution in marine sediments from the southwest coast of Spain. Chemosphere. 55 (3), 431-442.

Morse, J. W., Arvidson, R. S., Lüttge, A., 2007. Calcium carbonate formation and dissolution. Chem. Rev. 107 (2), 342-381.

Moum, J. N., 2021. Variations in ocean mixing from seconds to years. Ann. Rev. Mar. Sci. 13, 201-226.

Mulrooney, S. B., Hausinger, R. P., 2003. Nickel uptake and utilization by microorganisms. FEMS Microbiol. Rev. 27 (2-3), 239-261.

Munksgaard, N. C., Parry, D. L., 2001. Trace metals, arsenic and lead isotopes in dissolved and particulate phases of North Australian coastal and estuarine seawater. Mar. Chem. 75 (3), 165-184.

Murray, J. W., Spell, B., Paul, B., 1983. The contrasting geochemistry of manganese and chromium in the eastern tropical Pacific Ocean, in: C. S. Wong, Boyle, E., Bruland, K. W., Burton, J. D., Goldberg, E. D. (Eds.), In *Trace metals in Sea Water*, Springer, Boston, pp. pp 643-669.

Muyssen, B. T., Brix, K., DeForest, D., Janssen, C., 2004. Nickel essentiality and homeostasis in aquatic organisms. Environ. Rev. 12 (2), 113-131.

Nadella, S. R., Fitzpatrick, J. L., Franklin, N., Bucking, C., Smith, S., Wood, C. M., 2009. Toxicity of dissolved Cu, Zn, Ni and Cd to developing embryos of the blue mussel (Mytilus trossolus) and the protective effect of dissolved organic carbon. Comp. Biochem. Physiol. C Toxicol. Pharmacol. 149 (3), 340-348.

Nagelkerken, I., Connell, S. D., 2022. Ocean acidification drives global reshuffling of ecological communities. Glob. Chang. Biol. 28 (23), 7038-7048.

Naidu, A., Blanchard, A., Kelley, J., Goering, J., Hameedi, M., Baskaran, M., 1997. Heavy metals in Chukchi Sea sediments as compared to selected circum-arctic shelves. Mar. Pollut. Bull. 35 (7-12), 260-269.

Nakagawa, S., Johnson, P. C., Schielzeth, H., 2017. The coefficient of determination R 2 and intra-class correlation coefficient from generalized linear mixed-effects models revisited and expanded. J. R. Soc. Interface 14 (134), 20170213.

Nations, U., 1998. Kyoto protocol to the United Nations framework kyoto protocol to the United Nations framework. Rev. Eur. Community Int. Environ. Law. 7, 214-217.

Naz, A., Chowdhury, A., Chandra, R., Mishra, B. K., 2020. Potential human health hazard due to bioavailable heavy metal exposure via consumption of plants with ethnobotanical usage at the largest chromite mine of India. Environ Geochem Health. 42, 4213-4231.

Needham, S., Worden, R., Mcilroy, D., 2004. Animal-sediment interactions: the effect of ingestion and excretion by worms on mineralogy. Biogeosciences. 1 (2), 113-121.

Neto, J. B., Smith, B., McAllister, J., 2000. Heavy metal concentrations in surface sediments in a nearshore environment, Jurujuba Sound, Southeast Brazil. Environ. Pollut. 109 (1), 1-9.

Neuparth, T., Correia, A. D., Costa, F. O., Lima, G., Costa, M. H., 2005. Multi-level assessment of chronic toxicity of estuarine sediments with the amphipod Gammarus locusta: I. Biochemical endpoints. Mar. Environ. Res. 60 (1), 69-91.

Neuparth, T., Costa, F. O., Costa, M. H., 2002. Effects of temperature and salinity on life history of the marine amphipod Gammarus locusta. Implications for ecotoxicological testing. Ecotoxicology. 11 (1), 61-73.

Nielsen, F., 2021. Nickel. Adv. Nutr. 12 (1), 281.

NIVA, 2007. PNEC for metals in the marine environment derived from species sensitivity distributions. https://niva.brage.unit.no/niva-xmlui/bitstream/handle/11250/213463/5336-STK_72dpi.pdf?sequence=2&isAllowed=y (accessed 2023-08-09).

Noailly, J., 2012. Improving the energy efficiency of buildings: The impact of environmental policy on technological innovation. Energy Econ. 34 (3), 795-806.

Noor, T., Batool, N., Mazhar, R., Ilyas, N., 2015. Effects of siltation, temperature and salinity on mangrove plants. Eur. Acad. Res. 2 (11), 14172-14179.

Novelli, A. A., Losso, C., Ghetti, P. F., Ghirardini, A. V., 2003. Toxicity of heavy metals using sperm cell and embryo toxicity bioassays with Paracentrotus lividus (Echinodermata: Echinoidea): comparisons with exposure concentrations in the lagoon of Venice, Italy. Environ. Toxicol. Chem. 22 (6), 1295-1301.

Nys, C., Van Regenmortel, T., Janssen, C. R., Oorts, K., Smolders, E., De Schamphelaere, K. A., 2018. A framework for ecological risk assessment of metal mixtures in aquatic systems. Environ. Toxicol. Chem. 37 (3), 623-642.

Nys, C., Versieren, L., Cordery, K. I., Blust, R., Smolders, E., De Schamphelaere, K. A., 2017. Systematic evaluation of chronic metal-mixture toxicity to three species and implications for risk assessment. Environ. Sci. Technol. 51 (8), 4615-4623.

O'Day, P. A., Carroll, S. A., Randall, S., Martinelli, R. E., Anderson, S. L., Jelinski, J., Knezovich, J. P., 2000. Metal speciation and bioavailability in contaminated estuary sediments, Alameda Naval Air Station, California. Environ. Sci. Technol. 34 (17), 3665-3673.

Oelkers, E. H., Declercq, J., Saldi, G. D., Gislason, S. R., Schott, J., 2018. Olivine dissolution rates: A critical review. Chem. Geol. 500, 1-19.

Olerud, S., 1993. NORWAY'S INDUSTRIAL MINERALS. PRODUCTION & DEVELOPMENT TRENDS. Industrial Minerals. (307), 55-63.

Olsen, A. A., Rimstidt, J. D., 2008. Oxalate-promoted forsterite dissolution at low pH. Geochim. Cosmochim. Acta. 72 (7), 1758-1766.

Orihuela-Pinto, B., England, M. H., Taschetto, A. S., 2022. Interbasin and interhemispheric impacts of a collapsed Atlantic Overturning Circulation. Nat. Clim. Change. 12 (6), 558-565.

Orr, J. C., Fabry, V. J., Aumont, O., Bopp, L., Doney, S. C., Feely, R. A., Gnanadesikan, A., Gruber, N., Ishida, A., Joos, F., 2005. Anthropogenic ocean acidification over the twenty-first century and its impact on calcifying organisms. Nature. 437 (7059), 681-686.

Oshida, P. S., Word, L. S., 1982. Bioaccumulation of chromium and its effects on reproduction in Neanthes arenaceodentata (Polychaeta). Mar. Environ. Res. 7 (3), 167-174.

Ouyang, Y., Zhang, J., Ou, L. T., 2006. Temporal and spatial distributions of sediment total organic carbon in an estuary river. J Environ Qual. 35 (1), 93-100.

Oze, C., Fendorf, S., Bird, D. K., Coleman, R. G., 2004. Chromium geochemistry in serpentinized ultramafic rocks and serpentine soils from the Franciscan complex of California. Am. J. Sci. 304 (1), 67-101.

Palacios, S. L., Zimmerman, R. C., 2007. Response of eelgrass Zostera marina to CO2 enrichment: possible impacts of climate change and potential for remediation of coastal habitats. Mar. Ecol. Prog. Ser. 344, 1-13.

Palaniappan, P. R., Karthikeyan, S., 2009. Bioaccumulation and depuration of chromium in the selected organs and whole body tissues of freshwater fish Cirrhinus mrigala individually and in binary solutions with nickel. J. Environ. Sci. 21 (2), 229-236.

Pan, Y., Li, Y., Ma, Q., He, H., Wang, S., Sun, Z., Cai, W.-J., Dong, B., Di, Y., Fu, W., 2021. The role of Mg2+ in inhibiting CaCO3 precipitation from seawater. Mar. Chem. 237, 104036.

Panneerselvam, K., Marigoudar, S. R., Dhandapani, M., 2018. Toxicity of Nickel on the Selected Species of Marine Diatoms and Copepods. Bull Environ Contam Toxicol. 100 (3), 331-337.

Parkhurst, D. L., Appelo, C., 2013. Description of input and examples for PHREEQC version 3—a computer program for speciation, batch-reaction, one-dimensional transport, and inverse geochemical calculations. US geological survey techniques and methods. 6 (A43), 497.

Parra, S., Bravo, M. A., Quiroz, W., Querol, X., Paipa, C., 2015. Distribution and pollution assessment of trace elements in marine sediments in the Quintero Bay (Chile). Mar. Pollut. Bull. 99 (1-2), 256-263.

Partheeban, E. C., Anbazhagan, V., Arumugam, G., Seshasayanan, B., Rajendran, R., Paray, B. A., Al-Sadoon, M. K., Al-Mfarij, A. R., 2021. Evaluation of toxic metal contaminants in the demersal flatfishes (Order: Pleuronectiformes) collected from a marine biosphere reserve. Reg. Stud. Mar. Sci. 42, 101649.

Pattnaik, B. K., Equeenuddin, S. M., 2016. Potentially toxic metal contamination and enzyme activities in soil around chromite mines at Sukinda Ultramafic Complex, India. J. Geochem. Explor. 168, 127-136.

Penman, D. E., Rugenstein, J. K. C., Ibarra, D. E., Winnick, M. J., 2020. Silicate weathering as a feedback and forcing in Earth's climate and carbon cycle. Earth-Sci. Rev. 209, 103298.

Peters, A., Merrington, G., Schlekat, C., De Schamphelaere, K., Stauber, J., Batley, G., Harford, A., Van Dam, R., Pease, C., Mooney, T., 2018. Validation of the nickel biotic ligand model for locally relevant species in Australian freshwaters. Environ. Toxicol. Chem. 37 (10), 2566-2574.

Pettine, M., 2000. Redox processes of chromium in sea water, in: A. Gianguzza, Pelizetti, E., Sammartano, S. (Eds.), In *Chemical processes in marine environments*, Springer, Berlin, pp. pp 281-296.

Poirier, L. A., Clements, J. C., Coffin, M. R., Craig, T., Davidson, J., Miron, G., Davidson, J. D., Hill, J., Comeau, L. A., 2021. Siltation negatively affects settlement and gaping behaviour in eastern oysters. Mar. Environ. Res. 170, 105432.

Pokrovsky, O. S., Schott, J., 2000a. Forsterite surface composition in aqueous solutions: a combined potentiometric, electrokinetic, and spectroscopic approach. Geochim. Cosmochim. Acta. 64 (19), 3299-3312.

Pokrovsky, O. S., Schott, J., 2000b. Kinetics and mechanism of forsterite dissolution at 25 C and pH from 1 to 12. Geochim. Cosmochim. Acta. 64 (19), 3313-3325.

Posthuma, L., van Gils, J., Zijp, M. C., van de Meent, D., de Zwart, D., 2019. Species sensitivity distributions for use in environmental protection, assessment, and management of aquatic ecosystems for 12 386 chemicals. Environ. Toxicol. Chem. 38 (4), 905-917.

Precht, E., Huettel, M., 2003. Advective pore-water exchange driven by surface gravity waves and its ecological implications. Limnol. Oceanogr. 48 (4), 1674-1684.

Pruszak, Z., Zeidler, R. B., 1994. Sediment transport in various time scales, in: B. L. Edge (Eds.), Coastal Engineering 1994, Japan, pp. 2513-2526.

R Core Team, 2022. R: A language and environment for statistical computing. R foundation for statistical computing, Vienna, Austria. URL http://www.R-project.org/.

Raghavan, K., Bernitsas, M., 2011. Experimental investigation of Reynolds number effect on vortex induced vibration of rigid circular cylinder on elastic supports. Ocean Eng. 38 (5-6), 719-731.

Raj, S. M., Jayaprakash, M., 2008. Distribution and enrichment of trace metals in marine sediments of Bay of Bengal, off Ennore, south-east coast of India. Environ. Geol. 56 (1), 207-217.

Ramos-Vázquez, M. A., Armstrong-Altrin, J. S., 2021. Microtextures on quartz and zircon grain surfaces in the Barra del Tordo and Tesoro beaches, northwestern Gulf of Mexico. Arab. J. Geosci. 14 (11), 949.

Rao, A. M., Malkin, S. Y., Montserrat, F., Meysman, F. J., 2014. Alkalinity production in intertidal sands intensified by lugworm bioirrigation. Estuar. Coast. Shelf Sci. 148, 36-47.

Rao, A. M., Polerecky, L., Ionescu, D., Meysman, F. J., De Beer, D., 2012. The influence of pore-water advection, benthic photosynthesis, and respiration on calcium carbonate dynamics in reef sands. Limnol. Oceanogr. 57 (3), 809-825.

Rao, J. V., Kavitha, P., Srikanth, K., Usman, P., Rao, T. G., 2007. Environmental contamination using accumulation of metals in marine sponge, Sigmadocia fibulata inhabiting the coastal waters of Gulf of Mannar, India. Toxicol. Environ. Chem. 89 (3), 487-498.

Ratié, G., Jouvin, D., Garnier, J., Rouxel, O., Miska, S., Guimarães, E., Vieira, L. C., Sivry, Y., Zelano, I., Montarges-Pelletier, E., 2015. Nickel isotope fractionation during tropical weathering of ultramafic rocks. Chem. Geol. 402, 68-76.

Rau, G. H., Willauer, H. D., Ren, Z. J., 2018. The global potential for converting renewable electricity to negative-CO_2-emissions hydrogen. Nat. Clim. Change. 8 (7), 621-625.

Reddy, M. S., Basha, S., Joshi, H., Ramachandraiah, G., 2005. Seasonal distribution and contamination levels of total PHCs, PAHs and heavy metals in coastal waters of the Alang–Sosiya ship scrapping yard, Gulf of Cambay, India. Chemosphere. 61 (11), 1587-1593.

Reddy, M. S., Basha, S., Kumar, V. S., Joshi, H., Ramachandraiah, G., 2004. Distribution, enrichment and accumulation of heavy metals in coastal sediments of Alang–Sosiya ship scrapping yard, India. Mar. Pollut. Bull. 48 (11-12), 1055-1059.

Reish, D. J., 1981. Effects of chromium on the life history of Capitella capitata, in: J. F. Vernberg, Calabrese, A., Thurberg, F. P., Vernberg, W. B. (Eds.), Physiological responses of marine biota to pollutants, Academic Press, London, pp. 199-207.

Rejomon, G., Balachandran, K., Nair, M., Joseph, T., 2008. Trace metal concentrations in marine zooplankton from the western Bay of Bengal. Appl. Ecol. Environ. Res. 6 (1), 107-116.

Rejomon, G., Kumar, P. D., Nair, M., Muraleedharan, K., 2010. Trace metal dynamics in zooplankton from the Bay of Bengal during summer monsoon. Environ. Toxicol. 25 (6), 622-633.

Ren, H., Hu, Y., Liu, J., Zhang, Z., Mou, L., Pan, Y., Zheng, Q., Li, G., Jiao, N., 2021. Response of a Coastal Microbial Community to Olivine Addition in the Muping Marine Ranch, Yantai. Front. Microbiol. 12, 805361.

Renforth, P., 2012. The potential of enhanced weathering in the UK. Int. J. Greenh. Gas Control. 10, 229-243.

Renforth, P., Henderson, G., 2017. Assessing ocean alkalinity for carbon sequestration. Rev. Geophys. 55 (3), 636-674.

Riebesell, U., Basso, D., Geilert, S., Dale, A. W., Kreuzburg, M., Meysman, F., 2023. Mesocosm experiments in ocean alkalinity enhancement research. State of the Planet Discussions. 2023, 1-21.

Rigopoulos, I., Harrison, A. L., Delimitis, A., Ioannou, I., Efstathiou, A. M., Kyratsi, T., Oelkers, E. H., 2018. Carbon sequestration via enhanced weathering of peridotites and basalts in seawater. Appl. Geochem. 91, 197-207.

Rimstidt, J. D., Brantley, S. L., Olsen, A. A., 2012. Systematic review of forsterite dissolution rate data. Geochim. Cosmochim. Acta. 99, 159-178.

Rios-Yunes, D., Tiano, J. C., van Rijswijk, P., De Borger, E., van Oevelen, D., Soetaert, K., 2023. Long-term changes in ecosystem functioning of a coastal bay expected from a shifting balance between intertidal and subtidal habitats. Cont. Shelf Res. 254, 104904.

Ritz, C., Baty, F., Streibig, J. C., Gerhard, D., 2015. Dose-response analysis using R. PLoS One. 10 (12), e0146021.

Rix, R. R., Guedes, R. N. C., Cutler, G. C., 2022. Hormesis dose–response contaminant-induced hormesis in animals. Curr. Opin. Toxicol. 30, 100336.

Rosen, G., Rivera-Duarte, I., Colvin, M., Dolecal, R., Raymundo, L., Earley, P., 2015. Nickel and copper toxicity to embryos of the long-spined sea urchin, Diadema savignyi. Bull Environ Contam Toxicol. 95, 6-11.

Rubio, B., Nombela, M., Vilas, F., 2000. Geochemistry of major and trace elements in sediments of the Ria de Vigo (NW Spain): an assessment of metal pollution. Mar. Pollut. Bull. 40 (11), 968-980.

Rueda, O., Mogollón, J., Tukker, A., Scherer, L., 2021. Negative-emissions technology portfolios to meet the 1.5° C target. Glob Environ Change. 67, 102238.

Saengsupavanich, C., Pranzini, E., Ariffin, E. H., Yun, L. S., 2023. Jeopardizing the environment with beach nourishment. Sci. Total Environ. 868, 161485.

Saha, R., Nandi, R., Saha, B., 2011. Sources and toxicity of hexavalent chromium. J. Coord. Chem. 64 (10), 1782-1806.

Santore, R. C., Ryan, A. C., 2015. Development and application of a multimetal multibiotic ligand model for assessing aquatic toxicity of metal mixtures. Environ. Toxicol. Chem. 34 (4), 777-787.

Santos, I. R., Eyre, B. D., Huettel, M., 2012. The driving forces of porewater and groundwater flow in permeable coastal sediments: A review. Estuar. Coast. Shelf Sci. 98, 1-15.

Santos, R. M., Van Audenaerde, A., Chiang, Y. W., Iacobescu, R. I., Knops, P., Van Gerven, T., 2015. Nickel extraction from olivine: effect of carbonation pre-treatment. Metals. 5 (3), 1620-1644.

Sarmiento, J. L., 2013. Ocean biogeochemical dynamics, Princeton University Press, Princeton.

Sarmiento, J. L., Gruber, N., Brzezinski, M., Dunne, J., 2004. High-latitude controls of thermocline nutrients and low latitude biological productivity. Nature. 427 (6969), 56-60.

Scherer, C., Brennholt, N., Reifferscheid, G., Wagner, M., 2017. Feeding type and development drive the ingestion of microplastics by freshwater invertebrates. Sci. Rep. 7 (1), 17006.

Schielzeth, H., Dingemanse, N. J., Nakagawa, S., Westneat, D. F., Allegue, H., Teplitsky, C., Réale, D., Dochtermann, N. A., Garamszegi, L. Z., Araya-Ajoy, Y. G., 2020. Robustness of linear mixed-effects models to violations of distributional assumptions. Methods Ecol. Evol. 11 (9), 1141-1152.

Schlacher, T. A., Noriega, R., Jones, A., Dye, T., 2012. The effects of beach nourishment on benthic invertebrates in eastern Australia: impacts and variable recovery. Sci. Total Environ. 435, 411-417.

Schlekat, C. E., Garman, E. R., Vangheluwe, M. L., Burton Jr, G. A., 2016. Development of a bioavailability-based risk assessment approach for nickel in freshwater sediments. Integr. Environ. Assess. Manag. 12 (4), 735-746.

Schott, J., Berner, R. A., 1985. Dissolution mechanisms of pyroxenes and olivines during weathering. The chemistry of weathering. 35-53.

Schuiling, R., De Boer, P., 2010. Coastal spreading of olivine to control atmospheric CO2 concentrations: A critical analysis of viability. Comment: Nature and laboratory models are different. Int. J. Greenh. Gas Control. 4 (5), 855.

Schuiling, R. D., De Boer, P. L., 2011. Rolling stones; fast weathering of olivine in shallow seas for cost-effective CO2 capture and mitigation of global warming and ocean acidification. Earth Syst. Dyn. Discuss. 2, 551-568.

Schuiling, R. D., Krijgsman, P., 2006. Enhanced weathering: an effective and cheap tool to sequester CO 2. Clim. Change. 74 (1), 349-354.

Schulz, K. G., Bach, L. T., Dickson, A. G., 2023. Seawater carbonate system considerations for ocean alkalinity enhancement research. State of the Planet Discussions. 2023, 1-24.

Scott, A., Oze, C., Shah, V., Yang, N., Shanks, B., Cheeseman, C., Marshall, A., Watson, M., 2021. Transformation of abundant magnesium silicate minerals for enhanced CO 2 sequestration. Commun. Earth Environ. 2 (1), 1-6.

Serrano, R., Gras, L., Giménez-Casalduero, F., del-Pilar-Ruso, Y., Grindlay, G., Mora, J., 2019. The role of Cymodocea nodosa on the dynamics of trace elements in different marine environmental compartments at the Mar Menor Lagoon (Spain). Mar. Pollut. Bull. 141, 52-60.

Serreze, M. C., 2010. Understanding recent climate change. Conserv. Biol. 24 (1), 10-17.

Seuront, L., Duponchel, A.-C., Chapperon, C., 2007. Heavy-tailed distributions in the intermittent motion behaviour of the intertidal gastropod Littorina littorea. Phys. A: Stat. Mech. Appl. 385 (2), 573-582.

Seuront, L., Ng, T. P., Lathlean, J. A., 2018. A review of the thermal biology and ecology of molluscs, and of the use of infrared thermography in molluscan research. J. Molluscan Stud. 84 (3), 203-232.

Seyama, H., Soma, M., Tanaka, A., 1996. Surface characterization of acid-leached olivines by X-ray photoelectron spectroscopy. Chem. Geol. 129 (3-4), 209-216.

SEYER, J.-O., 1992. Resolution and sensitivity in the eye of the winkle Littorina littorea. J. Exp. Biol. 170 (1), 57-69.

Shahzad, B., Tanveer, M., Rehman, A., Cheema, S. A., Fahad, S., Rehman, S., Sharma, A., 2018. Nickel; whether toxic or essential for plants and environment-A review. Plant Physiol. Biochem. 132, 641-651.

Shanmugam, G., 2020. Mass transport, gravity flows, and bottom currents: Downslope and alongslope processes and deposits, Elsevier, 608.

Sherman, S., Chen, W., Blewett, T., Smith, S., Middleton, E., Garman, E., Schlekat, C., McGeer, J., 2021. Complexation reduces nickel toxicity to purple sea urchin embryos (Strongylocentrotus purpuratus), a test of biotic ligand principles in seawater. Ecotoxicol. Environ. Saf. 216, 112156.

Shum, K., 1992. Wave-induced advective transport below a rippled water-sediment interface. Journal of Geophysical Research: Oceans. 97 (C1), 789-808.

Shur, M. Y., Perchuk, A., 2015. Omphacite paradox in mantle peridotites. Russ. Geol. Geophys. 56 (11), 1568-1577.

Sibley, P. K., Benoit, D. A., Ankley, G. T., 1997. The significance of growth in Chironomus tentans sediment toxicity tests: relationship to reproduction and demographic endpoints. Environ. Toxicol. Chem. 16 (2), 336-345.

Silinski, A., Heuner, M., Troch, P., Puijalon, S., Bouma, T. J., Schoelynck, J., Schröder, U., Fuchs, E., Meire, P., Temmerman, S., 2016. Effects of contrasting wave conditions on scour and drag on pioneer tidal marsh plants. Geomo. 255, 49-62.

Simpson, S., Campana, O., Ho, K. (2016). Sediment toxicity testing. In *Marine ecotoxicology* (pp. 199-237): Elsevier.

Simpson, S. L., Batley, G. E., 2007. Predicting metal toxicity in sediments: a critique of current approaches. Integr. Environ. Assess. Manag. 3 (1), 18-31.

Simpson, S. L., Batley, G. E., 2016. Sediment quality assessment: a practical guide, 2nd, CSIRO Publishing, Clayton South.

Singh, V., Singh, N., Verma, M., Kamal, R., Tiwari, R., Sanjay Chivate, M., Rai, S. N., Kumar, A., Singh, A., Singh, M. P., 2022. Hexavalent-chromium-induced oxidative stress and the protective role of antioxidants against cellular toxicity. Antioxidants. 11 (12), 2375.

Sissmann, O., Daval, D., Brunet, F., Guyot, F., Verlaguet, A., Pinquier, Y., Findling, N., Martinez, I., 2013. The deleterious effect of secondary phases on olivine carbonation yield: Insight from time-resolved aqueous-fluid sampling and FIB-TEM characterization. Chem. Geol. 357, 186-202.

Skjærseth, J. B., 2021. Towards a European Green Deal: The evolution of EU climate and energy policy mixes. INT ENVIRON AGREEM-P. 21 (1), 25-41.

Smetacek, V., Klaas, C., Strass, V. H., Assmy, P., Montresor, M., Cisewski, B., Savoye, N., Webb, A., d'Ovidio, F., Arrieta, J. M., 2012. Deep carbon export from a Southern Ocean iron-fertilized diatom bloom. Nature. 487 (7407), 313-319.

Smith, P., Davis, S. J., Creutzig, F., Fuss, S., Minx, J., Gabrielle, B., Kato, E., Jackson, R. B., Cowie, A., Kriegler, E., 2016. Biophysical and economic limits to negative CO2 emissions. Nat. Clim. Change. 6 (1), 42-50.

Solan, M., Ward, E. R., White, E. L., Hibberd, E. E., Cassidy, C., Schuster, J. M., Hale, R., Godbold, J. A., 2019. Worldwide measurements of bioturbation intensity, ventilation rate, and the mixing depth of marine sediments. Sci. Data. 6 (1), 1-6.

Son, S., Newton, A. G., Jo, K.-n., Lee, J.-Y., Kwon, K. D., 2019. Manganese speciation in Mn-rich CaCO3: A density functional theory study. Geochim. Cosmochim. Acta. 248, 231-241.

Søndergaard, J., 2013. Dispersion and bioaccumulation of elements from an open-pit olivine mine in Southwest Greenland assessed using lichens, seaweeds, mussels and fish. Environ. Monit. Assess. 185, 7025-7035.

Sorgog, K., Kamo, M., 2019. Quantifying the precision of ecological risk: Conventional assessment factor method vs. species sensitivity distribution method. Ecotoxicol. Environ. Saf. 183, 109494.

Spencer, K. L., 2002. Spatial variability of metals in the inter-tidal sediments of the Medway Estuary, Kent, UK. Mar. Pollut. Bull. 44 (9), 933-944.

Speybroeck, J., Bonte, D., Courtens, W., Gheskiere, T., Grootaert, P., Maelfait, J. P., Mathys, M., Provoost, S., Sabbe, K., Stienen, E. W., 2006. Beach nourishment: an ecologically sound coastal defence alternative? A review. Aquat. Conserv.: Mar. Freshw. Ecosyst. 16 (4), 419-435.

Srichandan, S., Panigrahy, R., Baliarsingh, S., Pati, P., Sahu, B. K., Sahu, K., 2016. Distribution of trace metals in surface seawater and zooplankton of the Bay of Bengal, off Rushikulya estuary, East Coast of India. Mar. Pollut. Bull. 111 (1-2), 468-475.

Srikanth, K., Ahmad, I., Rao, J. V., 2014. Seasonal trend of potential toxic elements in seawater and sediments from Tuticorin coast. Water, Air, Soil Pollut. 225 (8), 2069.

Stauber, J., Golding, L., Peters, A., Merrington, G., Adams, M., Binet, M., Batley, G., Gissi, F., McKnight, K., Garman, E., 2021. Application of Bioavailability Models to Derive Chronic Guideline Values for Nickel in Freshwaters of Australia and New Zealand. Environ. Toxicol. Chem. 40 (1), 100-112.

Steenkamp, R. C., Webb, R. M., 2023. Legal Considerations relevant to the Research of Ocean Alkalinity Enhancement. State Planet Discuss. 2023, 1-30.

Steffy, D. A., Nichols, A. C., Morgan, L. J., Gibbs, R., 2013. Evidence that the Deepwater Horizon oil spill caused a change in the nickel, chromium, and lead average seasonal concentrations occurring in sea bottom sediment collected from the eastern Gulf of Mexico continental shelf between the years 2009 and 2011. Water, Air, Soil Pollut. 224 (11), 1-11.

Straub, S., Hirsch, P. E., Burkhardt-Holm, P., 2017. Biodegradable and petroleum-based microplastics do not differ in their ingestion and excretion but in their biological effects in a freshwater invertebrate Gammarus fossarum. Int. J. Environ. Res. Public Health. 14 (7), 774.

Strefler, J., Amann, T., Bauer, N., Kriegler, E., Hartmann, J., 2018. Potential and costs of carbon dioxide removal by enhanced weathering of rocks. Environ. Res. Lett. 13 (3), 034010.

Struyf, E., Smis, A., Van Damme, S., Meire, P., Conley, D. J., 2009. The global biogeochemical silicon cycle. Silicon. 1, 207-213.

Subhas, A. V., Marx, L., Reynolds, S., Flohr, A., Mawji, E. W., Brown, P. J., Cael, B., 2022. Microbial ecosystem responses to alkalinity enhancement in the North Atlantic Subtropical Gyre. Front. clim. 4, 784997.

Sun, M., Wu, W., Ji, X., Wang, X., Qu, S., 2019. Silicate weathering rate and its controlling factors: A study from small granitic watersheds in the Jiuhua Mountains. Chem. Geol. 504, 253-266.

Sun, W., Jayaraman, S., Chen, W., Persson, K. A., Ceder, G., 2015. Nucleation of metastable aragonite $CaCO_3$ in seawater. Proc. Natl. Acad. Sci. U.S.A. 112 (11), 3199-3204.

Szczybelski, A. S., Kampen, T., Vromans, J., Peeters, E. T., van den Heuvel-Greve, M. J., van den Brink, N. W., Koelmans, A. A., 2018. Avoidance tests as a tool to detect sublethal effects of oil-impacted sediments. Environ. Toxicol. Chem. 37 (6), 1757-1766.

Szefer, P., Glasby, G., Stüben, D., Kusak, A., Geldon, J., Berner, Z., Neumann, T., Warzocha, J., 1999. Distribution of selected heavy metals and rare earth elements in surficial sediments from the Polish sector of the Vistula Lagoon. Chemosphere. 39 (15), 2785-2798.

Taylor, L. L., Quirk, J., Thorley, R. M., Kharecha, P. A., Hansen, J., Ridgwell, A., Lomas, M. R., Banwart, S. A., Beerling, D. J., 2016. Enhanced weathering strategies for stabilizing climate and averting ocean acidification. Nat. Clim. Change. 6 (4), 402-406.

Tebo, B. M., Bargar, J. R., Clement, B. G., Dick, G. J., Murray, K. J., Parker, D., Verity, R., Webb, S. M., 2004. Biogenic manganese oxides: properties and mechanisms of formation. Annu. Rev. Earth Planet. Sci. 32, 287-328.

Thompson, J. F., Barnes, S. J., Duke, J. M., 1984. The distribution of nickel and iron between olivine and magmatic sulfides in some natural assemblages. Can. Mineral. 22 (1), 55-66.

Todd, V. L., Todd, I. B., Gardiner, J. C., Morrin, E. C., MacPherson, N. A., DiMarzio, N. A., Thomsen, F., 2015. A review of impacts of marine dredging activities on marine mammals. ICES J. Mar. Sci. 72 (2), 328-340.

Toffoli, A., Bitner-Gregersen, E. M., 2017. Types of ocean surface waves, wave classification. Encyclopedia of maritime and offshore engineering. 1-8.

Tréguer, P., Bowler, C., Moriceau, B., Dutkiewicz, S., Gehlen, M., Aumont, O., Bittner, L., Dugdale, R., Finkel, Z., Iudicone, D., 2018. Influence of diatom diversity on the ocean biological carbon pump. Nat. Geosci. 11 (1), 27-37.

Trevizani, T. H., Figueira, R. C. L., Ribeiro, A. P., Theophilo, C. Y. S., Majer, A. P., Petti, M. A. V., Corbisier, T. N., Montone, R. C., 2016. Bioaccumulation of heavy metals in marine organisms and sediments from Admiralty Bay, King George Island, Antarctica. Mar. Pollut. Bull. 106 (1-2), 366-371.

Tuckett, R. (2019). Greenhouse gases. In *Encyclopedia of Analytical Science* (pp. 362-372): Elsevier.

Tyle, H., Scott-Fordsmand, J., 2008. European Union Risk Assessment Report: Nickel and nickel compounds. https://echa.europa.eu/documents/10162/cefda8bc-2952-4c11-885f-342aacf769b3 (accessed 2023-08-08).

Umarani, R., Kumaraguru, A., Nagarani, N., 2012. Investigation of acute toxicity of heavy metals in Artemia salina acclimated to different salinity. Toxicol. Environ. Chem. 94 (8), 1547-1556.

Unceta, N., Séby, F., Malherbe, J., Donard, O. F. X., 2010. Chromium speciation in solid matrices and regulation: a review. Anal. Bioanal. Chem. 397, 1097-1111.

UNFCC. (2015). Paris agreement. Paper presented at the Report of the Conference of the Parties to the United Nations Framework Convention on Climate Change (21st Session, 2015: Paris).

Urien, N., Farfarana, A., Uher, E., Fechner, L., Chaumot, A., Geffard, O., Lebrun, J., 2017. Comparison in waterborne Cu, Ni and Pb bioaccumulation kinetics between different gammarid species and populations: Natural variability and influence of metal exposure history. Aquat. Toxicol. 193, 245-255.

Urrutia, C., Rudolph, A., Lermanda, M. P., Ahumada, R., 2008. Assessment of EDTA in Chromium (III–VI) Toxicity on Marine Intertidal Crab (Petrolisthes laevigatus). Bull Environ Contam Toxicol. 80 (6), 526.

USEPA, 1995. National Recommended Water Quality Criteria - Aquatic Life Criteria Table. https://www.epa.gov/wqc/national-recommended-water-quality-criteria-aquatic-life-criteria-table (accessed 2023-08-08).

Väänänen, K., Leppänen, M. T., Chen, X., Akkanen, J., 2018. Metal bioavailability in ecological risk assessment of freshwater ecosystems: from science to environmental management. Ecotoxicol. Environ. Saf. 147, 430-446.

Vader, W., Tandberg, A. H. S., 2019. Gammarid amphipods (Crustacea) in Norway, with a key to the species. Fauna Norv. 39, 12-25.

Van Alsenoy, V., Bernard, P., Van Grieken, R., 1993. Elemental concentrations and heavy metal pollution in sediments and suspended matter from the Belgian North Sea and the Scheldt estuary. Sci. Total Environ. 133 (1-2), 153-181.

Van Cappellen, P., Wang, Y., 1995. Metal cycling in surface sediments: modeling the interplay of transport and reaction, in: H. E. Allen (Eds.), In *Metal contaminated aquatic sediments*, Ann Arbor Press, Inc., Michigan, pp. pp 21-64.

van de Velde, S., Meysman, F. J., 2016. The influence of bioturbation on iron and sulphur cycling in marine sediments: a model analysis. Aquat. Geochem. 22 (5), 469-504.

Van den Berg, C., Nimmo, M., 1987. Determination of interactions of nickel with dissolved organic material in seawater using cathodic stripping voltammetry. Sci. Total Environ. 60, 185-195.

van den Berg, C. M., Boussemart, M., Yokoi, K., Prartono, T., Campos, M. L. A., 1994. Speciation of aluminium, chromium and titanium in the NW Mediterranean. Mar. Chem. 45 (4), 267-282.

Van Ginneken, M., De Jonge, M., Bervoets, L., Blust, R., 2015. Uptake and toxicity of Cd, Cu and Pb mixtures in the isopod Asellus aquaticus from waterborne exposure. Sci. Total Environ. 537, 170-179.

Varadachari, C., Barman, A. K., Ghosh, K., 1994. Weathering of silicate minerals by organic acids II. Nature of residual products. Geoderma. 61 (3-4), 251-268.

Veerasingam, S., Venkatachalapathy, R., Ramkumar, T., 2014. Distribution of clay minerals in marine sediments off Chennai, Bay of Bengal, India: Indicators of sediment sources and transport processes. Int. J. Sediment Res. 29 (1), 11-23.

Verriopoulos, G., Dimas, S., 1988. Combined toxicity of copper, cadmium, zinc, lead, nickel, and chrome to the copepod Tisbe holothuriae. Bull Environ Contam Toxicol. 41 (3), 378-384.

Vithanage, M., Kumarathilaka, P., Oze, C., Karunatilake, S., Seneviratne, M., Hseu, Z.-Y., Gunarathne, V., Dassanayake, M., Ok, Y. S., Rinklebe, J., 2019. Occurrence and cycling of trace elements in ultramafic soils and their impacts on human health: A critical review. Environ. Int. 131, 104974.

Wang, F., Giammar, D. E., 2013. Forsterite dissolution in saline water at elevated temperature and high CO2 pressure. Environ. Sci. Technol. 47 (1), 168-173.

Wang, J. F., Bashir, M., Engelsberg, B. N., Witmer, C., Rozmiarek, H., Billings, P. C., 1997a. High mobility group proteins 1 and 2 recognize chromium-damaged DNA. Carcinogenesis. 18 (2), 371-375.

Wang, M., Wang, G., 2010. Oxidative damage effects in the copepod Tigriopus japonicus Mori experimentally exposed to nickel. Ecotoxicology. 19, 273-284.

Wang, R.-M., Archer, C., Bowie, A. R., Vance, D., 2019. Zinc and nickel isotopes in seawater from the Indian Sector of the Southern Ocean: the impact of natural iron fertilization versus Southern Ocean hydrography and biogeochemistry. Chem. Geol. 511, 452-464.

Wang, W.-X., Griscom, S. B., Fisher, N. S., 1997b. Bioavailability of Cr (III) and Cr (VI) to marine mussels from solute and particulate pathways. Environ. Sci. Technol. 31 (2), 603-611.

Wang, X., Wang, J., Zhang, J., 2012. Comparisons of three methods for organic and inorganic carbon in calcareous soils of northwestern China. PLoS One. 7 (8), e44334.

Wang, X. C., Feng, H., Ma, H. Q., 2007. Assessment of metal contamination in surface sediments of Jiaozhou Bay, Qingdao, China. CLEAN–Soil, Air, Water. 35 (1), 62-70.

Wang, Z., Kwok, K. W., Lui, G. C., Zhou, G.-J., Lee, J.-S., Lam, M. H., Leung, K. M., 2014. The difference between temperate and tropical saltwater species' acute sensitivity to chemicals is relatively small. Chemosphere. 105, 31-43.

Wang, Z., Yeung, K. W., Zhou, G.-J., Yung, M. M., Schlekat, C. E., Garman, E. R., Gissi, F., Stauber, J. L., Middleton, E. T., Wang, Y. Y. L., 2020. Acute and chronic toxicity of nickel on freshwater and marine tropical aquatic organisms. Ecotoxicol. Environ. Saf. 206, 111373.

Wanninkhof, R., 2014. Relationship between wind speed and gas exchange over the ocean revisited. Limnol Oceanogr-Methods. 12 (6), 351-362.

Ward, E. J., MacDonald, B. A., 1996. Pre-ingestive feeding behaviors of two sub-tropical bivalves (Pinctada imbricata and Arca zebra): responses to an acute increase in suspended sediment concentration. Bull. Mar. Sci. 59 (2), 417-432.

Ward, S. L., Neill, S. P., Van Landeghem, K. J., Scourse, J. D., 2015. Classifying seabed sediment type using simulated tidal-induced bed shear stress. Mar. Geol. 367, 94-104.

Warne, M. S. J., Batley, G., Braga, O., Chapman, J., Fox, D., Hickey, C., Stauber, J., Van Dam, R., 2014. Revisions to the derivation of the Australian and New Zealand guidelines for toxicants in fresh and marine waters. Environ. Sci. Pollut. Res. 21, 51-60.

Wheeler, J., Grist, E., Leung, K., Morritt, D., Crane, M., 2002. Species sensitivity distributions: data and model choice. Mar. Pollut. Bull. 45 (1-12), 192-202.

Whitmarsh, L., Poortinga, W., Capstick, S., 2021. Behaviour change to address climate change. Curr Opin Psychol. 42, 76-81.

Willoughby, L., Earnshaw, R., 1982. Gut passage times in Gammarus pulex (Crustacea, Amphipoda) and aspects of summer feeding in a stony stream. Hydrobiologia. 97, 105-117.

WMO, G., 1979. Proceedings of the World Climate Conference; a conference of experts on climate and mankind Geneva, 12-23 Feb 1979.

Wogelius, R. A., Walther, J. V., 1992. Olivine dissolution kinetics at near-surface conditions. Chem. Geol. 97 (1-2), 101-112.

Wong, Y., Tam, N., Lau, P., Xue, X., 1995. The toxicity of marine sediments in Victoria Harbour, Hong Kong. Mar. Pollut. Bull. 31 (4-12), 464-470.

Xie, T., Zhao, L., Wu, Y., 2023. Peridotite dissolution in the presence of green microalgae: Implications for a geoengineering strategy of CO2 sequestration. J Asian Earth Sci. 241, 105486.

Xin, X., Faucher, G., Riebesell, U., 2023. Phytoplankton Response to Increased Nickel in the Context of Ocean Alkalinity Enhancement. Biogeosci. Disc. 2023, 1-15.

Yamagishi, T., Katsumata, M., Yamaguchi, H., Shimura, Y., Kawachi, M., Koshikawa, H., Horie, Y., Tatarazako, N., 2016. Rapid ecotoxicological bioassay using delayed fluorescence in the marine cyanobacterium Cyanobium sp.(NIES-981). Ecotoxicology. 25 (10), 1751-1758.

Yavuz, Ö., Altunkaynak, Y., Güzel, F., 2003. Removal of copper, nickel, cobalt and manganese from aqueous solution by kaolinite. Water Res. 37 (4), 948-952.

Yousefi, S. R., Masjedi-Arani, M., Morassaei, M. S., Salavati-Niasari, M., Moayedi, H., 2019. Hydrothermal synthesis of DyMn2O5/Ba3Mn2O8 nanocomposite as a potential hydrogen storage material. Int. J. Hydrog. Energy. 44 (43), 24005-24016.

Yu, F., Hunt, A. G., 2017. Damkohler number input to transport-limited chemical weathering calculations. ACS Earth Space Chem. 1 (1), 30-38.

Yu, K.-C., Tsai, L.-J., Chen, S.-H., Ho, S.-T., 2001. Correlation analyses on binding behavior of heavy metals with sediment matrices. Water Res. 35 (10), 2417-2428.

Yunus, K., Zuraidah, M., John, A., 2020. A review on the accumulation of heavy metals in coastal sediment of Peninsular Malaysia. Ecofeminism and Climate Change. 1 (1), 21-35.

Yusuf, M., Fariduddin, Q., Hayat, S., Ahmad, A., 2011. Nickel: an overview of uptake, essentiality and toxicity in plants. Bull Environ Contam Toxicol. 86, 1-17.

Zeebe, R. E., Wolf-Gladrow, D., 2001. CO2 in seawater: equilibrium, kinetics, isotopes, Gulf Professional Publishing,

Zhang, C., Yu, Z.-g., Zeng, G.-m., Jiang, M., Yang, Z.-z., Cui, F., Zhu, M.-y., Shen, L.-q., Hu, L., 2014. Effects of sediment geochemical properties on heavy metal bioavailability. Environ. Int. 73, 270-281.

Zhang, X., Li, J., Wei, D., Li, B., Ma, Y., 2018. The solid-solution distribution of copper added to soils: influencing factors and models. J Soils Sediments. 18, 2960-2969.

Zhong, S., Mucci, A., 1989. Calcite and aragonite precipitation from seawater solutions of various salinities: Precipitation rates and overgrowth compositions. Chem. Geol. 78 (3-4), 283-299.

Curriculum vitae

Personal information

Name	Gunter Flipkens
Mobile phone	+32 496 40 61 66
E-mail	gunter.flipkens@gmail.com
Date and place of birth	07/04/1996, 3960 Bree

Education

<u>University of Antwerp</u>

2019 - 2024	PhD researcher at the ECOSPHERE group, University of Antwerp: *"Coastal enhanced olivine weathering for climate change mitigation: investigating the CO_2 sequestration potential and ecotoxicological risks".*
2017 - 2019	Master of Science: Biology: Ecology and Environment (Great Distinction) Thesis: *"Effects of binary mixtures (cadmium-copper) on metal accumulation, ionoregulation and oxidative stress in common carp (Cyprinus carpio L.)"*

<u>Hasselt University</u>

2014 - 2017	Bachelor of Science: Biology Thesis: *"Onderzoek naar het broedgedrag bij nachtzwaluwen (Caprimulgus europaeus)".*

Publications

Castaldo, G., **Flipkens, G**., Pillet, M., Town, R. M., Bervoets, L., Blust, R., & De Boeck, G. (**2020**). Antagonistic bioaccumulation of waterborne Cu (II) and Cd (II) in common carp

(Cyprinus carpio) and effects on ion-homeostasis and defensive mechanisms. Aquatic Toxicology, 226, 105561**.**

Flipkens, G., Blust, R., & Town, R. M. (**2021**). Deriving nickel (Ni(II)) and chromium (Cr(III)) based environmentally safe olivine guidelines for coastal enhanced silicate weathering. Environmental Science & Technology, 55(18), 12362-12371.

Flipkens, G., Horoba, K., Bostyn, K., Geerts, L. J., Town, R. M., & Blust, R. (**2023**). Acute bioaccumulation and chronic toxicity of olivine in the marine amphipod Gammarus locusta. Aquatic Toxicology, 262, 106662.

Flipkens, G., Fuhr, M., Fiers, G., Meysman, F. J., Town, R. M., & Blust, R. (**2023**). Enhanced olivine dissolution in seawater through continuous grain collisions. Geochimica et Cosmochimica Acta, 359, 84-99.

Flipkens, G., Dujardin, V., Salden, J., T'Jollyn, K., Town, R.M., & Blust, R. (**2024**). Olivine avoidance behaviour by marine gastropods (*Littorina littorea* L.) and amphipods (*Gammarus locusta* L.) within the context of ocean alkalinity enhancement. Ecotoxicology and Environmental Safety, 270, 115840.

Flipkens, G., Fiers, G., Winardhi, C. W., Meysman, F.J.R., Blust, R., & Town, R.M. (**in prep.**). Effects of current on olivine dissolution kinetics in permeable marine sediment: a flume experiment.

Presentations at conferences

Flipkens, G., Town, R. M., & Blust, R. (2019). Negative emissions through enhanced mineral weathering in the coastal zone: ecosystem impacts. Biology Research Day, Antwerp, Belgium. **Poster presentation**.

Flipkens, G., Town, R. M., & Blust, R. (2020). Nickel and chromium marine ecotoxicity: relevant for risk assessment of enhanced olivine weathering in coastal zones. SETAC Europe 30th annual meeting, online. **Poster presentation**.

Flipkens, G., Town, R. M., & Blust, R. (2021). Enhanced olivine weathering through physical stress: Implications for CO_2 sequestration and possible ecosystem impacts. SETAC Europe 31st annual meeting, online. **Oral presentation**.

Flipkens, G., Town, R. M., & Blust, R. (2022). Deriving nickel (Ni(II)) and chromium (Cr(III)) based environmentally safe olivine guidelines for coastal enhanced silicate weathering. Enhanced Weathering Conference 2022, Amsterdam, The Netherlands. **Invited speaker, oral presentation**.

Flipkens, G., Blust, R., & Town, R. M. (2022). Deriving nickel (Ni(II)) and chromium (Cr(III)) based environmentally safe olivine guidelines for coastal enhanced silicate weathering. SETAC Europe 32nd annual meeting, Copenhagen, Denmark. **Oral presentation**.

Flipkens, G., Town, R. M., & Blust, R. (2022). Enhanced olivine weathering in seawater via continuous grain tumbling: implications for CO_2 capture and possible ecosystem impacts. The 2nd International Conference on Negative CO_2 Emissions, Gothenburg, Sweden. **Poster presentation**.

Flipkens, G., Blust, R., & Town, R. M. (2022). Deriving nickel (Ni(II)) and chromium (Cr(III)) based environmentally safe olivine guidelines for coastal enhanced silicate weathering. Interfaces Against Pollution 2022: Chemical and Biological Perspectives, Antwerp, Belgium. **Oral presentation**.

Flipkens, G., Fuhr, M., Fiers, G., Meysman, F. J. R., Town, R. M., & Blust, R. (2023). Enhanced olivine weathering in seawater via continuous grain tumbling: implications for

CO_2 capture and possible ecosystem impacts. Faculty of Science Research Day, Antwerp, Belgium. **Poster presentation**.

Flipkens, G., Horoba, K., Bostyn, K., Geerts, L., Town, R. M., & Blust, R. (2023). Acute and chronic effects of olivine exposure in the marine amphipod *Gammarus locusta*. SETAC Europe 33rd annual meeting, Dublin, Ireland. **Oral presentation**.

Flipkens, G., Horoba, K., Bostyn, K., Geerts, L., Town, R. M., & Blust, R. (2023). Acute and chronic effects of olivine exposure in the marine amphipod *Gammarus locusta*. Double Nature Summit: Rock Weathering Day, Delft, The Netherlands. **Oral presentation**.

Awards and grants

Award(s)

Best presentation: Olaf Schuiling award by the Climate Cleanup Foundation at the Enhanced weathering conference 2022. Awarded to the most promising innovation in the field of enhanced olivine weathering.

Grant(s)

Training course and travel grant (2020): Society of environmental toxicology and chemistry (SETAC) for the SETAC Europe 30th Annual Meeting, online.

Free meeting registration grant (2022): Society of environmental toxicology and chemistry (SETAC) for attending SETAC Europe 32nd annual meeting in Copenhagen, Denmark.